Experimental thermodynamic measurements of biofuel-related associating compounds and modeling using the PC-SAFT equation of state

Chien-Bin Soo

ParisTech
INSTITUT DES SCIENCES ET TECHNOLOGIES
PARIS INSTITUTE OF TECHNOLOGY

MINES ParisTech

Ecole doctorale n°432 : Sciences des Métiers de l'Ingénieur

Doctorat ParisTech

T H È S E

pour obtenir le grade de docteur délivré par

l'École Nationale Supérieure des Mines de Paris

Spécialité« Génie des Procédés »

présentée et soutenue publiquement par

Chien-Bin SOO

le 15 juin 2011

Mesures Expérimentales "Thermodynamiques" de Composés Associatifs dans les Mélanges de Biocarburants et Modélisation avec l'Équation d'État PC-SAFT

Experimental Thermodynamic Measurements of Biofuel-related Associating Compounds and Modeling using the PC-SAFT Equation of State

Directeur de thèse : **Dominique RICHON**
Co-directeur de thèse : **Deresh RAMJUGERNATH**

Jury

M. George JACKSON, Professor, Department of Chemical Engineering, Imperial College London	*Président*
M. Theodoor W. DE LOOS, Associate Professor, Process & Energy Laboratory, TU Delft	*Rapporteur*
M. Joachim GROß, Professor, ITT, University of Stuttgart	*Rapporteur*
M. Jean-Charles DE HEMPTINNE, Professeur IFP School, IFP Energies nouvelles	*Examinateur*
M. Kai FISCHER, Senior Research Thermodynamicist, Royal Dutch Shell Company	*Examinateur*
M. Deresh RAMJUGERNATH, Professor, School of Chemical Engineering, UKZN	*Examinateur*
M. Christophe COQUELET, Maître Assistant, CEP Fontainebleau/TEP, MINES ParisTech	*Examinateur*
M. Dominique RICHON, Directeur de recherche, CEP Fontainebleau/TEP, MINES ParisTech	*Examinateur*

T H È S E

MINES ParisTech
Centre Énergétique et Procédés - Laboratoire CEP/TEP
35, rue Saint Honoré, 77305 Fontainebleau cedex, France

ParisTech
INSTITUT DES SCIENCES ET TECHNOLOGIES
PARIS INSTITUTE OF TECHNOLOGY

MINES ParisTech

Ecole doctorale n°432 : Sciences des Métiers de l'Ingénieur

Doctorat ParisTech

T H È S E

pour obtenir le grade de docteur délivré par

l'École Nationale Supérieure des Mines de Paris

Spécialité« Génie des Procédés »

présentée et soutenue publiquement par

Chien-Bin SOO

le 15 juin 2011

Mesures Expérimentales "Thermodynamiques" de Composés Associatifs dans les Mélanges de Biocarburants et Modélisation avec l'Équation d'État PC-SAFT

Experimental Thermodynamic Measurements of Biofuel-related Associating Compounds and Modeling using the PC-SAFT Equation of State

Directeur de thèse : **Dominique RICHON**
Co-directeur de thèse : **Deresh RAMJUGERNATH**

Jury

M. George JACKSON, Professor, Department of Chemical Engineering, Imperial College London	*Président*
M. Theodoor W. DE LOOS, Associate Professor, Process & Energy Laboratory, TU Delft	*Rapporteur*
M. Joachim GROß, Professor, ITT, University of Stuttgart	*Rapporteur*
M. Jean-Charles DE HEMPTINNE, Professeur IFP School, IFP Energies nouvelles	*Examinateur*
M. Kai FISCHER, Senior Research Thermodynamicist, Royal Dutch Shell Company	*Examinateur*
M. Deresh RAMJUGERNATH, Professor, School of Chemical Engineering, UKZN	*Examinateur*
M. Christophe COQUELET, Maître Assistant, CEP Fontainebleau/TEP, MINES ParisTech	*Examinateur*
M. Dominique RICHON, Directeur de recherche, CEP Fontainebleau/TEP, MINES ParisTech	*Examinateur*

T H È S E

MINES ParisTech
Centre Énergétique et Procédés - Laboratoire CEP/TEP
35, rue Saint Honoré, 77305 Fontainebleau cedex, France

獻給　我的母親

Acknowledgements

This thesis is a gift from my families, friends and colleagues, who gave me the love and support to see this work through to the very end.

I would first like to thank my thesis director, Prof. Dominique Richon, for accepting me into the prestigious establishment that is TEP, and my co-director, Prof. Deresh Ramjugernath, for promoting my studies in Europe. I would like to mention the irreplaceable role of my *maître assistant*, Dr. Christophe Coquelet, who dedicated his time to supervising my work and my interests. It has been a pleasure to work with the lab staff and personnel of TEP, and I thank them for the friendship, the ambiance, and the energy that they have brought to my daily life at Fontainebleau.

During my studies, I had the privilege of working abroad at different academic establishments. I would like to thank Prof. Joachim Gross of the University of Stuttgart, without whom the modeling work of this study would probably remain incomplete. I am indebted to his generosity for prolonging my sabbatical at the ITT institute. Dr. Patrice Paricaud of ENSTA, who unselfishly shared his modeling experiences, and to whom I had great pleasure in collaborating with. Dr. Jean-Yves Coxam and Dr. Karine Ballerat-Busserolles of the University of Blaise-Pascal, for facilitating my calorimetry training at such short notice. The staff and students at my *alma mater*, the University of KwaZulu-Natal, whose assistance allowed me to maximize my experimental time in South Africa. A special mention must go to the Chang family, who accommodated my visit there and treated me like their own. Finally, I would like to thank Iris and David, who helped me with the French translations of the thesis. Without them, most of the French parts in here would have been unreadable.

I would also like to acknowledge the financial supports of CARNOT MINES and SESAME for making this research initiative possible. I am grateful to the members of the examining jury for their presence and kind advice in the thesis defense.

To my very special group of friends:

Xavier, for helping me during the difficult times when I arrived in France, and being my first friend here. You reminded me that there is a life outside the thesis, and encouraged me to live it to the fullest. Despite what people may tell you, you're still the best Ph.D. I have met from our lab.

Paolo, for showing me how to think laterally and maturely. It seems there is something to be learnt from you everyday, not only how to be a better scientist, but to be a better person.

JuanMa, for taking care of a complete stranger, and becoming my closest friend in Germany. You were someone that I could trust and rely on. Your calm demeanor brought me much comfort in times of need (especially when my hard drive crashed, you still have my thanks!).

Ali, for being a compassionate friend, giving to others without asking for anything in return. I'm sure you're going to succeed in becoming the professor that you wish to be.

V, for being an amazing colleague and friend; for being understanding at all times. I couldn't have asked for better company, both within and outside work.

Xiaohua, for all the excellent scientific advice you imparted towards the end of my thesis. You are indeed the true PC-SAFT expert!

Diani, for your prayers and your support. We may be distances apart, but your words of encouragement reached me clear as ever. Thank you.

Vale, for being a special friend and someone I could confide in. Knowing that you're always there to talk to, even into the early hours of the morning, made those long nights so much more bearable.

Shalen, for keeping me sane on the weekends during second year. Thoroughly enjoyed our sessions of toasted sandwiches, plastic 5 L kegs, Chinese buffets, and ridding the world of zombies. Good times.

Steve, for the amazing friendship; for making it fifteen years, and counting.

Finally, I dedicate this thesis to my mother, who endured with me all the hardships over the past four years. Mama, you loved me unconditionally, no matter what the result was. This is the result, and it is for you.

Fontainebleau, June 2011

Chien-Bin Soo

Contents

List of Figures

List of Tables

Introduction

Accurate experimental data and *reliable thermodynamic models* are basic requirements for cost-effective and safe process design. In this thesis, both these aspects are addressed in the context of a novel energy source - biological fuels. When considered as a transportation fuel or chemical intermediate, biofuels are unique through its ensemble of oxygenated compounds, exhibiting the type of interactions and phase equilibria not encountered as frequently in petroleum engineering applications. As a technology in development, the integration of biofuels on a process level relies heavily on the two fundamentals which form the central themes of this work: the acquisition of thermo-physical data; and a means to model complex molecular interactions.

The aim of the thesis is to address this seemingly two-part *conundrum* in each of the experimental and modeling sections. Biofuel is first introduced as an energy alternative, in which its positive and negative impacts on the ecosystems are critically reviewed. By examining the chemistry of bioethanols, biodiesels and biomass oils, the oxygenated compounds to be studied in this work is brought to the fore. The thesis focuses mainly on the first generation biofuels. The following chapter highlights the behaviour of real fluids that exhibit both physical and quasi-chemical interactions. The identification of pertinent forces in oxygenated compounds provides the justification for adopting a SAFT-type approach in the later modeling part of the work. The second chapter ends with a review of the Helmholtz free energy terms in the model of choice, the PC-SAFT equation of state.

The crux of the work begins in the third, and first of two experimental chapters. In this chapter, new vapour-liquid equilibrium data, at pressures ranging from 0.01 to 5 MPa, were measured for nine systems including alkanes, alcohols, acids, and ketones. For pressures up to atmospheric conditions, the measurements were effectuated using an ebulliometer-type apparatus based on the "dynamic-analytic" method. At conditions above atmospheric, an apparatus based on the "static-analytic" method, with two electromagnetic ROLSI™ capillary samplers, was employed. The features of both apparatuses were examined as means of obtaining reliable experimental data, which have been shown to be valid.

In the fourth chapter, an efficient and reliable "dynamic-synthetic" method is proposed for the measurement of critical properties of a variety of pure compounds, binary mixtures, and one ternary mixture. The critical phenomenon is observed via the critical opalescence in a view cell, which withstands conditions up to 543 K and 20 MPa. The apparatus incorporates a slight modification to commonly documented procedures, with promising results. Excellent agreements were obtained between the measured pure compounds' properties and those listed in recent databases. Accurate critical data provides a reference to which modeling work on SAFT-type equations, which lack constraints in the critical region, can be developed.

The fifth chapter focuses on the modeling of biofuel systems, including but not limited to, the measured data of the first part. The first of two modeling chapters acts as a systematic study in the application of the PC-SAFT equation of state to polar and associating mixtures. Dealing mainly with fluid phase equilibria, we examine the manner in which different non-idealities shown by various oxygenated compounds can be approached by utilizing the available variants of PC-SAFT. The chapter proceeds to discuss the modeling of excess enthalpies and thermodynamic consistency testing with the equation of state.

The final and sixth chapter deals with the modeling aspects in the critical region. To account for long-range density fluctuations in the critical region, renormalization group corrections, according to White, are applied to the PC-SAFT equation of state. The result is a model which scales correctly at the critical point, and could be used to model the critical data obtained experimentally. Where critical properties were originally over-estimated, the renormalization group corrections bring about significant improvements in the description of the critical region.

Introduction

Des données expérimentales précises et des modèles thermodynamiques fiables sont des conditions de base pour la conception de procédés rentables et fonctionnant en toute sécurité. Dans cette thèse, ces deux aspects sont abordés dans le cadre d'une source d'énergie originale via les biocarburants. Si l'on s'intéresse aux carburants de transport ou aux intermédiaires chimiques, les biocarburants sont uniques par l'ensemble des composés oxygénés qu'ils contiennent, présentant des types d'interactions et d'équilibres de phase que l'on ne rencontre pas fréquemment dans des applications liées à l'ingénierie pétrolière. Comme technologie à l'étude, l'intégration des biocarburants au niveau procédé se base fortement sur les deux principes fondamentaux qui forment les thèmes centraux de ce travail : l'acquisition de données thermo-physiques; et des moyens de modéliser des interactions moléculaires complexes.

Le but de la thèse est s'intéresser à cette apparente énigme en deux parties dans chacune des sections expérimentales et modélisation. Les biocarburants sont tout d'abord présentés comme une énergie alternative, dans laquelle ses impacts positifs et négatifs sur les écosystèmes sont passés en revue de manière critique. Suite à l'examen de la chimie des bioéthanols, biodiesels et huiles de biomasse, les composés oxygénés à étudier dans ce travail sont mis en lumière. La thèse se concentre principalement sur les biocarburants de première génération. Le chapitre suivant pointe le comportement des fluides réels qui présentent des interactions physique et quasi-chimique. L'identification des forces pertinentes pour la représentation des composés oxygénés fournit la justification pour adopter une approche de type SAFT dans la partie de modélisation du travail. Le deuxième chapitre se termine par l'examen des termes de l'énergie libre de Helmholtz dans le modèle retenu, l'équation d'état PC-SAFT.

L'essentiel du travail commence dans le troisième, et le premier des deux chapitres expérimentaux. Dans le chapitre 3, de nouvelles données d'équilibres liquide-vapeur ont été mesurées pour des pressions s'étendant de 0.01 á 5 MPa sur neuf systèmes comprenant des alcanes, des alcools, des acides, et des cétones. Aux pressions atmosphériques et subatmosphériques, les mesures ont été effectuées au moyen d'un ébulliomètre basé sur la méthode "dynamique-analytique". Pour les pressions supérieures à la pression atmosphérique, nous avons utilisé un appareil basé sur la méthode "statique-analytique", faisant appel à deux échantillonneurs électromagnétiques à capillaires ROLSI™. Les caractéristiques des deux appareils ont été examinées en tant que moyens d'obtenir les données expérimentales fiables, ce qui a permis de les déclarer aptes.

Dans le quatrième chapitre, on propose une méthode "dynamique-synthétique" efficace et fiable pour la mesure des propriétés critiques d'une série de composés purs, de mélanges binaires, et d'un mélange ternaire. On observe le phénomène critique par l'intermédiaire de l'opalescence critique dans une cellule transparente, conçue pour résister jusquà 543 K et à 20 MPa. L'appareil incorpore une légère modification

aux procédures généralement décrites, avec des résultats prometteurs. D'excellents accords ont été obtenus entre les propriétés des composés purs étudiés et celles énumérées dans les bases de données récentes. Les données critiques précises fournissent une référence sur laquelle un travail de modélisation par les équations de type SAFT, qui manquent de contraintes dans la région critique, peut être développé.

Le cinquième chapitre se concentre sur la modélisation des systèmes de biocarburants, incluant les valeurs expérimentales mesurées dans la première partie et autres. Le premier des deux chapitres de modélisation est une étude systématique de l'application de l'équation d'état PC-SAFT aux mélanges polaires et associatifs. Traitant principalement les équilibres de phases fluides, nous examinons la façon dont différentes non-idéalités présentés par divers composés oxygénés peuvent être approchées en utilisant les variantes disponibles de PC-SAFT. Le chapitre se poursuit avec la discussion de la modélisation des enthalpies d'excès et des tests de cohérence via une équation d'état.

Le sixième chapitre qui est le chapitre final traite les aspects de modélisation dans la région critique. Pour tenir compte des fluctuations de densité à longue portée dans la région critique, des corrections de groupe de renormalisation, selon White, sont appliquées à l'équation d'état PC-SAFT. Le résultat est un modèle satisfaisant au point critique qui peut être employé pour modéliser les données critiques obtenues expérimentalement. Là où des propriétés critiques ont été à l'origine surestimées, les corrections de groupe de renormalisation conduisent à des améliorations significatives de la description de la région critique.

CHAPTER 1

Biofuel as a Global Initiative

The use of vegetable oils for engine fuels may seem insignificant today. But such oils may become in course of time as important as petroleum and the coal tar products of the present time.

- Rudolf Christian Karl Diesel (1858-1913)

Biocarburant, une initiative globale

Ce premier chapitre introduit le rôle des biocarburants comme une énergie renouvelable. Tout d'abord, un bref historique concernant les carburants d'origines fossiles est présenté - ressources d'énergie qui ont servi la communauté durant plusieurs décennies. Bien que leur importance soit essentielle, leurs utilisations ont été récemment mal gérées conduisant à des impacts sociaux très négatifs. Quelques exemples notables sont : les émissions de gaz à effet de serre, la propriété non-renouvelable, un prix monétaire instable, et une forte implication politique.

Des débats ont amené certains pays à engager des initiatives afin de réduire leur dépendance aux carburants d'origines fossiles. Une énergie alternative envisageable doit être renouvelable, dans le sens qu'elle est naturellement recyclable, avec une empreinte carbone négligeable. Ce chapitre recense plusieurs types d'énergies renouvelables, incluant l'énergie issue de la biomasse, l'énergie solaire, celle du vent, la géothermie et l'énergie hydroélectrique. Le niveau d'intégration des énergies alternatives dans le marché est défini par les législations multinationales, tel que le Kyoto Protocol de 1997 et la directive européenne. Le premier vise à réduire grandement l'émission mondiale de gaz à effet de serre (CO2, CH4, N2O, SF6, HFC et PFC) pour 2012. Le dernier se focalise notamment sur les émissions provenant du secteur des transports afin de promouvoir l'utilisation de carburants issus de la biomasse - une source d'énergie qui est le thème centrale de ce travail.

Les biocarburants sont issus de matière organique végétale et présentent un intérêt particulier grâce à leur polyvalence. Ils sont quasiment neutres en carbone, puisque le dioxyde de carbone libéré lors de sa combustion est réabsorbé par les plantes pour leur croissance. Ils sont divisés en plusieurs générations, selon la nature de la matière première utilisée dans la production. Ce travail étudie principalement les biocarburants de première génération, qui extraient leur source d'énergie à partir de sucres, de l'amidon et d'huiles végétales. Les biocarburants de première génération comprennent les carburants utilisés pour le transport - le bioéthanol, l'ETBE et le biodiesel. Les biocarburants de deuxième génération sont dérivés des parties non comestibles des plantes, comme la bio-huile et le biobutanol. Un type de biocarburants de troisième génération, également connu comme carburants des algues, sera examiné brièvement ci-après.

Il est important de noter que les biocarburants, comme les autres énergies renouvelables, ne sont pas sans inconvénients. Certains types de matières premières n'ont pas un potentiel égal de réduction de carbone et peuvent même contribuer à d'autres émissions nocives, telles que le formaldéhyde. La promotion des biocarburants dans certains pays peut rivaliser avec les ressources alimentaires provoquant ainsi une augmentation des prix. Si la culture des plantes pour les biocarburants résulte à la déforestation et à des dommages à l'écosystème, les avantages des biocarburants sont réduits de manière importante. Par conséquent, une planification sociale et environnementale est nécessaire pour maximiser les effets positifs des biocarburants.

Une revue bibliographique sur la production des biocarburants est donnée dans le chapitre I, afin d'identifier les principaux types de procédés de séparation. Il est clair que les séparations thermiques et mécaniques sur un large assortiment de composés sont concernées. Il est nécessaire d'étudier le comportement de phase des alcools (le bioéthanol et biobutanol), des éthers (l'ETBE), des esters (biodiesel) et des acides carboxyliques (bio-huile), qui sont en mélange avec des composés du pétrole tels que des hydrocarbures, des aromatiques et des cétones.

Pour la conception et la simulation efficace des procédés de production de biocarburants, l'importance des données expérimentales et des modèles thermodynamiques ne peut être négligée. L'introduction d'un large assortiment de composés oxygénés mentionnés précédemment nécessite de nouvelles données expérimentales couvrant une large gamme de conditions. Les équations d'état classiques cubiques telles que l'équation de Peng-Robinson ont été abordées et ont montré un manque de précision dans le cas de certaines interactions spécifiques, telles que la liaison hydrogène. Dans les chapitres suivants, la thèse vise à proposer des techniques expérimentales et de modélisation pour la connaissance et la compréhension du comportement de phase des mélanges de biocarburants.

In recent times, the focus on the economic price of fossil crude has overshadowed its environmental cost - a price of 300 kg of CO_2 per barrel - a non-negotiable price from a non-renewable resource. The reduction of such a greenhouse gas is one of the main factors promoting renewable energies in the global market. Among the numerous forms of renewable energies recognized today, biological fuels, or *biofuels*, remain key players in reshaping the petroleum industry. The continuous need for biofuels to re-invent itself, when faced with oncoming social and economical challenges, is of our scientific interest and concern.

The chapter begins with an account of how petroleum has evolved to become the global powerhouse it is today. This provides the groundwork for understanding the need of alternative renewable energy sources. After defining necessary concepts, biofuels are singled out as the focus of this thesis. An overview of its characterization, chemical structures, and production is provided, before outlining the challenges and the structure for the remainder of the thesis.

1.1 A brief history of oil

The inventor of the engine of the same name, Diesel, along with motor forerunners such as Otto and Ford, were visionaries of bio-energy at a time of fossil fuel dominance. The beginning of the 20th century was, undoubtedly, the golden era of crude refining. It started in 1859, when Edwin Drake drilled the first oil well in Pennsylvania to send the United States (US) into their first oil rush. By 1878, more than 500 million barrels of recoverable crude oil were discovered in Azerbaijan alone, in what was probably the world's first giant oilfield then. By 1900, petroleum interests had spread to most parts of Europe, Middle East and the Americas [1].

Swift advancements in drilling technology followed, such as the rotary cone drill and the blowout preventers, which allowed deeper wells to be drilled safely. The timing could not have been better - a time when automobiles defined the new look of transportation. Oil demands were further fueled by the onset of World War I, where governments reaped the benefits of motorized warfare and became the major shareholders of petroleum companies. The low cost and availability of fossil-based crude at the time easily dismissed any contentions of an alternative energy resource. After a quarter of a century, there were more than 23 million registered vehicles, compared to the 8000 at the beginning of the century [1]. The US was uncovering giant oilfields, similarly to those in Azerbaijan, at a rate of three to five oilfields per annum. During World War II, the petroleum industry spread its markets to synthetic manufactures, plastics, rubber and wax. There were rare moments in the war when vegetable oils were used as diesel substitutes, but only in emergency situations [2].

Between 1950 and 1970, Middle Eastern producers rose to the global scene and shifted the tide of global crude wealth, thanks to timely oilfield discoveries. While the power players of the early 1900s were faced with escalating post World War II oil demands, the Middle East helped to drive a worldwide oil expansion that proceeded at an unprecedented annual rate of nearly 5 % [2]. The powers Iran, Iraq, Kuwait, Saudi Arabia, Venezuela went on to found the Organization of Petroleum Exporting Countries (OPEC[1]) in 1960. This marked the beginning of major political influence on crude oil prices, such that to the present day, one can no longer be mentioned without the other. Today, members of OPEC remain the owners of the majority of the world's proven oil reserves, up to 77 % as shown in Figure 1.1. The US, which produced about 53 % of the world's crude oil in 1950, was slowly losing its place as the leading global petroleum producer. It had, in fact, become one of the most import-dependent nations due to its perpetual oil demands. Inevitably, the rate of oilfield discoveries, and the discovered oilfield sizes were rapidly declining that, during the 1990s, only about 40 oilfields were discovered with not more than 50 giga barrels in total [2].

OPEC has had a hand in decades of crude price fluctuations since its formation. Two political incidents, namely the Yom Kippur War (1973) and the Iranian Revolution (1979), resulted in the two most notable oil price shocks

[1] Also referred in other languages as OPEP (L'Organisation des Pays Exportateurs de Pétrole / La Organización de Países Exportadores de Petróleo)

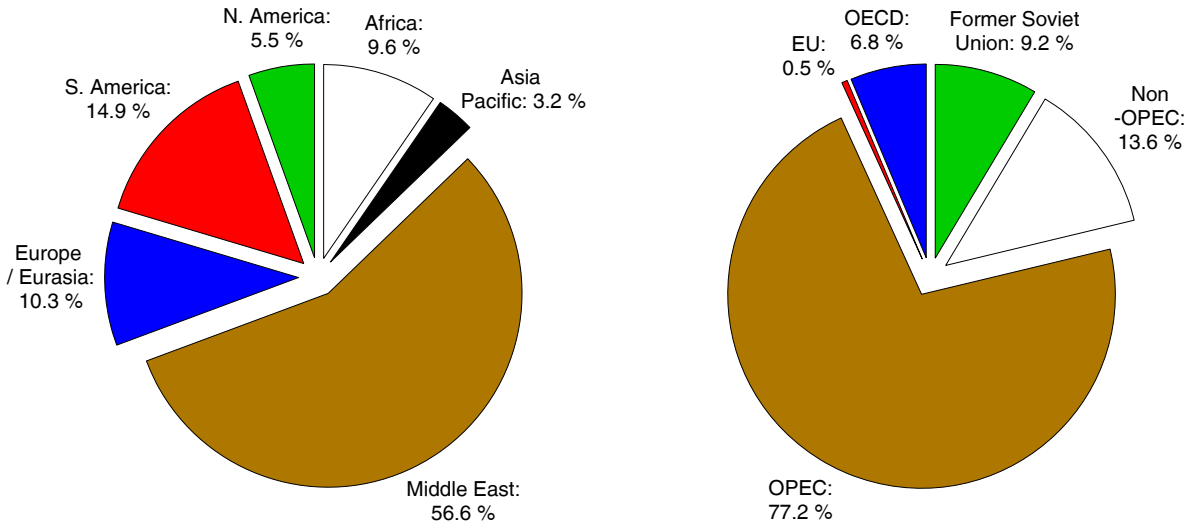

Figure 1.1: Distribution of the world's proven oil reserves at the end of 2009 between (*left*) the respective continents, and (*right*) notable global organizations, namely EU (European Union), OPEC, OECD (Organization for Economic Co-operation and Development), and others [3].

of the 20th century. The former saw the crude price quadruple from $ 3.01 to $ 11.65 per barrel, in a matter of three months, while the latter incident resulted in the price doubling from $ 13.62 to $ 32.95 per barrel, this case over a longer period of time [2]. In essence, such exaggeration of the oil price did much to harm OPEC in return, as non-OPEC countries strived for higher energy efficiency among themselves, and promoted oil exploration developments of their own. Brazil and the US, who were then the global leaders of sugar cane and maize, hit back with their own national incentives to develop ethanol-based fuel. By the end of the seventies, Brazil was on the verge of commercializing a blend of 25 % ethanol in gasoline; as well as a hydrous ethanol fuel containing no petroleum whatsoever. France, themselves not a huge excavator of petroleum, countered their import dependence by launching the *Carburol* plan, aimed at producing biological fuels from lignocellulosic biomass [4]. At that time, the research motives were more of an economic nature, rather than environmental, with a hint of snubbing at the OPEC leaders.

Regardless, OPEC budged, and global oil demands, for the first time since the 1860s, declined and along with it the oil prices, much to the unwillingness of several OPEC members. Oil prices plummeted from $33.62 in 1982 to below $10 per barrel by 1986 [2]. This did much to stem the development of sustainable energy resources. The *Proalcohol* programme, the cornerstone of much of Brazil's 1970 ethanol advancements, lost its support from the government. Even the *Carburol* plan of France was dispatched at the start of the 1990 [4]. However, some initiatives remained, notably the European directive 85/536/EC of 5 December 1985, which proposed future incorporations of ethanol and ethyl *tert*-butyl ether (ETBE) in gasoline.

Towards the end of the 20th century, it was evident that oil prices would show few signs of stability, as it continued its fluctuating trend into the new millennium. *Demand* remains the primary governing factor of oil prices, causing the trend to move in tandem with the current global energy demand. Along the way, the advent of human nature - political disputes, wars, corruption, and a history of oil shortage propaganda - has done just enough to keep the everyday investor guessing. Figure 1.2 shows the year-to-year changes of oil prices between 1981 to 2007, with significant dates shown in red and elaborated in Table 1.1. The most influenced periods are scattered far from the center of Fig. 1.2, where large relative changes in oil prices were experienced within consecutive years

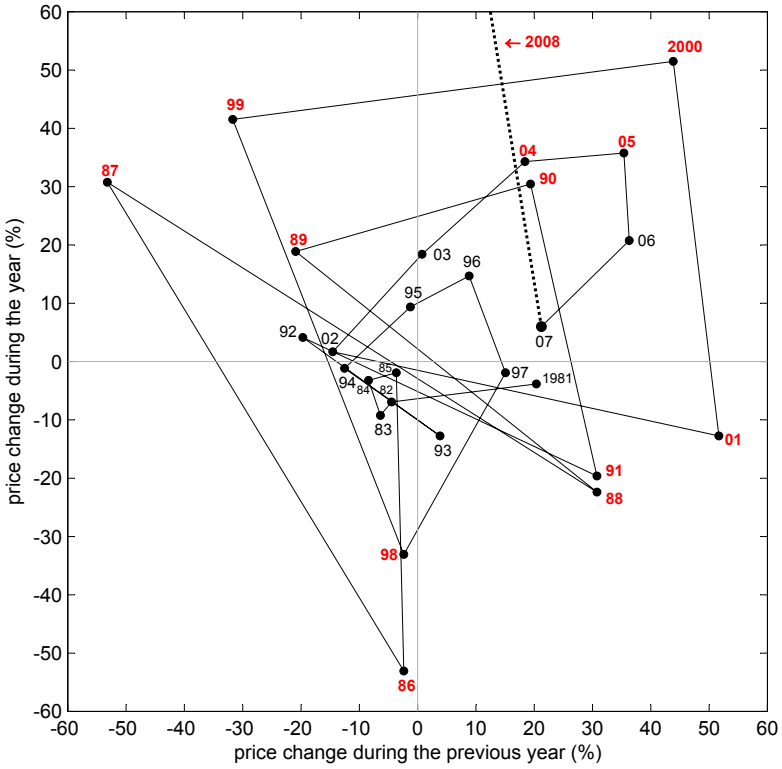

Figure 1.2: Year to year changes of oil prices from 1981 to 2007 [2]. The year is given next to each node, with significant dates shown in red and listed in Table 1.1.

1.2 The debate for alternative energy

In the combustion of fossil fuels, hydrocarbons disintegrate to elemental carbons and hydrogens, the low and high energy constituents of their structure. In the excess of oxygen, the combustion is complete and 'clean', and all the carbons are oxidized to form carbon dioxide, and the hydrogens water,

$$\text{fuel} + \text{oxidizer} \rightarrow CO_2 + H_2O + \text{energy} \tag{1.1}$$

Regardless of the complexity of the combustor, such complete combustion are rarely, if ever, encountered. Incomplete combustion occur when insufficient oxygen is present to transform all the fuel to carbon dioxide and water. The result of the combustion is thus a mixture of carbon dioxide, water, as well as unburned hydrocarbons, and trace emissions [6],

$$\text{fuel} + \text{oxidizer} \rightarrow CO_2 + H_2O + \text{energy} + C, CO, H_2, N_2, NO_x, SO_x \tag{1.2}$$

The trace emissions in reaction (1.2) make up a list of some of the most hazardous air pollutants. In fact, applying the above reaction to methane recovers half of all six greenhouse gases (see later), while those species that do not reach the atmosphere (NO_x, SO_x) are capable of inflicting adverse environmental and health effects at ground level.

Almost in an unsurprising manner, it took some unconventional methods, such as that of a certain cinematic featuring US congressman A. Gore [7], to initiate the general public on the state of our environment, and have its place reinstated in oil markets. The Goddard Institute of Space Studies at NASA have been observing the global

Table 1.1: Significant global influences on the oil prices from 1981 to 2007 [5], shown as red texts in Figure 1.2.

Year	Chronology
1986	Netback pricing on oil costs.
1987	Crude formula pricing. Iran/Iraq war cease fire.
1988	Crude oil prices jump in anticipation of possible production accord, which OPEC successfully reaches.
1989	ExxonMobil tanker Valdez spills 11 million gallons of crude oil.
1990	Iraq invades Kuwait
1991	US launches Operation Desert Storm, driving Iraq out of Kuwait, and wrecking Iraqi infrastructure.
1998	Asian Economic Crisis.
1999 - 2000	Oil costs react to strong world demands, OPEC oil production cutbacks, and other factors, including weather and low oil stock levels.
2001	9/11 Attacks.
2004 - 2005	Hurricane Ivan, Dennis, Katrina and Rita hit the Gulf of Mexico.
2008	Oil price reaches all-time high (+ $100) due to rising demands, low spare capacity, and geopolitical concerns.

average temperature and anomalies from as early as 1880, and reports show that there has been a gradual increase in the earth surface temperature, particularly towards the end of the 20^{th} century. With the increased demand for energy in all sectors, most significantly transport, levels of atmospheric carbon dioxide have intensified over the past fifty years. There is enough evidence to support that the carbon dioxide and methane released from the burning of fossil-fuels, have contributed directly to global changes such as ozone depletion, greenhouse effect, acid rains, and environmental pollution. Emissions from the combustion of fossil-fuels contain pollutants which are harmful to the human health and well-being, the effects of which can be short and long term depending on dosage levels. In face of the ongoing environmental deterioration, world leaders have converged to enforce legislations committed to reducing the level of greenhouse gas emissions. Conferences such as the decennial Earth Summit and Kyoto (1997) are some of the past instances where environmental laws have been established and evaluated. Figure 1.3 is an indication of the relentless and seemingly never-ending increase in atmospheric CO_2, global population, energy consumption, and average global temperature over the past few decades.

Suppose our earth *does* hold out for the next couple of decades, one must remember that oil is still a non-renewable energy, and like all non-renewable raw materials, its reserves are finite. With a global demand thats seems unabating, a time will surely come when man can no longer enjoy unearthing the commodity at the same rate, to generate the same profit, at the same price. Ever since M. King Hubbert accurately predicted in 1956 the US oil production peak of 1970, there has been countless philosophies, listed in Table 1.2, although rarely in agreement with each other and the facts, which foretold the year of global oil peak. While these ill-assorted opinions of oil peak sound like tireless innuendos and does little but alleviate the seriousness of the matter, an oil peak is more than just a brainchild of public paranoia, but an actuality to which the US stand testament. Most of the forecasts do share a common belief that, at the current rate of energy usage, the global oil peak will occur, if not already, before 2020 and that reserves will run dry before the end of 2100. Indeed, statistical reviews on the estimated ultimate recovery (EUR) of oil reveal that half of the world's crude resources will be extracted in the next few years, depending on the conservation of the estimates. Since the curve of oil production is said to be bell-shaped, similar to that a standard normal distribution, the production can only decline steeply after the peak.

Nonetheless, several theorists have constructively argued that the prospects of a crude oil peak are but 'a

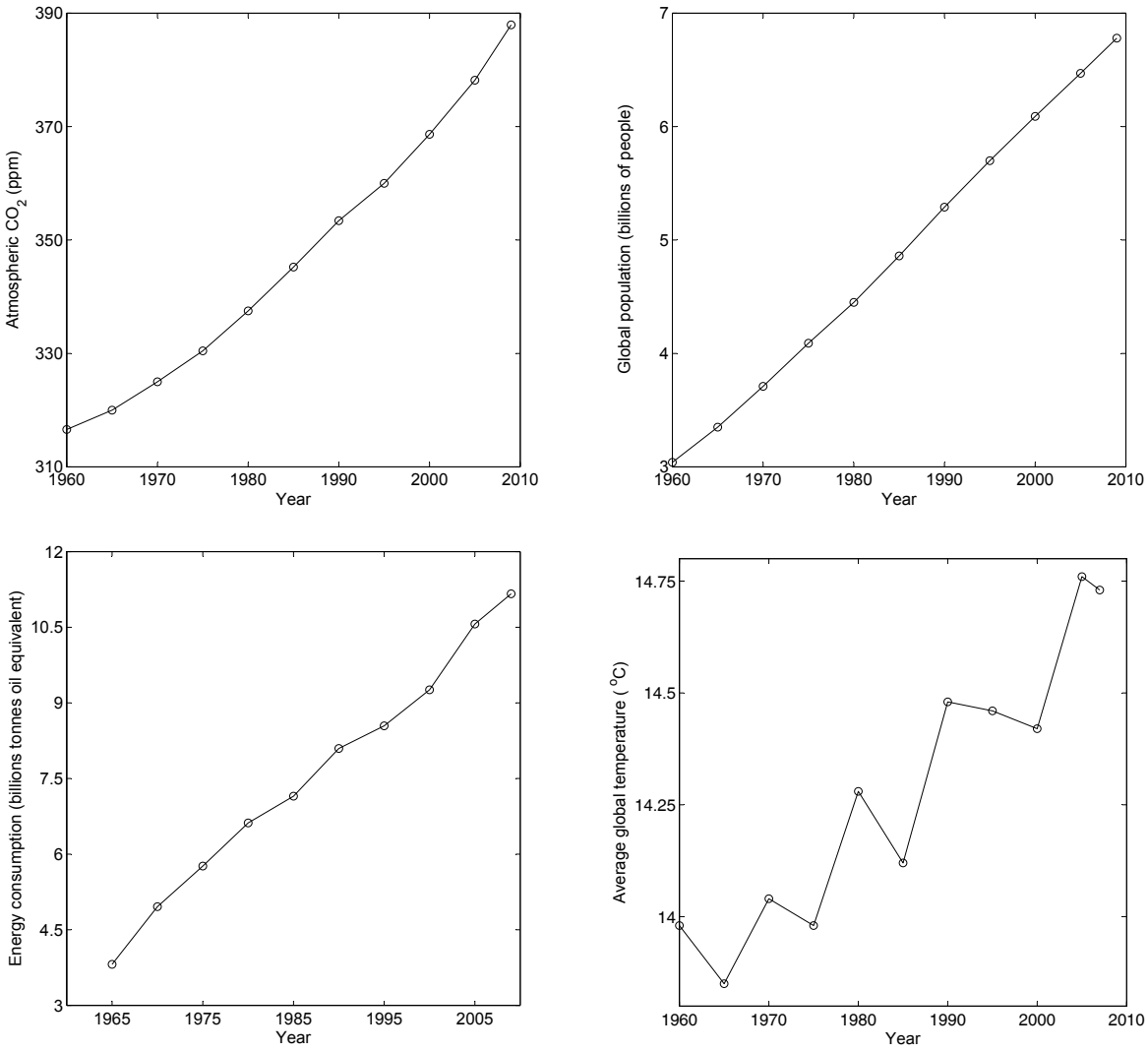

Figure 1.3: Graphs showing the ever-increasing trends of atmospheric CO_2 (*top left*, Source: Scripps Institution of Oceanography), global population (*top right*, Source: US Census Bureau), energy consumption (*bottom left*, Source: BP Statistical Review of World Energy 2010), and average global temperature (*bottom right*, Source: Goddard Institute of Space Studies).

long history of failed peak forecasts,' based on flawed assumptions [2, 14, 15]. This is legitimate considering the number of thwarted predictions; the oversimplified, bell-shaped production curve; and the omission of oil shales, tar sands, and natural gases in the calculation of the forecasts. The economist Michael Lynch believes that market and technological advancements will sustain our oil needs in the immediate future [14, 15]. Since there is a delicate balance between oil production and consumption rate, any increase in oil price is met with economic slowdown, followed by decreased oil use, alternative energy initiatives, and ending in a price decrease again - it is an action-reaction process. Smil [2] cited that the major obstacle is in not recognizing and reacting to the potential oil shortage. Afterwards, the intellect of man will ensure its prosperity even long after the depletion of oil, as opposed to the ideas of Ivanhoe [11] who believes the end of the oil era will bring 'the inevitable doomsday.' Figure 1.4 shows the historical trend of the reserves-to-production (R/P) ratio, a measure of the remaining amount of oil, in years. At 2009, the R/P ratio is at 45.7 years, with recent trends described as a fluctuating, but by no means subsiding, plateau.

Table 1.2: Forecasts of the global oil peak, listed in chronological order.

Reference	Forecasts
Hubbert [8]	Global oil peak occurs between 1993 and 2000.
Wilson [9]	Global oil peak to occur between 1994 and 1997.
Flower [10]	Global oil peak before the onset of the 21st century.
Ivanhoe [11]	Global oil peaks at 2000.
Deffeyes [12]	Global oil peaks at 25 November, 2005.
Campbell and Laherrère [13]	Global oil peak to occur before 2010.

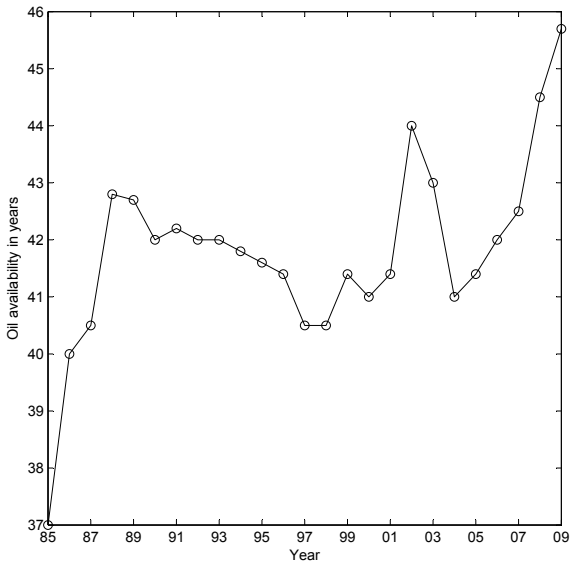

Figure 1.4: Global reserves-to-production ratio, with the ordinate indicating the oil availability in years. A fluctuating plateau has been experienced for the past few decades. The ratio at the end of 2009 is 45.7 years [3].

Furthermore, the unreliable fluctuations of the crude oil prices in the past has led to a general consensus among nations to suppress their dependence on crude, particularly Middle-Eastern imports. Today, the price of crude stands at $109.7 per barrel (15 April, 2011. *Source*: US Energy Information Administration). For major importers of the world, such as the US, this undoubtedly places a substantial toll on their economies. Despite OPEC not having the same dominance it once did, five out of the top ten oil producers today are still OPEC members (Iran, Iraq, Kuwait, Saudi Arabia, Venezuela), guaranteeing them a healthy portion of the oil monopoly. Experiences in the past have shown the effects of political disputes among OPEC members on oil prices, and with OPEC still possessing more than three-quarters of the world's oil resources [16], there is a collective realization worldwide to invest in an alternative, renewable source of energy. The concept of renewable energy is nothing new, *viz.* hydro-, wind- and solar power, and while most of them are generally non-polluting, only a few of them addresses the emission problems stemming from a growing vehicle population, those being biofuels and hydrogen cells.

So will biomass energy be the solution to our oil problems? The misinterpretation of the matter, as far as the public is concerned, is whether biomass energies, be it bioethanol, biodiesel or biogas, will step into petroleum's shoes when its last drop is used up, if it comes down to that. The irony is that, like its fossil-based counterpart, biomass energies are not without some severe flaws. However, these drawbacks, discussed in § 1.5.2, should only complicate the situation as much as the observer allows it to. In the opinion of the author, the bottom line is this: renewable energy has been around for years, and despite it being case-specific, has enjoyed numerous successes

in several countries. The same will apply for biofuels. While Brazil and the US are already reaping the benefits of bioethanol, it will be several more years before its full implementation in Asia, who relies heavily on vegetable imports. Even if biofuels are not the ultimate solution to the global environmental crisis, there is no reason for believing that 'green-living' should not consist of one, but rather many combinations of renewable energy strategies. In 2006, Sweden announced its goal of becoming oil-free in 2020 [17], without the use of nuclear power, and it is unlikely to do so relying on only one form of energy[2]. The ultimate goal is for countries to find the right balance between the economy and the environment, using the resources available to them.

1.3 Renewable energy processes

Renewable energies are energies based on natural resources derived from planetary motion. Energy from radiation of the sun (solar), movement of oceans (tidal), and transfer of air pressures (wind) can be harnessed and replenished in a natural manner; thus they are termed *renewable*. There is no definitive lifespan for such energy resources, with their first application dating back to the earliest civilizations.

The cloud of uncertainty over alternative energy resources means that most renewable energies only came into contention in the late 20th century. In recent years, a major factor boosting the development of renewable energy is the decrease in its operation cost. According to the Energy Information Administration (EIA), renewable energies made up about 8 % of the total global energy consumption in 2003, the equivalent of approximately 32.7 quadrillion Btu, and is projected to reach double of this amount in 2030 [19]. This is however only a 1 % projected increase, to 9 %.

This section discusses briefly some of the more common forms of renewable energy. This work places additional emphases on transportation fuels (bioethanol, biodiesel) arising from biomass energies. These are discussed in further details in § 1.5. As seen in Figure 1.5, biomass is the dominating renewable energy resource, but it is also the broadest in category (heating, electricity, transport, etc). Solar and geothermal energy, despite its theoretical potential, remains the smallest contribution to date, although its usage is on the rise.

Table 1.3 provides an overview of the discussed renewable energies in terms of land usage, cost, and disadvantages.

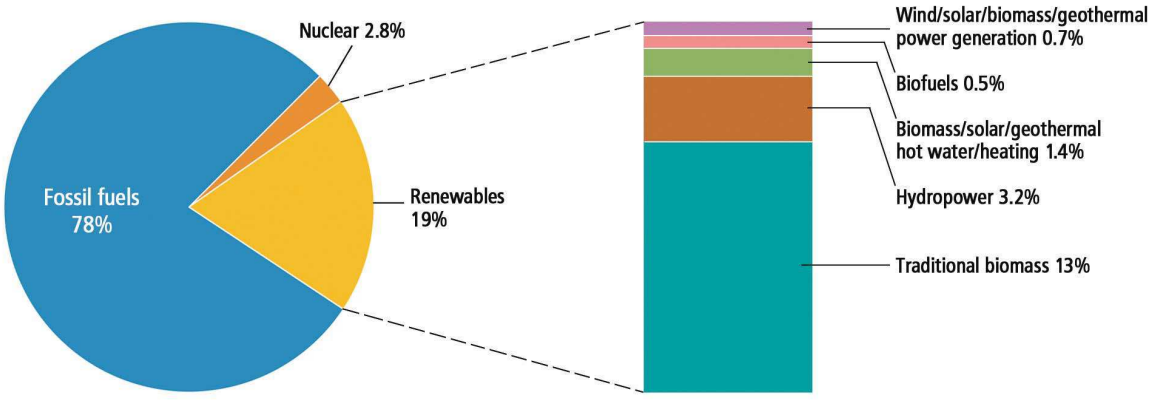

Figure 1.5: Share of renewable energy in the global final energy consumption for the year 2008 [20].

[2]By 2005, Sweden is already the second leading European country in integrating biofuel into its oil markets [18].

Solar Power

Solar power processes harness radiant energy from the sun and converts them to electric energy. The power density of solar radiation, or insolation, is used either as a heat source for driving working fluids, or is converted to electric currents through photovoltaic effects. To convert thermal energy into electricity, it is necessary to capture the radiation, either in solar ponds or parabolic troughs [21]. Only a fraction of the total solar radiation reaches the earth's surface, and is affected by surface orientation, latitude and meteorological conditions. Thus, solar power is generally stored or supplemented by another energy source, e.g. wind power (see later) to provide continuous power [22].

Photovoltaic cells is another form of energy source utilizing sunlight, by converting radiation to current electricity using semiconductors such as silicon. The small sizes of the cells make them cost-effective, and requires little or no additional land space. This flexibility enables their use in both domestic and industries. However, the manufacture of photovoltaic cells uses toxic chemicals such as cadmium sulphide that make their disposal and recycling difficult [21].

Geothermal Power

Geothermal energy systems use the natural heat that is created in some parts of the interior of the earth as a result of radioactive disintegration of atomic nuclei [23]. Several forms of geothermal energy sources can be found. Hot springs and underground steam reservoirs (hydrothermal resources) are used for electricity generation, although their location is somewhat limited. More common sources include superheated brine-methane mixtures (geo-pressurized systems) and dry rock accumulations of heat. Overall, existing sites for the extraction of geothermal energy are limited, and are not necessarily large in relation to possible usage. A further downfall is that the rate of regeneration / renewal of such energy reservoirs are not comparable with the rate at which they are exhausted. The average lifespan of a geothermal energy source is between 40 - 100 years, making them hardly 'renewable' [21].

Table 1.3: Land usage, costs, top producers, and drawbacks of different renewable energies.

Renewable Energy	Land Required (ha)	Cost per kWh ($)	Top world producer	Drawbacks
Solar	1100 - 5200	0.01 - 0.20	Germany	Generally low efficiency Heavy geographic dependence High installation costs Cannot store the energy over extended periods
Geothermal	30	0.04 - 0.07	China United States	Limited reservoirs with limited lifespan May produce toxic waste sludge and H_2S
Water	75000	0.03 - 0.12	China	Requires considerable land space Sedimentation may decrease dam efficiencies Dams alter existing marine ecosystems
Wind	9500	0.05 - 0.14	United States	Limited optimal sites Cause deaths of migrating birds Results in noise pollution at short distances
Biomass (excl. fuels)	200000	0.05 - 0.12	United States	Requires the most land due to forestry Combustion of biomass can still release pollutants

Hydroelectric Power

Hydroelectric power processes derive its energy from gravitational forces or directional movements of water, waves or tides. Its application ranges from simple mechanical power, such as watermills, to large-scale ocean wave power engines sustained through tidal energy. The power density of ocean waves are functions of wave depth, height, velocity, and density, with onsets of floods and storms driving the potential power generation to the scale of a few kilowatts per square meter (significantly greater than that of solar or wind energy) [22].

Hydroelectric dams and tidal power are used efficiently in some ports of China, Brazil, Canada and Russia. Its versatility, reasonably low cost, and high energy potential makes it the most common renewable energy in the world, marred only by disadvantages of wave instabilities, and disruption of aqueous marine life. At the end of 2009, hydroelectric power supplies around 15 % (980 giga watts) of the share of global electricity, only second to fossil fuels [20].

Wind Power

Wind power processes, as the name implies, involve the driving of generators by wind energy to generate electricity. Power density derived from aerodynamics is largely dependent on wind velocity which is affected by altitude and the geography of the site. Most wind farms produce a modest power density of a few hundred watts per square meter.

Wind power, like solar power, is an intermittent, non-dispatchable resource, meaning it is highly variable in intensity, unavailable at all times, and needs to be optimized when it is available. It is possibly the cleanest form of renewable energy, and has been deployed throughout all parts of the world, although its popularity has been often been plagued by reports of low efficiencies, noise, and a complicated cost factor.

Biomass

Biomass, in the global sense of the word, encompasses all forms of the energy routes that one obtains from living, or recently living biological materials. The simplest form of deriving biomass energy dates back to prehistoric times, where thermal conversion, in the form of fire, is used to burn wood to provide heating and cooking. Currently, liquid biomass extracted from plants is used directly as petroleum blends in biofuels. The potential of biomass energy is manifested in its wide range of products, including biochar, biogas, bioalcohol and biodiesel. A variety of raw materials can be used, from forestry residues to common crops to algae, depending on the end product.

The use of biomass energy remains loyal to the concept of carbon neutrality. The carbon released during the burning of biomass is reabsorbed by the autotrophs (plants, phytoplankton) of the biosphere, via photosynthesis, for growth. These plants are then harvested to be processed again as biomass energy. This form of carbon neutrality, known as the carbon cycle, effectively reduces, although does not completely nullify, a net gain of CO_2 [1]. A life cycle analysis[3] performed by Tan and Culaba concludes that biofuels benefits primarily with respect to global warming and fossil fuel resource depletion [24]. Biomass energy is currently the world's largest source of renewable energies, forming around 50 % among all forms of renewable energy [19].

As mentioned in the preceding section, only fuels from biomass, and hydrogen fuel cells, directly addresses the emission problems stemming from the transportation factor. Hydrogen fuel cells are safe and pollution-free, but the heavy cost factor prevents a mass market along the same scales as biofuels.

1.4 Major climate change initiatives

Since the beginning of the 21st century, there has been a slow, yet undeniable transition into biomass energy. This is, of course, with the help of some political intervention. Without the tax-cuts and subsidiaries involved in the

[3]The scientific and technical analysis of impacts associated with a product or a system [23].

manufacturing of biomass fuels, the promotion of the technology would be far from its current state. Biomass energy has been implemented with great success, notably in countries such as Brazil, US, and several countries of the European Union. In this section, some of the major global climate change initiatives are briefly outlined, in particular those involving biofuels.

The Kyoto Protocol

The Kyoto Protocol of 1997 is an international agreement under which ratified countries will aim to reduce greenhouse gas (GHG) emissions by 5.2 % compared to the year 1990. The goal of the protocol is to lower the overall emissions, averaged over 2008 to 2012, for a group of six greenhouse gases, namely carbon dioxide (CO_2), methane (CH_4), nitrous oxide (N_2O), sulphur hexafluoride (SF_6), hydrofluorocarbons (HFCs) and perfluorocarbons (PFCs). The limits of national reduction range from 8 % for countries of the European Union, 7 % for the U.S., some zero percent for countries (Russia, Ukraine) that are requested to stabilize current emissions, and permitted increase in emissions for others such as Australia and Iceland [25].

The fact that several of the countries' GHG emissions has increased since 1990 means that they would have to cut their emissions by some 30 %, if they are to still achieve the target of 5.2 % by the end of 2012. As a result, the Protocol, under the United Nations Framework Convention on Climate Change (UNFCCC), has granted countries flexible mechanisms with which they can fulfil their GHG reductions. Programs such as the Clean Development Mechanism and Joint Implementation [25] allow developed countries to set-up emission-reduction projects in developing countries, and in doing so, receive 'carbon-credits' which could be traded among countries as financial incentives. This form of credit-trading among countries stimulates sustainable development and allows equal opportunities for countries of various prevailing environmental standards.

The European Union Emission Trading

Economist Nicolas Stern, in his 2006 review [26], expressed the need to allow market forces to develop low carbon technologies. This is the concept behind Emission Trading, where transparent prices are designated to carbon emissions, and traded across businesses with a competitiveness that ensures emission reductions are made where the cost is the lowest. In this scheme, units known as allowances, equivalent to 1 ton of CO_2, are distributed to its participants. These allowances form the 'caps' or the limits of emissions permitted for a participant over a certain period. At the end of the period, usually 12 months, the participants measure their total emissions and surrender a number of allowances equivalent to their CO_2 emissions. Those participants who have used up all of their allocated allowances have the flexibility to buy additional allowances, at a cost, from other participants who has accrued a surplus through more cost-effective emission reduction. The result is a drive for businesses to reduce emissions cheaply, without placing cumbersome regulations and taxes.

The European Union Emission Trading Scheme (EU ETS) is currently the largest, multi-national emission trading scheme in the world. It was operational prior to the Kyoto Protocol, and has since then functioned in tandem with the International Emission Trading, a flexible mechanism of the Protocol. The EU ETS foresees an overall reduction of greenhouse gases of 21 % in 2020, compared to 2005 emissions. The United Kingdom, not being part of the European Union, established its own UK ETS from 2002 to 2006.

European Directives

The European Directives are a series of regulations established by the European commission to promote development of the energy sectors, in particular, the heat, electricity and biofuel divisions. One of the earliest significant directives, with regard to biofuels, was the 85/536/EC as mentioned in § 1.1. In 2000, the Green Paper of the European commission [27] aimed at replacing 20 % of all conventional fuels for road transport, divided among the three most viable potentials, *viz.*, biofuels, natural gas and hydrogen. Table 1.4 below shows the optimal scenario, as proposed

Table 1.4: Optimal scenario of alternative fuels introduction until 2020 according to the EU

Year	Biofuels	Natural Gas	Hydrogen	Total
2005	2 %	–	–	2 %
2010	5.75 %	2 %	–	7.75 %
2015	7 %	5 %	2 %	14 %
2020	8 %	10 %	5 %	23 %

by the Green Paper, on alternative fuel introduction. The following discussion focuses on biofuel-related directives only.

European Directive 98/70/EC Initiated on 13 October 1998, this was the first directive focusing on commitments relating to the quality of petrol and diesel fuels. It introduced environmental specifications to fuels, with effect from the year 2000, promoting the substantial reduction of pollutant emissions. This laid the foundation for future initiatives.

European Directive 2003/17/EC The successor of the European Directive 98/70/CE, this directive, which was brought into force on 3 March 2003, fixed the environmental specifications of unleaded petrol and diesel fuel marketed in the territory. These regulations, known as European Norms (EN), defined the standards of the incorporation of biodiesel in diesel (EN590) and bioethanol in gasoline (EN228) to be limited to 5 % vol. The incorporation of ETBE is limited to 15 % vol [28].

European Directive 2003/30/EC Formalized on 8 May 2003 with the aim of promoting the use of biofuels and other renewable fuels, the European directive 2003/30/EC specifies that member states must ensure a minimum share of biofuels and other renewable fuels are placed on the market. National targets for fuel for transport purposes were set at 2 % for all gasoline and diesel by 31/12/2005 and 5.75 % by 31/12/2010. The term biofuels included the wide range of pure and blended bioethanol, biodiesel, biogas, etc, including their derivatives such as ETBE. An annual report is demanded of each member state, the contents of which outlines its annual policies and resources implemented, as well as current progress, in achieving the final targets.

European Directive 2003/96/EC The directive restructured the formalities on the taxation of energy products and electricity. On 27 October 2003, it was passed onto member states to grant 'total or partial exemption or reductions in the level of taxation to taxable products used under fiscal control in the field of pilot projects for the technological development of more environmental friendly produces or in relation to fuels from renewable sources.' This was aimed at making inroads into the operation of internal energy markets. The actual level of tax exemption on environmental-friendly energy products, including biofuels, was decided by each of the member states.

Despite the incentives, the penetration in the market share of biofuels, at the end of 2007, failed to exceed 1 % averaged over the 27 countries of the European Union (compared to the initial 2 % target laid out in the 2005/30/EC directive). Germany and Sweden were the leading countries at this stage, having already a biofuel market share of 3.75 and 2.23 % by 2005. France, having only achieved a 0.97 % biofuel market share in 2005, improved their share to 1.77 % in 2006, and may still achieve the stipulated 5.75 % for 2010, if the current rate continues. Figure 1.6 shows the position of some of the member states in biofuel market share at the year 2005. The Biomass Action Plan [29], drawn up towards the end of 2005, contains guidelines to help countries achieve the objectives of the European Directive 2003/30/EC. In 2007, it was proposed that the 5.75 % target for 2010 should be relaxed to 4 %.

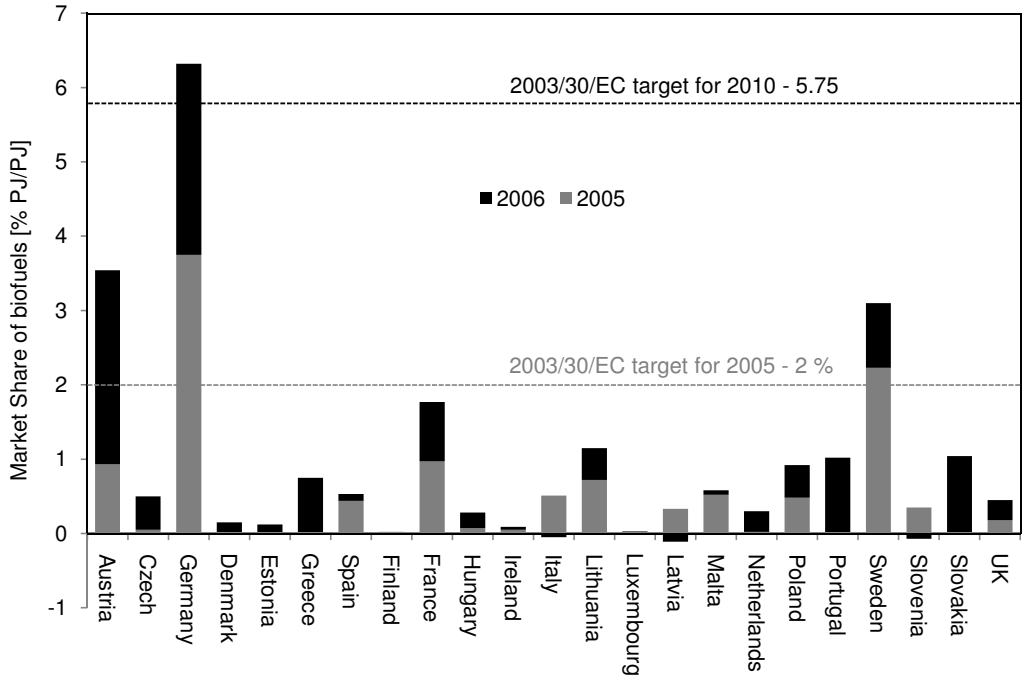

Figure 1.6: Market share of biofuels of some member states of the European Directive 2003/30/EC [18]. The two targets stipulated by the directive are given in dotted lines

The Advance Energy Initiative

The Advanced Energy Initiative (AEI) was initiated by U.S. President George W. Bush in 2006 with the aim of proposing a 22 % increase in funding for cleaner alternative energy resources. It was focused on searching new ways of fueling vehicles, such as biofuels or hydrogen fuel cells; and new ways of powering domestic and industrial sectors, e.g. nuclear, wind and solar energy. The 2009 budget for AEI reached 3.17 billion dollars, an 80 % increase of the initial 2006 investment of 1.6 billion dollars.

1.5 Biofuel review and production

The remainder of this chapter focuses on biofuels - solid and liquid fuels derived from organic matter. First generation biofuels (see below) are central to the objectives of the thesis. In order to satisfactorily measure and model the thermodynamic properties of these fuels, it is vital to first understand the nature and complexity of their structures. The following sections serve to characterize and illustrate the chemistry of first generation biofuels, their pros and cons, and the processes of manufacturing market products.

1.5.1 Definition and characterization of biofuels

Solid and liquid fuels are derived from the burning or treatments of a wide range of biological materials, specifically plant matters capable of self-renewal. This allows the fuel to be classified into different *generations*, depending on the nature of their original raw material.

First generation biofuels

First generation biofuels are fuels which extract their energy sources from sugars, starch and vegetable oils. These fuels are also known as *food oils*, since the fuel is derived from feed-stocks that enter the human and animal food chain. Depending on the product, conventional technologies are used to extract the oil out of the raw material, including fermentation, transesterification, and anaerobic digestion.

Bioalcohols are liquid transportation fuels consisting of a blend of gasoline and biologically produced alcohols, usually ethanol or butanol. Bioethanol (specification **E**, designed for gasoline engines), is the most common bioalcohol, consisting of ethanol - which may or may not be transformed in the form of ETBE - blended in gasoline. The level of ethanol incorporation in gasoline varies from 5 % (E5), which can be used in most modern automobiles without much modifications, to pure or almost pure (E85-E100) ethanol, restricted to modified engines such as those in flexible-fuel vehicles [30]. National standards of low ethanol blends are usually set at 5 or 10 (E10) %, with the levels rising up to 25 % in Brazil, a leader of ethanol production.

Biodiesels (specification **B**, designed for diesel engines) are formed by blending standard diesel with vegetable oil esters, typically in 20 % blends known as B20. Germany and France are currently world leaders in biodiesel production, largely due to well-structured national development schemes. Figure 1.7 shows the leading global producers of ethanol and vegetable oil based fuel, at the end of 2009 [20].

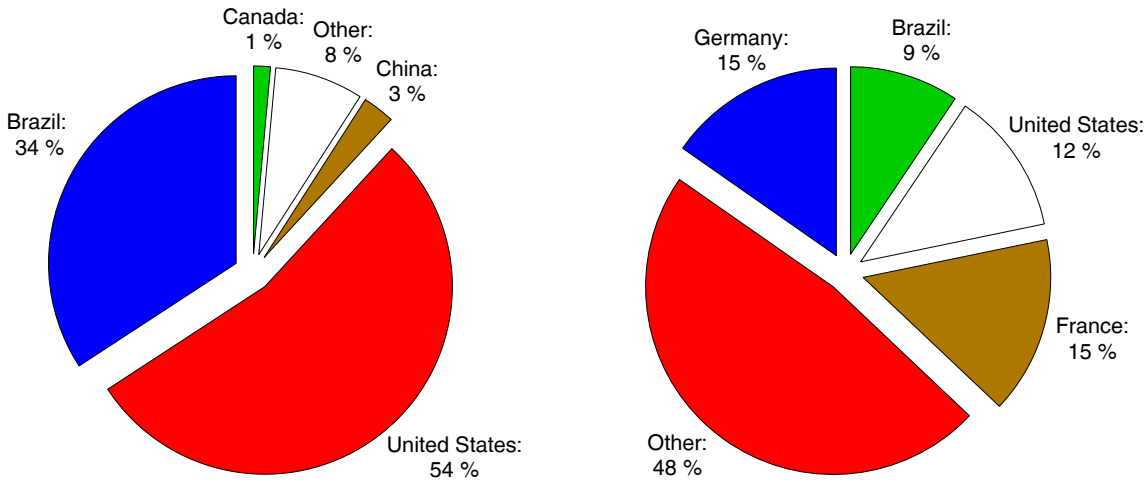

Figure 1.7: Top global producers of (*left*) bioethanol and (*right*) biodiesel at the end of 2009 [20].

Biogas is a mixture of methane and carbon dioxide prepared from the anaerobic digestion of biodegradable materials by methanogenic bacterial species [31]. As the feed-stocks usually include manures and wastes, biogas has historically served as a low-cost source of heating for rural communities. The byproducts of the anaerobic digestion further serves as fertilizers for agricultural use. Also known as landfill gas, biogas may contain carbon monoxide and hydrogen sulphide, thus requiring careful management to prevent free emissions to the atmosphere.

Second generation biofuels

The main disadvantage of the first generation biofuels is its inevitable disruption on the food economy and biodiversity. For first generation biofuels to remain on par with fossil fuel prices, it cannot avoid competing with local subsidiary food supplies, which is a major problem particularly for rural sectors.

Second generation biofuels is the collective term given to renewable fuels from non-edible food parts of plants. Some examples include residues of stems, leaves and husks; non-food crops such as jatropha; and agricultural wastes such as woodchips and fruit pulps. The final products of first and second generation biofuels do not always differ. Ethanol, for example, is extracted from the direct fermentation of corn and wheat in first generation bioethanols (free glucose); whereas second generation bioethanols require the additional task of extracting the locked glucose within non-edible cellulose, before conventional fermentation. This is no trivial matter, among numerous other technicalities, meaning second generation biofuels remain currently in the development stages. Among the second generation biofuels, only bio-oils are covered in this work. Bio-oil, also known as *pyrolysis oil* or *wood oil*, is a dark brown, free-flowing liquid originating from the thermal or biochemical conversion of woody lignocellulosic plants. Bio-oil is chemically heavy, with a high oxygen content between 45 - 50 % by weight. This oil is used as a substitute for diesel, as well as providing electricity when combusted in boilers, heaters and furnaces [32]. As a result of the complex structures of ligno-cellulosic biomass, several compounds are formed during the cleavage and fragmentation of the lignin, cellulose and hemicellulose during pyrolysis. These include, and are not restricted to: acids, alcohols, aldehydes, esters, ethers, ketones, phenols, furans, guaiacols, aromatics, syringols and sugars. The highest concentration of any single compound in bio-oil, besides water and hydroacetaldehyde, is formic and acetic acid, at ~ 3 % and ~ 5 % wt respectively [33].

Some other common second generation biofuels include,

- biohydrogen
- bioDME
- biobutanol
- Fischer-Tropsch biomass-to-liquid fuel

Both biohydrogen and bioDME are analogous to the existing technology in hydrogen fuel cells, and the usage of dimethyl ether in compression engines, except they are manufactured using biomass gasification methods. Biobutanol is an advanced, but less commercialized, form of bioalcohol, manufactured via ABE (acetone, butanol and ethanol) fermentation. Biobutanol displays high potential with respect to its superior energy content compared to ethanol. In addition, butanol/gasoline blends are less susceptible to immiscibility in the presence of water, than its ethanol/gasoline counterpart. Fischer-Tropsch fuels uses the Fischer-Tropsch (FT) gas-to-liquid technology, but applying it to cellulosic biomass to produce the syngas necessary for the main FT reaction [31].

Third generation biofuels

The concept of algae fuel, the third generation biofuel, was postulated as early as 1998 by the US Department of Energy [31]. Algae feedstock grown in artificial ponds does not interfere with the availability of arable land and agricultural resources for food crops. Microalgae has a high energy content, with some species containing an oil content of up to 80 % wt. on a dry basis [34]. This greatly exceeds most of the best oil-producing terrestrial plants. Furthermore, microalgae photosynthesizes sunlight in a much more efficient manner, leading to rapid growth rates. Early development of algae fuel was hindered by high costs, even when flue gas was used to provide the CO_2 for algae growth. Nonetheless, with the current trends in fossil fuel prices several magnitudes higher than that of last decade, algae fuel has gathered renewed interest as a viable form of alternative energy, notably as a diesel substitute (biodiesel).

1.5.2 The cases for and against biofuels

Biofuel is a double-edged sword. Each *n*th generation biofuel is manifested as a means of addressing inherent flaws found in the most recent predecessor. This section discusses some of the main advantages and disadvantages associated with the biofuels, starting with the former:

Reduction of greenhouse gases Carbon neutrality, is an idealized concept in which the net release of atmospheric carbon dioxide arising from a process or life cycle is zero. Biofuels is said to be *closely* carbon-neutral, since the majority of the CO_2 released in burning biofuels is recycled by the next generation of crops for growth, as depicted in Figure 1.8. Farming for biofuels enriches the soil fertility and reduces erosion, and any increase in soil organic matter greatly contributes to atmospheric CO_2 reduction. According to sources [1], an increase of 1 % in the soil organic matter level results in a reduction of over 40 tons of atmospheric CO_2 per hectare of farmland. Investigations on biofuel emissions show a significant reduction in other harmful constituents, such as CO and SO_x, which were responsible for the adverse health effects from petroleum.

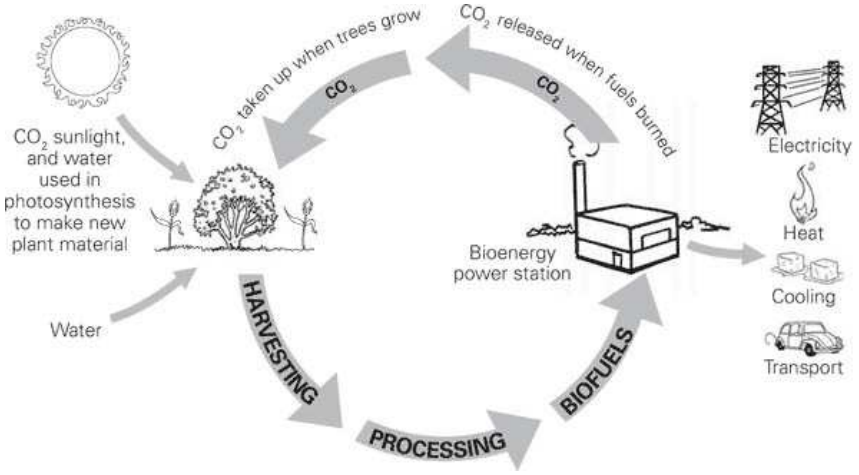

Figure 1.8: A standard carbon cycle, with biomass as the energy source, depicting the continuous return of atmospheric CO_2 to the energy plant (Source: State of New South Wales through the Department of Water and Energy).

Economy and security of energy Biofuels can be manufactured from common crops distributed throughout the world, thus relieving the pressure on many countries from Middle-Eastern imports. There is not one fixed type of feed-stock, meaning that there is potential for biofuel development in every part of the world. Biofuel stimulates the rural sector output, providing job employments and promoting the farming industry.

Waste disposal The production of biogas and bio-oils from agricultural waste - such as manures, wood chips, rice straws - provides an energy-efficient method of waste disposal. The byproducts of both processes return to the earth as valuable fertilizers.

It is worthwhile mentioning that while the implementation of biofuels is advantageous, largely due to tax benefits and subsidies, this is not an inherent advantage of the fuel itself. The following paragraphs outline biofuel disadvantages:

Remains carbon positive in several cases It is widely believed that the reported carbon saving of burning biofuels is often bolstered by omitting the carbon dioxide released in the production of the fuel. In several cases, the use of fossil fuels to power ethanol distillation plants and long-distance transportation of energy crops can actually *increase* the total greenhouse gas emissions. Corn, the pioneering energy crop of the United States, is no longer considered a major player in GHG reductions. By itself, it would reduce emissions from the transport sector by 10 % at most [35]. While other sources report slightly higher values for different parts of the world (12 - 14 %), many base their calculations on the assumption that corn is an 'indigenous' crop, which is far from reality [31]. In Figure 1.9, ethanol fuel derived from corn shows little or no savings on the CO_2 emissions per kilometre than coal

and gasoline/MTBE [36]. Second generation biofuels - biomethanol and cellulosic ethanol - do however show more promising results.

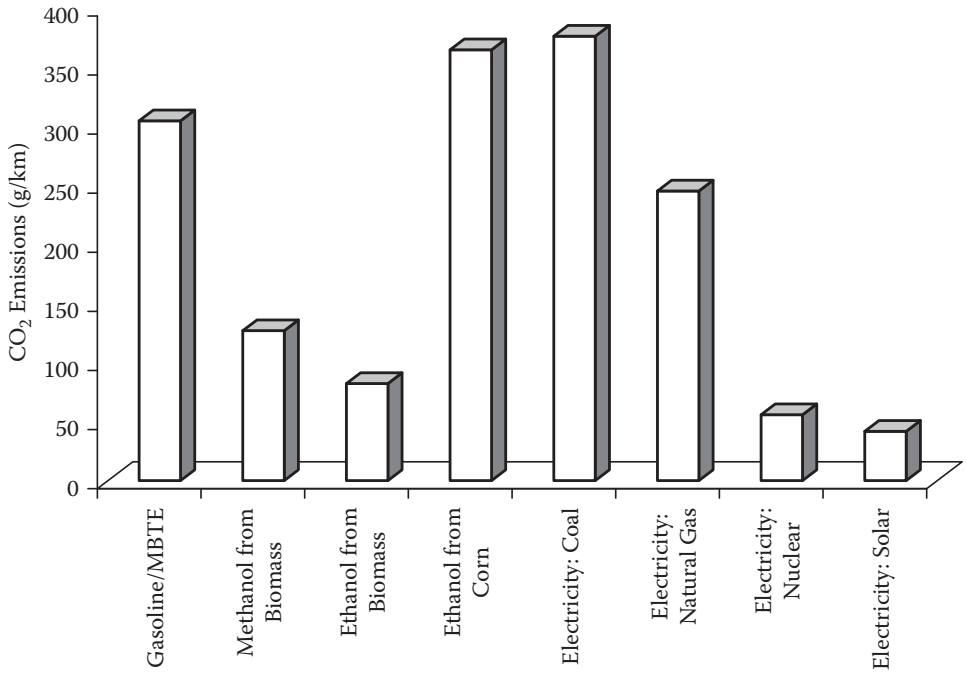

Figure 1.9: Comparisons of the total fuel cycle CO_2 emissions between corn ethanol and other forms of energy.

In general, bioethanols, when effectively reducing GHG emissions, do little to suppress the other harmful pollutants such as NO_x and particulates. Former Nobel Laureate Paul Crutzen, in a conservative study, stated that the release of nitrous oxide (N_2O) from biofuel production using high nitrogen content crops, such as rapeseed and maize, can in fact contribute 1 - 1.7 times more to global warming than the global cooling effect due to fossil-fuel saving. Crutzen highlighted this fact, as rapeseed is the source of 80 % or more of global bio-diesel production, especially in Europe [37]. More optimistic results were yielded with crops of lower nitrogen content (palm oil, grasses). Stump et al. [38] observed tailpipe emissions of a bioethanol powered vehicle, and observed that although some pollutants (CO, hydrocarbon, benzene, etc.) were reduced, formaldehyde and acetaldehyde emissions were almost doubled, both chemicals of which are highly toxic and carcinogenic.

Food supply As discussed previously, in order to meet the demands of the energy sector, energy crops have to compete with food crops for land, fertilizers, labour, infrastructures, etc [39]. In the US, the need to meet both demands from the food and energy sector has led the corn price to escalate, as shown in Figure 1.10, to the extent that unless an alternative source of ethanol extraction is found in due course, the US corn production will struggle in the forthcoming years [40]. The morality of putting foods, that could go to alleviate world hunger, into a motor vehicle, is indeed a bitter pill to swallow.

Alterations to the ecosystem The production of biofuels has often led to changes in land use and the replacement of native crops to energy crops. The search for fertile land for biofuel crops has resulted in deforestation and the clearing of grasslands, which originally store large amounts of carbon.

In conclusion, while biofuels is not all it seems to be, its vital feature is that the production is non-selective in the feed-stock. This makes it versatile enough to accommodate various difficulties, such was the objective of

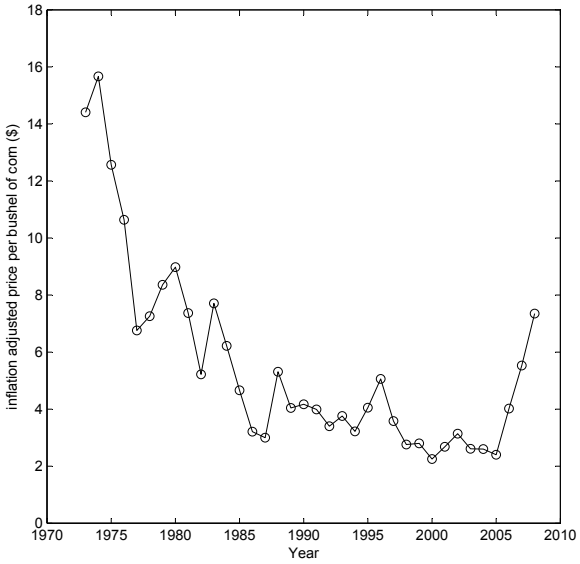

Figure 1.10: The real (inflated adjusted) price per bushel of corn in the US over the past thirty years, rising gradually again towards the end of 2008.

developing cellulosic, and other second generation biofuels. It is perhaps this, that is its strength above all other forms of renewable energies.

1.5.3 Bioethanol

Ethanol is fuel of choice of American motor pioneer Henry Ford, and not without justification. The octane number, a measure of the anti-knock property of the fuel, of pure ethanol is large, around 110. When ethanol is blended even in small quantities in gasoline as in E5 or E10, it brings a bonus of one to two indices to the octane number. Apart from having several properties similar to standard gasoline, the oxygenated molecules promote complete combustion of the fuel, and prevents emission of uncombusted hydrocarbons or partially oxygenated products, such as carbon monoxide [4].

While it is possible to produce ethanol from the catalytic hydration of ethylene [41], the most common method of ethanol production remains the fermentation of glucose from raw vegetation [42],

$$C_6H_{12}O_6 \longrightarrow 2C_2H_5OH + 2CO_2 \tag{1.3}$$

The reaction is dependant on several factors, such as the final ethanol quantity and the temperature, as well as the oxygen levels, minerals, and the optimal pH for the specific enzyme used. The reacting glucose is derived either from *sugary plants*, such as beetroot and sugar cane; or *common crops*, notably maize, wheat and barley. The latter types require a more involved process, as the sugars are not present in simple carbohydrates, but as polymeric starch molecules that needs to be hydrolyzed first in the presence of enzymes. The enzyme species *Saccharomyces* is currently the most exploited enzyme due to its superior adaptation in high alcoholic and low pH conditions. For both categories of raw materials, a yield of up to 92 % of the maximum theoretical yield, 51.1 %, can be achieved at an industrial scale [4].

The process of ethanol extraction from sugar plants is straight-forward, while two types of processes are present with regard to extraction from crops, namely wet and dry milling. The difference lies in that for wet milling, the feed for ethanol fermentation is the effluent of several sugar extraction processes preceding it; thus the quality of the ethanol depends on the demand of all preceding products. In general, all ethanol manufacturing processes

require a preparation stage, followed by the fermentation of glucose, the extraction of ethanol by distillation, and finally the removal of water by dehydration to yield the anhydrous ethanol (99.8 %). The preparation stages are all mechanical processes such as cleaning, pulping, and grinding of the raw material to free its sugars. Where crops such as maize are used as feeds, this would include an additional stage of enzymatic hydrolysis, known as liquefaction-saccharification, immediately after pulp grinding. This is followed by the fermentation stage, which takes place in cascades of fermenters in series. To maintain a high activity of the micro-organisms, weak aeration is supplied to the first two fermenters of the cascade. Agitation, in the form of stirrers, ensures homogeneity of the reactor contents, and maximizes the rate of fermentation. At the end of the fermentation stage, the enzyme culture is separated by centrifugation or filtration, and washed before being recycled to the head of the cascade. The ethanol, about 10 % in volume, proceeds to azeotropic distillation, where it is concentrated to a purity as high as the permitted by the azeotrope. The effluents from the distillation are concentrated by centrifugation and, depending on the type of raw materials used, returned to the earth as fertilizer, used as animal feed, or recycled to the start of fermentation. On the other hand, the ethanol moves to a final dehydration step, either carried out by azeotropic distillation with cyclohexane, or more commonly by pressure swing adsorption with molecular sieves, yielding the desired 99.8 % anhydrous ethanol. A schematic diagram of the dry milling process is shown in Figure 1.11 [4].

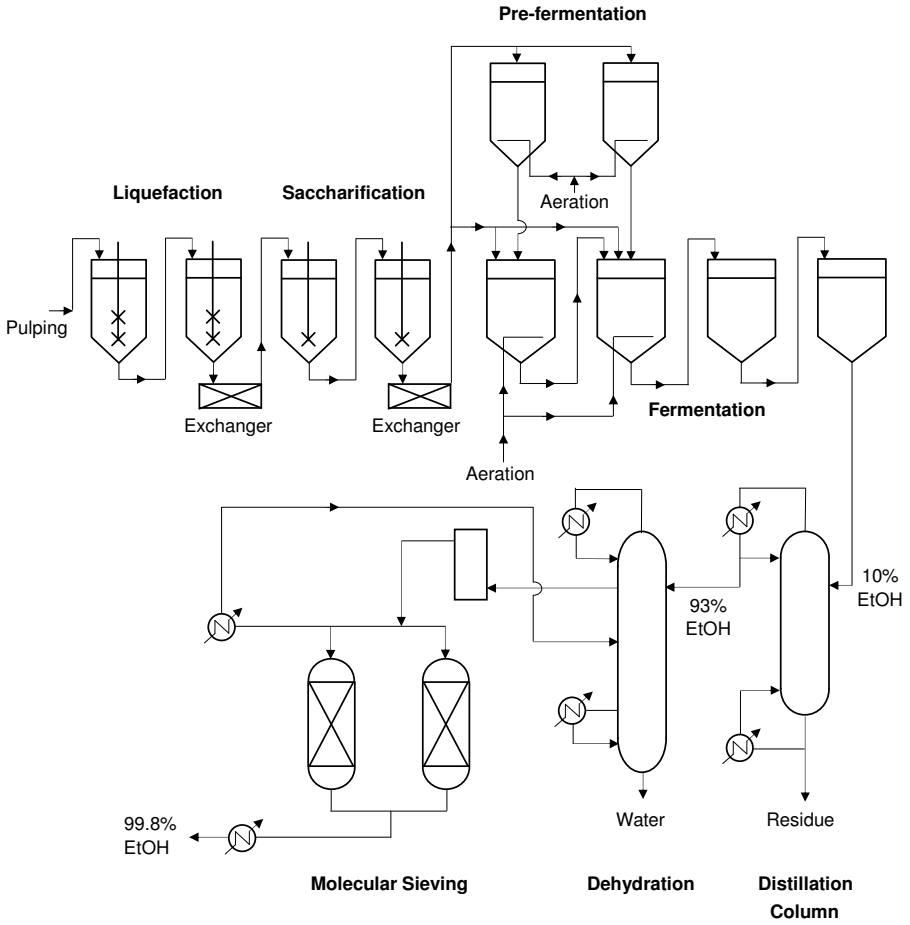

Figure 1.11: Process flow diagram of ethanol production via the dry milling process, using starch plants as a raw feed.

Currently, ethanol is still not blended in gasoline at more than 10 % in volume in several countries, and this is not without reason. The presence of ethanol results in many inconveniences [4]:

Fuel economy The large presence of oxygen, not encountered previously in standard gasoline, results in a lower overall energy content, and consequently an increased consumption of the fuel.

Azeotrope formation Mixtures of ethanol with light hydrocarbons (C_4 - C_6) form azeotropes, which increases the vapour pressure and its emissions thereof.

Cold-starts The high latent heat of vaporization provokes difficulties in its performance at colder conditions, particularly with regard to start-ups.

Immiscibility in water In the presence of water, at low temperatures, the phenomenon of liquid-liquid equilibria (LLE) can occur, where an ethanol-water phase separates from the hydrocarbon phase, resulting in a lowering of octane number.

Material compatibility The oxygen contents of the fuel has a tendency to form acetic acid by oxidation, resulting in incompatibilities with certain metallic materials and polymers.

Emission of aldehydes The combustion of ethanol emits formaldehyde and acetaldehyde, which has negative effects on humans.

The issue of volatility is a particularly serious one, and is illustrated in Figure 1.12. For a base gasoline of approximately 62 kPa vapour pressure, the increase in the vapour pressure of the gasoline increases proportionally with the addition of ethanol until 5 %. This increase diminishes thereafter, with the vapour pressure decreasing gradually and stabilizing for higher additions [43]. It has been shown that similar phenomenons result with base gasolines of varying vapour pressures [4]. With a 5-10 % incorporation of ethanol (E5 and E10), this would result in a worsening rate of emission by evaporation than that of pure gasoline. While using pure ethanol would appear to solve the problem, this would in contrast worsen the problem regarding cold starts. This problem is currently rectified in two ways; the first is to incorporate into a gasoline a compromise - a mixture of 85 % ethanol and 15 % light hydrocarbons (E85), instead of pure ethanol. The second method, more complicated, is the conversion of the ethanol into ETBE by isobutene. The latter approach has the added advantage of overcoming cold-starts.

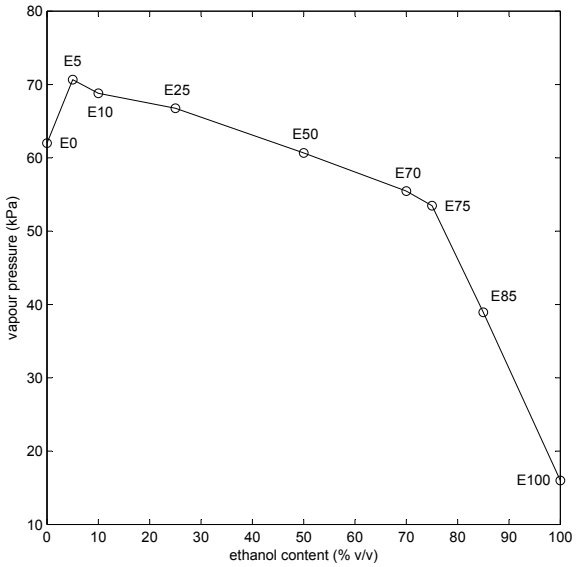

Figure 1.12: Diagram illustrating the relation between the vapour pressure of a generic gasoline and the percentage ethanol blended by volume [43]. The test temperature is approximately 313 K.

Table 1.5: Physical and performance properties of ETBE, pure ethanol and standard gasoline

	ETBE	Ethanol	Gasoline
Molecular Mass (g/mol)	102	46.07	102.5
C (wt %)	70.6	52.2	86.5
H (wt %)	13.7	13.1	13.5
O (wt %)	15.7	34.7	0
Density at 288 K (kg/m^3)	750	794	735 - 760
Latent Heat of Vaporization at 338 K (kJ/kg)	321	854	289
Boiling Point (K)	345	352	303 - 463
Research Octane Number	117	111	95
Motor Octane Number	101	92	85

The operating conditions (temperature, pressure, reactor residence time) of ethanol production are optimized to achieve the highest possible yield at the lowest energy cost. At the same time, care is taken to produce a product conforming to the criteria stated by the respective government legislations.

1.5.4 Ethyl *tert*-butyl ether (ETBE)

Ether-incorporated fuel has existed from as early as 1975, where methyl *tert*-butyl ether (MTBE) was first added to gasoline as a means of increasing the octane number and reducing the emissions of CO and benzene. Its use has since then faded, when findings exposing its slow biological degradation, and solubility in potable water resulted in its ban across the world. However, these drawbacks are not encountered when ethanol is transformed to ETBE; allowing it to reap both the benefits of MTBE and ethanol, while avoiding the setbacks of both. More importantly, ETBE is not carcinogenic, unlike MTBE [44]. The path of etherification of ETBE is identical to that of MTBE (Figure 1.13), although the current global production of ETBE is far from that of MTBE during its peak (about 0.6 Mt ETBE/yr

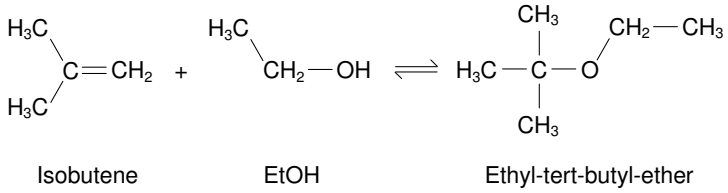

Figure 1.13: Synthesis reaction of ETBE from isobutene and ethanol

currently, compared to 20 Mt MTBE/yr at 1998). The etherification should be carried out below 353 K, where the equilibrium constant of ETBE formation is sufficiently high [45]. The by-products of the above reaction depend on the source crop of the ethanol, and the amount of water present during the reaction. Mostly, secondary reactions result in varying quantities of acetic acid, acetaldehyde, *tert*-Butanol, and diethyl-ether. Catalysts in the form of reticulated sulphur polystyrene is used. To prevent deactivation of the catalyst, the temperature and the pressure of the reaction is limited to 353 K and 3 MPa, respectively. Table 1.5 illustrates the close resemblance of ETBE to standard gasoline, along with properties also for ethanol [4],

Most of the industrial processes and units that manufactures ETBE today are derived from those originally designed for MTBE productions [4]. A process flow diagram for ETBE manufacturing is given in Figure 1.14. Prior to arrival of the reaction section of the process, the isobutene charge is cleansed with water to remove impurities that may be catalyst-poisoning. The ethanol and isobutene are then mixed before entering principle reactors, containing ion exchange resins that act as catalysts of etherification. This is followed by a debutanizer section, where ETBE is

separated from the isobutene and unreacted ethanol by catalytic distillation. The ETBE, which appears at the bottom of the debutanizer, will contain a little more than 1 % of ethanol, although this is unavoidable. The raffinate (distillate) of the debutanizer is further processed in a wash column, where water reduces the ethanol contents in the raffinate to less than 50 ppm, making it safe for downstream alkylation processes. The aqueous ethanol is taken from the bottom of the wash column to an ethanol recycling unit, where pure water at the bottom of the column is recycled for use in the wash column, and ethanol at the top returns to the initial charge lines of the process.

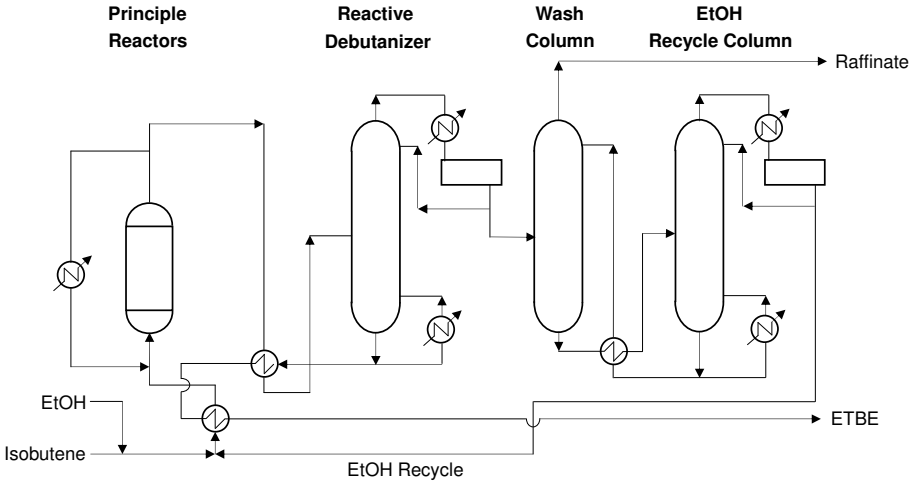

Figure 1.14: Process flow diagram of ETBE production.

1.5.5 Biodiesel and vegetable oil esters

First employed in 1900 by Rudolph Diesel, who used peanut oil to power his diesel engine, vegetable oil esters are the biomass-based substitutes of diesel. The oil is derived from a wide range of raw materials, usually plants (rapeseeds, sunflower, soya), but may also originates from animal fats. The choice of the feedstock depends on the cost, availability, government legislations, which in turn will affect the choice of process technology. The fatty acid esters blended into diesel (such as those in B20) are manufactured by transesterification of triglycerides, the main component of plant oil, the reaction of which is shown in Figure 1.15. The alkyl groups on the triglyceride may

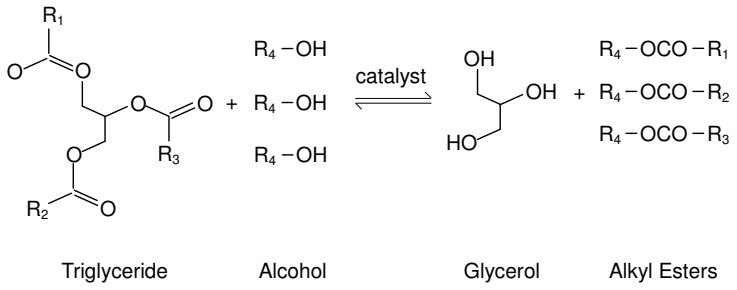

Figure 1.15: Transesterification reaction of alkyl esters from triglyceride and alcohol. R_i can be any alkyl group.

be the same, or all different, depending on the type of source plant. The transesterification is in fact a three stage process, with three different reaction rates, and enhanced by a catalyst [4]. The alcohol used is usually methanol due to its lower cost, forming *methyl* esters, although ethanol could also be used to yield *ethyl* esters. Heavier alcohols are possible, but not preferred due to steric hinderance. An excess of alcohol is used to achieve close to 99 % yield

Table 1.6: Comparison between a catalytic and non-catalytic approach in the transesterification of vegetable oils using methanol for the production of biodiesel.

	Catalytic method	Non-catalytic method
Catalyst	Alkali / Acidic	None
Reaction temperature (K)	< 500	523 - 573
Reaction pressure (MPa)	0.1 - 6	10 - 25
Reaction time (min)	0.1 - 6	10 - 25
Methyl ester yield (% wt)	96	98
Removal for purification	Methanol, catalyst glycerol, soaps	Methanol
Free fatty acids	Saponified products	Methyl esters, water

esters. Currently, alkali catalysts (KOH or NaOH) are almost always preferred over acidic ones since they have higher activity, and do not risk corroding industrial units. The methyl esters are viscous, heavy compounds with large carbon numbers ranging from 14 in methyl myristate ($C_{15}H_{30}O_2$) to 19 in methyl oleate ($C_{19}H_{36}O_2$). These are blended in petroleum diesel fuel containing non-branched saturated hydrocarbons of 12 to 18 carbon atoms.

Transesterification processes via methanol can be divided into two categories, depending on whether or not the reaction temperature exceeds the critical temperature of methanol. Whereas catalysts are always present in the case of subcritical transesterifications, it is not a prerequisite in supercritical transesterifications [46, 47]. Table 1.6 compares the general features between a subcritical catalytic transesterification, and a supercritical non-catalytic method [48].

The main variables affecting the yield of a transesterification reaction are reaction temperature, molar ratio of alcohol and oil, catalyst, reaction time, and the presence of moisture and free fatty acid [1].

The production of vegetable oil esters can be batch or continuous, although the former is usually older and less preferred, especially due to high operating costs. Continuous processes with homogenous catalysts have higher activity in the reactors, although the catalyst is lost in the process, and expensive post-processing stages are required. Heterogeneous catalysis, on the other hand, have the added advantage of less emission of pollutants, while being less cost-intensive in general. The continuous, heterogeneous catalytic process developed by the Institut Français du Pétrole (IFP) [49], uses a zinc aluminate catalyst ($ZnAl_2O_4$), and with the process in Figure 1.16. The mixture of methanol and vegetable oil, at a methanol:oil ratio of 0.35 - 0.50:1, is introduced in the first of two fixed-bed reactors in series. The temperatures and pressures of the reactors are set between 453 - 493 K and 4 - 6 MPa, the former due to the high activation energy of the catalyst. The effluent, which contains about 95 % methyl esters, is subjected to a partial evaporation to remove excess methanol, hence displacing the reaction equilibrium in the direction of product formation. The glycerol is separated from the esters via a sequence of decanters, exiting each time as the heavier product. After the second transesterification reactor, a distillation stage evaporates and fully recovers the methanol for recycling, while the bottoms are centrifuged to yield separately esters and glycerol each with a purity of at least of 98 %. A final step of purification of the methyl esters consists of the elimination of soluble glycerol by passing through a column of selective adsorbents.

The methyl esters produced industrially, from processes such as the one above, possesses characteristics that resembles standard diesel astoundingly well. Table 1.7 shows a comparison of the characteristics between diesel and methyl esters [4, 31].

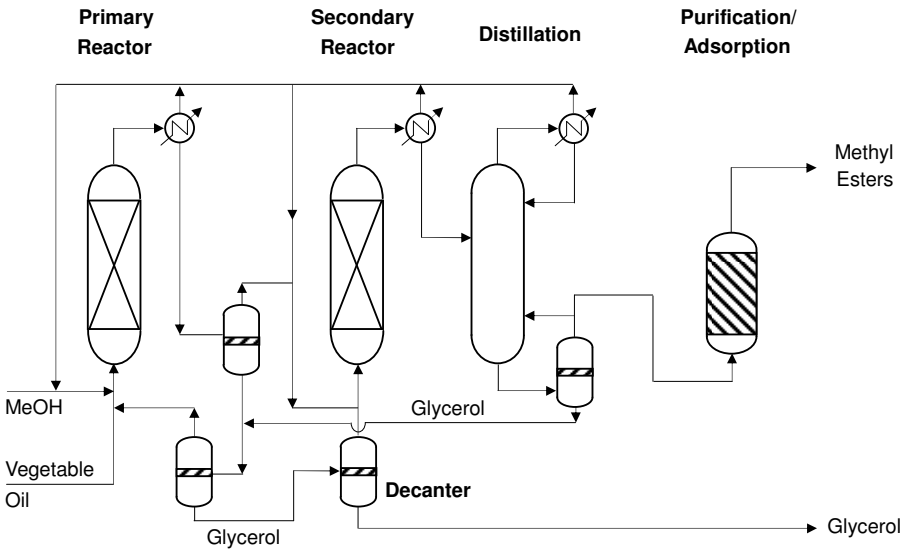

Figure 1.16: Process flow diagram of methyl ester production, as proposed by the Institut Français du Pétrole (IFP) [49].

Table 1.7: Comparison of the physical and performance properties between methyl esters and diesel.

	Methyl Esters	Diesel
Onset of volatilization (K)	343	343
End of volatilization (K)	523	533
90 % distillation temperature (K)	515	493
Density at 288 K (g/ml)	0.88	0.83 - 0.85
Viscosity at 293 K (mm^2/s)	7	5.5
Cetane Number	48 - 58	45 - 54
Flash Point (K)	443 - 453	$\geq$ 373
Cloud Point (K)	272	274

1.5.6 Pyrolysis Oil

In the context of biofuels, pyrolysis is a technology used for the thermal decomposition of cellulosic biomass, i.e. cellulose, hemicellulose and lignin, in the absence of oxygen. The product of the pyrolysis depends on the technique employed, as well as several parameters including the pyrolysis temperature, residence time, heating rate, particle size, etc [50]. Regardless, the thermal degradation of biomass always yields heavy liquid products, non-condensable gases (CO, CO_2, H_2, saturated and unsaturated C_1 - C_3 hydrocarbons [51]), solid char, water and ashes. Slow pyrolysis[4] is characterized by low heating rates, with reported rates usually around 5 - 30 K/min [52, 53, 54]. Therefore, slow pyrolysis occurs over a longer period of time and favours the production of solid char (biochar), as well as a small yield of liquid (pyrolysis oil). Fast pyrolysis has employed heating rates from 300 K/min to even 10000 K/s, resulting generally in higher liquid yields up to an increase of 10 % compared to that of slow pyrolysis [52, 54, 55]. The design considerations for different feed-stocks and impact of the process variables on the pyrolysis oil properties have been extensively discussed in literature [32, 51, 52, 53, 54, 56, 57, 58].

[4]The terms 'slow' and 'fast' pyrolysis are arbitrary as there is no clear definition of the boundary of the heating rate between the two. Intermediate heating rates, those that lie between commonly employed heating rates of slow and fast pyrolysis, could be used [32].

In this work, one is interested in the principal associating compounds found in pyrolysis oils, a fluid regarded as a petroleum substitute. Due to the extreme complexity of lignin, a complete characterization of pyrolysis oil is impossible using gas or liquid chromatography [57]. Approximately 300 organic compounds have been identified to date, which can be classified broadly as acids, alcohols, ketones, aldehydes, phenols, ethers, esters, sugars and furans. Prior to the characterization of pyrolysis oils, the oil is fractionated into separate, analyzable fractions. This is done either using water and diethyl-ether with filtration (Figure 1.17 [59, 60]), or using a silica-gel packed column eluated with *n*-pentane, toluene, ether and methanol to separate into different fractions corresponding to each functional group [61].

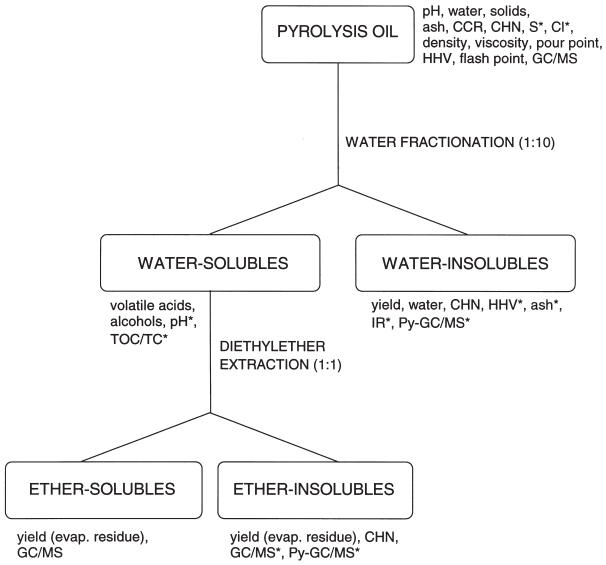

Figure 1.17: Fractionation scheme with basic and additional analyses for pyrolysis oils, using water and vacuum filtration. Additional analyses are marked with an asterisk [60].

The preceding sections encompassed three important functional groups occurring in oxygenated compounds, namely alcohols, water (bioethanol), ethers (ETBE) and esters (biodiesel). It is hereby noted three further functional groups that are relevant to the study, shown in Table 1.8, choosing in each case major components of pyrolysis oils [62].

In addition, multi-functional compounds spanning several functional groups are frequently encountered. These compounds are complex, often containing one or more oxygenated branches. Figure 1.18 gives the molecular structures of three instances in furfural, glycerol and phenol. The modeling approach to these compounds proves a challenging and interesting task that will be examined in later chapters.

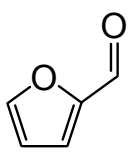

(a) Furfural

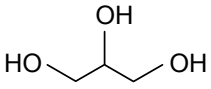

(b) Glycerol

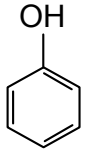

(c) Phenol

Figure 1.18: Molecular structures of three typical multi-functional compounds encountered in pyrolysis oil.

Table 1.8: Oxygenated functional groups found in pyrolysis oils, along with the compounds present in the highest percentage.

Functional group	Molecular structure	Compounds	% wt weight[a]
Carboxylic acids	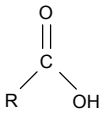	Formic acid Acetic acid	0.3 - 14 2.1 - 11
Aldehydes	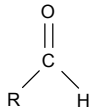	Formaldehyde Acetaldehyde	0.3 - 14 0.01 - 2
Ketones	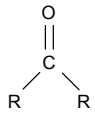	Acetone 2-Butanone	0.01 - 0.21 0.01 - 0.46

[a] based on wet liquid

1.6 Thermodynamics in biofuel research: an example

Thermodynamic calculation in phase equilibria plays a defining role in the design of chemical processes. A clear understanding of the distribution of materials between co-existing phases is particularly vital for the dimensioning of separation units. Since more than 40 % of the total energy cost of a chemical plant comes from separation activities alone, this is an area with a minimal margin for error.

In thermodynamics, there is a fine balance maintained between *experimental* data and *theoretical* models. These tools, by themselves, are no more that their name implies - data are merely discrete, momentary observations of a behaviour dependant on the individuals' judgements and the equipment precision; while models are theoretical at best, and are as true as the fundamentals that underlie its development. However, when applied in tandem, data and model form a powerful partnership that enables understanding of the behaviour of fluids.

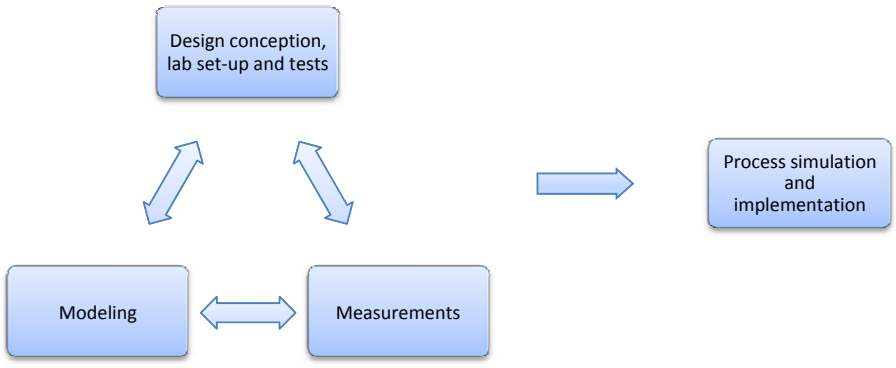

Figure 1.19: Strategy cycle for the design of processes, starting from the conception of ideas to the final implementation of the process.

Process design is a cyclic strategy starting with the conception stage, where one evaluates the vital components needed to accomplish an objective. In the context of unit operations, this objective may be anything from the simple mixing of two liquids, to the catalytic reaction of products formation, to the separation of effluent streams for recycle.

In the foremost conception stage, it becomes understood the necessary disciplines for achieving the objective, as well as the vital decisions, in terms of data and model selection, required for designing the process. In the absence of information, laboratory-scale tests and pilot-plants are setup to perform experiments in order to obtain such data. The experimental data are used to develop or 'fine-tune' the new, or available, models. The adapted model may, or may not, contain all the necessary information for the satisfactory description of the process. At this stage one needs to evaluate the possibility of additional measurements - either of the same type, at different conditions, or completely new properties - thus resulting in revisits of previous stages. This strategy is shown in Figure 1.19, and terminates with the simulation of the process and its implementation.

Cubic equations of state (EoS) such as Peng-Robinson (PR, [63]) and Soave-Redlich-Kwong (SRK, [64]) remain models of choice in petroleum industries, where they excel in multicomponent hydrocarbon mixtures. There are, however, doubts whether its simplified fluid theory would be able to address new molecular interactions brought upon by oxygenated biofuel components. Let us consider the case of ethanol in mixture with the petroleum compound benzene, and with the gasoline alternative ETBE. Experimental data for the corresponding binary pairs are taken from Oh and Park [65]. The data for each binary pair are used to optimize, where specified, adjustable binary interaction parameters for three variants of the PR EoS, each differing in complexity. For each case, the original unmodified form of the Peng-Robinson equation of state is used. One denotes **PR0** for the PR EoS with the interaction parameter set to zero; **PR** for the PR EoS with an adjusted interaction parameter arising from the van der Waal's one-fluid mixing rule (k_{12}); and **PR-WS-NRTL** for the PR EoS with the Wong-Sandler mixing rule [66] coupled with the NRTL g^{E} function [67] ($k_{12}, \tau_{12}, \tau_{21}$)[5]. Figure 1.20 shows comparisons between each of the different forms of the PR EoS, for each of the binary pairs.

At this stage, it is necessary to define the terms *correlation* and *prediction*, which in this work hold different meanings. *Correlations* refer to model representation of properties, where the properties have previously been the subject of optimization to 'fine-tune' the model, in an attempt to reproduce as closely as possible the same properties. *Predictions* of properties are model representations carried out without having any prior knowledge or information of the properties themselves. A calculation is also considered a prediction if the model used is correlated to some alternative properties which have little or no connection with the properties being calculated.

Referring to Figure 1.20, it is clear that, without adjusted interaction parameters, PR0 cannot predict non-idealities exhibited by oxygenated systems (black lines). Even with the aid of a single interaction parameter from the van der Waals one-fluid mixing rule (k_{12}), the correlation between model and data is only satisfactory for the most ideal of the three systems (ETBE + benzene). The erroneous calculations of the minimum-boiling azeotropes render PR impractical for simulation purposes. The multi-parameter PR-WS-NRTL, containing more flexible mixing rules, is more versatile. The increase in the number of binary interaction parameters improve markedly the correlation, as shown by the red lines, although this is expected of the sheer large number of adjustable parameters. These interaction parameters, among with the previous models, are displayed in Table 1.9. An inspection of the magnitude and sign of the parameters provide some evidence in the manner in which specific intermolecular forces were treated by the PR EoS. These are given as below:

- Abnormally high τ_{12} and τ_{21} values within the NRTL g^{E} function, in the excess of 2, are usually indications of specific intermolecular forces. These forces, not explicitly accounted for in the EoS, are compensated by larger parameters. In this case, ethanol is present as a strong self-associating compound possessing a dipole moment [69], leading to hydrogen bonding and dipolar forces.
- The solvating system ETBE + ethanol can only be aptly described with either negative k_{ij} or τ_{ij} values. This is due to the inability of the London theory of dispersion forces to describe strong cross-energy interactions [70].

A further shortcoming not apparent in the above binary calculations is the heavy temperature dependence of the interaction parameters. The large number of adjustable parameters in the PR-WS-NRTL cannot be extrapolated

[5]There is a fourth adjustable interaction parameter α when using the NRTL g^{E} function, although this is fixed at 0.3 for this example.

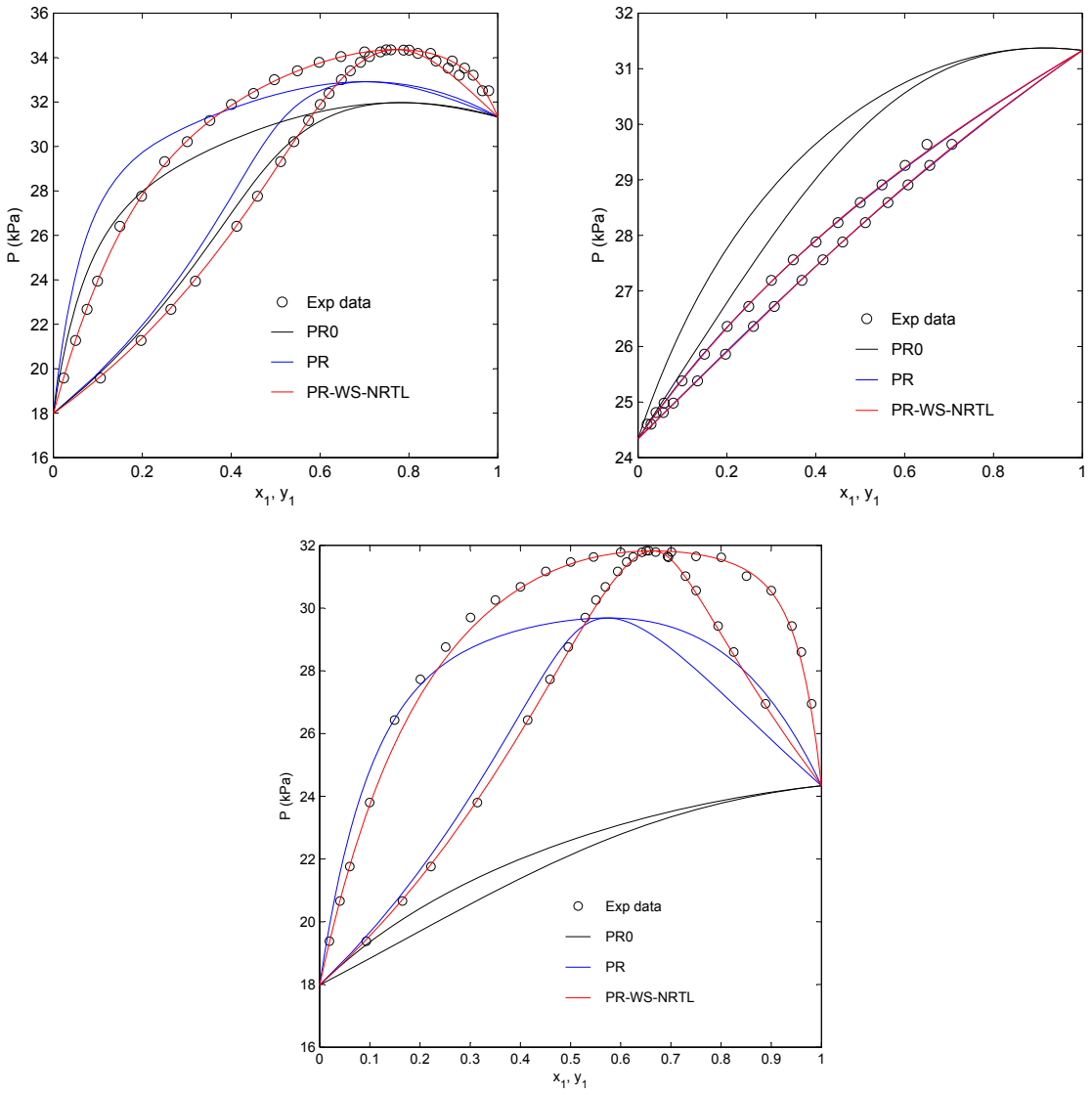

Figure 1.20: Vapour-liquid equilibria modeling of three binary systems, using forms of the PR EoS of varying complexities, along with experimental data (○) at 313.2 K taken from Oh and Park [65]. *Top left*: ETBE + ethanol; *Top right*: ETBE + benzene; and *bottom*: ethanol + benzene. In all cases, black lines are calculations using PR0, blues lines using PR, reds lines using PR-WS-NRTL. Pure parameters for the models are taken from [68].

Table 1.9: Dimensionless binary interaction parameters for three variants of the PR EoS of increasing complexity, for the systems ETBE (1) + ethanol (2); ETBE (1) + benzene (3); and ethanol (2) + benzene (3). The models were fitted to experimental data from Oh and Park [65] using a flash type algorithm[a].

Model	k_{12}	k_{13}	k_{23}	τ_{12}	τ_{21}	τ_{13}	τ_{31}	τ_{23}	τ_{32}
PR0	0	0	0						
PR	-0.012	-0.016	0.067						
PR-WS-NRTL	0.41	0.22	-0.41	2.7	-1.1	-0.23	0.082	2.51	-0.22

[a] Objective function $F = \sum \left|\left(x_{exp} - x_{cal}\right)/x_{exp}\right| + \left|\left(y_{exp} - y_{cal}\right)/y_{exp}\right|$

across wide temperature ranges, thus several isothermal measurements are required in order to get a clear picture of the evolution of the parameters with temperature. For ease of usage in process simulations, a model with fewer parameters and extrapolative properties is usually preferred.

In conclusion, cubic EoS such as the PR-WS-NRTL remain feasible choices for modeling phase equilibria of most systems containing oxygenated compounds. Nonetheless, this work focuses on an alternative approach, based on more theoretically sound fluid theories, to tackle this problem. In order to understand the reasons as to why the cubic EoS are less adapted in dealing with oxygenated compounds, it is necessary to first understand the underlying intermolecular potentials of these models, and the fluid interactions which are present. This knowledge, which is covered in detail in the next chapter, justifies the selection of new strategies in the approach of this modern problem.

1.7 Industrial context and thesis objectives

Biofuel research, regarding lignocellulosic types, is a revolutionary science in need of modern tools capable of characterizing complex molecules and their behaviour. The search for such tools currently branches into three areas of expertise. The first is through molecular simulation, usually Monte Carlo ensembles, to predict thermodynamic properties and fluid phase equilibria. The second is using *ab initio* quantum chemistry methods, typically the COSMO (COnductor-like Screening MOdel) models and its variants COSMO-RS [71] and COSMO-SAC [72], which predicts phase equilibria well. Both these two methods allow the characterization of compounds in the absence of experimental data. This thesis is concerned with the third approach, i.e. conventional equation of states with a heavy reliance on molecular thermodynamics, addressing directly the underlying molecular interactions. A common notion among all the above methods is the emphasis placed on interactions on a microscopic level, a subject which has often been overlooked in the past and addressed with approximate means.

The use of equation of states, as described in § 1.6, requires experimental data - those useful not only for industrial design, but also for the development of models. A lack of data may appear for more unfamiliar compounds, such as those shown in Figure 1.18, but in fact this deficiency extends even to systems containing compounds which are not uncommon in industries. As an example, we take an advance on Chapter 3 results to illustrate, in Figure 1.21, the vapour-liquid equilibria predictions for the toluene (1) + acetic acid (2) system using the modified UNIFAC (with database from the Dortmund data bank [73, 74]) and PSRK (Predictive Soave-Redlich-Kwong [75]).

Failures of the predictive models such as those shown in Figure 1.21 are often an indication of the lack of experimental data present during the development of the predictive terms of the model. The above experimental data from Zawidzki [76] have been repeated in the duration of the thesis with good agreements. The need for reliable experimental data remains strong. This thesis focuses on experimental measurements of phase equilibria (Chapter 3), and critical points (Chapter 4) as means of acquiring data necessary in the field of biofuels.

This thesis investigates the capabilities of the Perturbed-Chain Statistical Associating Fluid Theory (PC-SAFT) equation of state in the field of biofuel modeling. Although no longer a recent approach, the PC-SAFT EoS remains a powerful tool versatile enough to account for the several quasi-chemical forces that cubic EoS do not. If applied correctly, the PC-SAFT, without any group contribution modifications, borders on being predictive, and have recently been implemented in commercial simulators such as AspenPlus™ and ChemCad™. In the two modeling chapters that follow, the PC-SAFT is employed not only in modeling the measured experimental data, but also extends to systems of other oxygenated compounds, presenting a systematic study of biofuel mixtures. Chapter 5 examines in turn possible ways to apply the PC-SAFT EoS to a wide range of oxygenated compounds, focusing mainly on fluid phase equilibria, before diverting the reader's attention to excess enthalpies and consistency testings. In Chapter 6, the PC-SAFT EoS is used to model the measured binary critical data, with the aid of White's renormalization group theory for mixtures. This recent development accounts for the long-range density fluctuations at the critical region, which are otherwise omitted by classical equations of states. The results of the thesis is relevant to current industrial partnerships, such as the French projects MEMOBIOL and NESOREACH.

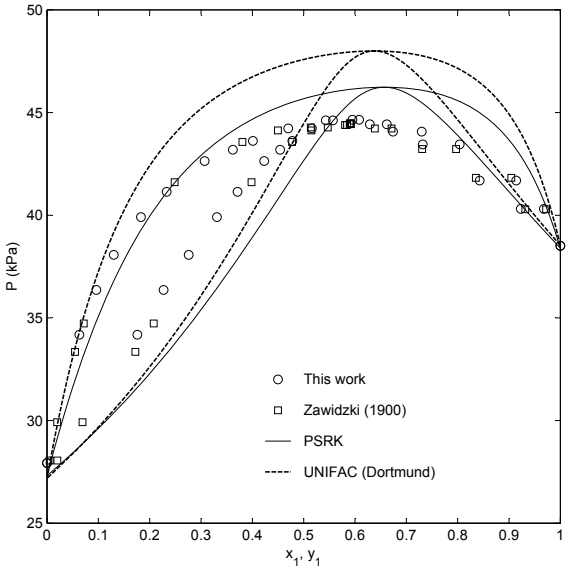

Figure 1.21: Predictions of vapour-liquid equilibria for the binary system toluene (1) + acetic acid (2) at 353 K using the PSRK EoS and the modified UNIFAC (Dortmund) model. Experimental data (•) taken from Zawidzki [76].

To understand the modeling approaches chosen for this work, it is vital to understand the concept of *real fluids* and its behaviour on a microscopic level. This is the subject of the next chapter.

CHAPTER 2

Fundamentals of the Perturbed-Chain Statistical Associating Fluid Theory (PC-SAFT)

On the particles of a gas no forces act; on the particles within a liquid the forces neutralize each other. In both cases the motion will go on undisturbed so long as no collision occurs.

- Johannes Diderik van der Waals (1837-1923)

Les Bases Fondamentales de Perturbed-Chain Statistical Associating Fluid Theory (PC-SAFT)

Contrairement aux gaz parfaits, les fluides réels contiennent des molécules qui interagissent les unes avec les autres au moyen d'interactions spécifiques. Ce comportement devient de plus en plus complexe avec la présence de molécules oxygénées, ces dernières permettent des interactions supplémentaires, telles que les liaisons hydrogène. Ce chapitre expose l'état de l'art sur l'équation d'état PC-SAFT (Perturbed-Chain Statistical Associating Fluid Theory), qui a été identifiée comme fiable dans le domaine de la modélisation des composés oxygénés et associatifs. Dans son développement PC-SAFT prend en compte la mécanique statistique ainsi que la thermodynamique moléculaire. Il en résulte un modèle de l'énergie libre de Helmholtz, répondant aux problmès dus aux nombreuses non-idéalités présentes.

Pour tirer tous les avantages de cette équation, il est impératif de comprendre et surtout de tenir compte des différents types d'interactions moléculaires présentes dans les fluides réels. Ces dernières sont discutées en début de ce chapitre. Une molécule mise en présence d'une deuxième molécule se trouve soumise à des interactions attractives et répulsives. La puissance de ces interactions dépend de la distance entre les centres intermoléculaires, et de l'orientation des molécules. La structure atomique de la molécule joue un rôle important dans la détermination des types de forces d'attraction présentes. Alors que les forces répulsives ne sont pas parfaitement bien comprises, les forces d'attraction sont divisées en deux types : physiques et chimiques. Les forces physiques sont de nature électrostatique, et se produisent sur de longues distances. La forces de London (dispersion) sont communes aux forces de Van der Waals, elles sont proportionnelles à la valeur de la polarisabilité et des potentiels d'ionisation de la molécule. Les molécules polaires possèdent un dipôle électrique qui introduit des interactions additionnelles, telles que les forces de Keesom (dipôle-dipôle), et les forces de Debye (dipôle-dipôle induit). Ces forces sont importantes dans les composés oxygénés, notamment dans les cétones et les aldéhydes, qui possèdent de forts moments dipolaires.

La liaison hydrogène est considérée comme une force chimique ou quasi-chimique. Aussi connue que la force d'association, la liaison hydrogène se produit sur une courte distance, mais elle est souvent plus forte que les forces physiques et électrostatiques. Les liaisons hydrogène sont responsables de la formation de polymères et de complexes, qui confèrent des comportements particuliers aux propriétés de corps purs des composés fortement associés, comme les alcools et les acides. Un objectif principal de ce travail est l'application d'un modèle thermodynamique qui tient compte en particulier des forces associatives.

Dans le cadre de ces modèles thermodynamiques, les interactions entre les molécules sont simplifiées par des fonctions de potentiel intermoléculaire. Bien que mathématiquement simples, les expressions conservent dans une certaine mesure le comportement physique entre les molécules. Lorsqu'elles sont utilisées avec la fonction de distribution radiale en thermodynamique statistique, les fonctions de potentiel intermoléculaire conduisent à la détermination des principales propriétés thermodynamiques des fluides : corps purs et mélanges. Les fonctions de distribution radiale sont cependant complexes et ne peuvent être résolues facilement pour les fonctions de potentiel intermoléculaire les plus rigoureuses. En utilisant la théorie de perturbations, Zwanzig, et Barker et Henderson, ont reformulés le problème comme un développement de l'énergie libre de Helmholtz. Cette technique utilise seulement les expressions les plus simples de la fonction de distribution radiale et des fonctions de potentiel intermoléculaire. Le résultat est une forme générale de l'équation d'états non-cubique de l'énergie de Helmholtz.

L'équation d'état PC-SAFT, développée par Gross et Sadowski, est une équation d'état écrite comme un développement des perturbations de l'énergie libre de Helmholtz. Dans ce développement, chaque terme de l'énergie de Helmholtz contribue à une interaction spécifique. Ces contributions sont examinées en détail dans ce chapitre. Les interactions entre les monomères de sphères dures sont décrites par l'expression de Boublík et Mansoori. La contribution prenant en compte les interactions associatives entre composés oxygénés est basée sur la théorie des perturbations thermodynamiques de premier ordre, développée par Wertheim. La contribution de la chaîne mis au point par Chapman prend en compte le facteur de taille de la molécule en formant des chaînes de monomères simples. Le terme de dispersion de Gross et Sadowski décrit les interactions de dispersion entre les chaînes, en utilisant un potentiel de type Lennard-Jones. Une revue bibliographique des différents types de contributions dipolaires utilisées dans ce travail est également donnée.

Equations of states (EoS) remain an active field of research, largely due to its wide applicability in chemical and related industries. Non-empirical EoS allow both correlations and predictions of thermodynamic properties and phase equilibria of pure and multi-component systems, giving them a large role in chemical process design and simulation. While no single EoS exists that can handle all engineering purposes, its development has branched to dedicated areas of research, including non-ideal, highly polar systems, electrolyte mixtures, polymers, and supercritical fluids. An equation of state that is true to its application has several advantages. It can be used for a wide range of temperatures and pressures, from light gases to heavy fluids, and perform equilibrium calculations of any phase combination in a natural manner. The fundamental thermodynamic relations, to which all fluid properties are bounded to, can be derived from a succinct set of expressions, making EoS a powerful tool in chemical engineering.

Over the years, the progress in chemical technology has ensured that EoS evolved to meet new challenges. One of the most pertinent advancements has been the incorporation of statistical mechanics and molecular theory in the development of equation of states. With the improvements in computing power, it is now possible to bridge, albeit not completely, the gap between the macroscopic fluid and its microscopic properties. These theoretically-based equations of states are highly accurate for real fluids and mixtures, and are central to the approach in this thesis. Contrary to ideal gases, molecules of a real fluid exhibit volume and interact with atoms of neighbouring molecules. These specific interactions impart unique properties to fluids, such as elevated melting points, polarity, pH changes, etc, that could not be accounted for otherwise. Intermolecular forces provide a useful, and often, only explanation for the state of existence of matter.

The aim of the chapter is to introduce the principles and theories underlying the Perturbed-Chain Statistical Associating Fluid Theory (PC-SAFT), a model which lends its basis from statistical and molecular thermodynamics. The layout of the chapter is a systematic buildup to the final form of the model as it is known today, and provides some light for its selection for this work. As a model concerned with interactions between free moving molecules, the chapter begins with a review of intermolecular forces in nature - those which are physical and quantifiable, and those which are quasi-chemical and specific. In equations of states, the repulsion and attraction between molecules are simplified to intermolecular potential functions - empirical expressions that can be coupled with radial distribution functions to impart knowledge of the local fluid density. The perturbation theory is shown to be a powerful tool for addressing complex radial distribution functions, leading to expressions for the Helmholtz free energy. The different contributions to the Helmholtz energy in the PC-SAFT EoS are then reviewed, before formulating the procedure for the model parameterization that will be used throughout this work.

2.1 Intermolecular forces in nature

Atoms, whether viewed as hard or soft spheres, obey the repulsive-attractive relation at a microscopic level. Two molecules attract each other when they are far apart, and repel each other when they are brought close together. All molecular interactions are thus governed by the distance r between intermolecular centers. The function between the force $F(r)$ and the potential energy $u(r)$ of interactions is commonly expressed as,

$$F(r) = -\frac{du(r)}{dr} \tag{2.1}$$

where the total potential $u(r)$ can be decomposed into a repulsive and an attractive part,

$$u(r) = u_{repulsive}(r) + u_{attractive}(r) \tag{2.2}$$

Intermolecular potentials play a particularly important role in the calculation of second virial coefficients, which describe the interactions between pairs of molecules. A functional form of Eqn. (2.2) requires mathematical simplicity, while accounting for the necessary contributions on the right-hand side. The attractive forces, in particular, of polar, oxygenated molecules are more involved than non-polar ones, and cannot always be handled with a mean dispersive field.

2.1.1 Physical forces

Physical forces are electrostatic in nature, arising from unequal distribution of point charges on a molecule. Among non-ionic molecules, van der Waal's forces dominate the physical attractions, i.e. dispersion (London), dipole (Keesom), and dipole-induced dipole (Debye) forces. These interactions occur over long ranges, but are weaker than chemical forces.

The contribution of different physical forces among strongly and weakly polar molecules can be demonstrated by considering separately, molecules of toluene and of acetone in vacuum. Quantitatively, the total physical force between two identical molecules of toluene and acetone are the same, with the negative sign denoting an attraction (Fig. 2.1 *left*). The makeup of the total forces are, however, vastly different in each case (Fig. 2.1 *right*), which would have an effect in their modeling approach. We refer to this example in the review of physical forces.

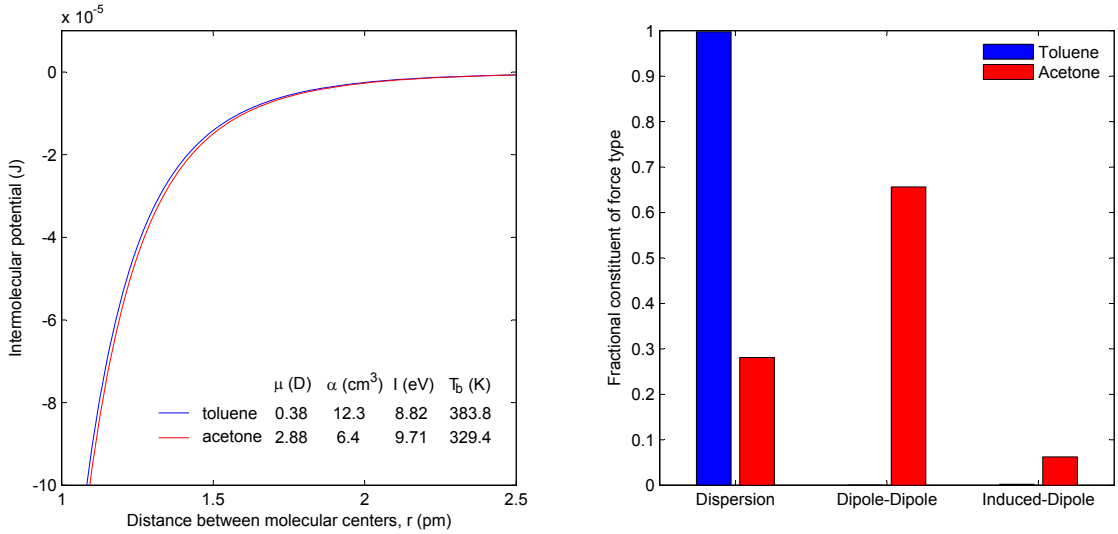

Figure 2.1: *left:* Physical attractive forces between pairs of toluene molecules and pairs of acetone molecules. Quantitatively, the two substances exert almost the same force between themselves. Electrostatics data are taken from Lide [77]. *right:* Fractional constituents of the total force between toluene and acetone molecules.

Dipole-dipole (Keesom) forces

Polar molecules are electrically neutral, but possess an electric dipole due to the asymmetry and orientation of the molecule. The potential energy between two permanent dipoles i and j depends on the distance between the dipole centers and the dipole axes orientation. Hirschfelder et al. [78] derived an average dipole-dipole potential by statistical averaging over all orientations of charge distribution:

$$\bar{u}_{DD,ij} = -\frac{2}{3}\frac{\mu_i^2\mu_j^2}{(4\pi\epsilon_0)^2\, kTr^6} \tag{2.3}$$

or between two identical dipoles of the same type of molecule:

$$\bar{u}_{DD,ii} = -\frac{2}{3}\frac{\mu_i^4}{(4\pi\epsilon_0)^2\, kTr^6} \tag{2.4}$$

Quantity μ is the permanent dipole moment of the charge distribution, ϵ_0 is the electric permittivity of vacuum and k is the Boltzmann's constant. Dipole-dipole forces are inversely proportional to temperature, and are particularly important at low T. Furthermore, these forces are proportional to the fourth power of the dipole moment; thus have a

profound effect in charged molecules with μ larger than one. Nonetheless, point charge effects are subject to dilution in large molecules. An appropriate measure of the intensity of the dipole effect is given by:

$$\text{Dipole intensity} = \frac{\mu^2}{\text{molecular volume}} \tag{2.5}$$

Therefore, the larger the molecule, the less important are the dipole effects.

In Fig. 2.1, the dipole-dipole forces are felt strongly by acetone, which has a dipole moment of 2.88 D [77]. In the modeling of acetone and its mixtures, the dipole-dipole interactions must be accounted for explicitly. On the contrary, toluene's dipole moment of 0.45 D explains why weakly-polar compounds may be modeled as a non-polar molecule with minimal losses of accuracy.

Dipole-induced dipole (Debye) forces

Both polar and non-polar molecules may experience an induced, temporary dipole moment when subjected to an external field. Such induced dipole moment μ^i is proportional to the field strength E,

$$\mu^i = \alpha E \tag{2.6}$$

where α is known as the polarizability of the molecule, i.e. the ease in which the electrons of a molecule may be displaced when introduced to an electric field. Although polarizability is an intensive variable, Debye forces occur only in the presence of a permanent dipole, which acts as a field inductor. Debye derived the expression for the mean potential energy due to the induction of permanent dipoles:

$$\bar{u}_{ID,ij} = -\frac{\alpha_i \mu_j^2 + \alpha_j \mu_i^2}{(4\pi\epsilon_0)^2 r^6} \tag{2.7}$$

or between two identical molecules:

$$\bar{u}_{ID,ii} = -\frac{2\alpha_i \mu_i^2}{(4\pi\epsilon_0)^2 r^6} \tag{2.8}$$

Dipole-induced dipole forces are scaled more importantly by the dipole moment μ than the polarizability α, making them negligible in weakly-polar molecules. That being said, the contribution of Debye forces in a strongly-polar molecule such as acetone remains modest, accounting for only 6 % of the total attractive force for acetone in Fig. 2.1. Induced dipole interactions are the weakest van der Waal's forces, and are also assessed in relation to molecular size. The inclusion of the dipole-induced dipole effects in modeling polar molecules is a rigorous, albeit not always rewarding, approach.

Dispersion (London) forces

The above discussions confirm that dispersion forces, and not permanent dipole forces, are responsible for the attractions between non-polar and weakly-polar molecules. Dispersive interactions are based on quantum mechanical effects, and originates from temporary dipoles induced by instantaneous separation of charges from the oscillation of the electrons about the nucleus. This dipole moment rapidly changes magnitude and direction, averaging zero over a short period of time. The average dispersion interaction between two different molecules is given by,

$$\bar{u}_{DISP,ij} = -\frac{3}{2}\frac{\alpha_i \alpha_j}{(4\pi\epsilon_0)^2 r^6}\left(\frac{I_i I_j}{I_i + I_j}\right) \tag{2.9}$$

and between the same type of molecule:

$$\bar{u}_{DISP,ii} = -\frac{3}{4}\frac{\alpha_i^2 I_i}{(4\pi\epsilon_0)^2 r^6} \tag{2.10}$$

where I is first ionization potential. Dispersion forces are the only universal van der Waal's force, since all molecules have non-zero polarizabilities and first ionization potentials. London forces are strong, and scales more importantly to the polarizability than the relatively constant first ionization potential. Dispersive forces are temperature independent and offer some thermal resistance to molecules. This is shown in the high boiling point of toluene, where 99 % of the attractive force is dispersive.

2.1.2 Hydrogen Bonding

It is well-established that highly electronegative atoms attract free electrons of a hydrogen atom in close proximity, forming hydrogen bonds. An intermolecular hydrogen bond is a specific, quasi-chemical attractive force that are several orders of magnitude stronger than physical forces. Hydrogen bonds result from the overlapping of electron clouds, and cannot be quantitatively expressed as algebraic expressions, as was done previously. They are understood, through experimental observations, to be short-ranged, directional forces that respond exponentially to changes in intermolecular distance [78].

Hydrogen bonding are responsible for the formation of long-lived polymers, with properties different to those shown by monomers. In this thesis, we focus on oxygenated molecules that *associate* or *solvate* with one another. We refer to the term *association* when hydrogen bonding occurs between molecules possessing both electron donors and acceptors (alcohols and acids). This may occur between associating molecules of the same (self-association) or different (cross-association) type. On the other hand, molecules such as ketones and aldehydes, which are either electron donors or acceptors, can hydrogen bond only in the presence of their missing complement, i.e. another donor or acceptor. This is a form of cross-association referred to as solvation, and occurs uniquely between unlike molecules. In reality, the behaviour of an associating fluid is complex, and may participate in combinations of the aforementioned phenomena.

Most models accounting for hydrogen bonding to date are simplifications of the true quantum mechanical effect. That said, a model without any hydrogen bonding contributions will struggle to describe the phase equilibria of the associating fluid. This is true for the classical Peng-Robinson EoS in Fig. 1.20.

2.1.3 Intermolecular potential functions

Unlike attractive interactions at intermediate to long ranges, repulsive interactions at short distances are not as well understood. It is intuitive that two impenetrable spheres repel each other with an infinite force when they touch, i.e. when the distance between their centers is equal to the rigid diameter. A more correct and modern view of real molecular repulsion is the soft repulsion, where spheres are allowed to interpenetrate beyond a softer core upon collision. This is true as two molecules have a collision diameter equal to the sphere diameter only when they collide at infinitely slow speed [69].

Depending on the realism required, several forms of intermolecular potential function (Eqn. 2.2) have been proposed to represent repulsive and attractive interactions. A comprehensive listing is found in Prausnitz et al. [69], Kontogeorgis and Folas [70], and Hirschfelder et al. [78]. To facilitate easy usage, potential functions are necessarily empirical, with a number of adjustable parameters to reproduce the properties of real fluids. An example is Mie's expression for intermolecular potential [79], which contains four possible adjustable parameters:

$$u(r) = \frac{A}{r^m} - \frac{B}{r^n} \tag{2.11}$$

In this section, we cover those potentials pertinent to later discussions, starting with the potential between hard spheres.

The hard sphere potential

The potential function between two rigid, impenetrable hard spheres of diameter σ is:

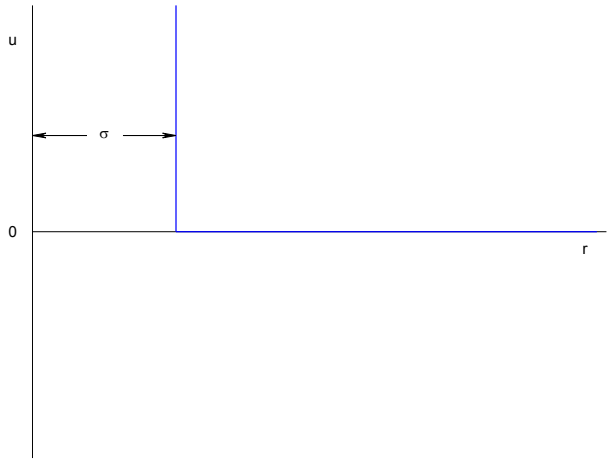

$$u(r) = \begin{cases} \infty & r \leq \sigma \\ 0 & r > \sigma \end{cases} \tag{2.12}$$

It is clear that the hard-sphere is but a simple modification of an ideal gas potential ($u(r) = 0$ for all r). Hard spheres of diameter σ exert no attractive forces on each other, but are susceptible to strong, infinitely large repulsive forces upon contact. Despite its simplicity, hard sphere potentials are useful in allowing exact solutions to statistical thermodynamic calculations.

The Lennard-Jones potential

The Lennard-Jones (LJ) potential is derived from the Mie potential [79], with a 12-6 exponential:

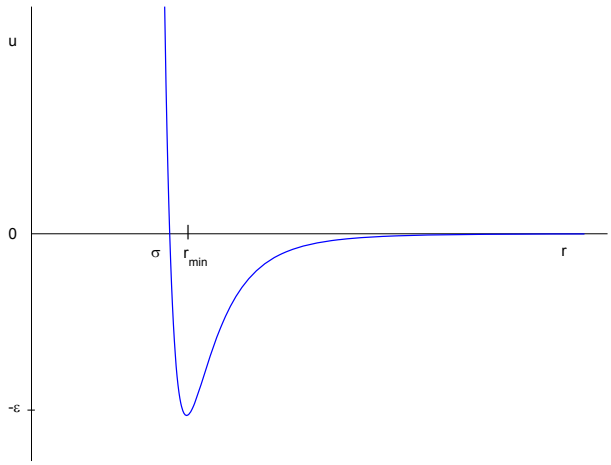

$$u(r) = 4\epsilon\left[\left(\frac{\sigma}{r}\right)^{12} - \left(\frac{\sigma}{r}\right)^{6}\right] \tag{2.13}$$

The van der Waal's dispersive attraction is represented in the inverse sixth power relation, while the inverse twelfth power representing repulsion is of mathematical convenience. The Lennard-Jones potential provides a good approximation for small, non-polar molecules such as argon and methane. Flexibility is achieved with two adjustable parameters: the depth of the energy well ϵ and the collision diameter σ. The soft repulsion of real fluid behaviour is correctly captured at $r < r_{min}$.

The square-well potentials

The basic square-well potential was proposed as an attempt to simplify the Lennard-Jones potential:

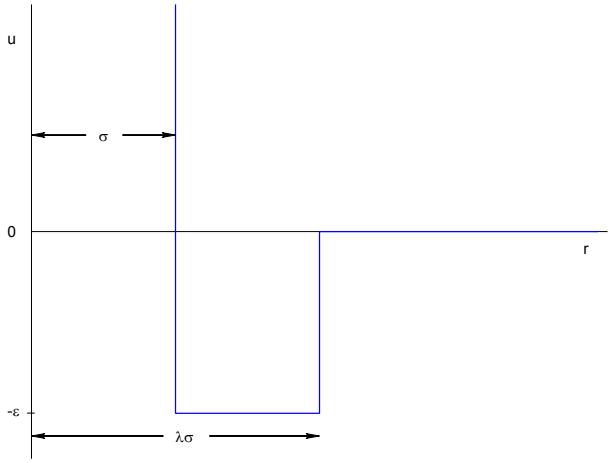

$$u(r) = \begin{cases} \infty & r \leq \sigma \\ -\epsilon & \sigma < r \leq \lambda\sigma \\ 0 & r > \lambda\sigma \end{cases} \tag{2.14}$$

The potential makes use of the mathematical simplicity from the piecewise formulation, whilst a third adjustable parameter λ, the width of the energy well, achieves further flexibility. Chen and Kreglewski [80] proposed a modified square-well potential to introduce the soft repulsion:

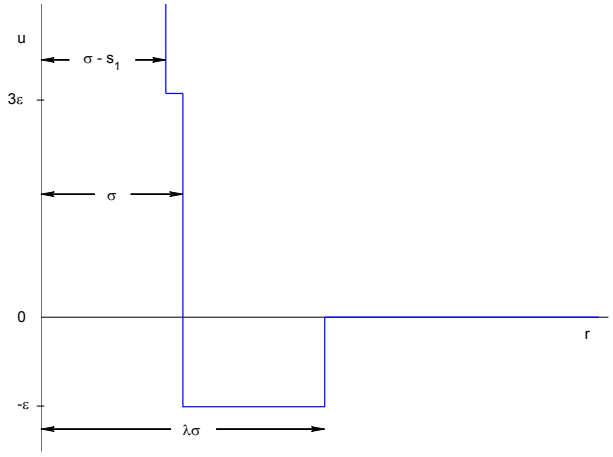

$$u(r) = \begin{cases} \infty & r \leq \sigma \\ 3\epsilon & (\sigma - s_1) \leq r \leq \sigma \\ -\epsilon & \sigma \leq r < \lambda\sigma \\ 0 & r > \lambda\sigma \end{cases} \tag{2.15}$$

where $s_1 = 0.12\sigma$ is an empirical relation defining the limit of interpenetrable distance upon sphere collision.

Intermolecular potentials can be broken up into their respective repulsive and attractive parts. An example could be a truncated Lennard-Jones potential [81]:

$$u(r) = \begin{cases} 0 & r < \sigma \\ 4\epsilon\left[\left(\frac{\sigma}{r}\right)^{12} - \left(\frac{\sigma}{r}\right)^{6}\right] & r > \sigma \end{cases} \tag{2.16}$$

where only the attractive part is retained. This is an important result in perturbation theory, which is discussed next.

2.2 Perturbation theory in equation of states

2.2.1 The radial distribution function

To appreciate the value of the perturbation theory, it is appropriate to explain the role played by the radial distribution function (rdf). We do so here in the simplest manner possible. At a molecular level, a fluid (gas, solid or liquid) is characterized by density fluctuations that deviate from the conventional macroscopic density. This leads to the concept of local densities within a given volume element around a fixed molecule (typically a shell for hard spheres). The radial distribution function is a *probability index* of finding another molecule in the volume element, at a distance of r from the fixed molecule. The rdf may be defined between like and unlike atoms or molecules. An example of the rdf between two oxygen atoms, $g_{oo}(r)$, is given in Fig. 2.2.

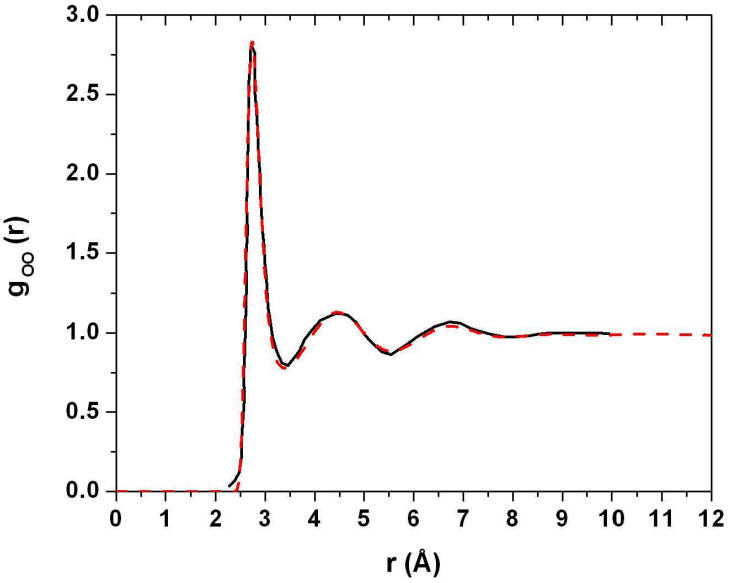

Figure 2.2: Oxygen-oxygen radial distribution function of liquid water, $g_{oo}(r)$, at $T = 298$ K and $P = 1$ atm, comparison between experimental data (solid line) and simulation results (dashed line) [82].

At short distances, less than the core diameter, the rdf is necessarily zero due to strong, repulsive forces. The rdf is amplified at a small distance for the first volume element, due to strong attractive forces that operate at short ranges (hydrogen bonding in this case[1]). This amplification leaves a lesser distribution in the adjacent element, only to allow slightly more packing for the next volume element, and so on. In any fluid medium, the radial distribution function approaches one at the limit of infinite distance, and local density necessarily approaches the macroscopic density.

In statistical thermodynamics, the radial distribution relates, within certain assumptions, to the configuration integral of the canonical partition function. This makes the rdf a key property in determining the thermodynamic

[1]For non hydrogen-bonding species, the rdf is dominated by repulsive forces

functions of pure fluids and mixtures [83]:

$$\text{internal energy:} \qquad \frac{U}{NkT} = \frac{3}{2} + \frac{\rho}{2kT}\int_0^\infty u(r)\, g(r)\, 4\pi r^2 dr \tag{2.17}$$

$$\text{compressibility factor:} \qquad \frac{PV}{NkT} = 1 - \frac{2\pi\rho}{3kT}\int_0^\infty \frac{du(r)}{dr} g(r)\, r^3 dr \tag{2.18}$$

$$\text{chemical potential:} \qquad \frac{\mu}{NkT} = \ln \Lambda^3\rho + \frac{4\pi\rho}{kT}\int_0^1\int_0^\infty \frac{\partial u(r,\xi)}{d\xi} g(r,\xi)\, r^2 dr d\xi \tag{2.19}$$

$$\text{isothermal compressibility:} \qquad kT\left(\frac{\partial\rho}{\partial P}\right)_{T,V} = 1 + 4\pi\rho\int_0^\infty [g(r) - 1]\, r^2 dr \tag{2.20}$$

The quantity N is the number of molecules, Λ is the de Broglie thermal wavelength, and ξ is a perturbation coupling parameter [84]. The solution of Eqns. (2.17) - (2.20) requires, together with potential functions, the integration of a known rdf, although the latter is far from trivial. Rdf are complex expressions dependent on distance, density, temperature, and mixture composition. This holds for even simple potential functions, such that analytical forms of the distribution function are available only for hard spheres and Lennard-Jones molecules. The perturbation theory addresses this limiting factor.

2.2.2 First and second-order perturbation expansions

In perturbation theory, the total intermolecular potential energy of a system is written as the sum of a reference and perturbation part:

$$u(r) = u_0(r) + u_a(r) \tag{2.21}$$

u_0 is the potential energy of an unperturbed system, of which the solution is not only exact but also related to the total $u(r)$. u_a, the perturbation energy, is a series expansion approximating the residual between the total and the reference energy. In statistical thermodynamics, the expansion is kept to the third order at most to avoid mathematical complexity.

From Eqn. (2.21), Zwanzig [85] applied a perturbation expansion to the system Helmholtz energy up to the second order:

$$\frac{A}{NkT} = \frac{A_0}{NkT} + \frac{A_1}{NkT} + \frac{A_2}{NkT} \tag{2.22}$$

where A_0 is the reference Helmholtz energy, and A_i is the ith-order perturbation expansion. Using a multinomial expansion, Zwanzig derived an exact expansion for the first order perturbation expansion,

$$\frac{A_1}{NkT} = \frac{1}{2}N\rho\int_0^\infty u_1(r)\, g_0(r)\, 4\pi r^2 dr \tag{2.23}$$

The significance of Eqn. (2.23) lies in g_0 - only information on the reference rdf, which would have been known, is required to solve the expansion. Zwanzig and later Barker and Henderson [86] derived the exact expression for the second order expansion A_2/NkT. However, the exact form is awkward and could not be solved without considerable effort. Barker and Henderson simplified the second order expansion using the concept of macroscopic compressibility,

$$\frac{A_2}{NkT} = -\frac{1}{4}\frac{N\rho}{kT}\int_0^\infty u_1^2(r)\, g_0(r)\, kT\left(\frac{\partial\rho}{\partial P}\right)_0 dr \tag{2.24}$$

where again, we exploit the rdf of the reference term, and additionally a $(\partial\rho/\partial P)_0$ term, the macroscopic compressibility of the reference fluid. The approach using the perturbation theory were first tested by Frisch et al. [81], Zwanzig [85], Barker and Henderson [86], and Smith and Alder [87] against experiment and simulation with good agreements.

The benefits of the perturbation theory are shown in Eqns. (2.22) - (2.24). The Helmholtz energy of real systems could be solved using a limited knowledge from simpler potential functions (u_0, u_1) and the reference radial distribution functions (g_0). Of vital importance is the selection and exactness of solution of the reference fluid. This is often chosen as the hard sphere fluid, to which accurate expressions for the rdf are given by Percus and Yevick [88], Wertheim [89], Carnahan and Starling [90], and Mansoori et al. [91].

2.3 Residual Helmholtz contributions of the PC-SAFT

The Perturbed-Chain Statistical Associating Fluid Theory (PC-SAFT) was first proposed by Gross and Sadowski as a general equation of state for square-well chains [92]. The publicized form, from the same authors [93, 94], applies a Lennard-Jones attraction and modified square-well repulsion for interacting chains. As with SAFT-type equations, it could be cast into a Helmholtz energy expansion, a result of the perturbation theory:

$$a = a^o + \underbrace{a^{hs} + a^{chain} + a^{disp} + a^{assoc} + a^{multipole}}_{a^R} \tag{2.25}$$

where a is shorthand for A/NkT, the dimensionless (reduced) total Helmholtz energy. Each term on the right-hand side of (2.25) is a contribution to the total Helmholtz energy due to the presence of the molecular phenomenon in superscript. o is the ideal-gas energy, hs denote hard spheres, $disp$ are the dispersion interactions, $chain$ is chain formation, $assoc$ are the association effects, and $multipole$ are additional expansions including dipolar and quadrupolar contributions. The contributions following the ideal-gas make up the total residual Helmholtz energy, a^R.

An equation of state in Helmholtz energy form has the benefit of deriving all thermodynamic properties using only derivatives and ideal-gas integrals. The foremost properties are given in Table 2.1. In this section, we are concerned with how each of the residual Helmholtz contributions are formulated, to resemble a simple fluid to a real fluid.

2.3.1 Wertheim's TPT1 theory and the association term

In dense, liquid-like phases, regular perturbation theory applied to Lennard-Jones spheres at short ranges fails to represent the radial distribution of associating fluids. This is because the rdf of the reference fluid, generally a hard sphere, do not take into account highly attractive forces, such as hydrogen bonding, which are dominant at short-ranges. The result is a severe underestimation of the local density of the fluid.

Wertheim, in a four-part publication [96, 97, 98, 99], addressed the matter by deriving a formulation for associating interactions through graph theory and cluster expansion. Wertheim's model for hydrogen bonding is based on a physical perturbation theory, as opposed to other chemical [100, 101, 102] or quasi-chemical (lattice) [103] theories. In Wertheim's approach, the intermolecular pair potential $\phi(12)$ is represented by the sum of a repulsive reference part ϕ_R, and an attractive part made up of a number of short range interactions:

$$\phi(12) = \phi_R + \sum_{\alpha} \sum_{\beta} \phi_{\alpha\beta} \left(\left| r_2 + d_\beta(\Omega_2) - r_1 - d_\alpha(\Omega_1) \right| \right) \tag{2.26}$$

r_i and Ω_i denote the molecular center and orientation of molecule i, while d_α and d_β are directional vectors from the molecule center to a site. The attractive sites α and β interact on a short range via a potential $\phi_{\alpha\beta}$. Wertheim's potential has the immediate advantages of:

- accounting for sites which are off-center and near the core edge.
- representing discrete interactions between specific pairs of sites.
- allowing multiple sites on one molecule, i.e. no limit is imposed on the number of sites.

Table 2.1: Thermodynamic property relations for Helmholtz energy equation of states, adapted from Stringari [95]. Properties in capital letters are molar properties, while dimensionless (reduced) forms are given in small letters. Superscripts '$\circ$' denote the ideal gas state, while 'R' denote the residual state. Subscripts '0' indicate the property is at the reference state (temperature T_0 and pressure P_0).

Nomenclature[a] (where M may be either one of ρ or T)	
$a_M = \left(\frac{\partial a}{\partial M}\right)_{N\neq M}$ $\quad a_{MM} = \left(\frac{\partial^2 a}{\partial M^2}\right)_{N\neq M}$ $\quad a_{\rho T} = \left(\frac{\partial a}{\partial \rho \partial T}\right)_{N\neq\rho, Q\neq T}$	
Fundamental ideal gas relations and useful temperature derivatives	
a°	$\frac{H_0}{RT} - 1 + \frac{1}{RT}\int_{T_0}^{T} C_p^\circ dT - \frac{S_0}{R} - \frac{1}{R}\int_{T_0}^{T}\frac{C_p^\circ}{T}dT + \ln\frac{P}{P^\circ}$
Ta_T°	$1 - \frac{H_0}{RT} - \frac{1}{RT}\int_{T_0}^{T} C_p^\circ dT$
$T^2 a_{TT}^\circ + 2Ta_T^\circ$	$1 - \frac{C_p^\circ}{R}$
Property	**Relation**
Internal energy	$u = -Ta_T^\circ - Ta_T^R$
Enthalpy	$h = 1 - Ta_T^\circ - Ta_T^R + \rho a_\rho^R$
Helmholtz energy	$a = a^\circ + a^R$
Gibbs energy	$g = 1 + a^\circ + a^R + \rho a_\rho^R$
Entropy	$s = -Ta_T^\circ - Ta_T^R - a^\circ - a^R$
Compressibility factor	$Z = 1 + \rho a_\rho^R$
Isochoric heat capacity	$c_v = -\left(T^2 a_{TT}^\circ + 2Ta_T^\circ\right) - T^2 a_{TT}^R - 2Ta_T^R$
Isobaric heat capacity	$c_p = \frac{\left(1 + \rho a_\rho^R + \rho T a_{\rho T}^R\right)^2}{1 + 2\rho a_\rho^R + \rho^2 a_{\rho\rho}^R}$
Speed of sound[b]	$\frac{w^2}{RT} = \frac{c_p}{c_v}\left(1 + 2\rho a_\rho^R + \rho^2 a_{\rho\rho}^R\right)$
Fugacity coefficient	$\phi = \exp\left(\rho a_\rho^R - \ln Z + a^R\right)$
First pressure derivative with respect to density	$\left(\frac{\partial P}{\partial \rho}\right)_T = RT\left(1 + 2\rho a_\rho^R + \rho^2 a_{\rho\rho}^R\right)$
Second pressure derivative with respect to density	$\left(\frac{\partial^2 P}{\partial \rho^2}\right)_T = RT\left(2a_\rho^R + 4\rho a_{\rho\rho}^R + \rho^2 a_{\rho\rho\rho}^R\right)$

[a] In the context of PC-SAFT, $a_\rho = \left(\pi/6 \times \sum_i x_i m_i d_i^3\right) a_\eta$, while $\rho a_\rho = \eta a_\eta$, $\rho^2 a_{\rho\rho} = \eta^2 a_{\eta\eta}$, etc.

[b] R on the left-hand side of the equation is the universal gas constant, expressed in $J.kg^{-1}.K^{-1}$.

A comprehensive knowledge of graph theory is required to fully appreciate Wertheim's perturbation theory, and the explanation provided below are but extracts of key results of his work. For a review of graph theory and cluster expansion, the reader is referred to Hansen and McDonald [104]. In brief, Wertheim expressed the Helmholtz energy as an arithmetic series of cluster graphs. The cluster nodes are connected by specific bonds described exactly by the Mayer f-function. Through physical arguments, Wertheim simplified his model using the concept of *steric incompatibility*, along with other bonding rules enabling him to eliminate several graphs within the energy expansion. The model approximations of Wertheim's association theory are given in Fig. 2.3, although these approximations can be relaxed if needed.

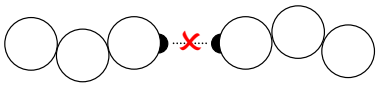

(a) Acceptor-acceptor and donor-donor type bonds are prohibited. Only acceptor-donor type bonds are permitted.

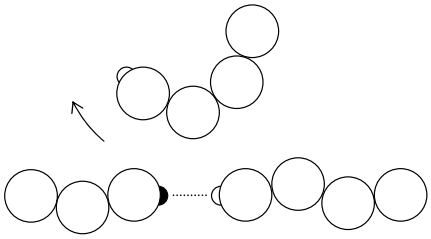

(b) The repulsive core of two bonded molecules prevent any other incoming molecules from bonding at the same site.

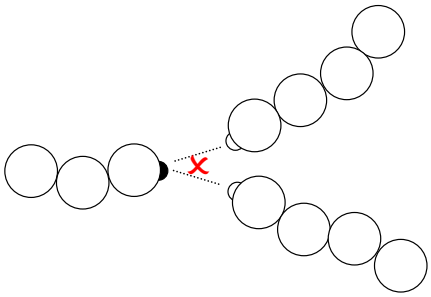

(c) No site on one molecule can bond simultaneously to two sites of another molecule.

Figure 2.3: Illustrations depicting the bonding rules of Wertheim's thermodynamic perturbation theory of first-order (TPT1).

The main outcome of Wertheim's work was a relatively simple expression relating the number density of the fluid ρ to the monomer density ρ_M. For a system where only dimers are present, Wertheim's thermodynamic perturbation theory of first order (TPT1) gives,

$$\rho = \rho_M + \rho_M^2 \int g^{MM}(r) \left[\exp\left(-\frac{u^{assoc}(r)}{kT} \right) - 1 \right] dr\,(12) \tag{2.27}$$

where g^{MM} is the rdf between monomers, u^{assoc} is the association potential function, and $dr\,(12)$ integrates over all orientations of molecules 1 and 2, and all separations of molecules 1 and 2. A more practical form of Eqn. (2.27) is obtained by introducing a fraction, X_A, for unbonded monomers of single site A, where $X_A = \rho_M/\rho$. Upon

rearranging, Eqn. (2.27) can be written as:

$$X_A = \frac{1}{1 + \rho X_A \Delta} \tag{2.28}$$

where,

$$\Delta = \int g^{MM}(r) \left[\exp\left(-\frac{u^{assoc}(r)}{kT} \right) - 1 \right] dr\,(12) \tag{2.29}$$

The quantity Δ can be viewed as an association strength, i.e. the tendency to form n-mers from monomers. The residual Helmholtz energy due to dimerisation (association) is the difference between the Helmholtz energy of a dimerising ideal gas, and that of the non-associating ideal gas:

$$\begin{aligned} a^{assoc} &= \frac{A_D^{ig}}{NkT} - \frac{A^{ig}}{NkT} \\ &= \frac{\mu_D^{ig}}{kT} - \frac{P_D^{ig} V}{NkT} - \frac{\mu^{ig}}{kT} + 1 \end{aligned} \tag{2.30}$$

where we have used the thermodynamic relation $A = N\mu - PV$. The chemical potential of an ideal gas is given by:

$$\mu^{ig} = kT \ln\left(\rho \Lambda^3\right) \tag{2.31}$$

The monomers and dimers in the dimerising ideal gas are in equilibrium, and thus have equal chemical potentials, $\mu_M^{ig} = \mu_D^{ig}$. The pressure of the dimerising ideal gas is:

$$P_D^{ig} = kT\left(\rho_M + \rho_D\right) \tag{2.32}$$

Substituting equations (2.31) and (2.32) into (2.30), we have

$$\begin{aligned} a^{assoc} &= \ln\left(\rho_M \Lambda^3\right) - \frac{\rho_M + \rho_D}{\rho} - \ln\left(\rho \Lambda^3\right) + 1 \\ &= \ln \frac{\rho_M}{\rho} - \frac{\rho_M + \rho_D}{\rho} + 1 \end{aligned} \tag{2.33}$$

In the formation of dimers, we have additionally the mass-action equation $\rho = \rho_M + 2\rho_D$, which reduces Eqn. (2.33) to

$$\begin{aligned} a^{assoc} &= \ln \frac{\rho_M}{\rho} - \frac{1}{2}\frac{\rho_M}{\rho} + \frac{1}{2} \\ &= \ln X^A - \frac{X^A}{2} + \frac{1}{2} \end{aligned} \tag{2.34}$$

The above equation for dimers can be extended to multiple sites by summation of Eqn. (2.34) over all sites,

$$a^{assoc} = \sum_A \left[\ln X^A - \frac{X^A}{2} \right] + \frac{1}{2} S \tag{2.35}$$

where S is the number of associating sites.

The remaining task was finding an expression for the rdf of the monomers, g^{MM}. Chapman, concerned with deriving an association term for engineering purposes, simplified the picture to a coarse-grain model - the location of the bonding site, and the angle between sites, would be neglected. This allowed viewing the monomers as non-bonded hard spheres, approximated by the hard sphere rdf g^{hs}. The potential between associating spheres resembles a short-range square-well, which would not be incorrect for two perfectly-aligned bonding sites. The integral in (2.29) reduces to a simpler expression in two characteristic parameters, κ^{assoc} and ϵ^{assoc} [105, 106],

$$\Delta = \kappa^{assoc} \sigma^3 g^{hs}(r) \left[\exp\left(\frac{\epsilon^{assoc}}{kT} \right) - 1 \right] \tag{2.36}$$

representing an association volume and energy respectively. The hard sphere rdf used in the association, and later chain terms, are taken from Mansoori et al. [91] and Boublìk [107].

The association contribution was extended by Chapman et al. to mixtures of associating molecules [108]. No composition-dependent mixing rule was required in the extension, i.e. extension to multicomponents is facilitated in a natural manner.

$$a^{assoc} = \sum_{i}^{NC} x_i \sum_{A} \left[\ln X^{A_i} + \frac{X^{A_i}}{2} \right] + \frac{1}{2} S \tag{2.37}$$

$$X^{A_i} = \left[1 + \sum_{i} x_i \sum_{A} \rho X^{A_i} \Delta \right]^{-1} \tag{2.38}$$

$$\Delta = \kappa^{A_i B_j} \sigma_{ij}^3 g^{hs}(r) \left[\exp\left(\frac{\epsilon^{A_i B_j}}{kT} \right) - 1 \right] \tag{2.39}$$

where X^{A_i} is the monomer fraction of component i not bonded at site A. In Eqn. (2.39), $\kappa^{A_i B_j}$ is the association volume between site A on component i and site B on component j, and $\epsilon^{A_i B_j}$ is the association strength between site A on component i and site B on component j. The combining rule for σ_{ij}^3 is defined in § 2.3.3. The only ambiguity is the way in which cross-associations between different types of molecules are handled. Simple combining rules from Wolbach and Sandler are applied to the association parameters [109]:

$$\epsilon^{A_i B_j} = \frac{1}{2} \left(\epsilon^{A_i B_i} + \epsilon^{A_j B_j} \right) \tag{2.40}$$

$$\kappa^{A_i B_j} = \sqrt{\kappa^{A_i B_i} \kappa^{A_j B_j}} \left(\frac{\sqrt{\sigma_i \sigma_j}}{0.5 \left(\sigma_i + \sigma_j \right)} \right)^3 \tag{2.41}$$

Equations (2.40) and (2.41) are somewhat grotesque representations of the quantum mechanical effect governing cross-association. One would need to consider, at the outset, size differences in the square-well potential between cross-associating molecules, a matter already far from trivial. Gross and Sadowski have shown the current approach to be acceptable for cross-associating molecules belonging to the same functional group [94].

Equations (2.28) and (2.38) are implicit in monomer fraction, and are usually solved iteratively before substitution in Eqns. (2.35) and (2.37). Various acceleration methods in solving X^{A_i} have been suggested by Elliott [110], Michelsen and Hendriks [111], and Tan et al. [112].

Bonding scheme allocation and the role of spectroscopy

Prior to solution of Eqns. (2.28) and (2.38), one needs to consider the number and allocation of bonding sites for the associating molecules. Such assignments are often subjective, and based on assumptions varying from generally correct, to considerably simplified. The nature of the coarse-grained model is such that the most rigorous schemes do not guarantee the most improved result. This makes determining bonding schemes a matter of trial-and-error.

The effects of different bonding schemes are reflected most prominently in the values of the monomer fractions, which should act as a reference point in the validation. The number of molecules not participating in hydrogen bonding can be experimentally determined using FTIR or NMR spectroscopy. Von Solms et al. [113] remarked that it is not possible to conclude decisively the correct bonding scheme without spectroscopic data, as alternate data, such as vapour pressure, alone cannot determine the bonding scheme. Despite their importance, experimental data are few and far between, with most studies limited to systems of water and alcohols [69, 114, 115, 116, 117, 118, 119, 120, 121, 122, 123, 124]. When presented in numerical form, many of these data are ill-reconciliated, with confusion over the exact quantity being reported [118].

In the absence of experimental X^{A_i}, which is most often the case, a sound knowledge of the chemical nature of the compound in study, should allow the modeler to narrow down the possible bonding schemes. As this stage, the final choice can often be made based on the representation of the pure fluid and mixture properties; on the

experience of the modeler; and on the complexity desired in the calculation. Complexity is a significant factor, as over-rigorous schemes yielding marginal improvements are often less preferred for engineering purposes. Typical bonding schemes for different functional groups will be discussed in Chapter 5.

2.3.2 The chain term

Equation of states which view fluids as free-moving hard spheres with mean-field attraction terms are rigorous only for simple near-spherical molecules such as methane and argon. Real fluids are non-spherical in nature, and exist as flexible chains exhibiting size and shape effects. A more realistic reference fluid for EoS would be to replace spheres with chains of tangentially bonded spherical segments. The formation of hard chains from hard spheres is viewed as a perturbation that must be accounted for explicitly in the total Helmholtz energy.

Chapman et al. [106] derived the Helmholtz contribution for chain formation by recognizing that monomeric fractions decrease with increasing association energy ϵ^{AB}, such that at the limit of infinite association, associating spheres can be forced to form a fully bonded chain. The chains would contain m segments of equal-sized spheres of diameter σ. This further allowed Chapman to exploit the result of Wertheim's association theory, i.e. Eqns (2.28) and (2.36). In the case of a component with a single associating site, the fluid is composed of dimers only, resembling a hard-dumbbell-fluid. Eqn. (2.28) can be rewritten for single-site spheres:

$$\rho\Delta^{AA}\left(X^A\right)^2 + X^A - 1 = 0 \tag{2.42}$$

where Δ^{AA} is the association strength between like sites, A-A. By taking the limit of infinite association, we have $\Delta^{AA} \to \infty$, and X^A necessarily becomes:

$$\lim_{\Delta^{AA}\to\infty} X^A = X^{A,D} = \frac{1}{\sqrt{\rho\Delta^{AA}}} \tag{2.43}$$

where superscript D indicates a dimer case. Equation (2.43) reduces to zero, which is in accordance with the complete depletion of monomers in total bonding. Substituting the result of (2.43) into (2.35), for $S = 1$ bonding site,

$$\begin{aligned} a^D = \frac{A^D}{N^D kT} = 2\frac{A^{assoc}_{\Delta\to\infty}}{NkT} &= 2\ln X^{A,D} - X^{A,D} + 1 \\ &= -\ln\left(\rho\Delta^{AA}\right) + 1 \end{aligned} \tag{2.44}$$

Following Chapman's approach, the compressibility factor of a fully associated dimer fluid is,

$$\begin{aligned} Z^D = \rho\left(\frac{\partial a^D}{\partial\rho}\right)_{T,\rho} &= -\frac{1}{\Delta^{AA}}\left(\Delta^{AA} + \rho\frac{\partial\Delta^{AA}}{\partial\rho}\right) \\ &= -\left(1 + \frac{\rho}{\Delta^{AA}}\frac{\partial\Delta^{AA}}{\partial\rho}\right) \end{aligned} \tag{2.45}$$

The only density dependence of Δ^{AA} is given by the reference radial distribution function, which are the contacting hard spheres:

$$Z^D = -\left(1 + \rho\frac{\partial\ln g^{hs}}{\partial\rho}\right) \tag{2.46}$$

where g^{hs} is the rdf for like-sized hard sphere in the hard sphere mixture. To recover the contribution to the compressibility factor due to chain formation, it is necessary to subtract the ideal gas contribution:

$$\begin{aligned} Z^{chain} &= Z^D - \lim_{\rho\to 0} Z^D \\ &= -1 - \rho\frac{\partial\ln g^{hs}}{\partial\rho} + 1 \\ &= -\rho\frac{\partial\ln g^{hs}}{\partial\rho} \end{aligned} \tag{2.47}$$

The Helmholtz energy contribution due to chain formation is obtained by integrating Z^{chain} with respect to density,

$$a^{chain} = -\ln g^{hs} \tag{2.48}$$

Equation (2.48) can be extended to a chain of any number of segments by recognizing that for every chain of m segments, there will be $m-1$ bonds; thus giving,

$$a^{chain} = -(m-1)\ln g^{hs} \tag{2.49}$$

Similar to the association term, the chain term is extended trivially to mixtures,

$$a^{chain} = -\sum_i x_i\,(m-1)\ln g_{ii}^{hs} \tag{2.50}$$

where the index ii in the rdf denotes equal-sized segments of the same component.

2.3.3 The dispersion term

In the SAFT formulation, the perturbation theory imparts to the repulsive reference fluid, an attractive potential resembling the target fluid. In the original SAFT by Chapman and coworkers [125], the hard sphere fluid is perturbed with dispersive attractions from a Lennard-Jones potential [126], prior to being strung into a chain.[2] Each segment α_i of a chain interacts with the $\beta_{i,\ldots,m}$ segments of a neighbouring chain through a segment rdf $g^{seg} \simeq g^{hs}$ (or g^{LJ}, see footnote 1). This, however, does not reflect the *correlation-hole effect*: a down-scaling of the segment-segment rdf, so that the probability of segment α_i encountering the segment β_i decreases, due to shielding-off by the neighbouring segments $\beta_{j\neq i}$ of the chain.

Gross and Sadowski modified the SAFT by first forming a chain of hard spheres, and thereafter imparting an average dispersive energy to hard chains. The hard chain acts as the reference fluid in the perturbation theory; thus yielding the concept of a Perturbed-Chain (PC) version of SAFT. To do this, the authors used an average inter-chain segment-segment rdf g^{hc} proposed by Chiew [129], instead of rigorously accounting for each and every segment-segment interaction. This approximation was tested with good agreements to molecular simulation [92]. In addition, the g^{hc} exhibits the aforementioned correlation-hole effect. The dispersion contribution to the total Helmholtz energy could be written as a perturbation expansion of second order:

$$a^{disp} = a_1 + a_2$$

where

$$a_1 = -2\pi\rho m^2\left(\frac{\epsilon}{kT}\right)\sigma^3 \underbrace{\int_1^\infty u(x)\,g^{hc}\left(m,\eta,x\frac{\sigma}{d}\right)x^2dx}_{I_1} \tag{2.51}$$

$$a_2 = -\pi\rho mkT\left(\frac{\partial\rho}{\partial P}\right)_{hc} m^2\left(\frac{\epsilon}{kT}\right)^2\sigma^3 \underbrace{\frac{\partial}{\partial\rho}\left[\rho\int_1^\infty u(x)^2\,g^{hc}\left(m,\eta,x\frac{\sigma}{d}\right)x^2dx\right]}_{I_2} \tag{2.52}$$

The quantities x and $u(x)$ are reduced distance and potential respectively; see Refs. [92] and [93] for details. The perturbation integrals I_1 and I_2 can be solved for any intermolecular potential $u(x)$, although an analytical expression for I_1 and I_2 is difficult to obtain due to the complexity of g^{hc}. Gross and Sadowski simplified the problem by removing partly the temperature dependency from the hard chain rdf, so that the only temperature dependence of g^{hc}

[2] The chain term, Eqn. (2.50), contains the rdf of the target fluid. This was not done in Chapman's work, where $a^{chain} = \sum_i x_i(1-m_i)\ln g_{ii}^{hs}$ should have been replaced by $a^{chain} = \sum_i x_i(1-m_i)\ln g_{ii}^{LJ}$ for chains of Lennard-Jones spheres. It was presumed that Chapman was extending his developments of Wertheim's association theory; thus keeping the g^{hs} he suggested therein. The LJ approach was followed rigorously in LJ-SAFT [127, 128], with promising results.

remains in the packing fraction, i.e. $g^{hc} = f(m, \eta)$. The packing fraction is related to the soft repulsion diameter d, the latter described here by the step function of a modified square-well potential,

$$d = \sigma \left[1 - 0.12 \exp\left(-3 \frac{\epsilon}{kT} \right) \right] \tag{2.53}$$

d exhibits a moderate temperate dependency not too different from the exact form of g^{hc}, and Eqn. (2.53) serves well to give I_1 and I_2 a moderate overall temperature dependency. The integral I_1 and I_2 were replaced by a power series of sixth order in m and η.

$$I_1(m, \eta, T) \rightarrow I_1(m, \eta) = \sum_{i=0}^{6} a_i(m) \eta^i \tag{2.54}$$

$$I_2(m, \eta, T) \rightarrow I_2(m, \eta) = \sum_{i=0}^{6} b_i(m) \eta^i \tag{2.55}$$

The remaining task involved obtaining $a_i(m)$ and $b_i(m)$ for chain molecules. The dependency of a_i and b_i on the chain segment number m is well described by Liu and Hu [130]. n-Alkanes of varying lengths were used as model substances to capture the non-sphericity of chains. The coefficients were obtained in the following manner:

1. For an n-alkane, with pure parameters $\{m, \sigma, \epsilon\}$, Eqns. (2.51) and (2.52) are solved exactly with a Lennard-Jones attractive potential in $u(x)$.
2. The regression parameters $\{m, \sigma, \epsilon\}$ were optimized by minimizing an objective function in vapour pressure, and liquid, vapour and supercritical densities. This is done for the n-alkane species methane, and propane to n-decane[3] [131].
3. I_1 and I_2 in Eqns. (2.51) and (2.52) were replaced by power series (2.54) and (2.55). The regression parameters switch to $\{a_{0,\ldots,6},\ b_{0,\ldots,6}\}$, and are optimized to the same objective function in step 2, for all n-alkanes that were considered in step 2.

The coefficients obtained in this manner were declared as universal model coefficients, and possess two important features. Firstly, a realistic potential in Lennard-Jones was employed; and secondly, experimental data were compared in the objective function, so that coefficients were based on real fluid behaviour. It is clear from the above explanation that PC-SAFT chains would interact with a modified square-well-Lennard-Jones potential:

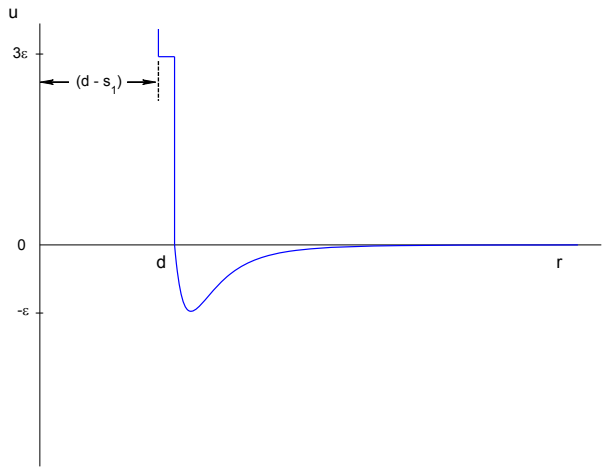

$$u(r) = \begin{cases} \infty & r \leq (d - s_1) \\ 3\epsilon & (d - s_1) \leq r \leq d \\ 4\epsilon \left[\left(\frac{d}{r} \right)^{12} - \left(\frac{d}{r} \right)^{6} \right] & r > d \end{cases} \tag{2.56}$$

The universal coefficients a_i and b_i are given in Ref. [93], while the same coefficients for pure square-well chains are given in Ref. [92] (the latter is obtained slightly differently, and is not used in this work).

[3] Ethane was not used in the original regression, as it possesses a quadrupole-quadrupole interaction, which, albeit weak, could not be accounted for at the time the dispersion term was developed.

The dispersion is extended to mixtures by applying the van der Waal's one-fluid mixing rule to yield [93]:

$$a_1 = -2\pi\rho I_1 \sum_i \sum_j x_i x_j m_i m_j \left(\frac{\epsilon_{ij}}{kT}\right) \sigma_{ij}^3 \tag{2.57}$$

$$a_2 = -\pi\rho\bar{m}\left(1 + Z^{hc} + \rho\frac{\partial Z^{hc}}{\partial\rho}\right)^{-1} I_2 \sum_i \sum_j x_i x_j m_i m_j \left(\frac{\epsilon_{ij}}{kT}\right)^2 \sigma_{ij}^3 \tag{2.58}$$

where $\bar{m} = \sum_i x_i m_i$. The Berthelot-Lorentz combining rule is used for σ_{ij} and ϵ_{ij}:

$$\sigma_{ij} = \frac{1}{2}\left(\sigma_i + \sigma_j\right) \qquad \epsilon_{ij} = \sqrt{\epsilon_i \epsilon_j}\left(1 - k_{ij}\right) \tag{2.59}$$

where k_{ij} is an adjustable binary interaction parameter. For difficult mixtures, a second asymmetric l_{ij} parameter could be employed, based on a formulation by Mathias et al. [132]:

$$a_1 = -2\pi\rho I_1 \left[\sum_i \sum_j x_i x_j m_i m_j \left(\frac{\epsilon_{ij}}{kT}\right)\sigma_{ij}^3 + \sum_i x_i m_i \left(\sum_j x_j m_j \sigma_{ij}\left(\frac{\epsilon_{ij}}{kT} l_{ij}\right)^{1/3}\right)^3\right] \tag{2.60}$$

2.3.4 The multipole terms

The $a^{multipole}$ term refers to any contributions of the relevant contributions developed to account for polar interactions. The complete expansion of the term can be given by:

$$a^{multipole} = a^{DD} + a^{QQ} + a^{DQ} \tag{2.61}$$

where superscripts DD account for dipole-(induced) dipole interactions, QQ the quadrupole-quadrupole interactions, and DQ the dipole-quadrupole cross-interactions. Dipole-dipole and dipole-induced dipole are the most prominent electrostatic forces in oxygenated compounds, and will be discussed in more detail. We consider only the dipole-dipole expressions from Gross and Vrabec (PC-SAFT-GV) [133], and from Jog and Chapman (PC-SAFT-JC) [134, 135], as well as the induced dipole expression from Kleiner and Gross (PCIP-SAFT) [136].

The less-encountered quadrupole-quadrupole and dipole-quadrupole terms are taken from the works of Gross [137], and Vrabec and Gross [138] respectively. The former contribution excels typically in systems containing carbon dioxide, while the latter is suited for refrigerant systems. These applications are not within the scope of the study. Nonetheless, the two contributions follow similar derivations as Ref. [133], and may be cross-referred by the reader if necessary.

The Gross and Vrabec dipolar term

The dipolar contribution of Gross and Vrabec [133] adopts an approach similar to that of Saager and Fischer [139], who sought to improve polar representations by employing a two-center Lennard-Jones (2CLJ) model, rather than the classical LJ [140], plus point dipoles. The method of Saager and Fischer showed superior agreement to molecular simulation data than previous theories, despite the EoS being somewhat empirical (28 coefficients were required). While this points to the 2CLJ plus point dipole fluid as a suitable reference model, it serves to know that a different model, the tangent sphere (TS) fluid, has been employed as a reference leading up to that stage. As shown in Fig. 2.4, the 2CLJ plus point dipole is more elaborate, consisting of two Lennard-Jones spheres of diameters σ, separated at a distance L apart, with a point dipolar site of moment μ situated at the geometric center and aligned along the horizontal axis. Following the work of Saager and Fischer, the intermolecular potential is given as the sum of the 2CLJ reference and an attractive dipole acting as a perturbation, cf. Eqn. (2.21)

$$u\left(\mathbf{r}_{ij}, \omega_i, \omega_j\right) = u^{2CLJ}\left(\mathbf{r}_{ij}, \omega_i, \omega_j\right) + u^{DD}\left(\mathbf{r}_{ij}, \omega_i, \omega_j\right) \tag{2.62}$$

where $\mathbf{r}_{ij}$ is the vector between the two LJ centers, and ω_i denotes a set of two molecular orientation angles σ_i and ϕ_j. This suggests an expansion of the residual Helmholtz energy of a polar fluid in the framework of the perturbation theory,

$$a^R = a^{2CLJ} + a^{DD} \tag{2.63}$$

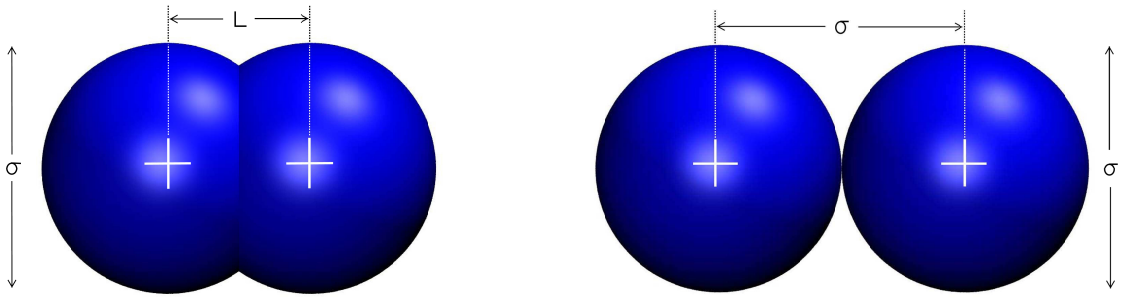

(a) two-center Lennard-Jones (2CLJ) model **(b)** tangent sphere (TS) model

Figure 2.4: Molecular ball models depicting the structural differences between the 2CLJ and TS model.

Such approach was followed by Saager and Fischer, although refinements would be required to integrate the 2CLJ fluid into the current TS setup of SAFT. Different reference fluids means that a simple translation between models is not possible for most molecular parameters, e.g. $\epsilon^{2CLJ} \neq \epsilon^{TS}$. In addition, Saager and Fischer used a fixed elongation $L/\sigma = 0.505$ in their EoS, thereby choosing a strongly spherical reference as opposed to the non-spherical tendency of SAFT. Gross [137] proposed an alternative by expanding a^{2CLJ} in the TPT1 framework for asymmetric (chain) fluids,

$$a^{2CLJ} = ma^{LJ} + (1-m)\ln g^{LJ} \tag{2.64}$$

opting to use the accurate Helmholtz energy and rdf expressions available for LJ monomers [141, 142]. Assuming the segment diameters σ of both models are identical, a scheme was proposed [143], using recent 2CLJ simulation data [144], to translate molecular parameters between 2CLJ and TS models. Using this relation, the features of the 2CLJ model could be brought, with good precision, to the TS model framework.

Due to the long-range nature of electrostatic forces, the perturbation expansion of the a^{DD} converges slowly; thus requiring higher-order terms. Gray and Gubbins [145] showed that the first-order expansion a_1 is a non-weighted average of angles, and is zero. However, terms higher than the third-order expansion become computationally expensive, whilst not being sufficiently small to be truncated without inducing errors. A compromise is reached via a Padé approximant, as suggested by Stell et al. [146].

$$a^{DD} = a_2 + a_3 + a_4 + \cdots \simeq \frac{a_2}{1 - a_3/a_2} \tag{2.65}$$

and in doing so the full series is represented by the lesser intensive terms a_2 and a_3:

$$a_2 = -\pi\rho \sum_i \sum_j x_i x_j \frac{\epsilon_i}{kT}\frac{\epsilon_j}{kT}\frac{\sigma_i^3\sigma_j^3}{\sigma_{ij}^3} n_{\mu,i} n_{\mu,j} \mu_i^{*2} \mu_j^{*2} J_{2,ij}^{DD} \tag{2.66}$$

$$a_3 = -\frac{4\pi^2}{3}\rho^2 \sum_i \sum_j \sum_k x_i x_j x_k \frac{\epsilon_i}{kT}\frac{\epsilon_j}{kT}\frac{\epsilon_k}{kT}\frac{\sigma_i^3\sigma_j^3\sigma_k^3}{\sigma_{ij}\sigma_{ik}\sigma_{jk}} n_{\mu,i} n_{\mu,j} n_{\mu,k} \mu_i^{*2} \mu_j^{*2} \mu_k^{*2} J_{3,ijk}^{DD} \tag{2.67}$$

where $\mu_i^{*2} = \mu_i^2 / \left(m_i \epsilon_i \sigma_i^3\right)$ is the dimensionless dipole in vacuo. The quantity $n_{\mu,i}$ denotes the number of dipolar moments of component i, a value which is one for monofunctional compounds. The complicated, yet unavoidable

perturbation integrals, taken over the angle-weighted rdf, are manifested in the J terms, where they are approximated by simple power series in m and ρ. This concept has been introduced in § 2.3.3, and in this case model parameters were fitted to phase equilibrium data generated by molecular simulations of 2CLJ fluids [144]. This implies that the dipole should only be stretched over a maximum of two spheres ($m = 2$), due to the geometrical restrictions of the 2CLJ fluid. The relevant parameters and relations pertaining to $J^{DD}_{2,ij}$ and $J^{DD}_{3,ijk}$ can be found in Ref. [133], and are analogous to Eqns. (2.54) - (2.55).

Extension to Dipole-induced dipole interactions Kleiner and Gross [136] extended the dipole term of Gross and Vrabec [133] to account for dipole-induced dipole effects, in addition to the permanent dipole-dipole effects already addressed from Eqns. (2.64) - (2.67). By applying the renormalized perturbation theory of Wertheim [147, 148] to bulk fluid properties, the polarizability of molecules α were integrated into the conventional dipole in vacuo μ, thereby giving an increased, effective dipole moment μ^{eff} with no polarizability. This simplification avoids working with higher-order perturbation expansions, effectively reducing the problem to the two- and three-body correlations adopted for permanent dipoles.

In this approach, the dimensionless effective dipole moment μ_i^{*eff} for species i is written for an average electric field strength and polarizability, yielding the implicit equation,

$$\mu_i^{*eff} = \mu_i^* - \frac{\alpha_i^* T_i^*}{x_i} \frac{\partial a'^{DD}}{\partial \mu_i^{*eff}} \tag{2.68}$$

where only the value of μ_i^*, but not μ_i^{*eff}, is known *a priori*. The a'^{DD} term is the dipolar term of Gross and Vrabec (§ 2.3.4), with the prime indicating that the effective dipole, rather than the permanent dipole, is used. The expression is analogously written in Padé approximant:

$$a'^{DD} = \frac{a'_2}{1 - a'_3/a'_2} \tag{2.69}$$

The induced-dipole effect is introduced in the second- and third-order expansions above through two quantities z_i^A and z_i^B, yielding the expressions:

$$a'_2 = -\pi\rho \sum_i \sum_j x_i x_j \frac{\epsilon_i}{kT} \frac{\epsilon_j}{kT} \left(z_i^A z_j^A - z_i^B z_j^B \right) \frac{\sigma_i^3 \sigma_j^3}{\sigma_{ij}^3} n_{\mu,i} n_{\mu,j} J^{DD}_{2,ij} \tag{2.70}$$

$$a'_3 = -\frac{4\pi^2}{3} \rho^2 \sum_i \sum_j \sum_k x_i x_j x_k \frac{\epsilon_i}{kT} \frac{\epsilon_j}{kT} \frac{\epsilon_k}{kT} \left(z_i^A z_j^A z_k^A - z_i^B z_j^B z_k^B \right) \frac{\sigma_i^3 \sigma_j^3 \sigma_k^3}{\sigma_{ij}\sigma_{ik}\sigma_{jk}} n_{\mu,i} n_{\mu,j} n_{\mu,k} J^{DD}_{3,ijk} \tag{2.71}$$

with the following definitions for z_i^A and z_i^B:

$$z_i^A = \left(\mu_i^{*eff}\right)^2 + 3\alpha_i^* T_i^*$$

$$z_i^B = 3\alpha_i^* T_i^*$$

The reduced quantities α_i^* and T_i^* can both be found in Ref. [136]. The polarizability of a molecule α_i is expressed through the quantity α_i^*, and is not treated as an adjustable parameter. Similar to the permanent dipole moment, values of polarizability will be taken from the experimental data.

An iteration scheme is required to solve Eqn. (2.68), using either Newton-Raphson or successive substitution methods. The analytical expression for $\partial a'^{DD}/\partial \mu_i^{*eff}$ is not given in Ref. [136], but has been solved in this work and included in Appendix B, along with other useful derivatives. An initial value of $\mu_i^{*eff} = \mu_i^*$ is used for the iteration. Upon solution of the value of μ_i^{*eff}, the effective dipolar contribution, which replaces the a^{DD} term on the right of Eqn. (2.61), is given as:

$$a^{DD,eff} = a'^{DD} + \frac{1}{2} \sum_i \frac{\alpha_i^* T_i^*}{x_i} \left(\frac{\partial a'^{DD}}{\partial \mu_i^{*eff}} \right)^2 \tag{2.72}$$

The Jog and Chapman dipolar term

Jog and Chapman [134, 135] developed a dipolar contribution by visualizing non-spherical polar molecules as hard-sphere chains containing both polar and non-polar segments. In this approach, the reference fluid is an equimolar mixture of non-polar and polar hard spheres, where the latter possesses a dipole vector at the center of the sphere. The thermodynamic properties of the polar hard spheres were calculated using the u-expansion [145]. Similar to the manner in which Chapman derived the SAFT chain term [106], the authors considered the limit of total bonding in Wertheim's theory, effectively stringing the assorted segments into a chain. For this step, the radial distribution function between the reference polar and non-polar monomers, g^R, needed to be known. Jog and Chapman showed, using computer simulation, that g^R can be approximated by the hard-sphere rdf, g^{hs}, up to a moderate dipole strength provided that the segment dipole vector is aligned perpendicularly to the line joining the center of the dipole segment to that of the adjacent segment. The dipolar term was presented as a perturbation expansion in Padé approximant:

$$a_2 = -\frac{2\pi}{9}\frac{\rho}{(kT)^2}\sum_i\sum_j x_i x_j m_i m_j x_{p_i} x_{p_j}\frac{\mu_i^{*2}\mu_j^{*2}}{d_{ij}^3} I_{2,ij}^{DD} \tag{2.73}$$

$$a_3 = \frac{5\pi^2}{162}\frac{\rho^2}{(kT)^3}\sum_i\sum_j\sum_k x_i x_j x_k m_i m_j m_k x_{p_i} x_{p_j} x_{p_k}\frac{\mu_i^{*2}\mu_j^{*2}\mu_k^{*2}}{d_{ij}d_{jk}d_{ik}} I_{3,ijk}^{DD} \tag{2.74}$$

where $I_{2,ij}^{DD}$ and $I_{3,ijk}^{DD}$ are the Rushbrooke approximations for the perturbation integrals of second and third order [149]. The introduction of x_p, the fraction of polar segments in a chain, gives rise to an extra pure component parameter, assuming experimental dipole moments are used in Eqn. (2.73) and (2.74).

The notion of x_p as an adjustable parameter is, however, not entirely correct. For chains of tangentially connected segments containing a single dipolar site, x_p is exactly $1/m$, although this will not be the case for non-integer m values, as in SAFT. Various authors [135, 150, 151] chose to correlate x_p by assigning a constant value to the product mx_p for a particular homologous group (e.g. $mx_p = 0.50$ for ketones [150]). To determine this constant, the smallest member of the series is fitted to vapour pressure and liquid density data, with no constraints on x_p. The product mx_p stemming from the final set of parameters is then held constant for the rest of the homologous group. Dominik et al. [151] observed the problem of multiple solutions when fitting a set of $\{m, \sigma, \epsilon/k\}$ parameters, and suggested the incorporation of a single set of binary data in the regression. Any mixture with a second component free of functionality (e.g. n-alkanes) could be used. Not a great deal of detail regarding the type of measurement data used were provided by the authors; the systems employed in their work included both isothermal vapour-liquid equilibria and isobaric liquid-liquid equilibria data. The handling of the x_p parameter is a rather arduous procedure, and one that may cause the JC term to be overlooked as a 'quick-fix'.

Such segment approach of the JC term differs from that of the GV term in that the dipolar moment is not placed along the molecular axis of the molecule. In the GV approach, the location of the stretchable dipole in the chain is not considered. This is depicted graphically in Fig. 2.5. The dipole segments exist site-like in a JC chain; thus the distance of closest approach of the dipole is represented. Furthermore, the segment approach also accounts for multiple dipolar functional groups. Al-Saifi et al. [152] compared the Helmholtz free energy contribution to the reduced chemical potential from the two dipolar terms, and found the JC approach to have a higher contribution among the two.

2.4 Systematic parameterization of the PC-SAFT

Depending on the form of the PC-SAFT employed, different numbers of pure component parameters must be determined for the model. To reflect real substance behaviour, the parameters are regressed to experimental data of thermodynamic properties. For both associating and non-associating substances, the **chain segment** m; the **segment diameter** σ; and the **depth of energy well** ϵ are always included in the regression. The parameters m and σ are

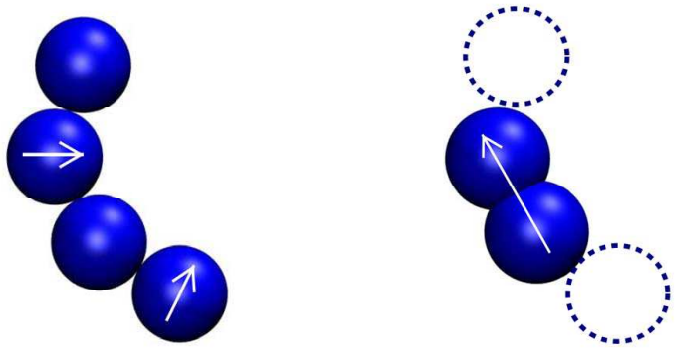

(a) Jog and Chapman **(b)** Gross and Vrabec

Figure 2.5: Orientation of the dipole moment within a chain molecule, following the JC or the GV approach. In the JC approach, the dipole vectors, shown as white arrows, are placed on specific segments within a chain, perpendicular to the vector connecting the centers of adjacent segments. In the GV approach, the dipole moment is stretched across a maximum of two segments, and placed along the central axis. Its position, with respect to the other non-polar segments, is irrelevant.

geometric parameters, and reflect the packing extent of the molecule. Data on liquid density (ρ^L) supply information on the magnitude of these two parameters. ϵ is an attractive energetic parameter that holds molecules together; its magnitude affects the molecules' tendency to disperse and form a vapour phase. Values of the vapour pressure (P^{sat}) is required to tune the parameter. For associating compounds, two additional parameters i.e. the **association energy** ϵ^{AB} and **association volume** κ^{AB}, are required (§ 2.3.1). The electrostatic parameters μ and α found in the dipolar contributions to the Helmholtz energy are not strictly adjustable, and retain their experimental values in this work, unless stated otherwise.

As with multi-parameter EoS, the parameterization of PC-SAFT is subjected to the modeler's preferences. The central theme of this work is the application of PC-SAFT to the calculation of thermodynamic properties; thus we devise herein a systematic procedure for tuning the model for phase equilibria purposes. The procedure outlined below can be easily modified to yield different sets of parameters adapted for alternative purposes.

1. ***Visualize the compound.*** This helps to identify whether the compound is associating/non-associating, polar/non-polar, and the possible hydrogen bonding combinations, if applicable. Decisions can thus be made on the correct forms of PC-SAFT to use.

2. ***Compile data.*** As explained, experimental data on liquid densities and vapour pressures are essential, and as many data as possible should be collected from the triple point to the critical point. This ensures the parameters are applicable for the entire range of vapour-liquid coexistence. In the case of insufficient data, it is possible to compensate using subcooled liquid or superheated vapour volumes. Heat of vaporization can also be used, its relation to vapour pressure and fluid densities is given by the Clausius-Clapeyron equation. Second virial coefficient data can also be considered, although the fitting is usually difficult. For associating compounds, spectroscopic data on monomer fractions, provided that they are available and correctly interpreted, can be used.

3. ***Eliminate unwanted data.*** It is useful to obtain empirical correlations for the liquid volumes and vapour pressures. A plot of the collected data and an empirical correlation on the same axes may reveal significant outliers that would otherwise mislead the regression if retained. These outliers should be removed. Repeated experimental results at an identical condition should be filtered. Unless explicitly required, very low vapour pressures in the range of a few hundred Pascal should be omitted. These data points are often not reliable

to within several percentages in uncertainties, leading to unnecessary efforts in the minimization routine to reduce the deviations.

Empirical correlations for density and pressure correlations can be found in standard databases, notably DIPPR [68], NIST [153], and Perry et al. [154].

4. ***Parameter regression.*** Using logical initial guesses, regress the relevant parameters as to minimize the objective function F,

$$F = 100 \sum_{T_p}^{N_{T_p}} \frac{1}{N_{exp,T_p}} \sum_{i}^{N_{exp,T_p}} \left(\frac{\theta_{T_p,i}^{exp} - \theta_{T_p,i}^{cal}}{\theta_{T_p,i}^{exp}} \right)^2 \tag{2.75}$$

where T_p is the thermodynamic property to be fitted; N_{T_p} is the total number of different types of thermodynamic properties to be considered in the overall regression; N_{exp,T_p} is the total number of experimental data points considered for thermodynamic property T_p; and $\theta_{T_p,i}^{exp/cal}$ is the i^{th} experimental/calculated value of the thermodynamic property T_p. Only discrete experimental data are used in the regression.

5. ***Evaluate the results.*** Both the closeness of the fit and the nature of the parameters should be inspected. The former is indicated by the *absolute average deviation*, *AAD*,

$$AAD_{T_p} = \frac{100}{N_{exp,T_p}} \sum_{i}^{N_{exp,T_p}} \left| \frac{\theta_{T_p,i}^{exp} - \theta_{T_p,i}^{cal}}{\theta_{T_p,i}^{exp}} \right| \tag{2.76}$$

with the quantities defined above. Values for *AAD* for the liquid volumes and vapour pressures should ideally be below 2 %, if possible. However, this evaluation is insufficient, as nonsensical parameters may mathematically give good fits to experimental data. The identification of obscure parameters are often based on experience, and can be guided by the following pointers:

- The segment number m should conform to the size of the molecule. Large m values correspond to large molecules, and vice versa. No values of m should be smaller than one, the value of m designated to methane.
- Abnormally large ϵ parameters, that stand out from other values of similar compounds, are often indications of neglected contributions. Unaccounted molecular interactions, such as hydrogen bonding, may manifest themselves by lumping their effects in the available energy parameters as a compensation. This is analogous to abnormally large binary interaction parameters in mixture calculations.
- For some associating compounds, small values of *AAD* are obtained at the price of driving the effective association volume κ^{AB} close to zero. This may occur along with common values for ϵ^{AB}. Since the effective volume is strongly correlated with the association energy, it is acceptable to prescribe a constant value for the κ^{AB} value. The prescribed value should be physically representative. An example uses a fixed $\kappa^{AB} = 0.001$, for hydrogen sulphide [155].

PC-SAFT should not be treated as a *reference* equation of state, i.e. models specialized in complete description of a substance, parameterized using five or more thermodynamic properties. The number of adjustable parameters in PC-SAFT is not sufficiently high for such purpose, and over-expansion of Eqn. (2.75) only serves to complicate the optimization routine. However, we show in Fig. 2.6 the predictions of the heat capacity and the speed of sound for some non-associating and associating compounds, whose parameters were regressed to liquid densities and vapour pressures. Even though c_p and w were not included in the regression of pure-component parameters, qualitative agreements with experimental data could still be achieved. This emphasizes the appropriateness of the choice of ρ^L and P^{sat} as target properties, as well as the physical basis of the model.

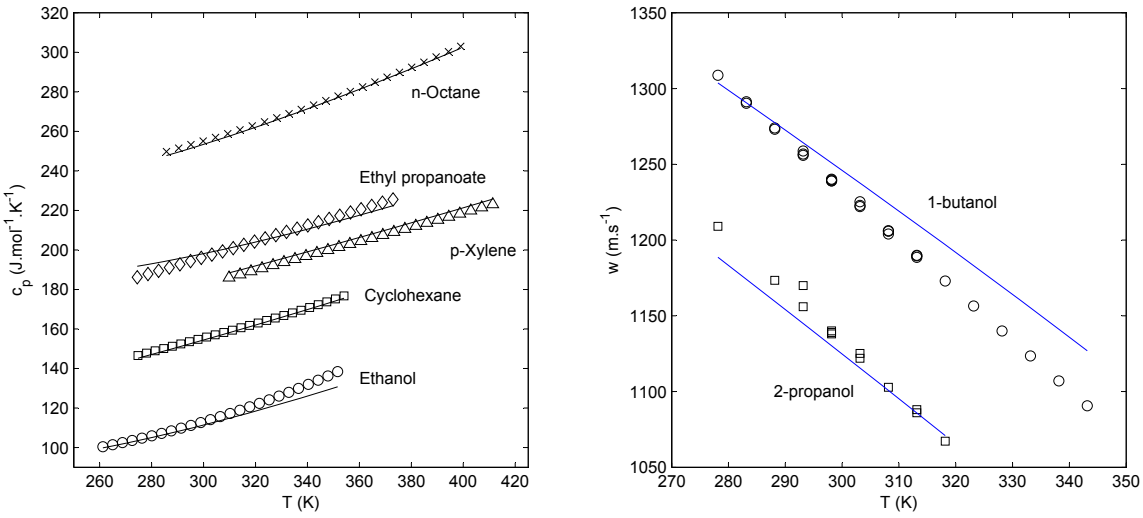

Figure 2.6: Predictions of thermodynamic properties indirectly related to the vapour pressure and liquid densities, for several compounds using variants of the PC-SAFT EoS. *left*: Isobaric heat capacity c_p in the liquid phase at atmospheric pressure, using the non-polar form of the PC-SAFT. *right*: Speed of sound w in the liquid phase at atmospheric pressure, using PC-SAFT with the Jog and Chapman dipolar term. Pure component parameters were taken from [93, 94, 152]. Experimental data taken from Daubert et al. [68], Outcalt et al. [156], and the DDB Explorer Edition (http://www.ddbst.com/en/products/Products_Explorer.php).

2.5 Concluding remarks

The Perturbed-Chain Statistical Associating Fluid Theory (PC-SAFT) is identified as a prospect in the modeling of phase behaviour and thermodynamic properties of systems of oxygenated compounds. By harnessing the power of molecular simulation and perturbation theory, various types of molecular interactions are contained in a multi-parameter equation of state. Several of the interactions pertinent to oxygenated compounds, such as association and dipole-related types, are not explicitly accounted for in cubic EoS.

This review chapter emphasized the role of intermolecular forces in the phase behaviour of compounds and mixtures, and the need to account for necessary interactions in their modeling. The state of art of the PC-SAFT EoS was shown to achieve this goal by examining each of its Helmholtz free energy contributions in sufficient detail. The concepts introduced in this chapter will be used in the modeling of experimental results obtained in this work (Chapters 5 and 6).

CHAPTER 3

Vapour-liquid equilibrium measurements of binary systems

The strongest arguments prove nothing so long as the conclusions are not verified by experience. Experimental science is the queen of sciences and the goal of all speculation.

- Roger Bacon (1214-1294)

Mesures Expérimentales d'Équilibres "Liquide-Vapeur" sur des Systèmes Binaires

Ce chapitre présente deux techniques expérimentales permettant de réaliser des mesures d'équilibres "liquide-vapeur" (ELV) aux basses et hautes pressions.

Sept systèmes binaires ont été étudiés à des pressions inférieures à la pression atmosphérique, et deux à des pressions supérieures. Chaque système contient au moins un composé oxygéné, et les mesures ont été réalisées dans des conditions non publiées dans la littérature. Les sept mélanges binaires, considérés comme des systèmes à basse pression, sont mesurés en utilisant un appareillage basé sur la méthode "dynamique-analytique". L'équipement est une modification de l'ébulliomètre de Yerazunis, apportée par Raal. Le mélange liquide est introduit dans l'appareillage et porté à ébullition dans une chambre agitée. Le mélange liquide-vapeur chauffé se déplace dans un tube de Cottrell par capillarité, et arrive dans la chambre d'équilibre. Dans cet espace, le garnissage en acier inoxydable permet le transfert de masse entre les deux phases. Au bas de la chambre d'équilibre, les phases liquide et vapeur sont séparées. La phase vapeur est dirigée vers un condenseur, et les deux phases liquide et vapeur condensée sont échantillonnées à l'aide d'une seringue, pour analyse par chromatographie en phase gazeuse. Le condensat dans les chambres d'échantillonnages est recirculé au niveau de la chambre d'ébullition initiale, un fonctionnement en continu dynamique est ainsi atteint. Le capteur de température a été étalonné dans un bain d'huile silicone, et le capteur de pression a été étalonné à l'aide d'une pompe à main pneumatique. Les deux étalonnages ont été effectués par rapport aux normes nationales. Le TCD du chromatographe en phase gazeuse a été étalonné en utilisant une méthode proposée par Raal, où des échantillons de mélanges standards de compositions connues ont été injectés successivement dans le chromatographe. Les incertitudes de mesures de la température, de la pression et de la composition molaire ont été déterminées suivant les procédures développées par le NIST.

Les deux autres systèmes, dont les pressions varient de 4 à 40 bars, sont considérés comme des systèmes à haute pression et sont étudiés à l'aide d'un appareillage basé sur la méthode "statique-analytique". Le mélange est introduit dans une cellule en titane et porté à l'équilibre rapidement par des agitateurs magnétiques. La température de la cellule est maintenue en utilisant une enceinte à air régulée. Le mélange à l'équilibre est échantillonné directement à l'intérieur de la cellule par deux échantillonneurs ROLSI™ électromagnétiques à capillaire, un pour chacune des phases présentes. Les échantillons des phases prélevés sont transférés, en ligne au chromatographe pour analyse. Deux capteurs de température et de pression sont reliés à la cellule d'équilibre. Comme pour l'appareillage basé sur la méthode "dynamique-analytique", le capteur de température est étalonné en utilisant un bain d'huile silicone, tandis que le capteur de pression est étalonné par rapport à une balance à poids mort. Le TCD du chromatographe est étalonné par injection à la seringue de volumes connus de chacun des deux composés.

Les deux appareils ont permis de reproduire les résultats de la littérature avec une bonne précision. Alors qu'ils nécessitent des temps similaires pour atteindre l'équilibre, la méthode "statique-analytique" offre une technique de prélèvement plus fiable, grâce aux deux échantillonneurs ROLSI™. En conséquence, la répétabilité de l'échantillonnage pour la méthode "statique-analytique" est supérieure à la méthode "dynamique-analytique". La méthode d'étalonnage TCD proposées pour la méthode "dynamique-analytique" est plus simple que la méthode présentée pour la méthode "statique-analytique". Le problème le plus important rencontré lors de l'étalonnage par des injections directes de corps purs à la seringue est que l'incertitude dans les compositions molaires est amplifiée lorsque le nombre de moles dans l'échantillon est proche de l'erreur d'étalonnage. Pour s'assurer que le niveau d'incertitude est réduit au minimum, de grands échantillons doivent être prélevés durant toutes les mesures avec la méthode "statique-analytique". La méthode d'étalonnage TCD proposée pour l'appareillage "dynamique-analytique" est avantageuse car elle fournit directement le niveau d'incertitude dans la composition molaire finale.

Avec la bonne procédure, les deux appareillages peuvent être utilisés pour mesurer efficacement un grand nombre de systèmes contenant des composés oxygénés, et sur une large gamme de conditions.

Experimental data and modeling are part and parcel in the understanding of phase behaviour and thermodynamic properties. Accurate data and reliable experimental techniques continue to be highly regarded in modern industries [157, 158]. Mixtures of oxygenated compounds are often highly non-ideal due to the formation of hydrogen bonds and polar interactions; thus theoretical approaches and model predictions are often insufficient without the support of actual experimental data. Of equal importance is the numerous phenomena present in the phase equilibria that make such systems useful for testing equations of states. The apparatuses presented in this chapter are considered to be of sufficient accuracy for the design and development of thermodynamic models and unit operations. Human errors aside, the apparatus operate with an uncertainty in repeatability within 1 % of the final values.

This chapter is the first of two experimental chapters, and is divided into sections concerning low and high pressure vapour-liquid equilibria (VLE) measurements. In each section, the layout of the apparatus is presented, followed by the experimental procedures, and the results obtained. Isothermal and isobaric data for nine binary systems containing oxygenated compounds are presented herein. The chapter also proceeds to discuss steps in evaluating the experimental uncertainties that can be applied for both Chapters 3 and 4. The modeling of the VLE results, using the PC-SAFT equation of states, is presented from Chapter 5 onwards.

3.1 Low pressure vapour-liquid equilibria by a "dynamic-analytic" method

3.1.1 Overview

Synthetic biofuel components, such as methyl esters, pyrolysis oil and ETBE, are low pressure in mixture due to their large molecular size and specific operating conditions. Methyl esters, for example, are separated using liquid-liquid extraction from transesterification products glycerol and methanol at atmospheric pressures due to the low boiling points of the components [159]. ETBE, at maximum etherification conditions (~ 353 K), exerts a vapour pressure of barely more than 2 bars when in mixture with other reactor products [160, 161].

From the vast range of possible biofuel mixtures, this work focuses on cyclic compounds in mixture with oxygenated substances such as ethanol and acetic acid. Carboxylic acid data are particularly significant in gaining insight to the thermodynamic properties of pyrolysis oils, as well as addressing a domain of modeling less ventured from a PC-SAFT point of view. In this work, vapour-liquid equilibria measurements at atmospheric pressures and below are carried out using a "dynamic-analytic" apparatus developed by Raal [162]. In the "dynamic-analytic" method, the two-phase mixture is re-circulated continuously (dynamic) in a closed environment, thereby attaining steady-state equilibrium. Upon equilibrium, provisions are made for sampling separately the present phases for analysis (analytic).

The binary systems measured in this section are summarized in Table 3.1, including the test system (ethanol + cyclohexane) and the systems where new data have been recorded. The materials and their respective suppliers are provided in Table 3.2. All chemicals, except for acetone, were used without further purification, but their pure component vapour pressures were measured for consistency with literature values (see § 3.1.5). The acetone was further purified using a spinning band distillation column (from B/R Instrument Corp, Model 9600 Series, USA). The purified acetone was tested on an Atago refractometer (Model RX-7000α, Japan) to have a refractive index of 1.35841 at 293 K, comparing favourably to the literature value of 1.3588[1].

3.1.2 Description of the dynamic-analytic apparatus

The VLE apparatus is, in brief, a modification of the still of Yerazunis et al. [163] for low pressure measurements. The apparatus is constructed of glass, thus allowing a maximum pressure of 1 atm. Liquid in a stirred reboiler chamber of ~ 80 cm^3 is heated via two heaters, *viz*, an external heater for reducing the surrounding heat loss; and an internal heater for smooth boiling and control of circulation rate. The boiled vapour-liquid mixture moves up a

[1] http://invsee.asu.edu/nmodules/engmod/proprefrac.html

Table 3.1: Binary systems measured by the "dynamic-analytic" apparatus for low pressure vapour-liquid equilibria.

Component 1	Component 2	Temperature (K)	Pressure (kPa)
ethanol	cyclohexane	323 - 354	29 - 100
n-hexane	1-propanol	338 - 365	99
ethanol	*m*-xylene	323 - 410	4 - 95
ethanol	ethylbenzene	323 - 343	8 - 73
benzene	acetic acid	323 - 343	8 - 74
toluene	acetic acid	353 - 363	28 - 64
acetone	formic acid	323	16 - 82

Table 3.2: Purity and supplier of the compounds used in the measurement of low pressure vapour-liquid equilibria.

Compound	Formula	CAS number	Purity (% analysis)	Supplier
acetic acid	$C_2H_4O_2$	64-19-7	≥ 98 % v/v	Merck
acetone	C_3H_6O	67-64-1	≥ 98 % v/v	Merck
benzene	C_6H_6	71-43-2	≥ 99 % GC	Sigma-Aldrich
cyclohexane	C_6H_{12}	110-82-7	≥ 99.5 % GC	Merck
ethanol	C_2H_6O	64-17-5	≥ 99.8 % v/v	Sigma-Aldrich
ethylbenzene	C_8H_{10}	100-41-4	≥ 98 % GC	Fluka
formic acid	CH_2O_2	64-18-6	≥ 98 % GC	Fluka
n-hexane	C_6H_{14}	110-54-3	≥ 98 % GC	Merck
1-propanol	C_3H_8O	71-23-8	≥ 99 % v/v	Merck
toluene	C_7H_8	108-88-3	≥ 99.9 % GC	Sigma-Aldrich
m-xylene	C_8H_{10}	108-38-3	≥ 99.9 % GC	Sigma-Aldrich

Table 3.3: GC column temperatures for each of the measured, low pressure binary systems

System	T_{column} (K)
ethanol + cyclohexane	333
n-hexane + 1-propanol	378
ethanol + *m*-xylene	373
ethanol + ethylbenzene	373
benzene + acetic acid	423
toluene + acetic acid	423
acetone + formic acid	423

vacuum-jacketed Cottrell tube by capillary action, and discharges into the overhead space of the equilibrium chamber. Upon discharge, the mixture is brought in contact with a Pt-100 temperature surface element connected to an Agilent data acquisition unit (model 34401A, 6½ digits). The vapour-liquid mixture is forced down a packed section of the equilibrium chamber, consisting of stainless steel (SS.) wire mesh cylinders of 3 mm dimensions. This allows rapid mass transfer between the existing phases with minimal pressure drops [162]. At the bottom of the equilibrium chamber, the mixture, which is in equilibrium, exits through small holes in the bottom of the chamber. The liquid disengages from its vapour phase, and flows downwards to a small liquid trap with a built-in teflon septum. The septum is encased by a plastic cap, thus the maximum temperature of the apparatus should not exceed ~ 443 K. Samples of the liquid phase are taken from the septa (S1) with a plastic syringe for analysis by gas chromatography.

The disengaged vapour phase flows upwards around a concentric layer of the equilibrium chamber, and downwards again through a third concentric layer before arriving at a double condenser. This seemingly long-winded route is an effort to provide thermal insulation to the equilibrium chamber. The system pressure is controlled at the top of the condenser via a vacuum pump with an electronic manostat (BÜCHI, model B-721) utilizing a pressure transducer (Sensotec, model HM) and solenoid valve. A needle valve and two 5-liter ballast flasks in series with the manostat and the vacuum pump smooth pressure fluctuations. The vapour is condensed at the double condenser with re-circulating ethylene glycol cooling fluids. The vapour condensate falls down a droplet counter en route to a stirred condensate receiver, with a sampling setup similar to that of the liquid phase, through septa S2. The overflows of both the liquid and vapour condensate traps are returned to the reboiler chamber, to be mixed and recirculated again. The reboiler and equilibrium chambers, and the double condensers are insulated with cotton wool and aluminium foil for thermal regulation.

As indicated above, the analysis work was carried out using a gas chromatograph (Shimadzu, model GC-2010) equipped with a thermal conductivity detector (TCD) connected to a computer fitted with the Shimadzu GC Solutions software. In addition, the gas chromatograph is fitted with a Shimadzu AOC-20i auto-injector equipped with a 1 μL syringe (SGE, Australia). A capillary-type analytical column is used for all the systems measured - a Cwax 20M Bonded with 25 m length, 0.53 mm inner diameter, and 1 μm film thickness. Helium was used as the carrier gas, and the temperatures of the TCD and the injector were maintained at 513 K for all aforementioned systems. The column temperatures for each of the systems measured can be found in Table 3.3.

3.1.3 Experimental procedures

Temperature and pressure sensor calibrations

The Pt-100 surface element, connected to an Agilent data acquisition unit, is calibrated against a standard Pt-100 reference probe connected to a WIKA CTH 6500 display. Both Pt-100 sensors are submersed in a WIKA 9100 oil bath with silicon oil. The temperature of the oil bath is increased and decreased monotonically until the working

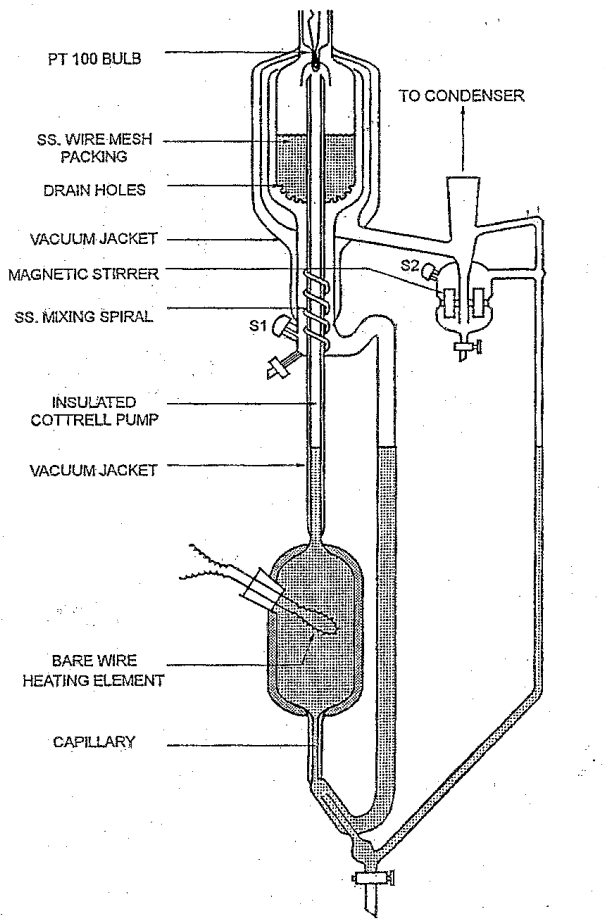

Figure 3.1: Illustration of the "dynamic-analytic" VLE apparatus, developed by Raal, and used for measurements of low pressure vapour-liquid equilibria. Taken from Raal and Mühlbauer [162].

range is covered. This ensures that hysteresis within the instrument is detected. At each consignment of temperature, the displays on the WIKA CTH 6500 and the Agilent 34401 A are allowed to stabilize before being recorded. The relationship between the true temperature T_{true}, given by the WIKA CTH 6500 display, and the experimental temperature T_{exp}, given by the Pt-100 surface element, can be described with good accuracy using a second-order equation. This is shown in Fig. 3.2, which presents the second-order relation and equation, and the deviation of T_{exp} from T_{true}. The red symbol is the point of maximum departure of the experimental value from the true value; thus we report the temperature calibration *error*[2] as ± 0.1 K. The calibration correlation errors in this work will always be given as the maximum value from the calibrations.

The Sensotec pressure transducer is calibrated against a WIKA CPH 6000 digital calibrator multimeter, fitted with a standard reference transducer (WIKA) of 1 atm maximum pressure. A pneumatic hand pump (WIKA, model WICP M500) is attached to both the reference and the Sensotec transducer. The pressure to the reference and Sensotec transducers can be increased by compressing the hand pump, and decreased via a precision needle valve. In this way, the entire working range is covered from ~ 10 - 101 kPa with almost uniform intervals. The drift for the

[2] To avoid confusion at this stage, the term *error* is simply defined as the difference between the measured value and the true value, of the quantity being studied. The only other quantitative way to express experimental imperfection, that will be used in this work, is *uncertainty*. Uncertainty reporting is less trivial than error reporting, and a separate section (§ 3.1.4) has been designated for this.

Sensotec pressure transducer in the current apparatus is observed to be very large, possibly due to its age. A single equation, in second-order, relates the true (CPH 6000) and experimental (Sensotec) pressures. The second-order relationship offers a slightly smaller deviation, in hundredths of kPa, than the first-order. This keeps the correlation tight, even at the low pressure ranges of operation. Pressure calibration correlation errors are given to be ± 0.02 kPa.

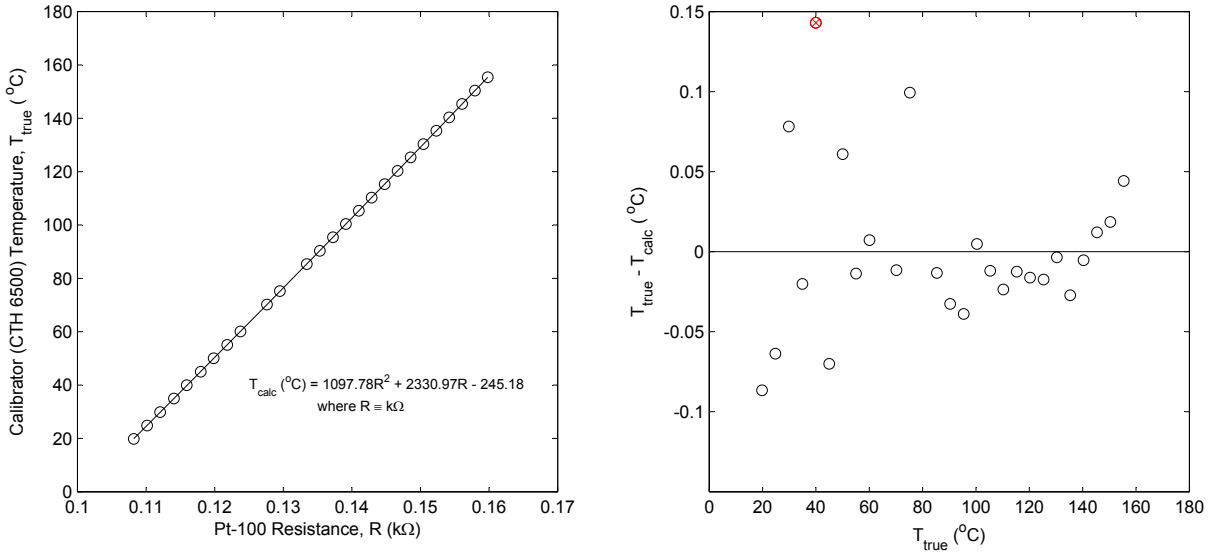

Figure 3.2: Calibration of the Pt-100 surface element for the "dynamic-analytic" apparatus. *left:* Second-order relation between the true and probe temperatures. *right:* Deviations from the true temperature, resulting from the use of a second-order relation. The ⊗ symbol denotes the furthest departure.

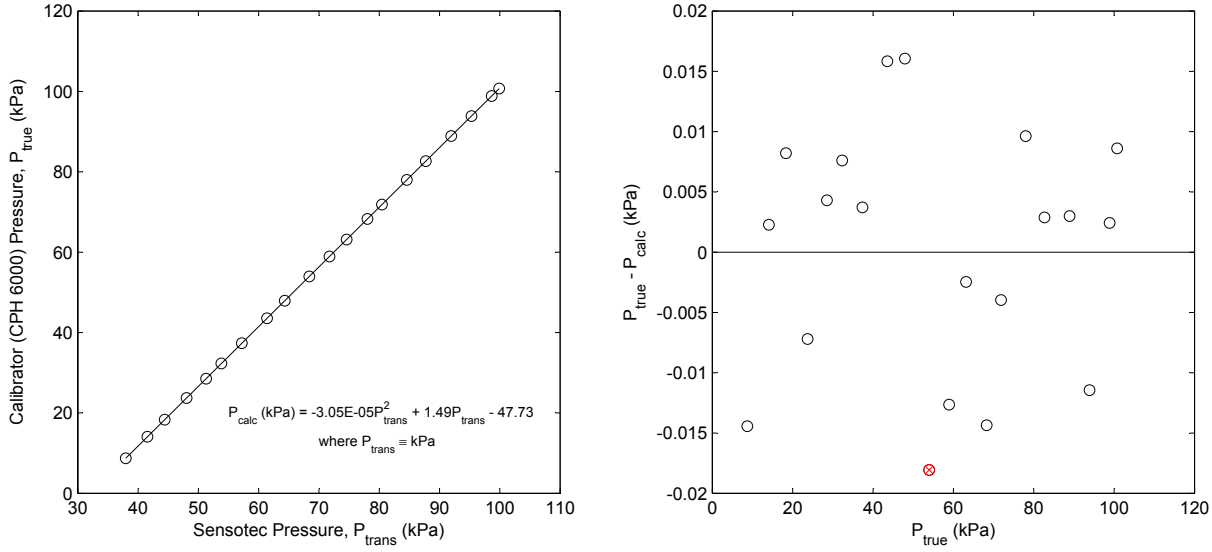

Figure 3.3: Calibration of the pressure transducer for the VLE dynamic-analytic apparatus. *left:* Second-order relation between the true and transducer pressures. *right:* Deviations from the true pressure, resulting from the use of a second-order equation. The ⊗ symbol denotes the furthest departure.

TCD calibration

The detector in a gas chromatograph produce peaks proportional to the amount of the material passing at its retention time. It provides no additional information on the relation between peak area and actual mole numbers, other than those given by the user through the calibration. All experimental values are no more accurate than the calibration used.

For liquid phase components at ambient conditions, we employ the method of TCD calibration as suggested by Raal and Mühlbauer [162]. In this method, standard mixtures of known compositions are prepared by gravimetrically weighing predetermined masses on a balance (Ohaus Adventurer, Model AR2140, maximum error 0.1 mg). The standard solutions are thoroughly mixed, with as little vapour space as possible left in the container after both components have been added. The entire volume of the container within which the solutions are prepared should be filled in order to prevent flashing of the mixture. With each mixture, the auto-injector (Shimadzu AOC-20i) delivers a constant volume - 0.1 μL - to the detector, yielding two TCD peaks with the ratio of the peak areas as A_i/A_j. With the application of the auto-injector, repeatability with syringe injections is somewhat improved, although inherent faults in the syringe, and other error sources such as adsorption, persist. Unlike the calibration of a gaseous component, which will be discussed in § 3.2.3, the actual volume passing through the TCD is irrelevant, as the method of Raal and Mühlbauer does not use volume in the calculation of mole fractions. The only requirement is that the syringe and auto-injector should be sufficiently functional to deliver the same volume throughout the entire experiment. By considering the errors stemming from the mass balance as negligible, there are very few sources of uncertainties for this calibration method.

In their method, Raal and Mühlbauer defines the TCD response factor F_i as a proportionality constant between n_i moles of a component i passing through the detector, and the resulting peak area A_i. Applying this definition for a binary mixture of components i and j, we can write the following relations:

$$n_i = F_i A_i \qquad n_j = F_j A_j \tag{3.1}$$

$$\frac{n_i}{n_j} = \frac{x_i}{x_j} = \left(\frac{F_i}{F_j}\right)\left(\frac{A_i}{A_j}\right) \tag{3.2}$$

In practice, the mole number ratios n_i/n_j are more linearly proportional to their peak area ratios A_i/A_j (Eqn. 3.2), than mole numbers n_i are to their peak areas A_i in the presence of $A_{j\neq i}$ (Eqn. 3.1). The linear slope in each case may be determined using a least squares method from a set of x_i-A_i data, where a smaller deviation is obtained if the TCD is characterized by the relation of Eqn. (3.2). We adopt only response factor ratios in this work, and respect the limiting condition that $x_i = 0$ at $A_i = 0$. The peak area ratios A_i/A_j obtained during the experiment will always remain within the calibration range, provided the slope passes through the origin.

Raal and Mühlbauer stated that the response factor ratio F_i/F_j is usually not a constant value across the entire range of composition, save for some binary systems. They advised to divide the composition range into a dilute and concentrated region, based on one of the components. Thus, for any acquisition of peak areas, the dilute region uses the equation:

$$x_1 = \frac{a\,A_1}{A_2 + a\,A_1} \qquad \text{where} \qquad a = \frac{F_1}{F_2} \tag{3.3}$$

whereas in the concentrated region, the ordering of Eqn. (3.2) is reversed, i.e. x_2/x_1 is plotted against A_2/A_1, with the slope being F_2/F_1:

$$x_1 = \frac{A_1}{A_1 + bA_2} \qquad \text{where} \qquad b = \frac{F_2}{F_1} \tag{3.4}$$

For most of the systems studied in this work, the response factor ratios of the dilute region is approximately the reciprocal of that of the concentrated region ($a \simeq 1/b$). This implies that a single response factor ration could even be used for the entire range of composition. The percentage error in the mole fraction may be slightly increased by doing so, but the effects on the final mole fractions were only noticeable in the third decimal place. The manner in which the boundary between the dilute and rich region is established is arbitrary, provided that a common fraction is shared in both calibration ranges, and the correct equation (3.3 or 3.4) is chosen for the calculation.

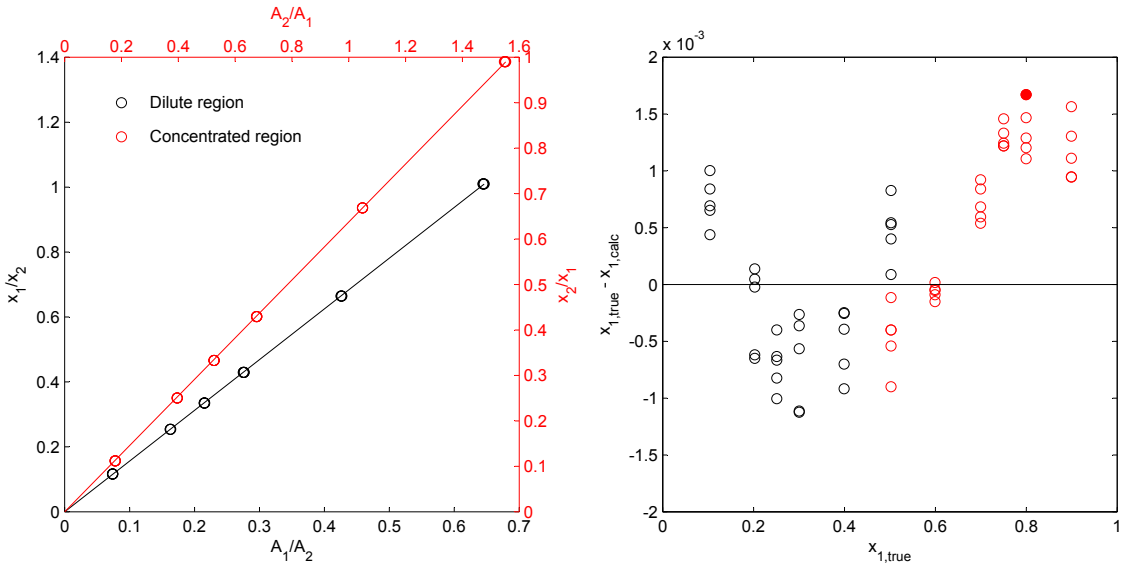

Figure 3.4: TCD Calibration for the ethanol (1) + cyclohexane (2) system using the method of Raal and Mühlbauer. *left:* Linear relation between the area and mole fraction ratios. The black line (and axes) depicts the dilute region calibration, the region defined as $0 < x_1 \leq 0.5$, while the red depicts the concentrated region calibration, used for $0.5 \leq x_1 < 1$. *right:* Error compared to the true composition, resulting from the use of Eqn. (3.3) and (3.4). The filled symbol denotes the maximum error, in mole fraction.

TCD calibration in the presence of an impurity

The above calibration technique was valid for all but the acetone + formic acid system, which proved a challenge due to the presence of the impurity, water, in the formic acid reserves. Due to time constraints, it was not possible to purify the formic acid via vacuum distillation to remove the 2 % water specified by the manufacturer. Standard purification was not possible due to the acid's tendency to oxidize at high temperatures in contact with air, neither could the water be removed via molecular sieving, as the acid proved too corrosive upon contact. The optimum GC conditions for this binary system were difficult to find, because a single pass of formic acid through the TCD produces two peaks, the acid and impurity water, which are spaced well apart. When the water peak, denoted here by A_w, superimposes with the peak of the second component (acetone), the acetone peak A_a is either obscured (for small acetone mole numbers), or enlarged (for high acetone mole numbers). This is illustrated in Fig. 3.5.

With the current setup, it was not able to split the peaks, as the water peak may at times be completely contained in the acetone peak, thus not be visible. In both cases in Fig. 3.5, one has access to the formic acid area A_f, and an *apparent* acetone area $A'_a = A_a + A_w$, provided that peak integration is performed from baseline to baseline. We know the *true* acetone area A_a is the difference between the apparent acetone area, and that of water A_w. A simple way of obtaining the desired A_a for each pass of acetone + formic acid mixture through the TCD, is to know in advance the size of A_w as a function of the formic acid peak area, i.e. $A_w = f(A_f)$. This is done by injecting into the TCD different volumes of pure formic acid using the auto-injector, and noting each time the area of the two peaks on the chromatogram. Once a sufficiently wide range of A_f and A_w has been covered, the relationship between the two peaks is described by a second-order polynomial. To remain physically consistent, the polynomial necessarily passes through the origin.

The calibration of the acetone + formic acid mixture, from the preparation of standard solutions, proceeds as before. For each apparent acetone peak integrated, it is necessarily to subtract from the calculated area the contribution which is water, using the second-order relation determined beforehand. The slope or response factor

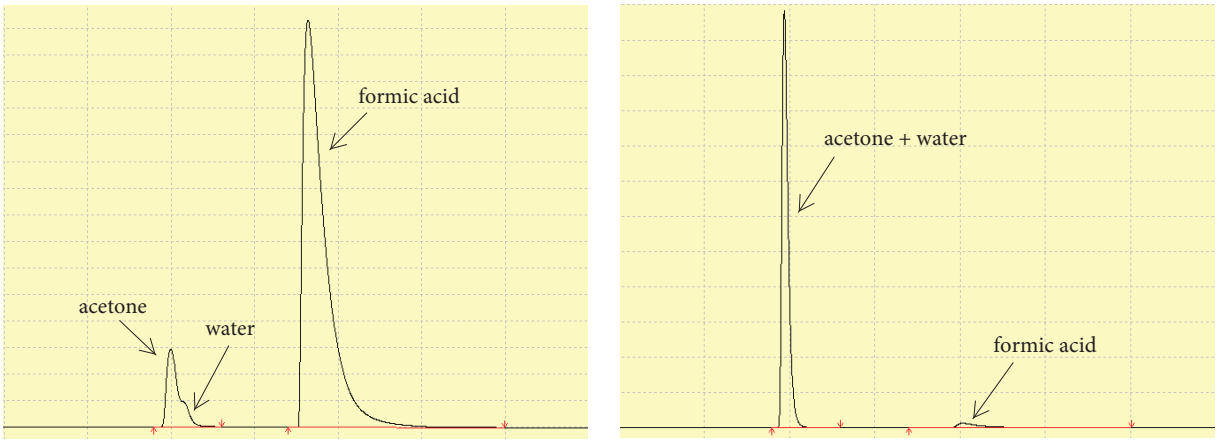

Figure 3.5: Chromatograms of a 5 % acetone - 95 % mol formic acid mixture (*left*), and a 90 % acetone - 10 % mol formic acid mixture (*right*). In the *left* figure, the 'first' peak is in fact a combination of two peaks, that of acetone, and water. The latter is present in formic acid as an impurity. The impurity obscures the shape of the desired, acetone peak. In the *right* figure, the water peak is completely invisible within the first acetone peak. The impurity in this case is contained in the first peak, making the peak larger than intended.

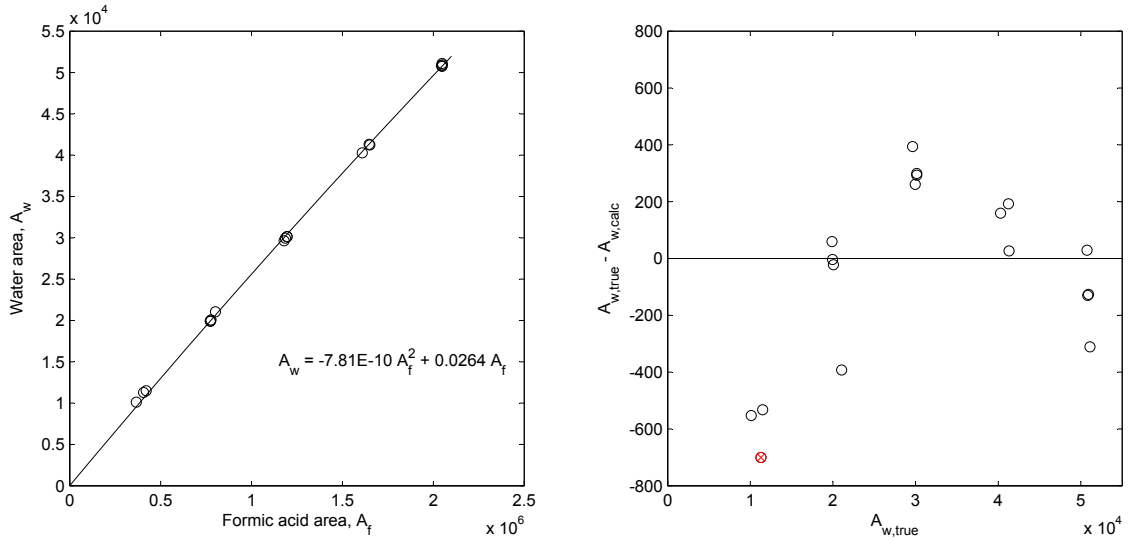

Figure 3.6: Calibration of the water (impurity) peak area A_{w} as a function of the peak area of formic acid A_{f}, the desired component. *left:* Second-order relation between A_{w} and A_{f}. *right:* Deviations from the true A_{w}, resulting from the use of a second-order equation. The ⊗ symbol denotes the furthest departure

ratio obtained in this manner pertains to the true acetone peak area. The mole fraction calculated using Eqn. (3.3) or (3.4) is based on a water-free (true) acetone area; thus the water portion must be removed prior to its use.

The above approach is not a standard laboratory procedure, and should not be preferred over testing more suitable GC columns. It will be shown later that increasing the number of relations used in determining x_1 only serves to increase its final uncertainty. The method should be regarded as a last resort only.

Experimental method

The equilibrium still is loaded with the first of two components, through one of the sampling ports (S1 or S2), until the reboiler chamber has been filled (~ 80 cm^3). Degassing prior to loading is not mandatory, as the pressure is controlled by the setpoint on the electronic manostat. The external and internal heaters are adjusted, in tandem, until a fasting pumping action in the Cottrell pump is achieved. As the temperature approaches that of equilibrium, its value will gradually remain constant, plateauing off and becoming independent of the input voltage from the two heaters. Thereafter, the operator is only required to intervene by fine-tuning the internal heating such that:

- a healthy drop rate in the droplet counter, of approximately 2 - 3 drops per second, is observed.
- a good recirculation is achieved within the apparatus, with constant recycling from both the liquid and vapour condensate traps.
- no admixture occurs between the sampling traps and the returning liquid/condensates through over-boiling.
- the system remains at all times in the plateau temperature region, where temperature does not respond to changes in heating cartridge voltages.

Equilibrium is usually attained within 45 - 60 minutes for mixtures, and less for pure components. The second component is then injected with a syringe, altering the temperature in the process to correspond to the first temperature measurement. In the case of isothermal operation, the pressure setpoint is in turn adjusted such that a constant temperature is maintained upon each addition. Care is taken that the equilibrium still is not flooded through over-loading. Upon equilibrium, the constant temperature and pressure values are recorded. Samples of both the liquid and vapour phases are withdrawn, using 2 mL plastic syringes, from their respective sampling chambers. Small samples of ~ 0.5 mL were taken in rapid succession, and analyzed repeatedly in the gas chromatograph for repeatability. Samples not being analyzed immediately are kept in small 2 mL vials in ice baths to prevent flashing. This manual sampling, albeit convenient, is considered to be the weaker, less accurate part of the procedure. At extremely low pressures (~ 20 kPa), near-vacuum within the apparatus needs to be overcome in order to withdraw the smallest of samples, a failure of which may displace the system from equilibrium. Furthermore, the two teflon septa fitted to the apparatus are damaged easily through the manual sampling, and needs to be replaced regularly. In the case where a septum needs replacement during an experiment, it is necessary to stop the apparatus and empty its contents.

More amounts of the second component are added after each sampling and analysis, until the entire phase diagram has been traversed.

3.1.4 Estimation of uncertainty for low pressure measurements

Prior to presenting the results, it is necessary to digress to the topic of uncertainty estimation. Uncertainty results from doubts that originate from the measurement, and is quantified as an interval within which the true value of measurement has a high probability of residing. Error reporting and uncertainty reporting are not the same (see footnote on page 74). The error is a straightforward observation, used also in the calculation of uncertainty, the latter of which is statistics-based exercise. Only uncertainty, and not error, is expressed alongside NIST measurement results [164]. Several approaches exist for reporting uncertainties, and the reader can refer to standard textbooks on metrology for terminologies employed throughout this chapter. Evaluation of uncertainties are subject to the interpretation of the experimentalist; the sources of uncertainties considered in the calculations are those believed to be non-negligible.

Regardless of the nature of the quantity θ being studied, the objective is to express for θ an interval of uncertainty that is a combination of all the possible sources of uncertainties. This is referred to as the combined standard

uncertainty $u_c(\theta)$:

$$u_c(\theta) = \pm \sqrt{\sum_i u_i(\theta)^2} \tag{3.5}$$

where $u_i(\theta)$ could be any source of uncertainty, such as errors resulting from the use of a calibration polynomial, or the standard deviation from averaging multiple observations. The possible entries for $u_i(\theta)$ are discussed below.

Temperature and pressure uncertainty

Uncertainties in temperature and pressure arise from calibration imperfections and repeated readings of a single transducer. The estimation is straightforward and can be applied to both the low and high pressure measurements. The following steps are shown for temperature but can be interchanged with pressure. We have already identified the sources of uncertainties to insert in Eqn. (3.5):

$$u_c(T) = \pm \sqrt{u_{\text{calib}}(T)^2 + u_{\text{rep}}(T)^2} \tag{3.6}$$

with subscripts *calib* and *rep* denoting that of calibration and of repeatability, respectively. The upper and lower limits of uncertainty from the temperature calibration is determined from the calibration polynomial, and is illustrated in Fig. 3.2 to be, rounded off, ± 0.1 K. We assume that the temperature is equally likely to fall anywhere between the two limits, such that a uniform or rectangular distribution is followed. Uncertainties based on this prescribed distribution is referred to as a *type B* calculation (random uncertainty), and is given for a rectangular distribution as:

$$u_{\text{calib}}(T) = \frac{b}{\sqrt{3}} \tag{3.7}$$

The quantity b is the half-width between the upper and lower limits, i.e. $b = 0.1$ K in our case, the quantity that we have referred to as *error* (see Fig. 3.2 for more details).

For calibrations, a range of T and P has to be considered; thus we did not use a Gaussian distribution there. However, consider during an experiment, that unless the temperature remains perfectly constant at the moment of every sampling, the withdrawal of n samples will result in n temperature readings being recorded. The averaging of repeated readings yields a mean $\bar{T}$ with a standard deviation σ. As before, this can be statistically converted to an uncertainty due to *repeatability of the measurements*, via:

$$\begin{aligned} u_{\text{rep}}(T) &= \frac{\sigma}{\sqrt{n}} \\ &= \sqrt{\frac{1}{n(n-1)} \sum_{i=1}^{n} \left(T_i - \bar{T}\right)^2} \end{aligned} \tag{3.8}$$

where n is the number of repeated measurements. A Gaussian type of distribution is the likely behaviour here, since the repeated readings are likely to fall close to the mean. This is known as a *type A* evaluation (systematic uncertainty), where only statistical methods are required to interpret the uncertainty.

Molar composition uncertainty

The two sources of uncertainties that arise with each determination of molar composition are the imprecision that is present in the TCD calibration, and the standard deviation from the averaging of the repeated samples. The combined standard uncertainty for molar composition is analogous to that of temperature and pressure:

$$u_c(x_i) = \pm \sqrt{u_{\text{calib}}(x_i)^2 + u_{\text{rep}}(x_i)^2} \tag{3.9}$$

where the subscript i denotes component i. The manner in which the TCD is calibrated for low pressure measurements differs from that of high pressure (§ 3.2.3), therefore the method given herein is based on the procedure of Raal

and Mühlbauer. In general, when a quantity θ is determined from the measurement of other quantities α_i, then the uncertainty $u(\theta)$ will be governed by the uncertainties present in each of the measured quantities $u(\alpha_i)$. This is the definition of the root-sum-squared uncertainty:

$$\theta = f(\alpha_1, \alpha_2, \ldots, \alpha_n)$$
$$u(\theta) = \sqrt{\left[\left(\frac{\partial\theta}{\partial\alpha_1}\right)_{\alpha_{i\neq1}} u(\alpha_1)\right]^2 + \left[\left(\frac{\partial\theta}{\partial\alpha_2}\right)_{\alpha_{i\neq2}} u(\alpha_2)\right]^2 + \ldots + \left[\left(\frac{\partial\theta}{\partial\alpha_n}\right)_{\alpha_{i\neq n}} u(\alpha_n)\right]^2} \tag{3.10}$$

In $u_{\text{calib}}(x_i)$, uncertainties exist in the preparation of the standard solutions as a result of the imperfections in the balance (denoted B). Furthermore, the use of Eqn. (3.2) results in an error that is demonstrated in Fig. 3.4 (denoted corr). Applying Eqn. (3.5) again, we have:

$$u_{\text{calib}}(x_i) = \sqrt{u_{\text{B}}(x_i)^2 + u_{\text{corr}}(x_i)^2} \tag{3.11}$$

Since x_i is dependent on the measurement of the masses m_i and m_i:

$$u_{\text{B}}(x_i) = \sqrt{\left[\left(\frac{\partial x_i}{\partial m_1}\right)_{m_2} u(m_1)\right]^2 + \left[\left(\frac{\partial x_i}{\partial m_2}\right)_{m_1} u(m_2)\right]^2} \tag{3.12}$$

Using the definition $x_i = n_i/(n_i + n_j)$ and $n_i = m_i/MM_i$, where MM is the molecular mass, Eqn. (3.12) can be simplified to:

$$u_{\text{B}}(x_i) = x_1 x_2 \sqrt{\left(\frac{u(m_1)}{m_1}\right)^2 + \left(\frac{u(m_2)}{m_2}\right)^2} \tag{3.13}$$

Both values of $u(m_1)$ and $u(m_2)$ stem from the same balance and will be equal in this case. A type B evaluation (Eqn. 3.7) is employed here using the upper and lower limits given by the manufacturer. However, Eqn. (3.13) is somewhat ambiguous as several suitable combinations of m_1 and m_2 can make up a desired x_1, and that during the analytical part of a low pressure VLE experiment, no values for m_1 and m_2 are yielded. Intuitively, the small value of the balance imprecision (± 0.1 mg) would lead to a small $u(m_i)$ term, with $u(m_i) \ll m_i$, followed by $u_{\text{B}}(x_i) \ll u_{\text{corr}}(x_i)$. While it is not unreasonable to ignore the $u_{\text{B}}(x_i)$ term altogether, we evoke a constant value for the square root term in Eqn. (3.13). By evaluating the square root term for each standard solution made for a particular binary system, the maximum value obtained is used in place of the square root term for all subsequent calculations of $u_{\text{B}}(x_i)$.

In calculating $u_{\text{corr}}(x_1)$, we use instead the *maximum error* observed when using the linear correlation, $\left|x_{1,\,\text{true}} - x_{1,\,\text{calc}}\right|_{\text{max}}$, and calculate $u_{\text{corr}}(x_1)$ using a rectangular distribution as before. $u_{\text{rep}}(x_1)$ can be calculated via a type A evaluation, as described before.

Uncertainty when calibrating in the presence of an impurity

By using the procedure described in § 3.1.4 for calibrating the TCD in the presence of an impurity, one introduces an additional source of error stemming from the formic acid-water area relation. As a result, Eqn. (3.3) is no longer exact, since $A_{\text{a}} = A'_{\text{a}} - A_{\text{w}}$ is not exact. We can consider that the two peak areas readily available from GC chromatograms - the formic acid A_{f}, and the apparent acetone A'_{a}, have negligible uncertainties. It follows for the

acetone + formic acid system, for the acetone dilute region (Eqn. 3.3):

$$x_a = \frac{\frac{F_1}{F_2} A_a}{A_f + \frac{F_1}{F_2} A_a} = \frac{\frac{F_1}{F_2} (A'_a - A_w)}{A_f + \frac{F_1}{F_2} (A'_a - A_w)}$$

$$u_{imp}(x_a) = \sqrt{\left[\left(\frac{\partial x_a}{\partial A_w}\right)_{A_f, A'_a} u(A_w)\right]^2} \tag{3.14}$$

where, $u(A_w)$ is the term given for the uncertainty that exists in the estimation of the water peak area. Additionally,

$$\left(\frac{\partial x_a}{\partial A_w}\right)_{A_f, A'_a} = -\frac{x_a x_f}{A'_a - A_w}$$

The x_a for the concentrated region can be solved similarly. $u(A_w)$ should be evaluated as a type B uncertainty with rectangular distribution and a maximum departure from the A_w correlation shown in Fig. 3.6. Furthermore, $u_{calib}(x_a)$ is modified as:

$$u_{calib}(x_a) = \sqrt{u_B(x_a)^2 + u_{corr}(x_a)^2 + u_{imp}(x_a)^2}$$

Reporting of uncertainties

As a last step, we apply a coverage factor k to re-scale the combined standard uncertainties calculated above. This is often referred to as the *expanded uncertainty* $U(\theta) = k\, u_c(\theta)$. The role of the coverage factor is to impart a particular confidence level by expanding the uncertainty interval, for $k > 1$:

$$\theta_{final} = \theta_{measured} \pm k\, u_c(\theta) \tag{3.15}$$

A value of $k = 2$ gives an approximate 95 % confidence level on the uncertainty, *if the distribution of errors follow a normal Gaussian (type A) distribution*. In this work, $u_c(\theta)$ combines both type A and B methods. Specifically, a k value of 1.65 is sufficient to give a 95 % confidence for a rectangular distribution [165]. The value of 2 employed here is simply common practice, and therefore claims to give at least a 95 % confidence level overall.

3.1.5 Results of low pressure vapour-liquid equilibrium measurements

Pure component vapour pressures

Measurements of pure component vapour pressures were carried out using the aforementioned procedure, without the phase sampling. With the exception of formic and acetic acid, which had a slightly lower purity, the experimental values were within ± 1 kPa of the literature values from Daubert et al. (DIPPR version 11, [68]). The results for formic acid were the least satisfactory, showing a marked departure from the literature values. This is expected to result from the water impurity.

Binary mixtures

The pressure-composition and/or temperature-composition phase diagrams for seven binary systems measured in this section are given in Figs. 3.9 - 3.15, with the tabulated values given in Appendix C. Error bars for each phase diagram have been included for molar compositions, but not for temperature and pressure values, due to their small

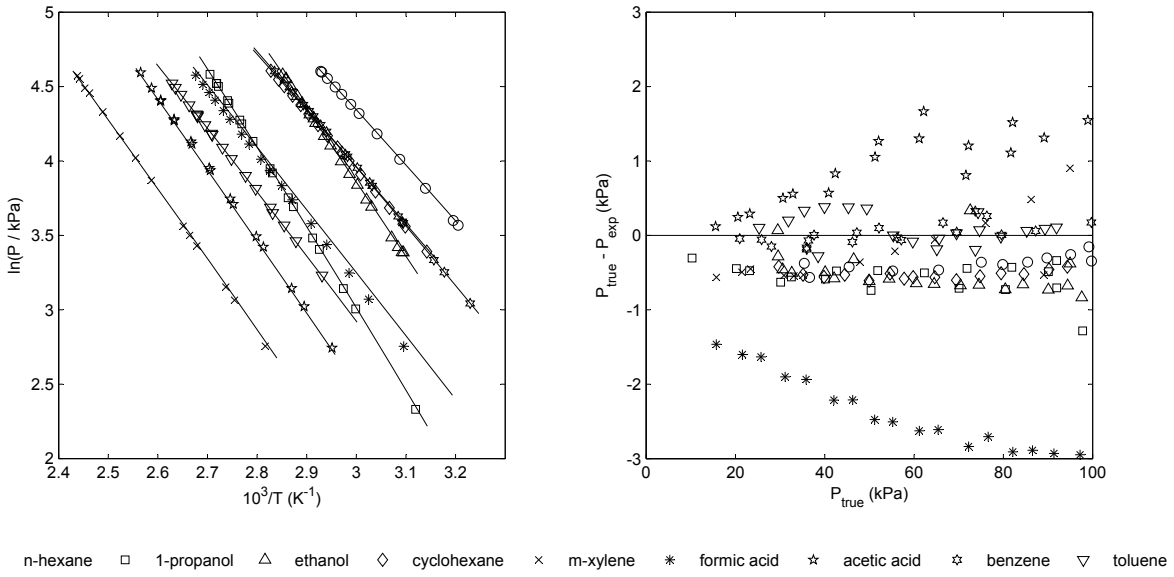

Figure 3.7: Measurements of pure component vapour pressures for the nine compounds used in the low pressure study. *left*: logarithms of pressures against inverse temperature; *right*: deviation plot between literature and experimental vapour pressures. Generally good agreements are observed with values from the DIPPR ver. 11 database of Daubert et al. [68], given as solid lines.

overall uncertainties. In general, almost all the uncertainties on the molar compositions arise from the errors in the calibration polynomial, with the other uncertainties (balance, repeatability, etc) making up ~ 1 % of the final uncertainty. A negligible uncertainty on repeated samples is particularly encouraging, since the manual sampling aspect of the apparatus is not ideal. Averaged uncertainties for the temperature, pressure and compositions of the measured systems are given in Table 3.4. The procedures outlined in § 3.1.4 determines the temperature, pressure and composition uncertainties for a single equilibrium condition, in which several repeated measurements were carried out. For a set of presented results in a single isotherm/isobar, the uncertainties are averaged over the entire dataset, which is slightly less rigorous, but the impact on the final value is negligible for the low pressure VLE measurements. The uncertainties given in the table should be regarded as averages over the entire data set.

The uncertainties on temperatures and pressures are slightly high, possibly due to the age of the transducers

Table 3.4: Averaged temperature, pressure, and mole fraction uncertainties for the binary systems measured with an apparatus based on the "dynamic-analytic" method.

		Expanded uncertainties $\bar{U}(\theta)$ with $k = 2$			
Component 1	Component 2	$\bar{U}(T)$ (K)	$\bar{U}(P)$ (kPa)	$\bar{U}(x)$	$\bar{U}(y)$
ethanol	cyclohexane	± 0.1	± 0.2	± 0.005	± 0.005
n-hexane	1-propanol	± 0.1	± 0.2	± 0.012	± 0.012
ethanol	*m*-xylene	± 0.1	± 0.2	± 0.006	± 0.006
ethanol	ethylbenzene	± 0.1	± 0.2	± 0.006	± 0.006
benzene	acetic acid	± 0.1	± 0.2	± 0.009	± 0.009
toluene	acetic acid	± 0.1	± 0.2	± 0.017	± 0.017
acetone	formic acid	± 0.1	± 0.2	± 0.022	± 0.022

used in the apparatus. The uncertainties on composition, and that of the TCD calibration, are favourably low. This outlines the effectiveness of the calibration procedure, which should be regarded as the method of choice when both the components are liquids at room temperature. This method is however not applicable to gaseous components.

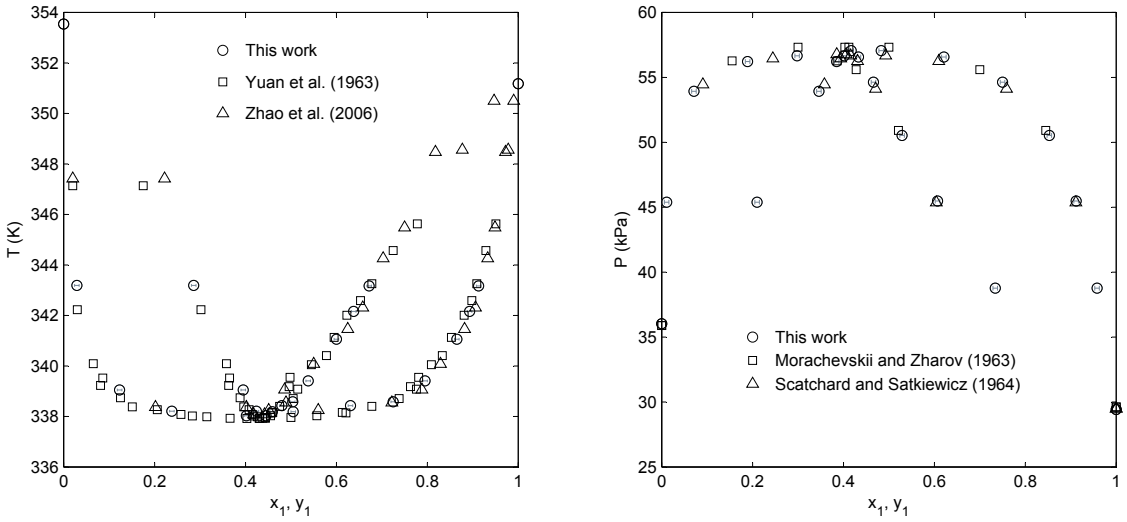

Figure 3.8: Experimental VLE data for the ethanol (1) + cyclohexane (2) binary system at 99.9 kPa (*left*) and 323.4 K (*right*), with comparison to literature data [166, 167, 168, 169].

The apparatus was first tested against the well-documented ethanol + cyclohexane system, for which good agreements were observed between the experimental and literature values. The measurements for the *n*-hexane + 1-propanol system appears erroneous when compared to the two sources of literature data [170, 171]. However, we leave this system for further discussion in Chapter 5, where we observe an interesting modeling result. For the moment, it is sufficient to note that neither of the two literature sources here are fully consistent when tested with DECHEMA standards [172, 173]. For the ethanol + *m*-xylene system, the only existing literature was by Vittal Prasad et al. at 95 kPa [174], which indicated a minimum temperature azeotrope in the ethanol-rich region. This however was not observed in our experiment, where not only was azeotropy not encountered, very little resemblance exists between the two sets of data at the same pressure. The data presented herein were verified to be consistent with predictions using the modified UNIFAC [73, 74] for the liquid phase and the Soave-Redlich-Kwong EoS [64] for the vapour phase. Several of the isotherms in Fig. 3.11 exhibit near-azeotropic behaviour, although we reinstate that no azeotropes were found for the ethanol + *m*-xylene system. This was verified by starting the measurement with pure ethanol, and adding small amounts of *m*-xylene. By observing the changes in the pressure of the system, we concluded that a local maxima in pressure/minima in temperature does not exist. The same conclusions could be reached for the ethanol + ethylbenzene system. It is worth noting that the ethanol + toluene system, the aromatic compound having one carbon atom less, exhibits prominent azeotropes (for example, the data of Kretschmer and Wiebe [175]).

For compounds in mixture with acetic acid, the addition of a branched methyl group to a benzene ring, as in toluene, leads to the presence of a clear-cut azeotrope, whereas benzene alone does not exhibit azeotropy with acetic acid. The data from Zawidzki [76] for the toluene + acetic acid system, while outdated, is surprisingly consistent with the results of this work, and as pointed out in § 1.7, not obtainable from predictive models.

For the acetone + formic acid system, the TCD response factor was highly non-linear. It was required to use two different response factors, one for each of the dilute and concentrated acetone regions, in order to obtain a good representation of the calibration data. When using a single response factor for the entire composition range, as was possible for all the other systems, errors of up to 0.05 mole fractions were observed for some area ratios.

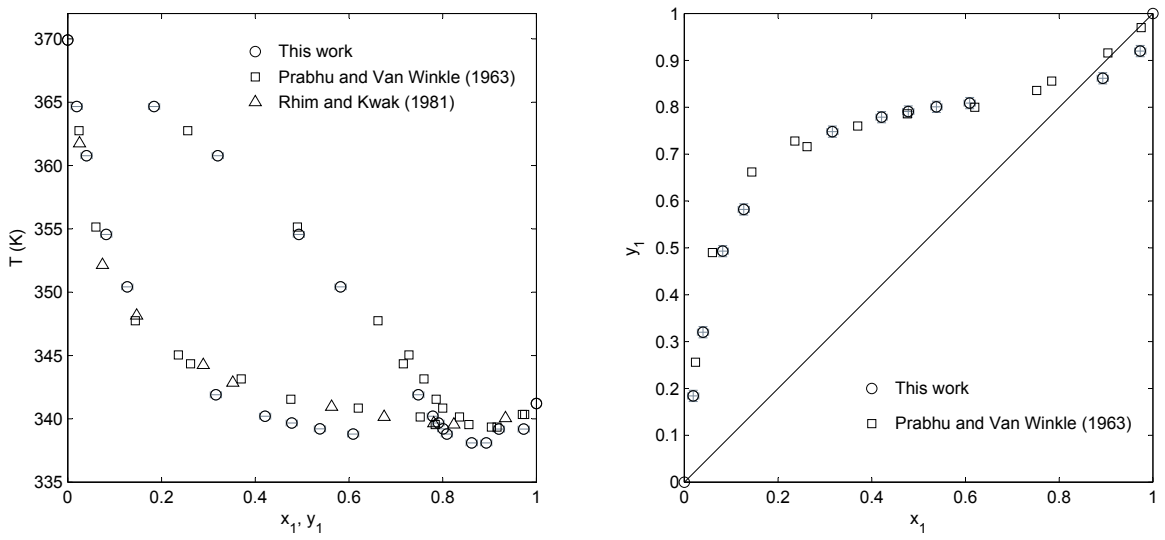

Figure 3.9: Experimental VLE data for the *n*-hexane (1) + 1-propanol (2) binary system at 98.9 kPa, with comparison to literature data [170, 171].

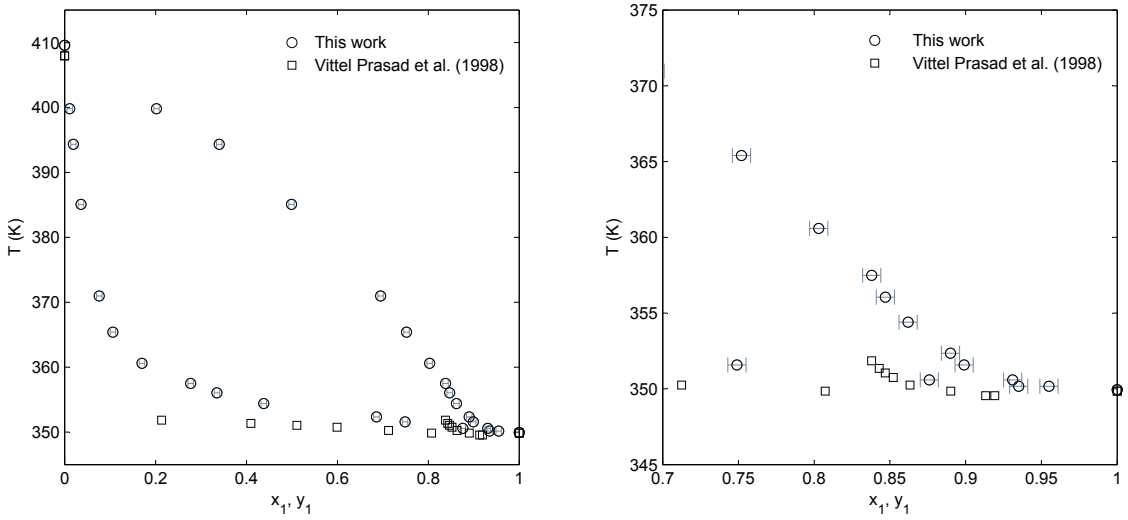

Figure 3.10: Experimental VLE data for the ethanol (1) + *m*-xylene (2) binary system at 94.9 kPa. The right figure is a zoom of the ethanol-rich region, where no azeotrope was observed in our measurements. The literature data was taken from Vittal Prasad et al. [174].

Similarly, each region will have a different $u_{\text{corr}}(x_1)$, which should be referred to accordingly when calculating uncertainties. With the formic acid not entirely pure, it is likely that the VLE curves are somewhat shifted slightly. The vapour pressure of pure formic acid, at $T = 323$ K, recorded at the start of the experiment was 15.8 kPa, which is noticeably lower than the literature values of ~ 17.3 kPa [68]. While the aforementioned calibration method may take into account the impure water peak area, it does not address the effects that water may have on the overall phase behaviour.

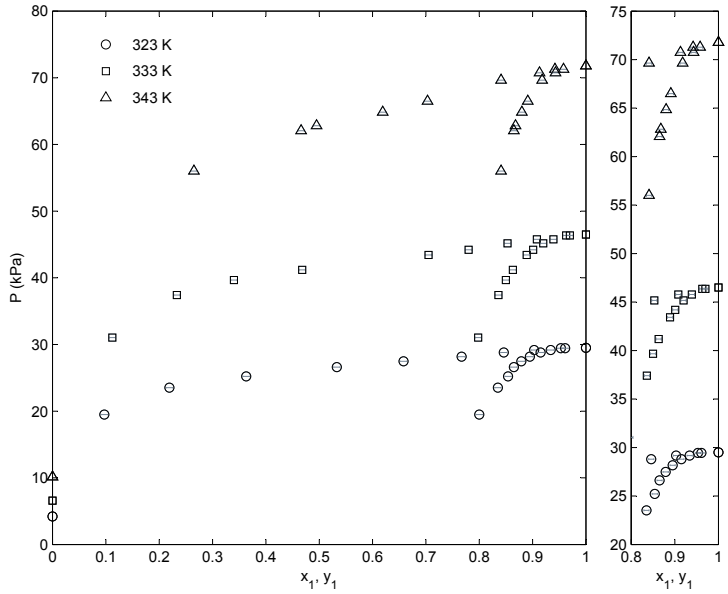

Figure 3.11: Experimental VLE data for the ethanol (1) + *m*-xylene (2) binary system at 323 - 343 K. A more detailed view of the ethanol-rich region is given alongside the figure.

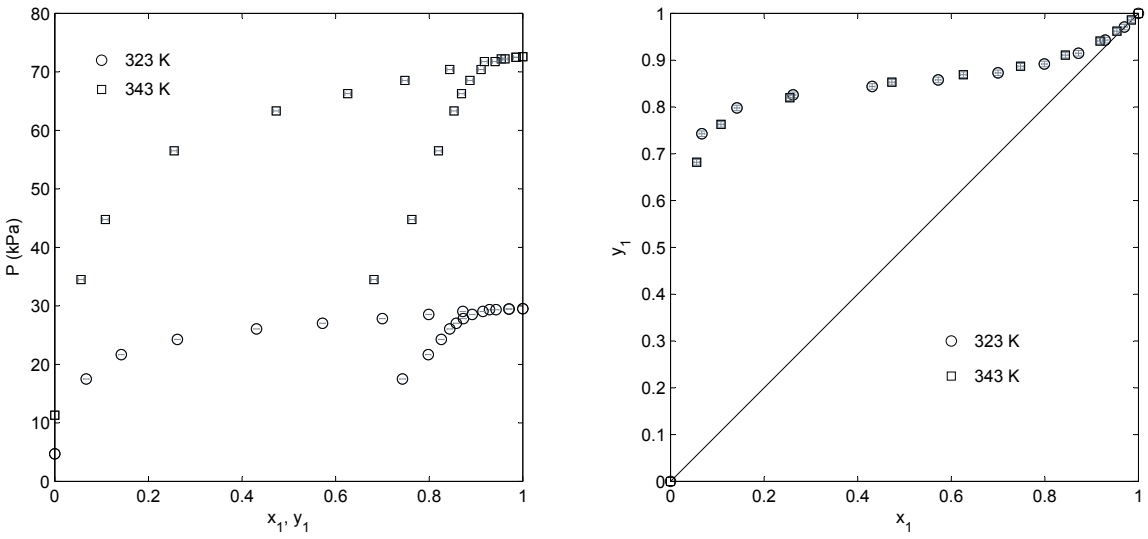

Figure 3.12: Experimental VLE data for the ethanol (1) + ethylbenzene (2) binary system at 323.3 and 343.3 K.

3.2 High pressure vapour-liquid equilibria by a "static-analytic" method

3.2.1 Overview

Systems exhibiting high pressures among biofuels are mainly restricted to bio-alcohols in mixture with light hydrocarbons. Catalyst-free transesterification of triglycerides, using supercritical methanol, require high-pressure vapour-liquid equilibria data for downstream methanol recycling. Such measurements have been performed by Shimoyama et al. [176]. This work focuses on two binary bioethanol systems, namely propane + ethanol and *n*-butane + ethanol. The former has been investigated previously by various sources [177, 178, 179, 180], although

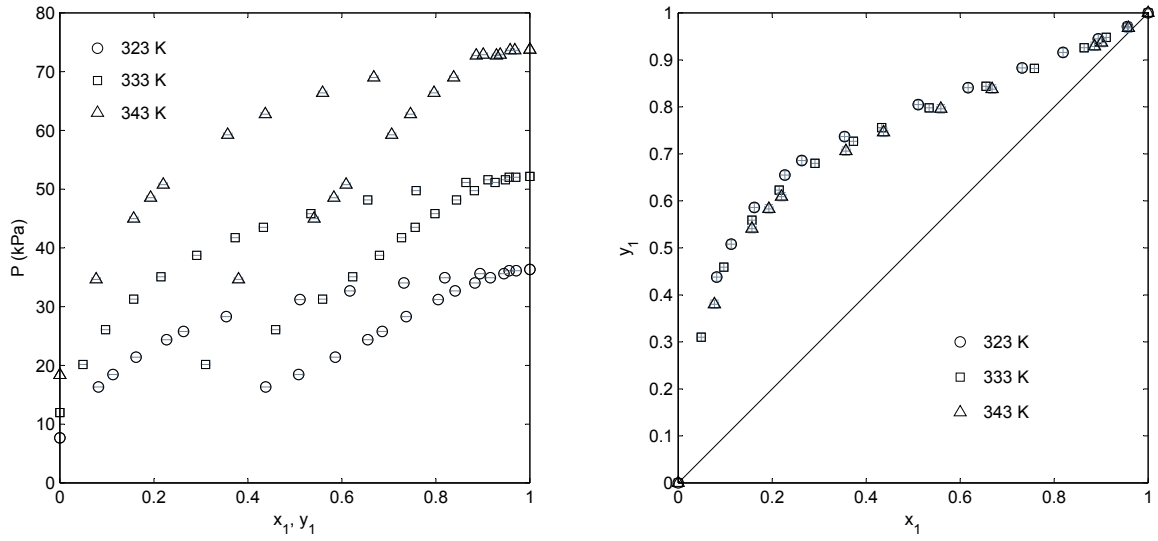

Figure 3.13: Experimental VLE data for the benzene (1) + acetic acid (2) binary system at 323-343 K. Literature data at 323 K is taken from Zawidzki [76]

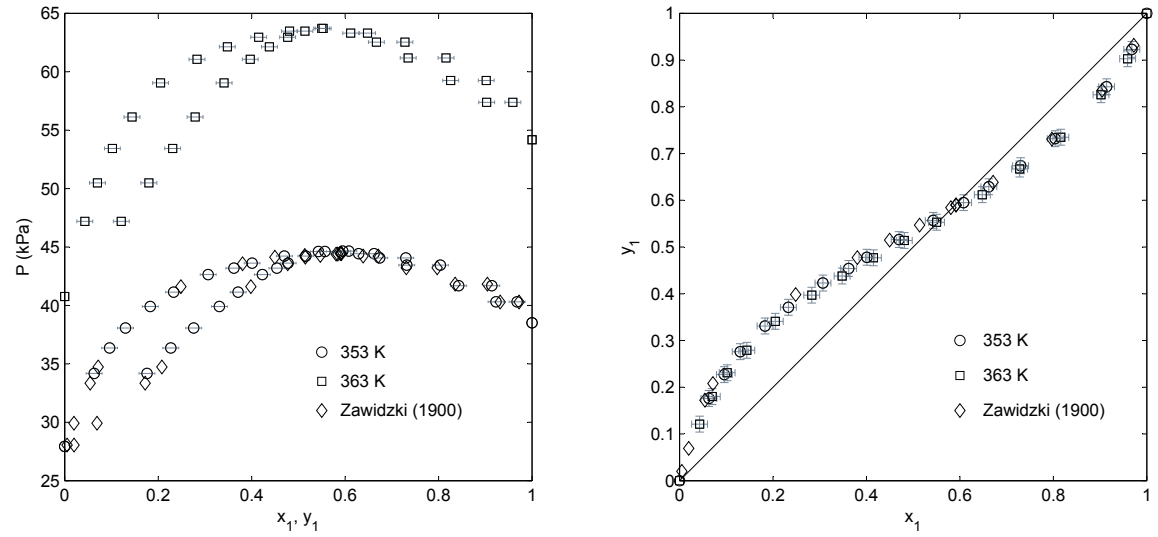

Figure 3.14: Experimental VLE data for the toluene (1) + acetic acid (2) binary system at 353.2 and 363.1 K. Literature data is from Zawidzki [76].

there is very little agreement amongst them, with certain literature being some 40 % different than others. VLE data for the full range of *n*-butane composition in mixture with ethanol were measured by Holderbaum et al. [181] and Deák et al. [182]. The literature indicates maximum pressure azeotropes within the system, although only bubble point curves (*P*-*x*) have been measured. Dew point curves were constructed solely based on modeling results.

A vapour-liquid equilibria still using the "static-analytic" method has been used to carry out the high pressure measurements. For such methods, the two-phase mixture is kept in a closed environment (static), and equilibrium is attained via rapid agitation, usually by means of stirrers. Upon equilibrium, provisions are made for sampling separately the present phases for analysis (analytic). The two bioethanol-related systems measured in this work are given in Table 3.5 with information on the materials given in Table 3.6. All the chemicals were degassed carefully

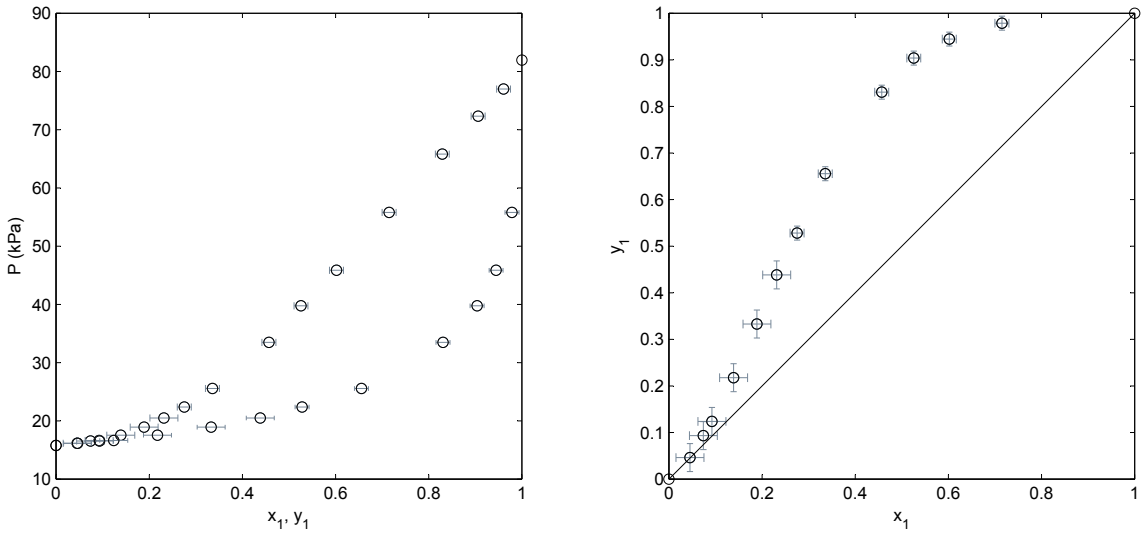

Figure 3.15: Experimental VLE data for the acetone (1) + formic acid (2) binary system at 323.1 K.

Table 3.5: Binary systems measured by the "static-analytic" apparatus for high pressure vapour-liquid equilibria.

Component 1	Component 2	Temperature (K)	Pressure (MPa)
propane	ethanol	344 - 403	0.07 - 5.7
n-butane	ethanol	323 - 423	0.03 - 3.7

prior to measurement. This was done either by venting for pressurized gases, or by vacuum for liquids.

3.2.2 Description of the static-analytic apparatus

The apparatus, shown schematically in Fig. 3.16, is based on the "static-analytic" method which is described extensively by Raal [162]. Both liquid and vapour phase sampling is undertaken within the apparatus. The equilibrium cell **EC** consists of a titanium body of 80 cm^3 cell volume, and operates at maximum conditions of pressure and temperature of 20 MPa and 425 K respectively. Two sapphire windows **SW** on either side of the cell body allow visualization of the cell contents, while a variable-speed, magnetic bar stirrer **VSS** prevents any gradients within the cell. The cell is placed in an air bath **O**, where a fan oven (France Etuves, model C3000) maintains the desired temperature. In order to perform accurate temperature measurements in the cell and check for thermal gradients, two 100 Ω platinum resistance thermometers probes **TT** are inserted inside wells drilled at two locations, corresponding to the vapour and liquid phases. Similarly, cell pressures are measured by two

Table 3.6: Purity and supplier of the compounds used in the measurement of high pressure vapour-liquid equilibria.

Compound	Formula	CAS number	Purity (% analysis)	Supplier
n-butane	C_4H_{10}	106-97-8	≥ 99.95 % v/v	Air Liquide
ethanol	C_2H_6O	64-17-5	≥ 99.8 % v/v	Fluka
propane	C_3H_8	74-98-6	≥ 99.95 % v/v	Messer-Griesheim

pressure transducers (Druck, model PTX 611): a high pressure transducer **HPT** (maximum 20 MPa abs) which is always connected, and a low pressure transducer **LPT** (maximum 4 MPa abs), which could be bypassed by the isolation valve **IV**. For pressure readings less than 4 MPa, the value of the low pressure transducer is considered to be more accurate and is the reported pressure. For pressures above 4 MPa, the same transducer is bypassed to prevent diaphragm damage. The pressure transducers are maintained at a constant temperature (383 K throughout this work) by means of a PID regulator **TR** (WEST, model 6100). Both the signals from the temperature and pressure sensors are transmitted to a data acquisition unit (Actifa), which is connected to a personal computer/data acquisition system **DAS** via the Ltc10 interface. This system allows real time readings and storage of temperatures and pressures throughout the different isothermal runs.

Three valves (**V1**, **V2**, **V3**) connected to the cell allow for loading, discharging, degassing and evacuation operations. Two electromagnetic ROLSI™ capillary samplers [183] fitted to the cell lid serves for sampling of the liquid phase (**LS**) and vapour phase (**VS**). The analytical work was carried out using a gas chromatograph (PERICHROM, model PR-2100) equipped with a thermal conductivity detector (TCD). Peak integration and analysis was performed using the data acquisition software WINILAB III (ver. 4.6, from Perichrom, France). The analytical column used for this study are:

propane + ethanol Porapak Q, 80/100 mesh column (length: 2 m, diameter: 1/8 in. silcosteel, from Restek France), maintained at 473 K.

***n*-butane + ethanol** HayeSep T, 80/100 mesh column (length: 1 m, diameter: 2 mm, silcosteel, from Restek France), maintained at 413 K.

A helium flow rate of ~ 30 mL.min^{-1} was passed through the column.

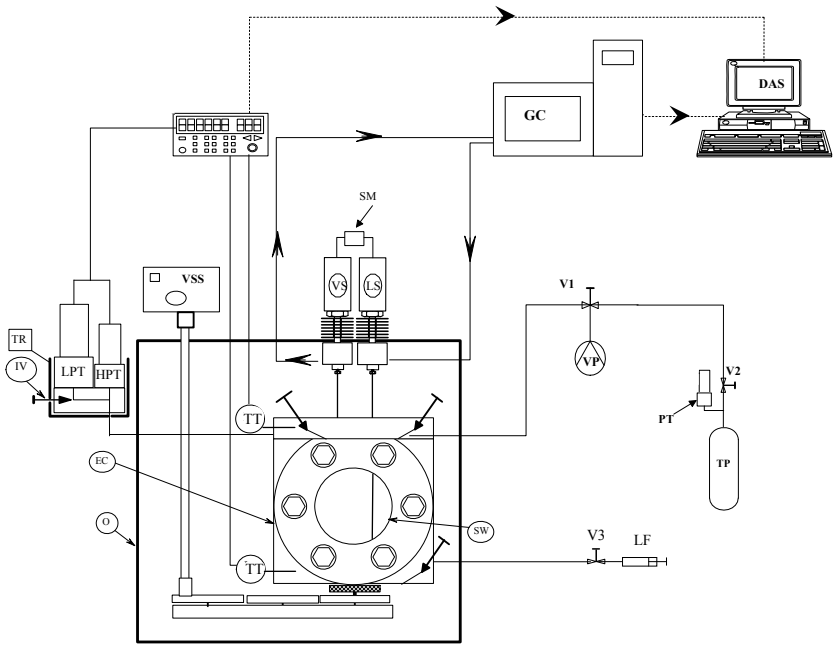

Figure 3.16: Flow diagram of the "static-analytic" apparatus used for measurements of high pressure vapour-liquid equilibria. DAS: Data Acquisition System; EC: Equilibrium Cell; GC: Gas Chromatograph, HPT: High Pressure Transducer; IV: Isolation Valve; LF: Liquid Feed; LPT: Low Pressure Transducer; LS: Liquid Sampler; O: Oven/Air Bath; PT: Pressure Transducer; SM: Sample Monitor; SW: Sapphire Window; TP: Thermal Press; TR: Temperature Regulator; TT: Platinum resistance temperature transducer; V_i: Valve; VP: Vacuum Pump; VS: Vapour Sampler; VSS: Variable Speed Stirrer.

3.2.3 Experimental procedures

Temperature and pressure sensor calibrations

The two 100 Ω platinum temperature probes were calibrated by submerging in a HAAKE DC 50 oil bath (maximum 473 K), together with a 25 Ω reference platinum resistance thermometer (TINSLEY Precision Instruments, Type 5187 A). The 25 Ω reference platinum resistance thermometer was calibrated by the Laboratoire National d'Essais (Paris) based on the 1990 International Temperature Scale (ITS 90). Two separate coils in the bath, each for heating and cooling regulates the temperature of the oil to the specified set point. The reference probe is connected to a micro-ohmmeter (Hewlett-Packard, model 34420 A), from which the value of the resistance displayed can be converted to a temperature reading via a polynomial. The two 100 Ω platinum probes are connected to the same data acquisition unit (refer to Fig. 3.16), en route to a computer installed with the Actifa Ltc10 interface. As before, the temperature of the oil bath is increased and decreased monotonically, in order to check for hysteresis, until the working range is covered. Second-order trendlines correlate the two 100 Ω probe temperatures to the real temperature. Back calculation with the trendlines gives the maximum correlation error as ± 0.01 K.

The pressure calibration is effectuated by connecting the inlet of the equilibrium cell to a dead weight balance (Desgranges & Huot, 5202S, CP 0.3-40 MPa, Aubervilliers, France), which in turn is connected to a source of pressure higher than the maximum working pressure of the experiment. Nitrogen is used as the high pressure source. The balance consists of the central piston of 200 g, to which calibrated known weights can be added. The total pressure exerted on the balance is thus the sum of the pressure from the gravitational force of the piston and any added weights, as well as the atmospheric pressure measured by a digital barometer (Druck, model DPI 141). After addition of the weights, nitrogen is charged to the cell, passing the dead weight balance en route, and counter-balancing the downward forces of the piston and its weights. To ensure that the inlet pressure matches exactly the downward pressure, fine-tuners are provided on the balance to control the inlet pressure. When this is achieved and allowed to stabilize, the pressures detected by the cell pressure transducers **LPT** and **HPT** are recorded against the real pressure, calculated from the number of weights on the piston. Second-order trendlines are used to correlate the transducer pressure to the real pressure, as shown in Fig. 3.17. Pressure correlation errors are estimated to be ± 1 kPa and ± 8 kPa for the low and high pressure transducers, respectively.

TCD calibration

High-pressure vapour-liquid equilibria measurements require calibrating the TCD for both liquid and gaseous substances. In this work, the TCD of the gas chromatograph was calibrated by a syringe injection technique. Syringes (SGE, Australia) of volumes ranging from 0.1 to 5 μL were used for liquid, while volumes ranging from 10 to 500 μL were used for gases. In the case of components existing as gases at room temperature, the number of moles injected each time into the TCD is known beforehand by using the ideal gas law $n = PV/RT$, where the pressure P is measured with a digital barometer (see above), the temperature T by a calibrated Pt-100 probe of maximum deviation ± 0.025 K (Leris, France), and the volume V is read as precisely as possible off the syringe via a magnifying eye-piece. The temperatures and pressures are measured at the exit nozzle of the gas cylinder, and is considered to be representative of its contents. More accurate equation of states for the gas phase (Pitzer correlations [184], for example) offer only slight differences for the compounds studied. The area under the injected peak is integrated using the WINILAB III software, and a graph of mole number versus peak area is generated. Simple polynomials (of orders not more than two) can be fitted to the calibration using a least squares method.

For the case of liquids at room temperature, TCD calibrations require a knowledge of liquid molar densities as a function of temperature. Such correlations can be found in literature [68, 185]. Only the temperature and volume of the injected liquid needs to be known, since the density of an incompressible liquid is not a strong function of pressure.

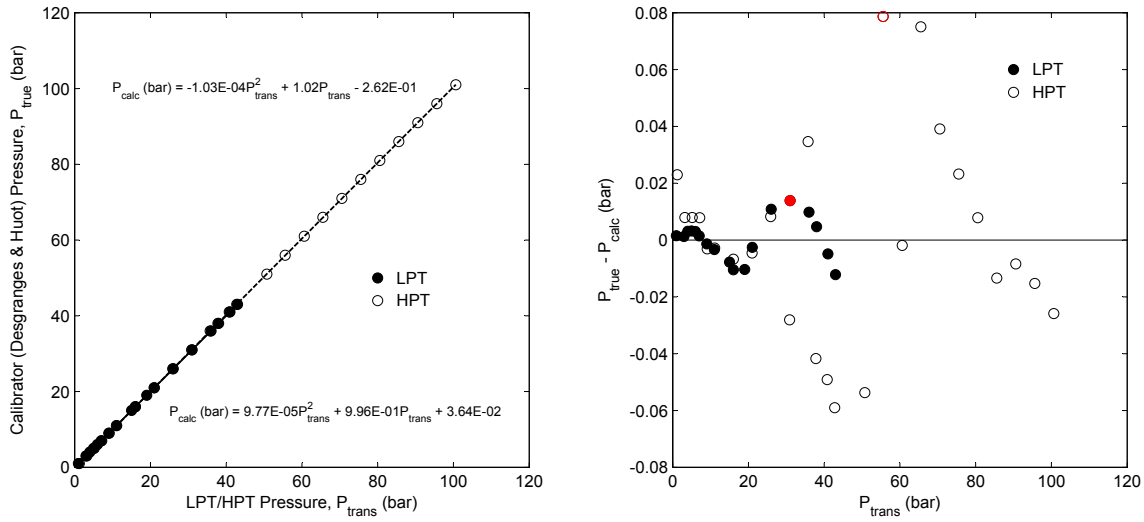

Figure 3.17: Calibration of the pressure transducers for the "static-analytic" VLE apparatus. *left:* Second-order relation between the true and transducer pressures. The calibration for both the high and low pressure transducers (**HPT** and **LPT**) are shown. The relation for **LPT** is given by the solid trendline, and the dashed line for the **HPT**. *right:* Deviations from the true pressure, resulting from the use of a second-order relation. The red symbols denote the furthest departures for each respective transducer.

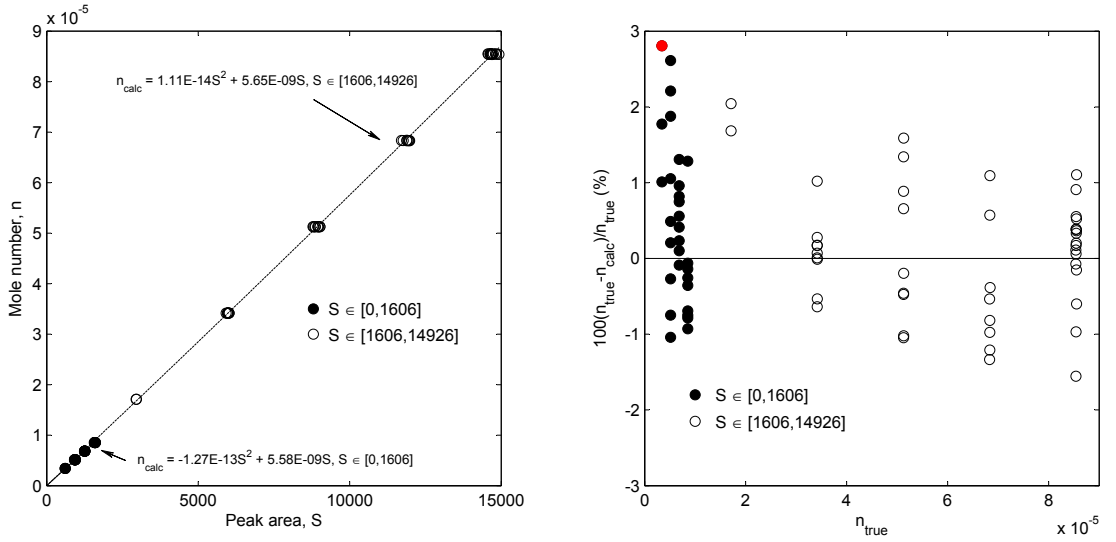

Figure 3.18: TCD calibration for ethanol, performed using direct syringe injections, to be used for the propane + ethanol system. *left:* Two second-order relations, solid and dashed lines, from two syringes of different volumes, are used to correlate the GC peak surface areas to the number of moles of ethanol passing through the TCD. *right:* Percentage deviations from the true composition, given for each of the two second-order relations. The red symbol denotes the furthest departure.

Fig. 3.18 illustrates the instance where two syringes are not sufficiently consistent with one another to pass one trendline through both syringe results with adequate accuracy. One should note that all calibration methods, involving the use of syringes, are subject to errors such as dead volume in needle, fluid expansion or adsorption, and manufacturer imperfections. This implies that the volume of substances injected in the TCD does not always

correspond to that indicated on the syringe. This inaccuracy is somewhat worsened, inevitably, in the method of direct injections, through imperfections of the operator. As the method employed in § 3.1.3 for low pressure TCD calibration cannot be used here, it may be beneficial in future work to consider alternate calibration techniques where the volume passed through the TCD can be accurately determined in advance.

For gases having a low vapour pressure at room temperature, such as *n*-butane, condensation of the gas can occur in the syringe. In this instance, the peak areas vary for a seemingly constant syringe volume, and repeatability of injections becomes difficult. As a result, calibration by direct syringe injections is not recommended. The TCD is alternatively calibrated by first determining the detector response to inert nitrogen using vapour type syringes of 10 to 500 μL. This can be done normally using the above-mentioned procedure. Thereafter, a nitrogen + *n*-butane mixture of known composition y_{C_4} and y_{N_2} - from knowledge of partial pressures P_{C_4} and P_{N_2} - is prepared in the cell. Using the ROLSI™ samplers, samples of different sizes can be taken and the TCD calibrated to *n*-butane by *difference*. For each sample taken, two peaks will be obtained on the WINILAB III software, and the mole number of *n*-butane is determined by mass balance:

$$n_{C_4} = \frac{y_{C_4} n_{N_2}}{1 - y_{C_4}} \tag{3.16}$$

where n_{N_2} is known upon each sampling from the nitrogen calibration determined beforehand. Any inert substances may be used for this procedure, as long as the peak onset and retention time does not coincide with the other component of interest. The temperature of the cell should be set, before loading, to a value such that only a single phase is observed in the cell. While sampling was carried out here only in the vapour phase, the experiment and Eqn. (3.16) can be setup for the liquid phase as well.

Experimental method

The equilibrium cell and its loading lines are evacuated. For this work, the heavier component is liquid and is introduced via a syringe **LF**, and degassed extensively by vacuum while being heated to the desired temperature. In the meantime, adequate stirring is maintained throughout the cell. The lighter, usually gaseous component is charged via a thermal press **TP** to a pressure level corresponding to the pressure of the first measurement. Phase equilibrium is assumed to be achieved when the two pressure transducers and temperature probes have stabilized to within their instrument uncertainty, for at least 10 minutes. For each equilibrium condition, at least six samples of both the liquid and vapour phases are withdrawn using the ROLSI™ electromagnetic samplers, and analyzed to ensure that repeatability is achieved within ± 1 % of the samples taken. Averages of the samples were then taken for each phase. More of the lighter component is introduced after each sampling and analysis, stepping up to the highest composition of the second component. When required, the thermal press is heated using a hotplate to facilitate charging from a higher pressure source. Relative care must be taken for this step.

3.2.4 Estimation of uncertainty for high pressure measurements

The uncertainties in the temperature and pressure sensors are treated in the same manner as those in the low pressure measurements (§ 3.1.4). The usage of models, such as the ideal gas law, in the calibration procedure means that further sources of uncertainties, from a measurement point of view, are introduced. The reporting of the composition uncertainty for high pressure measurements is thus examined here in detail.

We recall that the combined standard uncertainty for molar composition is made up of a calibration and repeatability part (Eqn. 3.9), the latter of which can be determined by a type A evaluation. For the calibration of gaseous compounds, the number of moles *n* calculated by the ideal gas law will be affected somewhat by imprecisions in the measurement of T, P and V (The gas constant R is assumed to have a value of negligible uncertainty). In

general,

$$u_{\text{calib}}(x_i) = \sqrt{\left[\left(\frac{\partial x_i}{\partial n_1}\right)_{n_2} u(n_1)\right]^2 + \left[\left(\frac{\partial x_i}{\partial n_2}\right)_{n_1} u(n_2)\right]^2}$$
$$= \sqrt{\left(\frac{1-x_i}{n_1+n_2} u(n_1)\right)^2 + \left(\frac{x_i}{n_1+n_2} u(n_2)\right)^2} \tag{3.17}$$

To obtain the values for $u(n_1)$ and $u(n_2)$, we again have two uncertainties that must be combined. For gaseous compound, these are the ideal gas law (ig), and the calibration polynomial (corr).

$$u(n_i) = \sqrt{u_{\text{ig}}(n_i)^2 + u_{\text{corr}}(n_i)^2} \tag{3.18}$$

The former is written out here using the root-sum-squared formula for component i:

$$n_i = \frac{PV}{RT}$$
$$u_{\text{ig}}(n_i) = \sqrt{\left[\left(\frac{\partial n_i}{\partial P}\right)_{V,T} u(P)\right]^2 + \left[\left(\frac{\partial n_i}{\partial V}\right)_{P,T} u(V)\right]^2 + \left[\left(\frac{\partial n_i}{\partial T}\right)_{P,V} u(T)\right]^2}$$
$$= n_i \sqrt{\left(\frac{u(P)}{P}\right)^2 + \left(\frac{u(V)}{V}\right)^2 + \left(\frac{u(T)}{T}\right)^2} \tag{3.19}$$

The uncertainties $u(P)$, $u(T)$ and $u(V)$ can be obtained from their instrument specifications, i.e. the DRUCK DPI 141 for the pressure and the Leris Pt-100 for the temperature. The uncertainty in the reading of the syringe volume is difficult to quantify, and we allow in this work an error of ± 2 % for each volume reading. A type B evaluation with rectangular distribution is applied to all three uncertainties. As was done for the low pressure measurements, $u_{\text{corr}}(n_i)$ is evaluated by assuming the maximum error observed, from the calibration polynomials, as the limits of a rectangular distribution.

The calculation is slightly modified when calibrating a substance in the liquid phase. In this case, the ideal gas law is replaced by an empirical model for liquid densities as a function of temperature. This empirical correlation is given in DIPPR 11 [68] as:

$$\rho = \frac{n}{V} = \frac{A}{B^{\left(1+\left(1-\frac{T}{T_c}\right)^C\right)}} \tag{3.20}$$

where A, B, C are empirical constants regressed from experimental data, and T_c is the critical temperature. Uncertainties in the number of moles is influenced only by the temperature (from the Pt-100) and volume precisions (from the syringe). Thus, we replace $u_{\text{ig}}(n_i)$ in Eqn. (3.18) with $u_{\text{ld}}(n_i)$ for liquid density, the latter given by:

$$u_{\text{ld}}(n_i) = \sqrt{\left[\left(\frac{\partial n_i}{\partial T}\right)_V u(T)\right]^2 + \left[\left(\frac{\partial n_i}{\partial V}\right)_T u(V)\right]^2} \tag{3.21}$$

where

$$\left(\frac{\partial n_i}{\partial T}\right)_V = n_i \frac{C}{T_c} \ln B \left(1 - \frac{T}{T_c}\right)^{C-1}$$
$$\left(\frac{\partial n_i}{\partial V}\right)_T = \frac{n_i}{V}$$

Therefore,

$$u_{\text{ld}}(n_i) = n_i \sqrt{\left(\frac{C}{T_c} \ln B \left(1 - \frac{T}{T_c}\right)^{C-1} u(T)\right)^2 + \left(\frac{u(V)}{V}\right)^2} \tag{3.22}$$

Note that the value of temperature used for calculating the liquid density is measured using the same Leris Pt-100 as before. In addition, the 2 % error in syringe volume reading is applied. Certainly, the DIPPR correlation for liquid density in Eqn. (3.20) may possess an error, which should to be further combined in the uncertainty evaluation. However, this details of this error is not given and will not be included in the calculation.

A worked example is given in Appendix D to illustrate the procedure, using measurements from the propane + ethanol system.

Uncertainty from calibrations using a ROLSI™ sampler

We mentioned in § 3.2.3 that the ROLSI™ sampler was incorporated into the calibration of *n*-butane, and that the overall procedure resembles part-syringe (for the nitrogen), and part-ROLSI™. This long-winded procedure brings about additional uncertainties, a glaring source is the precision on the nitrogen calibration, by direct syringe injections, which will have a large bearing on the quality of the *n*-butane calibration. We have also a relation in Eqn. (3.16), where the uncertainty on y_{C_4} must be considered. We underline here the steps that need to be undertaken.

The objective is to find an uncertainty for this ROLSI™ calibration procedure, which we denote by rc, that can be combined with $u_{\text{corr}}\left(n_{C_4}\right)$ in Eqn. (3.18). The n_{C_4} value calculated in Eqn. (3.16) should reveal three sources of uncertainties, if one uses Dalton's law to replace $y_{C_4} = P_{C_4}/(P_{C_4} + P_{N_2})$:

$$n_{C_4} = \frac{P_{C_4} n_{N_2}}{P_{N_2}} \tag{3.23}$$

$$\begin{aligned} u_{\text{rc}}\left(n_{C_4}\right) &= \sqrt{\left(\frac{\partial n_{C_4}}{\partial P_{C_4}} u\left(P_{C_4}\right)\right)^2 + \left(\frac{\partial n_{C_4}}{\partial P_{N_2}} u\left(P_{N_2}\right)\right)^2 + \left(\frac{\partial n_{C_4}}{\partial n_{N_2}} u\left(n_{N_2}\right)\right)^2} \\ &= n_{C_4} \sqrt{\left(\frac{u\left(P_{C_4}\right)}{P_{C_4}}\right)^2 + \left(\frac{u\left(P_{N_2}\right)}{P_{N_2}}\right)^2 + \left(\frac{u\left(n_{N_2}\right)}{n_{N_2}}\right)^2} \end{aligned} \tag{3.24}$$

keeping all other variables constant at each derivative. We note that $u\left(P_{C_4}\right) = u\left(P_{N_2}\right) = u_{\text{corr}}(P)$ since the pressure of both these components are read directly from the same equilibrium cell transducer (Druck, model PTX 611). In addition, P_{C_4} and P_{N_2} are constants, a requirement of the method described in earlier text. Nitrogen is calibrated like any other gaseous component, with direct syringe injections, and the uncertainty $u\left(n_{N_2}\right)$ have already been covered.

3.2.5 Results of high pressure vapour-liquid equilibrium measurements

The experimental results for the propane + ethanol and *n*-butane + ethanol systems at various temperatures are given in Figs. 3.19 and 3.20. The uncertainties, included only for composition in the graphics, are calculated with the method described in § 3.2.4, and presented in Table 3.7 as averages over all isotherms. As with the low pressure apparatus, the uncertainties on repeatability are negligible, the molar compositions in this case sampled automatically by the ROLSI™ samplers. Of more importance are the uncertainties stemming from the TCD calibration correlations, which have higher contributions to the uncertainties of molar compositions. A distinct difference between the methods of calibration for low and high pressure measurements is the large number of variables in the high pressure case that can contribute to errors. In the method of Raal and Mühlbauer, the compositions are calculated from GC peak areas, which we assume to have negligible error, and a response factor ratio, which has been optimized to yield as little error as possible. With the error in the balance considered negligible, the final expanded uncertainty is expectedly smaller than the method of syringe calibration.

For the high pressure measurements, the calibration of the TCD for a gaseous component, by syringe injections, is generally quite good, with percentage deviations rarely exceeding 2 %. The assumption of a 2 % error on syringe volume readings is usually noticeable only in the regions where the gaseous compound is in bulk, and will not be

Table 3.7: Averaged temperature, pressure, and mole fraction uncertainties for the binary systems measured with an apparatus based on the "static-analytic" method.

		Expanded uncertainties $\bar{U}(\theta)$ with $k = 2$			
Component 1	Component 2	$\bar{U}(T)$ (K)	$\bar{U}(P)$ (bar)	$\bar{U}(x)$	$\bar{U}(y)$
propane	ethanol	± 0.02	± 0.04	± 0.027	± 0.021
n-butane	ethanol	± 0.02	± 0.02	± 0.024	± 0.028

contested here. Conversely, syringe calibration with a liquid component is less precise, with percentage deviations on mole numbers between 2.5 and 3.5 %. In addition, the uncertainties on calibration $u_{\text{calib}}(x_i)$ will depend on the total number of moles sampled each time. Examining Eqn. (3.17), the term $n_1 + n_2$ in the denominators have a pronounced effect on the value of the uncertainty. Different size samples taken by the ROLSI™ samplers do not change the value of x_1, but a smaller sample will result in a smaller $n_1 + n_2$ value which will amplify the uncertainty. It is thus recommended to take as large a sample as is reasonable, at all times, in order to increase the term $n_1 + n_2$ in the expression for $u_{\text{calib}}(x_i)$. This not only helps to decrease the value of the uncertainty, but is generally good sampling practice with the ROLSI™ samplers, ensuring that no dead volume or unwanted flashing occurs in the sampling capillaries. In cases where this was not followed rigorously, insufficiently large samples have led to some of the data to having very wide compositional uncertainty bands in Figs. 3.19 and 3.20. High uncertainties also occurs at the extreme ends of the composition, since the sample size that can be taken is bounded by one of the two components that is close to peak saturation.

The performance of the "static-analytic" apparatus is poorer at equilibrium pressures below 4 bars. This is due to the insufficient gradient between the pressures of the system and the carrier gas circulating inside the ROLSI™ samplers. For these purposes, capillaries with larger internal diameters are recommended. However, this may prove to be an inconvenient option, as it would require emptying and dismantling the apparatus during the course of an isothermal measurement. The approach adopted here is to activate the ROLSI™ samplers for larger periods of time (~ 5 seconds), in an attempt to take sufficiently large samples. This should be done without visibly distorting the peaks, which may at times result from such a procedure.

The step in Eqn. (3.17) involving n_i is not required in the calibration procedure of Raal and Mühlbauer, in fact, their method translates the mole fractions directly from the GC peak areas, synonymous to a temperature/pressure transducer. This is possible since the only other uncertainty $u_{\text{B}}(x_i)$ is negligible. Note that the volume injected into the GC during calibration or during sampling is irrelevant in this method. From an uncertainty estimation point of view, calibration by preparing standard mixtures of known composition is a more favoured approach.

In Chapter 5, the data of the propane + ethanol system are modeled by the PC-SAFT EoS, with the results used to evaluate the quality of the existing literature data. For the *n*-butane + ethanol system, experimental liquid compositions are in relatively good agreement with the literature values of Deák et al. with deviations not exceeding 3 %.

3.3 Concluding remarks

In the first of two experimental chapters, vapour-liquid equilibria measurements were performed for nine biofuel-related binary systems, with the aim of employing two different types of equipment. Systems of near-atmospheric conditions were regarded as low pressure types, and measured using an apparatus based on the "dynamic-synthetic" method. The apparatus is a modified form of the glass ebulliometer, with manual sampling facilitated by gas-tight syringes. For elevated pressures extending over several bars, we employed a "static-synthetic" apparatus, with two on-line electromagnetic ROLSI™ samplers.

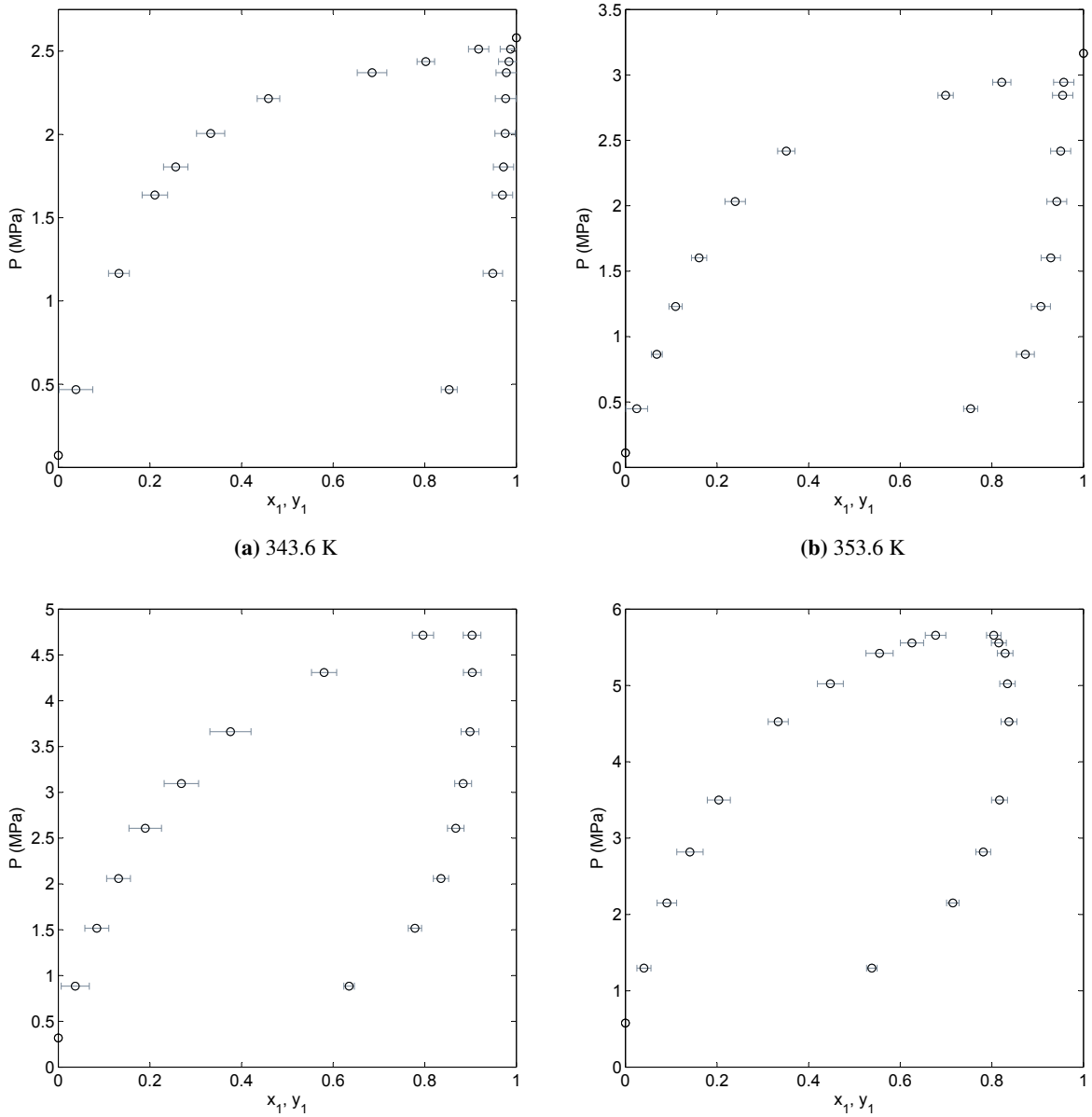

(a) 343.6 K

(b) 353.6 K

(c) 383.6 K

(d) 403.0 K

Figure 3.19: Experimental pressures against liquid and vapour phase mole fractions for the system propane (1) + ethanol (2) at isotherms 344 - 403 K.

Both apparatuses lead to good reproducibility of the results. Good agreements with literature data were observed. Some emphasis have been placed on the manner in which uncertainties of the measured variable have been reported. This is important for identifying the areas of the experiment which could be improved.

The equipments discussed in this chapter are among the several existing apparatuses for VLE measurements; they are by no means universal methods, and some shortcomings of both apparatuses were given in the chapter. There exists an intermediate pressure region of 1 - 4 bars where sampling in the "static-analytic" method is less well-facilitated, unless one is prepared to modify the ROLSI™ capillary diameter during the course of the experiment. It was concluded that the calibration of the thermal conductivity detector of the gas chromatograph remains a

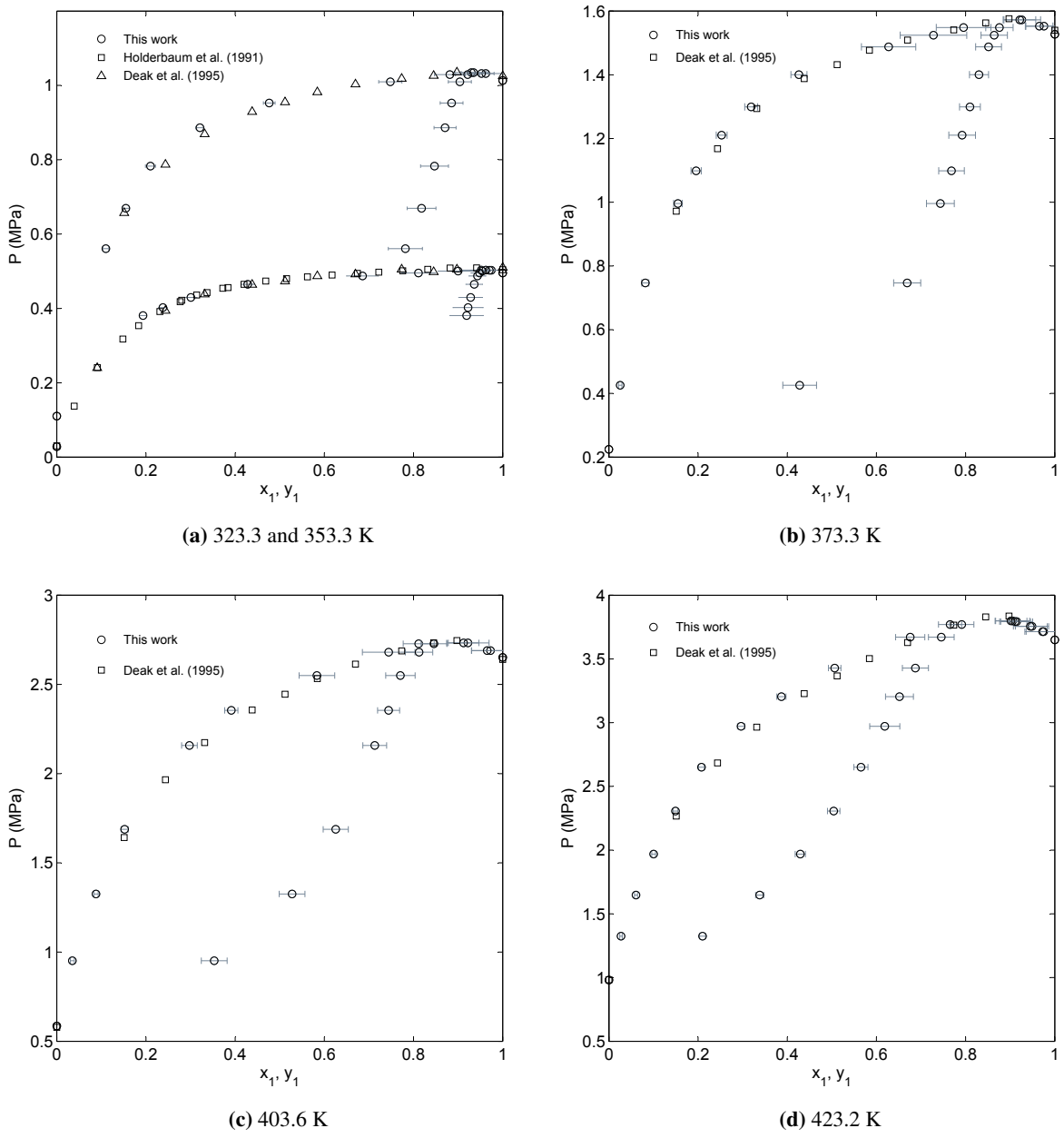

(a) 323.3 and 353.3 K

(b) 373.3 K

(c) 403.6 K

(d) 423.2 K

Figure 3.20: Experimental pressures against liquid and vapour phase mole fractions for the system *n*-butane (1) + ethanol (2) at isotherms 323 - 403 K. Literature data were taken from Refs. [181, 182].

common area for improvement. Several alternatives exist, one is the preparation of standard, monophasic mixtures with known compositions in the equilibrium cell, and calibrate using the ROLSI™ sampler, similar to the method of Raal and Mühlbauer (with an auto-injector). Other methods can be found in most texts regarding experimental techniques [162, 186, 187]. In considering alternate calibration procedures, one should question the extent of improvement the alternative will bring, in the context of an uncertainty estimation, to determine its usefulness.

CHAPTER 4

Experimental determination of critical points using a "dynamic-synthetic" apparatus

Nothing tends so much to the advancement of knowledge as the application of a new instrument.

- Sir Humphry Davy (1778-1829)

La détermination expérimentale
de points critiques au moyen d'un appareillage "dynamique-synthétique"

La connaissance des valeurs des points critiques des mélanges est essentielle pour l'optimisation des procédés liés au pétrole et à extraction supercritique. Ces données fournissent des informations sur le comportement des fluides réels aux conditions de limite d'équilibre. Le quatrième chapitre présente un appareillage, utilisant la méthode de "dynamique-synthétique", capable de permettre la mesure des propriétés critiques de composés purs et de mélanges jusqu'à 543 K et 20 MPa. Les propriétés critiques de treize composés purs, sept systèmes binaires et un système ternaire ont été mesurées. Bien que les données critiques ne soient pas directement liées aux processus relatifs aux biocarburants, à l'exception de la fabrication de certains biodiesels, ces données sont certes très utiles pour évaluer et améliorer les performances du modèle étudié: l'équation d'état PC-SAFT.

L'appareillage se compose de trois sections différentes, une pour le chargement, une pour la mesure, et une dernière pour le contrôle de débit. Le composé pur ou le mélange est préparé dans une presse volumétrique. Dans le cas d'un mélange, sa composition est déterminée par pesées différentielles sur une balance analytique avant et après ajout de chacun des composés. Cette procédure dite synthétique garantit des compositions de mélange de faible incertitude. Le contenu de la presse maintenu sous forme liquide en exerçant une pression supérieure à la pression de bulle par l'intermédiaire du piston de la presse volumétrique est transféré dans une pompe ISCO. La pompe délivre le fluide à la cellule d'équilibre, qui comprend un tube vertical en saphir situé dans une enceinte à air. En utilisant la pompe, et les vannes manuelles se trouvant dans la section de contrôle de débit, le niveau de fluide est maintenu au centre de la cellule alors que la température de l'enceinte à air est progressivement augmentée jusqu'à approcher le point critique. Lorsque le point critique est proche, la couleur du liquide vire au rouge, et enfin au noir, ce qui indique son passage à l'état critique. La température et la pression critique sont enregistrées au cours de cette transition, grâce aux capteurs reliés à la cellule d'équilibre. Les capteurs de température sont étalonnés par rapport à une sonde étalon à l'intérieur d'un bain d'huile silicone. Le capteur de pression est lui étalonné en référence à une balance à poids morts, respectivement. La procédure de mesure des propriétés critiques est répétée plusieurs fois pour définir une valeur moyenne.

Les résultats expérimentaux pour plusieurs composés purs sont en bon accord avec les valeurs publiées dans la littérature. Les points critiques de certains fluides frigorigénes, pour lesquels peu d'informations sont disponibles dans la littérature, ont également été mesurés. Ces données ont été utilisées pour évaluer la performance de plusieurs modèles prédictifs empiriques. Pour les réfrigérants étudiés, la méthode de Marrero et Pardillo a donné les prédictions les plus proches au niveau de température critique, alors que la méthode de Wilson et Jasperson fournit les meilleures prédictions de la pression critique. Les valeurs des points critiques des systèmes binaires, dont la plupart contient des composés oxygénés tels que l'éthanol, pourraient être corrélés avec une expression de Redlich-Kister. Ceux du mélange ternaire : n-pentane + éthanol + n-hexane ont été corrélés en utilisant une expression semblable à celle des travaux de Cibulka, et de Singh et Sharma.

Plusieurs modifications ont été proposées en fin de chapitre pour améliorer les performances de l'appareillage. Les plus importantes de ces modifications comprennent une réduction du volume de la cellule, l'utilisation d'un bain liquide pour un contrôle de température plus fin, et l'introduction d'un agitateur à l'intérieur de la cellule d'équilibre. La présence d'un agitateur permet également le fonctionnement de l'appareillage sous forme "statique-synthétique". Cela a été testé sur des corps purs et a conduit à des résultats identiques, aux incertitudes expérimentales près, à ceux obtenus avec l'appareillage prototype en mode dynamique-analytique présenté dans ce chapitre.

Critical point data of mixtures are essential for the optimization of petroleum and supercritical extraction processes. These data supply information on real fluid behaviour at limiting conditions of equilibrium. Due to strong fluctuations of densities at near-critical conditions, it is difficult for most thermodynamic models to satisfactorily predict the phase behaviour near the critical region. This is more so for multi-parameter equations of state (EoS), such as the PC-SAFT, which under normal conditions are not constrained at the critical region.

Despite the usefulness of such data, it comprises only a small percentage of the open literature. According to the Dortmund Data Bank 2009 (http://www.ddbst.com), data sets dedicated to mixture critical data form less than 1 % of the database, that is excluding the occasional critical points reported in vapour-liquid equilibria (VLE), which themselves appear few and far between. Strictly speaking, supercritical fluids are not associated with biofuel processes, save for certain biodiesel productions, but within the context of evaluating and improving the performance of the PC-SAFT EoS at the critical region, accurate measurements of critical data is of high value to this work.

The second of the two experimental chapters is focused on the experimental aspect of attaining mixture critical profiles. A "dynamic-synthetic" apparatus, which allows the observation of the critical opalescence, has been used for pure compounds and mixtures. As indicated in Chapter 3, a "dynamic" apparatus re-circulates its contents to facilitate efficient mixing, and with the "synthetic" aspect, the global composition of the mixture is synthesized and known *ab initio*, by direct weighing with a mass balance. The performance of the apparatus is illustrated in a series of measurements involving pure compounds, and binary mixtures. The critical *P-T* projections for the ternary *n*-pentane + ethanol + *n*-hexane system are also presented. The measurements are not restricted to biofuels in nature; we present also several refrigerants less well described in open literature (C_3F_6, C_3F_6O, R365mfc)

Mixture critical data provide a stern modeling test for the PC-SAFT EoS, and this is a topic that will be investigated further in Chapter 6. For this chapter, experimental results for binary mixtures are correlated empirically using the Redlich-Kister equation [188]. We present forms of the Cibulka [189] and Singh and Sharma's [190] equation suitable for correlating ternary critical properties.

4.1 Description of "dynamic-synthetic" apparatus

Table 4.1 summarizes the purities of the chemicals used in the study. A large inventory of materials is required for the duration of the experiment, due to the flow nature of the apparatus. Experimental techniques for the measurement of critical properties are almost all synthetic as opposed to analytic in operation. A comprehensive review on recent methods is provided by Teja and Mendez-Santiago [191]. The apparatus presented in this work is a typical flow-type setup based on the works of Roess [192], and Rosenthal and Teja [193], with a maximum residence time of 10 - 15 seconds at the highest flowrates.

The apparatus, based on the "dynamic-synthetic" method, has been previously described in open literature, and is similar to that constructed for the works of Horstmann et al. [194, 195, 196, 197], Guilbot et al. [198] and Gil et al. [199]. The apparatus is presented in Fig. 4.1, and the circuit is designed to allow complete evacuation of the cell and its lines prior to loading. Starting from the bottom-right corner of the schematic, the sample is prepared in a volumetric press **VPr**, its composition being accurately determined through weighing. Thereafter, the synthesized sample is transferred via pressure, in the form of compressed nitrogen **PS**, to a thermostated syringe pump **SP**. The syringe pump (ISCO, model 260D) is capable of delivering its contents at constant flowrate or pressure. An external jacket surrounds the pump length, within which water, thermally regulated by a water bath **WB** (Julabo, model F32), maintains the pump contents at a constant temperature.

The main difference between the current setup and that reported in previous literature is the use of a single pump with a volumetric press, where mixture compositions are prepared at high precision by

Table 4.1: Purity and supplier of the compounds used in the measurement of critical points.

Compound	CAS number	Purity (% analysis)	Supplier
Propane	74-98-6	≥ 99.95 % v/v	Messer-Griesheim
n-Butane	106-97-8	≥ 99.95 % v/v	Air Liquide
n-Pentane	109-66-0	≥ 99.0 % GC	Sigma-Aldrich
n-Hexane	110-54-3	≥ 99.0 % GC	Merck
n-Heptane	142-82-5	≥ 99.5 % GC	Fluka
n-Octane	111-65-9	≥ 99.0 % GC	Fluka
Ethanol	64-17-5	≥ 99.8 % v/v	Fluka
1-Propanol	71-23-8	98.0 % GC	Prolabo
Hexafluoropropylene oxide (HFPO)	428-59-1	≥ 99.9 % v/v	Pelchem
Hexafluoropropylene (R1216)	116-15-4	≥ 99.9 % v/v	Pelchem
Pentafluoroethane (R125)	345-33-6	≥ 99.5 % v/v	ARKEMA
1,1,1,2-Tetrafluoroethane (R134a)	811-97-2	99.95 % v/v	Dehon
1,1,1,3,3-Pentafluoropropane (R245fa)	460-73-1	≥ 99.9 % v/v	ARKEMA
1,1,1,3,3-Pentafluorobutane (R365mfc)	406-58-6	≥ 99.9 % v/v	ARKEMA
Perfluorobutane (R610)	355-25-9	≥ 98.5 % v/v	Pelchem

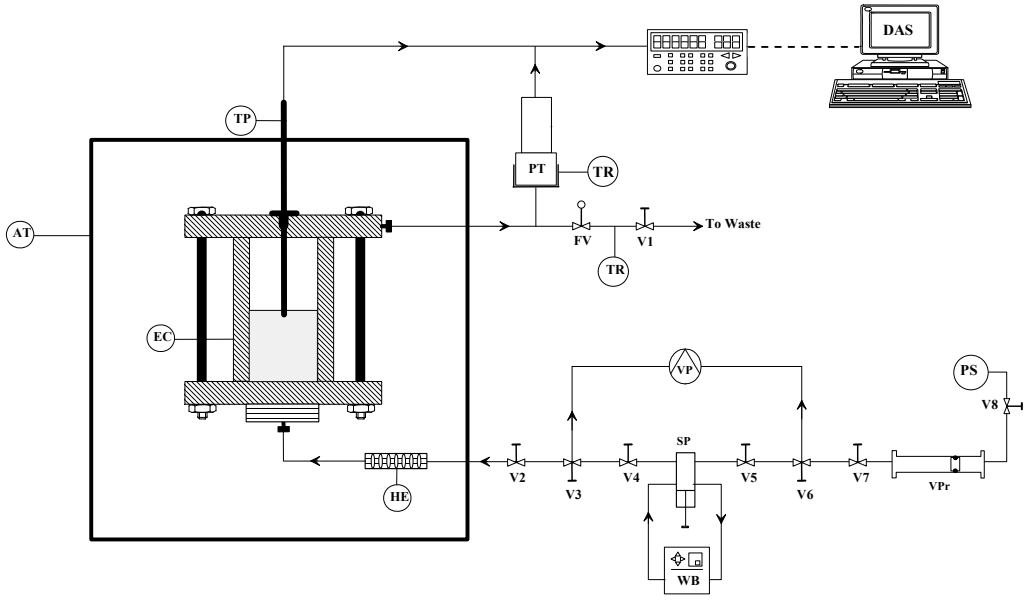

Figure 4.1: Flow diagram of the "dynamic-synthetic" apparatus used for critical point measurements. AT: Air Thermostat; DAS: Data Acquisition System; EC: Equilibrium Cell; FV: Flow Control Valve; HE: Heat Exchanger; PS: Pressurized Source (Nitrogen); PT: Pressure Transducer; SP: Syringe Pump; TP: Platinum Resistance Temperature Probe; TR: Temperature Regulator; V_i: Valve; VP: Vacuum Pump; VPr: Volumetric Press; WB: Water Bath.

weighing on a Mettler Toledo XP2004S balance of ± 0.1 mg maximum error. Knowledge of the capacity of the press (100 cm^3) enables one to calculate the quantity of materials required to prepare the desired mixture compositions.

The titanium-flanged sapphire cell **EC** operates up to 20 MPa and the maximum temperature is limited

by the air thermostat **AT** (France Etuves, model XU 125) - 543 K. The cell is situated within the air thermostat, where a strategically-placed mirror reflects rays of light onto the cell for enhancing the visual access of the critical opalescence. The mirror is not shown in Fig. 4.1. A coiled heat exchanger **HE** in the entry line ensures that liquids entering the cell is at the same temperature as the interior of the cell; thus minimizing possible temperature gradients. A 100 Ω platinum resistance thermometer probe **TP** (from Actifa) extends down the central axis of the sapphire cell, such that a half-filled cell submerses ~ 15 mm of length from the tip of the probe. The pressure transducer **PT** is supplied by Druck (model PTX 611), and is kept at constant temperature by means of a heating cartridge regulated via a PID temperature regulator (**TR**, from WEST, model 6100). Both the signals from the temperature and pressure probes are transmitted to a data acquisition unit, supplied by Actifa, and displayed on a personal computer/data acquisition system **DAS** via a Ltc10 interface.

The final, flow-monitoring, part consists of two valves, with which variations of the cell volume can be achieved. The valve **FV** in Fig. 4.1 is a flow control valve (TOP INDUSTRIE), as opposed to **Vi**, which are a standard shut-off valves. The exit line emerging from the air thermostat is regulated at a constant temperature by a WEST PID regulator **TR** (model 6100). This prevents rapid condensation of the cell contents upon leaving the air thermostat, and in doing so, avoids unexpected drops in pressure. The exit line from the entire setup is in the form of a stainless steel capillary, with an internal diameter between 100 - 160 microns.

4.2 Experimental procedures

Temperature and pressure sensor calibrations

The pressure transducer is calibrated against a dead weight pressure balance (Desgranges & Huot, 5202S, CP 0.3-40 MPa, Aubervilliers, France). The procedure for the pressure calibration has already been described in § 3.2.3. Pressure calibration errors are estimated to be ± 0.4 kPa, in the range of 0.1 to 7.1 MPa that sufficiently covers the working ranges of this study. This is shown in Figure 4.2.

The 100 Ω platinum resistance thermometer probe is calibrated against a 25 Ω reference platinum resistance thermometer (TINSLEY Precision Instruments, Type 5187 A). Following the same procedures outlined in § 3.2.3, a silicon oil bath (HAAKE, model DC 50) is used for the 323 - 443 K range, while a fluidized alumina bath (Techne, model FB-08) is used for the 443 - 573 K range. The 25 Ω reference platinum probe was calibrated by the Laboratoire National d'Essais (Paris), based on the 1990 International Temperature Scale (ITS 90). From Fig. 4.3, maximum sensor calibration errors for temperature are ± 0.02 K in the 323 - 443 K range, and ± 0.1 K in the 443 - 573 K range.

Experimental method

The transfer of the press contents to the ISCO pump is carried out in the monophasic liquid state at elevated pressures. Upon charging the ISCO pump with the prepared sample from the press, the contents are again pressurized to a single liquid phase, and maintained at a high temperature for a sufficient amount of time. This ensures that diffusion accounts for any remaining unmixed portions within the mixture, as no stirrer is present in the pump. For mixtures containing less soluble components, it may be necessary to induce further mixing through raising and lowering the pump piston continuously.

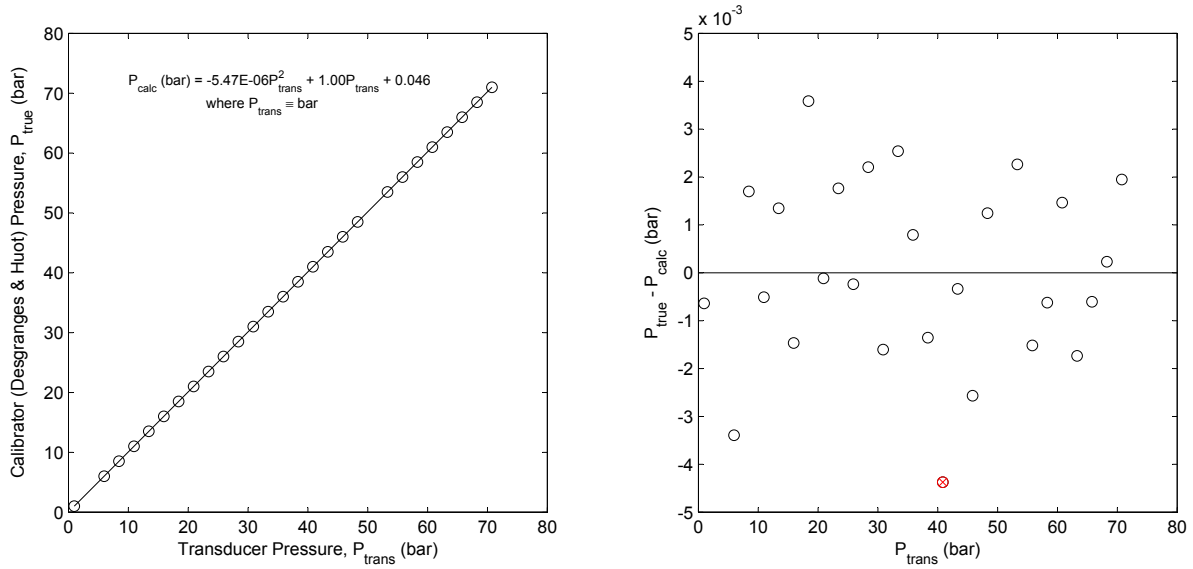

Figure 4.2: Calibration of the pressure transducer for the critical point apparatus. *left*: Second-order relation between the true and transducer pressures. *right*: Deviations from the true pressure, resulting from the use of the second-order equation. The ⊗ symbol denotes the furthest departure from the true pressure.

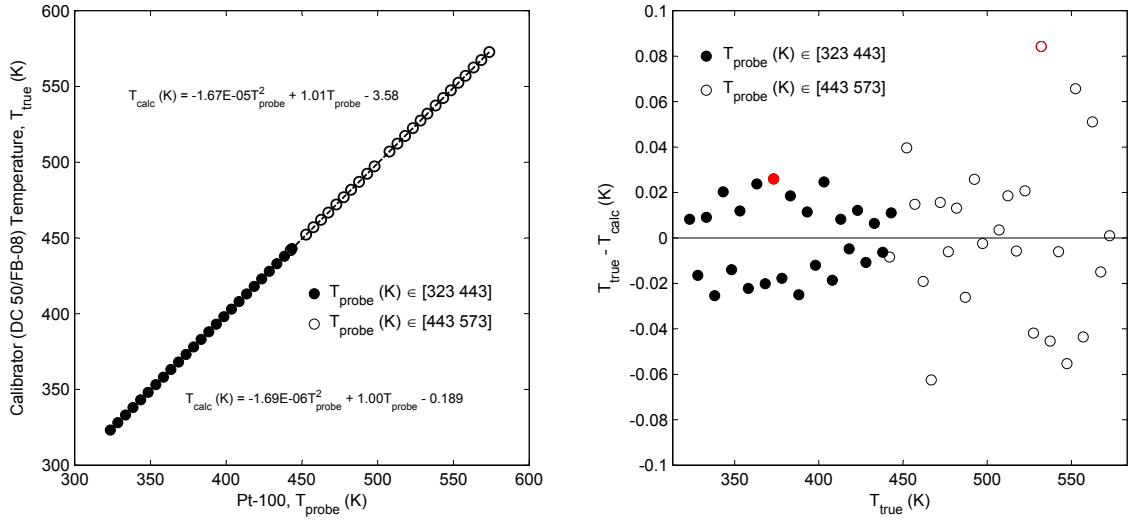

Figure 4.3: Calibration of the Pt-100 temperature probe for the critical point apparatus. *left:* Two calibrators divide the working range into two second-order relations between the true and probe temperatures. The calibrations are shown for a low (323 - 443 K) and high (443 - 573 K) range. The relation for the lower range is given by the solid trendline, with the dashed line for the higher range. *right:* Deviations from the true temperature, resulting from the use of the second-order equations. The red symbols denote the furthest departures for each respective range.

The cell is first heated to a temperature a few kelvins below the expected critical temperature. The pump contents are then transferred to the cell at a constant flowrate, usually at 2 - 3 cm^3/min. Considerable flashing of the liquid occurs until sufficient pressure is achieved to maintain a liquid phase. The cell is allowed to fill to the halfway mark, at which time the flow control valves (FV and V1) are opened to

maintain the liquid level halfway. The temperature is then slowly raised at a rate of ± 1 K/min, during which any changes in the liquid level are compensated by the flow control valves (for coarse adjustments) or the pump flowrate (for finer adjustments). This small gradient in temperature ensures that the response time of the temperature and pressure sensors, which results in an undesirable delay in registering the true values, have minimal impact on the recorded value. The temperature and pressures within the cell are monitored continuously, in real-time. As the cell contents approach its critical temperature, the solution starts to become cloudy, then dark and finally a deep red colour, marking the disappearance of the interface separating liquid and vapour. The sequence of color changes does not vary according to the compounds, for the transparent compounds in this work. The critical temperature (T_c) and pressure (P_c) are recorded at the instant the dark color become red, where the liquid is also at its darkest state (Fig. 4.4). The temperature is then decreased slowly from the supercritical state, where the reversed sequence of the colours can now be observed in the cell. The cyclic procedure is repeated at least eight times to reduce the uncertainty, with the reported value taken as the average of the runs. Fig. 4.5 shows the temperature and pressure profiles as the experiment proceeds. At each t_i, the dark red colour is observed in the cell, and the values of the temperature and pressure are recorded.

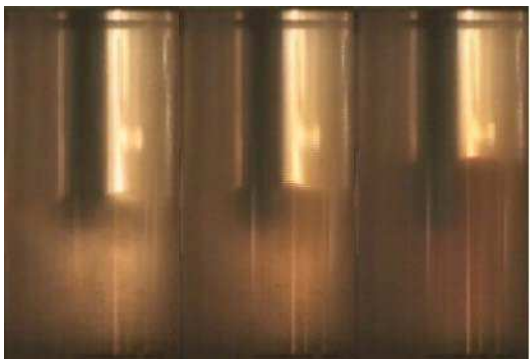

Figure 4.4: The transition of a fluid mixture to the critical state, from a cloudy subcritical state (left frame), to dark (middle), and finally a red color at the point of transition (right). The critical point is recorded at the instant the red color appears.

4.3 Results and discussions

Pure compounds

All experimental data were subjected to the Dixon's Q-test [200] on a 95 % confidence level to remove outliers. The results for the critical temperatures and pressures of pure compounds are listed in Tables 4.2 and 4.3 respectively, with comparisons between DIPPR [68] and NIST [153] databases. Average expanded uncertainties for temperature and pressure, calculated using the methods described in § 3.1.4, are 0.02 K and 0.001 MPa for pure compounds. A coverage factor of $k = 2$ was applied for all uncertainty estimations of pure compounds and mixtures. The largest error compared to literature was shown to be hexafluoropropylene (R1216), although a technical report by *DuPont* [201] gives a T_c value of 359.95 K, which agrees favorably with the value from this work (no value of P_c was found in the

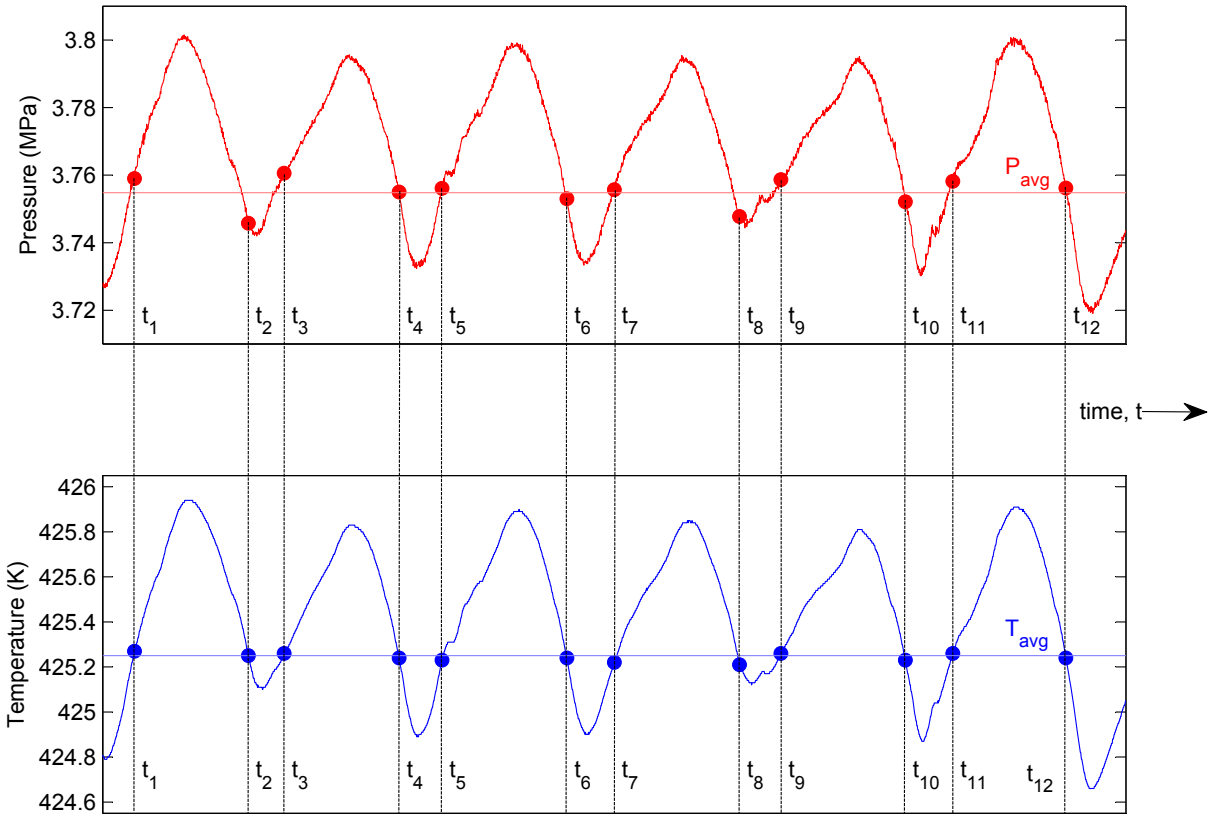

Figure 4.5: The temperature and pressure profiles of the cell contents during an experiment in which 12 recordings of (T_c, P_c) were made at $t_1, t_2, \ldots, t_{12}$. Each recording was done at the instant a dark red color was observed in the cell (third frame of Fig. 4.4.)

aforementioned report). Other recent sources, yet to be recorded in the databases, give similar values of (T_c, P_c) = (358.93 K, 3.134 MPa) [202], and (358.8 ± 0.1 K, 3.129 ± 0.001 MPa) [203]. These two results were determined using a vibrating tube densitometer. A *DuPont* report on hexafluoropropylene oxide (C_3F_6O) gives T_c and P_c values of 359.15 K and 2.896 MPa [204], while reference [202] reports (T_c, P_c) = (359.26 K, 2.931 MPa) using a vibrating tube densitometer, both of which match well with the values in Tables 4.2 and 4.3. Meanwhile, no literature values have been previously reported for the critical properties of 1,1,1,3,3 - pentafluorobutane (R365mfc).

The three uncommon compounds (R1216, C_3F_6O, R365mfc) were tested on three predictive group contribution methods of varying complexity, namely Wilson and Jasperson [205], Marrero and Pardillo [206], and Nannoolal et al. [207]. To obtain the normal boiling points T_b required for these methods, the vapour pressures of each of the compounds were first measured in a static VLE cell with efficient agitation devices. The expanded uncertainties for these vapour pressures were expected not to exceed ± 3 kPa. The temperatures at 1 atm were then calculated for each compound using a spline interpolation. The comparisons are summarized in Table 4.4. The Wilson and Jasperson method showed surprisingly good results, particularly for the critical pressures, for its relatively simple computational nature. One should note, however, that the critical pressure here is a function of critical temperature, and will thus be affected if the other is poorly predicted. With regard to C_3F_6O, neglecting the second-order correction, i.e. the

Table 4.2: Experimental critical temperatures (K) of pure compounds together with their uncertainties.

Compound	This work	DIPPR	NIST[a]
Propane	369.85 ± 0.03	369.83	369.90 ± 0.20
n-Butane	425.22 ± 0.03	425.12	425.00 ± 1.00
n-Pentane	470.10 ± 0.12	469.70	469.80 ± 0.50
n-Hexane	507.61 ± 0.12	507.60	507.60 ± 0.50
Ethanol	513.90 ± 0.12	513.92	514.00 ± 7.00
1-Propanol	536.44 ± 0.12	536.78	536.90 ± 0.80
HFPO	359.48 ± 0.03	-	-
R1216	359.02 ± 0.03	368.00	-
R125	339.26 ± 0.03	339.19	339.24 ± 0.11
R134a	374.23 ± 0.03	374.30	374.10 ± 0.20
R245fa	427.15 ± 0.03	427.00	-
R365mfc	459.91 ± 0.12	-	-
R610	386.41 ± 0.03	386.35	386.35 ± 0.20

[a] NIST values computed by averaging all the individual literature values, and subsequently eliminating data outside three standard deviations, repeating the process until no further outliers are present.

Table 4.3: Experimental critical pressures (MPa) for pure compounds.

Compound	This work	DIPPR	NIST[a]
Propane	4.243 ± 0.001	4.248	4.25 ± 0.01
n-Butane	3.787 ± 0.001	3.796	3.80 ± 0.01
n-Pentane	3.379 ± 0.001	3.370	3.36 ± 0.06
n-Hexane	3.031 ± 0.001	3.025	3.02 ± 0.04
Ethanol	6.128 ± 0.001	6.148	6.30 ± 0.40
1-Propanol	5.178 ± 0.001	5.175	5.20 ± 0.10
HFPO	2.936 ± 0.001	-	-
R1216	3.138 ± 0.001	2.900	-
R125	3.619 ± 0.001	3.595	3.60 ± 0.05
R134a	4.044 ± 0.001	4.064	4.06 ± 0.02
R245fa	3.657 ± 0.001	3.640	-
R365mfc	3.200 ± 0.001	-	-
R610	2.299 ± 0.001	2.323	2.32 ± 0.01

[a] NIST values computed by averaging all the individual literature values, and subsequently eliminating data outside three standard deviations, repeating the process until no further outliers are present.

Table 4.4: Comparison between experimental and predicted critical properties of pure R1216, C_3F_6O and R365mfc.

	R1216	C_3F_6O	R365mfc
Boiling point T_b (K)	243.80	244.46	313.13
Critical temperature T_c (K)			
This work	359.02	359.48	459.91
Wilson and Jasperson[a]	368.52	358.67	463.71
Marrero and Pardillo	364.28	358.37	456.08
Nannoolal et al.	361.23	351.24	461.06
Critical pressure P_c (MPa)			
This work	3.138	2.936	3.200
Wilson and Jasperson[a]	3.281	2.901	3.321
Marrero and Pardillo	2.903	2.881	2.652
Nannoolal et al.	2.712	3.257	3.314

[a] Only first-order considered

branched epoxide group, and treating the compound as a simple first-order molecule, yields a far better result (T_c = 373.74 K, P_c = 3.55 MPa when considered as a second-order molecule). This is rather misleading, but also not uncommon, and has been discussed [185]. The method of Marrero and Pardillo, being more recent but also more complex, gives fair predictions throughout. This method is more rigorous than the former as the compound is considered as a structure of subgroup pairs, rather than individual atoms. Nannoolal et al's method is the most recent and complete of the models, covering most of the essential issues such as extrapolations to large molecules, second-order corrections, and the presence of molecular interactions. As opposed to the Wilson and Jasperson method, the second-order corrections in this case aid, rather than harm, the predictions. Nonetheless, the critical pressure predictions for Nannoolal et al's method are not particularly good, considering its complexity. One needs to take into account that the breakdown of molecules for each method is not identical, leading to instances where certain groups in a particular method are not as well defined, due to lack of data during development. The fact that one is given the freedom to select any method to calculate each critical property, shows that no one method is capable of describing all types of existing compounds.

Impurities in a substance may, to various extents, affect the critical point. Isomers, and close-boiling impurities may not significantly affect the critical point of the bulk substance. Tests with mildly contaminated chemicals have been conducted with the apparatus, and inconsistencies with literature values have not gone undetected. It may be useful to parameterize cubic EoS with the compounds' experimental critical points, rather than literature values, for calculations in subsequent experiments (cf. adjusting constants of an alpha function to experimental, and not literature, vapour pressures).

Binary mixtures

The experimental binary critical properties T_c and P_c can be found in Appendix E, and are plotted in Figures 4.6 - 4.14. To avoid possible changes in the global compositions within the cell - a problem for binary pairs with vastly different volatilities - a flowrate of not lower than 2.5 cm^3/min was used at all times.

This caused the uncertainties on temperature and pressure to be higher than those of the pure components, although this is rarely more than ± 0.2 K and 0.01 MPa. The uncertainties in mole fractions, calculated using the procedure outlined in § 3.1.4, is in the range of 1E-06, and will not be shown in the figures. In contrast, the uncertainties in both T and P are more significant than those seen in VLE measurements, largely due to the errors stemming from repeated measurements.

The relatively ideal propane + *n*-butane mixture was chosen as a test system, due to its simple monotonous critical behaviour. Nonetheless, the system exhibits a maximum in the mixture critical pressures, indicating that the mixture can exist as two-phases at a pressure higher than the critical pressures of the two pure components. A positive agreement with literature was observed, with close matches with the more recent literature sources. To ensure that all literature sources are accounted for, critical points obtained from VLE measurements have also been included in the graphs. In each case, the critical co-ordinates are estimated using a simple yet effective form of the scaling law, which extrapolates to the critical composition x_c and P_c using solely a set of P-T-x-y data. For isotherms, this is in the form of two simultaneous equations [208, 209]:

$$y_i - x_i = \lambda_1 (P_c - P) + \vartheta (P_c - P)^{\gamma} \tag{4.1}$$

$$\frac{y_i - x_i}{2} - x_c = \lambda_2 (P_c - P) \tag{4.2}$$

where ϑ, λ_1, λ_2 are empirical constants, solved simultaneously with x_c and P_c by regressing to experimental VLE data for a given temperature. The constant γ is an universal critical constant equaling 0.325 [210], and applies to mixtures and pure compound forms of the above scaling laws [211]. In Eqn. (4.1), the P-x-y diagram is represented via a linear term, for the behaviour far away from the critical point, and an exponential term, which takes preference at the critical vicinity. In Eqn. (4.2), the distance between the average phase compositions, to the critical point, is proportional to the differences in corresponding pressures, i.e. the law of rectilinear diameters. At least six data points are used in the regression, with sufficient data points close to the vicinity of the critical point. The method itself is however not unsusceptible to erroneous experimental data. The scaling laws were tested on isothermal VLE literature data, consisting of experimentally determined critical points, of several hydrocarbon and alcohol systems, and yielded errors no more than 3 % for pressure and composition. In the graphical presentation of results, extrapolated data arising from Eqns. (4.1) and (4.2) are shown as closed symbols.

The ethanol + *n*-alkane (C_4-C_8) mixtures are non-ideal, azeotropic systems. This is most clearly seen in the T_c-x projection, where a minimum is observed in the critical temperature curve, yielding a maximum pressure azeotrope for these mixtures. The phenomenon is least evident in the *n*-butane + ethanol system, where the differences in the components' critical temperatures are reasonably large. The effect however becomes clear within the zoom (see Fig. 4.7 *right*), where points were measured at sufficiently small intervals in the *n*-butane rich region. There is little agreement between the critical points obtained in the VLE measurements using the "static-analytic" apparatus, and those obtained using the "dynamic-synthetic" apparatus. However, at the critical vicinity, a high level of difficulty were encountered in the "static-analytic" apparatus in terms of pressure control, and together with uncertainties in the TCD calibration, a large error is believed to exist in the two closed symbols.

The critical temperature minimum becomes more pronounced in *n*-pentane + ethanol system, and is most prominent in the ethanol + *n*-hexane mixture. The binary pair in this case has the smallest differences

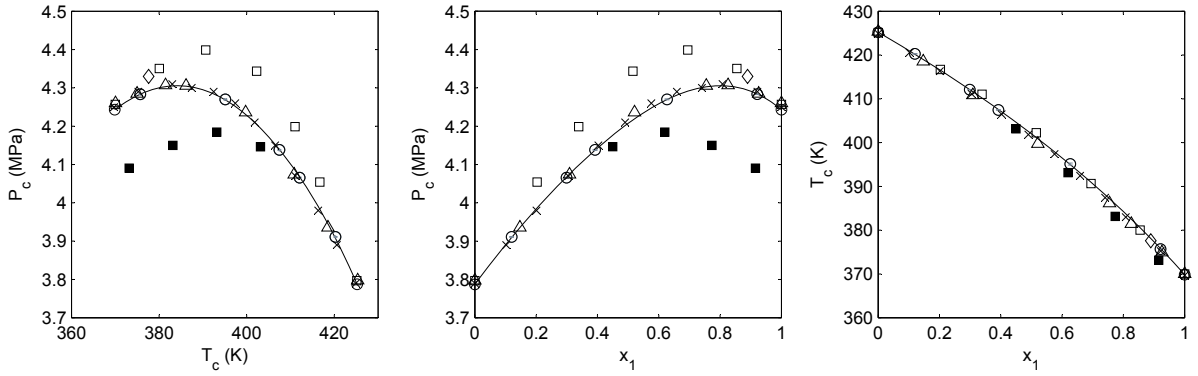

Figure 4.6: Experimental critical pressures and temperatures for the propane (1) + *n*-butane (2) system. ○: This work; □: Nysewander et al. [212]; △: Kreglewski and Kay [213]; ◇: Wiese et al. [214]; ×: Horstmann et al. [194]; ■: Kay [215], using Eqns. (4.1) and (4.2); −: Redlich-Kister correlation.

in pure component critical temperatures ($T_{c,n\text{-hexane}}$ = 507.61 K, $T_{c,\text{ethanol}}$ = 513.90 K), and *n*-hexane is the only hydrocarbon to form a bancroft point with ethanol (T_{bancroft} = 383.22 K, P_{bancroft} = 0.312 MPa). With hydrocarbons heavier than *n*-hexane, the curve minimum becomes less distinct as the differences in the components' critical temperatures increase again. In all cases, the curvatures of the critical loci can be generated in a natural, and less ambiguous manner compared to a typical VLE setup. This is clear from the disagreements of the extrapolated VLE data to the measured values.

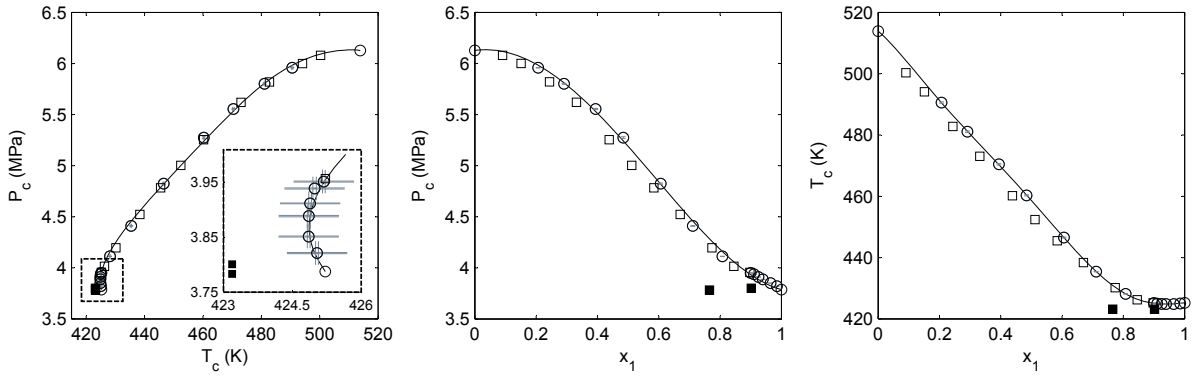

Figure 4.7: Experimental critical pressures and temperatures for the *n*-butane (1) + ethanol (2) system. ○: This work; □: Deák et al. [182]; ■: Soo et al. [216], using Eqns. (4.1) and (4.2), with data presented in Appendix C; −: Redlich-Kister correlation. The dashed inset figure is a zoom of the *n*-butane rich region, the curvature showing the presence of two critical pressures for each given temperature within the range $424.86 < T < T_{c,1}$.

For systems with no literature data, it is often difficult to approximate the location of the first synthesized mixture. In this case, the experimentalist may call upon experiences with similar systems or, if possible, gain insights from predictions using appropriate models. A trial-and-error procedure is also feasible by starting the measurements sufficiently far away from the critical region, and slowly heat the mixture in a controlled manner until critical phenomena is observed. As the shape of the critical profile is revealed, experimentation becomes intuitively easier. An example is the propane + 1,1,1,2-Tetrafluoroethane system, shown in Figure 4.13.

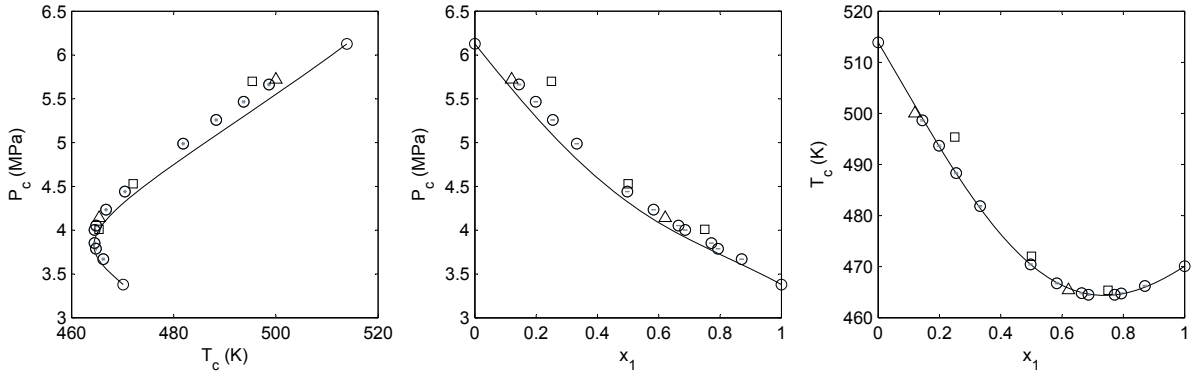

Figure 4.8: Experimental critical pressures and temperatures for the *n*-pentane (1) + ethanol (2) system. ○: This work; □: Seo et al. [217]; △: McCracken et al. [218]; −: Redlich-Kister correlation.

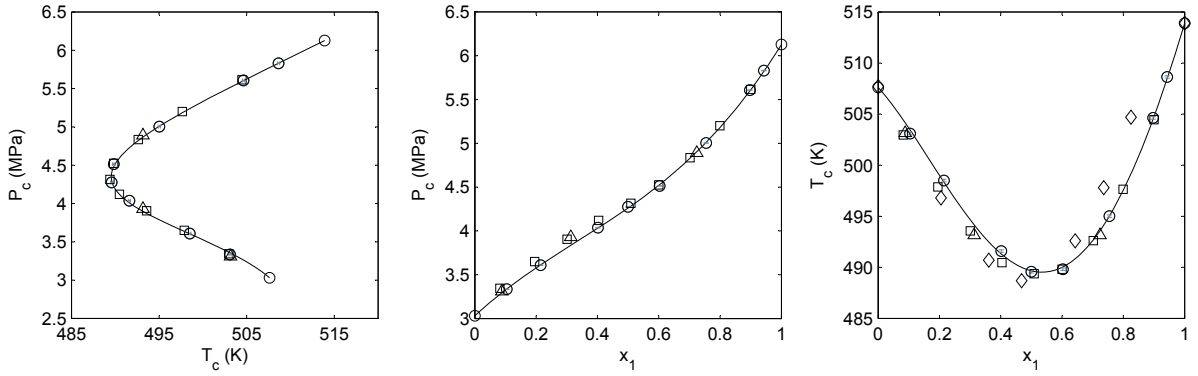

Figure 4.9: Experimental critical pressures and temperatures for the ethanol (1) + *n*-hexane (2) system. ○: This work; □: Sauermann et al. [219]; △: Seo et al. [220]; ◇: Morton et al. [221]; −: Redlich-Kister correlation.

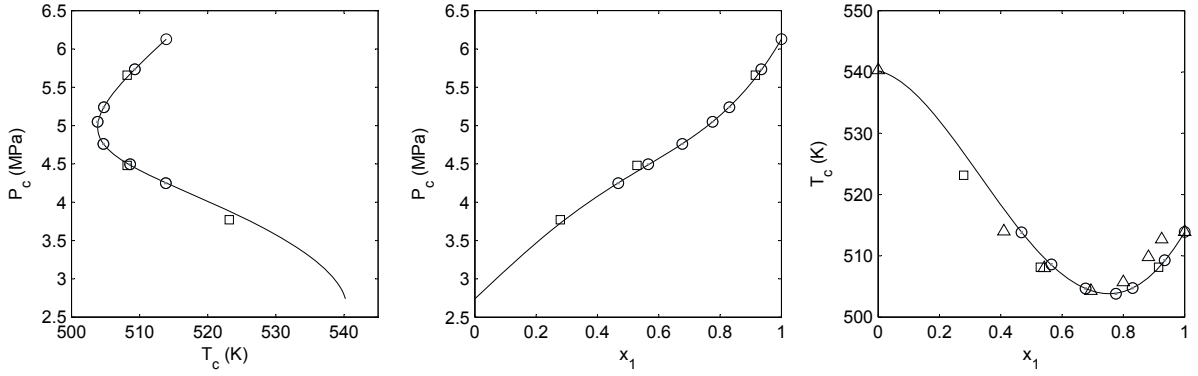

Figure 4.10: Experimental critical pressures and temperatures for the ethanol (1) + *n*-heptane (2) system. ○: This work; □: Seo et al. [222]; △: Morton et al. [221]; −: Redlich-Kister correlation.

The critical temperature and pressure of each of the binary mixtures is correlated using a Redlich-Kister

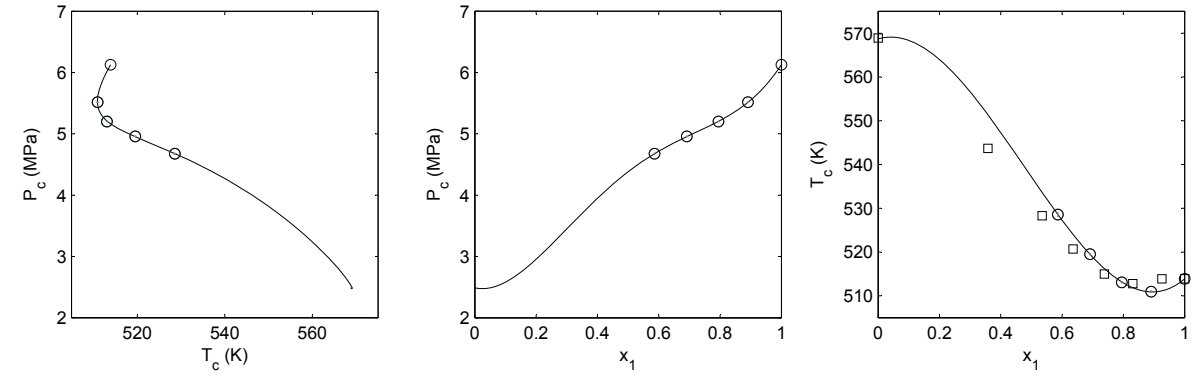

Figure 4.11: Experimental critical pressures and temperatures for the ethanol (1) + *n*-octane (2) system. ○: This work; □: Morton et al. [221]; −: Redlich-Kister correlation.

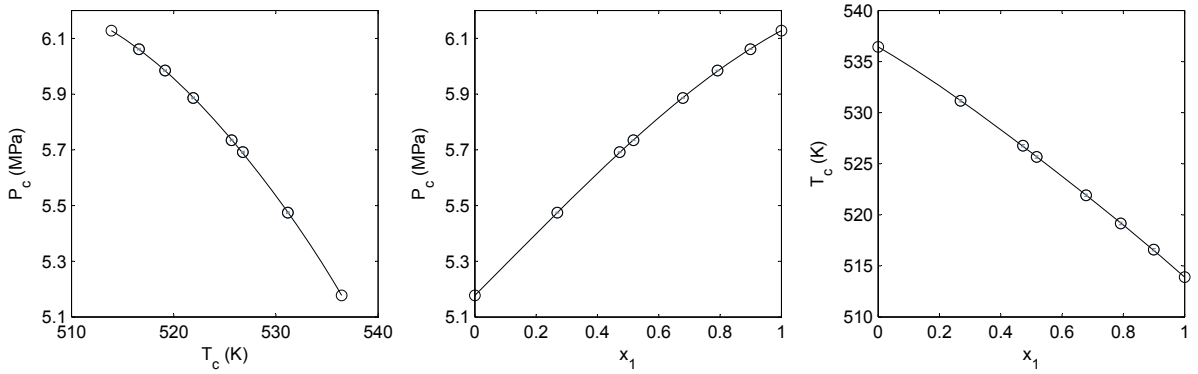

Figure 4.12: Experimental critical pressures and temperatures for the ethanol (1) + 1-propanol (2) system. Solid line is the Redlich-Kister correlation.

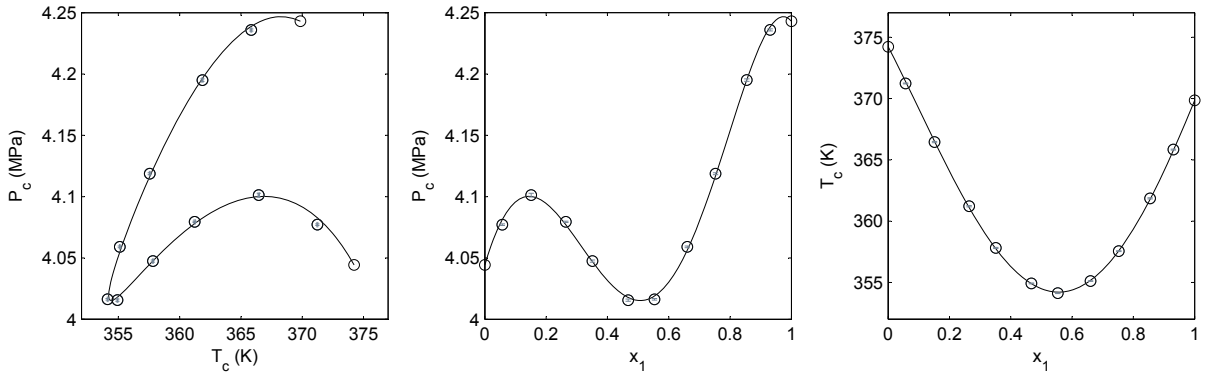

Figure 4.13: Experimental critical pressures and temperatures for the propane (1) + 1,1,1,2-Tetrafluoroethane/R134a (2) system. Solid line is the Redlich-Kister correlation.

type equation as follows:

$$T_{12} = x_1 T_{c,1} + x_2 T_{c,2} + \sum_{j=1}^{n} a_j x_1 x_2 (2x_1 - 1)^{j-1} \tag{4.3}$$

Table 4.5: Redlich-Kister constants for Eqns. (4.3) and (4.4) for the binary mixtures in this work.

System	a_1 (K)	a_2 (K)	a_3 (K)	a_4 (K)	a_5 (K)	$RMSD$ (K)
$C_3H_8 + C_4H_{10}$	17.996	4.229	0.7480	-	-	0.10
$C_4H_{10} + C_2H_6O$	-43.694	-49.151	-69.829	-1.058	68.678	0.08
$C_5H_{12} + C_2H_6O$	-86.741	-12.809	17.170	-	-	0.21
$C_2H_6O + C_6H_{14}$	-84.370	-27.197	18.006	-	-	0.20
$C_2H_6O + C_7H_{16}$	-60.394	-62.932	12.458	-	-	0.07
$C_2H_6O + C_8H_{18}$	-16.520	-94.506	-3.206	-	-	0.06
$C_2H_6O + C_3H_8O$	3.662	-0.565	1.048	-	-	0.01
$C_5H_{12} + C_6H_{14}$	7.980	0.288	-0.337	-	-	0.02
C_3H_8 + R134a	-70.207	-10.928	15.738	-	-	0.08
System	b_1 (MPa)	b_2 (MPa)	b_3 (MPa)	b_4 (MPa)	$RMSD$ (MPa)	
$C_3H_8 + C_4H_{10}$	0.769	0.252	0.114	-	9.9×10^{-4}	
$C_4H_{10} + C_2H_6O$	0.929	-2.127	-0.319	-	2.2×10^{-2}	
$C_5H_{12} + C_2H_6O$	-1.737	0.425	0.551	-	1.6×10^{-1}	
$C_2H_6O + C_6H_{14}$	-1.270	-1.328	0.064	-	8.9×10^{-3}	
$C_2H_6O + C_7H_{16}$	-0.411	-1.918	-1.170	-	5.2×10^{-3}	
$C_2H_6O + C_8H_{18}$	0.290	0.419	-4.659	-	2.7×10^{-3}	
$C_2H_6O + C_3H_8O$	0.262	0.104	9.210×10^{-3}	-	1.4×10^{-3}	
$C_5H_{12} + C_6H_{14}$	0.190	0.025	-0.058	-	1.3×10^{-3}	
C_3H_8 + R134a	-0.513	-0.442	1.085	0.361	2.3×10^{-3}	

$$P_{12} = x_1 P_{c,1} + x_2 P_{c,2} + \sum_{j=1}^{n} b_j x_1 x_2 (2x_1 - 1)^{j-1} \tag{4.4}$$

where $T_{c,i}$ and $P_{c,i}$ are the pure component critical temperature or pressure of the i^{th} component; n is the number of coefficients; and a_j and b_j are the empirical constants of the equations, obtained by minimizing the relative mean standard deviation (RMSD):

$$RMSD = \left[\frac{1}{M} \sum_{j} \left(\theta_{exp} - \theta_{cal} \right)_j^2 \right]^{0.5} \tag{4.5}$$

where θ is either T_c or P_c, and M is the number of data points. Thus, each mixture T_c or P_c can be seen as the sum of an *ideal* contribution, comprising of the first two terms of Eqns.(4.3) or (4.4), and a non-ideal, or *pseudo-excess*, contribution equal to the summation term (we avoid using a non-official term such as *excess critical temperature*). The coefficients for each binary system are listed in Table 4.5. The highest possible number of coefficients is used for each binary system, where no further improvements in correlation can be achieved.

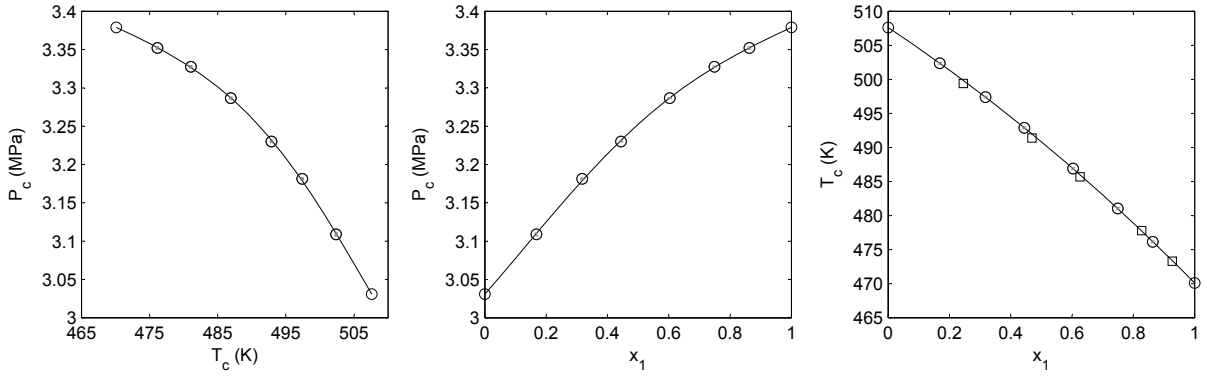

Figure 4.14: Experimental critical pressures and temperatures for the *n*-pentane (1) + *n*-hexane (2) system. ○: This work; □: Partington et al. [223]; −: Redlich-Kister correlation.

Ternary mixtures

To facilitate data treatment of the ternary *n*-pentane (1) + ethanol (2) + *n*-hexane (3) mixture, it is necessary to acquire data regarding all binary pairs. The binary *n*-pentane (1) + *n*-hexane (2) system was thus measured, with the coefficients for Eqns. (4.3) and (4.4) included in Table 4.5.

We formulate a correlation for ternary mixtures by assuming that the ternary critical property is the sum of the ideal contributions, the pseudo-excess contributions from the binary parts, as well as a further pseudo-excess contribution for the ternary part. We use Cibulka and Singh and Sharma's expressions for the ternary contribution.

Cibulka [189]:

$$T_{123} = x_1 T_{c,1} + x_2 T_{c,2} + x_3 T_{c,3} + \sum_{j=1}^{n} a_{12,j} x_1 x_2 (2x_1 - 1)^{j-1} + \sum_{j=1}^{n} a_{13,j} x_1 x_3 (2x_1 - 1)^{j-1} \\ \sum_{j=1}^{n} a_{23,j} x_2 x_3 (2x_2 - 1)^{j-1} + x_1 x_2 x_3 (\alpha_1 + \alpha_2 x_1 + \alpha_3 x_2) \tag{4.6}$$

$$P_{123} = x_1 P_{c,1} + x_2 P_{c,2} + x_3 P_{c,3} + \sum_{j=1}^{n} b_{12,j} x_1 x_2 (2x_1 - 1)^{j-1} + \sum_{j=1}^{n} b_{13,j} x_1 x_3 (2x_1 - 1)^{j-1} \\ \sum_{j=1}^{n} b_{23,j} x_2 x_3 (2x_2 - 1)^{j-1} + x_1 x_2 x_3 (\beta_1 + \beta_2 x_1 + \beta_3 x_2) \tag{4.7}$$

Singh and Sharma [190]:

$$T_{123} = x_1 T_{c,1} + x_2 T_{c,2} + x_3 T_{c,3} + \sum_{j=1}^{n} a_{12,j} x_1 x_2 (2x_1 - 1)^{j-1} + \sum_{j=1}^{n} a_{13,j} x_1 x_3 (2x_1 - 1)^{j-1} \\ \sum_{j=1}^{n} a_{23,j} x_2 x_3 (2x_2 - 1)^{j-1} + x_1 x_2 x_3 \left[\alpha_1 + \alpha_2 x_1 (x_2 - x_3) + \alpha_3 x_1^2 (x_2 - x_3)\right] \tag{4.8}$$

$$P_{123} = x_1 P_{c,1} + x_2 P_{c,2} + x_3 P_{c,3} + \sum_{j=1}^{n} b_{12,j} x_1 x_2 (2x_1 - 1)^{j-1} + \sum_{j=1}^{n} b_{13,j} x_1 x_3 (2x_1 - 1)^{j-1}$$
$$\sum_{j=1}^{n} b_{23,j} x_2 x_3 (2x_2 - 1)^{j-1} + x_1 x_2 x_3 \left[\beta_1 + \beta_2 x_1 (x_2 - x_3) + \beta_3 x_1^2 (x_2 - x_3)\right] \quad (4.9)$$

where α_{1-3} and β_{1-3} are the ternary parameters for temperatures and pressures, respectively. The T_c-x projection has a global minimum close to the pure *n*-pentane, which results from the behaviour of the binary *n*-pentane + ethanol system. The agreement of the Cibulka and Singh and Sharma's expressions to the data are comparable, both having correlation coefficients (r^2) above 0.9900, for α and β. The experimental results for the ternary system can be found in Appendix E, and the critical surfaces from Cibulka's equation are plotted in Fig. 4.15. The α and β values are summarized in Table 4.6.

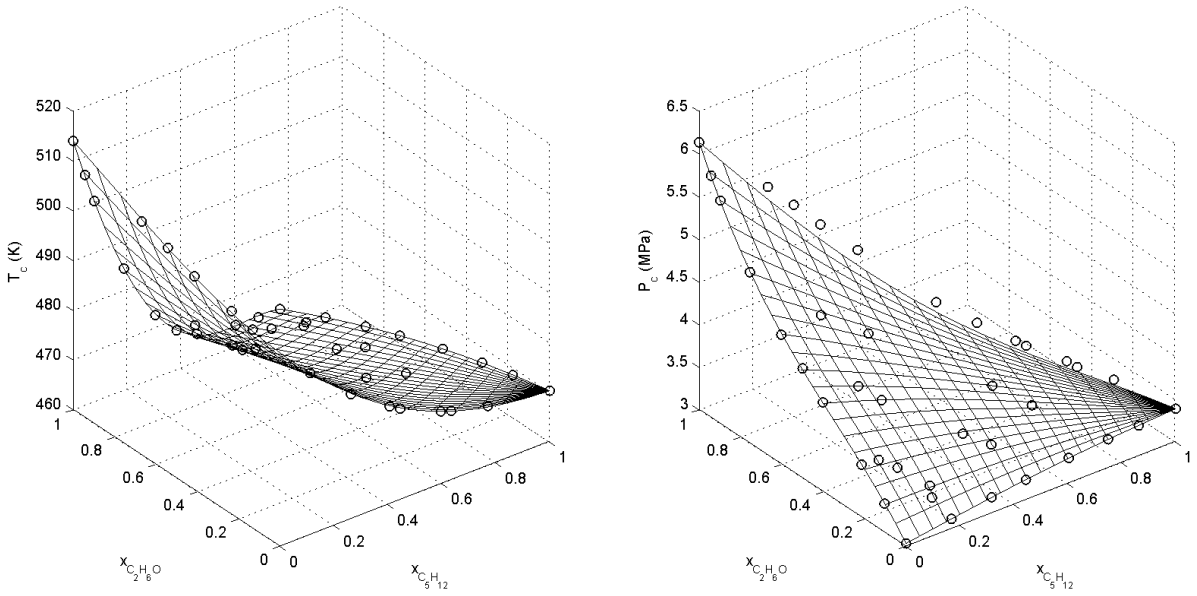

Figure 4.15: Experimental critical pressures and temperatures for the *n*-pentane (1) + ethanol (2) + *n*-hexane (3) system. The critical surface is generated using Cibulka's expression, i.e. Eqns. (4.6) and (4.7).

The constants in Tables 4.5 and 4.6 are empirical, and their limitations can be quickly exposed by extrapolation to systems other than those presented herein. Equations of states with fewer, and more meaningful parameters serve as a means of correlating mixture critical data. This is the approach taken in Chapter 6 of the thesis.

4.4 Recommendations for the apparatus

Critical measurement by visual observation are generally static methods; mostly with designs different to the presented apparatus:

1. ***Small cell volumes.*** The well-documented sealed ampoule method uses thin cells (ampoules) of 0.5 - 3 mm internal diameter and 5 - 10 cm in length [191]. This allows for a short meniscus and

Table 4.6: α and β constants for the *n*-pentane (1) + ethanol (2) + *n*-hexane (3) ternary mixture.

System	Cibulka	Singh and Sharma
α_1 (K)	64.2863	25.3234
α_2 (K)	34.5248	-455.8621
α_3 (K)	-144.1266	-1420.5424
$RMS\,D,\ T$ (K)	0.14	0.28
β_1 (MPa)	4.2641	4.4880
β_2 (MPa)	1.3644	-9.1400
β_3 (MPa)	-1.4655	-99.1569
$RMS\,D,\ P$ (MPa)	0.01	0.01

more sharply defined critical points. Stirrers may be avoided in the thinnest of cells, although rocking-motion type stirrers have been observed to reduce temperature gradients in the cell [224].

2. ***Fine temperature control.*** For thermally stable substances, the focus of the heating source is on fine, rather than rapid, temperature control. This suggests the use of liquid baths, with transparent silicon oil for viewing purposes. Gas and electric heaters have been used for thermally decomposing substances, due to their rapid temperature regulation (see Ref. [191] for a list of previous works). Air baths, such as that presented herein, are rarely encountered.

3. ***Visual enhancers.*** A magnified image of the static cell, can be superimposed with the time-temperature profile, as described in Refs. [191, 224]. Cameras are used for reviewing and re-examining the critical phenomenon.

Despite some modifications, the current cell measures 12.7 mm in inner diameter, and 30.03 mm in length. This is considered to be rather large in diameter. Although the continuous flow provides some means of stirring, the effect is still not ideal. The colour of the fluid changes initially, and most intensely, at the interface of the liquid, with a 1 - 2 second interval for complete colour dispersion within the cell. This is the reason the critical point is adjudged by observing only the liquid surface. The air furnace offers rapid heating/cooling speed, but not at the level documented by gas and electric heaters (for example, T = 640 K in 45 s [225]). It can, however, acquire fine temperature control (± 0.5 K/min) through careful flow regulations, although this may require some practice initially. The absence of a stirrer and the large cell volume are the two main reasons the present setup cannot be used in static mode. Tests reveal a meniscus which disappears too slowly over a long time interval.

The lack of a local stirrer makes the apparatus ineffective when faced with large, contrasting volatilities between the components of a mixture. An example is the propane + ethanol system shown in Figure 4.16. It was observed that the colouring phenomenon proposed, in Figure 4.4, for establishing critical points could only be obtained at very large flowrates (~ 4 - 5 cm^3/min). In addition, control of the level of the liquid within the cell becomes very difficult at such high flowrates, and the colour changes of the fluid are no longer clearly defined/sequenced. For mixtures of compositions in the mid-regions (x_1 =~ 0.5), it was not possible to obtain any distinct colour changes and results. While some success were had at the extremities of the compositions, results were obtained with consistently high uncertainties, reaching

± 0.4 K and ± 0.02 MPa, values which were larger than for previously discussed mixtures. The system was not pursued beyond compositions relatively rich in one component. Judging from the VLE data presented in Chapter 3, it is possible that the large relative volatilities present between propane and ethanol demand large flowrates in order to maintain the synthesized composition constant.

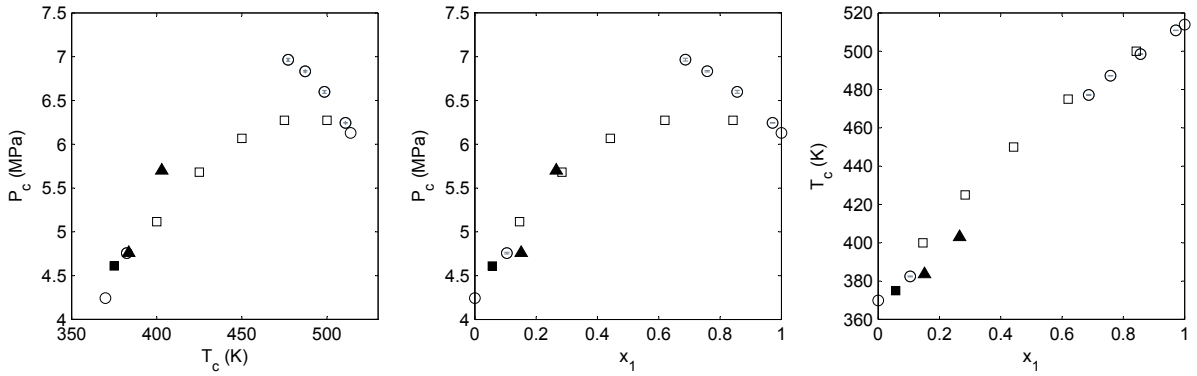

Figure 4.16: Experimental critical pressures and temperatures for the propane (1) + ethanol (2) system. Curve incomplete due to difficulties encountered in the large differences in volatilities between the two substances. ○: This work; □: Gomez-Nieto and Thodos [178]; ■: Horizoe et al. [179], using Eqns. (4.1) and (4.2); ▲: VLE measurements from this work (see Appendix C), using Eqns. (4.1) and (4.2)

In a recent modification of the apparatus, a magnetic stirrer has been placed within the cell, and driven by an external motor (Fig. 4.17). Critical point measurements in this setup are performed as a static-synthetic apparatus, where the contents remain in a closed circuit (the exit valve **V1** is kept fully shut). This modification has been tested on pure compounds, and gave identical results as the dynamic mode. Other forms of agitation, such as a rocking/oscillating stirrer, has also been employed.

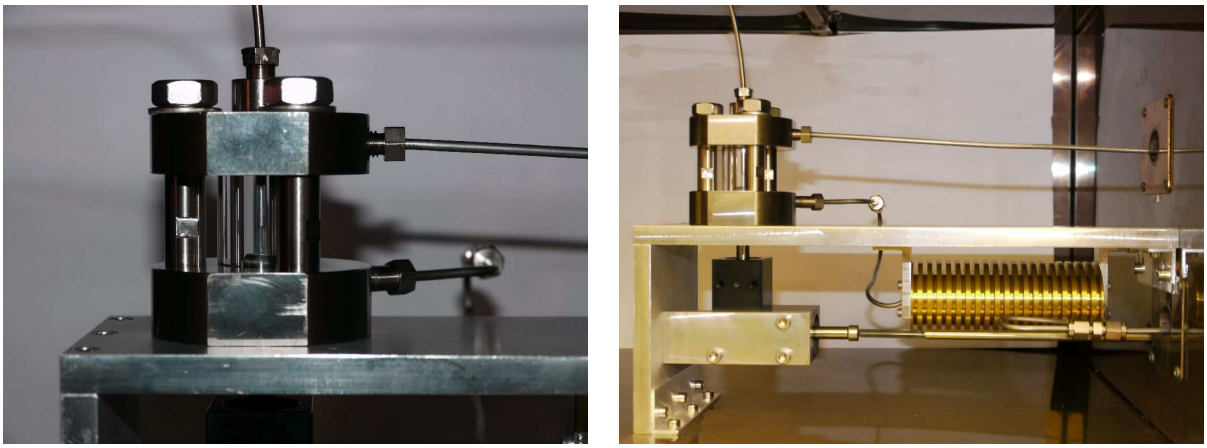

Figure 4.17: Photos of the modified equilibrium cell with an addition of a local magnetic stirrer, which can be seen on the *left* figure. The stirrer is driven by a motor situated outside the oven of the cell.

In addition to a stirrer, a further improvement is the light source in the furnace. While the current light-mirror combination is beneficial, it is more desirable to use a concentrated light source, such as laser. Rapid-frame cameras and video camcorders, as visual enhancers, are also useful. Automation of

the apparatus is not as crucial an improvement, due to the relatively short duration of each experiment - a single press volume is depleted within an hour. If available, the press can be replaced by two piston pumps [51, 179, 194, 195, 196, 197, 198] to rapidly change the mixture composition in-line during run-time. This requires a knowledge of the temperature in the entry lines to accurately calculate the molar flowrates and composition (only the volumetric flow is indicated by the piston pump).

Anselme et al. [226] proposed a method to calculate the critical density for static methods, from a knowledge of the cell volume and mass of the loading. This can be applied, in an *approximate* manner, to our apparatus - the mass is less easily defined here; and the cell volume needs to incorporate the volume in the lines, capillaries, etc. A *PVT* method such as the vibrating tube densitometer technique would better serve such a purpose [157]. The relatively low temperature limitation in the apparatus did not allow testing of thermally unstable materials. An extrapolative procedure, such as that described in Teja and Mendez-Santiago [191], is likely to be used.

4.5 Concluding remarks

We have presented an apparatus, using the "dynamic-synthetic" method, capable of measuring the critical properties of pure and multi-component systems, up to 543 K and 20 MPa. In this chapter, the critical properties of thirteen pure components, nine binary systems, and one ternary system have been measured. The experimental results show good agreement with literature values, where available. Critical points of mixtures could be measured rapidly and in a more clear-cut manner compared to a "static-analytic" apparatus. Various mathematical models have been applied in correlating the critical properties, and the outcomes discussed. The highly accurate nature of the critical data obtained with this apparatus is suitable for the characterization of mixture phase diagrams, and the development of thermodynamic models at high pressure.

Various improvements should be implemented for the apparatus to measure the critical profiles of more complex systems - those possessing components of highly varying volatilities, as well as extremely high and low temperature measurements. Such systems are not yet suitable for the prototype nature of the current apparatus. Possible recommendations to the current setup have been proposed in the chapter, some of which are already being deployed.

CHAPTER 5

Thermodynamic modeling of biofuel systems using the PC-SAFT equation of state

Remember that all models are wrong; the practical question is how wrong do they have to be to not be useful.

- George Edward Pelham Box (1919 -)

La modélisation thermodynamique
de systèmes de biocarburants en utilisant l'équation d'État PC-SAFT

Dans ce chapitre, les capacités de l'équation d'état PC-SAFT vis-à-vis du calcul des propriétés thermodynamiques sont démontrées systématiquement dans son application à l'étude de mélanges de biocarburants. Les mesures expérimentales présentées dans le troisiéme chapitre sont traitées, ainsi qu'une variété de systèmes issus de la littérature. En identifiant les interactions moléculaires notables présentes, des contributions de l'énergie de Helmholtz pertinentes peuvent être appliquées dans l'équation d'état PC-SAFT pour modéliser des systèmes non-idéaux. Dans plusieurs cas, un seul paramètre d'interaction binaire est suffisant pour modéliser une large gamme de conditions.

Pour modéliser des équilibres de phase des systèmes contenant des alcools, l'inclusion de termes dipolaires par Jog et Chapman, ou Gross et Vrabec, conduit à une baisse de la valeur numérique du paramètre d'interaction binaire. De cette manière, les mélanges d'alcools étudiés dans le chapitre 3 pourraient être représentés quantitativement avec de petits paramètres binaires. Une difficulté rencontrée avec les systèmes d'alcools est la prédiction de phases incorrectes, telles que l'apparition d'une deuxième phase liquide. Pour les systèmes d'acides carboxyliques, on a proposé de nouveaux paramètres PC-SAFT pour les acides linaires, de l'acide formique (CH2O2) à l'acide caproïque (C6H12O2). Les acides ont été modélisés avec un seul site d'association, qui est représentatif de la phase vapeur. Le paramétrage est basé sur l'approche décrite dans le chapitre 2. Dans ce calcul, le paramètre de volume d'association κ^{AB} est fixé à une valeur de 0.001, afin d'éviter de multiples solutions qui résultent de la procédure d'optimisation. Les nouveaux paramètres ont permis de reproduire avec précision les tensions de vapeur et les densités liquides des acides. Des résultats positifs ont également été obtenus pour les mélanges idéaux contenant des acides carboxyliques. Pour les systèmes non-idéaux contenant un azéotrope, il est souvent nécessaire d'introduire un deuxième paramètre d'interaction binaire l12 dans le terme de dispersion de PC-SAFT. La présence d'un deuxième paramètre offre plus de flexibilité au modèle, bien qu'il devienne moins prédictif. Le deuxième paramètre permet à des mélanges plus complexes d'être décrits par PC-SAFT.

Dans ce chapitre on procède à la modélisation de l'équilibre des phases des systèmes contenant des composés polaires, qui incluent des cétones, éthers, esters et aldéhydes. Pour des composés très polaires, tels que l'acétone, les termes dipolaires servent à améliorer les résultats de la modélisation, ainsi qu'à diminuer la valeur numérique du paramètre binaire. PC-SAFT polarisable ne permet que des améliorations légères, même pour les composés très polaires, et a trouvé peu d'applications dans ce travail. L'éther principal de ce travail est l'éthyle tertio butyle éther (l'ETBE), pour lequel on a proposé de nouveaux paramètres. De même, de nouveaux paramètres ont été déterminés pour les esters méthyliques lourds, qui sont des constituants importants des biodiesels. Les paramètres ont été testés par rapport à la modélisation des équilibres entre phases des systèmes binaires, avec des résultats positifs. Les paramètres d'esters méthyliques lourds peuvent encore être améliorés en incorporant des données plus complètes sur la pression et la densité. Dans un mélange contenant un composé polaire et un composé associatif, l'effet de solvatation doit être pris en compte, cela est réalisé en utilisant une technique proposé par Kleiner et Sadowski.

La modélisation de mélanges aqueux est une tâche difficile pour les équations d'états. Dans ce travail, on a modélisé l'eau comme une molécule possédant deux sites d'associations. Bien que la méthode soit simplifiée, une bonne description des équilibres de phase peut être réalisée. En utilisant deux paramètres d'interaction binaire, les équilibres liquide-vapeur et liquide-liquide de plusieurs mélanges aqueux peuvent être décrits en même temps.

Le reste du chapitre traite du calcul des enthalpies d'excès, et de l'application de PC-SAFT dans les tests de cohérence thermodynamique. Généralement, l'équation PC-SAFT n'est pas particulièrement adaptée pour décrire les enthalpies d'excès, car elle nécessite souvent aux deux paramètres d'interaction binaire de corréler quantitativement les données expérimentales. Pour la plupart des mélanges, la valeur du paramètre binaire utilisé pour corréler les données d'enthalpie d'excès ne peut pas être transférée pour la corrélation des équilibres entre phases. L'équation PC-SAFT fournit une option pour modéliser les enthalpies d'excès de systèmes de composés oxygénés, mais il est toujours préférable de faire appel à des modèles plus classiques, tels que NRTL ou UNIQUAC.

Un test de cohérence thermodynamiques peut être utilisé pour évaluer le niveau de cohérence entre le modèle et les données expérimentales. Il aide également à identifier de données moins correctes d'un ensemble de résultats. Dans ce travail, on a choisi le test de Christiansen et Fredenslund, et de Van Ness-Byers-Gibbs, pour les systèmes sous-critiques. Le test de Valderrama et Alvarez est utilisé pour les mélanges supercritiques. Les données expérimentales de ce travail ont été conclus pour être bien corréle avec les données expérimentales mesurées dans ce travail.

Application of the PC-SAFT equation of state (EoS) can almost be considered as an *art*. It involves, on the most basic level, the selection of the appropriate Helmholtz energy contributions from an impressive arsenal. Each contribution comes with its own decision-making process, which are not only interconnected with others, but also affects the model parameters and final results. Examples highlighting this nature include:

- Choice of pure component parameters, i.e. the association scheme, the need for multipolar contributions, and whether the introduction of additional contributions will bring about sufficient improvements to justify the increase in mathematical complexity and computational time.
- Thermodynamic properties to be included for regressing pure component parameters (Objective function used for the regression procedure).
- Number of binary interaction parameters (k_{12}, l_{12}) to be included in the dispersion term.

This seemingly lack of standardization and transparent implementation is often the reason that the SAFT family of EoS are still not widely considered in commercial simulators [158]. This is unfortunate, given that SAFT models, when used effectively, extrapolate well to extended regions of operation. As far as process simulations are concerned, this is a desirable feature which we shall exploit in this chapter.

This chapter is concerned with the modeling of thermodynamic properties of selected biofuel systems, including the treatment of experimental data covered in Chapter 3. We propose, in a systematic manner, strategies in modeling different functional groups found in oxygenated biofuel mixtures. Throughout the chapter, emphasis is placed on exploiting the full capabilities of the PC-SAFT in the event of different molecular structures and interactions. While the focus is mainly on fluid phase equilibria at the start, we eventually turn our attention to modeling excess enthalpies - an important aspect in gasoline blends. The chapter closes with a section on thermodynamic consistency testing, applied to the measurements of this work using the PC-SAFT EoS.

To avoid confusion in the referral of the different variants of the PC-SAFT EoS, the term PC-SAFT will be used in a general light to refer to the SAFT EoS of Chapman et al. [125] containing the modified dispersion term of Gross and Sadowski [92, 93]. In modeling discussions, the nomenclature and curve colours outline in Table 5.1 will be used. As previously, the cubic PR-WS-NRTL EoS when used, refers to the original Peng-Robinson equation with the Wong and Sandler mixing rule and NRTL g^{E} function.

Table 5.1: Abbreviations for the different variants of PC-SAFT EoS used in Chapter 5, together with the Helmholtz free energy contributions each form may choose to include.

Model name	a^{o}	a^{hs}	a^{chain}	a^{disp}	a^{assoc}	a^{DD}_{JC}	a^{DD}_{GV}	$a^{DD,eff}$
non-polar PC-SAFT	✓	✓	✓	✓	✓			
PC-SAFT-JC (polar)	✓	✓	✓	✓	✓	✓		
PC-SAFT-GV (polar)	✓	✓	✓	✓	✓		✓	
PCIP-SAFT (induced polar)	✓	✓	✓	✓	✓			✓

5.1 Modeling aspects and approach

For this work, a symmetric phi-phi (ϕ-ϕ) approach is followed to calculate both liquid and vapour phase fugacities. As described in § 2.3.3, the PC-SAFT is extended to mixtures using the Berthelot-Lorentz combining rules for the dispersive energy, resulting in a single binary interaction parameter k_{12} (Eqn. 2.59). In the treatment of data, this model parameter is adjusted to minimize the error between the experimental and calculated values of two of the four possible phase variables (P, T, x, y). This is a result of the Gibbs phase rule. In high pressure vapour-liquid equilibria (VLE), we select the temperature and pressure as the independent variables, as they have the lowest experimental

uncertainties. A flash-type objective function is used in the optimization:

$$F = \frac{100}{N}\left[\sum_{i}^{N}\left(x_{exp,i} - x_{cal,i}\right)^2 + \sum_{i}^{N}\left(y_{exp,i} - y_{cal,i}\right)^2\right] \tag{5.1}$$

where N is the number of data points, ($x_{exp,i}$, $x_{cal,i}$) and ($y_{exp,i}$, $y_{cal,i}$) are the i^{th} measured and calculated liquid and vapour compositions of the coexisting fluid phases at fixed temperature and pressure.

For low pressure systems, the mass balance criterion in flash calculations does not converge easily, hence we have opted for a bubblepoint pressure type objective function for isothermal measurements:

$$F = \frac{100}{N}\left[\sum_{i}^{N}\left(y_{exp,i} - y_{cal,i}\right)^2 + \sum_{i}^{N}\left(\frac{P_{exp,i} - P_{cal,i}}{P_{exp,i}}\right)^2\right] \tag{5.2}$$

and a bubblepoint temperature objective function for isobaric measurements:

$$F = \frac{100}{N}\left[\sum_{i}^{N}\left(y_{exp,i} - y_{cal,i}\right)^2 + \sum_{i}^{N}\left(\frac{T_{exp,i} - T_{cal,i}}{T_{exp,i}}\right)^2\right] \tag{5.3}$$

Irrespective of the objective functions used, the model calculations are verified for spurious phase-splitting. In the events where an automated optimization routine results in the appearance of an erroneous phase, the binary interaction parameter is adjusted manually by trial-and-error. In this work, k_{12} (and occasionally l_{12}) values are optimized using a Nelder-Mead algorithm [227], unless stated otherwise.

5.2 Application of the PC-SAFT in modeling fluid phase equilibria of polar mixtures

5.2.1 Alcohols

According to Huang and Radosz [228], each associating alcohol molecule can be modeled as either having one proton donor and one proton acceptor (2B scheme), or two proton donors and one proton acceptor (3B scheme). The latter scheme is generally accepted as the more rigorous of the two schemes [229, 230], although both schemes tend to yield similar results for most alcohols. There has been few cases within alcohol mixtures illustrating true improvements of the 3B over the 2B scheme, since the effects of the adjustable binary parameter are much larger than the choice in bonding scheme. Von Solms et al. [113] showed, using spectroscopy, that the 2B scheme is generally used for alcohols heavier than methanol. Wolbach and Sandler is in agreement with this statement [231]. A PC-SAFT systematic study by Gross and Sadowski [94] using only 2B schemes for alcohols gave excellent correlations. In this work, we adopt the simpler 2B scheme for alcohol-related mixtures, avoiding the use of over-rigorous schemes when the association term of Wertheim is in itself not fully rigorous (see § 2.3.1).

Alcohols are strong associating compounds that are considered as moderately polar, generally having a dipole moment of less than two Debye. While this suggests the use of the Helmholtz energy contribution a^{assoc} and a^{DD} for the association and dipole effects, such an approach is not rigorously correct. Two alcohol molecules are continuously subjected to short-range (association) and long-range (dipole) interactions; forces which are not entirely independent of one another, yet are being represented by separate terms. Nevertheless, this approach is commonly employed (for example, in Lennard-Jones SAFT [127, 128]), and its merits are shown for the propane + ethanol system in Figure 5.1. When the three EoS, i.e. the PC-SAFT, and the PC-SAFT with the two different dipolar terms JC (Jog and Chapman [134, 135]) and GV (Gross and Vrabec [133]), optimizes the binary interaction parameter k_{12} using Eqn. (5.1), they yield similar results. There is however a large decrease in the magnitude of k_{12} upon including a dipole term. In this case, PC-SAFT-GV can be considered as predictive for the system, as the interaction

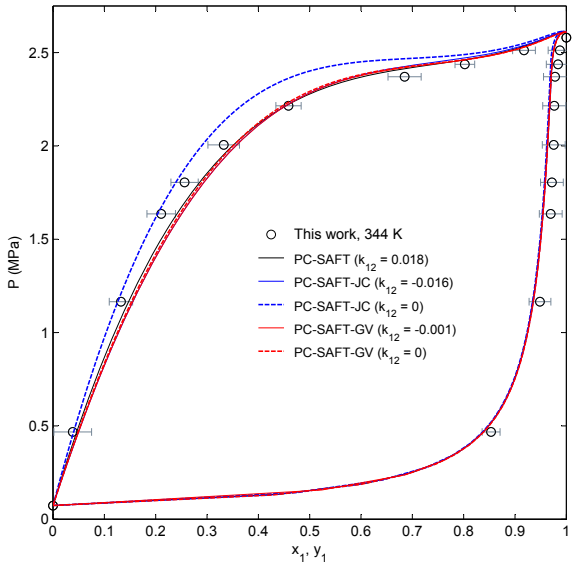

Figure 5.1: Experimental VLE and modeling results for the propane (1) + ethanol (2) system at 343.6 K. As correlations, PC-SAFT, PC-SAFT-JC and PC-SAFT-GV presented similar results. However, the PC-SAFT-GV achieves good predictability when used without a binary interaction parameter. Propane parameters are taken from Gross and Sadowski [93], and ethanol from Gross and Sadowski [94] and Al-Saifi et al. [152].

parameter can be ignored completely. This is less true for the PC-SAFT-JC. In this chapter, we shall exploit, as much as possible, the predictive capabilities of the polar PC-SAFTs.

In Figure 5.2, the experimental VLE data of the propane + ethanol system from this work are first modeled using a single transferable k_{12} parameter for non-polar PC-SAFT, as well as the two polar variants. No temperature dependency is required for the regressed parameter, allowing extrapolation to extended temperature ranges. The addition of the GV dipolar term further removes the need for the interaction parameter. This allows one to use the PC-SAFT-GV to represent selected literature isotherms, particularly at lower temperatures where the data appear ambiguous. It is found that available literature from Zabaloy et al. [180] are the most consistent with our model predictions. Gomez-Nieto and Thodos [178] provided isothermal measurements up to 500 K, but their data appear to be the least consistent with our calculations, and with other literature sources. The poor description of the critical isotherms at 384 and 403 K is a result of the mismatch between the critical parameters (T_c, P_c, V_c) of the individual components calculated by the EoS, and the experimental values. This is a common limitation of multi-parameter models not constrained at the critical point, and while we continue this chapter in the same vein, a method is proposed in the following chapter to improve the modeling of the critical region.

For the *n*-butane + ethanol system (Figure 5.3), we apply as before predictions from the two polar PC-SAFTs, and further introduce the PR-WS-NRTL EoS [63, 66, 67] as a comparison. This cubic EoS is used in the same manner as proposed in § 1.6, with up to three adjustable interaction parameters (k_{12}, τ_{12}, τ_{21}), which will be optimized using Eqn. (5.1) for each isotherm. For data representation, the correlation provided by PR-WS-NRTL is excellent, with good descriptions of the vapour phase, an area found lacking in both the polar PC-SAFTs. Here, we employ the PC-SAFT-JC in a slightly different manner for the associating compound ethanol. Rather than using ethanol parameters from Al-Saifi et al. [152], as we did for the propane + ethanol system, we refitted its five parameters (m, σ, ϵ/k, κ^{AB}, ϵ^{AB}) using vapour pressures and liquid densities from Daubert et al. [68], as well as a *key mixture* described by Dominik et al. [151]. The role of the key mixture is to avoid the problem of multiplicity in the parameter regression, and we have selected our data at 353 K, due to its good agreement with that of Deák et al. [182]. In fact, any good quality mixture data with a second component free of functionality groups can be used. Literature values

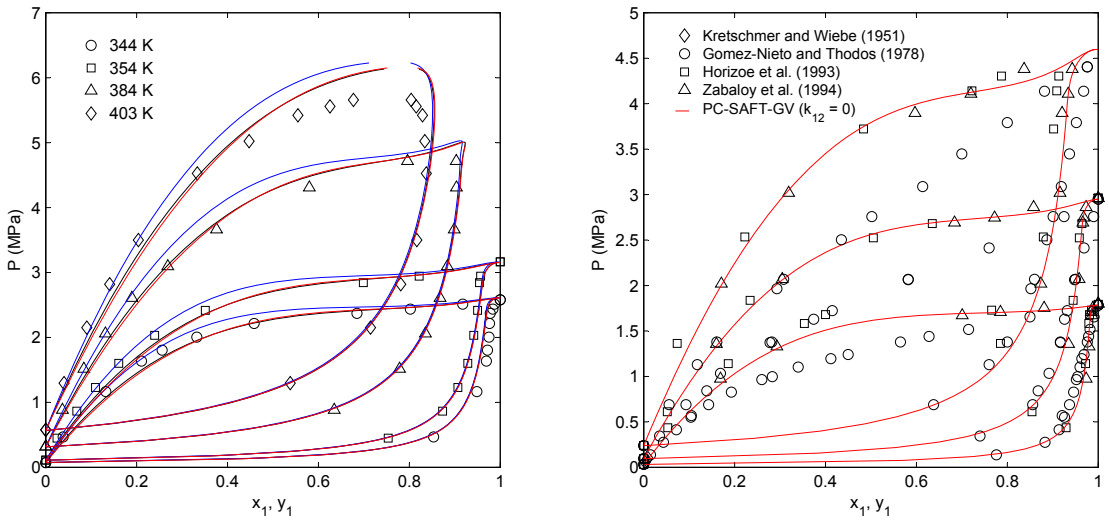

Figure 5.2: VLE modeling of the propane (1) + ethanol (2) system using three forms of the PC-SAFT, given by — : non-polar PC-SAFT ($k_{12} = 0.018$); — : PC-SAFT-JC ($k_{12} = 0$); — : PC-SAFT-GV ($k_{12} = 0$). *left*: Modeling of experimental VLE from this work. *right*: PC-SAFT-GV predictions for isotherms at 325, 350 and 375 K, compared with existing literature data. Data from Zabaloy et al. [180] appear to be the most consistent with model predictions.

were retained for the dipole moment ($\mu = 1.7$ D) and x_p ($x_p = 0.65/m$), and were not regressed [152]. When tested, our set of ethanol parameters gave very similar mixture results to those of Al-Saifi et al., prompting us to believe that a source of ambiguity may be present in parameterizing the PC-SAFT-JC. Such ambiguity is avoided altogether in the PC-SAFT-GV.

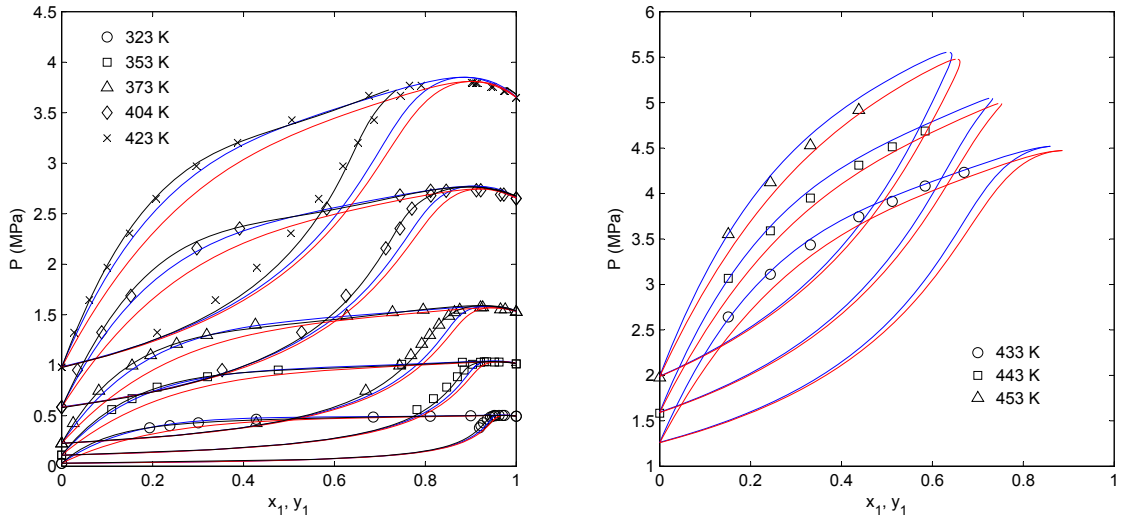

Figure 5.3: VLE modeling of the *n*-butane (1) + ethanol (2) system using both cubic and PC-SAFT EoS. — : PR-WS-NRTL, correlated at each temperature; — : PC-SAFT-JC ($k_{12} = 0$); — : PC-SAFT-GV ($k_{12} = 0$). Pure parameters for the PR-WS-NRTL are taken from [68], and for the polar PC-SAFTs from [93] and [152]. *left*: Modeling of experimental VLE from this work. *right*: PC-SAFT-JC and PC-SAFT-GV predictions for selected literature isotherms at 433, 443 and 453 K from Deák et al. [182].

At 423.2 K, slightly below the critical temperature of *n*-butane (425.12 K [68]), two separate VLE regions were observed experimentally, separated by a single phase region. At this temperature, the PR-WS-NRTL EoS is only able to calculate a very small VLE envelope in the *n*-butane rich region. The polar PC-SAFTs do not predict this two phase envelope phenomenon at 423.2 K due to the critical temperature of *n*-butane being calculated at a much higher value (± 431 K) with the employed pure parameters from [93]. As a result, the VLE behaviour predicted by the two polar PC-SAFTs remain, erroneously, azeotropic. The weakness of the PR-WS-NRTL is the strong temperature dependency of its three interaction parameters, making extrapolation to other temperatures ineffective. This is likely due to the inability of the cubic EoS to explicitly describe association, a task which is eventually taken care of by its binary parameters. As seen in the right-hand of Figure 5.3, this is easier handled by the polar PC-SAFTs, particularly the PC-SAFT-JC. Soo et al. [216] provide additional results for the PC-SAFT-JC EoS, using temperature-dependent k_{12} values, for the *n*-butane + ethanol system.

For highly non-ideal systems, usually containing short-chain alcohols, the polar PC-SAFTs may still require the interaction parameter. An example is the *n*-butane + methanol system, with experimental data from Courtial et al. [232]. By regressing simultaneously isotherms from 323 to 443 K, a value of $k_{12} = 0.055$ is obtained for the non-polar PC-SAFT. Figure 5.4 shows that, when applying this result to the 323.2 K isotherm, spurious phase splitting occurs, indicating the presence of vapour-liquid-liquid equilibria (VLLE) when none was observed experimentally (nor reported in literature). Predictions from PC-SAFT-JC and PC-SAFT-GV were even worse. The correct phase splitting (vapour-liquid) can be recovered by regressing each isotherm independently, as shown with the black, dashed curve ($k_{12} = 0.048$). A k_{12} value higher than 0.04 is considered as relatively large for a SAFT EoS. On the right-hand of Figure 5.4, temperature-dependent interaction parameters were used to describe six isotherms for both PR-WS-NRTL and non-polar PC-SAFT. These binary parameters are given in Courtial et al. [232] for both models, with a standard deviation on the parameters of 0.01 for PC-SAFT. As mentioned before, the supercritical isotherms are overestimated by the PC-SAFT, and an azeotrope is erroneously calculated for the 423.1 K isotherm.

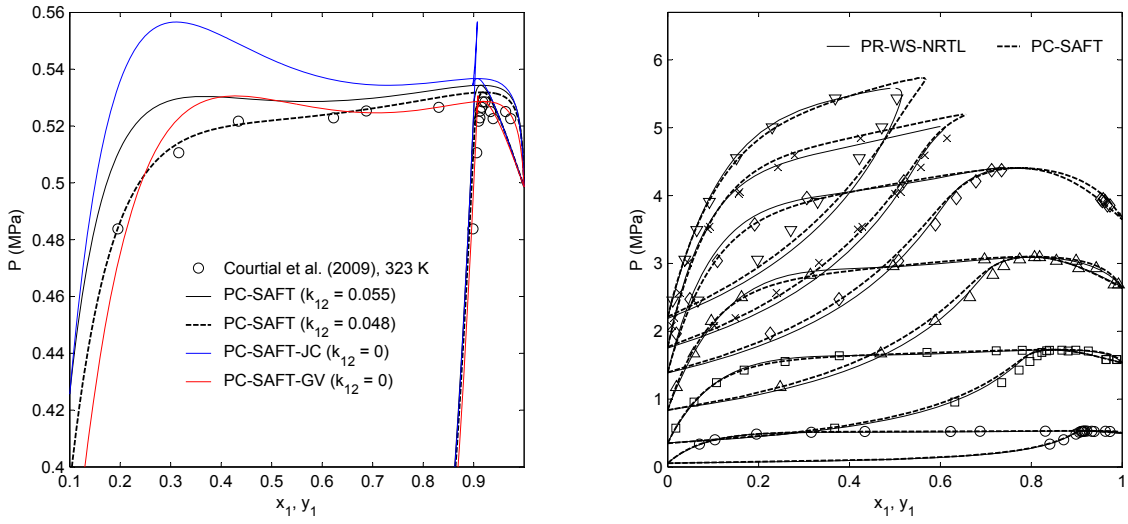

Figure 5.4: VLE modeling of the *n*-butane (1) + methanol (2) system using both cubic and PC-SAFT EoS. Pure parameters for the PR-WS-NRTL are taken from [68], and for the PC-SAFTs from [93, 94, 152]. *left*: Vapour-liquid-liquid equilibrium is erroneously predicted at 323.2 K by the two polar PC-SAFTs with $k_{12} = 0$, as well as by the non-polar PC-SAFT with a single temperature-independent k_{12} value. Experimentally, only vapour-liquid equilibrium exists. Fitting k_{12} uniquely to the isotherm rectifies the problem. *right*: Modeling of experimental VLE data taken from Courtial et al. [232]. Temperature-dependent binary parameters are used for each isotherm. ○: 323.2 K; □: 373.2 K; △: 403.1 K; ◇: 423.1 K; ×: 433.2 K and ▽: 443.2 K

Another example of a highly non-ideal system is the ethanol + cyclohexane system, measured with the "dynamic-synthetic" apparatus. In Fig. 5.5, a k_{12} value of 0.045 is required for the non-polar PC-SAFT to correlate the data of the isotherm and isobar. Both the PC-SAFT-JC and PC-SAFT-GV are ineffective when used without the binary parameter. As a rule of thumb, the addition of either of the dipole terms discussed in this work will decrease the value of the binary interaction parameter by at most 0.03. An interesting feature of this figure is the ability of PC-SAFT to describe both isothermal and isobaric VLE using a single k_{12} value (the temperature dependency and pressure dependency of k_{12} are otherwise often dissimilar).

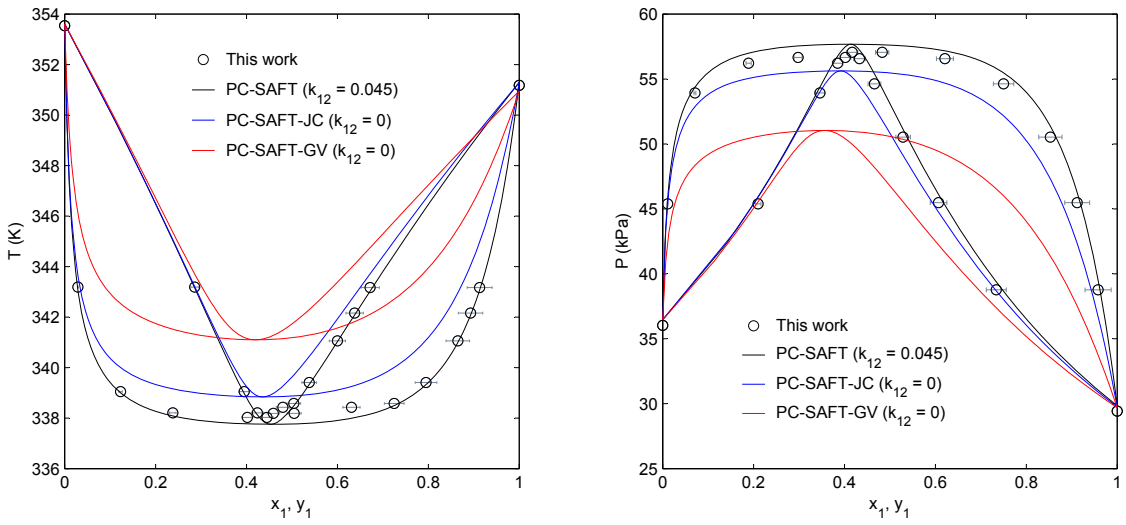

Figure 5.5: VLE modeling of the ethanol (1) + cyclohexane (2) system measured at 99.9 kPa (*left*) and 323.4 K (*right*), using different forms of the PC-SAFT EoS. Parameters for ethanol are taken from [94, 152] and for cyclohexane from [93]. A single, albeit large, value of k_{12} can be used for both isothermal and isobaric data.

In the *n*-hexane + 1-propanol case, we have the PC-SAFT-JC and PC-SAFT-GV each predicting a different data source being correct. The PC-SAFT-GV follows closely the data of Prabhu and Van Winkle [170], and Rhim and Kwak [171], while the PC-SAFT-JC passes through the data from this work. To gain more insight on the system, we predict also isotherms taken from different literature sources [233, 234], realizing that the PC-SAFT-GV is in fact the weaker of the two models. Shown on the right-hand of Fig. 5.6, a systematic error exists when applying the PC-SAFT-GV, which is likely to manifest in the isobaric plot shown on the left-hand. Using the predictive aspects of the polar PC-SAFTs, it is possible to make judgments on data quality, in the event of insufficient supporting literature.

For the isobaric VLE results of the ethanol + *m*-xylene system at 94.9 kPa, we verify using the modified UNIFAC (Dortmund) model [73, 74] that the data of Vittel Prasad et al. [174] may indeed be doubtful. Other predictive models support this finding. Both polar PC-SAFTs require a non-zero binary parameter to describe the system behaviour, with the PC-SAFT-GV being slightly more quantitative than the PC-SAFT-JC. The need for the binary interaction parameter could be attributed to the quadrupolar interactions from the *m*-xylene molecules, which were not accounted for here. Nevertheless, the two dipolar forms, while not entirely rigorous for the system, can still be extrapolated to several temperatures. Fig. 5.7 shows the modeling for the ethanol + *m*-xylene system, while Fig. 5.8 presents the ethanol + ethylbenzene system, with which similar conclusions may be drawn. No azeotropes in the ethanol + *m*-xylene system were calculated by any of the models shown in Fig. 5.7, which is consistent with the experimental findings.

In modeling the cyclohexane + cyclohexanol system, with the PC-SAFT-JC EoS, one is faced with the problem of parameterizing x_p (fraction of dipolar segments in a molecule) for a compound from an undocumented homologous

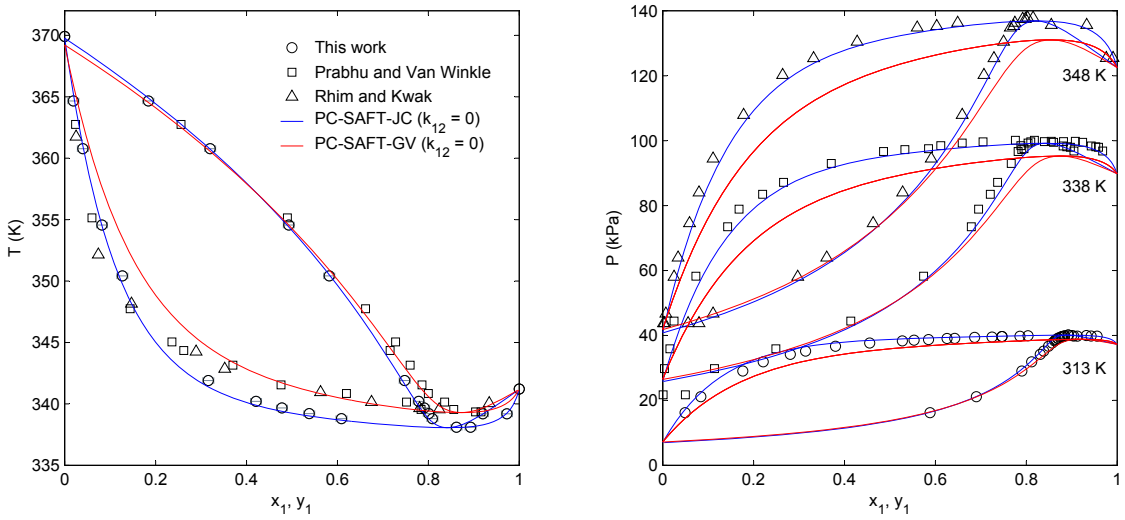

Figure 5.6: VLE modeling of the *n*-hexane (1) + 1-propanol (2) system measured at 98.9 kPa (*left*) and at various isotherms taken from literature (*right*) [233, 234]. Parameters for *n*-hexane are taken from [94] and for 1-propanol from [152]. Keeping the binary parameter as zero at all times, PC-SAFT-JC (—) has a better representation of the isotherms, as well as passing through the isobaric measurements from this work. This supports the claim that the isobaric measurements from this work cannot be deemed incorrect.

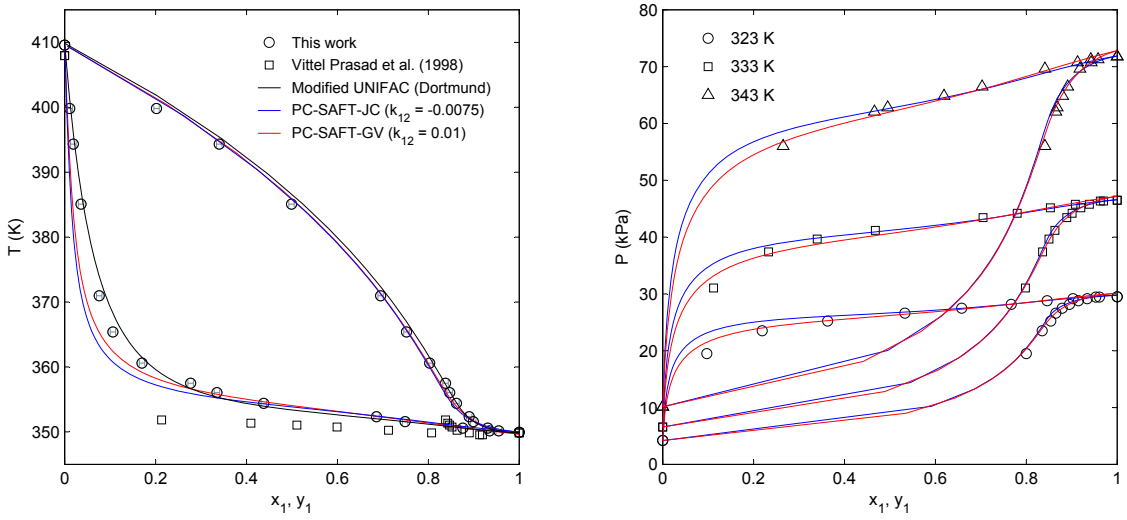

Figure 5.7: VLE modeling of the ethanol (1) + *m*-xylene (2) system measured at 94.9 kPa (*left*) and at isotherms 323 - 343 K (*right*). Parameters for ethanol are taken from [152] and for *m*-xylene from [93]. The same binary interaction parameters are used for both sides of the figure.

group - *cycloalcohols*. We recall that the product mx_p is a constant value for compounds of the same homologous group, or approximately $x_p = 1/m$ [135]. The two declarations cannot be fulfilled at the same time, and in general the first declaration is followed in work where parameters are published. Since no parameters have been published for the cycloalcohol group, the value for mx_p is not known here. In this work, we tentatively employ the same mx_p value used for aliphatic alcohols (methanol, ethanol, etc), i.e. $mx_p = 0.7$. Furthermore, cyclohexanol has a similar dipole moment to aliphatic alcohols, $\mu = 1.7$ D. No key mixture was selected in the regression procedure. For

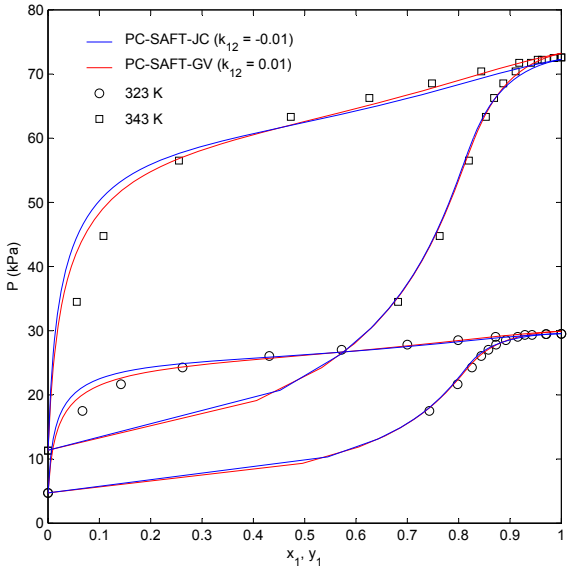

Figure 5.8: Modeling results for the ethanol (1) + ethylbenzene (2) system measured at isotherms 323.3 and 343.3 K. Parameters for ethanol are taken from [152] and for ethylbenzene from [93].

PC-SAFT-GV, cyclohexanol is parameterized like all other alcohols, with a fixed dipole moment. New parameters for cyclohexanol for usage in the PC-SAFT-JC have been published in Coquelet et al. [235], while we give here the parameters for PC-SAFT-GV (m = 2.5317, σ = 3.935 Å, ϵ/k = 326.95 K, κ^{AB} = 0.00089, ϵ^{AB}/k = 2933.70 K, μ = 1.7 D). The modeling results for this system are shown in Fig. 5.9 for PR-WS-NRTL and the two forms of the polar PC-SAFTs. The binary parameters of PR-WS-NRTL are regressed from the experimental data of Coquelet et al. [235]. Neglecting the binary parameter, the polar PC-SAFTs provide a qualitative representation of the VLE behaviour. Coquelet et al. showed that the inclusion of a non-zero k_{12} value for PC-SAFT-JC can yield highly quantitative descriptions. However, the true potential of the PC-SAFT EoS is shown in a plot of relative volatility against molar composition x_1. Experimental work from various sources [235, 236] suggest an exponential behaviour extending to low cyclohexane concentrations. This is followed in a natural manner by the polar PC-SAFTs, despite having a poorer representation compared to the PR-WS-NRTL. The PR-WS-NRTL follows an exponential trend only at the composition regions where data are present, veering off at low cyclohexane concentrations. When adjusted to the same data, the polar PC-SAFTs still retain the correct shape of the relative volatility curve. This is a case where the PR-WS-NRTL may describe well the discrete measured data, but to a lesser extent the underlying molecular interactions. This results in its deficiency to extrapolate even to regions within the same isotherm. Figure 5.10 shows the polar PC-SAFTs capability of extrapolating to isotherms as low as 298 K, an aspect not achievable with the PR-WS-NRTL.

5.2.2 Carboxylic acids

Among systematic studies involving the PC-SAFT to date, there is little to no exposure of modeling of carboxylic acids. Huang and Radosz, in their pioneering work on CK-SAFT [228], perceived chain acids as dimers. The proton donor and acceptor of two acid monomer units would hydrogen bond in a lock and key mechanism, i.e. in one manner only, to form strong dimers. This strong tendency of acids to dimerise is in agreement with chemical theories and experimentation [69, 70], and is a valid representation of the vapour phase dimerisation process [240]. This bonding scheme was referred to as the 1 model by Huang and Radosz, with which pure parameters for chain acids from one to ten carbon atoms were given for CK-SAFT [228]. Using the same 1 scheme, Fu and Sandler

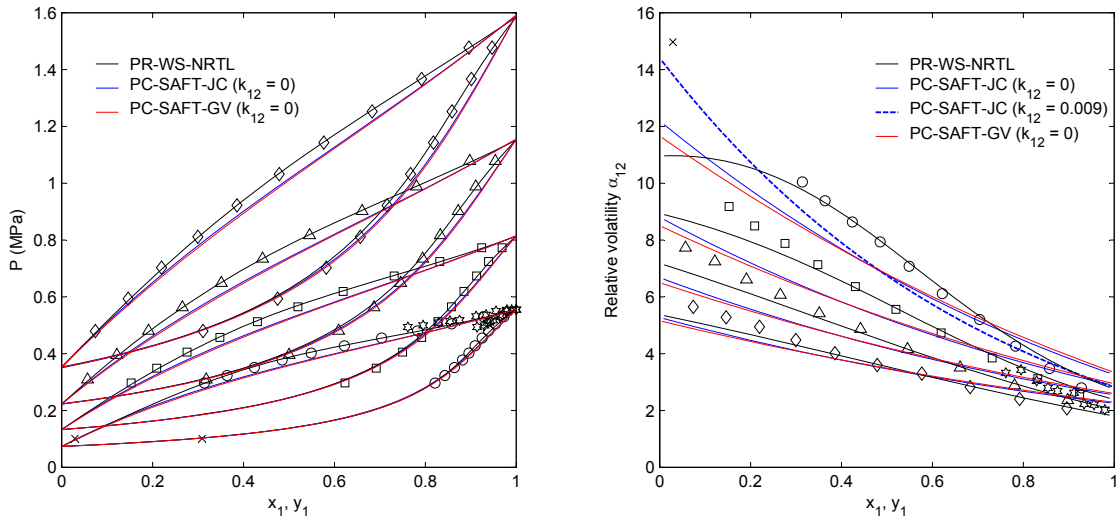

Figure 5.9: VLE modeling of the cyclohexane (1) + cyclohexanol (2) system from 424 - 484 K, with — : PR-WS-NRTL; — : PC-SAFT-JC ($k_{12} = 0$) and — : PC-SAFT-GV ($k_{12} = 0$). Pure parameters for cyclohexane are taken from [93, 68], and for cyclohexanol from [68, 235]. Experimental VLE data are taken from the work of Coquelet et al. [235], Steyer and Sundmacher [236], and Li et al. [237].

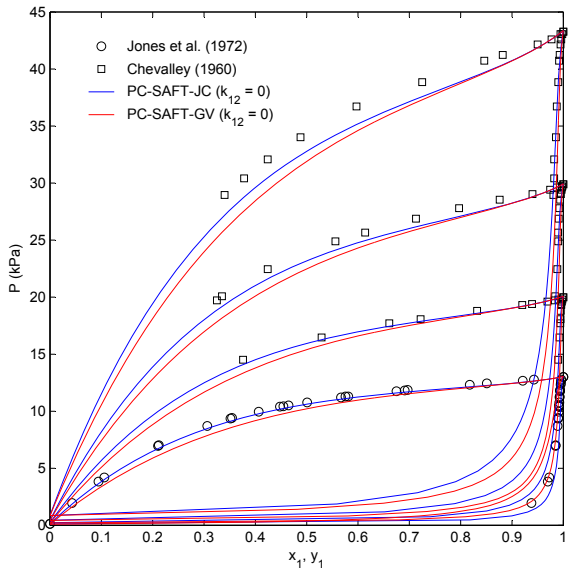

Figure 5.10: VLE modeling of the cyclohexane (1) + cyclohexanol (2) system from 298 - 328 K using different forms of the polar PC-SAFTs. Pure parameters for cyclohexane are taken from [93, 68], and for cyclohexanol from [68, 235]. Experimental VLE data are taken from the work of Jones et al. [238] and Chevalley [239].

proposed pure component parameters for acetic, propanoic and butanoic acids for simplified SAFT, and applied them to mixtures [241]. Gross and Sadowski [94] published pure component parameters for acetic acid, using a 2B bonding scheme, although this was not investigated further until later [70].

It is in the interest of this work to propose pure component parameters for chain acids which could be used with the PC-SAFT EoS. Only the 1 bonding scheme is considered in this work. We will determine parameters for the standard, non-polar form of the PC-SAFT, and the polar PC-SAFT-GV by Gross and Vrabec. No parameterization

is done with the PC-SAFT-JC, as the parameter x_p will be defined according to personal preferences, giving an ambiguous number of possible combinations of pure parameters. The only electrostatic parameter of PC-SAFT-GV for chain acids is the dipole moment, which will be fixed at its experimental value. The procedures followed for regressing pure component parameters are outlined in detail in § 2.4. Experimental vapour pressures and liquid densities for carboxylic acids from formic (C_1) to caproic (C_6) are taken from the DIPPR 11 compilation by Daubert et al. [68]. Experimental dipole moments are taken from the CRC Handbook of Chemistry and Physics (76th edition) by Lide [77]. For both forms of PC-SAFT, the adjustable parameters are $\left\{m, \sigma, \epsilon, \kappa^{AB}, \epsilon^{AB}\right\}$. An objective function based solely on vapour pressures and liquid densities was used (cf. Eqn. 2.75):

$$F = \frac{100}{N_{P^{sat}}} \sum_{i}^{N_{psat}} \frac{\left|P^{sat}_{exp,i} - P^{sat}_{cal,i}\right|}{P^{sat}_{exp,i}} + \frac{100}{N_{\rho^L}} \sum_{i}^{N_{\rho^L}} \frac{\left|\rho^L_{exp,i} - \rho^L_{cal,i}\right|}{\rho^L_{exp,i}} \tag{5.4}$$

The regressions were performed initially by varying all the five adjustable parameters. It was observed that while a good return on the absolute average deviation (Eqn. 2.76) could be obtained for the pressures and densities of most acids, a multiplicity of solutions exists for the regression, depending on the initial values. Convergence was achieved in each of the possible solutions; thus they were rejected on the basis of any nonsensical parameters present. We propose below a selection criteria, which, while appearing intuitively trivial, were not always met at the regression outcome.

- The parameter m should increase with size of the acid. Formic acid should have an m between 1 and 2.
- The parameter κ^{AB} should have a value less than 1.
- The parameter σ should be larger than 3 Å. Only a few documented gases have a σ value less than 3 Å (e.g. carbon dioxide [93]).
- The association strength ϵ^{AB}/k should be in the $>$ 4000 K range. This is a result of the 1 scheme model, whereby all the association tendencies will be lumped entirely under one site, as opposed to the alcohols, say, where 2 identical sites (2B scheme) distribute the association strength evenly ($\sim$ 2500 K each).

Interestingly, the above criteria lead to rejection of all the possible solutions. Alternatively, a step was taken to reduce the number of regression parameters from five to four, by prescribing a fixed value to κ^{AB}. This is considered on the basis that the value of κ^{AB} is strongly correlated to the association energy parameter ϵ^{AB}/k. This fixed value of κ^{AB}, however, cannot be known *a priori*. It was decided to test and assign the κ^{AB} value only to multiples of 0.1, i.e. $\kappa = \{0.1, 0.01, 0.001, 0.0001\}$. Immediately, the return on the absolute average deviation (for vapour pressures and liquid densities) were poor for $\kappa^{AB} = 0.1$ and $\kappa^{AB} = 0.0001$. These choices were rejected, leaving two remaining possibilities, which we refer here onwards as 0.01 and 0.001 parameters.

The 0.01 and 0.001 parameter sets differ mainly in the size of the association energy ϵ^{AB}/k. 0.01 parameters have lower ϵ^{AB}/k values for the acids, averaging around 4500 K, while 0.001 parameters have larger values, around 7000 K. This means that when adopting the 0.001 parameters, acids have a higher tendency to form dimers, compared to using the 0.01 parameters. The association energies for acetic acid have been experimentally shown to be in the range of 6949-8266 K, values which are in closer agreement with the 0.001 parameters [242, 243, 244]. When acids bond with the 1 bonding scheme, the available bonding site is 'used up' once two monomer units are locked with one another. This is unlike the 2B scheme of alcohols. Dimer acids resemble the properties of a non-associating hydrocarbon, since there are no further protons available for transfer. The more dimers formed, the more ideal is the acid, and essentially the mixture. This is an important factor in the illustration which follows.

In Figure 5.12, experimental VLE data for the benzene + acetic acid system are modeled using the non-polar PC-SAFT in two instances - with the κ^{AB} parameter fixed at 0.01, and at 0.001. While it is clear that the 0.001 parameters (dashed line) provides the better correlation, the focus should be on the right-hand figure, which shows a zoom of the benzene-rich region. The azeotrope shown here for the 0.01 parameters (solid line) should not be present at all, and is a case where non-ideality is over-compensated in the system. The acetic acid, with

0.01 parameters, exists mainly as associating monomers, whereas with the 0.001 parameters the formation of more ideal dimers is favoured, leading to a suppression of the azeotrope. Exaggeration of association can lead to unnecessary non-idealities (azeotropes, spurious phase splits) that cannot be avoided through changing the binary interaction parameter. In the end, we have chosen to use the 0.001 parameter sets, which can be found in Table 5.2 for formic acid to caproic acid. Figure 5.11 shows the vapour liquid equilibria of the pure acids in saturated T-P and T-ρ diagrams. Extended modeling on all measured isotherms of the benzene + acetic acid system is given in Figure 5.13.

Table 5.2: Pure component parameters for carboxylic acids used in this work. One association site (1 scheme) is assumed for all acids.

Compound	m	σ	ϵ/k	κ^{AB}	ϵ^{AB}/k	μ	AAD (%)		T_{range} (K)		Ref [a]
	(-)	(Å)	(K)	(-)	(K)	(D)	P^{sat}	ρ^L	P^{sat}	ρ^L	
formic acid (MM = 46.026 g/mol)											
PC-SAFT	1.1693	3.5089	305.04	0.001	7078.3		0.41	0.05	268 - 453	283 - 373	1
PC-SAFT-GV	1.0503	3.6651	296.11	0.001	7184.1	1.41	0.41	0.06			1, 2
acetic acid (MM = 60.052 g/mol)											
PC-SAFT	1.9826	3.3094	238.75	0.001	7133.5		0.58	2.1	298 - 583	298 - 553	1
PC-SAFT-GV	1.8702	3.3816	234.74	0.001	7067.8	1.70	0.66	2.3			1, 2
propanoic acid (MM = 74.079 g/mol)											
PC-SAFT	2.2147	3.5296	245.33	0.001	6368.8		0.77	0.32	323 - 438	273 - 493	1
PC-SAFT-GV	2.1246	3.5857	245.31	0.001	6309.5	1.75	0.77	0.32			1, 2
n-butanoic acid (MM = 88.105 g/mol)											
PC-SAFT	2.4821	3.6643	250.96	0.001	6210.8		1.2	0.37	343 - 498	278 - 553	1
PC-SAFT-GV	2.4564	3.6789	250.78	0.001	6198.4	1.50	1.1	0.38			1
n-pentanoic/valeric acid (MM = 102.132 g/mol)											
PC-SAFT	2.8292	3.8059	307.85	0.001	4415.1		0.93	1.3	361 - 573	233 - 533	1
PC-SAFT-GV	2.8149	3.8131	307.69	0.001	4415.7	1.60	0.93	1.2			1
n-hexanoic/caproic acid (MM = 116.158 g/mol)											
PC-SAFT	3.9412	3.5603	279.93	0.001	4195.3		1.1	0.41	379 - 533	273 - 573	1
PC-SAFT-GV	3.9306	3.5638	279.91	0.001	4196.2	1.57	1.1	0.41			1

[a] References: [1] T.E. Daubert, R.P. Danner, H.M. Sibul, and C.C. Stebbins. *DIPPR Data compilation of pure compound properties*. Version 11.0, Database 11. NIST Standard Reference Data Program, Gaithersburg, MD, 1996.

[2] D.R. Lide. *CRC Handbook of Chemistry and Physics*. CRC Press, Inc., Boca Raton, 76th edition, 1995.

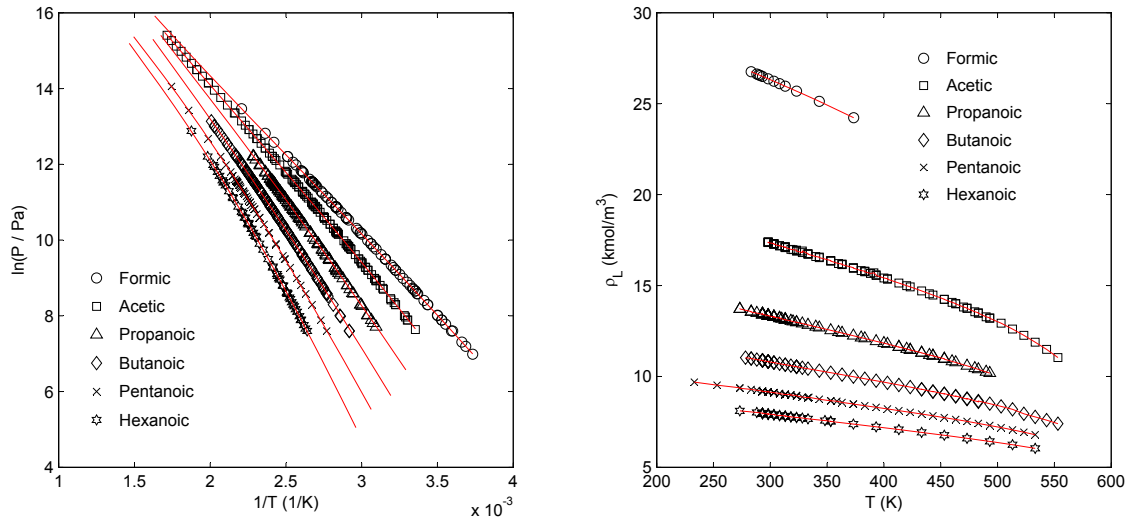

Figure 5.11: Saturated vapour pressures and liquid densities for C_1 to C_6 chain acids, using the parameters given in Table 5.2 with a fixed κ^{AB} value of 0.001. Comparison of the PC-SAFT-GV (—) to experimental data taken from DIPPR compilation [68].

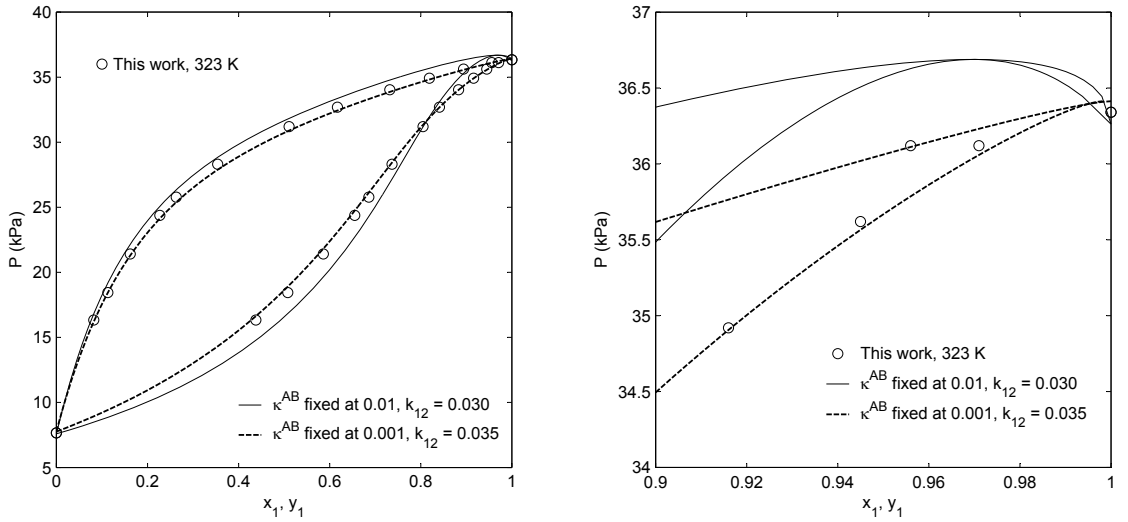

Figure 5.12: VLE modeling results for the benzene (1) + acetic acid (2) system measured at 323.3 K. Pure parameters for benzene were taken from [94]. Two sets of non-polar PC-SAFT pure parameters for acetic acid were tested in the correlations. When fixing the κ^{AB} value of acetic acid to 0.001, the description of the VLE is better than fixing at 0.01. The problem regarding the 0.01 parameter set is the suggestion a prominent azeotrope, in the benzene-rich region, which was not observed experimentally.

Citing work from Valtz et al. [246], VLE data for the cyclohexane + *n*-hexanoic acid (caproic acid) were modeled using the PR-WS-NRTL, and the PC-SAFT-GV with new acid parameters. The predictions from PC-SAFT-GV are not much different from the PR-WS-NRTL, the latter of which uses three temperature-dependent binary parameters. In Figure 5.14, we note that the skewed data of 413.5 and 423.5 K are handled badly by the PR-WS-NRTL, the behaviour of its relative volatility curves appear intuitively incorrect. This is conclusive by observing the curve shape and the value of α_{12} at infinitely dilute cyclohexane. This is not encountered with PC-SAFT-GV, and even when

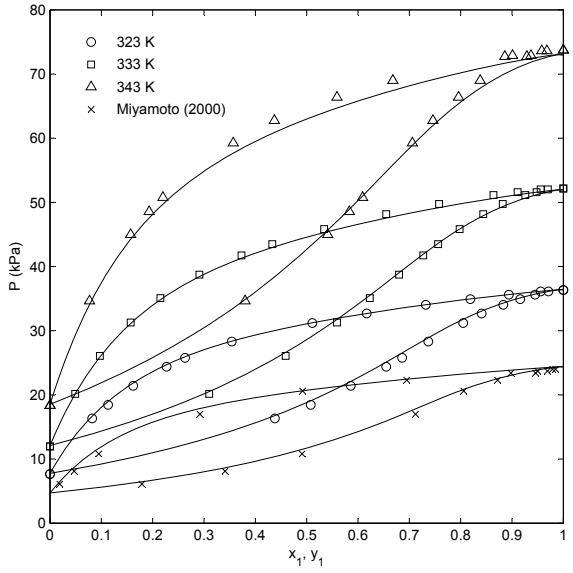

Figure 5.13: VLE modeling of the benzene (1) + acetic acid (2) system from 313 - 343 K, using the non-polar PC-SAFT (k_{12} = 0.038). Pure parameters for acetic acid are taken from Table 5.2. Literature data at 313 K are taken from Miyamoto et al. [245].

adjusted to the same skewed data, as described in Valtz et al., the PC-SAFT-GV is able to retain more realistic shapes for the relative volatility curves. In this case, the good predictive properties of the PC-SAFT-GV offers a simple modeling approach, making it also effective for simulation purposes.

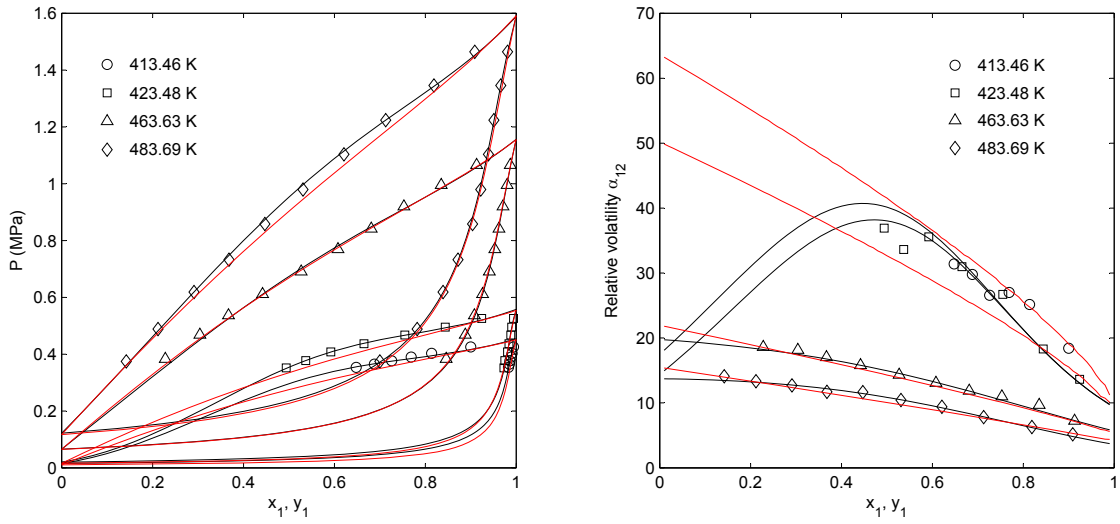

Figure 5.14: VLE modeling of the cyclohexane (1) + *n*-hexanoic acid (2) system from 413 - 484 K, with — : PR-WS-NRTL; — : PC-SAFT-GV (k_{12} = 0). Pure parameters for cyclohexane are taken from [93, 68], and *n*-hexanoic acid from Table 5.2. *left*: Modeling of experimental VLE taken from the work of Valtz et al. [246]. *right*: Experimental relative volatilities and modeling results for the data of the same system.

Acid-acid mixtures are relatively 'ideal', in the sense that no azeotropes occur in the phase behaviour. Nevertheless, for the two systems illustrated in Figures 5.15 and 5.16, a non-zero binary interaction parameter is required

for the PC-SAFT-GV in order to give a tight description of the VLE. Otherwise, the Wolbach-Sandler combining rules (Eqns. 2.40 and 2.41) appear applicable for cross-associating, similar, molecules.

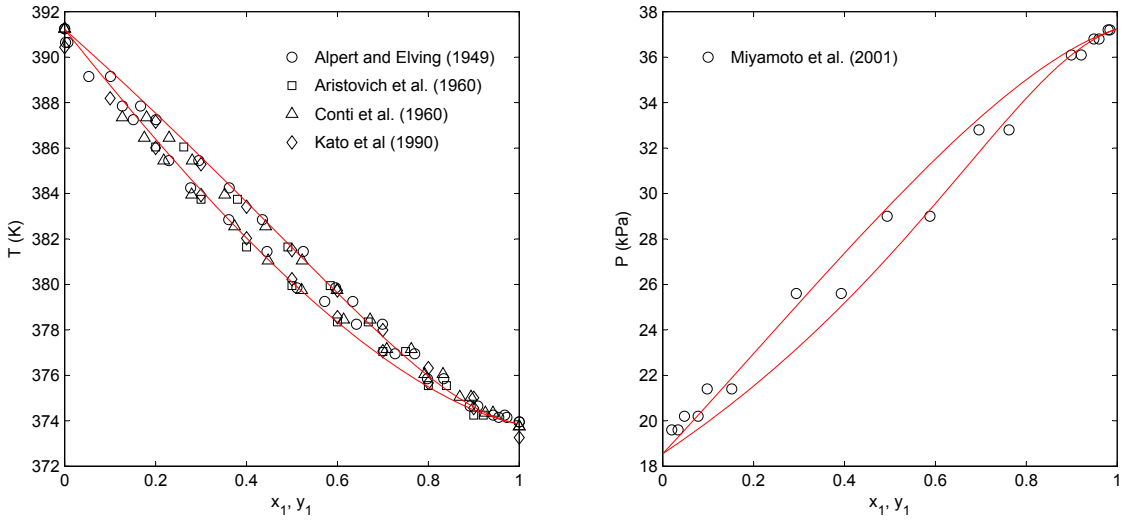

Figure 5.15: VLE modeling of the formic acid (1) + acetic acid (2) system at 101.3 kPa (*left*) and 343.2 K (*right*), using a correlated PC-SAFT-GV with $k_{12} = -0.0025$. Pure parameters for formic acid and acetic acid are taken from Table 5.2. Literature data are taken from [247, 248, 249, 250, 251].

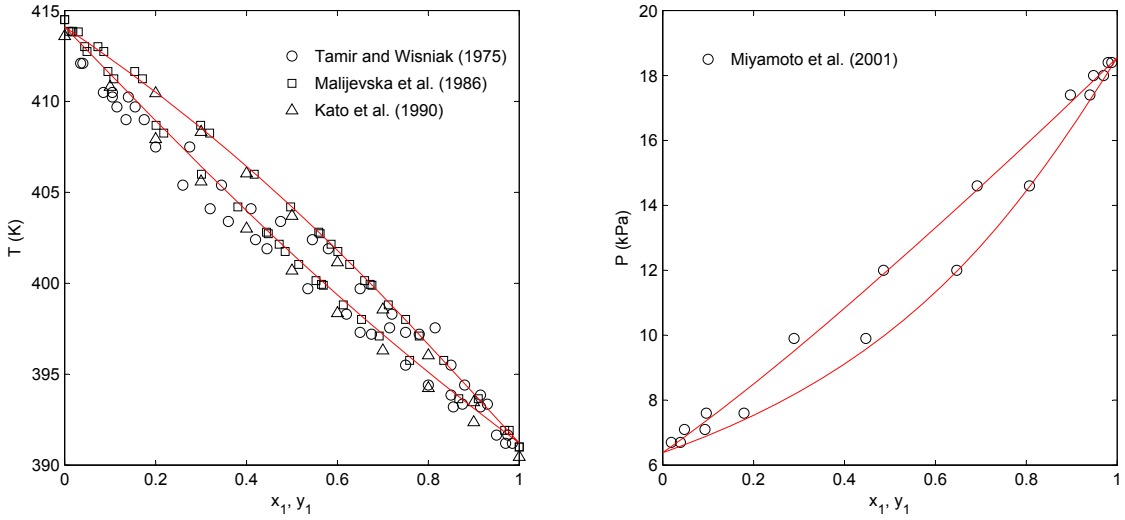

Figure 5.16: Modeling results for the acetic acid (1) + propionic acid (2) system at 101.3 kPa (*left*) and 343.2 K (*right*), using a correlated PC-SAFT-GV with $k_{12} = 0.01$. Pure parameters for acetic acid and propionic acid are taken from Table 5.2. Literature data are taken from [250, 251, 252, 253].

Non-ideal mixtures involving chain acids are rather complex, and using the above modeling approach gave mostly poor results. For example, with the acetic acid + *n*-octane mixture, initial treatment of VLE data from Plesnar et al. [254] suggest that the azeotropic pressure in the system may be increased by increasing the k_{12} value for PC-SAFT-GV. This can be illustrated in the left-hand of Figure 5.17. However, when the k_{12} value is at 0.056, the azeotropic pressure is matched to the data, but the azeotropic composition is incorrect. Of greater concern is the

appearance of a second spurious liquid phase, as shown on the right-hand of the figure. It was found that VLLE occurs at the condition $k_{12} > 0.052$, thereby achieving the correct azeotropic pressure is, in fact, not possible.

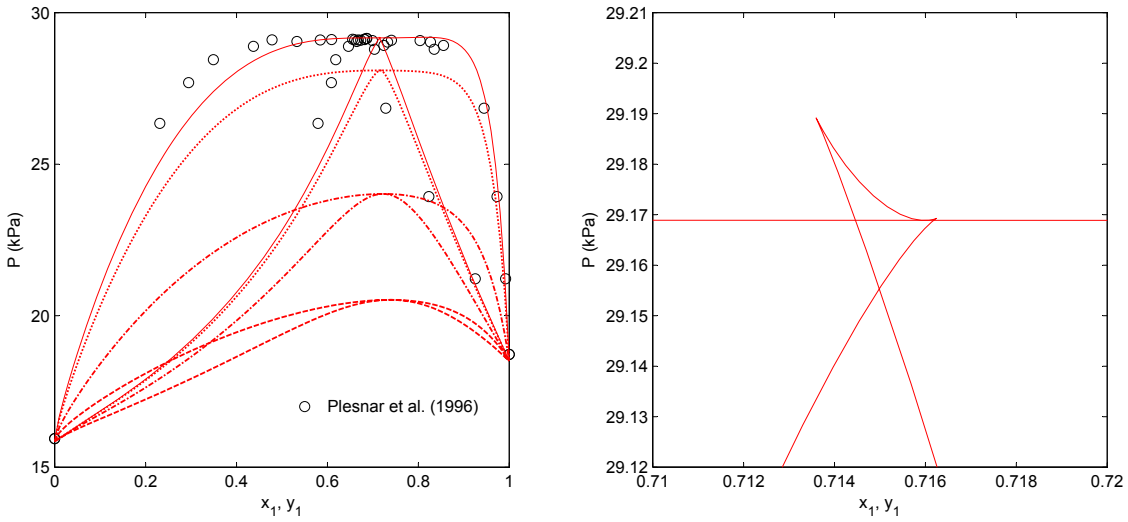

Figure 5.17: VLE modeling of the acetic acid (1) + *n*-octane (2) system at 343.2 K, using the PC-SAFT-GV with various k_{12} values. Dashed line: $k_{12} = 0$; dashed dotted line: $k_{12} = 0.025$; dotted: $k_{12} = 0.050$; solid: $k_{12} = 0.056$. Pure parameters for *n*-octane are taken from [93], and for acetic acid from Table 5.2. In the *left* figure, the top-most curve ($k_{12} = 0.056$) captures the correct azeotropic pressure, but in turn the azeotropic composition is mismatched, and spurious VLLE is induced, shown on the *right*. Experimental data taken from Plesnar et al. [254].

In this case, we found the introduction of the second asymmetric parameter l_{12}, given by Eqn. (2.60), to be a useful solution. As with most equation of states, a further adjustable binary parameter provides flexibility to data correlation. In this instance, the parameter l_{12} was able to subdue the appearance of the spurious liquid phase split, and allow the k_{12} to be adjusted more freely. Furthermore, the azeotropic composition could be manipulated more easily in the desired direction. As observed with the PR-WS-NRTL, the extrapolative property of PC-SAFT is somewhat lost in the exchange for having an additional binary parameter. Figure 5.18 shows an improved modeling of the system, albeit using different temperature-dependent k_{12} values. This is also caused by the high level of non-ideality inherent in the system, leading to large values of k_{12} parameters. Two further examples are given in Figure 5.19 for toluene + acetic acid, and cyclohexane + acetic acid. In the second system, the data of Baradarajan and Satyanarayana [255] was reported to be less accurate than that of Malijevska et al. [256].

In Figure 5.20, we present the modeling of systems containing a chain acid with another associating compound, 1-butanol. In general, experimental data of 1-butanol + an acid are rare, and difficult to measure due to its reactivity. We have selected data in which only short experimental time has been allowed to ensure that the formation of butyl esters is avoided [257, 258]. We note also that the 1-butanol + acetic acid system exhibits a minimum-pressure azeotrope. In the modeling of a mixture containing an acid and an alcohol, the two associating sites of the alcohol (2B scheme) is *different* to the lone associating site of the acid (1 scheme). This is an important aspect. The active sites of the alcohol are an oxygen (proton acceptor) and a hydrogen (proton donor), while the single acid site resembles the 'teeth' of a key (both hydrogen and oxygen viewed as one site). Due to the specificity of the acid site, only another acid site will 'fit' into the position of the site shape. This means that the alcohols would only associate among themselves, and so will the acids, in turn setting up a unique system where both compounds are only self-associating. Three distinct bonding sites are distinguished in the calculations. A single transferrable $k_{12} = 0.047$ value can be used for the non-polar PC-SAFT, for the 1-butanol + acetic acid system. While the same approach was adopted for the 1-butanol + butanoic acid system (k_{12} = -0.01), the correlation from the model was poorer. The authors Muñoz

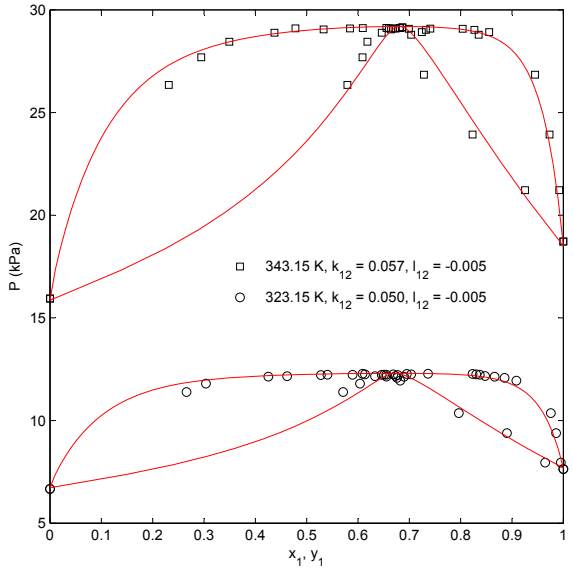

Figure 5.18: VLE modeling of the acetic acid (1) + *n*-octane (2) system at 323.2 and 343.2 K using a correlated PC-SAFT-GV with two binary interaction parameters k_{12} and l_{12}. While the same l_{12} value is used for the two isotherms, the k_{12} values vary with temperature. Experimental data again taken from Plesnar et al. [254].

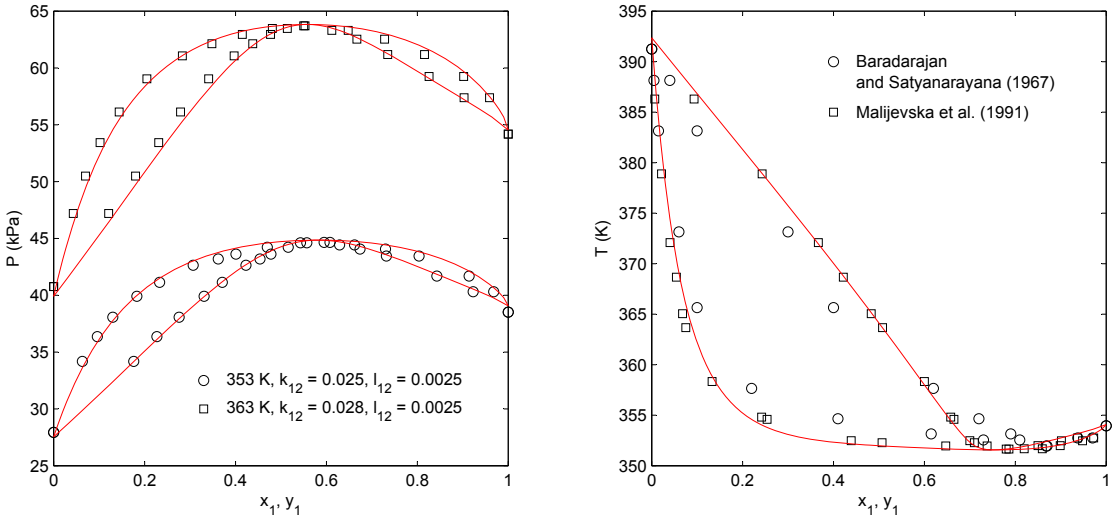

Figure 5.19: VLE modeling results, using a correlated PC-SAFT-GV with two binary interaction parameters k_{12} and l_{12}, for two binary systems. *left*: toluene (1) + acetic acid (2) at 353.2 and 363.1 K from this work. *right*: cyclohexane (1) + acetic acid (2) system at 101.3 kPa, data taken from Baradarajan and Satyanarayana [255], and Malijevska et al. [256]. The binary parameters for the system is $k_{12} = 0.067$ and $l_{12} = 0.005$. Pure parameters for toluene and cyclohexane are from [93], and for acetic acid from Table 5.2.

and Krähenbühl [258] modeled their experimental 1-butanol + butanoic acid data using a gamma-phi (γ-ϕ) approach, with liquid-phase activity coefficients from the NRTL [67], Wilson [259] and UNIQUAC [260] models. The vapour phase non-idealities and chemical equilibrium constants were accounted for by the Hayden and O'Connell correlation [261]. Interestingly, the correlation from the three aforementioned models (with chemical association) resemble each other, and that of the non-polar PC-SAFT (with physical association) in Figure 5.20.

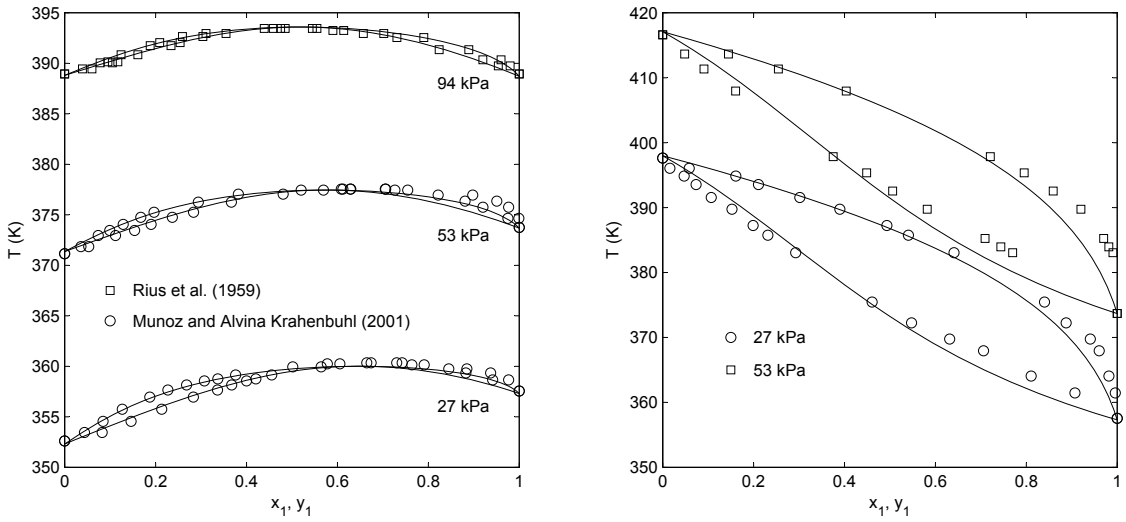

Figure 5.20: VLE modeling results, using a correlated non-polar PC-SAFT, for two 1-butanol (1) + chain acid (2) systems. *left*: 1-butanol (1) + acetic acid (2) system at various pressures, taken from Rius et al. [257] and Muñoz and Krähenbühl [258]. A single k_{12} value of 0.047 is used for all isobars. *right*: 1-butanol (1) + butanoic acid (2) system at 26.6 and 53.3 kPa, from Muñoz and Krähenbühl [258]. A single k_{12} value of -0.01 is used for the system. Pure parameters for 1-butanol are taken from [94], and for the acids from Table 5.2.

It is possible to model carboxylic acids with different bonding schemes for the different phases, e.g. a 1-site scheme for the vapour, as used in this work, and at least a 2-site scheme for the liquid phase. This only requires some minor changes to the calculation of the a^{assoc} term, and is a prospect for future work on the subject.

5.2.3 Polar Compounds

In this work, polar compounds refer to substances with notable dipole moments which may or may not self-associate. The range of polar mixtures that can be covered in this work is extensive; we have already dealt with two types of self-associating, weakly polar compounds through alcohols and acids. As mentioned in Chapter 1, we will also focus on the application of PC-SAFT on systems containing ketones, ethers, esters and aldehydes - polar compounds which do not self-associate. The modeling of these polar compounds involves two further considerations. Firstly, the effect of dipole-induced dipole (Debye) forces may, to an extent, play a role in the presence of small, but highly polar molecules such as acetone and acetaldehyde. Secondly, polar compounds possess electronegative oxygens that have a tendency to accept free electrons from the hydrogen of another associating compound. This is exemplified for an ether and an alcohol molecule in Fig. 5.21. This form of partial cross-association is referred specifically as solvation, and will be examined in further detail in this section.

Ketones

The applications of the polar PC-SAFT thus far have seen a decrease in the magnitude of the binary interaction parameter, i.e. an improvement in the predictive capabilities of the model. In cases where the species' dipoles are relatively weak ($\mu < 2.0$ D), the non-polar and polar forms of the PC-SAFT are equally feasible models, if one is more concerned with the overall representation rather than the magnitude of the k_{12} parameter (refer to Fig. 5.1). For systems containing compounds of a high dipole nature, such as ketones, the addition of a dipolar term becomes essential in achieving not only a reduced k_{12} value, but also a general improvement in the VLE description over the non-polar form. An example is given in Fig. 5.22 for the acetone + cyclohexane system,

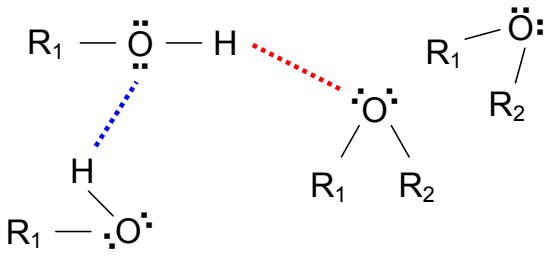

Figure 5.21: Partial cross-association (solvation) between an ether (R_1-O-R_2) and an alcohol (R_1-O-H) molecule, shown as the red dotted line. The hydrogen atom on the alcohol serves as the proton donor, while the oxygen atom on the ether acts as the acceptor. The alcohols may still self-associate among each other (blue dotted line), although the same cannot be said between the ethers.

where the polar PC-SAFTs (blue and red lines) clearly surpass the non-polar form (black line) in correlating the experimental data [262, 263, 264]. It is difficult to compare the effectiveness of the Jog and Chapman term to that of the Gross and Vrabec, even when the comparison is confined to certain species. The former formulation has an additional pure component parameter in the form of x_p, and uses mixture data in the regression of the pure component parameters, giving it a slight edge in mixture calculations. For this reason, the comparison is not on equal grounds. The PC-SAFT-GV has the advantage that its dipole-related parameters do not need to be regressed, and may be established solely from existing experimental data. This helps to bring some standardization to a modeling approach that has been criticized for its lack thereof. Compared to the PC-SAFT-GV, the PCIP-SAFT offers little improvements to the system, in terms of both the VLE representation and the magnitude of the binary parameter. This is in agreement with the observations in § 2.1, despite acetone being a relatively strong polarizable fluid. While one cannot deny the existence of Debye forces in this system, the improvements are rather insignificant in relation to the computational expenses.

Figures 5.23 - 5.25 show further systems well-handled by the polar variants of PC-SAFT, where extrapolations to wide temperature and pressure ranges are possible. Slightly more evident improvements from the PCIP-SAFT can be seen in the *n*-pentane + acetone system (Fig. 5.23). Cyclohexanone parameters for Fig. 5.24 for PC-SAFT-GV and PCIP-SAFT are not available in literature, and are determined in this work. These are given for PC-SAFT-GV as {m, σ, ϵ/k, μ} = {2.7229, 3.7901, 314.77, 3.2[1]}; and for PCIP-SAFT as {m, σ, ϵ/k, μ, α} = {2.8250, 3.7475, 302.78, 3.2[1], 11.15[2]}. The two sets of parameters are similar, and so are their representations in Fig. 5.24. Despite cyclohexanone having large μ and α values, the PCIP-SAFT continues to display similar results to the polar PC-SAFTs; thus we opt more often for the unrenormalized dipolar theories, due to their ease of computation. Dipolar interactions between two polar compounds are treated simply, requiring no explicit combining rules. The elevated isobars close to the critical pressures of acetone and 2-butanone (Fig. 5.25) are not as well represented by the PC-SAFT-JC, due the poorer descriptions of the pure fluids' boiling points at this vicinity.

As suggested before, the hydrogen atom of a carboxylic acid will have a low tendency to cross-associate with an oxygen atom of a non-acid, due to the specificity of the 1 bonding scheme. Under this assumption, self-association, rather than solvation, would be the predominant interaction in mixtures of carboxylic acids and ketones. Studies of two ketone + acid systems (Fig. 5.26) showed that this modeling approach does yield promising results.

[1] From Daubert et al. [68]

[2] http://www.drugbank.ca/drugs/DB02060

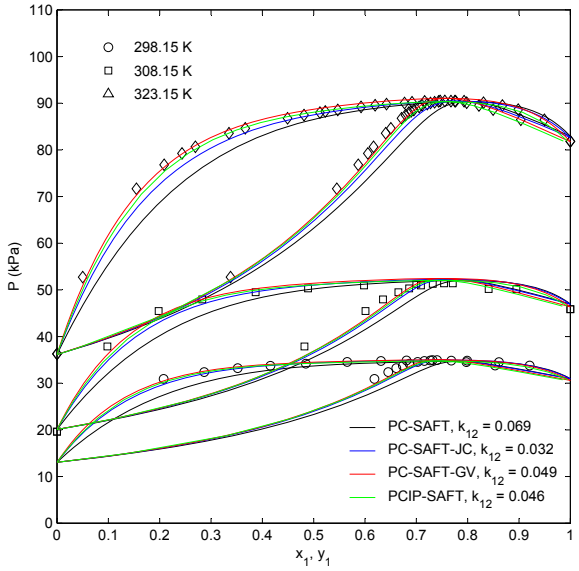

Figure 5.22: VLE modeling of the acetone (1) + cyclohexane (2) system at various temperatures using polar and non-polar forms of the PC-SAFT with a single binary interaction parameters k_{12}. Pure parameters for acetone are from [133, 135, 136], and for cyclohexane from [93]. Experimental data are taken from Marinichev and Susarev [262], Puri et al. [263], and Crespo Colin et al. [264].

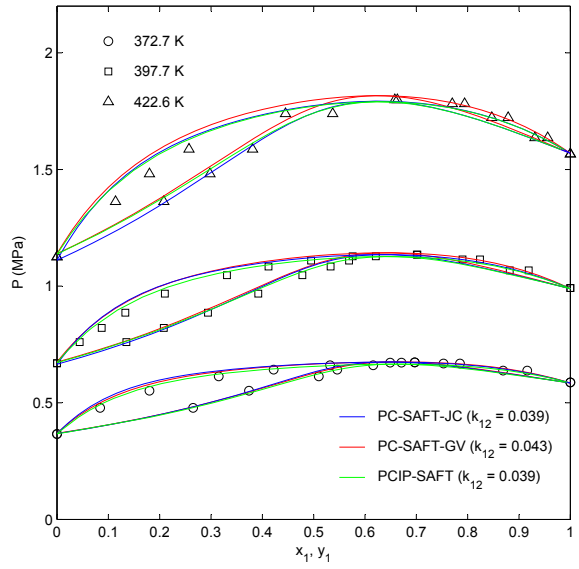

Figure 5.23: VLE modeling of the *n*-pentane (1) + acetone (2) system at various temperatures using polar variants of the PC-SAFT EoS. Pure parameters for polar PC-SAFTs are taken from [93, 133, 135, 136]. Experimental data taken from Campbell et al. [265].

Ethers

Regarding ethers, we are concerned mainly with systems of ethyl *tert*-butyl ether (ETBE), the 'green' alternative of methyl *tert*-butyl ether (MTBE). New parameters for ETBE for the non-polar PC-SAFT and the PC-SAFT-GV EoS are presented in Table 5.3. The parameters were obtained by fitting to pure vapour pressure and liquid density data

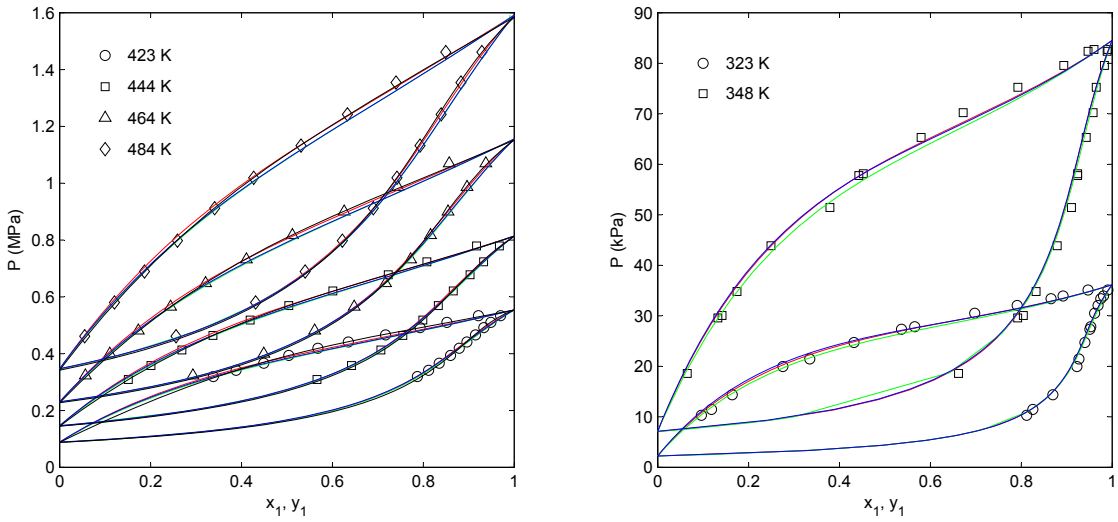

Figure 5.24: VLE modeling of the cyclohexane (1) + cyclohexanone (2) system at various temperatures, with — : PR-WS-NRTL; — : PC-SAFT-JC (k_{12} = 0.015), — : PC-SAFT-GV (k_{12} = 0.020) and — : PCIP-SAFT (k_{12} = 0.019). Pure parameters for cyclohexane are taken from [68, 93], and for cyclohexanone from [68, 266]. Experimental VLE data are taken from the work of Coquelet et al. [266], and Boublìk and Lu [267].

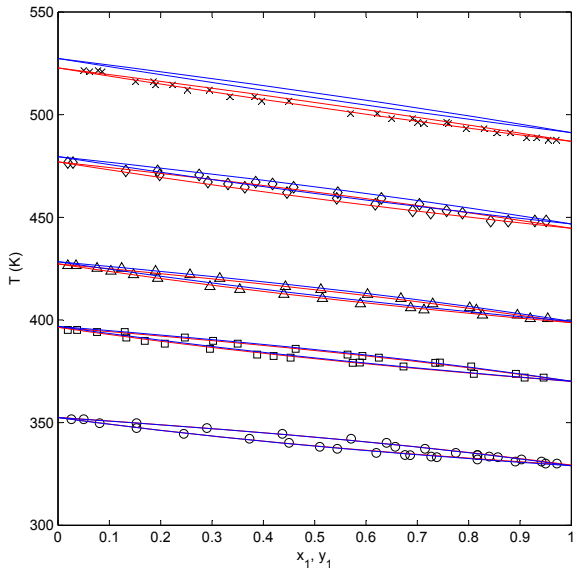

Figure 5.25: VLE modeling of the acetone (1) + 2-butanone (2) system at constant pressures, with — : PC-SAFT-JC (k_{12} = 0) and — : PC-SAFT-GV (k_{12} = 0). Pure parameters for acetone and 2-butanone were taken from [133, 135]. Experimental isobaric VLE data are taken from Othmer et al. [268], with ○: 0.1 MPa; □: 0.3 MPa; △: 0.7 MPa; ◇: 1.7 MPa; and ×: 3.4 MPa.

that were compiled from the DIPPR 11 database [68] and from Rarey et al. [160].

Vapour-liquid equilibria measurements of binary systems associated with the production of ETBE from isobutene and ethanol were published by Oh and Park [65], Rarey et al. [160], and Leu and Robinson [161]. In Fig. 5.27, we present the modeling of the isobutene + ETBE [161] and ETBE + benzene [271] systems, using the new parameters presented in Table 5.3. Both systems are relatively ideal, and can be represented by the models using small binary

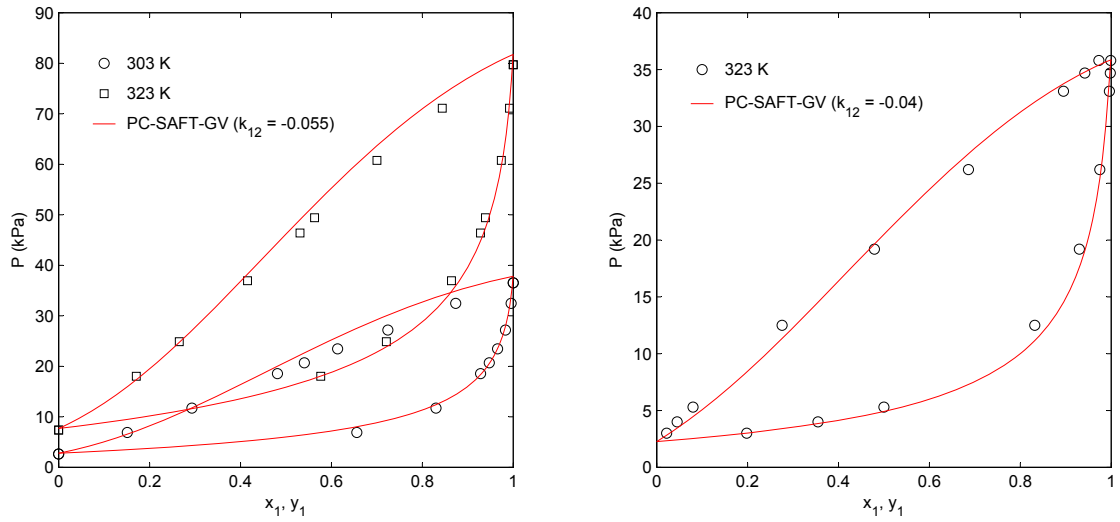

Figure 5.26: VLE modeling of the acetic acid (1) + acetone (2) system at 303.2 and 323.2 K (*left*), and of the 2-butanone (1) + propanoic acid (2) system at 323.2 K (*right*). The PC-SAFT-GV EoS with non-zero binary parameters were used for both cases. Pure parameters for acetone and 2-butanone were taken from [133], and for the acids from Table 5.2. Experimental isothermal VLE data for the left figure were taken from Meehan et al. [269] and Miyamoto et al. [270] for the right figure.

interaction parameters. Results for the ternary VLE system of 1-hexene + ETBE + benzene are given in Fig. 5.28, using small binary parameters.

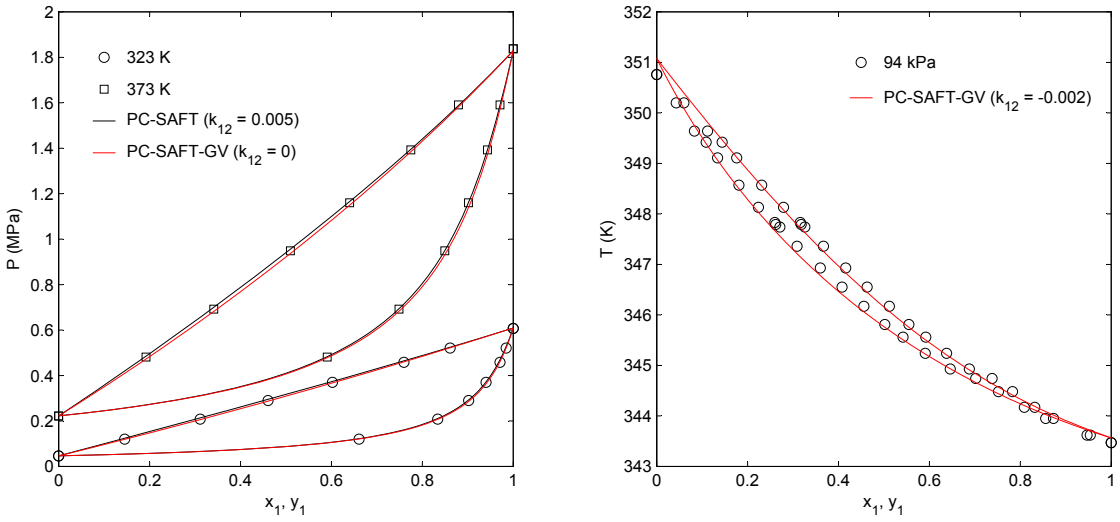

Figure 5.27: VLE modeling of the isobutene (1) + ETBE (2) system at 323.2 and 373.2 K (*left*), and of the ETBE + benzene system at 94.0 kPa (*right*). Pure parameters for isobutene and benzene were taken from [272], and for ETBE from Table 5.3. Experimental VLE data for the left figure were taken from Leu and Robinson [161] and from Segura et al. [271] for the right figure.

In modeling ETBE in the presence of ethanol, there is little agreement between the calculations of the PC-SAFT-GV and the experimental values from Rarey et al. [160], when solvation is not considered (Fig. 5.29). However,

Table 5.3: Pure component parameters for ethyl-*tert*-butyl-ether (ETBE) with the PC-SAFT and PC-SAFT-GV equation of states. Literature data for vapour pressures and liquid densities were taken from Daubert et al. [68] and Rarey et al. [160].

	PC-SAFT	PC-SAFT-GV
segment number, m	3.4279	3.4156
segment size, σ (Å)	3.7061	3.7107
segment energy, ϵ/k (K)	224.3808	224.5884
dipole moment, μ (D)	-	1.22
absolute average deviation, AAD (%)		
P^{sat}	0.42	0.43
ρ^L	0.15	0.17
temperature range, T_{range} (K)		
P^{sat}	278 - 503	
ρ^L	278 - 503	

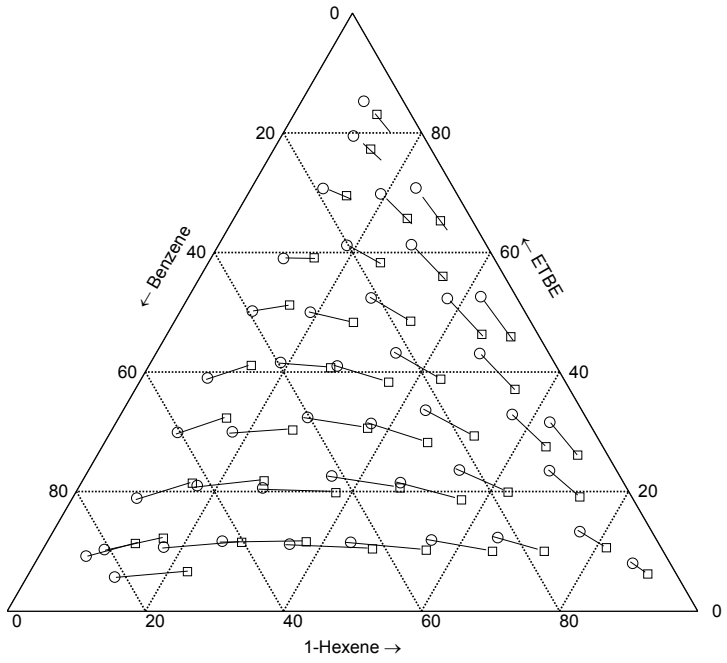

Figure 5.28: VLE modeling of the 1-hexene (1) + ETBE (2) + benzene (3) ternary system at 94.0 kPa, using the non-polar PC-SAFT (—) and the following binary interaction parameters: $k_{12} = 0.002$, $k_{13} = 0.006$ and $k_{23} = -0.002$. Experimental liquid phase mole percentages are given by circles (○), and vapour phase by squares (□). Pure parameters for 1-hexene and benzene were taken from [93], and for ETBE from this work. The non-isothermal binary and ternary VLE data were taken from Segura et al. [271, 273, 274].

solvation cannot be incorporated naturally into the current association model, since the association parameters ϵ^{AB}/k and κ^{AB} are only available for the self-associating component (ethanol). As a result, combining rules such as Eqns. (2.40) and (2.41) will not be able to induce solvation under the current setup. To account for cross-association between an associating and non-associating (ETBE) compound, we adopt the methodology proposed by Kleiner and Sadowski for induced-association interactions [275]. In their scheme, the ϵ^{AB}/k parameter of the polar, non-self-

associating compound remains zero, but the κ^{AB} parameter is adjusted to be equal to the value of the associating compound. In this case, $\kappa^{A_1B_1} = \kappa^{A_2B_2}$, and since $\epsilon^{AB}/k = 0$ for ETBE, the polar compound will, in accordance with the theory, not self-associate. Kleiner and Sadowski adopted a 2B bonding scheme for the association of the polar compound, on the basis of simplicity, which we will follow here. The inclusion of solvation greatly improves the performance of the PC-SAFT-GV, as well as decreases the value of the binary parameter required. As an alternative, we have also attempted to model this system using two binary parameters (k_{12} and l_{12}), which also yielded encouraging results. The drawback of using the two-parameter dispersion term is that it is usually less suited for extrapolative purposes across several temperatures.

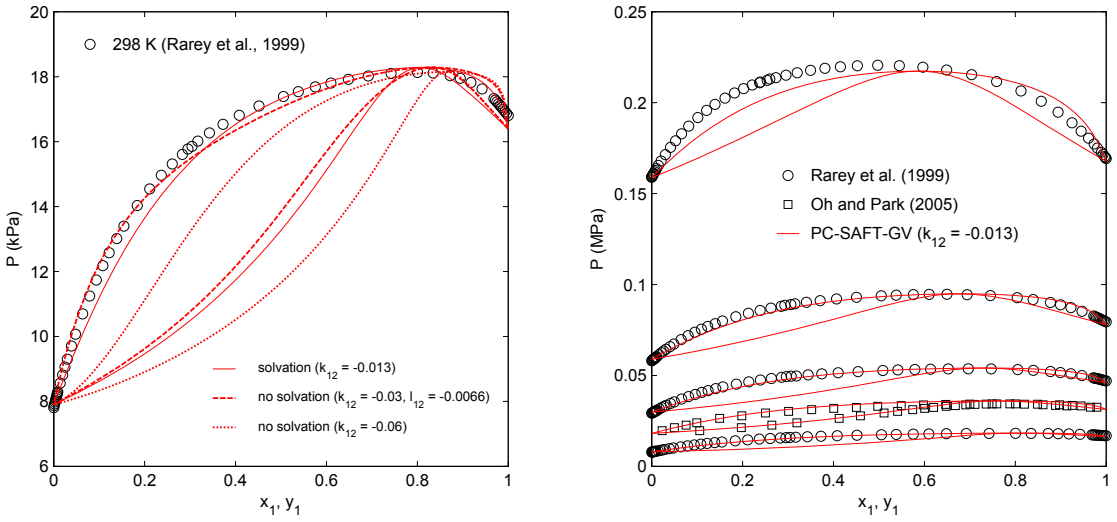

Figure 5.29: VLE modeling of the ETBE (1) + ethanol (2) system from 298-363 K, applying to the PC-SAFT-GV the solvation scheme proposed by Kleiner and Sadowski [275]. Pure parameters for ethanol were taken from [152], and for ETBE from Table 5.3. Experimental VLE data were taken from Rarey et al. [160] and Oh and Park [65].

Esters

Fatty acid methyl esters (FAME) of high molecular weights are the main products of the transesterification of triglycerides to form biodiesel components. Accurate determination of thermodynamic properties such as vapour pressure (normal boiling point), density, viscosity and latent heat of vaporization are important to ensure good fuel quality control. Nguyen Thi et al. [276] used a group-contribution SAFT (GC-SAFT) approach to model heavy esters from methyl propanoate to eicosanoate (C_{21}) using three different versions of SAFT (SAFT, SAFT-VR, PC-SAFT) and the Kraska and Gubbins dipolar term. NguyenHuyng et al. [277] later extended this work to mixtures of heavy esters, using the Jog and Chapman dipolar term. Tihić applied the group-contribution simplified PC-SAFT (sGC-PC-SAFT) to the prediction of vapour pressures of heavy esters, and presented calculations on phase equilibria and infinite dilution activity coefficients [272]. As far as the Perturbed-Chain form of the SAFT EoS is concerned, the various sources proceeded to present similar errors in predicting vapour pressures, ranging from 1 % to as high as 40 % deviations. While the different approaches adopted by the above sources make them not strictly comparable, most highlighted the importance of experimental data to improve the predictability of their models.

The objective in this work is to present parameters for FAME from methyl caprylate ($C_9H_{18}O_2$) to methyl oleate ($C_{19}H_{36}O_2$), which could be used with the PC-SAFT EoS. There is a strikingly lack of thermodynamic data for FAME (an overview can be found at http://www.ddbst.com/files/ddbsp/DDBSP-Biodiesel-2006.pdf), and most of the better quality data on FAME vapour pressures are believed to be from Scott et al. [278], Rose and Supina [279], Rose and Schrodt [280], and van Genderen et al. [281]. The number of data points decrease with the

increasing number of carbon atoms, due to difficulties in precise measurements of increasingly low pressures (e.g. the vapour pressure of methyl stearate at 316 K is 9.96 mPa [281]). Liquid density data can be found in the work of Pratas et al. [282] for methyl caprylate to methyl linoleate. The lack of data concerning dipole moments have led to the reluctance of including a polar term in our studies. The dipole moment was found for methyl caprate (μ = 2.08 D) and methyl laurate (μ = 1.70 D) from [68], but not for the remaining FAME. The deviations on vapour pressures and liquid densities using a non-polar PC-SAFT were not particularly high to suggest the need of a dipolar term. The large size of the ester molecules would make the dipole effect rather dilute in a molecular approach such as that of Gross and Vrabec. We have nonetheless tentatively parameterized the FAME for PC-SAFT-GV, using an averaged dipole moment of μ = 1.80 D for all the FAME. NguyenHuyng et al. treated the dipole moment as an adjustable parameter in their Jog and Chapman approach, an aspect we have avoided thus far.

Table 5.4 gives the pure component parameters for FAME used in this work. The T-P and T-ρ diagrams are given in Fig. 5.30. Using the new parameters, we also predict two important properties of fuel, the latent enthalpy of vaporization (H_{vap}) and the surface tension (γ), and these are presented in Fig. 5.31. H_{vap} can be calculated easily from the EoS, e.g. from Table 2.1. To calculate the surface tension, the PC-SAFT is written as Helmholtz energy functionals and coupled with the density functional theory, following the procedures of Gross [283]. For both the predictions, good agreements can be seen between the model and the experimental data for esters up to methyl palmitate. The predictions are poorer for methyl palmitate and methyl stearate, which we presume to have resulted from inconsistencies in the parameterization of the pure components, possibly caused by the data to which the parameters were adjusted to. Looking at the parameters in Table 5.4, there is a break in the increasing trend of the σ and ϵ/k occurring at these two esters, which are not likely in the same homologous group. However, without a great deal of vapour pressure and liquid density data to adjust to, this problem is not rectified easily. For the lighter esters, the results are encouraging as we have successfully predicted alternative properties using parameters adjusted only to vapour pressure and liquid density data. Both these properties are closely related to molecular structures, which further indicates the power of PC-SAFT in dealing with molecules of long chains. A more thorough conclusion can be reached, in the presence of more experimental thermo-physical data for the FAME compounds.

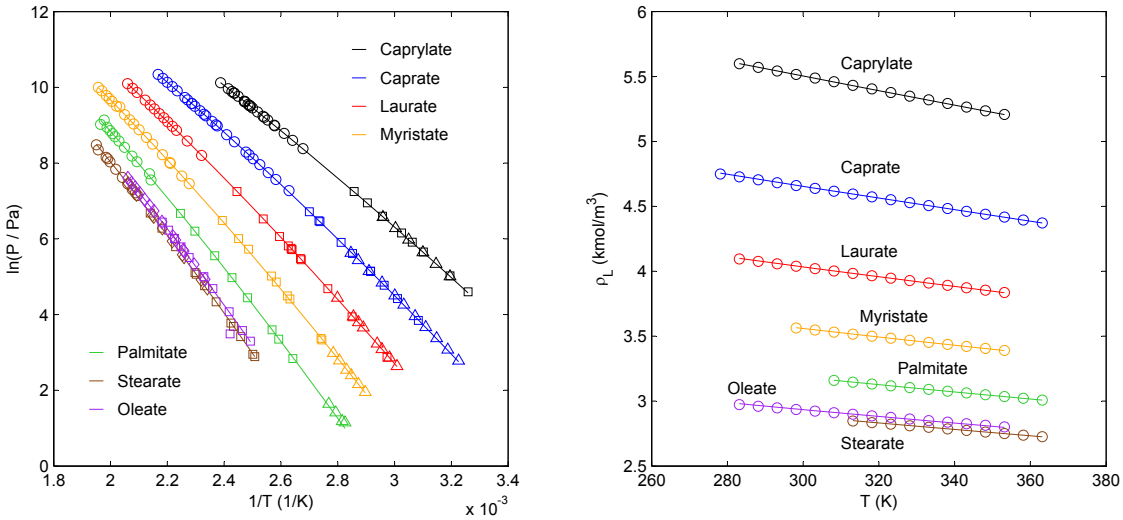

Figure 5.30: Calculation of thermodynamic properties of fatty acid methyl esters from methyl caprylate to methyl oleate, using the parameters given in Table 5.4 for non-polar PC-SAFT. *left*: Saturated vapour pressures for seven methyl esters, with the following experimental sources, □: [278]; ○: [279]; ◇: [280]; △: [281]. *right*: Saturated liquid densities, with experimental data taken from Pratas et al. [282].

Table 5.4: Pure component parameters for fatty acid methyl esters with the PC-SAFT/PC-SAFT-GV equation of state.

Compound	m	σ	ϵ/k	μ	AAD (%)		T_{range} (K)		N_{points}		Ref [a]
	(-)	(Å)	(K)	(D)	P^{sat}	ρ^L	P^{sat}	ρ^L	P^{sat}	ρ^L	
methyl caprylate/methyl octanoate ($C_9H_{18}O_2$)											
PC-SAFT	5.2074	3.6069	244.12		0.42	0.02	307 - 419	283 - 353	37	15	1,2,3,5
PC-SAFT-GV	5.1776	3.6139	244.61	1.8	0.31	0.02					
methyl caprate/methyl decanoate ($C_{11}H_{22}O_2$)											
PC-SAFT	5.8402	3.6871	248.27		0.37	0.04	324 - 461	278 - 363	36	18	1,2,3,5
PC-SAFT-GV	5.8298	3.6891	248.38	1.8	0.37	0.05					
methyl laurate/methyl dodecanoate ($C_{13}H_{26}O_2$)											
PC-SAFT	6.5153	3.7406	250.70		0.92	0.03	332 - 485	283 - 353	32	15	1,2,3,5
PC-SAFT-GV	6.5101	3.7415	250.73	1.8	0.92	0.04					
methyl myristate/methyl tetradecanoate ($C_{15}H_{30}O_2$)											
PC-SAFT	7.1197	3.7968	253.77		1.4	0.02	345 - 511	298 - 353	33	12	1,2,3,5
PC-SAFT-GV	7.1107	3.7986	253.88	1.8	1.4	0.02					
methyl palmitate/methyl hexadecanoate ($C_{17}H_{34}O_2$)											
PC-SAFT	7.8910	3.8140	253.71		2.2	0.01	378 - 509	308 - 363	20	12	1,2,5
PC-SAFT-GV	7.8966	3.8128	253.59	1.8	2.2	0.01					
methyl stearate/methyl octadecanoate ($C_{19}H_{38}O_2$)											
PC-SAFT	8.8759	3.7932	250.81		1.6	0.02	399 - 513	313 - 363	34	11	1,2,4,5
PC-SAFT-GV	8.8503	3.7975	251.15	1.8	1.6	0.03					
methyl oleate ($C_{19}H_{36}O_2$)											
PC-SAFT	8.6530	3.8036	252.00		0.76	0.09	401 - 485	283 - 353	24	14	2,4,5
PC-SAFT-GV	8.6812	3.7991	251.57	1.8	0.75	0.11					

[a] References: [1] A. Rose and W.R. Supina. *J. Chem. Eng. Data*, 6:173-179, 1961.

[2] T.A. Scott Jr., D. MacMillan, and E.H. Melvin. *Ind. Eng. Chem.*, 44:172-175, 1952.

[3] A.C.G. van Genderen, J. Cees van Miltenburg, J.G. Blok, M.J. van Bommel, P.J. van Ekeren, G.J.K. van den Berg, and H.A.J. Oonk. *Fluid Phase Equilibr.*, 202:109-120, 2002.

[4] A. Rose and V.N. Schrodt. *J. Chem. Eng. Data*, 9:12-16, 1964.

[5] M.J. Pratas, S. Freitas, M.B. Oliveira, S.C. Monteiro, A.S. Lima, and J.A.P. Coutinho. *J. Chem. Eng. Data*, 55:3983-3990, 2010.

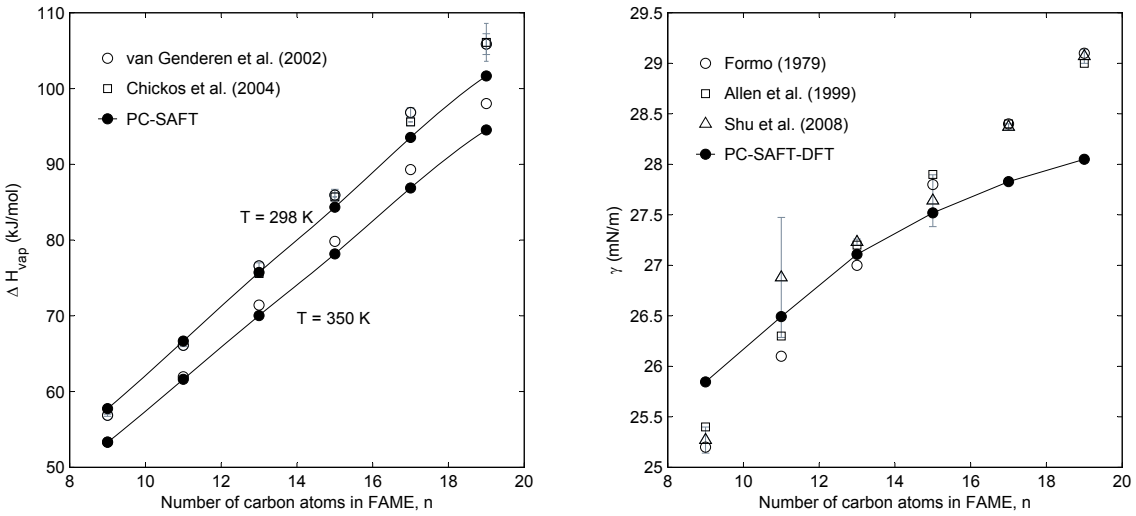

Figure 5.31: Calculation of latent heats of vaporization and surface tension of fatty acid methyl esters from methyl caprylate to methyl stearate, using the parameters given in Table 5.4 for non-polar PC-SAFT. The PC-SAFT is employed with the density functional theory in the calculation of the surface tension. Experimental data for H_{vap} were taken from [281, 284], and for γ from [285, 286, 287].

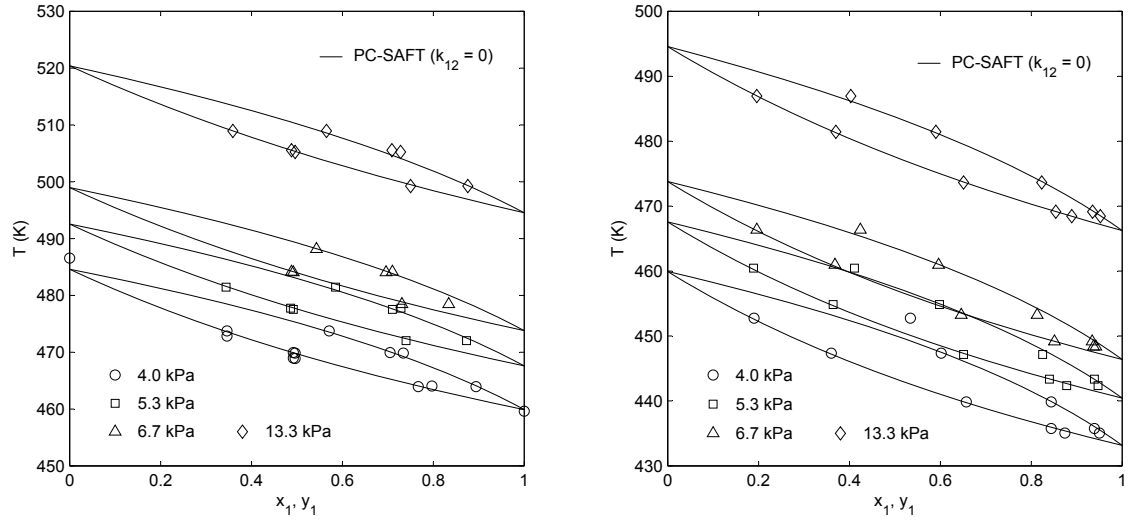

Figure 5.32: VLE modeling results using the non-polar PC-SAFT for the methyl myristate (1) + methyl palmitate (2) system (*left*) and methyl laurate (1) + methyl myristate (2) system (*right*). No binary parameter was used. Pure parameters for FAME were taken from Table 5.4. Experimental data taken from [279, 288].

Mixture equilibria data for FAME are scarce. We present the vapour-liquid equilibria of the methyl myristate + methyl palmitate [279, 288] and methyl laurate + methyl myristate [279] systems in Fig. 5.32. The phase behaviour between heavy esters are predicted easily at low pressures, even for the non-polar PC-SAFT. The phase equilibrium data for the methanol and methyl laurate/methyl myristate systems are particularly important for the production of biodiesel via transesterification using supercritical methanol [176]. Such an approach is known to be more rapid than the catalytic methods (cf. § 1.5.5), but the methanol should be recycled at the end of the process for it to be economical. In the modeling of both systems (Fig. 5.33), the results are similar with or without applying solvation

between the hydrogen of the alcohol and the oxygen of the ester. With the solvation effects included, the binary parameters are somewhat smaller than without. A zoom on the methanol-rich region shows that the representation of the vapour phase is only modest, possibly due to the lack of development of the PC-SAFT in the critical region.

Aldehydes

Aldehydes possess dipole moments of the same magnitudes as ketones ($\mu \simeq 2.5$ D), and are found predominantly in biomass fuels as formaldehyde, acetaldehyde, and furfural. While the aromatic structure of furfural is distinctly different from the linear aldehydes, its pure parameters are determined as with any other non-associating compounds. The presence of the second oxygen atom in the ring structure does suggest different bonding schemes upon cross-association, although Kleiner and Sadowski [275] had few difficulties representing the water + furfural system using a standard 2B scheme. The phase behaviours of furfural in a mixture with toluene, and with *n*-hexane are depicted in Figure 5.34. For the more complex vapour-liquid-liquid equilibrium (VLLE) system, a single k_{12} parameter was used to obtain a qualitative description of the system. The parameter value was adjusted to fit simultaneously the vapour-liquid and liquid-liquid boundaries, i.e. it was not fitted to one type of equilibria and applied to the other.

The modeling illustrated for linear aldehydes are shown herein for only acetaldehyde systems, due to a lack of data involving formaldehyde. Furthermore, pure parameters for acetaldehydes are not available in literature, which we shall provide here for the PC-SAFT-GV as: $m = 2.071$, $\sigma = 3.2737$ Å, $\epsilon/k = 232.48$ K, $\mu = 2.69$ D. For the acetaldehyde + acetic acid system, shown in Fig. 5.35, the implementation of solvation/cross-association between the polar and acid compounds has little effect on the overall phase description, as suggested earlier. However, the same cannot be said for the acetaldehyde + 2-propanol system, where the exclusion of hydrogen bonding between the aldehyde and alcohol compounds causes too much association in the system, and results in an azeotrope (pressure non-idealities) where none was observed. We note here that slightly incorrect values for the vapour pressure of 2-propanol were given from the data of Nikiforova et al. [292]. This was verified and confirmed with other sources, such as Daubert et al. [68].

5.2.4 Aqueous mixtures and other compounds

The influences of water on biofuels have been highlighted in the first chapter. Besides being a useful solvent for extraction, water forms a major constituent in biomass-derived fuels; whereas in bioethanols, it is identified as a demixtion agent that is monitored carefully in fuel quality control. Water is known for its strong hydrogen bonds, and is considered to be relatively polar for its dipole moment ($\mu \simeq 1.8$ D) and nearly spherical molecular size. The phase behaviour of aqueous systems is fairly complex; the common occurrence of two liquid phases often proving a challenge for most thermodynamic models. In this section, the second binary parameter l_{12} is used frequently to obtain quantitative (and at times, qualitative) description of the existing phases. The often negative, and obscurely large binary parameters needed are indications that not all specific interactions, or combinations thereof, within the systems can be accounted for.

Among the several investigations across different versions of the SAFT EoS, there is a general consensus, based on comparisons with available spectroscopic data, that water is best modeled as a 4-site associating molecule, or 4C scheme. The four sites in a 4C scheme are considered to be identical and indistinguishable from one another. Von Solms et al. [113] published seven different parameter sets for water, each set with a fixed m value and a 4C scheme, ranging from $m = 2.0$ to $m = 3.5$. The foremost observation was that water as a 4C molecule reproduces the vapour pressure and liquid densities better than a 2B water molecule, although different authors may have used different data sources. Compared with spectroscopic monomer fraction data from Luck [116], the 4C parameter sets with $3.0 < m < 3.5$ predicts most closely the experimental values, although such values for m is not fully consistent with the size factor of the molecule. Von Solms et al. cited the polarity of water as the main contribution to the observation. Aparicio-Martinez and Hall [295] also observed that the value of m will fall below 2, if allowed to freely adjust to pure properties, but this leaves a very large deviation in liquid densities. In their work, aqueous mixtures were

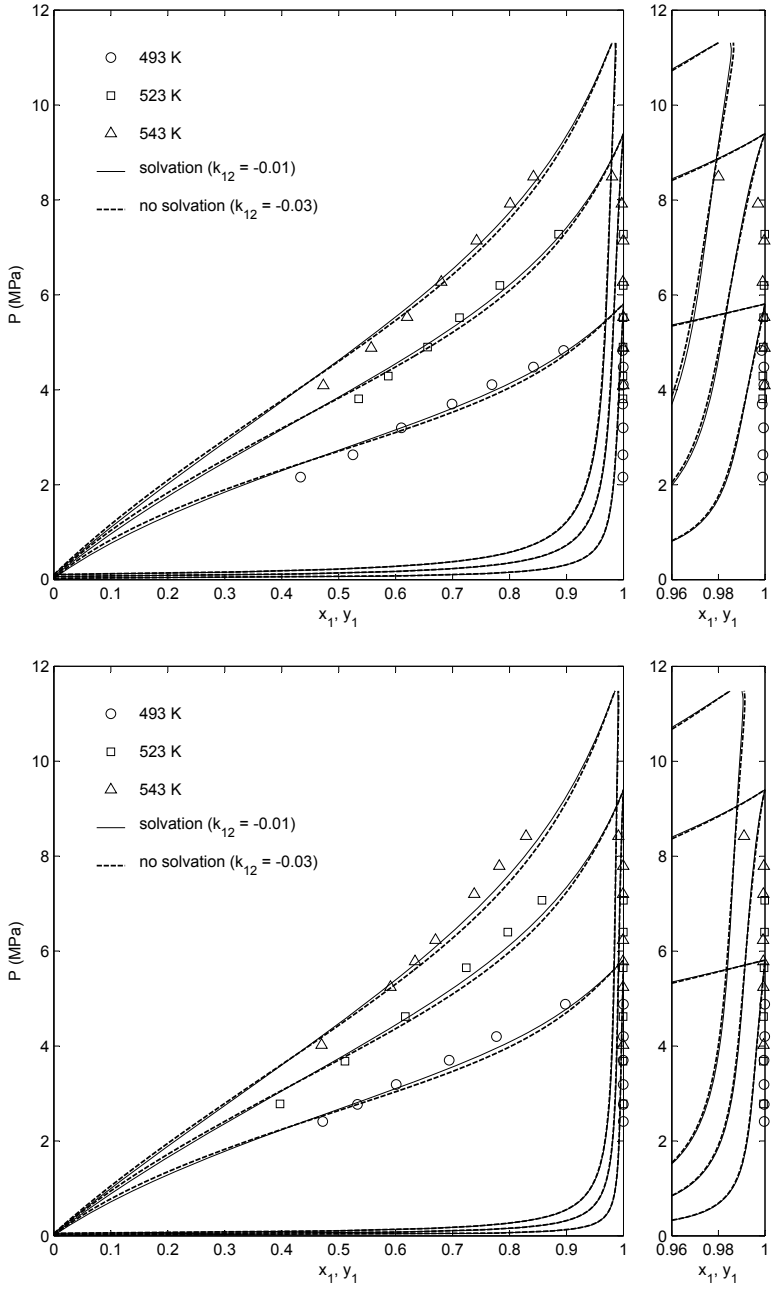

Figure 5.33: VLE modeling of the methanol (1) + methyl laurate (2) system (*top*) and of the methanol (1) + methyl myristate (2) system (*bottom*) at the critical region, using the non-polar PC-SAFT with and without solvation effects. Pure parameters for methanol were taken from [94], and for the FAME from Table 5.4. A zoom of the methanol-rich region is given alongside each figure, where the representation of the vapour phase can still be improved. Experimental VLE data were taken from Shimoyama et al. [176].

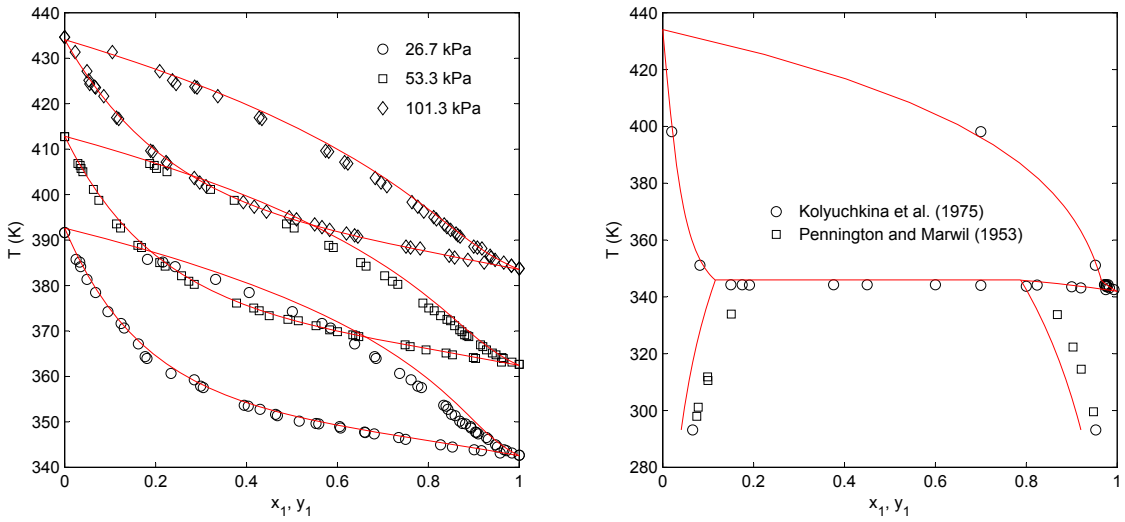

Figure 5.34: VLE modeling results using the PC-SAFT-GV for two furfural-containing systems. *left*: toluene (1) + furfural (2) [289], with $k_{12} = 0$. *right*: *n*-hexane (1) + furfural (2) [290, 291], with $k_{12} = 0.03$. Pure parameters for toluene and *n*-hexane were taken from [93], and for furfural from [275].

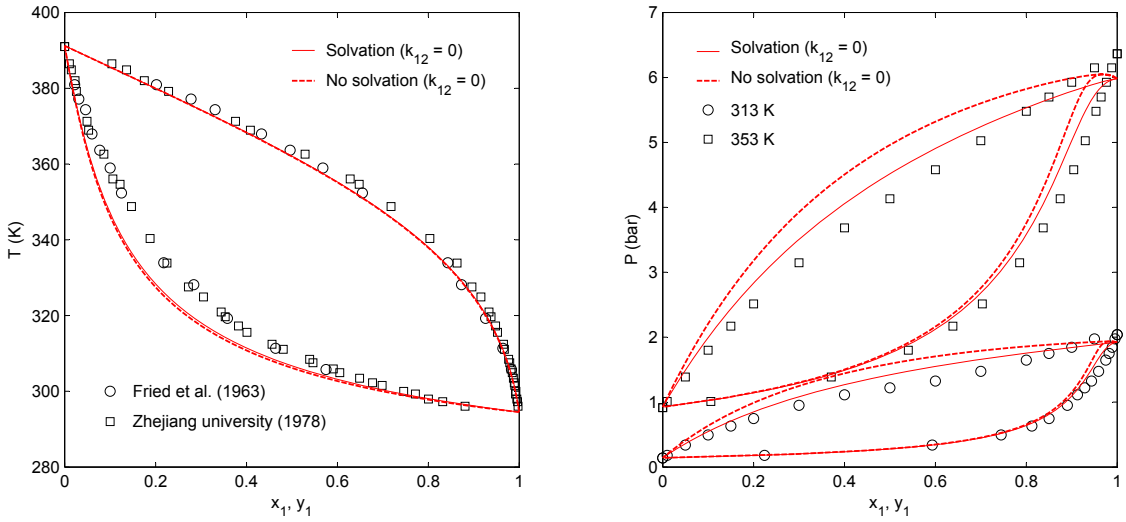

Figure 5.35: VLE modeling results using the PC-SAFT-GV for two acetaldehyde-containing systems, with $k_{12} = 0$ for both cases. *left*: acetaldehyde (1) + acetic acid (2) [293, 294], where the application of solvation or cross-association has little effects on the overall calculations. *right*: acetaldehyde (1) + 2-propanol (2) [292], where solvation is essential in order to suppress an azeotrope at low concentrations of 2-propanol. Pure parameters for 2-propanol were taken from [152], while those for acetaldehyde and acetic acid are from this work.

modeled using a three site model for water with the non-polar PC-SAFT. The three site model possesses two proton donors in the hydrogens, and a single proton acceptor in the oxygen (3B scheme). Their choice was based on the structural consistency of the 3B scheme over the 4C, the latter unlikely to exist on the grounds of steric hinderance; and a comparison of experimental monomer fractions that was not too different from the optimal 4C scheme. This has not discounted the 2B scheme from being used, however, least of all as a simple and *ad hoc* approach to modeling aqueous systems [94, 152, 275, 296].

In this work, we will apply only the 2B bonding scheme to water, for the same reasons as for the alcohols. More rigorous bonding schemes, such as the 3B or 4C schemes, can only add some physicality to the model; they do little to override the original simplifications of Wertheim's association theory (bonding site angle, intramolecular interaction in network structures). In addition, it was observed in trial calculations that for several systems, the inclusion of polarity to water did not improve modeling results, but may oftentimes have the opposite effect, particularly in the presence of a second liquid phase. While one cannot overlook the existence of *both* the electrostatic and associative effects of water, it is not physically correct to couple the two effects through separate Helmholtz energy terms in the model (a^{DD} and a^{assoc}). Kleiner and Sadowski have also reported an adverse effect in modeling results, when polarity is applied to water, particularly if the other compound is also polar [275]. In this section, we will model water as a non-polar ($\mu = 0$ D), but associating compound, using the parameters taken from Gross and Sadowski [94]. An example where water is better modeled this way is the water + 1-butanol system, shown in Fig. 5.36. When polarity is applied to water (thick red line), the liquid-liquid miscibility gap becomes too wide, and very large binary parameters are needed to bring the curves to the liquid-liquid equilibrium (LLE) data. The result is that some accuracy in the VLE portion had to be sacrificed in the overall representation. In the second figure alongside, the water + acetic acid system, large absolute values were used for both the k_{12} and l_{12} parameters. Despite passing through most of the data points, the shape of the curve is somewhat distorted (cf. 'overfitting' the data in Figs. 5.9 and 5.14).

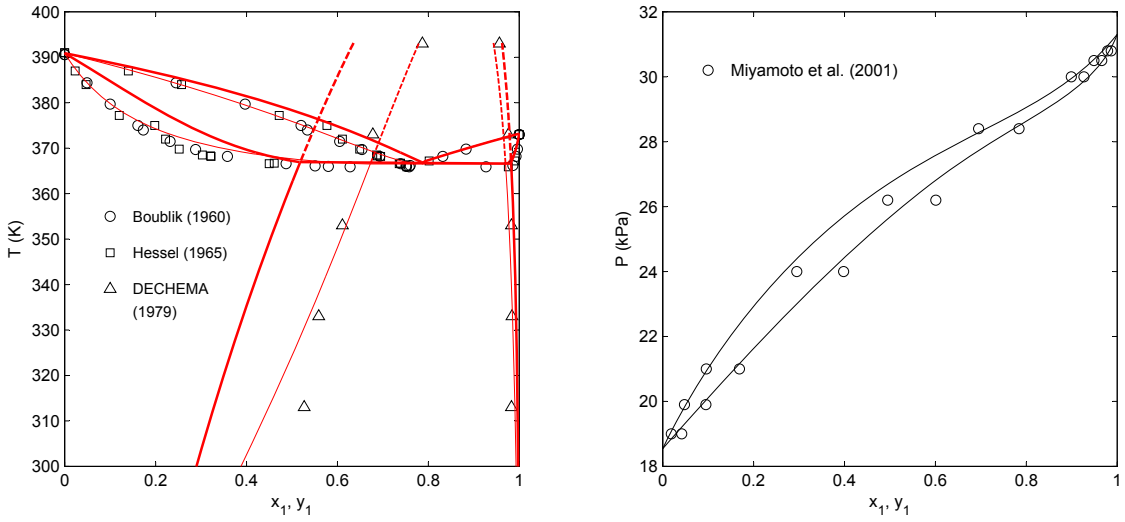

Figure 5.36: VLLE and VLE modeling results for two water-containing systems, using different forms of the PC-SAFT EoS. *left*: water (1) + 1-butanol (2) system [297, 298, 299], using the PC-SAFT-GV EoS in two cases: the thick line ($k_{12} = -0.05$, $l_{12} = 0.01$) includes polarity in water, whereas the thin line ($k_{12} = 0.005$, $l_{12} = -0.02$) does not. *right*: water (1) + acetic acid (2) system [270], using the non-polar PC-SAFT ($k_{12} = -0.055$, $l_{12} = -0.025$). Pure parameters for water and 1-butanol were taken from [94, 152], while those for acetic acid are from this work.

Modeling the VLE portion of the ETBE + water system is an instance where the inclusion of solvation effects does not improve the overall representation of the data, even when the phenomenon is expected to be present in the system (Figure 5.37). There are no rigorous cross-association theories to date, the approach used in this work remains empirical, and only trial and error will determine the extent of its effect. There are other techniques to simulate solvation, as long as available bonding sites can become occupied and non-idealities suppressed. NguyenHuyng et al., for example, modeled the solvation between an alcohol and an ester by setting *both* the κ^{AB} and ϵ^{AB}/k parameters of the ester to those of the alcohol [277]. For choosing a suitable bonding scheme in their approach, the best scheme between one to four sites that described the methyl propanoate + 1-propanol system was kept for all remaining

mixtures. This lack of standardization in addressing solvation is likely to continue until more theoretical approaches are developed. For the purposes of modeling the binary water + butyraldehyde system, and the ternary furfural + 2-butanone + water system, the inclusion of solvation is once again necessary. Both furfural and 2-butanone employ the association volume parameter of water in order to take solvation into account ($\kappa^{A_1B_1} = \kappa^{A_2B_2} = \kappa^{A_3B_3}$).

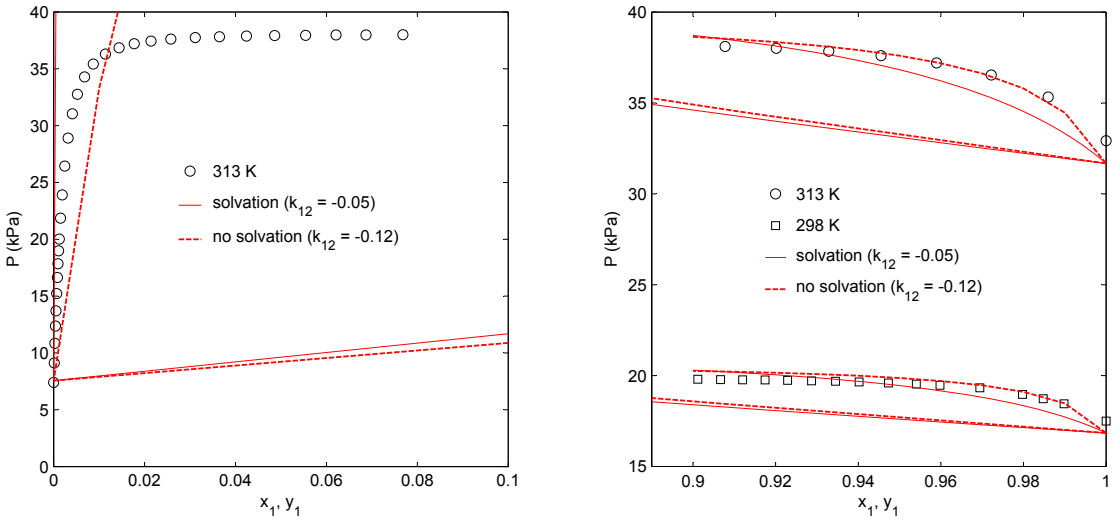

Figure 5.37: VLE modeling of the ETBE (1) + water (2) system at 298.3 and 313.2 K, using the PC-SAFT EoS, showing the two extreme ends of ETBE composition. The data representation is slightly better when the solvation effect is ignored, even when the phenomena is expected to be present in the system. Pure parameters for water were taken from [94], while those for ETBE are from Table 5.3. Experimental data were taken from Rarey et al. [160].

It was mentioned in earlier text that the thermal upgrading of lignocellulosic biomass results in molecules of a more complex nature. These molecules may possess several functional groups, and are often used as reaction intermediates in the manufacture of important chemicals. The types of molecules that may be derived from the decomposition of cellulose, hemicellulose and lignin are listed elsewhere, and we have selected a few here, in mixture with organic solvents, such as water and toluene. Phase equilibria data for these binaries are typically scarce, and those exhibiting solid-liquid equilibria are beyond the scope of this work. This limits our study to phenolics, and glycerol (furfural, a major product of cellulose decomposition, has been discussed in § 5.2.3, and further in [275]). We present, firstly, the PC-SAFT and PC-SAFT-GV parameters for these compounds in Table 5.5. For the phenolics, it was observed that the values of κ^{AB} tend to drop to very low values, when attempting to fit to vapour pressures and liquid densities. To once again avoid unconventional κ^{AB} values, we fix a value of 0.0001 to κ^{AB}, which we deem to be the lowest feasible number for this parameter. Values higher than 0.0001 gave poorer fits to vapour pressures and liquid densities. We have chosen to treat the phenolics as polar and associating compounds, although their large m values ($m \simeq 4$) and small dipole moments ($\mu < 2.0$ D) make modeling results much the same even if they are simply considered as a non-polar (but not non-associating) molecule. Furthermore, we do not tamper with the $n_{\mu,i}$ variable (cf. Eqn. 2.66, 2.67) within the GV dipolar term. These terms are reserved for copolymers and polar repeated units, which are not the cases here. For guaiacol, which appears to have dipolar effects coming from both the -OH and -OCH_3 terms, we have blanketed this effect by treating it collectively as a single polar group and used an average dipole moment.

The new parameters for the phenolics and miscellaneous compounds have been applied to mixture VLE and LLE systems, with good effects. Several examples of various complexities have been given in Figures 5.39 - 5.43, most of which require only small values for the binary interaction parameter. The results for the systems involving glycerol are particularly interesting (Figs. 5.42 and 5.43). The 1-alkanol + glycerol systems could be qualitatively

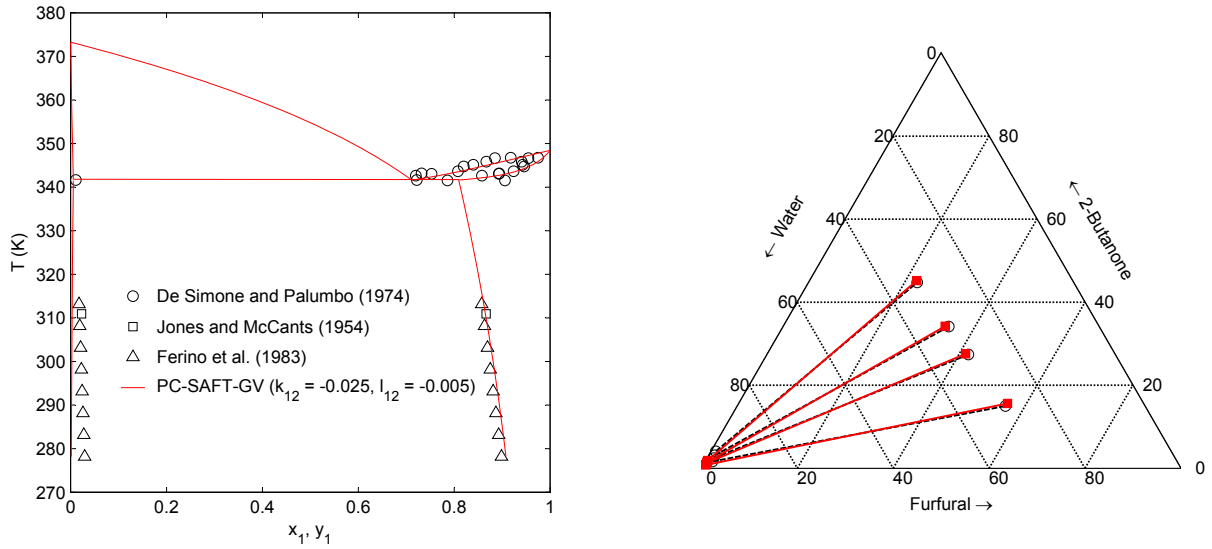

Figure 5.38: *left*: VLE modeling of the water (1) + butyraldehyde (2) system at 101.3 kPa, using the PC-SAFT-GV EoS, with solvation effects and two binary parameters included. Pure parameters for water were taken from [94], and for butyraldehyde from [133]. Experimental data were taken from [300, 301, 302]. *right*: LLE modeling of the furfural (1) + 2-butanone (2) + water (3) ternary system at 298.2 K and 101.3 kPa, using PC-SAFT-GV (—) and the following binary interaction parameters: $k_{12} = 0.018$, $k_{13} = -0.027$ and $k_{23} = -0.065$. Pure parameters for were taken from [94, 275, 133]. Experimental data (○) and tie lines (- -) were taken from Krupatkin and Glagoleva [303].

represented by the PC-SAFT-GV without aid of binary parameters. For the ternary methyl oleate (1) + methanol (2) + glycerol (3) system, no VLE or LLE data was located nor obtainable for the binary pairs of methyl oleate (1) + methanol (2) and methyl oleate (1) + glycerol (3). We have thus approached the modeling in a slightly different manner. We set a zero value for k_{12}, but include the solvation effect between methyl oleate + methanol, assuming that this may decrease the 'true' value of k_{12} to around zero in any case. This is grounded on the fact that small k_{12} values were also used in Fig. 5.33. We do not, however, use k_{12} values from the same figure, as methyl oleate is a branched, rather than linear, ester. We proceed to adjust the value of k_{13} to fit the experimental data, and found that only small values (±0.01) are required to satisfactorily describe the LLE.

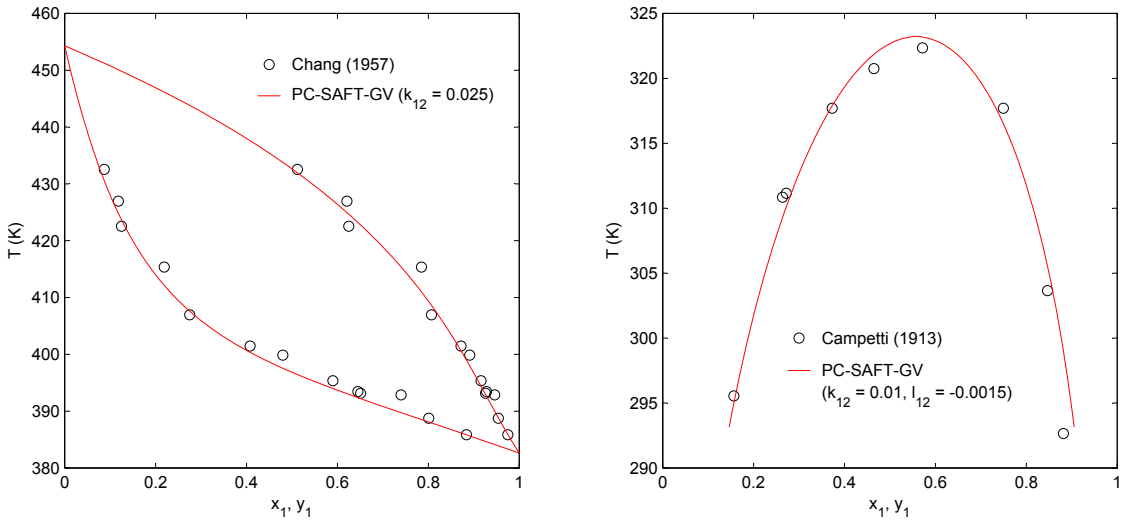

Figure 5.39: VLE and LLE modeling, at 101.3 kPa, of the toluene (1) + phenol (2) (*left*), and *n*-octane (1) + phenol (2) (*right*) systems using the PC-SAFT-GV EoS. Pure parameters for toluene and *n*-octane were taken from [93], and for phenol from Table 5.5. Experimental values were taken from [304] and [305].

Table 5.5: Pure component parameters for phenolics and miscellaneous compounds with the PC-SAFT/PC-SAFT-GV equation of state. Vapour pressure, liquid density and dipole moment values are taken from Daubert et al. [68]. For associating compounds, a 2B bonding scheme has been assumed.

Compound	m	σ	ϵ/k	κ^{AB}	ϵ^{AB}/k	μ	AAD (%)		T_{range} (K)	
	(-)	(Å)	(K)	(-)	(K)	(D)	P^{sat}	ρ^L	P^{sat}	ρ^L
phenol (MM = 94.111 g/mol)										
PC-SAFT	4.0721	3.1017	285.52	0.0001	2805.20		0.81	0.61	353 - 690	315 - 533
PC-SAFT-GV	4.0656	3.1035	285.28	0.0001	2798.87	1.43	0.81	0.62		
m-cresol (MM = 108.138 g/mol)										
PC-SAFT	4.2217	3.2607	288.69	0.0001	3078.89		0.80	1.2	343 - 695	293 - 493
PC-SAFT-GV	4.2156	3.2625	288.44	0.0001	3074.57	1.59	0.80	1.2		
o-cresol (MM = 108.138 g/mol)										
PC-SAFT	4.2682	3.2273	280.69	0.0001	2532.64		0.38	0.66	333 - 688	298 - 453
PC-SAFT-GV	4.2635	3.2286	280.52	0.0001	2524.29	1.45	0.39	0.66		
p-cresol (MM = 108.138 g/mol)										
PC-SAFT	4.5368	3.1775	278.42	0.0001	3002.29		0.55	1.1	323 - 695	289 - 493
PC-SAFT-GV	4.5312	3.1790	278.21	0.0001	2997.97	1.56	0.55	1.1		
anisole (MM = 108.138 g/mol)										
PC-SAFT	3.4921	3.4951	284.09				0.53	0.16	323 - 640	273 - 425
PC-SAFT-GV	3.4866	3.4973	283.99			1.33	0.53	0.17		
guaiacol (MM = 124.137 g/mol)										
PC-SAFT	2.4616	4.0500	383.95	0.0001	3408.89		2.9	0.30	362 - 479	278 - 478
PC-SAFT-GV	2.4059	4.0856	384.34	0.0001	3405.92	2.43	2.9	0.34		
glycerol (MM = 92.094 g/mol)										
PC-SAFT	1.5728	4.1901	554.73	0.0007	4364.57		3.4	0.59	339 - 563	193 - 563
PC-SAFT-GV	2.5250	3.5473	413.11	0.0042	3638.49	2.68	3.7	0.47		

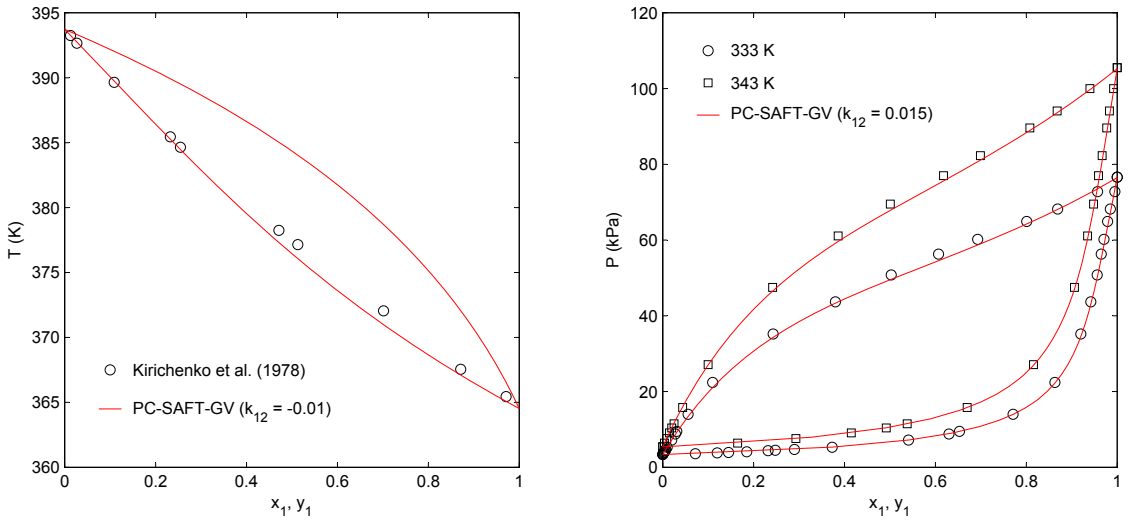

Figure 5.40: VLE modeling of the anisole (1) + phenol (2) (*left*), and *n*-hexane (1) + anisole (2) (*right*) systems using the PC-SAFT-GV EoS. Solvation is accounted for in the anisole (1) + phenol (2) system. Pure parameters for *n*-hexane were taken from [93], and the rest were newly determined from Table 5.5. Experimental values were taken from [306] and [307].

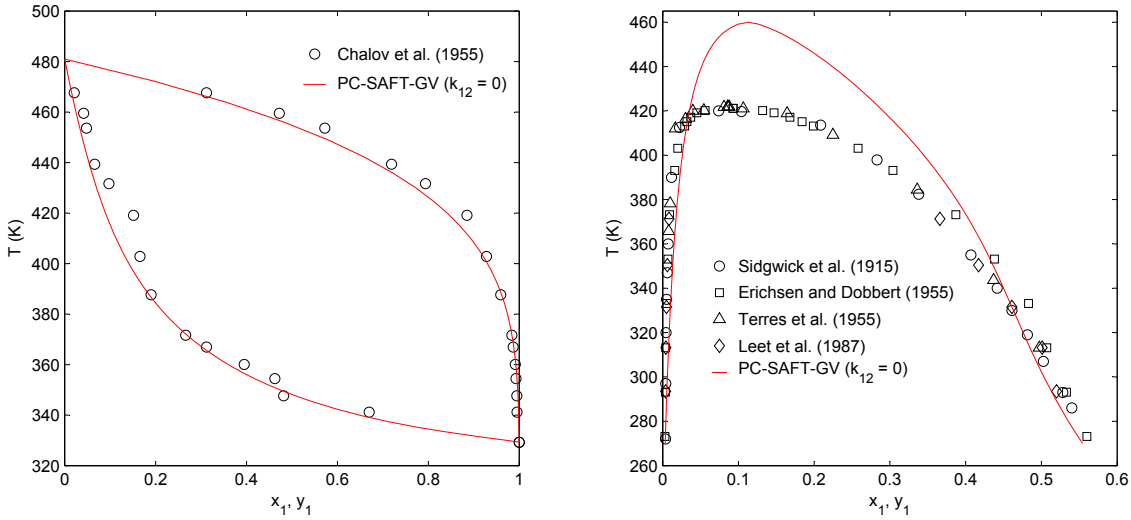

Figure 5.41: *left*: VLE modeling of the acetone (1) + guaiacol (2) system using the PC-SAFT-GV EoS. Pure parameters for acetone were taken from [133], and for guaiacol from Table 5.5. Experimental values were taken from [308]. *right*: LLE modeling of the *m*-cresol (1) + water (2) system at 101.3 kPa using the PC-SAFT-GV EoS. Water is regarded as a non-polar compound. Pure parameters for water were taken from [94], and *m*-cresol from Table 5.5. Experimental values were taken from [309, 310, 311, 312].

5.3 Calculation of Excess Enthalpy

The molecular simulation data used in the development of the SAFT EoS were mainly equilibrium types, with focus on pressures, densities and compressibility factors. No excess enthalpy (h^{E}) data were used for comparison, and

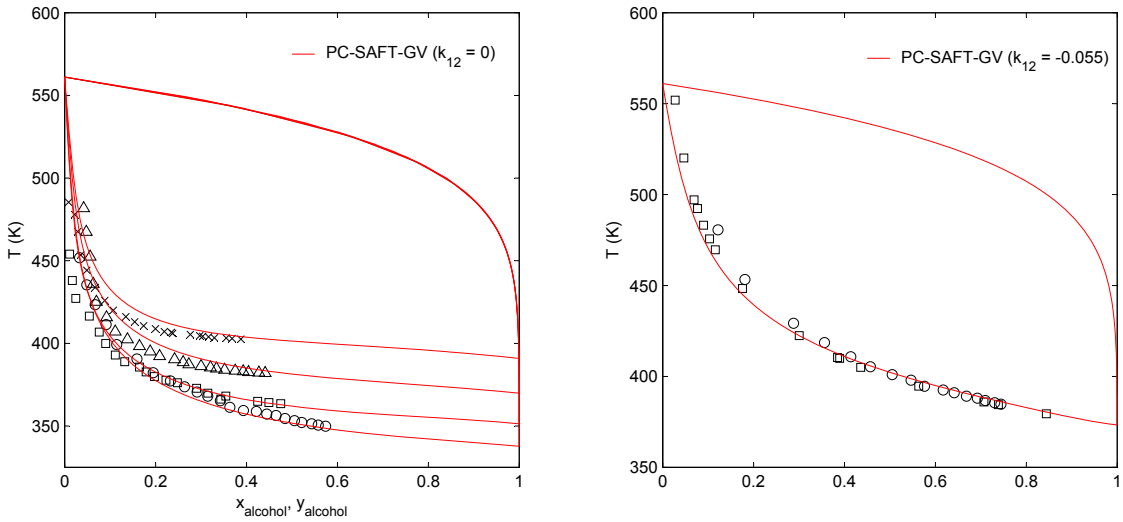

Figure 5.42: VLE modeling of the (*left*): alcohol (1) + glycerol (2) systems, with experimental data for methanol (○), ethanol (□), 1-propanol (△) and 1-butanol (×), and of the (*right*): water (1) + glycerol (2) system. Both systems measured at 101.3 kPa, and taken from [159, 313]. Pure parameters for alcohols were taken from [152], water from [94], and glycerol from Table 5.5.

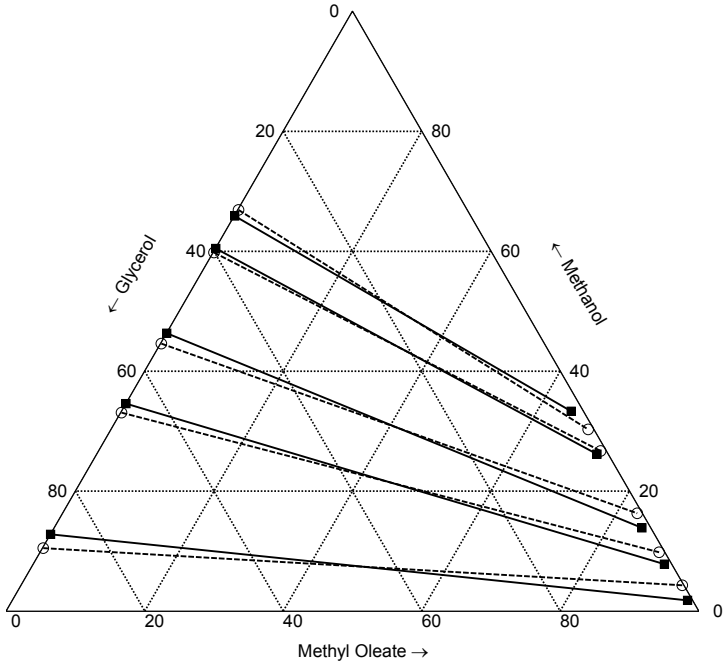

Figure 5.43: LLE modeling of the methyl oleate (1) + methanol (2) + glycerol (3) ternary system at 333.2 K and 101.3 kPa, using the non-polar PC-SAFT (—) and the following binary interaction parameters: $k_{12} = 0$, $k_{13} = 0.01$ and $k_{23} = -0.04$. Pure parameters for methanol were taken from [94], and the others from this work. Experimental data (○) and tie lines (- -) were taken from Negi et al. [314].

none were chosen to be fitted against in determining the pure component parameters. In practice, solution models dealing with liquid non-idealities, such as the NRTL and UNIQUAC models, are more adapted and accessible to h^{E} calculations than EoS. The evaluation of excess enthalpy can be a revealing exercise, which calls upon the

temperature dependency ($\partial/\partial T$) of the state properties of an EoS, an area lesser explored in the phase equilibria calculations thus far.

In representing h^E as a function of molar composition, the location and magnitude of the enthalpy maximum (or minimum) is of most interest; thus the binary interaction parameter will be adjusted manually to match closely this region. While it is possible to correlate simultaneously VLE and h^E data, as is commonly done with solution models (e.g. with NRTL [315]), we choose not to follow this approach here. In essence, it is of more interest to fit the binary parameter solely on h^E data, and attempt to predict the VLE of the system, the purpose being that excess enthalpy measurements are, generally, less expensive to perform than VLE ones. As difficult as this can be, success would result in time saved on experimental work. It was expected that the PC-SAFT EoS, with its theoretical framework, may have some success, at least in simple systems consisting of non-associating, apolar molecules. Several systems were tested, and the results varied from complete quantitative description of the VLE, to zero agreement whatsoever. This occurred even for relatively ideal systems. We exemplify here using the *n*-hexane + cyclohexane system, a standard reference system used for validating calorimeters. Sabbah et al. [316] compiled over 400 experimental data points for the system; and is widely regarded as high quality h^E data. This makes a fair evaluation of the capabilities of the PC-SAFT EoS in representing h^E behaviour and, furthermore, predicting the VLE. When the EoS adequately describes the h^E curve, using a non-zero k_{12} parameter, it is only qualitative in its attempt to predict the VLE[3], taken from Martin and Youings [317], and Ott et al [318]. This is shown in Fig. 5.44. The VLE of the system is ideal, and this is supported by the relatively low h^E values and the zeotropic *P*-*x*-*y* behaviour. Expectedly, no binary interaction parameter is needed by the PC-SAFT to describe the VLE data. However, using a zero binary parameter for the h^E calculation will produce fruitless results. For such a system, the k_{12} value needs to be fitted simultaneously to both h^E and VLE data to obtain meaningful results. It was observed that h^E values, calculated by PC-SAFT, are more sensitive to changes in the binary parameter k_{12}, compared to phase equilibria calculations.

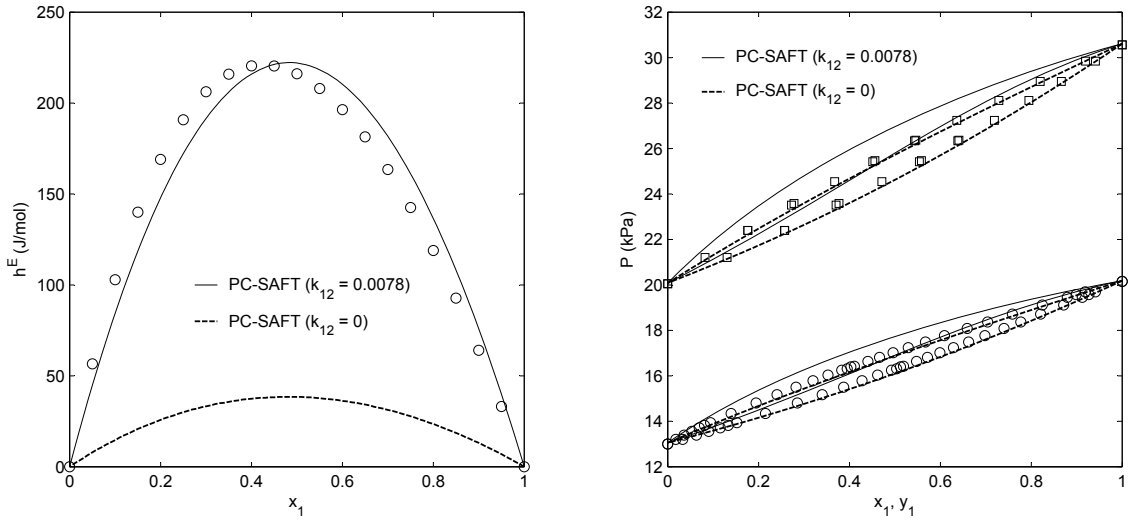

Figure 5.44: Prediction of the VLE, or h^E, behaviour by first fitting the k_{12} parameter of PC-SAFT to data of the other. The system is *n*-hexane (1) + cyclohexane (2). In the *left* figure, the non-polar PC-SAFT is optimized to give a good representation of h^E data (solid line), using $k_{12} = 0.0078$. However, this parameter only gave modest predictions when used in VLE, given in the *right* figure. The same could be said when the PC-SAFT is fitted to VLE data (dashed line) on the *right*, but a k_{12} value of zero transfers badly when used in the *left* for h^E predictions. Pure parameters for *n*-hexane and cyclohexane taken from [93], and experimental data are from [316, 317, 318].

[3]The VLE data used in this example is considered to be fully consistent when tested with DECHEMA standards.

The excess enthalpy is usually positive for a mixture containing an associating compound and a non-associating, apolar compound. The mixing is endothermic, as the energy required to disrupt hydrogen bonds usually dominates all others in the system. In an example using ethanol + benzene (Fig. 5.45), the PC-SAFT-GV using a single k_{12} parameter gave only modest description of h^E. The overestimation of h^E in the ethanol-rich portion suggests too much association was calculated by the model, while the dispersive interactions appears too weak on the other end of the composition. Changes in the k_{12} parameter shifts the peak of the h^E curve vertically; thus it was difficult to improve the representation other than employing the second asymmetric parameter l_{12}. The l_{12} parameter can be useful in this case, as it primarily displaces the curve peak in a horizontal manner. Whilst several solution models use two or more parameters to represent h^E, this is somewhat unconvincing in the framework of PC-SAFT, particularly for an example that is not overly complex from a structural and VLE point of view. A further shortcoming, for this and several other systems tested, is that a single interaction parameter cannot be used for wide temperature ranges; thus the model is not extrapolative for h^E. This is related to the high sensitivity of h^E values to the k_{12} parameter. As observed in VLE, the inclusion of a dipolar term may decrease the value of the k_{12} parameter in h^E calculations.

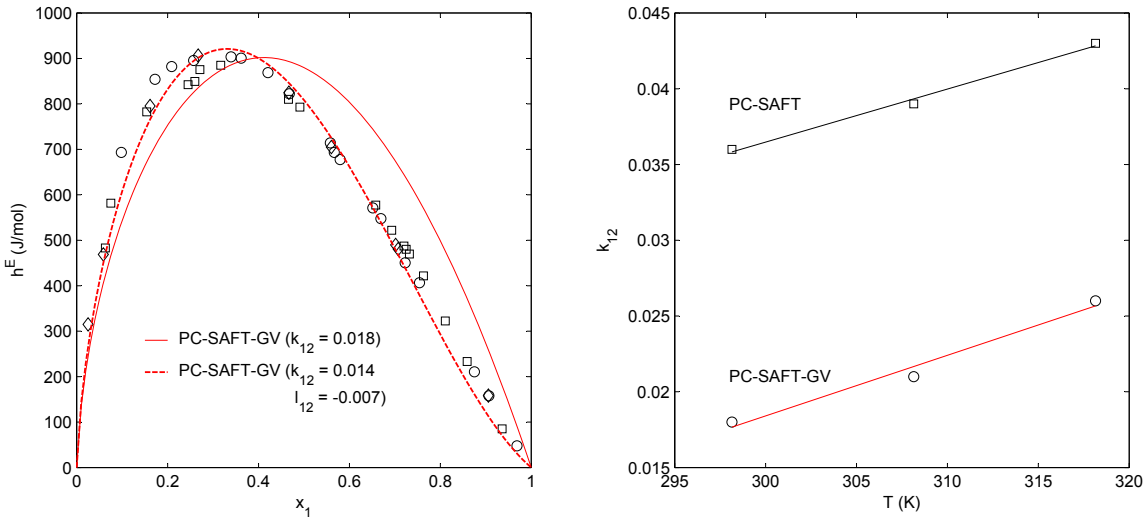

Figure 5.45: Modeling of the excess enthalpy of the ethanol (1) + benzene (2) system, using the PC-SAFT-GV EoS with one or two binary parameters. *left*: Excess enthalpy of the system at 298.2 K, where a two-parameter PC-SAFT-GV provides an improved description of the system. *right*: Binary interaction parameter k_{12} as a function of temperature, in order to represent h^E behaviour at 298, 308 and 318 K with the non-polar and polar PC-SAFT. Pure parameters for ethanol are taken from [94, 152] and for benzene from [93]. Experimental data from [319, 320, 321].

In the specific case where two structurally similar components are mixed, the PC-SAFT performs relatively well for both the h^E and VLE behaviour. In the methanol + 1-octanol system, a k_{12} value of 0.019 was used to correlate the h^E data [322], which could also be used to quantitatively describe the VLE behaviour [323]. Another system which shows some success in transferring the k_{12} value from h^E to VLE is the ETBE + *n*-heptane system. The addition of ETBE to gasoline as an octane-rating enhancer requires knowledge of the heats of mixing of ETBE in hydrocarbons. While this simultaneous description may seem promising, the same trend was not observed in the ETBE + *n*-hexane or *n*-octane systems. It is thus impossible to identify such a phenomenon *a priori*. In Figure 5.46, the excess enthalpy modeling is presented at the forefront, while the VLE modeling is shown as a lighter watermark to show, at a glance, the fit quality. The axes pertain to the forefront figure only.

The polar terms also proved useful in calculating the excess enthalpies of systems of high polarity. A single k_{12} value for PC-SAFT-GV could be transferred well between systems of acetone + *n*-alkanes, as shown in Fig. 5.47. The same k_{12} value is however only effective for predicting the VLE with *n*-decane, as shown in [133]. As we

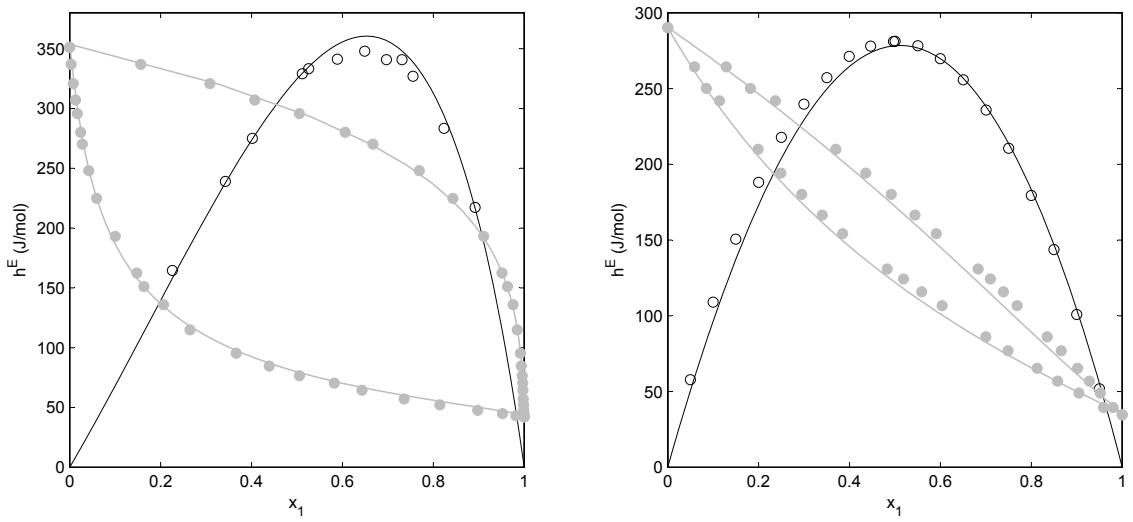

Figure 5.46: Prediction of the VLE behaviour by first fitting the k_{12} parameter of the non-polar PC-SAFT to h^{E} data. The excess enthalpy results are shown at the forefront in black, with the VLE results as a gray watermark. In the *left* figure, the methanol (1) + 1-octanol (2) system is modeled with $k_{12} = 0.019$, with experimental data taken from [322, 323]. The *right* figure shows the ETBE (1) + *n*-heptane (2) results, with $k_{12} = 0.010$ and various data taken from [324, 325]. Pure parameters are taken from [93, 94], except for those of ETBE from Table 5.3.

have shown that the inclusion of the solvation effect improves the VLE modeling between a polar, non-associating compound, and another associating compound, a similar observation could be made in the calculation of h^{E}. There is a marked improvement in representing the h^{E} behaviour of the ETBE + ethanol by adopting the solvation approach of Kleiner and Sadowski. When solvation effects were excluded, the model overestimates the h^{E}, shown herein for the 298 K case (dashed line in Fig. 5.47 *right*). Since the value of k_{12}, with solvation included, is the same as that used in the VLE modeling in Fig. 5.29, the parameter could be used for both h^{E} and VLE representations.

In overview, the PC-SAFT EoS cannot be regarded as a highly reliable model for representing excess enthalpy data, unless one is prepared to employ more than one binary interaction parameter. On those grounds, it may be simpler to use conventional excess Gibbs energy models (NRTL, UNIQUAC, etc) that are specially adapted for liquid mixtures and their phase behaviour.

5.4 Thermodynamic Consistency Testing

As the Gibbs Phase Rule and the Gibbs-Duhem equation must hold at equilibrium, both mathematical expressions signal the measurement of *P-T-x-y* data as an 'overdetermination' of state variables [162]. In fact, the Gibbs-Duhem equation requires only three out of the four measured variables to calculate, in a thermodynamically consistent manner, the remaining one (cf. Barker's method [330]). Nonetheless, the possession of an additionally measured, fourth variable provides a means in data assessment. If one is able to predict, through Gibbs-Duhem derived expressions, the values of the fourth variable, using other measurements and mathematical models, then it is possible to claim the data to be thermodynamically consistent.

The concept of data consistency is elusive, and how a set of consistent/inconsistent data is utilized depends on its purpose and context. The evaluation of data consistency is not transparent, there are no single tests (including the one mentioned above) that serve as the definite thermodynamic consistency test - the data should be subjected to several tests, while not all tests can be applied to the same dataset. Moon et al. [331] applied four different types of thermodynamic tests to 224 alcohol-hydrocarbon datasets, and, with a criterion established in their work, showed

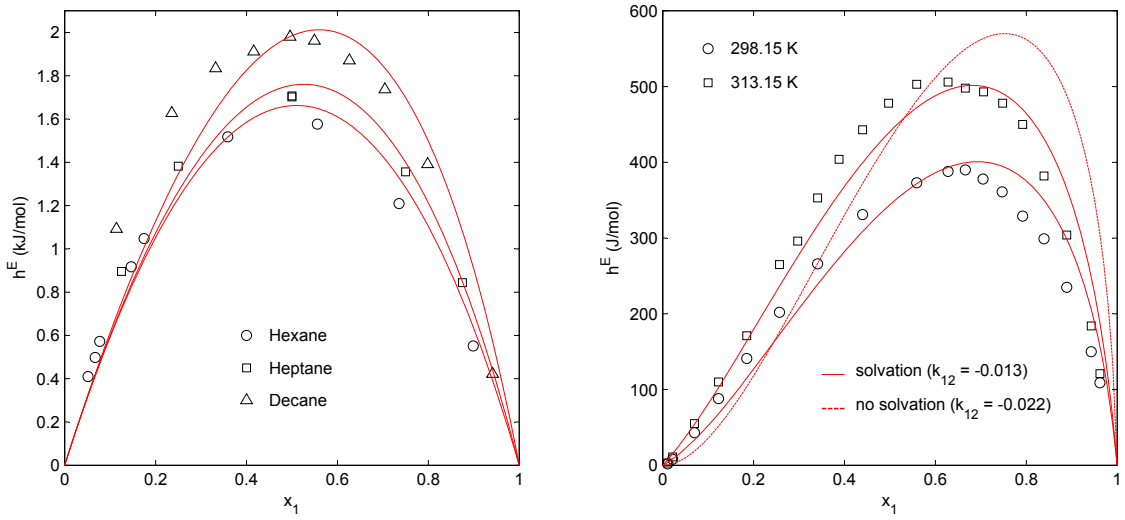

Figure 5.47: Modeling of the excess enthalpy using the PC-SAFT-GV EoS for acetone (1) + *n*-alkane (2) systems (*left*), and the ETBE (1) + ethanol (2) system (*right*). A single k_{12} value of 0.033 was used for all three binaries in the left figure. The inclusion of solvation effects positively improved the description of h^E in the ETBE + ethanol system. Pure parameters for the compounds are taken from [93, 133, 152] and Table 5.3. Experimental values taken from [326, 327, 328, 329].

that only 60 datasets were consistent. Nevertheless, datasets of difficult systems (e.g. MDEA systems) containing few experimental points will continue to benefit industries, who have expressed interests in 'informative' rather than 'accurate' data, regardless of consistency [157]. It is important to be cognizant of the role thermodynamic models play in the consistency test. A model that is hardly suitable for the system being tested, when coupled with Gibbs-Duhem relations, will inevitably result in a verdict of inconsistency. In this work, we prefer to claim that a set of data is thermodynamically consistent *with the particular model being used to carry out the test*. One should not confuse consistency with correctness. While thermodynamically inconsistent data is possibly incorrect, thermodynamically consistent data may not necessarily be correct. Jackson and Wilsak cautions how different analyses and tests may lead to different interpretations of a single set of data [332].

5.4.1 Methods and Test Criteria

There are innumerable consistency tests existing in literature, most of which are derived from the Gibbs-Duhem equation. In this work, we will not be conducting comprehensive testing spanning several tests; only a few selected tests will be applied with the PC-SAFT to the measured VLE data from Chapter 3. The way we perform the tests are as follows: for each system, the form of PC-SAFT that gives the best representation of the data is used for the test, with the appropriate binary interaction parameter(s). For subcritical conditions at constant temperature, we employ the test by Christiansen and Fredenslund [333]. In this method, the Gibbs-Duhem relations, written as non-linear differential equations in Gibbs energy, are solved using the method of orthogonal collocation [334]. The test uses minimal information from the data and model, as the equations are solved at collocation x compositions different to those of the experiment, and interpolated at the end using Lagrangian interpolation to obtain a set of consistent y compositions for the experimental x's. The collocation x compositions are roots of the Jacobian polynomial. The empirical criterion for consistency for any given y_i is given as:

$$|y_i\,(calc) - y_i\,(exp)| \leq U\,(x) + U\,(y) \tag{5.5}$$

where the subscripts *calc* and *exp* are the consistent and experimental vapour mole fractions, and U is the expanded uncertainty as described in Chapter 3. The test is almost model-free, especially if experimental data can be used for the liquid densities and the saturated fugacities, which are otherwise calculated with the help of an EoS. This moderate dependence on the model gives rise to the popularity of the method, which seeks to test the data with as little intervention from the model as possible. While the original paper was intended for consistency testing at high pressures, this test can also be done at low pressures through slight adjustments in the standard states of fugacities. The mathematical complexity of the model means slightly longer computational times are needed for this test.

The poor representation of the PC-SAFT EoS in the supercritical isotherms are somewhat carried over in applying the Christiansen and Fredenslund test, and we have opted to rather use an alternative test for supercritical isotherms. Valderrama and Alvarez proposed a test for asymmetric phase equilibrium data at high pressures, which does not require data for the entire concentration range [335, 336]. The basis of the test is the comparison of two integrals, one of which is based solely on experimental values, and the other on the model calculations. A simple Riemann sum have been used to evaluate the integrals. Interpretations for the test are provided for zero to absolute coherence of the two integral values, with a cutoff of 80 % coherence regarded as consistent. The model selection is manifested more strongly in this test, but the advantage is that the reference for consistency, i.e. the integral of the experimental values, is determined from the start, whereas the reference for the previous test, i.e the consistent y composition, is affected to some extent by the model chosen.

For isobaric systems, there are considerably less consistency tests available in literature, as the Gibbs-Duhem equation written out for constant pressure requires information on the excess enthalpies, which may not be available. Since we have only three isobaric cases, we simply apply the conventional Van Ness-Byer-Gibbs test [337] to the systems. The test is a modeling test, where the two least confident of the four state variables (x and y in our case) are calculated by the model, and the residuals plotted. Consistency for a particular data can be claimed if the absolute residuals fall below the experimental uncertainties (see Eqn. 5.5), and that the data is free from bias if the residuals themselves are scattered evenly about zero. Many authors have indicated the Van Ness-Byer-Gibbs test as an insufficient, but necessary test to be included in a thorough consistency testing [162, 332].

5.4.2 Results of tests

The results of thermodynamic consistency tests are open to interpretations, and should always be met with a clear idea of the contexts and roles of the data. Table 5.6 lists the results of the consistency testing using the methods described in the previous section. Where applicable, the maximum residuals on molar composition identified were given, and the number of points that were deemed consistent, via the criteria for each method. The results are slightly misleading for the high-pressure measurements, as large uncertainties were proclaimed in the experiments, making the fulfillment of Eqn. (5.5) somewhat simple. We have abstained from removing so-called inconsistent data points from our results, as in the context of a systematic PC-SAFT modeling study, both consistent and inconsistent data from a wide range of sources were resorted to, and little can be taken away from the merits of the model. Within such a role, the measured datasets remain useful to our study, despite the presence of several inconsistent points. Different individuals would interpret differently the results of Table 5.6, whose main purpose is to identify the number of points that were, firstly, not thermodynamically consistent with the model, and secondly, possibly reported with less certainty than others. A common observation is that the low pressure regions of an isotherm in low pressure VLE measurements yielded often inconsistent data, and this can be traced to the difficulties in pressure control and manual sampling experienced in this region. The test of Valderrama and Alvarez expectedly revealed the data points closely to the critical points of the supercritical isotherms as inconsistent, and this is identifiable with PC-SAFT's weakness in this region, rather than the data itself. Several of the points concluded as inconsistent may lie on the limits of the criteria, and would probably be consistent if temperature-dependent binary parameters, rather than a single transferrable one, were used for these. We have presented also examples in Fig. 5.48, where relatively good consistencies have been observed in the data and modeling, and areas where weaknesses in both have been identified.

These serve to explain the nature of the tests being conducted. Effects of impurities and poor model descriptions meant no tests were performed for our acetone + formic acid system.

Thermodynamic consistency testing remains a valuable tool for assessing the data-model relationship, providing the user with information on multiple aspects of experimental procedure and modeling techniques. If interpreted correctly, this modeling exercise may be used in conjunction with other techniques of data evaluation, such as calculating absolute average deviations (*AAD*). It remains to be said that a set of VLE data satisfying several consistency tests may find itself more compelling than its inconsistent counterparts.

Table 5.6: Results of the thermodynamic consistency tests for the binary systems measured in this work [333, 335, 337].

						Christiansen & Fredenslund		Van Ness-Byers-Gibbs				Valderrama & Alvarez	
System	Const T or P	Model	k_{12}	l_{12}	n_{total}	$\lvert\Delta y\rvert_{\max}$	$n_{\text{consistent}}$	$\lvert\Delta x\rvert_{\max}$	$n_{x,\text{consistent}}$	$\lvert\Delta y\rvert_{\max}$	$n_{y,\text{consistent}}$	$n_{\text{consistent}}$	Verdict
ethanol	99.91 kPa	PC-SAFT	0.045		11			0.173	7	0.031	8		
+ cyclohexane	323.81 K	PC-SAFT	0.045		9	0.038	7						
n-hexane	98.91 kPa	PC-SAFT-JC	0		11			0.096	6	0.025	10		
+ 1-propanol													
ethanol	94.89 kPa	PC-SAFT-GV	0.01		13			0.045	5	0.035	10		
+ *m*-xylene	323.39 K	PC-SAFT-GV	0.01		9	0.024	4						
	333.10 K	PC-SAFT-GV	0.01		9	0.026	6						
	343.16 K	PC-SAFT-GV	0.01		9	0.010	9						
ethanol	323.25 K	PC-SAFT-GV	0.01		10	0.024	5						
+ ethylbenzene	343.20 K	PC-SAFT-GV	0.01		10	0.011	10						
benzene	323.38 K	PC-SAFT	0.038		12	0.035	7						
+ acetic acid	333.15 K	PC-SAFT	0.038		13	0.027	10						
	343.16 K	PC-SAFT	0.038		9	0.065	4						
toluene	353.17 K	PC-SAFT-GV	0.025	0.0025	16	0.042	14						
+ acetic acid	363.14 K	PC-SAFT-GV	0.028	0.0025	15	0.030	15						
propane	343.63 K	PC-SAFT	0.018		9	0.008	9						
+ ethanol	353.62 K	PC-SAFT	0.018		7	0.026	7						
	383.60 K	PC-SAFT	0.018		9							6	NFC[a]
	402.98 K	PC-SAFT	0.018		9							6	NFC[a]
n-butane	323.25 K	PC-SAFT-JC	0		9	0.018	9						
+ ethanol	353.26 K	PC-SAFT-JC	0		8	0.070	6						
	373.27 K	PC-SAFT-JC	0		11	0.027	11						
	403.57 K	PC-SAFT-JC	0		8	0.046	8						
	423.19 K	PC-SAFT-JC	0		14	0.050	14						

[a] NFC ≡ Not Fully Consistent [335]

.

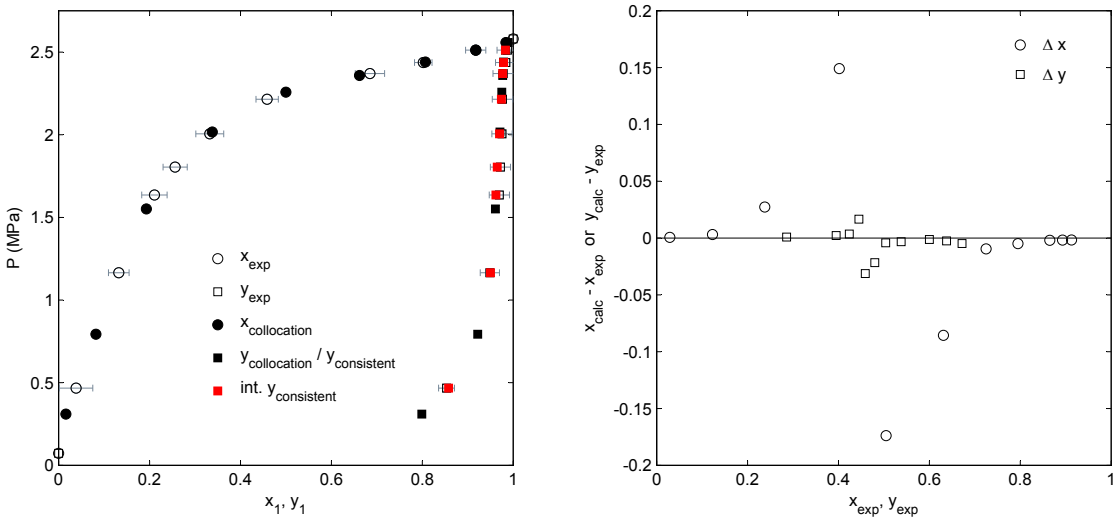

Figure 5.48: Examples of different thermodynamic tests used in this work. *left*: Christensen and Fredenslund test applied to the propane (1) + ethanol (2) system at 343.6 K. The nine $x_{\text{collocation}}$ points are determined from the Jacobian polynomial, the $y_{\text{collocation}}$ solved by orthogonal collocation, and the $y_{\text{consistent}}$ that corresponds to the x_{exp} is obtained via Lagrangian interpolation. *right*: Van Ness-Byers-Gibbs test applied to the ethanol (1) + cyclohexane (2) system at 99.9 kPa. The x and y residuals are scattered evenly and in a symmetrical manner along the abcissa. The less consistent points, which occur at the azeotropic region, can be seen clearly.

5.5 Concluding remarks

In a systematic manner, we have illustrated the capabilities of the PC-SAFT EoS in representing thermodynamic properties of various oxygenated compounds. The original, non-polar PC-SAFT by Gross and Sadowski [93] handles most associating chain molecules well, while for more advanced systems exhibiting specific interactions, such as polarity, the deployment of additional Helmholtz energy contributions is essential. The polar forms of the PC-SAFT, using either the Gross and Vrabec, or Jog and Chapman dipolar approach, have proved valuable in this regard. The polarizable PC-SAFT, which extends the PC-SAFT-GV EoS to account for molecular polarizability, was able of achieving results of the same quality as those of the PC-SAFT-GV, but did not bring about as much additional improvements as expected. By incorporating the suitable contributions in the model for the necessary interactions, one improves both the predictability and effectiveness of the final calculation. For most instances, a single binary interaction parameter k_{12} in the dispersion contribution a^{disp} is capable of describing azeotropic and non-azeotropic systems. Due to its theoretically sound basis, the PC-SAFT can be extrapolated across wide temperature ranges without a great loss in accuracy.

Table 5.7 shows the approaches adopted for modeling mixtures of different combinations of oxygenated species. For polar PC-SAFT instances, the PCIP-SAFT could be preferred if dealing with $\mu_i > 2$ D. It is hereby reminded that the methods followed in this work are but a few of the several possible means of modeling oxygenated compounds. An example is with aqueous mixtures, where we have used a simplistic 2B bonding scheme rather than the more popular 4C scheme, but were able to obtain nonetheless promising results. In dealing with biofuel mixtures, we have proposed new pure component parameters for several relevant compounds not published in literature. This included carboxylic acids, ethyl *tert*-butyl ether, fatty acid methyl esters, and other miscellaneous compounds. This was done using the approach outlined in § 2.4 for the PC-SAFT and PC-SAFT-GV; we have not exploited the PC-SAFT-JC in this regard as we felt the characterization of the x_p parameter is too loose for presenting a concrete set of parameters.

We have thus set aside this aspect for future work. Favourable results were obtained using the new parameters to calculate thermodynamic properties and phase equilibria, thereby justifying several decisions made in the regression procedure. The alcohol and acid mixtures measured in Chapter 3 could be represented quantitatively with a small binary interaction parameter. For more difficult mixtures consisting with acids and water, a second asymmetric l_{12} parameter provides some flexibility to the model.

Excess enthalpy is an important property in the blending of biofuels, and when calculated using the PC-SAFT, imparts information regarding the temperature derivatives of the model. In general, PC-SAFT does not perform well in excess enthalpy calculations, being both less extrapolative and more reliant on binary parameters, if compared to phase equilibria standards. There were a few instances, although nothing definitive, to suggest that a single binary parameters could be used for both h^{E} and VLE calculations. For difficult systems, such as those involving water, it is advisable to consider g^{E} models suited for liquid phase behaviour.

A short thermodynamic consistency testing was conducted for the VLE measurements presented in Chapter 3. The main objective here was to examine the level of consistency between the data and the model, which is generally acceptable. A more thorough investigation, involving several tests, is required to give more conclusive remarks on the data quality. The preliminary study performed here was useful in identifying most erroneous points, which would indicate several datasets not being fully consistent.

Acknowledgements

The author would like to thank Prof. Joachim Gross for the use of his code regarding the density functional theory. This enabled the calculation of surface tensions for the fatty acid methyl esters.

Table 5.7: Summary of the modeling approaches adopted in this work for modeling mixtures of oxygenated compounds. PC-SAFT refers to the original non-polar form from Gross and Sadowski. Polar PC-SAFT variants may refer to PC-SAFT-JC or PC-SAFT-GV EoS. Self-association and cross-association, the latter occurring between two unlike associating compounds, are facilitated with the Sandler and Wolbach combining rules [109], i.e. Eqns. (2.40) and (2.41). Solvation between associating and non-associating compounds is facilitated by the method of Kleiner and Sadowski [275]. Bonding schemes, where applicable, are indicated in parenthesis. Water is treated as a non-polar, associating molecule, as indicated in § 5.2.4.

Species (1) → Species (2) ↓	Apolar & non-associating	Alcohols (2B)	Carboxylic acids (1)	Polar compounds	Water (2B)
Apolar & non-associating	PC-SAFT k_{12}	Polar PC-SAFT k_{12} Self-association	Polar PC-SAFT k_{12}, l_{12} Self-association	Polar PC-SAFT k_{12}	PC-SAFT k_{12}, l_{12} Self-association
Alcohols (2B)	Polar PC-SAFT k_{12} Self-association	Polar PC-SAFT k_{12} Cross-association	Polar PC-SAFT k_{12} Self-association only	Polar PC-SAFT k_{12} Solvation	Polar PC-SAFT k_{12}, l_{12} Cross-association
Carboxylic acids (1)	Polar PC-SAFT k_{12}, l_{12} Self-association	Polar PC-SAFT k_{12} Self-association only	Polar PC-SAFT k_{12} Cross-association	Polar PC-SAFT k_{12} Self-association only	Polar PC-SAFT k_{12}, l_{12} Self-association only
Polar compounds	Polar PC-SAFT k_{12}	Polar PC-SAFT k_{12} Solvation	Polar PC-SAFT k_{12} Self-association only	Polar PC-SAFT k_{12}	Polar PC-SAFT k_{12}, l_{12} Solvation
Water (2B)	PC-SAFT k_{12}, l_{12} Self-association	Polar PC-SAFT k_{12}, l_{12} Cross-association	Polar PC-SAFT k_{12}, l_{12} Self-association only	Polar PC-SAFT k_{12}, l_{12} Solvation	

CHAPTER 6

Modeling aspects of the PC-SAFT in the critical region

The renormalization group (RG) is at present an approach of last resort, to be used only when all other approaches have been tried and discarded. The reason for this is that it is rather difficult to formulate RG methods for new problems; in fact the RG approach generally seems as hopeless as any other approach until someone succeeds in solving the problem by the RG approach.

- Kenneth G. Wilson (1936 -)

Aspects de la modélisation avec PC-SAFT dans la région critique

Il est bien connu que les équations d'état classiques ne tiennent pas compte des fluctuations à longue portée de la densité au voisinage du point critique. Cela est particulièrement vrai pour l'équation d'état PC-SAFT, dont les paramètres ne sont pas contraints au point critique. En conséquence, tous les calculs réalisés avec ce modèle ne sont pas en accord avec les observations expérimentales faites dans la région critique. La surestimation de la température et de la pression critiques est une erreur courante liée à l'utilisation de PC-SAFT. La divergence des longueurs d'onde de densité doit être abordée avec une théorie appropriée.

Dans ce chapitre, la théorie de groupe de renormalisation de White est combinée avec l'équation d'état PC-SAFT pour modéliser le comportement de phase des corps purs et des mélanges dans la région critique. Dans cette méthode, les longueurs d'onde de densité ayant des fluctuations à longue portée similaires sont regroupées dans des intervalles représentatifs. Dans une série d'intervalles, chaque intervalle successif est renormalisé par rapport à l'intervalle qui le précéde, ainsi les contributions de l'énergie d'Helmholtz résultant d'un changement dans les longueurs d'onde sont considérées. Un grand nombre d'intervalles de discrétisation permet de décrire suffisamment bien la contribution de l'énergie de Helmholtz issue des fluctuations à longue portée. La théorie de groupe de renormalisation introduit trois paramètres supplémentaires, dans les calculs, pour les composés purs. Ces paramètres sont ajustés pour reproduire les propriétés critiques expérimentales (température, pression, volume) de chaque corps pur. Afin de modéliser les données critiques mesurées dans le quatrième chapitre, les nouveaux paramètres de groupe de renormalisation ont été déterminés pour l'éthanol, le propanol et le 1,1,1,2-tétrafluoroéthane. Pour certains corps purs associatifs, le modèle PC-SAFT + RG ("renormalisation group") utilise jusqu'à huit paramètres, ce qui est un inconvénient de ce modèle. Deux méthodes d'approximation ont été utilisées pour étendre la théorie de groupe de renormalisation de White à des mélanges. Dans l'approximation dite de la "cellule d'espace de phases", la fluctuation de densité de chaque composé est traitée indépendamment de celles des autres composés, tandis que pour l'approximation isomorphe, les mélanges à plusieurs composés sont traités comme un corps pur, avec une moyenne molaire utilisée pour les propriétés physiques.

Au moyen des corrections de la théorie de groupe de renormalisation, les performances de PC-SAFT dans la région critique sont grandement améliorées. Les propriétés expérimentales critiques sont reproduites avec une précision plus élevée, et le comportement de phase est correctement représenté dans la région critique, avec un facteur d'échelle égal à celui de la constante de la loi universelle : 0.325. L'amélioration dans les calculs des corps purs impacte favorablement les résultats pour les mélanges. Par rapport à l'équation PC-SAFT originale, le modèle PC-SAFT + RG améliore grandement la description de la région critique. Alors que les deux méthodes d'approximation montrent, pour la plupart des mélanges, des résultats similaires, chaque méthode est certes plus performante pour certains types de systèmes. Ainsi l'approximation de la "cellule d'espace de phases" représente mieux les systèmes alcane-alcane, et les systémes d'éthanol en mélange avec un hydrocarbure court. Pour sa part l'approximation isomorphe se révèle supérieure pour les systèmes éthanol-hydrocarbures, quand la chaïne de l'hydrocarbure contient six atomes de carbone ou plus. Les deux méthodes d'approximation ont toutefois besoin d'un paramètre d'interaction binaire pour obtenir des résultats quantitatifs.

Nous avons constaté que dans de sa forme actuelle, le modèle utilisé ici, constitué de l'équation d'état PC-SAFT et de la théorie de groupe de renormalisation de White, n'est pas suffisamment précis pour décrire simultanément des équilibres liquide-vapeur et des points critiques de mélange.

Nous avons donc cherché des voies d'amélioration du modéle PC-SAFT-RG, Des voies ont été identifiées et sont détaillées à la fin du chapitre. La première voie d'amélioration concerne le problème de la surparamétrisation dans le terme de groupe de renormalisation (en effet trois paramètres sont ajustés sur les trois grandeurs critiques, alors que les paramètres de SAFT conservent leurs valeurs originales). Une sérieuse amélioration consisterait en un réajustement global de l'ensemble des paramètres SAFT et RG, de corps purs, sur les données critiques, les pressions de vapeurs et les densité de liquide.. La seconde voie d'amélioration de la description des propriétés des mélanges critiques serait l'introduction d'un paramètre binaire ajustable dans le terme de groupe de renormalisation. Un

objectif pourrait être celui de modéliser simultanément les équilibres de phase de la région critique et classique en utilisant un ou deux paramètres d'interaction binaire.

Close to criticality, the microscopic fluid contains non-ordered arrangements of pockets of random densities, which extends beyond several levels of coarse-graining. In the continuous transition to the critical point, the distinction between the gas and liquid phases vanishes, often referred to as the zero of the order parameter, where the correlation lengths of the density pockets become effectively infinite. The existence of collective fluctuations in densities at long-ranges is verifiable in the scattering of light passed through the medium, giving the critical colouring (opalescence) that was exploited in Chapter 4.

The divergence of the correlation length in the vicinity of the critical point is accountable with theories involving long-range density fluctuations. The prediction of critical points and stability limits, both of which are directly applicable to petroleum industries and supercritical fluid extractions, is usually done using equations of state (EoS). Cubic EoS with mean-field approximations, the latter of which do not take into account correlation lengths, tend to fail at the critical region. The same applies to the PC-SAFT EoS, where the perturbation expansions are formulated around the radial distribution function of the repulsive hard sphere, accounting for only short-range correlations. Privat et al. claimed that PC-SAFT can possibly exhibit two critical points for simple compounds, which is physically inconsistent [338]. By parameterizing model parameters to the critical temperature and pressure, a compromise in the accuracy between subcritical and supercritical regions is somewhat reached, although very limited success is expected for calculations very far from the critical point. Intuitively, the model should be equipped with two sets of parameters, for regions far and near to the critical region, so as to 'switch' effectively between the fluid states.

Such tedious parameterization could be avoided by incorporating a theory which incorporates long-range density fluctuations at the critical region, while reverting to classic fluid behaviour away from the critical point. Two approaches to have some success in this regard are the crossover equations, and the renormalization group (RG) theory. The former uses universal scaling laws asymptotically close to the critical point to accurately reproduce critical behaviour, and necessarily reduces to the ideal gas limit when extrapolated to low densities. The crossover equations have been coupled with variations of the SAFT models to represent thermodynamic properties of *n*-alkanes and 1-alkanols, with promising results [339, 340, 341, 342, 343, 344, 345, 346, 347, 348, 349, 350]. A disadvantage of the method is the introduction of several adjustable parameters required to represent thermodynamic properties, even for pure compounds. The renormalization group theory mostly commonly applied to engineering EoS is that of White [351], who first formulated the RG theory based on intermolecular potentials and introduced a Van der Waals (VdW)-like attraction accounting for diverging wavelengths in density. White used a phase-space cell method [352] to account for successive contributions from increasingly long wavelengths. White's theory was re-evaluated for non-VdW fluid theories [353], before being extended to mixtures [354, 355, 356, 357]. In the framework of SAFT, White's RG theory has been applied for pure components [358, 359, 360, 361], and for mixtures [356, 359, 362]. Tang and Gross [363] combined the PC-SAFT EoS, the density functional theory and White's RG theory to calculate surface tensions up to the critical point. A scheme whereby the number of RG parameters could be reduced, was introduced therein.

In this chapter, we use the PC-SAFT EoS based on White's renormalization group corrections to model the critical profiles of binary mixtures obtained experimentally in Chapter 4. The phase-space cell (PS) approximation and the isomorphic (I) approximation methods will be used for mixture calculations. For brevity, the former will be denoted as PC-SAFT-RG-PS, and the latter PC-SAFT-RG-I. Multipole terms have not been included in this work. We begin with a review of the mixture approximation methods, before presenting the results and discussions.

6.1 Recursive renormalization procedure for mixtures

The recursive nature of the RG corrections stems from the way similar wavelengths of a long-range density fluctuation can be binned in representative intervals, with the contributions to the overall Helmholtz energy from each interval being recursively accounted for. Each interval is renormalized with respect to the previous bin, such that only the contributions resulting from a change in wavelengths are captured. If we consider Figure 6.1, where the contributions to the Helmholtz energy due to density fluctuations f, resemble a smooth ramp plateauing at increasingly long

wavelengths λ. L signifies a cutoff length, where wavelengths less than L can be captured by the PC-SAFT EoS without RG corrections. If f_n is the Helmholtz energy contribution of any interval with the index n, then the next interval with a higher wavelength will contribute an additional δf_{n+1} larger than its predecessor. In other words, the Helmholtz energy *density* for the n^{th} recursive renormalization step is:

$$f_n = f_{n-1} + \delta f_n \tag{6.1}$$

where $f = a\rho$ is the Helmholtz energy density, with a being the reduced Helmholtz energy, and ρ the number density in $1/\text{Å}^3$. The renormalization procedure 'sees' only the contributional part of each bin (δf_n); thus there is no double counting. An infinite number of intervals should be discretized along the curve, although in practice, the contributions δf_n tails off at the plateau region, where successive intervals do not bring about any further significant contributions and the recursion converges. The overall Helmholtz energy density is thus:

$$f^{total} = f^{PC-SAFT} + \sum_{n=1}^{\infty} \delta f_n \tag{6.2}$$

The Helmholtz energy density $f^{PC-SAFT}$ naturally takes into account all the short-range fluctuations, and is the product of the number density ρ and the contributions in Eqn. (2.25).

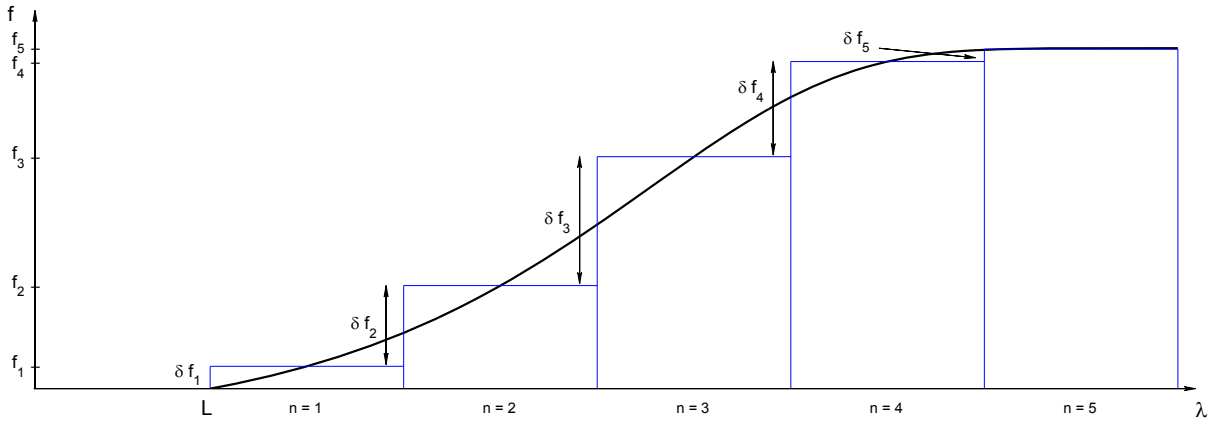

Figure 6.1: Schematic diagram showing the procedure for recursively renormalizing the Helmholtz energy contribution f due to density fluctuations of increasing wavelengths λ. Wavelengths shorter than L are considered short-range and does not feature in the method. The thick black line is traced by successive bins (blue bars) of representative wavepackets of index n, where only the contributional part δf_n is accumulated in the final f value as one traverses the curve. As n increases, the contribution δf_n becomes infinitesimally small, and the procedure can be assumed complete after five such intervals have been assessed.

6.1.1 Phase-space cell approximation

Wilson introduced the phase-space cell approximation for the semiquantitative analysis of the behaviour of systems near the critical point [352, 364]. In this approximation, the fluid is divided up into sufficiently small cells, such that long-range correlations can be neglected, and the mean-field theory approximates the molecular interactions within the cell. Each cell is then replaced with a representative molecule, and a coarse-graining procedure applied, where potential between cells are now approximated with the mean-field theory. This process is repeated until the entire physical space of the fluid is covered.

When applied to mixtures, the fluctuations can be calculated in density of each component independently of the other components density fluctuations. In this approach, the corrections for increasingly longer wavelengths are

given by:

$$\delta f_n(\rho_1,\rho_2) = -K_n \ln \frac{\int_0^{\min(\rho_2,\rho_2^{\max}-\rho_2)} \int_0^{\min(\rho_1,\rho_1^{\max}-\rho_1)} \exp\left(-\frac{G_n^D}{K_n}\right) d\tau_1 d\tau_2}{\int_0^{\min(\rho_2,\rho_2^{\max}-\rho_2)} \int_0^{\min(\rho_1,\rho_1^{\max}-\rho_1)} \exp\left(-\frac{G_n^0}{K_n}\right) d\tau_1 d\tau_2} \tag{6.3}$$

with the coefficients K_n defined as

$$K_n = \frac{k_b T}{(2^n L)^3} \tag{6.4}$$

The integral is taken over all possible amplitudes τ of density fluctuations, with the integration bounds ensuring that the densities cannot fluctuate to nonsensical values, i.e. below zero and above the density of closest segment packing, $\rho_i^{\max} = \sqrt{2}/\left(m_i d_i^3\right)$. The cutoff length L for a mixture is calculated from a mixing rule:

$$L^3 = \sum_{i=1}^{n} x_i \hat{m}_i L_i^3 \tag{6.5}$$

with

$$\hat{m}_i = \frac{m_i}{\sum_i x_i m_i} \tag{6.6}$$

The expressions G_n^D and G_n^0 in Eqn. (6.3) refer to the density fluctuations for the long-range and short-range attractions, respectively. The functionals are given as:

$$G_n^D = \frac{f_{n-1}(\rho_1+\tau_1,\rho_2+\tau_2) + f_{n-1}(\rho_1-\tau_1,\rho_2-\tau_2)}{2} - f_{n-1}(\rho_1,\rho_2) + \frac{16}{7}\pi\tau^2 \sum_{i=1}^{2}\sum_{j=1}^{2} x_i x_j m_i m_j \sigma_{ij}^5 \xi_{ij} \frac{\epsilon_{ij}}{kT} \frac{\phi_{ij}}{2^{2n+1} L_{ij}^2} \tag{6.7}$$

$$G_n^0 = \frac{f_{n-1}(\rho_1+\tau_1,\rho_2+\tau_2) + f_{n-1}(\rho_1-\tau_1,\rho_2-\tau_2)}{2} - f_{n-1}(\rho_1,\rho_2) + \frac{16}{9}\pi\tau^2 \sum_{i=1}^{2}\sum_{j=1}^{2} x_i x_j m_i m_j \sigma_{ij}^3 \xi_{ij} \frac{\epsilon_{ij}}{kT} \tag{6.8}$$

where $\tau = \tau_1 + \tau_2$. The combining rules for the three pure RG parameters ϕ_i, ξ_i, L_i are given by:

$$\phi_{ij} = \frac{1}{2}\left(\hat{m}_i \phi_i + \hat{m}_j \phi_j\right) \tag{6.9}$$

$$\xi_{ij} = \sqrt{\xi_i \xi_j} \tag{6.10}$$

$$L_{ij} = \sqrt{L_i L_j} \tag{6.11}$$

The quantity ϕ_i represents the average gradient of the considered wavelet, ξ is a characteristic constant accounting for segment-segment shielding effects (correlation hole effects), and L is the cutoff length as explained previously. The parameterization of these three RG parameters is discussed in § 6.1.3.

6.1.2 Isomorphic approximation

Fisher [365] developed the principle of isomorphism in critical phenomena by assuming that the universal property of a mixture near its critical point is isomorphic to that of a one-component fluid, provided that appropriate thermodynamic variables are kept constant. Under this assumption, the RG theory can be applied to mixtures in the same way as to pure fluids. Expression for mixture calculations using the isomorphic assumption are trivially

reduced to those suitable for pure fluid calculations, starting with the recursive contributions to the Helmholtz energy for Eqn. (6.2):

$$\delta f_n(\rho) = -K_n \ln \frac{\int_0^{\min(\rho,\rho^{\max}-\rho)} \exp\left(-\frac{G_n^D}{K_n}\right) d\tau}{\int_0^{\min(\rho,\rho^{\max}-\rho)} \exp\left(-\frac{G_n^0}{K_n}\right) d\tau} \tag{6.12}$$

with the short- and long-range attraction potentials given as:

$$G_n^D = \frac{f_{n-1}(\rho+\tau) + f_{n-1}(\rho-\tau)}{2} - f_{n-1}(\rho) + \frac{16}{7}\pi\tau^2 \sum_{i=1}^{2}\sum_{j=1}^{2} x_i x_j m_i m_j \sigma_{ij}^3 \xi_{ij} \frac{\epsilon_{ij}}{kT} \frac{\bar{w}^2\bar{\phi}}{2^{2n+1}L^2} \tag{6.13}$$

$$G_n^0 = \frac{f_{n-1}(\rho+\tau) + f_{n-1}(\rho-\tau)}{2} - f_{n-1}(\rho) + \frac{16}{9}\pi\tau^2 \sum_{i=1}^{2}\sum_{j=1}^{2} x_i x_j m_i m_j \sigma_{ij}^3 \xi_{ij} \frac{\epsilon_{ij}}{kT} \tag{6.14}$$

The quantities $\bar{w}$ and $\bar{\phi}$ are evaluated from:

$$\bar{w} = \sum_{i=1}^{n} x_i \hat{m}_i \sigma_i^2 \tag{6.15}$$

$$\bar{\phi} = \sum_{i=1}^{n} x_i \hat{m}_i \phi_i \tag{6.16}$$

where the expressions for L, $\hat{m}_i$ and ξ_{ij} have been defined in Eqns. (6.5), (6.6), and (6.10) respectively. The integrals in Eqns. (6.3) and (6.12) are solved using the trapezium rule, with the 400 equidistant density steps between zero and the maximum density, i.e. $\Delta\rho = \rho^{\max}/400$. Detailed numerical procedures for implementing the RG expressions in PC-SAFT can be found in Bymaster et al. [361], and Tang and Gross [362].

The two approximation methods for binary mixtures have the same expression for short-range density fluctuations G_n^0. For long-range density fluctuations G_n^D, the PC-SAFT-RG-PS uses combining rules for the cross RG parameters (subscript ij), i.e. it deals with pair interactions between different components (ϕ_{ij} and L_{ij}). On the other hand, the PC-SAFT-RG-I approach resembles a pure fluid calculation, and pair interactions are replaced by an average molar weighted value ($\bar{\phi}$ and L). The $\bar{w}$ variable is the isomorphic equivalent of σ_{ij}^2, which is adopted in Eqn. (6.7).

6.1.3 Parameterization of the PC-SAFT-RG

The RG corrections for pure fluids can be recovered by rewriting either of the mixture approximation methods for a single component. This gives the suggested set of expressions introduced by Bymaster et al. [361], which includes the third adjustable parameter ξ to allow matching of the critical density. Several authors adopt only two parameters in their implementation of White's RG method [359, 366], and oftentimes keeping one of the parameters constant, and fitting the other to critical temperature [354, 355, 360]. In this work, RG method is used as a three-parameter scheme, fitting simultaneously ϕ, L and ξ to the critical temperature, pressure and density. The first two quantities are particularly important in the modeling to follow, since the binary critical lines (in this work) start and end at the pure components' T_c and P_c. A mismatch of these properties is immediately exposed in the results, and will likely impact negatively on the intermediate portions of the curve.

RG parameters for the n-alkane series have been given by Bymaster et al. [361] and further by Tang and Gross [362]. The parameters for ethanol, 1-propanol and 1,1,1,2-tetrafluoroethane are determined in this work by fitting the parameters ϕ, L and ξ to their respective T_c, P_c and ρ_c. For the two alcohols, the parameters m, σ, ϵ, κ^{AB}, and ϵ^{AB} retain their original values given in the early work of Gross and Sadowski [94]. 1,1,1,2-tetrafluoroethane is parameterized in two parts, first as a non-polar molecule with no RG corrections - this yields the m, σ, and ϵ values that ideally describe the P^{sat} and ρ^L for the classical region. Thereafter, the three RG parameters are fitted to the

critical points. Literature values for the parameterization are taken from Daubert et al. [68]. While the application of three adjustable parameters in fitting three given properties appears a trivial exercise, many difficulties were encountered in the parameterization process. The RG parameters are closely correlated and do not complement each other well, with the result that either the critical temperature, or pressure, is matched, but rarely both. In addition, the matching of the critical density is particularly difficult due to the flatness of the T-ρ behaviour in the vicinity of the critical region, where numerical noises and multiple zero first derivatives occur. While all three critical properties were included in the regression routine, the parameters in this work have a higher tendency towards matching the critical temperature. The list of parameters used for this work are presented in Table 6.1, and a comparison between the calculated critical properties and the literature data is given in Table 6.2 for the newly determined compounds.

The parameterization of the RG parameters has been identified as a weakness of the model, since the regression of three parameters would require at least four reference data or more. Tang and Gross [363] suggested a scheme to reduce the number of parameters in the RG corrections, by fixing the value of L and ξ to 2σ and $1/m$, respectively. While this approximation is true for most pure compounds, the remaining ϕ parameter can match only one of the three critical properties. This approach is unsuitable for critical point modeling, where both T_c and P_c of the pure compound are particularly important. A possible solution is to re-define the entire set of pure parameters (geometric and energetic), along with the three RG parameters, to fit full-range vapour pressures, liquid densities, as well as critical properties.

Table 6.1: PC-SAFT-RG parameters used for this work. The critical temperatures, pressures and densities to which the RG parameters were regressed, were taken from Daubert et al. [68]. The m, σ, ϵ, κ^{AB} and ϵ^{AB} values for the n-alkanes and 1-alkanols are the same values as those originally published by Gross and Sadowski [93, 94].

Compound	m	σ (Å)	ϵ/k (K)	κ^{AB}	ϵ^{AB}/k (K)	ϕ	L/σ	ξ	Ref [a]
propane	2.0020	3.6184	208.11			20.37	1.63	0.397	1
n-butane	2.3316	3.7086	222.88			23.43	1.75	0.304	1
n-pentane	2.6896	3.7729	231.20			25.30	1.83	0.261	1
n-hexane	3.0576	3.7983	236.77			33.25	2.24	0.205	1
n-heptane	3.4831	3.8049	238.40			38.10	2.35	0.173	1
n-octane	3.8176	3.8373	242.78			42.06	2.63	0.155	1
methanol	1.5255	3.2300	188.90	0.0352	2899.49	17.4	1.57	0.38	2
ethanol	2.3827	3.1771	198.24	0.0324	2653.38	19.99	1.80	0.304	This work
1-propanol	2.9997	3.2522	233.40	0.0153	2276.78	20.95	1.90	0.284	This work
1,1,1,2-tetrafluoroethane (R134a)	3.2388	3.0220	170.80			23.17	1.83	0.262	This work

[a] References: [1] A. Bymaster, C. Emborsky, A. Dominik and W.G. Chapman. *Ind. Eng. Chem. Res.*, 47:6264-6274, 2008.
[2] X. Tang and J. Gross. *Ind. Eng. Chem. Res.*, 49:9436-9444, 2010.

Table 6.2: Critical properties of compounds with new parameters determined in this work for the PC-SAFT-RG, compared with literature values and the original PC-SAFT. Literature values are taken from Daubert et al. [68], and not from the experimental work in Chapter 4. The PC-SAFT values are those calculated using their original parameters from Refs. [93, 94].

	T_c (K)			P_c (MPa)			ρ_c (kg/m^3)		
Compound	lit	RG	PC-SAFT	lit	RG	PC-SAFT	lit	RG	PC-SAFT
ethanol	513.92	513.75	533.13	6.15	6.35	8.34	275.86	283.78	263.63
1-propanol	536.78	535.43	554.58	5.18	5.35	6.75	274.41	266.69	271.87
R134a	374.30	372.25	383.90	4.06	4.09	4.88	507.62	497.66	505.78

6.2 Results and Discussion

6.2.1 Pure components

Figure 6.2 gives a graphical comparison between the two different forms of the PC-SAFT EoS in modeling pure component VLE data of ethanol, 1-propanol and R134a. Literature values are given in their corresponding symbols, with the critical point highlighted by the closed symbol. The original PC-SAFT (dashed line) performs well away from the critical region, but over-predicts the critical points, as expected. The PC-SAFT-RG (solid line) resembles the original PC-SAFT at regions away from the critical point, where long-range density fluctuations are absent. In the vicinity of the critical points, density fluctuations longer than the cutoff length L are encountered, and the renormalization group corrections become significant. The improvements in the phase equilibrium description are clearly seen in both figures, particularly in the T-ρ diagram, where a flat, rather than parabolic, profile is achieved at the critical vicinity. At a temperature approach of ± 2 K to the critical temperature, one may inspect how closely the law of critical universality is conformed by the two models. For a pure component at the vicinity of the critical point:

$$\rho^L - \rho^V = \vartheta\,(T_c - T)^\gamma \tag{6.17}$$

where γ has been introduced earlier in Chapter 4 as the universal critical constant equaling 0.325. We proceed to plot $\ln(\rho^L - \rho^V)$ against $\ln(T_c - T)$ for ethanol, 1-propanol and R134a, using both PC-SAFT and PC-SAFT-RG. The PC-SAFT-RG yields the slopes 0.330, 0.333 and 0.322 for the three compounds respectively, i.e. the model calculations scale correctly to experimental observations at the critical region. The values from the PC-SAFT, in the same order, are less correct - 0.498, 0.498, 0.497 - which resembles the same behaviour as cubic EoS at the critical region ($\gamma = 0.5$).

6.2.2 Binary mixtures

In most cases, the well-documented Heidemann and Khalil method [370] was used for critical point calculations. By considering the criteria for phase stability and criticality, it was shown that for stability:

$$\left[A - A_0 - \sum_{i=1}^{N} \mu_{i0}\Delta n_i\right]_{T_0,V_0} > 0 \tag{6.18}$$

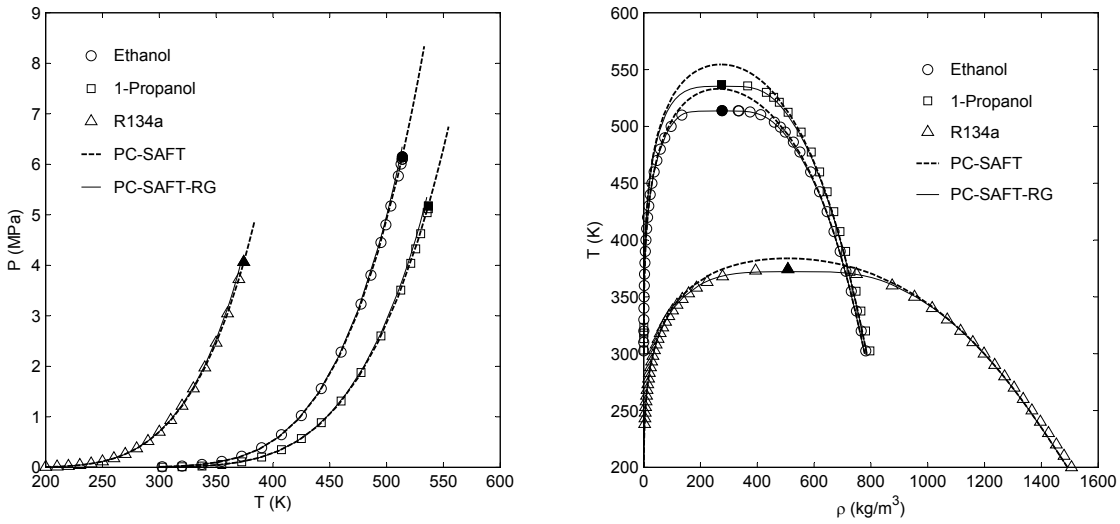

Figure 6.2: Saturated vapour pressures (*right*) and coexisting vapour and liquid densities (*left*) of ethanol, 1-propanol and R134a. Comparison between the PC-SAFT and the PC-SAFT-RG EoS, and experimental data [68, 367, 368, 369].

The Helmholtz free energy can be extended in Taylor series, to give the two criteria for critical points:

$$\sum_j \sum_i \left(\frac{\partial^2 A}{\partial n_j \partial n_i} \right) \Delta n_i \Delta n_j = 0 \tag{6.19}$$

$$\sum_k \sum_j \sum_i \left(\frac{\partial^3 A}{\partial n_k \partial n_j \partial n_i} \right) \Delta n_i \Delta n_j \Delta n_k = 0 \tag{6.20}$$

subject to the condition that the determinant of a matrix $\mathbf{Q}$ with elements:

$$q_{ij} = \left(\frac{\partial^2 A}{\partial n_j \partial n_i} \right)$$

is zero, and that $\mathbf{\Delta n} = (\Delta n_1,\ \Delta n_2,\ \ldots,\ \Delta n_N)$ contains non-zero entries. We use numerical derivatives to solve for PC-SAFT the sets of $\{x, T, V\}$ conditions satisfying Eqns. (6.19) and (6.20). Solution strategies and flowcharts for implementing the Heidemann and Khalil method are given by Stockfleth and Dohrn [371], and by Arce and Aznar [372].

The above method fails when applied to the PC-SAFT-RG variants, due to the large level of numerical noise encountered when taking numerical derivatives. This is illustrated in Fig. 6.3, which plots the values of the criterion of Eqn. (6.20) against volume, at a constant composition, for the system propane + *n*-butane using the PC-SAFT and PC-SAFT-RG. At each point, the criterion of Eqn. (6.19) has already been satisfied; thus the critical volume is solved as the root of each curve. While a unique solution $\{V, T\}$ can be found for both curves, the erratic behaviour of the PC-SAFT-RG is undesirable, since the first derivative changes sign rapidly, and regular root-searching methods that rely on the calculation of gradients are likely to be ineffective. In this work, we apply the Heidemann and Khalil method to the original PC-SAFT, i.e. $\{T_c, P_c\} = f(x_c)$, whereas for PC-SAFT-RG EoS we retrieve the critical compositions and pressures by plotting closely intervalled isotherms, with small approaches towards the critical points, i.e. $\{x_c, P_c\} = f(T_c)$.

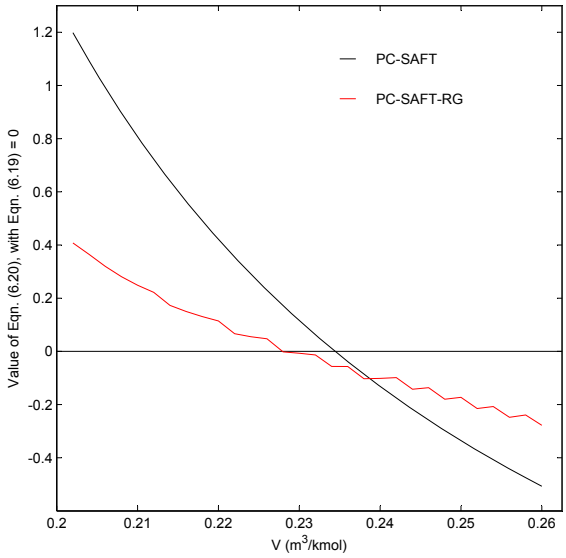

Figure 6.3: Behaviour of the triple sum criteria of the Heidemann and Khalil method, Eqn. (6.20), as a function of volume, using the PC-SAFT and the PC-SAFT-RG EoS. Calculations based on an equimolar propane + *n*-butane system, with pure parameters taken from Ref. [93] and Table 6.1. No binary parameters were used for either models.

The ability of the PC-SAFT-RG variants in matching the critical points of pure compounds is reflected positively in mixture calculations. We illustrate this with the PC-SAFT-RG-PS for the *n*-butane + methanol system. In Fig. 6.4, the previously observed azeotrope at 423.1 K is replaced correctly by two separate critical points, and a monophase between them. Isotherms above the critical temperature of *n*-butane (e.g. 443.2 K) are also improved significantly. Furthermore, a single binary interaction parameter of $k_{12} = 0.06$ for the PC-SAFT-RG-PS could be used in modeling several supercritical isotherms, as opposed to the PC-SAFT which requires temperature-dependent parameters for this system.

While the overall VLE representation from the PC-SAFT-RG appears conclusively superior than PC-SAFT, it remains to be seen whether both mixture VLE and critical behaviour can be calculated using a single interaction parameter. For this investigation to be meaningful, the supercritical VLE data, generally isothermal, should be measured up to the actual critical point. If this is not possible, it should approach, coherently, the critical point measured by a different apparatus (e.g. that given in Chapter 4). We choose as the binary system propane + *n*-butane, using isothermal VLE data from Refs. [215, 373] for T = 343 - 403 K, and critical data from the measurements in Chapter 4. For each model in Fig. 6.5, we fit the single binary interaction parameter k_{12} to the subcritical, but not supercritical, isotherms, i.e. T = 343 and 363 K. The reason for adopting this choice is that we noticed the four supercritical isotherms (T = 373 - 403 K) from Kay [215] are not consistent with our critical measurements. This has been shown previously in Fig. 4.6 as closed square symbols (■). Additionally, subcritical isotherms are measured with lower uncertainties than supercritical ones, as measurement uncertainties usually increase in the vicinity of the critical point. In general, the PC-SAFT-RG variants require a much larger binary parameter than the original PC-SAFT, in absolute terms, since focus is placed on the entire fluid state. In Fig. 6.5, all three EoS resemble one another within the two subcritical isotherms, which is consistent with the theory. At the critical region, the original PC-SAFT expectedly overestimates the

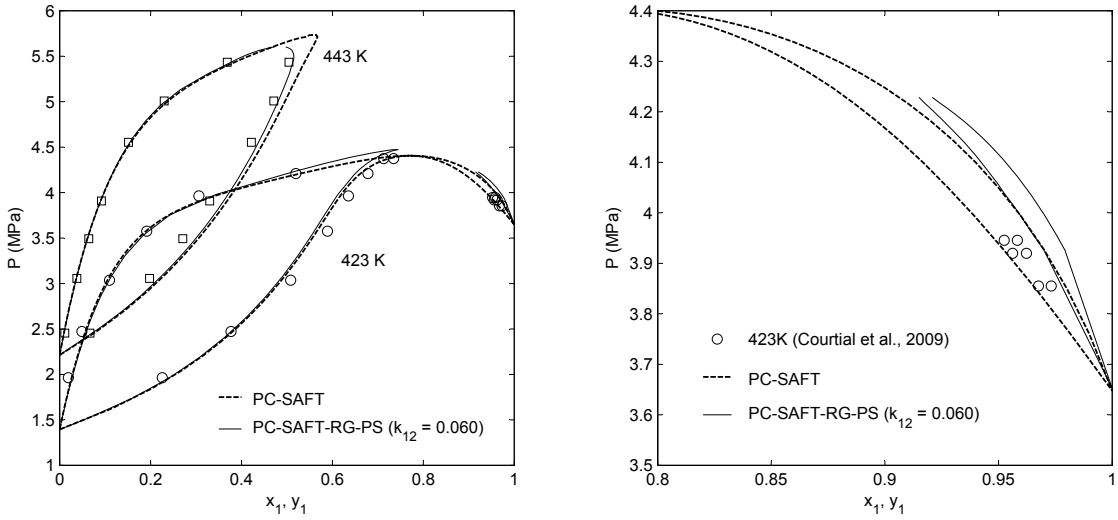

Figure 6.4: Modeling results for the *n*-butane (1) + methanol (2) system, at 423.1 and 443.2 K, using the PC-SAFT and PC-SAFT-RG-PS EoS. PC-SAFT uses a $k_{12} = 0.0658$ value for the 423 K isotherm, and $k_{12} = 0.0778$ for 443 K. Pure parameters for the PC-SAFT EoS were taken from [93, 94] and for the PC-SAFT-RG-PS from Table 6.1. The right figure is a zoom of the *n*-butane-rich region, where a second phase envelope results in the second critical point. This behaviour was supported by experiment [232].

critical point. The isomorphic approximation resembles the original PC-SAFT for most of the composition, but shows improved results near the critical region. The PC-SAFT-RG-PS applies the most renormalization corrections to the isotherms, and shows the best agreements with experimental data for the entire fluid state. The critical points determined by the models for each supercritical isotherms are given as the closed symbol corresponding to their colour. The addition of the RG corrections may also lead to unconventional values for the binary parameter, with a negative value ($k_{12} = -0.008$) observed for an alkane-alkane system. The same phenomenon was also observed with Tang and Gross [362] in their modeling of *n*-alkane mixtures. In the right-hand side of Fig. 6.5, the critical points of each supercritical isotherm is compared with the Redlich-Kister relation obtained from this work. While the two PC-SAFT-RG variants show some improvements to the PC-SAFT, they continue to overestimate the mixture critical points in terms of pressure.

It may be suggested that the k_{12} value within the two PC-SAFT-RGs should be fitted to *both* the mixture VLE and critical data, for a comprehensive description of the entire fluid state. However, we show in Fig. 6.6 that even such a compromising approach can become difficult, when dealing with large transformations in fluid properties across different fluid states. For a particular isotherm at 393.2 K, we vary the k_{12} value for the PC-SAFT-RG-PS in an attempt to match closely the VLE data, the critical composition ($x_p = 0.658$) and the critical pressure ($P_c = 4.28$ MPa). The latter two properties are obtained using the Redlich-Kister constants in Table 4.5 and Eqns. (4.3) - (4.4). It can be seen in the figure that the k_{12} which fits optimally the VLE data gives also the approximate value for x_c, but overestimates P_c. When P_c is represented correctly, with a different k_{12} value, the other two aspects are badly compromised. Each of the properties favour a different k_{12}; thus using a single binary parameter to accomplish all three aspects may prove to be unsatisfactory. Unlike before, a second parameter in the form of l_{ij} provided minimal

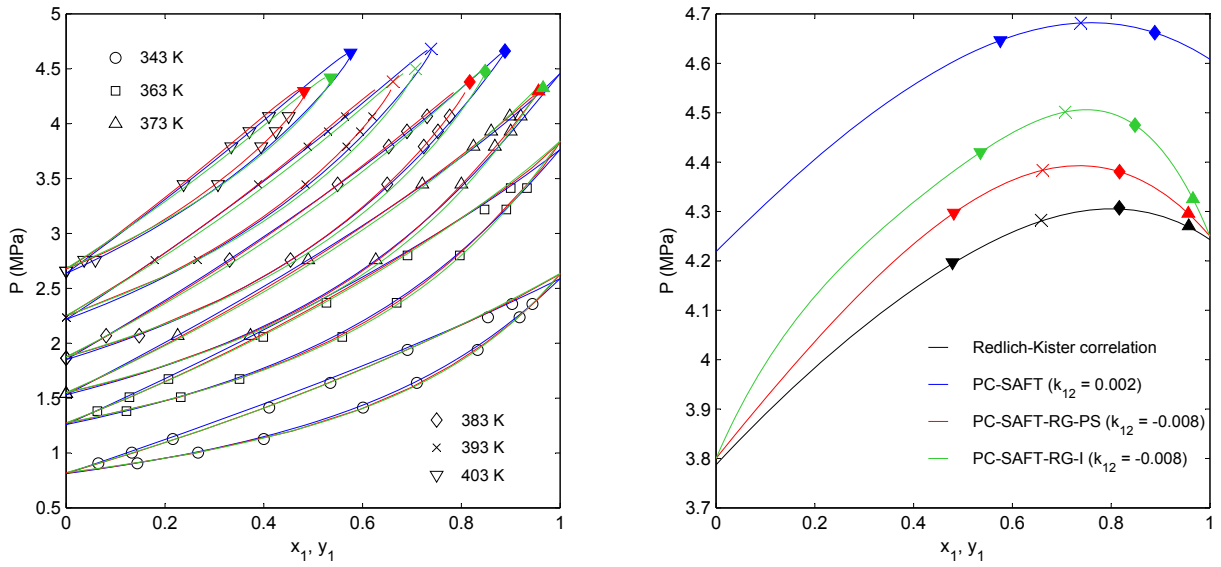

Figure 6.5: *left*: Modeling of subcritical and supercritical isotherms of the propane (1) + *n*-butane (2) system, using the PC-SAFT (—), PC-SAFT-RG-PS (—) and PC-SAFT-RG-I (—) EoS. The k_{12} parameters were adjusted to fit the VLE data, the latter taken from Refs. [215, 373]. The critical points determined for each supercritical isotherms are given as the closed symbol corresponding to the colour of the models. *right*: An enlarged view of the pressure scale from 3.7-4.7 MPa, where complete critical lines have been constructed using the optimal k_{12} values from VLE. The symbols have the same meaning for both figures. Redlich-Kister constants are taken from Table 4.5. Pure parameters taken from Ref. [93] and Table 6.1.

improvements, and often adversely affected the VLE at regions far from the critical point. If any additional binary parameters are to be introduced, it should manifest in the RG corrections, e.g. within the combining rules in Eqn. (6.9) - (6.11).

In modeling the experimental work from Chapter 4, it was chosen to neglect the binary interaction parameter altogether. One of the reasons has been mentioned previously, that only limited improvements can result from a single k_{12} value. By setting $k_{12} = 0$ for all models, one is able to observe the quality of the models, rather than the fit quality, in the critical region. A comparison between the PC-SAFT, PC-SAFT-RG-PS, and PC-SAFT-RG-I EoS will be on equal grounds, as the RG term aside, the three models are essentially identical, with the same geometric and energy parameters. Several authors working with PC-SAFT EoS in the critical region have used a *re-scaled* set of pure parameters by fitting them to critical properties, acentric factor, reduced ranges of vapour pressures and liquid densities, or a combination thereof [295, 372, 374, 375, 376, 377, 378, 379]. This approach makes the model very powerful at the critical region, and we have tested in this work that such a re-scaled model requires very small binary parameters to model our systems. However, the VLE representation of such re-scaled models are known to deteriorate rapidly at regions away from the critical point.

In the propane + *n*-butane system (Fig. 6.7 *left*), we have also designated a non-zero binary parameter to the PC-SAFT-RG-PS in an attempt to illustrate that, if needed, better fits to the experimental data can be achieved. The excellent agreement between the correlated model and experimental data is visualized on a *P*-*T* plane, where a k_{12} value of 0.015 matches very well the critical pressure. However, one should be aware that the same results plotted on the *T*-*x* plane would look less impressive. The representation

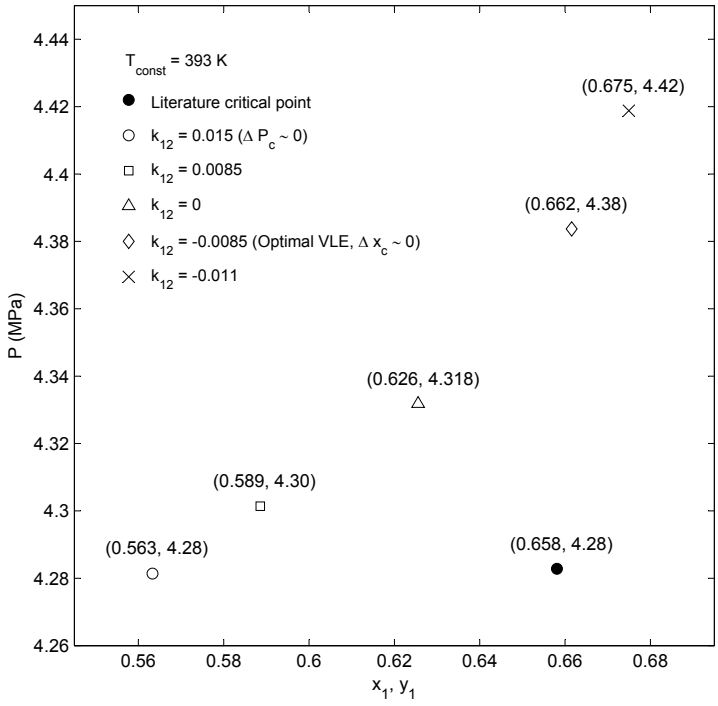

Figure 6.6: Response of the mixture critical point of the propane (1) + *n*-butane (2) system to changes in the k_{12} binary parameter of the PC-SAFT-RG-PS EoS. The system is isothermal at $T = 393.2$ K. The co-ordinate of the critical point for each different k_{12} value is given in parenthesis, i.e. (x_c, P_c).

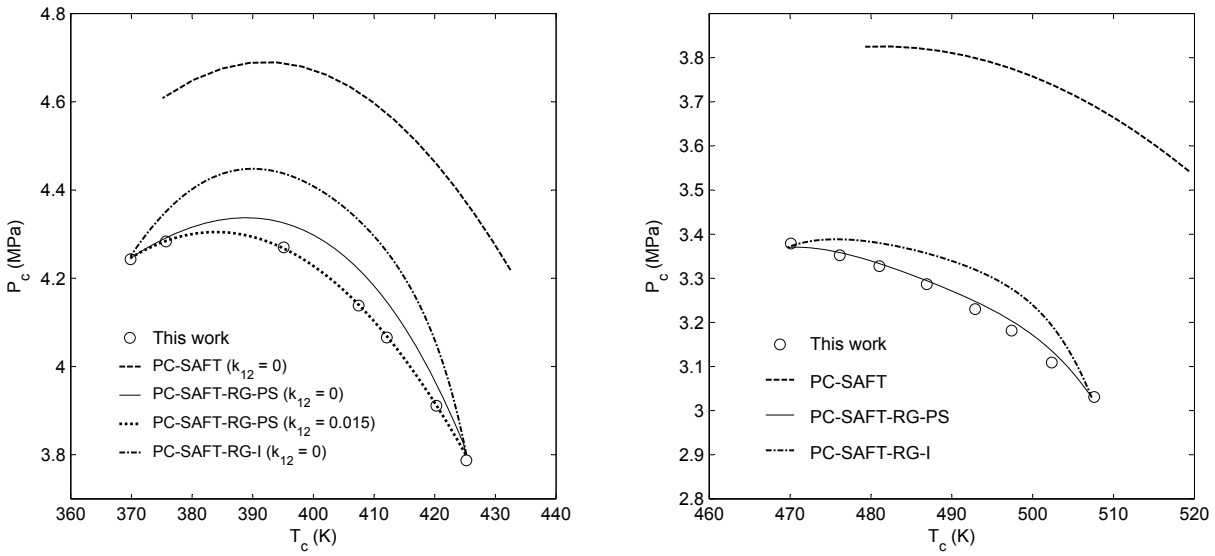

Figure 6.7: *left*: Critical line modeling of the propane + *n*-butane system, and *right*: the *n*-pentane + *n*-hexane system. Where the binary interaction parameters k_{12} are not specified, they are set to zero. Pure parameters for the PC-SAFT EoS are taken from [93], and for the PC-SAFT-RG EoS from Table 6.1.

of the original PC-SAFT is inevitably poor, due to the incorrect locations of the start and end points of the critical line, which are the pure components' critical points. The use of a fitted k_{12} value for

PC-SAFT has little bearing on the qualitative result. The use of any of the two RG variants, even with the binary parameter set to zero, is able to significantly improve the representation of the critical data. Compared to the isomorphic approximation on a zero k_{12} basis, the phase-space cell approach shows better agreement with the experimental data from this work. This is also observed with the *n*-pentane + *n*-hexane system (Fig. 6.7 *right*). The phase-space cell approximation attains both qualitative and quantitative representation of the experimental data without the aid of binary parameters. This is in agreement with Tang and Gross [362], whose study on alkane + alkane mixtures concluded the slight superiority of the phase-space cell approximation over the isomorphic approximation in representing the critical region.

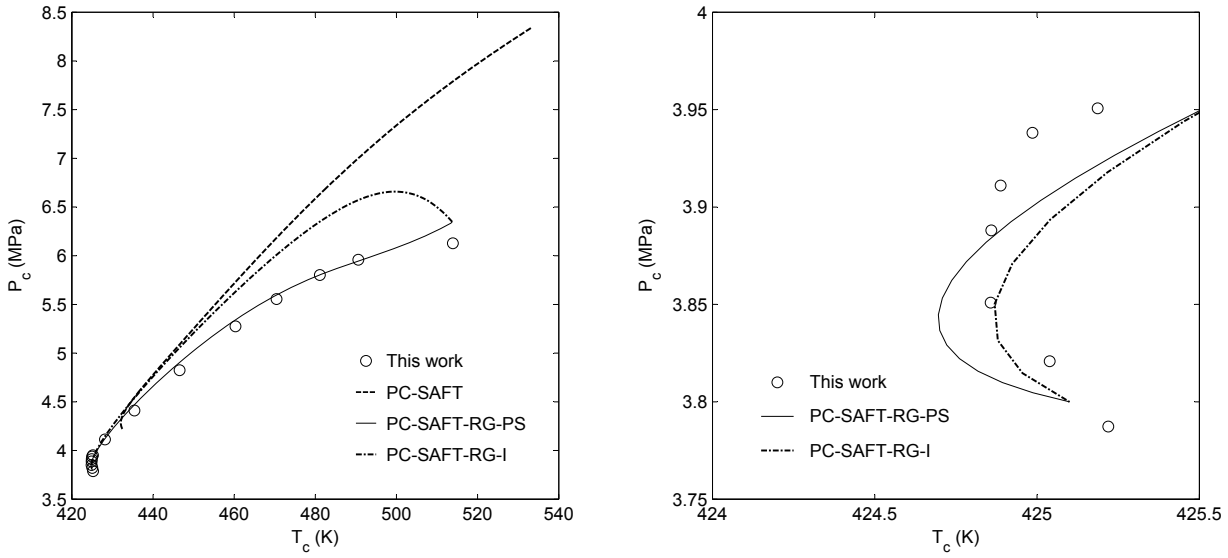

Figure 6.8: Critical line modeling of the *n*-butane + ethanol system. The *right* figure is a zoom of the *n*-butane rich region. Pure parameters for the PC-SAFT EoS are taken from [93, 94], and for the PC-SAFT-RG EoS from Table 6.1. All binary interaction parameters set to zero.

For the *n*-butane + ethanol system (Fig. 6.8), the PC-SAFT and PC-SAFT-RG-I representations proved to be poor. The critical pressure of pure ethanol for the RG variants is slightly over-predicted (see Table 6.2); thus one would expect a positive deviation for the pressure throughout the compositions. Interestingly, PC-SAFT-RG-PS were minimally affected by this factor, deviating only upon approaching pure ethanol, while maintaining a good representation of the critical data at the intermediate compositions. As the same parameters were used for both approximations, the theory behind the two different RG variants must play a role in the large differences of the results. Often with Type I Van Konynenburg and Scott phase diagrams [380] exhibiting an azeotropic behaviour, the azeotropic line is tangent to the critical line. The curvature at the pure *n*-butane approach, appears correctly described by both the PC-SAFT-RG models (Fig. 6.8 *right*). This suggests that the limit of azeotropic behaviour may also not be too badly predicted by the two RG variants.

The representations of the *n*-pentane + ethanol system (Fig. 6.9 *left*) from both RG approximation methods are reasonable, with a much improved result from the PC-SAFT-RG-I EoS. Regarding the ethanol + *n*-hexane system (Fig. 6.9 *right*), there appears to be a receding behaviour of the critical line, calculated by the RG models, in the direction of the pure components. The global minimum in the T-x plane is increased;

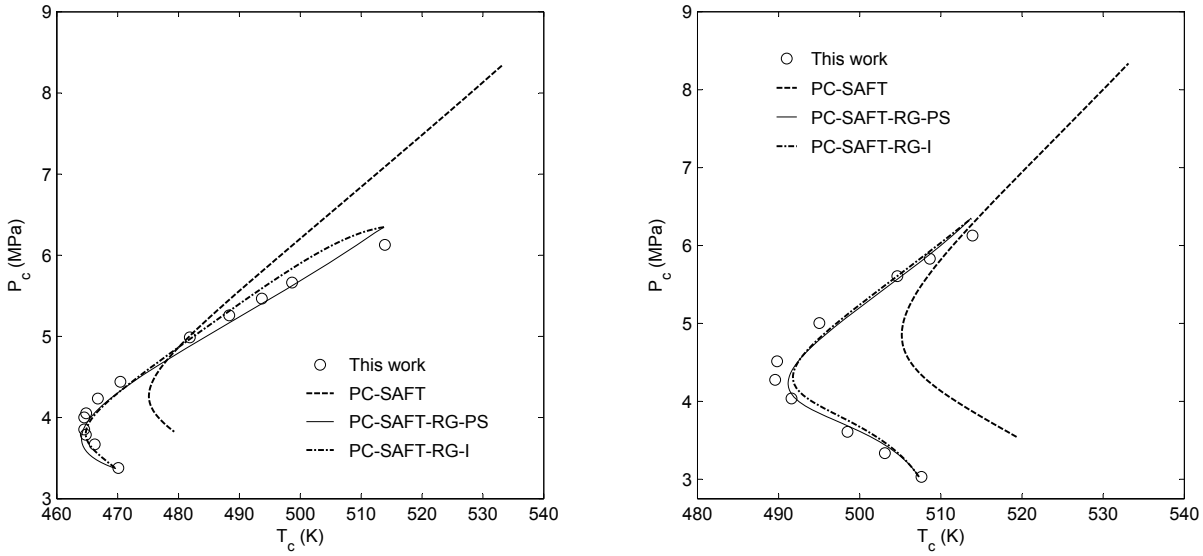

Figure 6.9: *left*: Critical line modeling of the *n*-pentane + ethanol system, and *right*: the ethanol + *n*-hexane system. All binary interaction parameters set to zero. Pure parameters for the PC-SAFT EoS are taken from [93, 94], and for the PC-SAFT-RG EoS from Table 6.1.

thus the terminal azeotrope (the point at which the azeotrope line intersects the critical line) occurs at a temperature slightly higher than anticipated. With this result, one would expect the representation of the subcritical VLE to be negatively affected as well. Upon increasing the length of the *n*-alkane chain, the aforementioned receding behaviour becomes more significant. This is observed in Fig. 6.10, where the undesirable behaviour occurs more prominently with the PC-SAFT-RG-PS than the PC-SAFT-RG-I. Referring to the ethanol + *n*-octane system, a temperature minimum no longer exists according to the PC-SAFT-RG-PS, which is inconsistent with our measurements, literature VLE [173, 381, 382] and literature critical data [221], and the remaining two models at the same zero k_{12}. A non-zero k_{12} value must be applied to the PC-SAFT-RG-PS to induce the temperature minimum again, as shown by the dotted line ($k_{12} = 0.05$). The PC-SAFT-RG-I is possibly the preferred model for the two systems in Fig. 6.10.

Figure 6.11 shows two binary systems where the models do not perform well. In the ethanol + 1-propanol system (*left*), the pure RG parameters for both pure components do not match perfectly with the literature values, and a systematic deviation was unavoidable. The feature of the propane + 1,1,1,2-tetrafluoroethane (R134a) system (Fig. 6.11 *right*) is the small pressure range that is covered by the critical line ($4.00 < P_{c,mix} < 4.25$ MPa). The pure RG parameters for 1,1,1,2-tetrafluoroethane (R134a) was regressed by prioritizing the pressure, to prevent the endpoints of the critical line from being too near one another. Regardless, the propane + 1,1,1,2-tetrafluoroethane (R134a) system would probably be best modeled considering a dipole-quadrupole Helmholtz energy contribution for R134a. Without the multipole term and a zero k_{12} value, the critical locus resembles a straight line connecting the two pure components. Application of the dipole-quadrupole term is not within the scope of this work. It was possible to *force* the qualitative shape of the curve by employing large k_{12} values for each model, although there were no quantitative results.

Table 6.3 gives a summary of the modeling results for the binary systems measured in Chapter 4. The

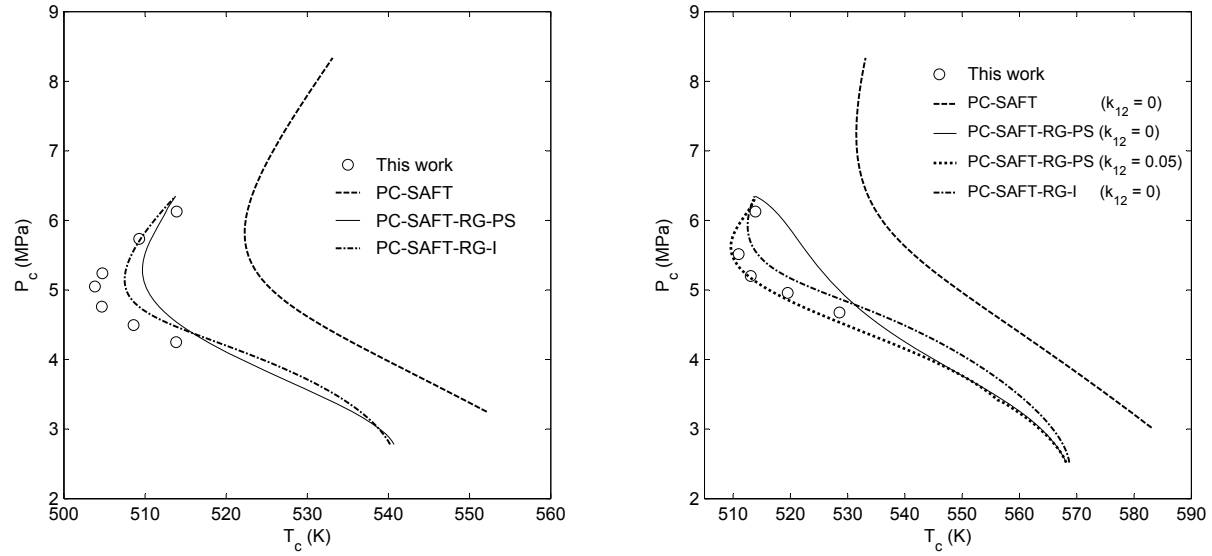

Figure 6.10: *left*: Critical line modeling of the ethanol + *n*-heptane system, and *right*: the ethanol + *n*-octane system. Where the binary interaction parameters k_{12} are not specified, they are set to zero. Pure parameters for the PC-SAFT EoS are taken from [93, 94], and for the PC-SAFT-RG EoS from Table 6.1.

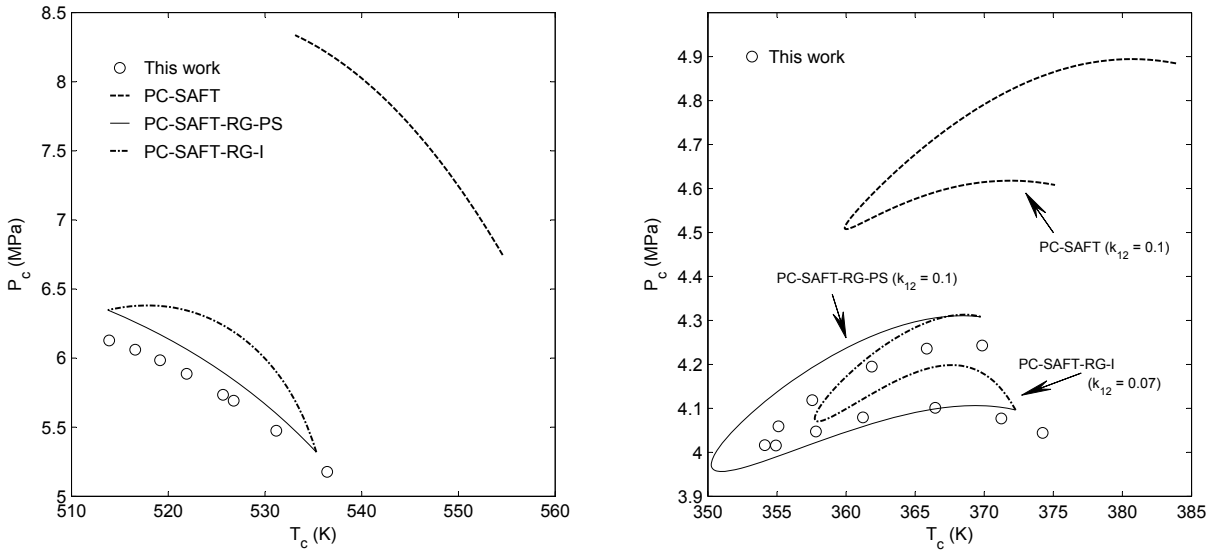

Figure 6.11: *left*: Critical line modeling of the ethanol + 1-propanol system, and *right*: the propane + R134a system. Where the binary interaction parameters k_{12} are not specified, they are set to zero. Pure parameters for the PC-SAFT EoS are taken from [93, 94], and for the PC-SAFT-RG EoS from Table 6.1.

two PC-SAFT-RG variants perform similarly for most of the systems, and it may be worthwhile to verify calculations with both approximation methods. One should note that the table gives the absolute error values in T and P, but does not emphasize the shape of the critical line depicted by each EoS, which is an important factor in assessing the overall quality of the representation. Depending on the application, it may be necessary to use a non-zero k_{12} parameter to remain coherent with VLE behaviour. Both variants of the PC-SAFT-RG were able to improve significantly the description of the critical line compared to the

Table 6.3: Comparison between the performances of the PC-SAFT and the PC-SAFT-RG models in the modeling of mixture critical points measured in this work. N_{pt} is the number of mixture measurements performed. RG-PS uses the phase space-cell approximation for binary mixtures, while RG-I uses the isomorphic approximation. $\Delta\bar{T}_c$ and $\Delta\bar{P}_c$ are the averaged absolute differences between the measured and calculated T_c and P_c. All binary interaction parameters were set to zero, unless specified otherwise.

		$\Delta\bar{T}_c$ (K)			$\Delta\bar{P}_c$ (MPa)		
System	N_{pt}	RG-PS	RG-I	PC-SAFT	RG-PS	RG-I	PC-SAFT
$C_3H_8 + C_4H_{10}$	5	1.34	0.90	6.10	0.07	0.14	0.41
$C_5H_{12} + C_6H_{14}$	6	1.08	0.35	10.4	0.02	0.07	0.49
$C_4H_{10} + C_2H_6O$	13	1.83	3.70	11.9	0.08	0.32	0.83
$C_5H_{12} + C_2H_6O$	11	2.08	2.85	15.3	0.04	0.15	0.98
$C_2H_6O + C_6H_{14}$	8	2.02	1.64	16.1	0.12	0.12	1.13
$C_2H_6O + C_7H_{16}$	6	3.95	2.52	16.8	0.22	0.12	1.11
$C_2H_6O + C_8H_{18}$	4	5.60	2.09	17.3	0.41	0.17	1.27
$C_2H_6O + C_3H_8O$	6	0.54	0.85	18.2	0.19	0.40	2.07
C_3H_8 + R134a [a]	10	2.90	2.33	6.47	0.04	0.07	0.56
Average		**2.37**	**1.91**	**13.2**	**0.13**	**0.17**	**0.98**

[a] $k_{12} = 0.1$ for both the PC-SAFT-RG-PS and the PC-SAFT. $k_{12} = 0.07$ for PC-SAFT-RG-I.

original PC-SAFT EoS. Application of the RG corrections to the ternary *n*-pentane + ethanol + *n*-hexane system is beyond the computational scope of this work, and is regarded herein as prospective work.

6.3 Concluding remarks

In this chapter, the renormalization group (RG) theory of White was applied to the PC-SAFT EoS to account for the long-range density fluctuations that characterize the critical region. The resulting PC-SAFT-RG model, employing three additional pure parameters, exhibits correctly the behaviour of universality at the critical region. At regions away from the critical point, the PC-SAFT-RG resembles the performance of the original PC-SAFT EoS [93, 94].

The PC-SAFT-RG and the original PC-SAFT EoS were applied to the critical point experiments conducted in this work, with the PC-SAFT-RG displaying promising results. New RG parameters for ethanol, 1-propanol and 1,1,1,2-tetrafluoroethane were determined and tested positively with experimental data across the entire fluid state. Two approximation methods were employed for extending the RG theory to mixtures, *viz.* the phase-space cell approximation (PS) and the isomorphic approximation (I). These two variants were applied to the critical data of binary mixtures measured in Chapter 4, showing vast improvements in the description of the critical region, compared with the original PC-SAFT. While performing similarly for most mixtures, each approximation method displays stronger cases for certain types of systems. The phase-space cell approximation tends to represent better the alkane-alkane systems, and systems of ethanol in mixture with a short hydrocarbon. The isomorphic approximation is superior for ethanol-hydrocarbon systems, where the hydrocarbon chain contains six carbon atoms or more.

Two areas of improvement have been identified for the PC-SAFT-RG. Firstly, the RG term is somewhat over-parameterized with three parameters fitting three critical properties. An alternative would be to regress the RG parameters, along with the other geometric (m, σ, κ^{AB}) and energetic (ϵ, ϵ^{AB}) parameters of PC-SAFT, to both thermodynamic (P^{sat}, ρ^{L}) and critical (T_c, P_c, ρ_c) properties. Secondly, a single binary interaction parameter can only fit the PC-SAFT-RG models to either experimental x_c-T_c or x_c-P_c data, but not both. In the event of modeling simultaneously the vapour-liquid equilibria and critical locus, PC-SAFT-RG models provide only a qualitative description of both aspects. It is possible that the introduction of another binary parameter within the RG combining rules may improve the results. It is limited to applications where acquiring general impressions of the phase behaviour across the entire fluid state is sufficient. A useful feature of the PC-SAFT-RG is that it remains extrapolative across wide temperature ranges. For systems where the mixture critical points cannot be measured, subcritical VLE data may be used to tune the binary parameter of the RG models, for it to be applied at supercritical temperatures to obtain a good *estimate* of the critical point.

Acknowledgements

The calculations in this chapter for the PC-SAFT-RG were facilitated using the code developed by Prof. Joachim Gross, who is gratefully acknowledged here.

Conclusions and Prospective Work

Experimental measurements and thermodynamic modeling are two essential elements in the ongoing research of biofuels. In the wake of increasing energy demands, there is a need to address the lack of reliable thermo-physical data, as well as improving current modeling approaches for increasingly complex compounds. These were the central themes of the thesis.

In Chapter 1, the role of biological fuels as an alternative energy source, was reviewed critically. Currently, biomass energies remain the most commonly used form of renewable energy, largely due to its wide-ranging sources, and flexibility in application. However, it is equally important to recognize the inherent flaws that reside in using biofuels, on social, economic, and environmental levels. It is of the author's opinion that biofuel legislations should be passed only after considering all three interlinking factors. Biofuels should be supplemented with other forms of existing renewable energy, for a truly carbon-reduction initiative. The understanding of the thermodynamics of biofuel is vital for implementing, safely and effectively, biofuels on a competitive level with non-renewable petroleum.

Chapter 2 is a bibliographic review, detailing the presence of intermolecular forces in nature that govern specific behaviours in fluids. The identification of pertinent forces in oxygenated compounds provides the justification for adopting a SAFT-type approach in modeling part of the work. The Perturbed-Chain Statistical Associating Fluid Theory (PC-SAFT) was chosen in this work as a theoretically sound equation of state (EoS), capable of handling associating and polar fluid behaviour, both characteristics of oxygenated compounds. The state of art of the PC-SAFT EoS was shown to achieve this goal by examining each of its Helmholtz free energy contributions in sufficient detail. The PC-SAFT is but one of several existing variations of the SAFT family equation of states, and other popular forms such as LJ-SAFT [127, 128] and SAFT-VR [383, 384] can equally be analyzed for biofuel applications in the future. A particularly exciting prospect, currently under investigation, is the application of the Group Contribution-SAFT (GC-SAFT) in the modeling of complex biofuel compounds [385, 386, 387].

The thesis focused mainly on experimental measurements under equilibrium, with Chapter 3 outlining two different apparatuses for obtaining low- and high-pressure vapour-liquid equilibrium (VLE) data. Seven binary systems, with pressures not exceeding atmospheric pressure, were measured using an ebulliometer-type apparatus based on the "dynamic-analytic" method. Two further systems, exhibiting pressures up to 5 MPa, were measured using an apparatus based on the "static-analytic" method, with two electromagnetic ROLSI™ capillary samplers. Both the setups and procedures for the two apparatuses were described in detail. Of particular emphasis was the estimation of measurement uncertainty, which is believed to be of sufficient rigour to identify weaknesses encountered during experimentation. The results from both apparatuses agreed favourably with literature data. It was identified that an intermediate

pressure region, of between 0.1 to 0.4 MPa, could not be measured as efficiently without changing the capillary size of the ROLSI™ samplers. This equipment modification may improve the results of certain isotherms measured in this work. Furthermore, the calibration of the thermal conductivity detector of the gas chromatograph is more accurately obtained when using standard, monophasic mixtures with known compositions. This may aid in reducing the uncertainties in the high-pressure measurements.

The scope of phase equilibria in biofuels is expansive. Several chemical intermediates in biofuels are large in molecular weight and often exhibit liquid-liquid (LLE) and solid-liquid equilibria (SLE). These types of equilibria deserve research merit, not only because they comprise but a small portion of existing databases, they play a major role in the separation technologies regarding biofuels. An LLE apparatus has been developed and verified in the CEP/TEP laboratory for this prospect. A schematic drawing of the LLE cell and its components are shown and explained in Fig. I:

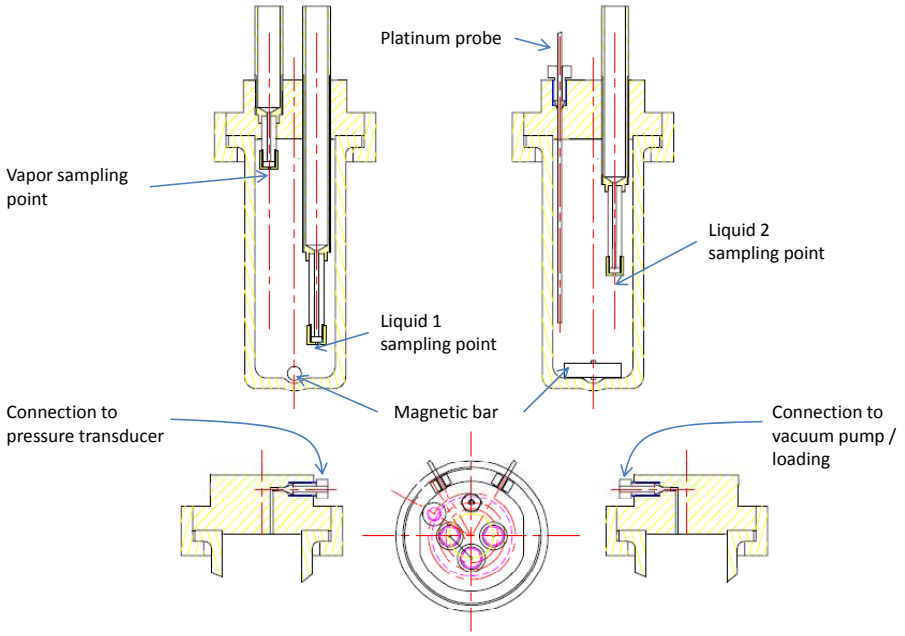

Figure I: Schematic drawing of a LLE cell suitable for measurement of liquid-liquid equilibria at atmospheric conditions. A single temperature probe and pressure measurement line provides the equilibrium T and P. The glass cell is accessed via a single loading line. Sampling of the organic and aqueous phases is facilitated at two points at different levels, using a 5 μL gas tight syringe. The apparatus requires manual sampling and injection into a calibrated gas chromatograph, i.e. it uses a "static-analytic" method.

An area of concern is the strong lack of data concerning fatty acid methyl esters (FAME), a component of biodiesel. The main difficulties in conducting their research is cost, availability, and the high fluid viscosity. There exists an opportunity for future work involving the measurement of thermodynamic properties of pure FAME and its mixtures, preferably those esters containing ten carbon atoms or more. These data are vital for model developments. Compounds that are derived from decomposition of woody matter, such as fumaric acid, vanillin and quinone, are found rarely in existing databases. These compounds exhibit mainly LLE and SLE, and contain multiple oxygenated functional groups.

Experimental critical data may have limited application in biofuel processes, but they provide valuable information for model development at the limit of phase coexistence. This is particularly relevant to

PC-SAFT, which lack constraints in the critical region. Chapter 4 presents an apparatus, using the dynamic-synthetic method, capable of measuring the critical properties of pure and multi-component systems, up to 543 K and 20 MPa. The critical phenomenon is observed via the critical opalescence in a view cell. The critical properties of up to thirteen pure components, seven binary systems, and one ternary system have been measured. The experimental results show good agreements with literature values, when available. Various mathematical models have been applied in correlating the critical properties, and the outcomes discussed. The apparatus is not well adapted for systems will large differences in volatilities, an aspect which needs improvement. Various recommendations have been suggested, the most prominent being the addition of a stirrer within the cell, and operation under static conditions. A recent modification, taking these factors into account, have been developed, giving results consistent with the dynamic setup, for pure compounds. Prospective work on mixtures of different volatilities should be conducted. A further proposal is the determination of the critical points of compounds subject to decomposition, via an extrapolation procedure [191].

Chapter 5 forms the main modeling work of this thesis, where the PC-SAFT equation of state is used to model phase equilibria of alcohols, acids, polar compounds, and water. Each functional group is examined in turn, with strategies for handling the different molecular structures and non-idealities in each case. The inclusion of appropriate Helmholtz energy contributions accounting for specific interactions, e.g. polarity, often improves both the predictability and effectiveness of the final calculation. For most instances, a single binary interaction parameter k_{12} in the dispersion contribution a^{disp} is capable of describing azeotropic and non-azeotropic systems. Due to its theoretically sound basis, the PC-SAFT can be extrapolated across wide temperature ranges without a great loss in accuracy. The binary parameter can be transferred between isobaric and isothermal conditions when modeling phase equilibria.

In modeling phase equilibria of alcohols, the inclusion of either dipolar terms discussed in this work has the positive effect of decreasing the value of the binary interaction parameter. In this way, the alcohol mixtures measured in Chapter 3 could be represented quantitatively with small binary parameters. Care should be taken to avoid spurious phase splits in the modeling of the azeotropic systems, a common feature among alcohol mixtures. The lack of modeling work done on carboxylic acids with the PC-SAFT has led to the determination of new pure component parameters for C_1 - C_6 chain acids. Adopting an approach where the κ^{AB} parameter is held constant, the proposed parameters were tested on thermodynamic properties of acids and their mixtures, with positive results. For difficult mixtures, such as the acetic acid + toluene system from this work, a second asymmetric parameter l_{12} in the dispersion can be used to tune the model for quantitative representations. The l_{12} parameter offers more flexibility to the PC-SAFT, but is less extrapolative to alternate temperatures. The polar compounds reviewed include ketones, ethers, esters and aldehydes, for which we have proposed new pure parameters for ethyl *tert*-butyl ether and seven FAMEs. For strongly polar compounds ($\mu > 2$ D), the inclusion of a contribution accounting for polarizable dipoles can lead to slight improvements in the description of phase equilibria. For FAMEs, a more concrete set of pure parameters can only be achieved in the event of more experimental data. In a mixture containing a polar and an associating compound, cross-association (solvation) must be accounted for, and this was carried out using an approach by Kleiner and Sadowski [275] to good effects. The modeling of aqueous mixtures proved a stern challenge for the model. The simultaneous description of liquid-liquid and vapour-liquid equilibrium could be achieved using both the k_{12} and l_{12} parameters.

The second half of Chapter 5 deals with the calculation of excess enthalpies and consistency testing. In

general, PC-SAFT does not perform well in excess enthalpy calculations, being both less extrapolative and more reliant on binary parameters, when compared to phase equilibria standards. A single binary parameter is often incapable of simultaneously describing the VLE and excess enthalpy. A short thermodynamic consistency testing was conducted for the VLE measurements presented in Chapter 3. The main objective here was to examine the level of consistency between the data and the model, which is generally acceptable. A more thorough investigation, involving several tests, is required to give more conclusive remarks on the data quality. The preliminary study performed here was useful in identifying most erroneous points, indicating that several datasets were possibly not fully consistent.

The modeling approach adopted in Chapter 5 is one of several possible approaches in the modeling of biofuel-related mixtures. In this work, we have not considered alternative bonding approaches, but have chosen to use the simple 2B bonding scheme for all associating compounds, apart from acids. We have omitted parameterizing new compounds for the PC-SAFT-JC (PC-SAFT + Jog and Chapman dipolar term) as it was felt that the characterization of the x_p parameter is subject to the individual modeler and needs. The goal of the chapter was to propose concrete sets of parameters for new compounds, with minimal ambiguities. We have thus set aside the parameters for PC-SAFT-JC as future work. A further modeling aspect that needs to be addressed in the future is the calculation of solid-fluid (liquid or vapor) equilibria in biofuel mixtures, using the PC-SAFT EoS [388].

In the final and sixth chapter, the PC-SAFT EoS was used to model the binary critical data measured previously in Chapter 4. To account for long-range density fluctuations that characterizes the critical region, the PC-SAFT was coupled with White's renormalization group (RG) theory, which allows the model to describe fluid properties far and near to the critical point. Two approximation methods were employed for extending the RG theory to mixtures, *viz.* the phase-space cell approximation and the isomorphic approximation. When applied to the binary mixtures of this work, the RG corrections provided significant improvements in representing the critical data, compared to the original PC-SAFT which tends to over-predict the critical properties. The RG parameters for ethanol, 1-propanol and 1,1,1,2-tetrafluoroethane were determined in the process. In several mixtures, the error between the experimental and calculated T_c and P_c were reduced to 1/10 of the value associated with PC-SAFT, upon inclusion of the RG corrections. The performances of the two approximation methods are comparable, with the phase-space cell approximation more suited for alkane-alkane systems, and the isomorphic approximation better adapted for ethanol + C_6-C_8 hydrocarbons.

The ternary *n*-pentane + ethanol + *n*-hexane system from Chapter 4 was not modeled in this work due to insufficient algorithm, and is regarded herein as prospective work. Two further recommendations for the RG term have been identified and detailed in Chapter 6. The first addresses the issue of over-parameterization in the RG term, by re-fitting *all* the possible pure parameters to both thermodynamic and critical properties. The second is the possibility of introducing a binary adjustable parameter within the RG term, in an attempt to improve the simultaneous descriptions of both mixture VLE and critical properties. At its current form, the PC-SAFT coupled with the RG term is not sufficiently accurate when describing mixture VLE and critical points at the same time.

Conclusions et Perspectives

Les mesures expérimentales et de modélisation thermodynamique sont deux éléments essentiels pour les recherches actuelles sur les biocarburants. Suite à la demande énergétique croissante, il est nécessaire de remédier au manque de fiabilité des données thermo-physiques, ainsi qu'à l'amélioration des approches actuelles de modélisation pour des composés plus complexes. Tels sont les thèmes centraux de la thèse.

Dans le chapitre 1, le rôle des combustibles biologiques comme source d'énergie alternative a été examiné de façon critique. Actuellement, les énergies issues de la biomasse demeurent une des formes les plus couramment utilisées pour les énergies renouvelables, principalement en raison de leurs sources abondantes et de la diversité dans leurs applications. Cependant, il est également important de reconnaître les défauts inhérents à l'utilisation des biocarburants au niveau social, économique et environnemental. Certains auteurs affirment que les législations sur les biocarburants doivent être transmises seulement après avoir examiné les trois facteurs de l'interconnexion. L'utilisation des biocarburants devraient être complétés par d'autres formes d'énergie renouvelable existante, pour une véritable réduction des émissions de carbone. La compréhension de la thermodynamique des biocarburants est donc vitale pour la mise en œuvre efficace et en toute sécurité des biocarburants à un niveau compétitif avec le pétrole non renouvelable.

Le chapitre 2 est une revue bibliographique, détaillant la présence de forces intermoléculaires dans la nature qui régissent les comportements spécifiques des fluides. L'identification des forces pertinentes des composés oxygénés permet de justifier, dans la partie modélisation de ce travail, l'adoption d'une approche de type SAFT. Le modèle "Perturbed-Chain Statistical Associating Fluid Theory" (PC-SAFT) a été choisie dans ce travail comme une équation d'état (EOS), capable d'aborder le comportement associatif et polaire, deux des caractéristiques des composés oxygénés. L'état de l'art de PC-SAFT EoS a été utilisé pour atteindre cet objectif en examinant chacune des contributions d'énergie libre de Helmholtz de façon suffisamment détaillée. Le PC-SAFT existe mais l'une des nombreuses variantes existantes de l'équation de la famille des équations d'état de SAFT, et d'autres formes courantes telles que LJ-SAFT [127, 128] et SAFT-VR [383, 384] pourront être également analysées pour des applications sur les biocarburants à l'avenir. Une perspective particulièrement intéressante, actuellement étudiée, est l'application de la Contribution de groupe SAFT (GC-SAFT) pour la modélisation des composés complexes de biocarburants [385, 386, 387].

La thèse porte principalement sur des mesures expérimentales à l'équilibre. Le chapitre 3 décrit deux appareils différents permettant l'obtention de données d'équilibre liquide-vapeur (ELV) à basse et à haute pression. Sept systèmes binaires, avec des pressions ne dépassant pas la pression atmosphérique, ont été mesurés en utilisant un appareil de type ébulliomètre basé sur la méthode "dynamique-analytique". Deux

autres systèmes, présentant des pressions allant jusqu'à 5 MPa, ont été mesurés en utilisant un appareil basé sur le méthode "statique-analytique", avec deux échantillonneurs capillaires électromagnétiques ROLSI™. Les deux configurations ainsi que les procédures pour les deux appareils ont fait l'objet d'une description détaillée. Un accent particulier a été mis sur l'estimation de l'incertitude, qui est censée être suffisamment précise pour identifier les faiblesses rencontrées lors de l'expérimentation. Les résultats des deux appareils concordent bien avec les données de la littérature. La conclusion et la prospective de la région de pression de travail, entre 0.1 à 0.4 MPa, ne pouvaient pas être mesurées de manière aussi efficace sans changer la taille des échantillonneurs capillaires ROLSI™. Cette modification de l'équipement peut améliorer les résultats de certains isothermes étudiés dans ce travail. Par ailleurs, l'étalonnage du catharomètre du chromatographe en phase gazeuse est obtenu plus précisément lors de l'utilisation de mélanges standard monophasiques de compositions connues. Cela peut aider à réduire les incertitudes pour les mesures à haute pression.

Le champ d'application des équilibres de phases pour les biocarburants est important. Plusieurs intermédiaires chimiques contenus dans les biocarburants ont de grandes masses moléculaires et présentent souvent des équilibres liquide-liquide (ELL) et liquide-solide (ELS). Ce type d'équilibre mérite une recherche soignée, non seulement parce qu'il alimente une petite portion de bases de données existantes, mais il joue un rôle majeur dans les technologies de séparation en matière de biocarburants. Un appareil ELL a été développé dans cette perspective et vérifié par le laboratoire CEP / TEP. Un schéma de la cellule ELL et de ses composants sont présentés et expliqués dans la Fig. **??**.

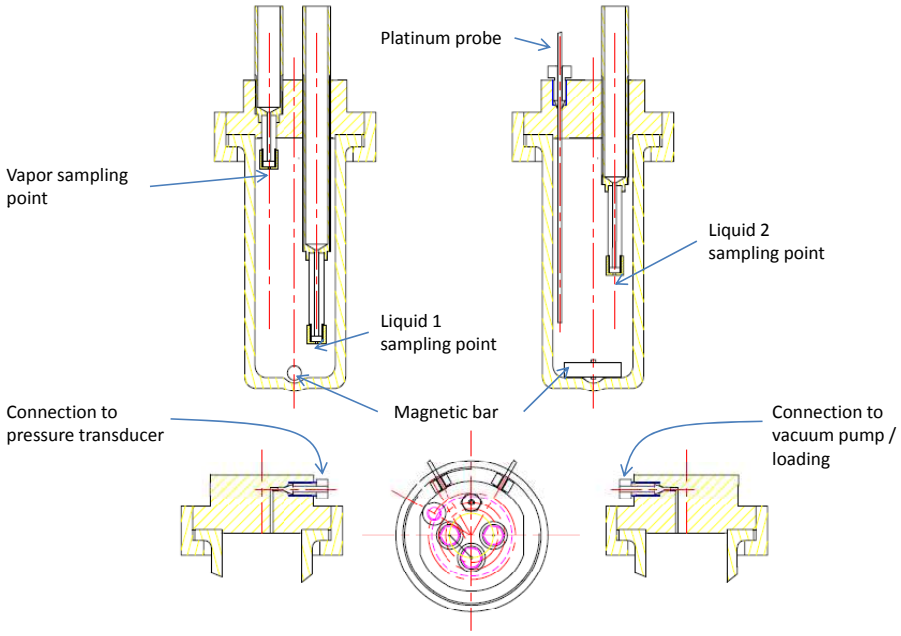

Schéma d'une cellule ELL adaptée à la mesure des équilibres liquide-liquide dans des conditions atmosphériques. Une seule sonde de température et une seule ligne de mesure de pression fournit le T et P à l'équilibre T et P. La cellule de verre est accessible via une ligne unique de chargement. L'échantillonnage des phases organique et aqueuse est facilité à deux points à des niveaux différents, en utilisant une seringue à gaz de 5 μL. L'appareil nécessite un échantillonnage manuel et une injection dans un chromatographe à phase gazeuse calibré, c'est à dire qu'il utilise une méthode "statique- analytique"

Un des sujets de préoccupation est le manque de données concernant les esters méthyliques d'acide gras (FAME), un composant du biodiesel. Les difficultés principales pour conduire ces recherches sont le coût, la disponibilité et la viscosité élevée des composés. Il apparait donc une opportunité pour des travaux futurs de mesure des propriétés thermodynamiques de composés FAME sous forme pure ou de mélange avec de préférence des esters contenant dix atomes de carbone ou plus. Ces données sont essentielles pour le développement de modèles. Les composés qui sont dérivés de la décomposition du bois, tels que l'acide fumarique, la vanilline et la quinone, sont rarement décrits dans les bases de données existantes. Ces composés possèdent des ELL et ELS et contiennent des groupes fonctionnels oxygénés multiples.

Les données critiques expérimentales peuvent avoir une application limitée aux procédés des biofuels, mais fournissent des informations valables pour le développement de modèle à la limite de la coexistence de phase. Ces données sont particulièrement appropriée au PC-SAFT qui manquent de contraintes dans la région critique. Le chapitre 4 présente un appareil qui utilise la méthode dynamique-synthétique et qui est capable de mesurer les propriétés critiques des systèmes purs et des systèmes multi-composés jusqu'à 543 K et 20 MPa. Le phénomène critique a été observé par l'intermédiaire de l'opalescence critique dans une cellule de vue. Les propriétés critiques de plus de treize composés purs, de sept systèmes binaires et d'un système ternaire ont été mesurées. Les résultats expérimentaux montrent de bonnes concordances avec des valeurs déjà publiées. Divers modèles mathématiques ont été appliqués en corrélant les propriétés critiques et leur résultats discutés. L'appareil n'est pas bien adapté aux systèmes possédant de grandes différences de volatilité et mériterait une amélioration. Diverses recommandations ont été suggérées et la plus importante serait d'ajouter un agitateur dans l'enceinte de la cellule et d'opérer dans des conditions statiques. Une récente modification tient compte de ces facteurs conduisant à des résultats conformes à l'installation dynamique pour les composés purs. Un travail complémentaire sur des mélanges de volatilités différentes devrait être conduit. Une autre proposition concerne la détermination des points critiques de composés sujets à la décomposition par l'intermédiaire d'un procédé d'extrapolation [191].

Le chapitre 5 constitue le travail de modélisation principal de cette thèse où l'équation d'état PC-SAFT est employée pour modéliser les équilibres de phase d'alcools, d'acides, de composés polaires et de l'eau. Chaque groupe fonctionnel a été examiné, avec des stratégies pour aborder de différentes structures moléculaires et non-idéales dans chaque cas. L'ajout de contributions d'énergie appropriées de Helmholtz pour des interactions spécifiques, comme par exemple la polarité, améliore souvent la prédiction et l'efficacité du calcul final. Pour la plupart des exemples, un paramètre d'interaction binaire simple k_{12} dans la contribution de dispersion a^{disp} est capable de décrire les systèmes azéotropiques et non-azéotropiques. En raison de sa base théoriquement solide, l'équation PC-SAFT peut être largement extrapolée aux conditions différents sans grande perte dans l'exactitude. Le paramètre binaire peut être transféré entre les conditions isobares et isothermes en modélisant les équilibres de phase.

En modélisant les équilibres de phase des alcools, l'ajout de l'une ou de l'autre contributions dipolaires discutée dans ce travail a pour effet positif de diminuer la valeur du paramètre binaire d'interaction. De cette façon, les mélanges d'alcool mesurés dans le chapitre 3 ont pu être représentés quantitativement avec de petits paramètres binaires. Le soin devrait être pris pour éviter de fausses séparations de phase dans la modélisation des systèmes azéotropiques, un dispositif commun parmi les mélanges d'alcool. Le manque de travail de modélisation fait sur les acides carboxyliques avec PC-SAFT a conduit à la détermination de nouveaux paramètres de composés purs pour les chaines C_1 - C_6. En adoptant une approche où le paramètre du κ^{AB} est maintenu constant, les paramètres proposés ont été examinés avec des résultats positifs sur

les propriétés thermodynamiques d'acides et de leurs mélanges. Pour des mélanges difficiles, tels que le système acide acétique/toluène étudié dans ce travail, un deuxième paramètre asymétrique l_{12} peut être employé dans la contribution de dispersion pour caler le modèle et obtenir des représentations quantitatives. Le paramètre l_{12} offre plus de flexibilité à l'équation PC-SAFT mais est moins extrapolable pour les températures alternatives. Les composés polaires passés en revue incluent les cétones, les éthers, les esters et les aldéhydes, pour lesquels nous avons proposé de nouveaux paramètres purs, notamment, pour l'éther tert-butylique d'éthyle et sept composés FAMEs. Pour les composés fortement polaires ($\mu > 2$ D), l'ajout d'une contribution expliquant les dipôles polarisables peut mener à de légères améliorations pour la description des équilibres de phase. Pour les composés FAMEs, un ensemble plus concret de paramètres purs peut seulement être réalisé dans le cas de plus de données expérimentales. Dans un mélange contenant un composé polaire et associé, l'association croisée (solvatation) doit être expliquée. Ceci a été effectué en utilisant l'approche de Kleiner et Sadowski [275] avec de bons résultats. La modélisation de mélanges aqueux s'est avéré être un défi pour ce modèle. La description simultanée de l'équilibre liquide-liquide et de l'équilibre de liquide-vapeur a pu être réalisée en utilisant les paramètres k_{12} et l_{12}.

La deuxième moitié du chapitre 5 traite de calcul des enthalpies et de test de cohérence thermodynamique. PC-SAFT ne fonctionne pas bien pour les calculs d'enthalpie d'excès car elle est moins extrapolable et plus dépendante sur des paramètres binaires, en comparaison de son performance à l'équilibre liquide-vapeur. Un paramètre binaire simple est souvent incapable de décrire simultanément l'ELV et l'enthalpie d'excès. Un test de cohérence thermodynamique court a été effectué pour les mesures d'ELV présentés au chapitre 3. L'objectif principal ici était d'examiner le niveau de l'uniformité entre les données et le modèle, qui est généralement acceptable. Une recherche plus complète, impliquant plusieurs tests est nécessaire pour obtenir des résultats plus concluants sur la qualité des données. L'étude préliminaire réalisée ici s'est avérée utile lors de l'identification de la plupart des points incorrects, indiquant que plusieurs ensembles de données n'étaient probablement pas entièrement conformes.

L'approche de modélisation adoptée au chapitre 5 est une parmi d'autres approches possibles pour la modélisation de mélanges présents dans les biofuels. Dans ce travail, nous n'avons pas considéré d'approches alternatives de liaison hydrogène, mais avons choisi d'employer l'arrangement simple de la liaison 2B pour tous les composés associés, sauf que des acides. Nous avons omis de paramétrer de nouveaux composés pour l'équation PC-SAFT-JC (PC-SAFT + Jog et Chapman terme dipolaire) car nous avons estimé que la caractérisation du paramètre x_p est sujet au modélisateur et à ses besoins. Le but du chapitre était de proposer des ensembles concrets de paramètres pour de nouveaux composés, avec des ambiguïtés minimales. Nous avons ainsi mis de côté les paramètres pour l'équation PC-SAFT-JC qui feront l'objet de travaux futurs. Un autre aspect de la modélisation, qui pourra être étudié à l'avenir, est le calcul des équilibres solide-fluide (liquide ou vapeur) dans des mélanges de biofuels, en utilisant l'équation PC-SAFT EoS [388].

Dans le dernier chapitre (chapitre 6), l'équation PC-SAFT EoS a été employée pour modéliser les données critiques binaires mesurées précédemment au chapitre 4. Pour expliquer les fluctuations de densités qui caractérisent la région critique, l'équation PC-SAFT a été couplée à la théorie de groupe de renormalisation de White (RG), qui permet au modèle de décrire des propriétés de fluide dans les région proche ou éloignée du point critique. Deux méthodes d'approximation ont été utilisées pour extrapoler la théorie RG aux mélanges, à savoir l'approximation de la cellule de d'espace de phase et l'approximation isomorphe. Quand elles sont appliquées aux mélanges binaires décrits dans ce travail, les corrections

de RG ont fourni des améliorations dans la représentation des données critiques, comparé à l'équation PC-SAFT originale qui tend à surévaluer les propriétés critiques. Les paramètres de RG pour l'éthanol, le 1-propanol et le 1,1,1,2-tétrafluoroéthane ont été déterminés dans ce travail. Dans plusieurs mélanges, l'erreur entre la T_c et la P_c expérimentales et ceux calculées a été réduite de 1/10 de la valeur liée à l'équation PC-SAFT original, lors de l'inclusion des corrections de RG. Les performances des deux méthodes d'approximation sont comparables, avec l'approximation de la cellule de d'espace de phase qui est davantage adaptée aux systèmes alcane-alcane et l'approximation isomorphe mieux adaptée pour les systèmes éthanol + les hydrocarbures de C_6-C_8.

Le système ternaire *n*-pentane + éthanol + *n*-hexane du chapitre 4 n'a pas été modelisé dans ce travail dû au manque d'algorithme et fera l'objet de travaux futurs. Deux autres recommandations pour la terme de RG ont été identifiées et détaillées dans le chapitre 6. La première aborde la question de sur-paramétrisation dans la terme de RG, par réajustement de *tous* les paramètres possibles des propriétés thermodynamiques et critiques. La seconde est la possibilité de présenter un paramètre binaire ajustable dans le terme de RG, afin d'essayer d'améliorer les descriptions simultanées du mélange de l'ELV et des propriétés critiques. Sous sa forme actuelle, l'équation PC-SAFT couplée à la terme de RG n'est pas suffisamment précise pour décrire simultanément l'ELV et les points critiques d'un mélange.

Bibliography

[1] A.K. Agarwal. *Prog. Energ. Combust.*, 33:233–271, 2007.

[2] V. Smil. *Oil: A Beginner's Guide*. One World Publications, Oxford, 2008.

[3] BP (beyond petroleum). *BP Statistical Review of World Energy*, June:1–50, 2010.

[4] D. Ballerini and N. Alazard-Toux. *Les Biocarburants*. IFP Productions, Paris, 2006.

[5] U.S. Energy Information Administration. *Annual Oil Market Chronology*. 2007.

[6] C.E. Baukal Jr. *Heat Transfer in Industrial Combustion*. CRC Press, Boca Raton, 2000.

[7] D. Guggenheim (Dir.). *An inconvenient truth (Film)*. Paramount Classics, United States, 2006.

[8] M. King Hubbert. Nuclear energy and the fossil fuels. In *Spring meeting of the Southern District, American Petroleum Institute*, March 1956.

[9] C.L. Wilson. *Energy: Global Prospects 1985-2000, Report on the Workshop on Alternative Energy Strategies*. McGraw-Hill, New York, 1977.

[10] A.R. Flower. *Scientific American*, 238:42–49, 1978.

[11] L.F. Ivanhoe. *World Oil*, October:77–88, 1995.

[12] K.S. Deffeyes. *Hubbert's Peak: The Impending World Oil Shortage*. Princeton University Press, Princeton, NJ, 2001.

[13] C.J. Campbell and J.H. Laherrère. *Scientific American*, 278:78–83, 1998.

[14] M.C. Lynch. The analysis and forecasting of petroleum supply: sources of error and bias. In D.H.E. Mallakh, editor, *Energy Watchers VII*. International Research Center for Energy and Economic Development, 1999.

[15] M.A. Adelman and M.C. Lynch. *Oil Gas J*, 95:56–60, 1997.

[16] J. Griffin (Ed.). *OPEC World Oil Outlook 2008*. OPEC Secretariat, Vienna, 2008.

[17] Commission on Oil Independence. *Making Sweden an OIL-FREE Society*. Sweden, 2006.

[18] Commission of the European Communities. *Biofuels Progress Report*. Brussels, 2007.

[19] Energy Information Administration. *International Energy Outlook 2008*. Washington, 2008.

[20] Renewable Energy Policy Network for the 21st Century (REN21). *Renewables global status report 2010*. France, 2009.

[21] D. Pimentel. *Biofuels, Solar and Wind as Renewable Energy Systems, Benefits and Risks*. Springer, United States, 2008.

[22] A.V. Da Rosa. *Fundamentals of Renewable Energy Processes*. Elsevier, London, 2005.

[23] B. Sorensen. *Renewable Energy*. Elsevier, London, 3rd edition, 2004.

[24] R.R Tan and A.B. Culaba. *Life-Cycle Assessment of Conventional and Alternative Fuels for Road Vehicles*. Manila, 2004.

[25] United Nations. *Kyoto Protocol to the United Nations Framework Convention on Climate Change*. Kyoto, 1998.

[26] N. Stern. *Stern Review Report on the Economics of Climate Change*. Cambridge University Press, Cambridge, 2006.

[27] Commission of the European Communities. *Green Paper*. Brussels, 2000.

[28] Commission of the European Communities. *Directive 2003/17/EC of the European Parliament and of the council of 3 March 2003*. 2003.

[29] Commission of the European Communities. *Biomass action plan*. Brussels, 2005.

[30] L. Ryan and H. Turton. *Sustainable Automobile Transport: Shaping Climate Change Policy*. Edward Elgar Publishing, England, 2007.

[31] D.M. Mousdale. *Biofuels: Biotechnology, Chemistry and Sustainable Development*. Boca Raton, 2008.

[32] D. Mohan, C.U. Pittman, and P.H. Steeles. *Energ. Fuel*, 20:848–889, 2005.

[33] J. Piskorz, D.S. Scott, and D. Radlien. *Pyrolysis Oils from Biomass: Producing Analyzing and Upgrading*. American Chemical Society, Washington, 1988.

[34] A. Singh, P. Singh Nigam, and J.D. Murphy. *Bioresource Technol.*, 101:4775–4800, 2010.

[35] H.S. Kheshgi, R.C. Prince, and G. Marland. *Ann. Rev. Energy Environ.*, 25:199–244, 2000.

[36] P. Bergeron. Environmental impacts of bioethanol. In C.E. Wyman, editor, *Handbook on Bioethanol: Production and Utilization*, Washington, 1996. Taylor & Francis.

[37] P.J. Crutzen, A.R. Mosier, K.A. Smith, and W. Winiwarter. *Atmos. Chem. Phys.*, 8:389–395, 2008.

[38] F. Stump, K. Knapp, and W. Racy. *J. Air Waste Manage Assoc.*, 46:1149–1161, 1996.

[39] E. Obwaka and D. Arnold. The limited case for biofuels. 2009.

[40] T. McMahon. *What is the Inflation Adjusted Price of Corn?* 2008. http://inflationdata.com/inflation/inflation_Articles/Corn_Inflation.asp.

[41] H. Scott Fogler. *Elements of Chemical Reaction Engineering*. Pearson Education, Inc., United States, 4th edition, 2006.

[42] M. Crosland. *Gay-Lussac, Scientist and Bourgeois*. Cambridge University Press, Cambridge, 1978.

[43] The Royal Society. *Sustainable biofuels: prospects and challenges (Policy document 01/08)*. The Royal Society, London, 2008.

[44] Fisher Scientific. Material safety data sheet: tert-butyl ethyl ether. Technical report, Fisher Scientific, 2007.

[45] A. Forestière. Rapports internes ifp 1991 et 1996. Technical report, IFP, 1996.

[46] A. Demirbas. *Energ. Source*, 24:835–841, 2002.

[47] K. Komers, J. Machek, and R. Stloukal. *Eur. J. Lipid Sci. Technol.*, 103:359–362, 2001.

[48] A. Demirbas. *Prog. Energ. Combust.*, 31:466–487, 2005.

[49] R. Stern, G. Hillion, J.J. Rouxel, and S. Leporq. *Procédé de fabrication d'esters à partir d'huiles végétales ou animales et d'alcools*. French Patent 2 752 242 (1996), US Patent 5 908 946 (1999).

[50] A.V. Bridgwater, D. Meier, and D. Radlein. *Org. Geochem.*, 30:1479–1493, 1999.

[51] P.A. Horne and P.T. Williams. *Fuel*, 75:1051–1059, 1996.

[52] E. Apaydin-Varol, E. Pütün, and A.E. Pütün. *Fuel*, 86:1892–1899, 2007.

[53] A.E. Pütün, E. Önal, B.B. Uzun, and N. Özbay. *Ind. Crops Prod.*, 26:307–314, 2007.

[54] O. Onay and E. Mete Kockar. *Renew. Energ.*, 28:2417–2433, 2003.

[55] A.V. Bridgwater. *Chem. Eng. J.*, 91:87–102, 2003.

[56] J.-L. Zheng. *J. Anal. Appl. Pyrol.*, 83:205–212, 2008.

[57] Q. Lu, W.-Z. Li, and X.-F. Zhu. *Energ. Convers. Manage.*, 50:1376–1383, 2009.

[58] W.T. Tsai, M.K. Lee, and Y.M. Chang. *J. Anal. Appl. Pyrol.*, 76:230–237, 2006.

[59] J. Yanik, C. Kornmayer, M. Saglam, and M. Yüksel. *Fuel Process Technol.*, 88:942–947, 2007.

[60] K. Sipilä, E. Kuoppala, L. Fagernäs, and A. Oasmaa. *Biomass Bioenerg.*, 14:103–113, 1998.

[61] A.E. Pütün, E. Apaydin, and E. Pütün. *Energy*, 29:2171–2180, 2004.

[62] A. Oasmaa and D. Meier. *J. Anal. Appl. Pyrol.*, 73:323–334, 2005.

[63] D.Y. Peng and D.B. Robinson. *Ind. Eng. Chem. Fundam.*, 15:59–64, 1976.

[64] G. Soave. *Chem. Eng. Sci.*, 4:1197, 1972.

[65] J.H. Oh and S.J. Park. *J. Ind. Eng. Chem.*, 11:456–464, 2005.

[66] D.S.H. Wong and S.I. Sandler. *AIChE J.*, 38:671–680, 1992.

[67] H. Renon and J.M. Prausnitz. *AIChE J.*, 14:135–144, 1968.

[68] T.E. Daubert, R.P. Danner, H.M. Sibul, and C.C. Stebbins. *DIPPR Data compilation of pure compound properties*. Version 11.0, Database 11. NIST Standard Reference Data Program, Gaithersburg, MD, 1996.

[69] J.M. Prausnitz, R.N. Lichtenthaler, and E. Gomes de Azevedo. *Molecular Thermodynamics of Fluid-Phase Equilibria*. Prentice Hall, New Jersey, 3rd edition, 1999.

[70] G.M. Kontogeorgis and G.K. Folas. *Thermodynamic Models for Industrial Applications: From Classical and Advanced Mixing Rules to Association Theories*. John Wiley & Sons, United Kingdom, 2010.

[71] A. Klamt and F. Eckert. *Fluid Phase Equilibr.*, 172:43–72, 2000.

[72] S.-T. Lin and S.I. Sandler. *Ind. Eng. Chem. Res.*, 41:899–913, 2002.

[73] U. Weidlich and J. Gmehling. *Ind. Eng. Chem. Res.*, 26:1372–1381, 1987.

[74] J. Gmehling, J. Li, and M. Schiller. *Ind. Eng. Chem. Res.*, 32:178–193, 1993.

[75] T. Holderbaum and J. Gmehling. *Fluid Phase Equilibr.*, 70:251–265, 1991.

[76] J. Zawidzki. *Z. Phys. Chem. Stoechiom. Verwandtschaftsl.*, 35:129–203, 1900.

[77] D.R. Lide. *CRC Handbook of Chemistry and Physics*. CRC Press, Inc., Boca Raton, 76th edition, 1995.

[78] J.O. Hirschfelder, C.F. Curliss, and R.B. Bird. *Molecular Theory of Gases and Liquids*. John Wiley and Sons, New York, 1954.

[79] G. Mie. *Ann. Phys.*, 11:657–675, 1903.

[80] S.S. Chen and A. Kreglewski. *Ber. Bunsen-Ges.*, 81:1048–1052, 1977.

[81] H. Frisch, J.L. Katz, E. Praestgaard, and J.L. Lebowitz. *J. Phys. Chem.*, 70:2016–2020, 1966.

[82] J.M. Castillo Sanchez. *Molecular simulation in microporous materials: adsorption and separation*. PhD thesis, Technische Universiteit Delft, 2010.

[83] D.A. McQuarrie. *Statistical Mechanics*. Harper & Row, New York, 1976.

[84] T. Boublìk. Perturbation theory. In J.V. Sengers, R.F. Kayser, C.J. Peters, and H.J. White Jr., editors, *Equations of State for Fluids and Fluid Mixtures: Part I*, Amsterdam, 2000. Elsevier.

[85] R.W. Zwanzig. *J. Chem. Phys.*, 22:1420–1426, 1954.

[86] J.A. Barker and D. Henderson. *J. Chem. Phys.*, 47:2856–2861, 1967.

[87] F.B. Smith and B.J. Alder. *J. Chem. Phys.*, 30:1190–1199, 1959.

[88] J.K. Percus and G.J. Yevick. *Phys. Rev.*, 110:1–13, 1958.

[89] M.S. Wertheim. *J. Math. Phys.*, 5:643–651, 1964.

[90] N.F. Carnahan and K.E. Starling. *J. Chem. Phys.*, 51:635–636, 1969.

[91] G.A. Mansoori, N.F. Carnahan, K.E. Starling, and T.W. Leland. *J. Chem. Phys.*, 54:1523, 1971.

[92] J. Gross and G. Sadowski. *Fluid Phase Equilibr.*, 168:183–199, 2000.

[93] J. Gross and G. Sadowski. *Ind. Eng. Chem. Res.*, 40:1244–1260, 2001.

[94] J. Gross and G. Sadowski. *Ind. Eng. Chem. Res.*, 41:5510–5515, 2002.

[95] P. Stringari. *Heuristic modeling of thermophysical properties of pure fluids and mixtures through innovative methods*. PhD thesis, Università Degli Studi Di Padova, 2008.

[96] M.S. Wertheim. *J. Stat. Phys.*, 35:19–34, 1984.

[97] M.S. Wertheim. *J. Stat. Phys.*, 35:35–47, 1984.

[98] M.S. Wertheim. *J. Stat. Phys.*, 42:459–476, 1986.

[99] M.S. Wertheim. *J. Stat. Phys.*, 85:2929–2936, 1986.

[100] R.A. Heidemann and J.M. Prausnitz. *Proc. Natl Acad. Sci. USA*, 73:1773–1776, 1976.

[101] A. Anderko. *Fluid Phase Equilibr.*, 45:39–67, 1989.

[102] A. Anderko. *Fluid Phase Equilibr.*, 50:21–52, 1989.

[103] C. Panayiotou and I.C. Sanchez. *J. Phys. Chem.*, 95:10090–10097, 1991.

[104] J.-P. Hansen and I.R. McDonald. *Theory of Simple Fluids*. Elsevier, Amsterdam, 3rd edition, 2006.

[105] W.G. Chapman. *Theory and Simulation of Associating Liquid Mixtures*. PhD thesis, Cornell University, 1988.

[106] W.G. Chapman, G. Jackson, and K.E. Gubbins. *Mol. Phys.*, 65:1057–1079, 1988.

[107] T. Boublìk. *J. Chem. Phys.*, 53:471–472, 1970.

[108] W.G. Chapman, K.E. Gubbins, G. Jackson, and M. Radosz. *Fluid Phase Equilibr.*, 52:31–38, 1989.

[109] J.P. Wolbach and S.I. Sandler. *Ind. Eng. Chem. Res.*, 37:2917–2928, 1998.

[110] J.R. Elliott Jr. *Ind. Eng. Chem. Res.*, 35:1624–1629, 1996.

[111] M.L. Michelsen and E.M. Hendriks. *Fluid Phase Equilibr.*, 180:165–174, 2001.

[112] S.P. Tan, H. Adidharma, and M. Radosz. *Ind. Eng. Chem. Res.*, 43:203–208, 2004.

[113] N. von Solms, M.L. Michelsen, C.P. Passos, S.O. Derawi, and G.M. Kontogeorgis. *Ind. Eng. Chem. Res.*, 45:5368–5374, 2006.

[114] A.N. Fletcher and C.A. Heller. *J. Phys. Chem.*, 71:3742–3756, 1967.

[115] T.R. Lien. *A study of the thermodynamic excess functions of alcohol solutions by IR spectroscopy: applications to chemical solution theory*. PhD thesis, University of Toronto, 1972.

[116] W.A.P. Luck. *Angew. Chem. Int. Ed. Engl.*, 19:28–41, 1980.

[117] S. Martinez. *Spectrochim. Acta A-M*, 42:531–536, 1986.

[118] R.B. Gupta and R.L. Brinkley. *AIChE J.*, 44:207–213, 1998.

[119] R.L. Brinkley and R.B. Gupta. *Ind. Eng. Chem. Res.*, 37:4823–4827, 1998.

[120] R.L. Brinkley and R.B. Gupta. *AIChE J.*, 47:948–953, 2001.

[121] N. Asprion, H. Hasse, and G. Maurer. *Fluid Phase Equilibr.*, 186:1–25, 2001.

[122] D. Missopolinou, K. Ioannou, I. Prinos, and C. Panayiotou. *Z. Phys. Chem.*, 216:1–14, 2002.

[123] F. Palombo, P. Sassi, M. Paolantoni, A. Morresi, and R.S. Cataliotti. *J. Phys. Chem. B*, 110:18017–18025, 2006.

[124] N. von Solms, L. Jensen, J.L. Kofod, M.L. Michelsen, and G.M. Kontogeorgis. *Fluid Phase Equilibr.*, 261:272–280, 2007.

[125] W.G. Chapman, K.E. Gubbins, G. Jackson, and M. Radosz. *Ind. Eng. Chem. Res.*, 29:1709–1721, 1990.

[126] R.L. Cotterman, B.J. Schwartz, and J.M. Prausnitz. *AIChE J.*, 32:1787–1798, 1986.

[127] T. Kraska and K.E. Gubbins. *Ind. Eng. Chem. Res.*, 35:4727–4737, 1996.

[128] T. Kraska and K.E. Gubbins. *Ind. Eng. Chem. Res.*, 35:4738–4746, 1996.

[129] Y.C. Chiew. *Mol. Phys.*, 73:359–373, 1991.

[130] H. Liu and Y. Hu. *Fluid Phase Equilibr.*, 122:75–97, 1996.

[131] J. Gross. *Entwicklung einer Zustandsgleichung für einfache, assoziierende und makromolekulare Stoffe*. PhD thesis, Technische Universität Berlin, Germany, 2000.

[132] P.M. Mathias, H.C. Klotz, and J.M. Prausnitz. *Fluid Phase Equilibr.*, 67:31–44, 1991.

[133] J. Gross and J. Vrabec. *AIChE J.*, 52:1194–1204, 2006.

[134] P.K. Jog and W.G. Chapman. *Mol. Phys.*, 97:307–319, 1999.

[135] P. Jog, S. Sauer, J. Blaesig, and W.G. Chapman. *Ind. Eng. Chem. Res.*, 40:4641–4648, 2001.

[136] M. Kleiner and J. Gross. *AIChE J.*, 52:1951–1961, 2006.

[137] J. Gross. *AIChE J.*, 51:2556–2568, 2005.

[138] J. Vrabec and J. Gross. *J. Phys. Chem. B.*, 112:51–60, 2008.

[139] B. Saager and J. Fischer. *Fluid Phase Equilibr.*, 72:67–88, 1992.

[140] K.S. Shing and K.E. Gubbins. *Mol. Phys.*, 45:129–139, 1982.

[141] K. Johnson, E.A. Müller, and K.E. Gubbins. *J. Phys. Chem.*, 98:6413–6419, 1994.

[142] M. Lisal, K. Aim, M. Lecke, and J. Fischer. *Int. J. Thermophys.*, 25:159–173, 2004.

[143] Y. Zhou, C.K. Hall, and G. Stell. *J. Chem. Phys.*, 103:2688–2695, 1995.

[144] J. Stoll, J. Vrabec, and H. Hasse. *Fluid Phase Equilibr.*, 209:29–53, 2003.

[145] C.G. Gray and K.E. Gubbins. *Theory of molecular fluids*, volume 1. Clarendon Press, Oxford, UK, 1984.

[146] G. Stell, J.C. Rasaiah, and H. Narang. *Mol. Phys.*, 27:1393–1414, 1974.

[147] M. Wertheim. *Mol. Phys.*, 34:1109–1124, 1977.

[148] M. Wertheim. *Mol. Phys.*, 37:83–94, 1979.

[149] G.S. Rushbrook, G. Stell, and J.S. Høye. *Mol. Phys.*, 26:1199–1215, 1973.

[150] S. Sauer and W.G. Chapman. *Ind. Eng. Chem. Res.*, 42:5687–5696, 2003.

[151] A. Dominik, W.G. Chapman, M. Kleiner, and G. Sadowski. *Ind. Eng. Chem. Res.*, 44:6928–6938, 2005.

[152] N.M. Al-Saifi, E.Z. Hamad, and P. Englezos. *Fluid Phase Equilibr.*, 271:82–93, 2008.

[153] E.W. Lemmon, M.O. McLinden, D.G. Friend, P.J. Linstroom, and W.G. Mallard. *Thermophysical Properties of Fluid Systems, NIST Chemistry WebBook*. NIST Standard Reference Database Number 69. National Institute of Standards and Technology, Gaithersburg, MD, 2005. http://webbook.nist.gov.

[154] P.E. Liley, G.H. Thomson, D.G. Friend, T.E. Daubert, and E. Buck. Physical and chemical data. In R.H. Perry, D.W. Green, and J.O. Maloney, editors, *Perry's Chemical Engineers' Handbook*, USA, 1999. McGraw-Hill Book Company.

[155] X. Tang and J. Gross. *Fluid Phase Equilibr.*, 293:11–21, 2010.

[156] S.L. Outcalt, A. Laesecke, and T.J. Fortin. *J. Mol. Liq.*, 151:50–59, 2010.

[157] C. Coquelet, L.A. Galicia-Luna, A.H. Mohammadi, and D. Richon. *Fluid Phase Equilibr.*, 296:2–3, 2010.

[158] E. Hendriks, G.M. Kontogeorgis, R. Dohrn, J.-C. de Hemptinne, I.G. Economou, L. Fele Žilnik, and V. Vesovic. *Ind. Eng. Chem. Res.*, 49:11131–11141, 2010.

[159] M.B. Oliveira, A.R.R. Teles, A.J. Queimada, and J.A.P. Coutinho. *Fluid Phase Equilibr.*, 280:22–29, 2009.

[160] J. Rarey, S. Horstmann, and J. Gmehling. *J. Chem. Eng. Data*, 44:532–538, 1999.

[161] A.-D. Leu and D.B. Robinson. *J. Chem. Eng. Data*, 44:398–400, 1994.

[162] J.D. Raal and A.L. Mühlbauer. *Phase Equilibria: Measurement and Computation*. Taylor & Francis, USA, 1999.

[163] S. Yerazunis, J.D. Plowright, and F.M. Smola. *AIChE J.*, 10:660, 1964.

[164] B.N. Taylor and C.E. Kuyatt. Guidelines for evaluating and expressing the uncertainty of NIST measurement results. Technical report, National Institute of Standards and Technology, Gaithersburg, MD, 1994.

[165] F. Authouart. *La métrologie mais c'est très simple!* Crisalis auto-édition, Le Havre, France,2nd edition, 2006.

[166] K.S. Yuan, J.C.K. Ho, A.K. Kespande, and B.C.-Y. Lu. *J. Chem. Eng. Data*, 8.

[167] J. Zhao, C.-C. Dong, C.-X. Li, H. Meng, and Z.-H. Wang. *Fluid Phase Equilibr.*, 242:147–153, 2006.

[168] A.G. Morachevskii and V.T. Zharov. *J. Appl. Chem. USSR*, 36.

[169] G. Scatchard and F.G. Satkiewicz. *J. Am. Chem. Soc.*, 86:130–133, 1964.

[170] P.S. Prabhu and M. Van Winkle. *J. Chem. Eng. Data*, 8:210–214, 1963.

[171] J.N. Rhim and C. Kwak. *Hwahak Konghak*, 19:199–206, 1981.

[172] J. Gmehling and U. Onken. *Vapor-liquid equilibrium data collection, organic hydroxy compounds: alcohols*, volume I, part 2a. DECHEMA Chemistry Data Series, Germany, 1977.

[173] J. Gmehling, U. Onken, and J.R. Rarey-Nies. *Vapor-liquid equilibrium data collection, organic hydroxy compounds: alcohols (supplement 3)*, volume I, part 2e. DECHEMA Chemistry Data Series, Germany, 1988.

[174] T.E. Vittal Prasad, K. Chandrika, M. Haritha, N.B Geetha, and D.H.L. Prasad. *Fluid Phase Equilibr.*, 149:121–125, 1998.

[175] C.B. Kretschmer and R. Wiebe. *J. Am. Chem. Soc.*, 71:1793–1797, 1949.

[176] Y. Shimoyama, Y. Iwai, B.S. Jin, T. Hirayama, and Y. Arai. *Fluid Phase Equilibr.*, 257:217–222, 2007.

[177] C.B. Kretschmer and R. Wiebe. *J. Am. Chem. Soc.*, 73.

[178] M. Gomez-Nieto and G. Thodos. *AIChE J.*, 24.

[179] H. Horizoe, T. Tanimoto, I. Yamamoto, and Y. Kano. *J. Chem. Eng. Jpn.*, 26:482–489, 1993.

[180] M.S. Zabaloy, H.P. Gros, S.B. Bottini, and E.A. Brignole. *J. Chem. Eng. Data*, 39.

[181] T. Holderbaum, A. Utzig, and J. Gmehling. *Fluid Phase Equilibr.*, 63:219–226, 1991.

[182] A. Deák, A.I. Victorov, and Th.W. de Loos. *Fluid Phase Equilibr.*, 107:277–301, 1995.

[183] P. Guilbot, A. Valtz, H. Legendre, and D. Richon. *Analusis*, 28:426–431, 2000.

[184] K.S. Pitzer. *Thermodynamics*. McGraw-Hill Book Company, New York, 3rd edition, 1995.

[185] B. Poling, J. Prausnitz, and J. O'Connell. *The Properties of Gases and Liquids*. McGraw-Hill Book Company, USA, 4th edition, 1988.

[186] R.D. Weir and Th.W. de Loos, editors. *Measurement of the thermodynamic properties of multiple phases*. Elsevier Academic Press, Amsterdam, 2000.

[187] B. Stuart and E. Prichard. *Practical Laboratory Skills and Training Guides: Gas Chromatography*. LGC (Teddington) Limited, United Kingdom, 2003.

[188] O. Redlich and A.T. Kister. *Ind. Eng. Chem.*, 48:345–348, 1952.

[189] I. Cibulka. *Collect. Czechoslov. Commun.*, 47:1414–1419, 1982.

[190] P.P. Singh and S.P. Sharma. *Can. J. Chem.*, 61:2321–2328, 1983.

[191] A.S. Teja and J. Mendez-Santiago. Critical parameters. In R.D. Weir and Th.W. de Loos, editors, *Measurement of the Thermodynamic Properties of Multiple Phases*, Amsterdam, 2000. Elsevier Academic Press.

[192] L.C. Roess. *J. Inst. Petrol. Tech.*, 22:665–705, 1936.

[193] A.S. Teja D.J. Rosenthal. *AIChE J.*, 35:1829–1834, 1989.

[194] S. Horstmann, K. Fischer, and J. Gmehling. *Chem. Eng. Techno.*, 22:839–842, 1999.

[195] S. Horstmann, K. Fischer, J. Gmehling, and P. Kolář. *J. Chem. Thermodyn.*, 32:451–464, 2000.

[196] S. Horstmann, K. Fischer, and J. Gmehling. *Chem. Eng. Sci.*, 56:6905–6913, 2001.

[197] S. Horstmann, K. Fischer, and J. Gmehling. *AIChE J.*, 48:2350–2356, 2002.

[198] P. Guilbot, P. Théveneau, A. Baba-Ahmed, S. Horstmann, K. Fischer, J. Gmehling, and D. Richon. *J. Chem. Thermodyn.*, 170:193–202, 2000.

[199] L. Gil, S.F Otín, J. Munoz Embid, M. Asunción Gallardo, S. Blanco, M. Artal, and I. Velasco. *J. of Supercritical Fluids*, 44:123–128, 2008.

[200] R.B. Dean and W.J. Dixon. *Anal. Chem.*, 23:636–638, 1951.

[201] DuPont. Technical information, dupont fluorointermediates: hexafluoropropylene. Technical report, DuPont, USA, 2007. http://www2.dupont.com/FluoroIntermediates/en_US/assets/downloads/h96535.pdf.

[202] C. Coquelet, G. Belaribi, F. Belaribi, A. Valtz, P. Naidoo, and D. Ramjugernath. Volumetric properties of hexafluoropropylene and hexafluoropropylene oxide. determination of phase diagram and critical properties. In *Proceedings of the AIChE Annual Meeting*, Nashville, TN, 2009.

[203] C. Coquelet, D. Ramjugernath, H. Madani, A. Valtz, P. Naidoo, and A. Hassen Meniai. *J. Chem. Eng. Data*, 55:2093–2099, 2010.

[204] DuPont. Push bulletin, dupont fluorointermediates: hexafluoropropylene oxide. Technical report, DuPont, USA, 2008. http://www2.dupont.com/FluoroIntermediates/en_US/assets/downloads/k05132.pdf.

[205] G.M. Wilson and L.V. Jasperson. Critical constants t_c, p_c, estimation based on zero, first and second order methods. In *Proceedings of the AIChE Spring Meeting*, New Orleans, LA, 1996.

[206] J. Marrero-Morejón and E. Pardillo-Fontdevila. *AIChE J.*, 45:615–621, 1999.

[207] Y. Nannoolal, J. Rarey, and D. Ramjugernath. *Fluid Phase Equilibr.*, 252:1–27, 2007.

[208] P. Ungerer, B. Tavitian, and A. Boutin. *Application of Molecular Simulation in the Oil and Gas Industry*. Editions Technip, Paris, 2005.

[209] M.A. Anisimov and J.V. Sengers. Critical region. In J.V. Sengers, R.F. Kayser, C.J. Peters, and H.J. White Jr., editors, *Equations of State for Fluids and Fluid Mixtures Part I*, Amsterdam, 2000. Elsevier Academic Press.

[210] N.B. Wilding. *Phys. Rev. E*, 53:602–611, 1995.

[211] J.J. Potoff and A.Z. Panagiotopoulos. *J. Chem. Phys.*, 109:10914–10920, 1998.

[212] C.N. Nysewander, B.H. Sage, and W.N. Lacey. *Ind. Eng. Chem.*, 32:118–123, 1940.

[213] A. Kreglewski and W.B. Kay. *J. Phys. Chem.*, 73:3359–3366, 1969.

[214] H.C. Wiese, J. Jacobs, and B.H. Sage. *J. Chem. Eng. Data*, 15:82–91, 1970.

[215] W.B. Kay. *J. Chem. Eng. Data*, 15:46–52, 1970.

[216] C.-B. Soo, E. El Ahmar, C. Coquelet, D. Ramjugernath, and D. Richon. *Fluid Phase Equilibr.*, 286:69–77, 2009.

[217] J. Seo, S. Lee, and H. Kim. *Fluid Phase Equilibr.*, 172:211–219, 2000.

[218] P.G. McCracken, T.S. Storvick, and J.M. Smith. *J. Chem. Eng. Data*, 5:130–132, 1960.

[219] P. Sauermann, K. Holzapfel, J. Oprzynski, F. Kohler, W. Poot, and Th.W. de Loos. *Fluid Phase Equilibr.*, 112:249–272, 1995.

[220] J. Seo, J. Lee, and H. Kim. *Fluid Phase Equilibr.*, 182:199–207, 2001.

[221] D.W. Morton, M.P.W. Lui, and C.L. Young. *J. Chem. Thermodyn.*, 35:1737–1749, 2003.

[222] J. Seo, J. Lee, and H. Kim. *J. Chem. Eng. Data*, 47:974–977, 2002.

[223] E.J. Partington, J.S. Rowlinson, and J.F. Weston. *Trans. Faraday Soc.*, 56:479–485, 1960.

[224] M.T. Gude and A.S. Teja. *AIChE Symp. Ser.*, 90(298):14–22, 1994.

[225] G.L. Eaton and C.A. Porter. *Ind. Eng. Chem.*, 24:819–822, 1932.

[226] M.J. Anselme, M. Gude, and A.S. Teja. *Fluid Phase Equilibr.*, 57:317–326, 1990.

[227] J.A. Nelder and R. Mead. *Comput. J.*, 7:308–313, 1965.

[228] S.H. Huang and M. Radosz. *Ind. Eng. Chem. Res.*, 29:2284–2294, 1990.

[229] H. Adidharma and M. Radosz. *J. Phys. Chem. B*, 105:9822–9827, 2001.

[230] J.-P. Passarello and P. Tobaly. *Ind. Eng. Chem. Res.*, 42:5383–5391, 2003.

[231] J.P. Wolbach and S.I. Sandler. *Ind. Eng. Chem. Res.*, 36:4041–4051, 1997.

[232] X. Courtial, C.-B. Soo, C. Coquelet, P. Paricaud, D. Ramjugernath, and D. Richon. *Fluid Phase Equilibr.*, 277:152–161, 2009.

[233] M.R.W. Maciel and A.Z. Francesconi. *J. Chem. Thermodyn.*, 20:539–544, 1988.

[234] J. Zielkiewicz. *J. Chem. Thermodyn.*, 23:605–612, 1991.

[235] C. Coquelet, C.-B. Soo, A. Valtz, D. Richon, D. Amoros, and H. Guyet. *Fluid Phase Equilibr.*, 298:33–37, 2010.

[236] F. Steyer and K. Sundmacher. *J. Chem. Eng. Data*, 49:1675–1681, 2004.

[237] J.-J. Li, S.-W. Tang, and B. Liang. *J. Chem. Eng. Data*, 55:3418–3421, 2010.

[238] D.E. Jones, I.A. Weeks, S.C. Anad, R.W. Wetmore, and G.C. Benson. *J. Chem. Eng. Data*, 17:501–506, 1972.

[239] J. Chevalley. *C.R. Hebd. Séances Acad. Sci.*, 250:3326–3328, 1960.

[240] S.O. Derawi, J. Zeuthen, M.L. Michelsen, E.H. Stenby, and G.M. Kontogeorgis. *Fluid Phase Equilibr.*, 225:107–113, 2004.

[241] Y.-H. Fu and S.I. Sandler. *Ind. Eng. Chem. Res.*, 34:1897–1909, 1995.

[242] R. Buttner and G. Maurer. *Ber. Bunsenges. Phys. Chem.*, 87:877–882, 1983.

[243] A.D.H. Clague and H.J. Bernstein. *Spectrochim. Acta*, 25A:563–596, 1969.

[244] R.C. Herman and R. Hofstadter. *J. Chem. Phys.*, 7:460–464, 1939.

[245] S. Miyamoto, S. Nakamura, Y. Iwai, and Y. Arai. *J. Chem. Eng. Data*, 45:857–861, 2000.

[246] A. Valtz, C.-B. Soo, C. Coquelet, D. Richon, D. Amoros, and H. Guyet. *Fluid Phase Equilibr.*, Submitted, 2011.

[247] N. Alpert and P.J. Elving. *Ind. Eng. Chem.*, 41:2864–2867, 1949.

[248] V.Y.U. Aristovich, N.V. Lutugina, and Y.U.I. Malenko. *Zh. Prikl. Khim.*, 33:2693, 1960.

[249] J.J. Conti, D.F. Othmer, and R. Gilmont. *J. Chem. Eng. Data*, 5:301–307, 1960.

[250] M. Kato, H. Yoshikawa, and M. Yamaguchi. *Fluid Phase Equilibr.*, 54:47–56, 1990.

[251] S. Miyamoto, S. Nakamura, Y. Iwai, and Y. Arai. *J. Chem. Eng. Data*, 46:405–409, 2001.

[252] A. Tamir and J. Wisniak. *Chem. Eng. Sci.*, 30:335–342, 1975.

[253] I. Malijevska, M. Sysova, and D. Vlckova. *Collect. Czech. Chem. Commun.*, 51:194–205, 1986.

[254] Z. Plesnar, Y.-H. Fu, S.I. Sandler, and H. Orbey. *J. Chem. Eng. Data*, 41:799–801, 1996.

[255] A. Baradarajan and M. Satyanarayana. *Indian J. Technol.*, 5:264–266, 1967.

[256] I. Malijevska, K. Chylkova, and M. Sysova. *Fluid Phase Equilibr.*, 68:219–228, 1991.

[257] A. Rius, J.L. Otero, and A. Macarron. *Chem. Eng. Sci.*, 10:105–111, 1959.

[258] L.A.L. Munoz and M. Alvina Krähenbühl. *J. Chem. Eng. Data*, 46:120–124, 2001.

[259] G.M. Wilson. *J. Am. Chem. Soc.*, 86:127–130, 1964.

[260] D.S. Abrams and J.M. Prausnitz. *AIChE. J.*, 21:116–128, 1975.

[261] J.G. Hayden and J.P. O'Connell. *Ind. Eng. Chem. Process Des. Dev.*, 14:209–216, 1975.

[262] A.N. Marinichev and M.P. Susarev. *J. Appl. Chem. USSR*, 38:371–375, 1965.

[263] P.S. Puri, J. Polak, and J.A. Ruether. *J. Chem. Eng. Data*, 19:87–89, 1974.

[264] A. Crespo Colin, A. Compostizo, and M. Diazpena. *J. Chem. Thermodyn.*, 16:497–502, 1984.

[265] S.W. Campbell, R.A. Wilsak, and G. Thodos. *J. Chem. Eng. Data*, 31:424–430, 1986.

[266] C. Coquelet, C.-B. Soo, A. Valtz, D. Richon, D. Amoros, and H. Guyet. *J. Chem. Eng. Data*, 55:4521–4524, 2010.

[267] T. Boublìk and B.C.-Y. Lu. *J. Chem. Eng. Data*, 22:331–333, 1977.

[268] D.F. Othmer, M.M. Chudgar, and S.L. Levy. *Ind. Eng. Chem.*, 44:1872–1881, 1952.

[269] G.F. Meehan and N.F. Murphy. *Chem. Eng. Sci.*, 20:757–769, 1965.

[270] S. Miyamoto, S. Nakamura, Y. Iwai, and Y. Arai. *J. Chem. Eng. Data*, 46:1225–1230, 2001.

[271] H. Segura, G. Galindo, J. Wisniak, and R. Reich. *Phys. Chem. Liq.*, 38:391–404, 2000.

[272] A. Tihić. *Group contribution sPC-SAFT equation of state*. PhD thesis, Technical University of Denmark, 2008.

[273] H. Segura, E. Lam, R. Reich, and J. Wisniak. *Phys. Chem. Liq.*, 39:43–54, 2001.

[274] H. Segura, J. Wisniak, G. Galindo, and R. Reich. *J. Chem. Eng. Data*, 46:506–510, 2001.

[275] M. Kleiner and G. Sadowski. *J. Phys. Chem. C*, 111:15544–15553, 2007.

[276] T.X. Nguyen Thi, S. Tamouza, P. Tobaly, J.-P. Passarello, and J.-C. de Hemptinne. *Fluid Phase Equilibr.*, 238:254–261, 2005.

[277] D. NguyenHuynh, A. Falaix, J.-P. Passarello, P. Tobaly, and J.-C. de Hemptinne. *Fluid Phase Equilibr.*, 264:184–200, 2008.

[278] T.A. Scott Jr., D. MacMillan, and E.H. Melvin. *Ind. Eng. Chem.*, 44:172–175, 1952.

[279] A. Rose and W.R. Supina. *J. Chem. Eng. Data*, 6:173–179, 1961.

[280] A. Rose and V.N. Schrodt. *J. Chem. Eng. Data*, 9:12–16, 1964.

[281] A.C.G. van Genderen, J. Cees van Miltenburg, J.G. Blok, M.J. van Bommel, P.J. van Ekeren, G.J.K. van den Berg, and H.A.J. Oonk. *Fluid Phase Equilibr.*, 202:109–120, 2002.

[282] M.J. Pratas, S. Freitas, M.B. Oliveira, S.C. Monteiro, A.S. Lima, and J.A.P. Coutinho. *J. Chem. Eng. Data*, 55:3983–3990, 2010.

[283] J. Gross. *J. Chem. Phys.*, 131:204705(1)–204705(12), 2009.

[284] J.S. Chickos, H. Zhao, and G. Nichols. *Thermochim. Acta*, 424:111–121, 2004.

[285] M.W. Formo. Physical properties of fats and fatty acids. In D. Swern, editor, *Bailey's Industrial Oil and Fat Products*, volume 1, USA, 1979. John Wiley and Sons.

[286] C.A.W. Allen, K.C. Watts, and R.G. Ackman. *J. Am. Oil Chem. Soc.*, 76:317–323, 1999.

[287] Q. Shu, J. Wang, B. Peng, D. Wang, and G. Wang. *Fuel*, 87:3586–3590, 2008.

[288] L.Y. Akisawa Silva, R.M. Matricarde Falleiro, A.J.A. Meirelles, and M.A. Krähenbühl. *Thermochim. Acta*, 512:178–182, 2011.

[289] F. Rivenq. *Bull. Soc. Chim. Fr.*, 9:2645, 1973.

[290] G.Ya. Kolyuchkina, V.N. Ponomarev, and V.S. Timofeev. *Izv. Vyssh. Uchebn. Zaved. Khim. Khim. Tekhnol.*, 18:1582, 1975.

[291] E.N. Pennington and S.J. Marwil. *Ind. Eng. Chem.*, 45:1371–1377, 1953.

[292] I.I. Nikiforova, B.N. Bobylev, and L.L. Karpacheva. *Osnovnoi Organ. Sintez. Neftekhim*, 21:49, 1985.

[293] V. Fried, A. Capkova, and J. Suska. *Collect. Czech. Chem. Commun.*, 28:3171, 1963.

[294] Zhejiang university. *J. Chem. Eng. (China)*, 1:75, 1978. Data taken from: J. Gmehling, U. Onken and J.R. Rarey. *Vapor-liquid equilibrium data collection, aldehydes (supplement 1)*, volume I, part 3a. DECHEMA Chemistry Data Series, Germany, 1993, page 15.

[295] S. Aparicio-Martinez and K.R. Hall. *Fluid Phase Equilibr.*, 254:112–125, 2007.

[296] S.J. Suresh and J.R. Elliot. *Ind. Eng. Chem. Res.*, 31:2783–2794, 1992.

[297] T. Boublìk. *Collect. Czech. Chem. Commun.*, 25:285–287, 1960.

[298] D. Hessel and G. Geiseler. *Z. Phys. Chem. (Leipzig)*, 229:199–209, 1965.

[299] J.M. Sørensen and W. Arlt. *Liquid-liquid equilibrium data collection: binary systems*, volume V, part 1. DECHEMA Chemistry Data Series, Germany, 1979.

[300] V. De Simone and P. Palumbo. *Chim. Ind. (Milan)*, 56:103, 1974.

[301] J.H. Jones and J.F. McCants. *Ind. Eng. Chem.*, 46:1956, 1954.

[302] I. Ferino, B. Marongiu, R. Monaci, V. Solinas, and S. Torrazza. *Thermochim. Acta*, 65:157–168, 1983.

[303] I.L. Krupatkin and M.F. Glagoleva. *Zh. Obshch. Khim.*, 40:261, 1970.

[304] Y.C. Chang. *Acta Focalia Sinica*, 2:1, 1957.

[305] A. Campetti and C. Del Grosso. *Nuovo Cimento*, 6:379–417, 1913.

[306] G.A. Kirichenko, V.N. Kiva, and V.S. Bogdanov. *Zh. Fiz. Khim.*, 52:1542, 1978.

[307] M.A.Y. Torres, S.B. Bottini, E.A. Brignole, V. Sanhueza, and R. Reich. *Fluid Phase Equilibr.*, 71:85–98, 1992.

[308] N.V. Chalov, E.F. Goryachikh, and L.Kh. Vobolazova. *Gidroliz. Lesokhim. Prom-St.*, 8:11, 1955.

[309] N.V. Sidgwick, W.J. Spurrell, and T.E. Davies. *J. Chem. Soc.*, 107:1202–1213, 1915.

[310] L.V. Erichsen and E. Dobbert. *Brennst.-Chem.*, 36:338–345, 1955.

[311] E. Terres, F. Gebert, H. Hulsemann, H. Petereit, H. Toepsch, and W. Ruppert. *Brennst.-Chem.*, 36:289, 1955.

[312] W.A. Leet, H.-M. Lin, and K.-C. Chao. *J. Chem. Eng. Data*, 32:37–40, 1987.

[313] D.H.T. Chen and A.R. Thompson. *J. Chem. Eng. Data*, 15:471–474, 1970.

[314] D.S. Negi, F. Sobotka, T. Kimmel, G. Wozny, and R. Schomäcker. *Ind. Eng. Chem. Res.*, 45:3693–3696, 2006.

[315] K.A.G. Schmidt, Y. Maham, and A.E. Mather. *J. Therm. Anal. Calorim.*, 89:61–72, 2007.

[316] R. Sabbah, X.-W. An, J.S. Chickos, M.L. Planas Leitao, M.V. Roux, and L.A. Torres. *Thermochim. Acta*, 331:93–204, 1999.

[317] M.L. Martin and J.C. Youings. *Aust. J. Chem.*, 33:2133–2138, 1980.

[318] J.B. Ott, K.N. Marsh, and R.H. Stokes. *J. Chem. Thermodyn.*, 12:1139–1148, 1980.

[319] J.R. Goates, R.L. Snow, and M.R. James. *J. Phys. Chem.*, 65:335–338, 1961.

[320] W. Renker and R. Kopp. *Kollektive Dissertation*. PhD thesis, Karl-Marx Univeristät (Leipzig), 1969.

[321] H.K. dEQ. Jones and B.C.-Y. Lu. *J. Chem. Eng. Data*, 11:488–492, 1966.

[322] M. Diaz Pena and F. Fernandez Martin. *An. Real. Soc. Espan. De Fis. Y Quim.*, 59:331–334, 1963.

[323] A. Arce, A. Blanco, A. Soto, and J. Tojo. *J. Chem. Eng. Data*, 40:1011–1014, 1995.

[324] D.-Y. Peng, Z. Wang, G.C. Benson, and B.C.-Y. Lu. *J. Chem. Thermodyn.*, 33:83–93, 2001.

[325] R. Reich, M. Cartes, H. Segura, and J. Wisniak. *Phys. Chem. Liq.*, 38:217–232, 2000.

[326] S. Murakami, K. Amaya, and R. Fujishiro. *Bull. Chem. Soc. Jpn.*, 37:1776–1780, 1964.

[327] D.O. Hansen and M. Van Winkle. *J. Chem. Eng. Data*, 5:30–34, 1960.

[328] U. Messow, U. Doye, S. Kuntzsch, and D. Kuchenbecker. *Z. Phys. Chem. (Leipzig)*, 258:90–96, 1977.

[329] W. Mier, G. Oswald, E. Tusel-Langer, and R.N. Lichtenthaler. *Ber. Bunsenges. Phys. Chem.*, 99:1123–1130, 1995.

[330] J.A. Barker. *Austral. J. Chem.*, 6:207–210, 1953.

[331] H.M. Moon, K. Ochi, and K. Kojima. *Fluid Phase Equilibr.*, 62:29–40, 1991.

[332] P.L. Jackson and R.A. Wilsak. *Fluid Phase Equilibr.*, 103:155–197, 1995.

[333] L.J. Christiansen and Aa. Fredenslund. *AIChE J.*, 21:49–57, 1975.

[334] M.L. Michelsen and J. Villadsen. *Chem. Eng. J.*, 4:64–68, 1972.

[335] J.O. Valderrama and V.H. Alvarez. *Fluid Phase Equilibr.*, 226:149–159, 2004.

[336] J.O. Valderrama and C.A. Faúndez. *Thermochim. Acta*, 499:85–90, 2010.

[337] H.C. Van Ness, S.M. Byers, and R.E. Gibbs. *AIChE J.*, 19:238–244, 1973.

[338] R. Privat, R. Gani, and J.-N. Jaubert. *Fluid Phase Equilibr.*, 295:76–92, 2010.

[339] S.B. Kiselev and J.F. Ely. *Ind. Eng. Chem. Res.*, 38:4993–5004, 1999.

[340] S.B. Kiselev and J.F. Ely. *Fluid Phase Equilibr.*, 174:93–113, 2000.

[341] S.B. Kiselev, J.F. Ely, I.M. Abdulagatov, and J.W. Magee. *Int. J. Thermophys.*, 21:1373–1405, 2000.

[342] S.B. Kiselev, J.F. Ely, H. Adidharma, and M. Radosz. *Fluid Phase Equilibr.*, 183-184:53–64, 2001.

[343] Z.-Q. Hu, J.-C. Yang, and Y.-G. Li. *Fluid Phase Equilibr.*, 205:1–15, 2003.

[344] Z.-Q. Hu, J.-C. Yang, and Y.-G. Li. *Fluid Phase Equilibr.*, 205:25–36, 2003.

[345] C. McCabe and S.B. Kiselev. *Fluid Phase Equilibr.*, 219:3–9, 2004.

[346] L. Sun, H. Zhao, S.B. Kiselev, and C. McCabe. *Fluid Phase Equilibr.*, 228-229:275–282, 2005.

[347] S.B. Kiselev, J.F. Ely, S.P. Tan, H. Adidharma, and M. Radosz. *Ind. Eng. Chem. Res.*, 45:3981–3990, 2006.

[348] F. Llovell and L.F. Vega. *J. of Supercritical Fluids*, 41:204–216, 2007.

[349] S.B. Kiselev and J.F. Ely. *J. Phys. Chem. C*, 111:15969–15975, 2007.

[350] A.M.A. Dias, F. Lovell, J.A.P Coutinho, I.M. Marrucho, and L.F. Vega. *Fluid Phase Equilibr.*, 286:134–143, 2009.

[351] J.A. White. *Fluid Phase Equilibr.*, 75:53–64, 1992.

[352] K.G. Wilson. *Phys. Rev. B*, 4:3184–3205, 1971.

[353] Y. Tang. *J. Chem. Phys.*, 109:5935–5944, 1998.

[354] L. Lue and J.M. Prausnitz. *J. Chem. Phys.*, 108:5529–5536, 1998.

[355] L. Lue and J.M. Prausnitz. *AIChE J.*, 44:1455–1466, 1998.

[356] J.G. Mi, Y.P. Tang, C.L. Zhong, and Y.G. Li. *J. Phys. Chem. B*, 109:20546–20553, 2005.

[357] J.G. Mi, C.L. Zhong, Y.G. Li, and Y.P. Tang. *AIChE J.*, 52:342–353, 2006.

[358] J.G. Mi, C.L. Zhong, Y.G. Li, and J. Chen. *Chem. Phys.*, 305:37–45, 2004.

[359] F. Llovell, J.C. Pámies, and L.F. Vega. *J. Chem. Phys.*, 121:10715–10724, 2004.

[360] D. Fu, X. Li, S. Yan, and T. Liao. *Ind. Eng. Chem. Res.*, 45:8199–8206, 2006.

[361] A. Bymaster, C. Emborsky, A. Dominik, and W.G. Chapman. *Ind. Eng. Chem. Res.*, 47:6264–6274, 2008.

[362] X. Tang and J. Gross. *Ind. Eng. Chem. Res.*, 49:9436–9444, 2010.

[363] X. Tang and J. Gross. *J. of Supercritical Fluids*, 55:735–742, 2010.

[364] K.G. Wilson. *Phys. Rev. B*, 4:3174–3183, 1971.

[365] M.E. Fisher. *Phys. Rev.*, 176:257–272, 1968.

[366] F. Llovell and L.F. Vega. *J. Chem. Phys. B*, 110:1350–1362, 2006.

[367] E.W. Lemmon, M.L. Huber, and M.O. McLinden. NIST standard reference database 23: Reference fluid thermodynamic and transport properties-refprop, version 9.0. Standard Reference Data Program, Gaithersburg, 2010. National Institute of Standards and Technology.

[368] V.A. Cymarnyi and V.M. Palaguta. *Zh. Prikl. Khim. (Leningrad)*, 63:905, 1990.

[369] G.K. Lavrenchenko, G.Y. Ruvinskii, S.V. Iljushenko, and V.V Kanaev. *Int. J. Refrig.*, 15:386–392, 1992.

[370] R.A. Heidemann and A.M. Khalil. *AIChE J.*, 26:769–778, 1980.

[371] R. Stockfleth and R. Dohrn. *Fluid Phase Equilibr.*, 145:43–52, 1998.

[372] P. Arce and M. Aznar. *J. of Supercritical Fluids*, 42:1–26, 2007.

[373] P. Beranek and I. Wichterle. *Fluid Phase Equilibr.*, 6:279–282, 1981.

[374] M.F. Alfradique and M. Castier. *Fluid Phase Equilibr.*, 257:78–101, 2007.

[375] D.N. Justo-García, F. García-Sánchez, N.L. Díaz-Ramírez, and A. Romero-Martínez. *Fluid Phase Equilibr.*, 265:192–204, 2008.

[376] M. Cismondi, E.A. Brignole, and J. Mollerup. *Fluid Phase Equilibr.*, 234:108–121, 2005.

[377] J.F. Blas and L.F. Vega. *J. Chem. Phys.*, 109:7405–7413, 1998.

[378] C. McCabe and G. Jackson. *Phys. Chem. Chem. Phys.*, 1:2057–2074, 1999.

[379] J.C. Pámies and L.F. Vega. *Mol. Phys.*, 100:2519–2529, 2002.

[380] P.H. Van Konynenburg and R.L. Scott. *Philos. Trans. R. Soc.*, 298:495–540, 1980.

[381] J. Gmehling, U. Onken, and W. Arlt. *Vapor-liquid equilibrium data collection, organic hydroxy compounds: alcohols (supplement 1)*, volume I, part 2c. DECHEMA Chemistry Data Series, Germany, 1981.

[382] J. Gmehling and U. Onken. *Vapor-liquid equilibrium data collection, alcohols: ethanol and 1,2-ethanediol (supplement 6)*, volume I, part 2h. DECHEMA Chemistry Data Series, Germany, 2006.

[383] A. Gil-Villegas, A. Galindo, P.J. Whitehead, S.J. Mills, G. Jackson, and A.N. Burgess. *J. Chem. Phys.*, 106:4168–4186, 1997.

[384] A. Galindo, L.A. Davies, A. Gil-Villegas, and G. Jackson. *Mol. Phys.*, 93:241–252, 1998.

[385] S. Tamouza, J.-P. Passarello, P. Tobaly, and J.-C. de Hemptinne. *Fluid Phase Equilibr.*, 222-223:67–76, 2004.

[386] S. Tamouza, J.-P. Passarello, P. Tobaly, and J.-C. de Hemptinne. *Fluid Phase Equilibr.*, 228-229:409–419, 2005.

[387] D. NguyenHuynh, J.-P. Passarello, P. Tobaly, and J.-C. de Hemptinne. *Fluid Phase Equilibr.*, 264:62–75, 2008.

[388] M. Seiler, J. Gross, B. Bungert, G. Sadowski, and W. Arlt. *Chem. Eng. Technol.*, 24:607–612, 2001.

[389] E. Calvet and H. Prat. *Recent Progresses in Microcalorimetry*. Pergamon Press, New York, 1963.

[390] Setaram Instrumentation. *C80 Calorimeter - Procedure experimental cells*. France, 2006.

[391] Setaram Instrumentation. *C80 Calorimeter - Commissioning*. France, 2006.

[392] J.B. Ott, G.V. Cornett, C.E. Stouffer, B.F. Woodfield, C. Guanquan, and J.J. Christensen. *J. Chem. Thermodyn.*, 18:867–875, 1986.

[393] J.B. Ott, C.E. Stouffer, G.V. Cornett, B.F. Woodfield, C. Guanquan, and J.J. Christensen. *J. Chem. Thermodyn.*, 19:337–348, 1987.

[394] D. Koschel. *Thermodynamics of acid gas, water and salt containing systems at high pressures and moderately elevated temperatures*. PhD thesis, Université Blaise Pascal, 2006.

[395] R. Zehioua, C. Coquelet, C.-B. Soo, D. Richon, and A.-H. Meniai. *Thermochim. Acta*, 495:72–80, 2009.

[396] C.G. Savini, D.R. Winterhalter, and H.C. Van Ness. *Int. Data Series, Sel. Data Mixtures Ser. A*, 11, 1976.

[397] S.E.M. Haman, G.C. Benson, and M.K. Kumaran. *J. Chem. Therm.*, 17:973–976, 1985.

Appendices

APPENDIX A

Determination of excess enthalpy by calorimetry

The measurement of excess enthalpy (h^{E}) is a mixing experiment, carried out primarily using calorimeters designed to detect changes in heat flux from a given reference state. All industrial mixing processes require, to some extent or another, knowledge of excess properties for the dimensioning of equipment and for transport calculations. Data on excess enthalpy can be used to tune models for excess Gibbs energy (NRTL, UNIQUAC), and is also required for thermodynamic consistency testing of isobaric VLE data. The blending of transport biofuels is such a mixing process, where one needs to cater for significant amounts of energy from the endothermic reactions.

Due to time constraints, a thorough investigation on calorimetric measurements of biofuel mixtures was not possible. We justify the inclusion of some preliminary calorimetry work here on the grounds of its relevance to the central theme of this work (biofuels), and as a foundation for future apparatus developments. In this work, we outline the experimental work conducted on Setaram micro-calorimeters operated in both the "static" and "dynamic" mode. We present, as before, the layout of the apparatuses and its experimental procedures, followed by some preliminary results. Recommendations for each mode of operation is discussed briefly thereafter.

A.1 The Setaram Calvet Calorimeters

The nature of two different calorimeters and setups were studied in this work, i.e. a "static" mode using the Calvet C80 calorimeter, and a "dynamic" mode using the BT2.15 calorimeter[1]. Both apparatus were manufactured by Setaram Instrumentation, France. While the circuits of the two setups differ, the design and functionalities of the two calorimeters are identical, and differ only in the temperature operating range. The Calvet C80 operates between room temperature and 573 K; while the BT2.15 has a lower maximum temperature of 473 K, but can operate at sub-zero conditions. The latter is possible due to an external jacket surrounding the body of the calorimeter, where a coolant present (usually liquid nitrogen or thermo-regulated ethanol) reduces the operating temperature. The BT2.15 is documented to withstand

[1]Work carried out in a two-week study at the *Laboratoire Thermodynamique et Interactions Moléculaire*, University of Blaise Pascal, France.

a minimum temperature of 77 K. The two calorimeters are based on the differential heat flux principle originally proposed by Tian and Calvet [389], which, under the correct setup, omits the need of knowing the heat capacity of the mixture. Both the calorimeters are versatile and can be modified for high pressure operation, as well as custom-made cells.

The C80 and BT2.15 calorimeters consist of a barrel-shaped, insulated enclosure attached to a base/console. The enclosure houses a large calorimetric block, within which two 12.5 cm^3 cylindrical wells are drilled for placement of the mixing cells. Highly sensitive heat flow detectors in the form of thermocouples surround the outer walls of the wells. These detectors send out signals upon detecting thermal exchanges between the cell and the calorimetric block, such as those present during mixing processes. Within the calorimetric block, a Pt-100 platinum probe monitors the sample temperature, whilst a Pt-200 platinum probe is used to control the temperature. This setup forms a compact assembly heated by a peripheral resistor. A sleeve surrounding the calorimetric block allows the circulation of cool air originating from the interior fan, for the purpose of ventilation.

The electronic circuits and the communication of data between the user and the calorimeter is identical in principle between the C80 and BT2.15. The analog signals from the internal heat flow detectors are transmitted to a receiver, where various analog commands may be performed. The principle CPU card and other auxiliary cards therein control and regulate the temperature of the calorimeter according to the user setpoint. The data signals are displayed in real time on a computer with the SetSoft software (ver. 2000, from Setaram Instrumentation), in a manner that can be interpreted by the operator.

A.2 Description of the apparatuses

Operation under "static" mode

The operation of the calorimeter under the "static" mode is a batch process, involving manual handling, downtime, cleaning, etc. The Calvet C80 calorimeter housed at the CEP/TEP laboratory is mounted off the ground on a reversal stand, the latter comprising a metallic shaft to which the entire calorimeter is attached to. It is capable of rotating the calorimeter through a one-dimensional, 180° arc. This automated mechanism enhances the mixing of liquids. The energy resulting from the rotation of the liquids has been verified to be negligible.

In this work, we use mainly membrane mixing cells, supplied by Setaram Instrumentation, for the measurement of excess enthalpies. These are batch-operating cells, as opposed to continuous mixing cells; thus the number of data points that can be measured within a specified time is considerably less. On the other hand, it requires much less chemicals and is less intensive on auxiliary equipments (continuous mixing cells require two additional syringe pumps for operation, see Fig. A.2). The membrane mixing cells are specifically adapted for the mixing of viscous fluids. Subject to a maximum condition of 493 K and 0.5 MPa, it consists of a cylindrical body partitioned into two isolated liquid compartments, each approximately 2.5 cm^3 in volume, by a membrane (13 mm diameter). The membrane must be made of an inert material, and one that can be broken with ease. Usually aluminium or teflon is used, although the former is preferred as it is easier to break. A command rod ending in a sharp fin runs along the central shaft of the cell and the cell well, piercing the membrane to bring the two liquids into contact. The energy associated with the breaking of an aluminium membrane has been verified to be negligible. The finned rod

also acts as a stirrer when rotated along the vertical axis. The components of the membrane mixing cells are shown in Fig. A.1.

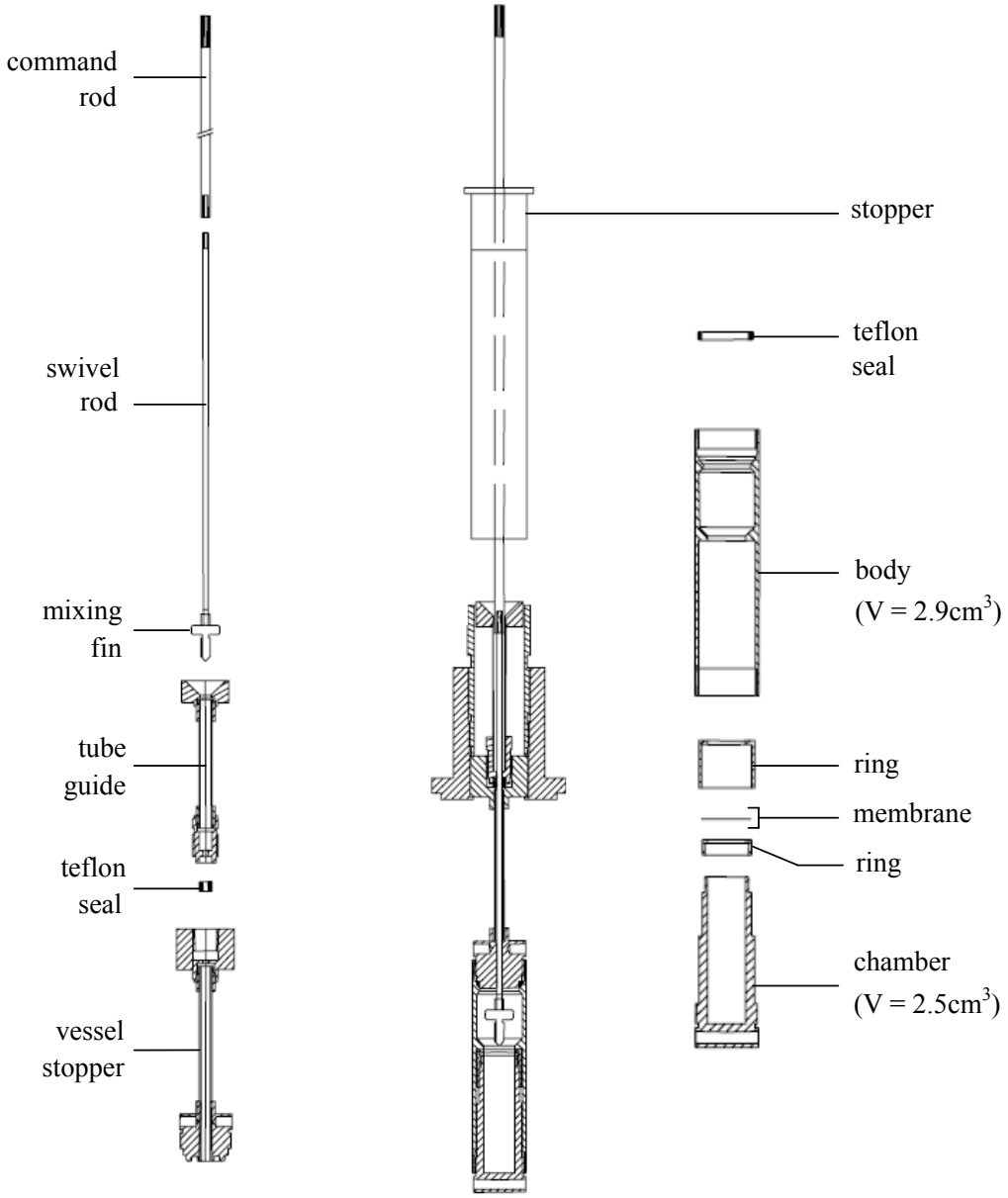

Figure A.1: Components of the stainless steel membrane mixing cell from Setaram Instrumentation, France [390].

A second type of mixing cell that was tested under the "static" setup is the reversal mixing cell (from Setaram Instrumentation). The reversal cell is exclusive to operation with the Calvet C80 adapted with the reversal fitting. The cell is designed such that the assembled cell, prior mixing, consists of two liquid chambers, stacked on top of each other, with a button covering the top chamber (tilting lid). Whereas membrane mixing is initiated by lowering a command rod, the reversal mixing is simply commenced via rotation of the reversal fitting. Upon rotation, the entire stacked structure within the cell collapses,

and the two liquids contact. Teflon O-rings confine the moving chambers to a small area in the cell body, where objects and liquid are thrown about as the calorimeter rotates. The higher density component is usually prepared in the bottom chamber. The reversal mixing cell was originally documented for use with mercury [390], a substance prohibited in modern laboratories. The reversal cell was not used in this work, since the membrane cell can act as a reversal cell, once the command rod is detached from the cell.

Operation under "dynamic" mode

The "dynamic" experimental setup is shown schematically in Fig. A.2, and is continuous in operation as opposed to the "static" batch operations. Two ISCO syringe pumps **SP**, of types 260D and 100DM, supplies liquid continuously to the calorimeter at a constant flowrate. The pump contents are thermally regulated along the length of its piston by a thermal jacket, within which a fluid (water in this case) circulates to and from a water bath **WB** (Julabo, model F-12). The fluid from the pumps passes through a series of three preheaters before reaching the calorimetric block. A cylindrical external preheater **EP**, where three access ways, drilled along the entire length of the preheater, allow for close thermal contact for the two entering and one exiting lines. The lines pass counter-currently to optimize available heat transfer and energy efficiency. The external preheater is regulated via a FLUKE 2200 temperature controller **TR**. Two internal preheaters **IP**, situated in the spaces above the calorimetric block, further brings the fluid to a temperature no less than 0.01 K to that regulated in the calorimetric block. This ensures that no energy is introduced within the calorimeter to bring the liquid to the experiment temperature - the only heat evolved is from the mixing process alone. The two internal preheaters are regulated via two ERO Electronic controllers. Lightbulbs of various power settings are placed sufficiently close to the external preheater to assist with fine regulation of the preheaters.

Continuous mixing cells, designed for dynamic modes of operation, were developed and constructed at the University of Blaise Pascal, France. The two arriving fluids enter the mixing cell separately in parallel tubes, and are discharged into a small mixing space/chamber at the tube endings. This mixing space is variable in size depending on the construction, and forms the beginning of a coil of tubes spiraling upwards along the length of the cell body. The fluids are mixed inside the coil, and leave the cell to counter-currently exchange heat with the incoming fluids through the three preheaters. The pressure of the exiting fluid is measured via a pressure transducer **PT** before being purged from the system.

A.3 Calibration of equipment

Temperature calibration

The temperature calibration is the first task required in the preparation for the measurements of excess enthalpy. The objective is to verify that the temperature inside the cell wells of the calorimetric block, within which the mixing cells are placed, corresponds to the temperature reading given by the calorimeter. The calorimeter temperature display is based on readings from the Pt-200 probe situated in the calorimetric block, between the two cell wells, thus there exists a slight displacement between the wells and the sensitive proportion of the Pt-200 probe.

The temperature calibration for isothermal conditions is performed as follows: A Pt-100 platinum temperature probe, embedded in a cylinder of the same dimensions as a measurement cell, is placed in the

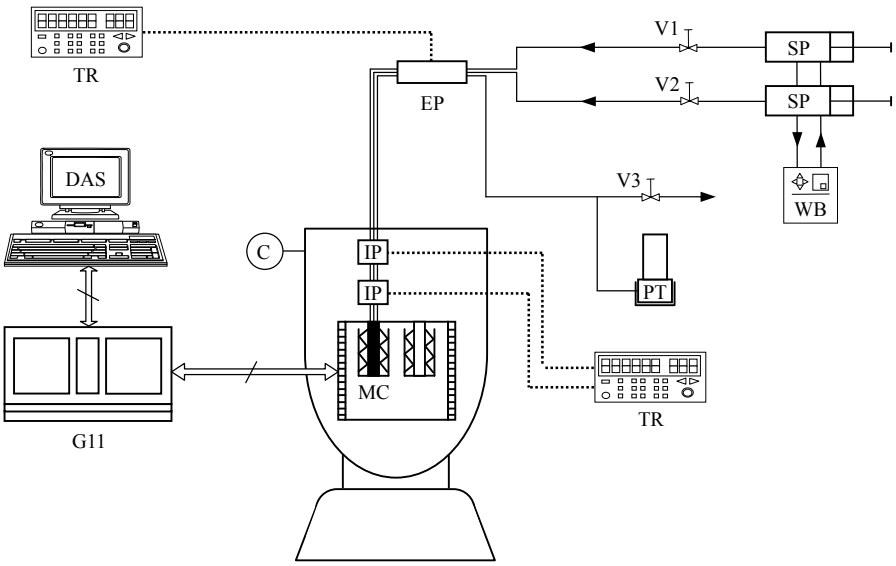

Figure A.2: Schematic diagram of the BT2.15 calorimeter and its external "dynamic" circuit setup. C: BT2.15 Calorimeter; DAS: Data Acquisition System; EP: External Preheater; G11: Setaram G11 interface controller; IP: Internal Preheater; MC: Mixing Cell; PT: Pressure Transducer; SP: Syringe Pumps; TR: Temperature Regulator; V_i: Valve; WB: Water Bath.

reference well. In the measurement well rests the cell used for the succeeding experiments. With such a configuration, the temperature measured on the Pt-100 platinum temperature probe can be compared directly to the value indicated on the computer/data acquisition system. Any necessary adjustments, if necessary, can then be carried out.

The temperature calibration for non-isothermal (ramped) measurements is performed by determination of fusion points of standard materials. This is not performed during the study, and is described elsewhere [390, 391]. Nonetheless, it is also possible to perform a temperature calibration using standard materials, when working at an isothermal condition. A prerequisite is the availability of standard materials of high purity, with a fusion temperature similar to that of the isothermal condition. This is less preferred than the method above, as there are only a limited selection of standard materials, and often the correction factor may need to be interpolated/extrapolated to the working condition.

Sensitivity calibration

The principles of Tian and Calvet was based on the prerequisite that galvanometric voltages, proportional to the heat flow, over a period of time could be converted to power, in the units of Watts. Indeed, the Calvet calorimeters provide information of heat flow in units of μV or μV.s; thus a calibration constant is required to translate between the equivalence of power (W) and electric (V) terms. This constant, denoted herein as S, is known as the sensitivity constant, and may be determined using either chemical or electric means.

The sensitivity constant is sensitive to any changes in the characteristics of the system. A specific calibration constant S is applicable only for a specific type of cell, with its specific material of construction, at a specific measurement condition. Changes in any one of the aforementioned variables would require

a new calibration; or at least a verification of; the sensitivity constant. This implies that sensitivity calibrations should be performed regularly.

In the electrical calibration, an electric impulse of constant magnitude is sent from the calibrator to a specifically-designed Joule-effect cell, over a known period of time t. At a constant temperature, the impulse results in a change in a heat flow at the calorimetric block, producing a peak signal on the interface with an area A in μV.s units. By measuring the power P delivered by the electric calibrator, the sensitivity constant can be determined, in units of μV/mW:

$$S = \frac{A}{Pt}$$

The accuracy of the calibration relies heavily on the precision of the value of P. It is necessary to repeat the calibration for different time intervals and impulse magnitudes, and verify that the same S can be obtained repeatedly for a given temperature. The chemical calibration is a more applied method for obtaining the sensitivity constant, and is the approach adopted in this work. Depending on the type of experiment to be conducted, a reference system of near or identical conditions is selected and performed first. The selected reference system must involve the same type of phases, and must be at the same temperature. The objective is to reproduce, as closely as possible, the values of the reference system by treating the calibration constant S as a degree of freedom in the calculation of h^{E}. For liquid-liquid h^{E} measurements, the reference system chosen is the ethanol + water system measured by Ott et al. [392, 393]. The authors of the publications give a sound argument as to the reasons for choosing ethanol + water as a reference mixture, including cost, ease of mixing, stability, toxicity, available purity, etc. The reported excess enthalpies themselves are rigorously measured, and span large temperature and pressure ranges. The chemical calibration is carried out as any other type of binary liquid-liquid h^{E} measurements (see below), except that the value of S is adjusted such that the values of the reference system are reproduced as closely as possible. If S is an independent parameter, then $h^{\mathrm{E}}_{\mathrm{calib}} = f(S)$ and the following objective function F can be applied:

$$F = \sum_i \left(h^{\mathrm{E}}_{\mathrm{calib}} - h^{\mathrm{E}}_{\mathrm{ref}}\right)^2 \tag{A.1}$$

For a constant $T = 303.15$ K, using the continuous flow mixing cell, the response of the $h^{\mathrm{E}}_{\mathrm{calib}}$ to changes in the value of S is shown in Fig. A.3. In this case, the optimal value of S is 3.67 μV/mW.

Once the sensitivity constant has been determined, it is a fixed value that is applied to the experiments which follow. It can also be input directly in the SetSoft program. Under the "dynamic" mode, it is preferential to prevent any dismantling of the calorimeter during the course of an experiment, to avoid the need of re-calibration. Koschel [394] compared the sensitivity constants determined by the electrical and chemical approach at different temperatures, and noted differences of less than 2 μV/mW between the two methods.

Regulation of preheaters ("dynamic" mode only)

A pure fluid, arriving at the calorimeter at the same temperature as that regulated within the calorimeter, will not cause a disturbance to a stable signal in the data acquisition. Conversely, a volumetric flow maintained at a constant temperature distinctly different from that of the calorimetric block, will induce a constant thermal effect. This in turn is reflected as a steady, deviated signal in the data acquisition

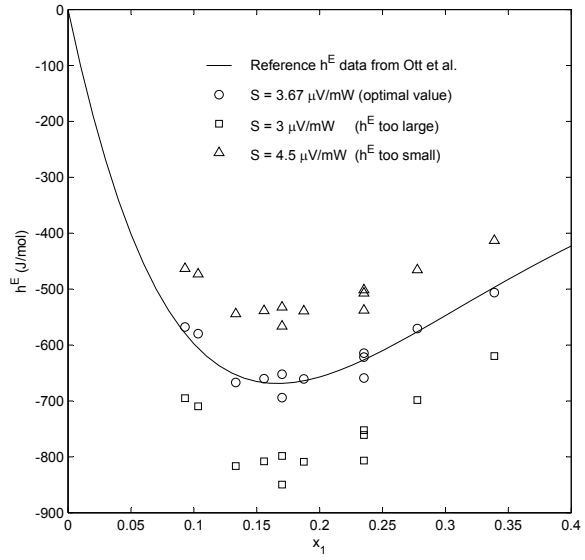

Figure A.3: Chemical calibration for the "dynamic" setup using the reference system ethanol (1) + water (2) at 303.1 K, from Ott et al. [392, 393]. The same set of measurements can be shifted vertically by varying the value of S, until the measurement values match those of the reference system, given by the solid line.

system, with a positive value indicating an endothermic effect (the fluid arrives at a lower temperature) and vice versa. The function of the water bath (**WB**) and the three preheaters (**EP**, 2×**IP**) is to ensure that the incoming fluids reach the mixing cell at a temperature not more than 0.01 K from the measurement temperature. This can be achieved by arranging the setpoints of all preheaters in such a way that a range of volumetric flowrates could be used during the experiment, without the occasion of the fluid arriving at the calorimeter at a temperature more than ± 0.01 K from the experimental temperature.

The procedure for finding the optimal combination of setpoints is as follows: one of the two components is passed to the calorimeter at a sufficiently low flowrate, usually 0.1 cm^3/min. This delivers a stable baseline signal after a sufficient amount of time, and is noted as the baseline value for the specific flowrate and the combination of the four setpoints. Depending on the working range of the excess enthalpy measurement, it may be required to adjust the preheater setpoints in order to bring the baseline value closer to zero. The correct combination of setpoints is determined by trial-and-error, and changes should always be made in small increments of 0.1 - 0.2 K.

When a satisfactory baseline value has been obtained at a reasonably low flowrate, the flowrate is increased slowly to observe the behaviour of the baseline. If the baseline changes significantly, it may be necessary to readjust the setpoint combination, and test once again throughout the desired flowrate range. This regulation process should be performed for both components, and every time a new component is used in the setup.

A.4 Experimental procedures

Operation under "static" mode

The temperature of the C80 calorimeter is first stabilized at the required setpoint. A Mettler AT 200 analytical balance, with a maximum deviation of 0.1 mg, is used to weigh the required masses in both compartments of the membrane cell to achieve the desired composition. The reference cell is kept empty. The cells are then placed in the calorimeter and isolated until the temperature and heat flow has stabilized on the SetSoft 2000 interface. Mixing is initiated via lowering the command rods of both cells and breaking the partition membrane, and followed by gentle rotation of the rod to aid mixing. Thereafter, both command rods (measurement and reference cells) are detached from their cell bodies, and the reversal stand is activated to rotate the calorimeter through semi-circular arcs until the end of the experiment. In this way, the features of both the membrane and reversal cells are achieved. An integration of the heat flow peak yields the excess enthalpy, and each composition measured is repeated at least two times. An example of an acquisition peak is shown in Figure A.4, where the calibration constant S has already been input into the software.

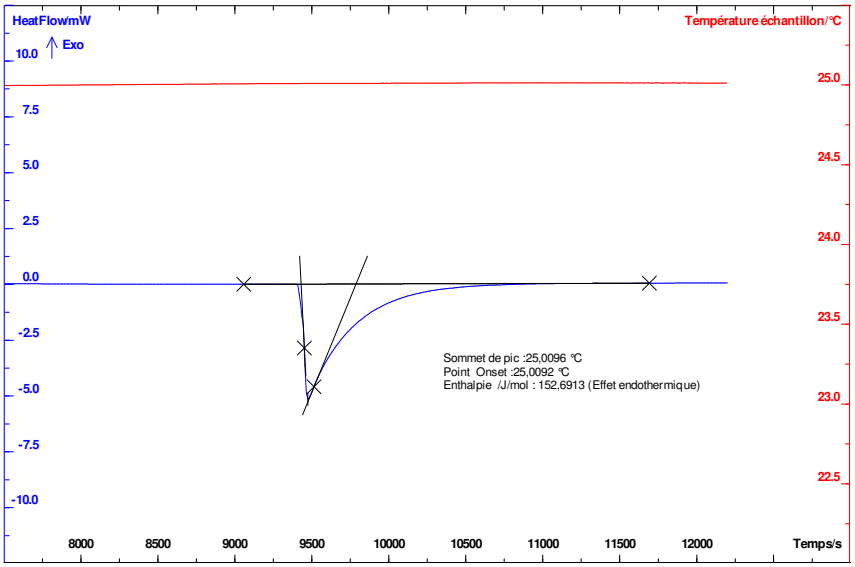

Figure A.4: Integration of an excess enthalpy experimental acquisition for the binary system cyclohexane (1) + *n*-hexane (2) at 298 K and 1 atm. The calorimeter was operated under the "static" mode, using the membrane mixing cell and aluminium membranes. The h^{E} value obtained from this acquisition is 152.7 J/mol.

Operation under "dynamic" mode

The two ISCO syringe pumps are loaded with each of the two pure components. No vacuum within the pumps was taken prior to loading. The loaded pumps were put under pressure and degassed thoroughly by venting any existing air spaces above the liquids. The pumps were then depressurized to ambient pressure.

The exit valve (**V3**) is maintained opened throughout the experiment. The component designated as the baseline component was pressurized slightly in its pump, and passed to the calorimeter by opening its corresponding valve (**V1** or **V2**). Designating this component as 1, component 1 is passed through the

calorimeter at a constant volumetric flowrate $\dot{v}_1 = \dot{v}_{max}$, where $\dot{v}_{max}$ is the maximum flowrate possible for liquids to enter the calorimeter without significantly affecting the baseline (see preheater regulation in § A.3). The baseline is established in approximately 30 minutes, when the heat flux value fluctuates at ± 0.05 μV of an average value. The average baseline value (q_{base}) is recorded. The mixing process is initiated by starting the second pump and releasing component 2 into the system at a flowrate such that the sum of the two flowrates, $\dot{v}_1$ and $\dot{v}_2$, should equal but not exceed the maximum flowrate that the preheaters are regulated, i.e. $\dot{v}_1 + \dot{v}_2 \leq \dot{v}_{max}$.

A second plateau, after that of the baseline, appears approximately 20 - 25 minutes upon introduction of the second component. This value ($q_{plateau}$) is again recorded, once the heat flux value fluctuates at ± 0.05 μV of an average value. The excess enthalpy h^E of the system, for a certain combination of $\dot{v}_1$ and $\dot{v}_2$ flows, is calculated via the following expression,

$$h^E = \frac{q_{plateau} - q_{base}}{\dot{n}_{total} S} \tag{A.2}$$

where h^E is in J/mol, q is a heax flux in μV, and S is the sensitivity constant determined beforehand, in units of μV/mW. The molar flowrate $\dot{n}$, in mol/s, can be calculated from the relation:

$$\dot{n}_{total} = \dot{n}_1 + \dot{n}_2 = \frac{\dot{v}_1 \rho_1}{MM_1} + \frac{\dot{v}_2 \rho_2}{MM_2} \tag{A.3}$$

where, for the ith component, $\dot{v}$ is the volumetric flowrate in cm^3/min, ρ is the density in g/cm^3, and MM is the molar mass in g/mol. The densities ρ at the temperature of the experiment can be found in standard handbooks [68, 153, 154]. A series of excess enthalpy values could thus be measured by varying the volumetric flowrates to achieve different mole fractions, as shown in Fig. A.5, for an arbitrary system.

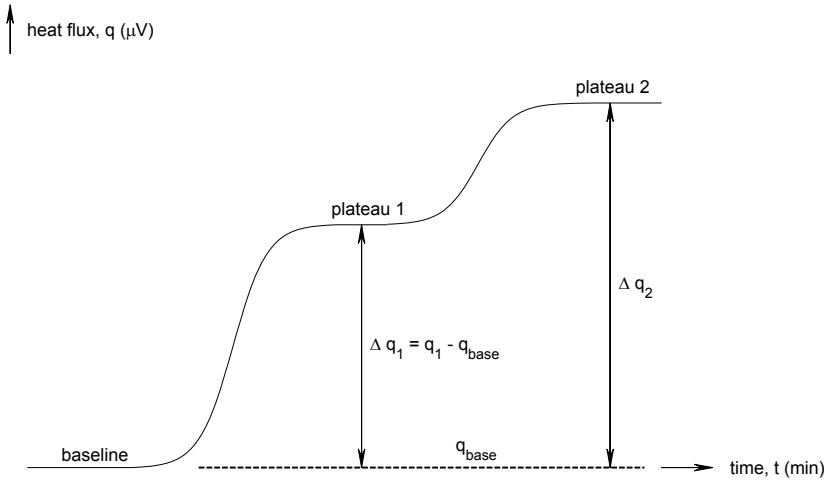

Figure A.5: Illustration of an *q-t* profile for an arbitrary system measured under the "dynamic" mode.

A flowrate higher than 0.05 cm^3/min should be maintained from either pumps at all times. For a particular mole fraction, more than one combination of flowrates, of the same ratio, should be used, to verify the excess enthalpy is not a function of the flowrates used to achieve the mole fraction. The "dynamic" setup also allows checking for hysteresis in the measurement.

A.5 Results and discussion

In this work, excess enthalpies were measured for the cyclohexane + *n*-hexane system under the "static" mode (system 1), and for the ethanol + *n*-hexane system under the "dynamic mode" (system 2). The values of h^{E} obtained are tabulated in Table A.1, and plotted in Fig. A.6. For system 1, it is important to ensure that the masses prepared in the two separate liquid compartments of the membrane cell utilizes as much available space as possible, i.e. vapour spaces are kept to a minimum in both compartments of the cell. As the heat flow signal takes a long time to stabilize after the batch cells are introduced to the calorimeter (± 45 mins), any volatile components will have the tendency to transfer to the vapour space, thereby altering the intended mole fraction. This can seriously affect the performance under "static" mode for dilute concentrations, where one of the components has a very small mass. The problem of volatility is resolved under the "dynamic" mode, where liquid phases are ensured in the circuits to the calorimeter, and the mixed solution is continuously removed from the system. In biofuel-related mixtures, where volatility is often a factor, the "dynamic" mode is likely to be the preferred method. Conversely, for viscous mixtures, where complete mixing becomes difficult, the operator may promote additional mixing by using the finned agitator under the "static" mode. For mixtures involving heavy esters, the volatility factor is negligible, and better mixing is possibly achieved with the "static" method. The same degree of mixing may be achieved with high volumetric flowrates under the "dynamic mode", although the mixing cells may require modifications to increase the retention time of the mixture in the measurement portion of the calorimeter. Furthermore, high volumetric flowrates may interfere with the regulation of preheaters upstream. An example of h^{E} measurements involving a highly viscous mixture is the water + triethylene glycol system [395], measured under the "static" mode and shown in Fig. A.7.

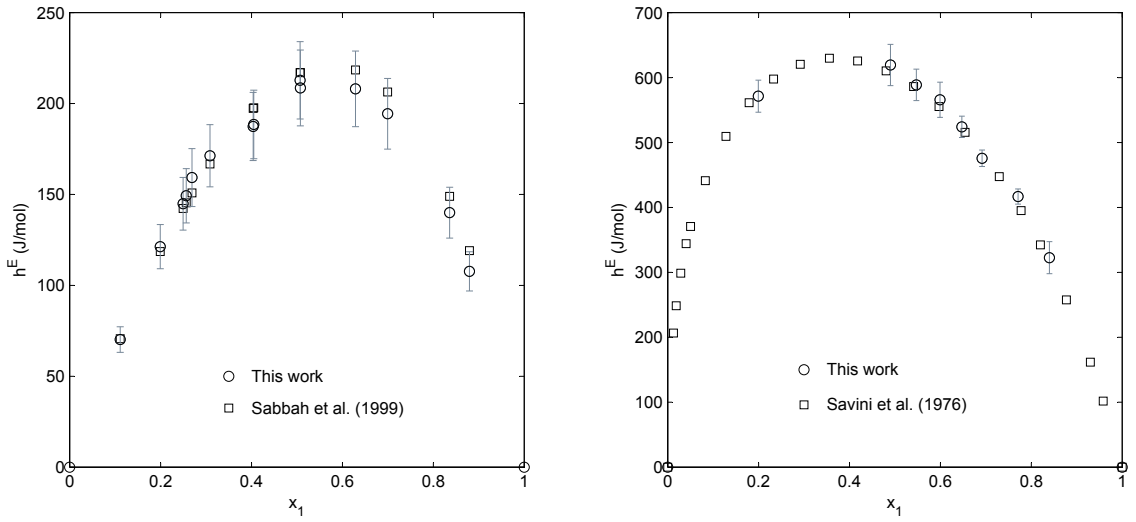

Figure A.6: Excess molar enthalpies for the cyclohexane (1) + *n*-hexane (2) system using the "static" mode at 298.2 K and 101.3 kPa (*left*), and for the ethanol (1) + *n*-hexane (2) system using the "dynamic" mode at 303.2 K and 101.3 kPa (*right*). Experimental data taken from Refs. [316, 396].

A major problem encountered in both modes of operation was the poor repeatability of the apparatus. Consecutive measurements, of the same mole fraction, but with different mass or flowrate ratios, may

Table A.1: Excess molar enthalpies for the cyclohexane (1) + *n*-hexane (2) and ethanol (1) + *n*-hexane (2) systems at 101.3 kPa.

x_1	h^E (J/mol)	x_1	h^E (J/mol)
	cyclohexane (1) + *n*-hexane (2)		
	T = 298.2 K		
0.111	70 ± 7	0.405	188 ± 19
0.199	121 ± 12	0.507	213 ± 21
0.249	145 ± 14	0.508	209 ± 21
0.257	149 ± 15	0.629	208 ± 21
0.269	159 ± 16	0.700	194 ± 19
0.309	171 ± 17	0.836	140 ± 14
0.404	187 ± 19	0.880	108 ± 11
	ethanol (1) + *n*-hexane (2)		
	T = 303.2 K		
0.200	571 ± 25	0.647	524 ± 16
0.490	619 ± 32	0.692	476 ± 13
0.547	589 ± 24	0.771	417 ± 12
0.599	566 ± 27	0.840	323 ± 25

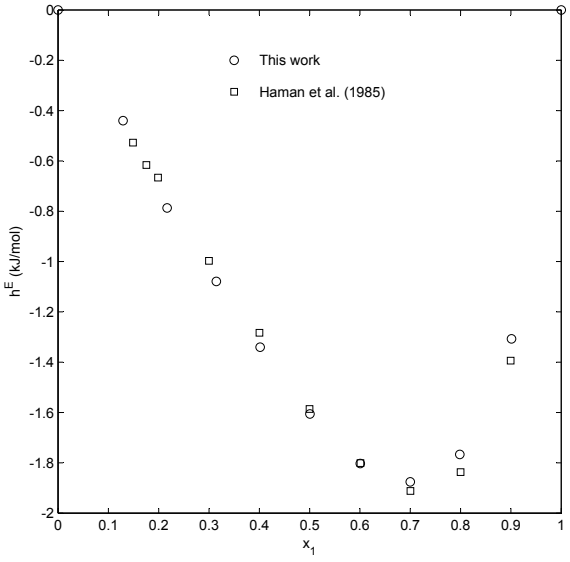

Figure A.7: Excess molar enthalpies for the water (1) + triethylene glycol (2) system using the "static" mode at 298.2 K and 101.3 kPa. Experimental data taken from Haman et al. [397].

differ by up to 5 %. This scattering of results is compromised by using an averaged value, together with a large uncertainty band. In fact, the uncertainties from elements such as volumetric flowrate and mass balances appear negligible compared to that which stems from repeated measurements. In Fig. A.6 we have based the uncertainty estimation solely on inconsistencies in repeatability, with a coverage factor

$k = 2$ ($U\left(h^{\mathrm{E}}\right) = 2u_{\mathrm{rep}}\left(h^{\mathrm{E}}\right)$), to show this effect. While more binary systems would have to be tested for both setups in order reach a conclusion, the "static" mode so far has appeared poor in measuring system 1, which contains two volatile components. An uncertainty of ± 10 % was observed throughout the experiment.

There are several possibilities to which the "static" mode may be improved. Mixing may be enhanced within the membrane cell by placing very fine glass pieces which move with the mixture as the calorimeter rotates aerially. One should ensure that no significant kinetic energy is introduced by the deployment of additional agitators, which may contribute undesirably to the final h^{E} value. This can be tested by rotating a pure fluid, of similar viscosity, containing the same amount of glass pieces, and observing any changes in the heat flux within the system. If necessary, the kinetic energy can be offset each time from the final h^{E} value. Any foreign objects included in the cell to assist with stirring should not react with the pure or mixed liquids, or cause damage to the finned agitator seated in the central axis. To decrease the long standby time needed for the heat flux to stabilize under the "static" mode, the calorimeter should be confined in an insulated and thermally-regulated enclosure. This also allows measurements to be carried out at below-ambient temperatures. The mixture at the end of a batch experiment may be analyzed in a calibrated refractometer or gas chromatograph to validate the true mixture composition.

In the "dynamic" mode, the mixing cell is the most commonly-modified aspect of the apparatus. There are no continuous flow cell designs which can accommodate the mixing of every fluid phase combination; thus cells are often constructed or manipulated for a specific type of measurement condition. The temperature/preheater regulation of the entering fluid remains a complication, which may possibly be improved by heating and insulating all exposed parts of the circuit, rather than employing preheaters at specific points of the circuit.

APPENDIX B

Analytical derivatives of the PCIP-SAFT equation of state

The Perturbed-Chain SAFT, combined with the polarizable dipole contribution (PCIP-SAFT), works with an effective Helmholtz energy ($A^{DD,eff}/NkT$) different to that of the A^{DD}/NkT in the unrenormalized theory, which does not account for the polarizability of dipole molecules. This section gives the analytical derivatives for the main expressions, such as the effective dipole moment, second and third order perturbation expansions, with respect to density (packing fraction), mole fractions and temperature. The nomenclature and definition of the terms are in accordance to the work of Kleiner and Gross [136], to which the reader may refer for guidelines. All Helmholtz free energies are written here in their reduced quantities, i.e. in lower caps, with no tilde (~).

$$a = \frac{A}{NkT}$$

In addition, the partial derivative are always taken with all other variables held constant, even if they are not indicated in subscripts. For example, a partial derivative taken with respect to the effective dipole moment of component i implies:

$$\frac{\partial a'^{DD}}{\partial \mu_i^{*eff}} = \left(\frac{\partial a'^{DD}}{\partial \mu_i^{*eff}}\right)_{\rho,T,\mathbf{x},\mu_{j\neq i}^{*eff}}$$

Since the polar contributions to the total residual Helmholtz free energy are usually written as a Pad prime e approximant, the following expressions apply also to the other multipole theories. The unrenormalized dipole theory is recovered by setting the polarizabilities of all components to zero. This implies a permanent dipole moment, and all derivatives of the effective dipole moment are subsequently zero. The expressions for the quadrupole-quadrupole contributions can be recovered similarly. The dipole moments are replaced by quadrupole moments, and the appropriate constants are used for the perturbation terms (a_2^{QQ}, a_3^{QQ}) and integral correlations ($J_{2,ij}^{QQ}$, $J_{3,ijk}^{QQ}$).

Table B.1: Quick referencing of the derivatives presented in Appendix B

Eqn.	Num.	Eqn.	Num.	Eqn.	Num.	Eqn.	Num.	Eqn.	Num.	Eqn.	Num.
$\frac{\partial a_2'^{DD}}{\partial \mu_i^{*eff}}$	B.1	$\frac{\partial^2 a_2'^{DD}}{\partial \mu_i^{*eff2}}$	B.2	$\frac{\partial^3 a_2'^{DD}}{\partial \mu_i^{*eff3}}$	B.3	$\frac{\partial^4 a_2'^{DD}}{\partial \mu_i^{*eff4}}$	B.4	$\frac{\partial a_3'^{DD}}{\partial \mu_i^{*eff}}$	B.5	$\frac{\partial^2 a_3'^{DD}}{\partial \mu_i^{*eff2}}$	B.6
$\frac{\partial^3 a_3'^{DD}}{\partial \mu_i^{*eff3}}$	B.7	$\frac{\partial^4 a_3'^{DD}}{\partial \mu_i^{*eff4}}$	B.8	$\frac{\partial \mu_i^{*eff}}{\partial \eta}$	B.9	$\frac{\partial^2 \mu_i^{*eff}}{\partial \eta^2}$	B.10	$\frac{\partial^n \mu_i^{*eff}}{\partial \eta^n}$	B.11	$\frac{\partial a'^{DD,eff}}{\partial \eta}$	B.12
$\frac{\partial^2 a'^{DD,eff}}{\partial \eta^2}$	B.13	$\frac{\partial^3 a'^{DD,eff}}{\partial \eta^3}$	B.14	$\frac{\partial a_2'^{DD}}{\partial \eta}$	B.15	$\frac{\partial^2 a_2'^{DD}}{\partial \eta^2}$	B.16	$\frac{\partial^3 a_2'^{DD}}{\partial \eta^3}$	B.17	$\frac{\partial^2 a_2'^{DD}}{\partial \eta \partial \mu_i^{*eff}}$	B.18
$\frac{\partial^3 a_2'^{DD}}{\partial \eta^2 \partial \mu_i^{*eff}}$	B.19	$\frac{\partial^4 a_2'^{DD}}{\partial \eta^3 \partial \mu_i^{*eff}}$	B.20	$\frac{\partial a_3'^{DD}}{\partial \eta}$	B.21	$\frac{\partial^2 a_3'^{DD}}{\partial \eta^2}$	B.22	$\frac{\partial^3 a_3'^{DD}}{\partial \eta^3}$	B.23	$\frac{\partial^2 a_3'^{DD}}{\partial \eta \partial \mu_i^{*eff}}$	B.24
$\frac{\partial^3 a_3'^{DD}}{\partial \eta^2 \partial \mu_i^{*eff}}$	B.25	$\frac{\partial^4 a_3'^{DD}}{\partial \eta^3 \partial \mu_i^{*eff}}$	B.26	$\frac{\partial \mu_i^{*eff}}{\partial x_k}$	B.27	$\frac{\partial a'^{DD,eff}}{\partial x_k}$	B.28	$\frac{\partial a_2'^{DD}}{\partial x_k}$	B.29	$\frac{\partial^2 a_2'^{DD}}{\partial x_k \partial \mu_i^{*eff}}$	B.30
$\frac{\partial a_3'^{DD}}{\partial x_k}$	B.31	$\frac{\partial a_3'^{DD}}{\partial x_k \partial \mu_i^{*eff}}$	B.32	$\frac{\partial \mu_i^{*eff}}{\partial T}$	B.33	$\frac{\partial^2 \mu_i^{*eff}}{\partial T^2}$	B.34	$\frac{\partial a'^{DD,eff}}{\partial T}$	B.35	$\frac{\partial^2 a'^{DD,eff}}{\partial T^2}$	B.36
$\frac{\partial a_2'^{DD}}{\partial T}$	B.37	$\frac{\partial^2 a_2'^{DD}}{\partial T^2}$	B.38	$\frac{\partial^2 a_2'^{DD}}{\partial T \partial \mu_i^{*eff}}$	B.39	$\frac{\partial^3 a_2'^{DD}}{\partial T^2 \partial \mu_i^{*eff}}$	B.40	$\frac{\partial a_3'^{DD}}{\partial T}$	B.41	$\frac{\partial^2 a_3'^{DD}}{\partial T^2}$	B.42
$\frac{\partial^2 a_3'^{DD}}{\partial T \partial \mu_i^{*eff}}$	B.43	$\frac{\partial^3 a_3'^{DD}}{\partial T^2 \partial \mu_i^{*eff}}$	B.44	$\frac{\partial^2 \mu_i^{*eff}}{\partial \eta \partial T}$	B.45	$\frac{\partial^2 a'^{DD,eff}}{\partial \eta \partial T}$	B.46	$\frac{\partial^2 a_2'^{DD}}{\partial \eta \partial T}$	B.47	$\frac{\partial^3 a_2'^{DD}}{\partial \eta \partial T \partial \mu_i^{*eff}}$	B.48
$\frac{\partial^2 a_3'^{DD}}{\partial \eta \partial T}$	B.49	$\frac{\partial^3 a_3'^{DD}}{\partial \eta \partial T \partial \mu_i^{*eff}}$	B.50								

Implicit equation for the effective dipole moment

$$\mu_i^{*eff} = \mu_i^* - \frac{\alpha_i^* T_i^*}{x_i} \frac{\partial a'^{DD}}{\partial \mu_i^{*eff}}$$

Derivatives of the polar perturbation terms with respect to the effective dipole moment

$$\frac{\partial a_2'^{DD}}{\partial \mu_i^{*eff}} = -4\pi\rho \sum_j x_i x_j \frac{\epsilon_i}{kT} \frac{\epsilon_j}{kT} z_j^A \mu_i^{*eff} \frac{\sigma_i^3 \sigma_j^3}{\sigma_{ij}^3} J_{2,ij}^{DD} \tag{B.1}$$

$$\frac{\partial^2 a_2'^{DD}}{\partial \mu_i^{*eff2}} = -8\pi\rho x_i^2 \left(\frac{\epsilon_i}{kT}\right)^2 \left(\mu_i^{*eff}\right)^2 \sigma_i^3 J_{2,ii}^{DD} - 4\pi\rho \sum_j x_i x_j \frac{\epsilon_i}{kT} \frac{\epsilon_j}{kT} z_j^A \frac{\sigma_i^3 \sigma_j^3}{\sigma_{ij}^3} J_{2,ij}^{DD} \tag{B.2}$$

$$\frac{\partial^3 a_2'^{DD}}{\partial \mu_i^{*eff3}} = -24\pi\rho x_i^2 \left(\frac{\epsilon_i}{kT}\right)^2 \mu_i^{*eff} \sigma_i^3 J_{2,ii}^{DD} \tag{B.3}$$

$$\frac{\partial^4 a_2'^{DD}}{\partial \mu_i^{*eff4}} = -24\pi\rho x_i^2 \left(\frac{\epsilon_i}{kT}\right)^2 \sigma_i^3 J_{2,ii}^{DD} \tag{B.4}$$

$$\frac{\partial a_3'^{DD}}{\partial \mu_i^{*eff}} = -8\pi^2\rho^2 \sum_j \sum_l x_i x_j x_l \frac{\epsilon_i}{kT} \frac{\epsilon_j}{kT} \frac{\epsilon_l}{kT} z_j^A z_l^A \frac{\sigma_i^3 \sigma_j^3 \sigma_l^3}{\sigma_{ij}\sigma_{il}\sigma_{jl}} \mu_i^{*eff} J_{3,ijl}^{DD} \tag{B.5}$$

$$\frac{\partial^2 a_3'^{DD}}{\partial \mu_i^{*eff2}} = -8\pi^2\rho^2 \left[4 \sum_j x_i^2 x_j \left(\frac{\epsilon_i}{kT}\right)^2 \frac{\epsilon_j}{kT} z_j^A \left(\mu_i^{*eff}\right)^2 \frac{\sigma_i^5 \sigma_j^3}{\sigma_{ij}^2} J_{3,iij}^{DD} + \sum_j \sum_l x_i x_j x_l \frac{\epsilon_i}{kT} \frac{\epsilon_j}{kT} \frac{\epsilon_l}{kT} z_j^A z_l^A \frac{\sigma_i^3 \sigma_j^3 \sigma_l^3}{\sigma_{ij}\sigma_{il}\sigma_{jl}} J_{3,ijl}^{DD}\right] \tag{B.6}$$

$$\frac{\partial^3 a_3'^{DD}}{\partial \mu_i^{*eff3}} = -32\pi^2\rho^2 \left[2x_i^3 \left(\frac{\epsilon_i}{kT}\right)^3 \left(\mu_i^{*eff}\right)^3 \sigma_i^6 J_{3,iii}^{DD} + 3 \sum_j x_i^2 x_j \left(\frac{\epsilon_i}{kT}\right)^2 \frac{\epsilon_j}{kT} z_j^A \mu_i^{*eff} \frac{\sigma_i^5 \sigma_j^3}{\sigma_{ij}^2} J_{3,iij}^{DD}\right] \tag{B.7}$$

$$\frac{\partial^4 a_3'^{DD}}{\partial \mu_i^{*eff4}} = -96\pi^2\rho^2\left[4x_i^3\left(\frac{\epsilon_i}{kT}\right)^3\left(\mu_i^{*eff}\right)^2\sigma_i^6 J_{3,iii}^{DD} + \sum_j x_i^2 x_j\left(\frac{\epsilon_i}{kT}\right)^2\frac{\epsilon_j}{kT}z_j^A\frac{\sigma_i^5\sigma_j^3}{\sigma_{ij}^2}J_{3,iij}^{DD}\right] \tag{B.8}$$

Density derivatives for the effective Helmholtz energy

$$\frac{\partial \mu_i^{*eff}}{\partial \eta} = -\frac{\alpha_i^* T_i^*}{x_i}\frac{\partial^2 a'^{DD}}{\partial\eta\partial\mu_i^{*eff}} \tag{B.9}$$

$$\frac{\partial^2 \mu_i^{*eff}}{\partial \eta^2} = -\frac{\alpha_i^* T_i^*}{x_i}\frac{\partial^3 a'^{DD}}{\partial\eta^2\partial\mu_i^{*eff}} \tag{B.10}$$

$$\frac{\partial^n \mu_i^{*eff}}{\partial \eta^n} = -\frac{\alpha_i^* T_i^*}{x_i}\frac{\partial^{n+1} a'^{DD}}{\partial\eta^n\partial\mu_i^{*eff}} \tag{B.11}$$

$$\frac{\partial a'^{DD,eff}}{\partial \eta} = \frac{\partial a'^{DD}}{\partial \eta} + \sum_i \frac{\alpha_i^* T_i^*}{x_i}\frac{\partial a'^{DD}}{\partial \mu_i^{*eff}}\frac{\partial^2 a'^{DD}}{\partial\eta\partial\mu_i^{*eff}} \tag{B.12}$$

$$\frac{\partial^2 a'^{DD,eff}}{\partial \eta^2} = \frac{\partial^2 a'^{DD}}{\partial \eta^2} + \sum_i \frac{\alpha_i^* T_i^*}{x_i}\left[\left(\frac{\partial^2 a'^{DD}}{\partial\eta\partial\mu_i^{*eff}}\right)^2 + \frac{\partial a'^{DD}}{\partial \mu_i^{*eff}}\frac{\partial^3 a'^{DD}}{\partial\eta^2\partial\mu_i^{*eff}}\right] \tag{B.13}$$

$$\frac{\partial^3 a'^{DD,eff}}{\partial \eta^3} = \frac{\partial^3 a'^{DD}}{\partial \eta^3} + \sum_i \frac{\alpha_i^* T_i^*}{x_i}\left[3\frac{\partial^2 a'^{DD}}{\partial\eta\partial\mu_i^{*eff}}\frac{\partial^3 a'^{DD}}{\partial\eta^2\partial\mu_i^{*eff}} + \frac{\partial a'^{DD}}{\partial \mu_i^{*eff}}\frac{\partial^4 a'^{DD}}{\partial\eta^3\partial\mu_i^{*eff}}\right] \tag{B.14}$$

$$\frac{\partial a_2'^{DD}}{\partial \eta} = \frac{-\pi\rho}{\eta}\sum_i\sum_j x_i x_j\frac{\epsilon_i}{kT}\frac{\epsilon_j}{kT}\frac{\sigma_i^3\sigma_j^3}{\sigma_{ij}^3}\left[2\left(\eta J_{2,ij}^{DD}\right)\left(z_j^A\mu_i^{*eff}\frac{\partial\mu_i^{*eff}}{\partial\eta} + z_i^A\mu_j^{*eff}\frac{\partial\mu_j^{*eff}}{\partial\eta}\right) + \left(z_i^A z_j^A - z_i^B z_j^B\right)\left(\eta J_{2,ij}^{DD}\right)_\eta\right] \tag{B.15}$$

$$\frac{\partial^2 a_2'^{DD}}{\partial\eta^2} = \frac{-\pi\rho}{\eta}\sum_i\sum_j x_i x_j \frac{\epsilon_i}{kT}\frac{\epsilon_j}{kT}\frac{\sigma_i^3\sigma_j^3}{\sigma_{ij}^3}\left[2\left(\eta J_{2,ij}^{DD}\right)\left[4\mu_i^{*eff}\mu_j^{*eff}\frac{\partial\mu_i^{*eff}}{\partial\eta}\frac{\partial\mu_j^{*eff}}{\partial\eta} + z_i^A\left(\frac{\partial\mu_j^{*eff}}{\partial\eta}\right)^2 + z_j^A\left(\frac{\partial\mu_i^{*eff}}{\partial\eta}\right)^2 + z_j^A\mu_i^{*eff}\frac{\partial^2\mu_i^{*eff}}{\partial\eta^2} + z_i^A\mu_j^{*eff}\frac{\partial^2\mu_j^{*eff}}{\partial\eta^2}\right] + 4\left(\eta J_{2,ij}^{DD}\right)_\eta\left(z_j^A\mu_i^{*eff}\frac{\partial\mu_i^{*eff}}{\partial\eta} + z_i^A\mu_j^{*eff}\frac{\partial\mu_j^{*eff}}{\partial\eta}\right) + \left(\eta J_{2,ij}^{DD}\right)_{\eta\eta}\left(z_i^A z_j^A - z_i^B z_j^B\right)\right] \tag{B.16}$$

$$\frac{\partial^3 a_2'^{DD}}{\partial\eta^3} = \frac{-\pi\rho}{\eta}\sum_i\sum_j x_i x_j \frac{\epsilon_i}{kT}\frac{\epsilon_j}{kT}\frac{\sigma_i^3\sigma_j^3}{\sigma_{ij}^3}\left[2\left(\eta J_{2,ij}^{DD}\right)\left[6\mu_j^{*eff}\frac{\partial\mu_j^{*eff}}{\partial\eta}\left(\frac{\partial\mu_i^{*eff}}{\partial\eta}\right)^2 + 6\mu_i^{*eff}\frac{\partial\mu_i^{*eff}}{\partial\eta}\left(\frac{\partial\mu_j^{*eff}}{\partial\eta}\right)^2 + 6\mu_i^{*eff}\mu_j^{*eff}\frac{\partial\mu_j^{*eff}}{\partial\eta}\frac{\partial^2\mu_i^{*eff}}{\partial\eta^2} + 6\mu_i^{*eff}\mu_j^{*eff}\frac{\partial\mu_i^{*eff}}{\partial\eta}\frac{\partial^2\mu_j^{*eff}}{\partial\eta^2} + 3z_i^A\frac{\partial\mu_j^{*eff}}{\partial\eta}\frac{\partial^2\mu_j^{*eff}}{\partial\eta^2} + 3z_j^A\frac{\partial\mu_i^{*eff}}{\partial\eta}\frac{\partial^2\mu_i^{*eff}}{\partial\eta^2} + z_j^A\mu_i^{*eff}\frac{\partial^3\mu_i^{*eff}}{\partial\eta^3} + z_i^A\mu_j^{*eff}\frac{\partial^3\mu_j^{*eff}}{\partial\eta^3}\right] + 6\left(\eta J_{2,ij}^{DD}\right)_\eta\left[4\mu_i^{*eff}\mu_j^{*eff}\frac{\partial\mu_i^{*eff}}{\partial\eta}\frac{\partial\mu_j^{*eff}}{\partial\eta} + z_i^A\left(\frac{\partial\mu_j^{*eff}}{\partial\eta}\right)^2 + z_j^A\left(\frac{\partial\mu_i^{*eff}}{\partial\eta}\right)^2 + z_j^A\mu_i^{*eff}\frac{\partial^2\mu_i^{*eff}}{\partial\eta^2} + z_i^A\mu_j^{*eff}\frac{\partial^2\mu_j^{*eff}}{\partial\eta^2}\right] + 6\left(\eta J_{2,ij}^{DD}\right)_{\eta\eta}\left(z_j^A\mu_i^{*eff}\frac{\partial\mu_i^{*eff}}{\partial\eta} + z_i^A\mu_j^{*eff}\frac{\partial\mu_j^{*eff}}{\partial\eta}\right) + \left(\eta J_{2,ij}^{DD}\right)_{\eta\eta\eta}\left(z_i^A z_j^A - z_i^B z_j^B\right)\right] \tag{B.17}$$

$$\frac{\partial^2 a_2'^{DD}}{\partial\eta\partial\mu_i^{*eff}} = \frac{-4\pi\rho}{\eta}\sum_j x_i x_j \frac{\epsilon_i}{kT}\frac{\epsilon_j}{kT}\frac{\sigma_i^3\sigma_j^3}{\sigma_{ij}^3}\left[z_j^A\mu_i^{*eff}\left(\eta J_{2,ij}^{DD}\right)_\eta + 2\mu_i^{*eff}\mu_j^{*eff}\left(\eta J_{2,ij}^{DD}\right)\frac{\partial\mu_j^{*eff}}{\partial\eta} + z_j^A\left(\eta J_{2,ij}^{DD}\right)\frac{\partial\mu_i^{*eff}}{\partial\eta}\right] \tag{B.18}$$

$$\frac{\partial^3 a_2'^{DD}}{\partial\eta^2\partial\mu_i^{*eff}} = \frac{-4\pi\rho}{\eta}\sum_j x_i x_j \frac{\epsilon_i}{kT}\frac{\epsilon_j}{kT}\frac{\sigma_i^3\sigma_j^3}{\sigma_{ij}^3}\left[z_j^A\mu_i^{*eff}\left(\eta J_{2,ij}^{DD}\right)_{\eta\eta} + 2\left(\eta J_{2,ij}^{DD}\right)_{\eta}\left[2\mu_i^{*eff}\mu_j^{*eff}\frac{\partial\mu_j^{*eff}}{\partial\eta} + z_j^A\frac{\partial\mu_i^{*eff}}{\partial\eta}\right]\right.$$
$$\left. + \left(\eta J_{2,ij}^{DD}\right)\left[4\mu_j^{*eff}\frac{\partial\mu_i^{*eff}}{\partial\eta}\frac{\partial\mu_j^{*eff}}{\partial\eta} + 2\mu_i^{*eff}\mu_j^{*eff}\frac{\partial^2\mu_j^{*eff}}{\partial\eta^2} + z_j^A\frac{\partial^2\mu_i^{*eff}}{\partial\eta^2} + 2\mu_i^{*eff}\left(\frac{\partial\mu_j^{*eff}}{\partial\eta}\right)^2\right]\right] \tag{B.19}$$

$$\frac{\partial^4 a_2'^{DD}}{\partial\eta^3\partial\mu_i^{*eff}} = \frac{-\pi\rho}{\eta}\sum_i\sum_j x_i x_j \frac{\epsilon_i}{kT}\frac{\epsilon_j}{kT}\frac{\sigma_i^3\sigma_j^3}{\sigma_{ij}^3}\left[z_j^A\mu_i^{*eff}\left(\eta J_{2,ij}^{DD}\right)_{\eta\eta\eta} + 3\left(\eta J_{2,ij}^{DD}\right)_{\eta\eta}\left(z_j^A\frac{\partial\mu_i^{*eff}}{\partial\eta} + 2\mu_i^{*eff}\mu_j^{*eff}\frac{\partial\mu_j^{*eff}}{\partial\eta}\right)\right.$$
$$+ 3\left(\eta J_{2,ij}^{DD}\right)_{\eta}\left[4\mu_j^{*eff}\frac{\partial\mu_i^{*eff}}{\partial\eta}\frac{\partial\mu_j^{*eff}}{\partial\eta} + 2\mu_i^{*eff}\left(\frac{\partial\mu_j^{*eff}}{\partial\eta}\right)^2 + 2\mu_i^{*eff}\mu_j^{*eff}\frac{\partial^2\mu_j^{*eff}}{\partial\eta^2} + z_j^A\frac{\partial^2\mu_i^{*eff}}{\partial\eta^2}\right]$$
$$+ \left(\eta J_{2,ij}^{DD}\right)\left[6\frac{\partial\mu_i^{*eff}}{\partial\eta}\left(\frac{\partial\mu_j^{*eff}}{\partial\eta}\right)^2 + 6\mu_j^{*eff}\frac{\partial\mu_j^{*eff}}{\partial\eta}\frac{\partial^2\mu_i^{*eff}}{\partial\eta^2} + 6\mu_j^{*eff}\frac{\partial\mu_i^{*eff}}{\partial\eta}\frac{\partial^2\mu_j^{*eff}}{\partial\eta^2}\right.$$
$$\left. + 6\mu_i^{*eff}\frac{\partial\mu_j^{*eff}}{\partial\eta}\frac{\partial^2\mu_j^{*eff}}{\partial\eta^2} + 2\mu_i^{*eff}\mu_j^{*eff}\frac{\partial^3\mu_j^{*eff}}{\partial\eta^3} + z_j^A\frac{\partial^3\mu_i^{*eff}}{\partial\eta^3}\right]\Bigg] \tag{B.20}$$

$$\frac{\partial a_3'^{DD}}{\partial\eta} = -\frac{4}{3}\pi^2\left(\frac{\rho}{\eta}\right)^2\sum_i\sum_j\sum_k x_i x_j x_k\frac{\epsilon_i}{kT}\frac{\epsilon_j}{kT}\frac{\epsilon_k}{kT}\frac{\sigma_i^3\sigma_j^3\sigma_k^3}{\sigma_{ij}\sigma_{ik}\sigma_{jk}}\times$$
$$\left[\left(\eta^2 J_{3,ijk}^{DD}\right)\left(z_i^A z_j^A z_k^A - z_i^B z_j^B z_k^B\right)_{\eta} + \left(z_i^A z_j^A z_k^A - z_i^B z_j^B z_k^B\right)\left(\eta^2 J_{3,ijk}^{DD}\right)_{\eta}\right] \tag{B.21}$$

$$\frac{\partial^2 a_3'^{DD}}{\partial\eta^2} = -\frac{4}{3}\pi^2\left(\frac{\rho}{\eta}\right)^2\sum_i\sum_j\sum_k x_i x_j x_k\frac{\epsilon_i}{kT}\frac{\epsilon_j}{kT}\frac{\epsilon_k}{kT}\frac{\sigma_i^3\sigma_j^3\sigma_k^3}{\sigma_{ij}\sigma_{ik}\sigma_{jk}}\left[\left(\eta^2 J_{3,ijk}^{DD}\right)\left(z_i^A z_j^A z_k^A - z_i^B z_j^B z_k^B\right)_{\eta\eta}\right.$$
$$\left. + 2\left(\eta^2 J_{3,ijk}^{DD}\right)_{\eta}\left(z_i^A z_j^A z_k^A - z_i^B z_j^B z_k^B\right)_{\eta} + \left(z_i^A z_j^A z_k^A - z_i^B z_j^B z_k^B\right)\left(\eta^2 J_{3,ijk}^{DD}\right)_{\eta\eta}\right] \tag{B.22}$$

$$\begin{aligned}\frac{\partial^3 a_3'^{DD}}{\partial\eta^3} &= -\frac{4}{3}\pi^2\left(\frac{\rho}{\eta}\right)^2\sum_i\sum_j\sum_k x_i x_j x_k\frac{\epsilon_i}{kT}\frac{\epsilon_j}{kT}\frac{\epsilon_k}{kT}\frac{\sigma_i^3\sigma_j^3\sigma_k^3}{\sigma_{ij}\sigma_{ik}\sigma_{jk}}\left[\left(z_i^A z_j^A z_k^A - z_i^B z_j^B z_k^B\right)\left(\eta^2 J_{3,ijk}^{DD}\right)_{\eta\eta\eta}\right.\\ &+ 3\left(z_i^A z_j^A z_k^A - z_i^B z_j^B z_k^B\right)_\eta\left(\eta^2 J_{3,ijk}^{DD}\right)_{\eta\eta} + 3\left(\eta^2 J_{3,ijk}^{DD}\right)_\eta\left(z_i^A z_j^A z_k^A - z_i^B z_j^B z_k^B\right)_{\eta\eta}\\ &\left.+ \left(\eta^2 J_{3,ijk}^{DD}\right)\left(z_i^A z_j^A z_k^A - z_i^B z_j^B z_k^B\right)_{\eta\eta\eta}\right]\end{aligned} \tag{B.23}$$

where the first, second and third density derivatives of $\left(z_i^A z_j^A z_k^A - z_i^B z_j^B z_k^B\right)$ are

$$\left(z_i^A z_j^A z_k^A - z_i^B z_j^B z_k^B\right)_\eta = 2\left[z_j^A z_k^A \mu_i^{*eff}\frac{\partial\mu_i^{*eff}}{\partial\eta} + z_i^A z_k^A \mu_j^{*eff}\frac{\partial\mu_j^{*eff}}{\partial\eta} + z_i^A z_j^A \mu_k^{*eff}\frac{\partial\mu_k^{*eff}}{\partial\eta}\right]$$

$$\begin{aligned}\left(z_i^A z_j^A z_k^A - z_i^B z_j^B z_k^B\right)_{\eta\eta} &= 2\left[z_j^A z_k^A\left(\frac{\partial\mu_i^{*eff}}{\partial\eta}\right)^2 + z_i^A z_k^A\left(\frac{\partial\mu_j^{*eff}}{\partial\eta}\right)^2 + z_i^A z_j^A\left(\frac{\partial\mu_k^{*eff}}{\partial\eta}\right)^2 + 4z_k^A\mu_i^{*eff}\mu_j^{*eff}\frac{\partial\mu_i^{*eff}}{\partial\eta}\frac{\partial\mu_j^{*eff}}{\partial\eta}\right.\\ &+ 4z_j^A\mu_i^{*eff}\mu_k^{*eff}\frac{\partial\mu_i^{*eff}}{\partial\eta}\frac{\partial\mu_k^{*eff}}{\partial\eta} + 4z_i^A\mu_j^{*eff}\mu_k^{*eff}\frac{\partial\mu_j^{*eff}}{\partial\eta}\frac{\partial\mu_k^{*eff}}{\partial\eta} + z_j^A z_k^A\mu_i^{*eff}\frac{\partial^2\mu_i^{*eff}}{\partial\eta^2}\\ &\left.+ z_i^A z_k^A\mu_j^{*eff}\frac{\partial^2\mu_j^{*eff}}{\partial\eta^2} + z_i^A z_j^A\mu_k^{*eff}\frac{\partial^2\mu_k^{*eff}}{\partial\eta^2}\right]\end{aligned}$$

$$
\begin{aligned}
\left(z_i^A z_j^A z_k^A - z_i^B z_j^B z_k^B\right)_{\eta\eta\eta} = \; & 2\left[z_j^A z_k^A\left(3\frac{\partial\mu_i^{*eff}}{\partial\eta}\frac{\partial^2\mu_i^{*eff}}{\partial\eta^2} + \mu_i^{*eff}\frac{\partial^3\mu_i^{*eff}}{\partial\eta^3}\right) + z_i^A z_k^A\left(3\frac{\partial\mu_j^{*eff}}{\partial\eta}\frac{\partial^2\mu_j^{*eff}}{\partial\eta^2} + \mu_j^{*eff}\frac{\partial^3\mu_j^{*eff}}{\partial\eta^3}\right)\right. \\
& + z_i^A z_j^A\left(3\frac{\partial\mu_k^{*eff}}{\partial\eta}\frac{\partial^2\mu_k^{*eff}}{\partial\eta^2} + \mu_k^{*eff}\frac{\partial^3\mu_k^{*eff}}{\partial\eta^3}\right) + 6z_k^A\left[\mu_j^{*eff}\frac{\partial\mu_j^{*eff}}{\partial\eta}\left(\frac{\partial\mu_i^{*eff}}{\partial\eta}\right)^2\right. \\
& \left.+\mu_i^{*eff}\frac{\partial\mu_i^{*eff}}{\partial\eta}\left(\frac{\partial\mu_j^{*eff}}{\partial\eta}\right)^2 + \mu_i^{*eff}\mu_j^{*eff}\frac{\partial\mu_j^{*eff}}{\partial\eta}\frac{\partial^2\mu_i^{*eff}}{\partial\eta^2} + \mu_i^{*eff}\mu_j^{*eff}\frac{\partial\mu_i^{*eff}}{\partial\eta}\frac{\partial^2\mu_j^{*eff}}{\partial\eta^2}\right] \\
& + 6z_j^A\left[\mu_k^{*eff}\frac{\partial\mu_k^{*eff}}{\partial\eta}\left(\frac{\partial\mu_i^{*eff}}{\partial\eta}\right)^2 + \mu_i^{*eff}\frac{\partial\mu_i^{*eff}}{\partial\eta}\left(\frac{\partial\mu_k^{*eff}}{\partial\eta}\right)^2 + \mu_i^{*eff}\mu_k^{*eff}\frac{\partial\mu_k^{*eff}}{\partial\eta}\frac{\partial^2\mu_i^{*eff}}{\partial\eta^2}\right. \\
& \left.+ \mu_i^{*eff}\mu_k^{*eff}\frac{\partial\mu_i^{*eff}}{\partial\eta}\frac{\partial^2\mu_k^{*eff}}{\partial\eta^2}\right] + 6z_i^A\left[\mu_k^{*eff}\frac{\partial\mu_k^{*eff}}{\partial\eta}\left(\frac{\partial\mu_j^{*eff}}{\partial\eta}\right)^2 + \mu_j^{*eff}\frac{\partial\mu_j^{*eff}}{\partial\eta}\left(\frac{\partial\mu_k^{*eff}}{\partial\eta}\right)^2\right. \\
& \left.+ \mu_j^{*eff}\mu_k^{*eff}\frac{\partial\mu_k^{*eff}}{\partial\eta}\frac{\partial^2\mu_j^{*eff}}{\partial\eta^2} + \mu_j^{*eff}\mu_k^{*eff}\frac{\partial\mu_j^{*eff}}{\partial\eta}\frac{\partial^2\mu_k^{*eff}}{\partial\eta^2}\right] \\
& \left. + 24\mu_i^{*eff}\mu_j^{*eff}\mu_k^{*eff}\frac{\partial\mu_i^{*eff}}{\partial\eta}\frac{\partial\mu_j^{*eff}}{\partial\eta}\frac{\partial\mu_k^{*eff}}{\partial\eta}\right]
\end{aligned}
$$

$$
\frac{\partial^2 a_3'^{DD}}{\partial\eta\partial\mu_i^{*eff}} = -8\pi^2\left(\frac{\rho}{\eta}\right)^2\sum_j\sum_l x_i x_j x_l\frac{\epsilon_i}{kT}\frac{\epsilon_j}{kT}\frac{\epsilon_l}{kT}\frac{\sigma_i^3\sigma_j^3\sigma_l^3}{\sigma_{ij}\sigma_{il}\sigma_{jl}}\left[z_j^A z_l^A\mu_i^{*eff}\left(\eta^2 J_{3,ijl}^{DD}\right)_\eta + \left(\eta^2 J_{3,ijl}^{DD}\right)\left(z_j^A z_l^A\mu_i^{*eff}\right)_\eta\right] \tag{B.24}
$$

$$
\begin{aligned}
\frac{\partial^3 a_3'^{DD}}{\partial\eta^2\partial\mu_i^{*eff}} = \; & -8\pi^2\left(\frac{\rho}{\eta}\right)^2\sum_j\sum_l x_i x_j x_l\frac{\epsilon_i}{kT}\frac{\epsilon_j}{kT}\frac{\epsilon_l}{kT}\frac{\sigma_i^3\sigma_j^3\sigma_l^3}{\sigma_{ij}\sigma_{il}\sigma_{jl}}\times \\
& \left[z_j^A z_l^A\mu_i^{*eff}\left(\eta^2 J_{3,ijl}^{DD}\right)_{\eta\eta} + 2\left(\eta^2 J_{3,ijl}^{DD}\right)_\eta\left(z_j^A z_l^A\mu_i^{*eff}\right)_\eta + \left(\eta^2 J_{3,ijl}^{DD}\right)\left(z_j^A z_l^A\mu_i^{*eff}\right)_{\eta\eta}\right]
\end{aligned} \tag{B.25}
$$

$$\frac{\partial^4 a_3'^{DD}}{\partial\eta^3\partial\mu_i^{*eff}} = -8\pi^2\left(\frac{\rho}{\eta}\right)^2\sum_j\sum_l x_i x_j x_l\frac{\epsilon_i}{kT}\frac{\epsilon_j}{kT}\frac{\epsilon_l}{kT}\frac{\sigma_i^3\sigma_j^3\sigma_l^3}{\sigma_{ij}\sigma_{il}\sigma_{jl}}\left[z_j^A z_l^A\mu_i^{*eff}\left(\eta^2 J_{3,ijl}^{DD}\right)_{\eta\eta\eta} + 3\left(z_j^A z_l^A\mu_i^{*eff}\right)_\eta\left(\eta^2 J_{3,ijl}^{DD}\right)_{\eta\eta}\right.$$
$$\left. + 3\left(\eta^2 J_{3,ijl}^{DD}\right)_\eta\left(z_j^A z_l^A\mu_i^{*eff}\right)_{\eta\eta} + \left(\eta^2 J_{3,ijl}^{DD}\right)\left(z_j^A z_l^A\mu_i^{*eff}\right)_{\eta\eta\eta}\right] \tag{B.26}$$

where

$$\left(z_j^A z_l^A\mu_i^{*eff}\right)_\eta = 2\mu_i^{*eff}\left(z_l^A\mu_j^{*eff}\frac{\partial\mu_j^{*eff}}{\partial\eta} + z_j^A\mu_l^{*eff}\frac{\partial\mu_l^{*eff}}{\partial\eta}\right) + z_j^A z_l^A\frac{\partial\mu_i^{*eff}}{\partial\eta}$$

$$\left(z_j^A z_l^A\mu_i^{*eff}\right)_{\eta\eta} = 4\frac{\partial\mu_i^{*eff}}{\partial\eta}\left(z_l^A\mu_j^{*eff}\frac{\partial\mu_j^{*eff}}{\partial\eta} + z_j^A\mu_l^{*eff}\frac{\partial\mu_l^{*eff}}{\partial\eta}\right) + 2\mu_i^{*eff}\left[4\mu_j^{*eff}\mu_l^{*eff}\frac{\partial\mu_j^{*eff}}{\partial\eta}\frac{\partial\mu_l^{*eff}}{\partial\eta}\right.$$
$$\left. + z_l^A\mu_j^{*eff}\frac{\partial^2\mu_j^{*eff}}{\partial\eta^2} + z_j^A\mu_l^{*eff}\mu_j^{*eff}\frac{\partial^2\mu_l^{*eff}}{\partial\eta^2} + z_l^A\left(\frac{\partial\mu_j^{*eff}}{\partial\eta}\right)^2 + z_j^A\left(\frac{\partial\mu_l^{*eff}}{\partial\eta}\right)^2\right] + z_j^A z_l^A\frac{\partial^2\mu_i^{*eff}}{\partial\eta^2}$$

$$
\begin{aligned}
\left(z_j^A z_l^A \mu_i^{*eff}\right)_{\eta\eta\eta} = {} & 6 z_l^A \mu_j^{*eff}\left(\frac{\partial \mu_j^{*eff}}{\partial \eta}\frac{\partial^2 \mu_i^{*eff}}{\partial \eta^2}+\frac{\partial \mu_i^{*eff}}{\partial \eta}\frac{\partial^2 \mu_j^{*eff}}{\partial \eta^2}\right)+6\frac{\partial \mu_i^{*eff}}{\partial \eta}\left[z_l^A\left(\frac{\partial \mu_j^{*eff}}{\partial \eta}\right)^2+z_j^A\left(\frac{\partial \mu_l^{*eff}}{\partial \eta}\right)^2\right] \\
& + 2 z_j^A \mu_l^{*eff}\left(3\frac{\partial \mu_l^{*eff}}{\partial \eta}\frac{\partial^2 \mu_i^{*eff}}{\partial \eta^2}+2\frac{\partial \mu_i^{*eff}}{\partial \eta}\frac{\partial^2 \mu_l^{*eff}}{\partial \eta^2}+\mu_j^{*eff}\frac{\partial \mu_i^{*eff}}{\partial \eta}\frac{\partial^2 \mu_l^{*eff}}{\partial \eta^2}\right) \\
& + 2\mu_j^{*eff}\mu_l^{*eff}\frac{\partial \mu_i^{*eff}}{\partial \eta}\left(12\frac{\partial \mu_j^{*eff}}{\partial \eta}\frac{\partial \mu_l^{*eff}}{\partial \eta}+z_j^A\frac{\partial^2 \mu_l^{*eff}}{\partial \eta^2}\right)+z_j^A z_l^A\frac{\partial^3 \mu_i^{*eff}}{\partial \eta^3}+2\mu_i^{*eff}\left[6\mu_l^{*eff}\frac{\partial \mu_l^{*eff}}{\partial \eta}\left(\frac{\partial \mu_j^{*eff}}{\partial \eta}\right)^2\right. \\
& + 6\mu_j^{*eff}\frac{\partial \mu_j^{*eff}}{\partial \eta}\left(\frac{\partial \mu_l^{*eff}}{\partial \eta}\right)^2+\mu_j^{*eff}\mu_l^{*eff}\left(6\frac{\partial \mu_l^{*eff}}{\partial \eta}\frac{\partial^2 \mu_j^{*eff}}{\partial \eta^2}+4\frac{\partial \mu_j^{*eff}}{\partial \eta}\frac{\partial^2 \mu_l^{*eff}}{\partial \eta^2}+2\mu_j^{*eff}\frac{\partial \mu_j^{*eff}}{\partial \eta}\frac{\partial^2 \mu_l^{*eff}}{\partial \eta^2}\right. \\
& \left. + z_j^A\frac{\partial^3 \mu_l^{*eff}}{\partial \eta^3}\right)+z_j^A\left(\mu_j^{*eff}\frac{\partial \mu_l^{*eff}}{\partial \eta}\frac{\partial^2 \mu_l^{*eff}}{\partial \eta^2}+\mu_l^{*eff}\frac{\partial \mu_j^{*eff}}{\partial \eta}\frac{\partial^2 \mu_l^{*eff}}{\partial \eta^2}+2\frac{\partial \mu_l^{*eff}}{\partial \eta}\frac{\partial^2 \mu_l^{*eff}}{\partial \eta^2}\right) \\
& \left. + z_l^A\left(3\frac{\partial \mu_j^{*eff}}{\partial \eta}\frac{\partial^2 \mu_j^{*eff}}{\partial \eta^2}+\mu_j^{*eff}\frac{\partial^3 \mu_j^{*eff}}{\partial \eta^3}\right)\right]
\end{aligned}
$$

Compositional derivatives for the effective Helmholtz energy

$$
\frac{\partial \mu_i^{*eff}}{\partial x_k} = \alpha_i^* T_i^*\left(\frac{\delta_{ik}}{x_i^2}\frac{\partial a'^{DD}}{\partial \mu_i^{*eff}}-\frac{1}{x_i}\frac{\partial^2 a'^{DD}}{\partial x_k \partial \mu_i^{*eff}}\right) \tag{B.27}
$$

where δ_{ik} is the Kronecker delta,

$$
\delta_{ik} = \begin{cases} 1 & i = k \\ 0 & \text{otherwise} \end{cases}
$$

$$
\frac{\partial a'^{DD,eff}}{\partial x_k} = \frac{\partial a'^{DD}}{\partial x_k}+\frac{1}{2}\sum_i \alpha_i^* T_i^*\left[\frac{2}{x_i}\frac{\partial a'^{DD}}{\partial \mu_i^{*eff}}\frac{\partial^2 a'^{DD}}{\partial x_k \partial \mu_i^{*eff}}-\frac{\partial_{ik}}{x_i^2}\left(\frac{\partial a'^{DD}}{\partial \mu_i^{*eff}}\right)^2\right] \tag{B.28}
$$

$$\frac{\partial a_2'^{DD}}{\partial x_k} = -\pi\rho\left[2\sum_i x_i\frac{\epsilon_i}{kT}\frac{\epsilon_k}{kT}\left(z_i^A z_k^A - z_i^B z_k^B\right)\frac{\sigma_i^3\sigma_k^3}{\sigma_{ik}^3}J_{2,ik}^{DD} + \sum_i\sum_j x_i x_j\frac{\epsilon_i}{kT}\frac{\epsilon_j}{kT}\frac{\sigma_i^3\sigma_j^3}{\sigma_{ij}^3}\left[4z_i^A\mu_j^{*eff}J_{2,ij}^{DD}\frac{\partial\mu_j^{*eff}}{\partial x_k} + \left(z_i^A z_j^A - z_i^B z_j^B\right)\left(J_{2,ij}^{DD}\right)_{x_k}\right]\right] \tag{B.29}$$

$$\frac{\partial^2 a_2'^{DD}}{\partial x_k\partial\mu_i^{*eff}} = -4\pi\rho\sum_j\frac{\epsilon_i}{kT}\frac{\epsilon_j}{kT}\frac{\sigma_i^3\sigma_j^3}{\sigma_{ij}^3}\left[z_j^A\mu_i^{*eff}J_{2,ij}^{DD}\left(\delta_{ik}x_j + \delta_{jk}x_i\right) + x_i x_j\left(z_j^A\mu_i^{*eff}\left(J_{2,ij}^{DD}\right)_{x_k} + 2\mu_i^{*eff}\mu_j^{*eff}J_{2,ij}^{DD}\frac{\partial\mu_j^{*eff}}{\partial x_k} + z_j^A J_{2,ij}^{DD}\frac{\partial\mu_i^{*eff}}{\partial x_k}\right)\right] \tag{B.30}$$

$$\frac{\partial a_3'^{DD}}{\partial x_k} = \frac{-4}{3}\pi^2\rho^2\left[3\sum_i\sum_j x_i x_j\frac{\epsilon_i}{kT}\frac{\epsilon_j}{kT}\frac{\epsilon_k}{kT}\left(z_i^A z_j^A z_k^A - z_i^B z_j^B z_k^B\right)\frac{\sigma_i^3\sigma_j^3\sigma_k^3}{\sigma_{ij}\sigma_{ik}\sigma_{jk}}J_{3,ijk}^{DD} + \sum_i\sum_j\sum_l x_i x_j x_l\frac{\epsilon_i}{kT}\frac{\epsilon_j}{kT}\frac{\epsilon_l}{kT}\frac{\sigma_i^3\sigma_j^3\sigma_l^3}{\sigma_{ij}\sigma_{il}\sigma_{jl}}\left[\left(z_i^A z_j^A z_l^A - z_i^B z_j^B z_l^B\right)\left(J_{3,ijl}^{DD}\right)_{x_k} + 6z_i^A z_j^A\mu_l^{*eff}J_{3,ijl}^{DD}\frac{\partial\mu_l^{*eff}}{\partial x_k}\right]\right] \tag{B.31}$$

$$\frac{\partial a_3'^{DD}}{\partial x_k\partial\mu_i^{*eff}} = -8\pi^2\rho^2\sum_j\sum_l\frac{\epsilon_i}{kT}\frac{\epsilon_j}{kT}\frac{\epsilon_l}{kT}\frac{\sigma_i^3\sigma_j^3\sigma_l^3}{\sigma_{ij}\sigma_{il}\sigma_{jl}}\left[z_j^A z_l^A\mu_i^{*eff}J_{3,ijl}^{DD}\left(\delta_{ik}x_j x_l + \delta_{jk}x_i x_l + \delta_{lk}x_i x_j\right) + x_i x_j x_l\left[z_j^A z_l^A\mu_i^{*eff}\left(J_{3,ijl}^{DD}\right)_{x_k} + 2z_l^A\mu_i^{*eff}\mu_j^{*eff}J_{3,ijl}^{DD}\frac{\partial\mu_j^{*eff}}{\partial x_k} + 2z_j^A\mu_i^{*eff}\mu_l^{*eff}J_{3,ijl}^{DD}\frac{\partial\mu_l^{*eff}}{\partial x_k} + z_j^A z_l^A J_{3,ijl}^{DD}\frac{\partial\mu_i^{*eff}}{\partial x_k}\right]\right] \tag{B.32}$$

Supplements:

$$\left(J_{2,ij}^{DD}\right)_{x_k} = \sum_{n=0}^{4}\left(a_{n,ij} + b_{n,ij}\frac{\epsilon_{ij}}{kT}\right)n\eta^{n-1}\zeta_{3,x_k}$$

$$\left(J_{3,ijl}^{DD}\right)_{x_k} = \sum_{n=0}^{4} c_{n,ijl} n \eta^{n-1} \zeta_{3,x_k}$$

Temperature derivatives for the effective Helmholtz energy

$$\frac{\partial \mu_i^{*eff}}{\partial T} = -\frac{\alpha_i^* T_i^*}{x_i}\left(\frac{1}{T}\frac{\partial a'^{DD}}{\partial \mu_i^{*eff}} + \frac{\partial^2 a'^{DD}}{\partial T \partial \mu_i^{*eff}}\right) \tag{B.33}$$

$$\frac{\partial^2 \mu_i^{*eff}}{\partial T^2} = -\frac{\alpha_i^* T_i^*}{x_i}\left(\frac{2}{T}\frac{\partial^2 a'^{DD}}{\partial T \partial \mu_i^{*eff}} + \frac{\partial^3 a'^{DD}}{\partial T^2 \partial \mu_i^{*eff}}\right) \tag{B.34}$$

$$\frac{\partial a'^{DD,eff}}{\partial T} = \frac{\partial a'^{DD}}{\partial T} + \frac{1}{2}\sum_i \frac{\alpha_i^* T_i^*}{x_i}\left[\frac{1}{T}\left(\frac{\partial a'^{DD}}{\partial \mu_i^{*eff}}\right)^2 + 2\frac{\partial a'^{DD}}{\partial \mu_i^{*eff}}\frac{\partial^2 a'^{DD}}{\partial T \partial \mu_i^{*eff}}\right] \tag{B.35}$$

$$\frac{\partial^2 a'^{DD,eff}}{\partial T^2} = \frac{\partial^2 a'^{DD}}{\partial T^2} + \sum_i \frac{\alpha_i^* T_i^*}{x_i}\left[\frac{2}{T}\frac{\partial a'^{DD}}{\partial \mu_i^{*eff}}\frac{\partial^2 a'^{DD}}{\partial T \partial \mu_i^{*eff}} + \left(\frac{\partial^2 a'^{DD}}{\partial T \partial \mu_i^{*eff}}\right)^2 + \frac{\partial a'^{DD}}{\partial \mu_i^{*eff}}\frac{\partial^3 a'^{DD}}{\partial T^2 \partial \mu_i^{*eff}}\right] \tag{B.36}$$

$$\frac{\partial a_2'^{DD}}{\partial T} = -\pi\rho \sum_i \sum_j x_i x_j \frac{\epsilon_i}{kT}\frac{\epsilon_j}{kT}\frac{\sigma_i^3 \sigma_j^3}{\sigma_{ij}^3}\left[\frac{2}{T}\left(z_i^B z_j^B - z_i^A z_j^A\right) J_{2,ij}^{DD} + J_{2,ij}^{DD}\left(z_i^A z_j^A - z_i^B z_j^B\right)_T + \left(z_i^A z_j^A - z_i^B z_j^B\right)\left(J_{2,ij}^{DD}\right)_T\right] \tag{B.37}$$

$$\begin{aligned}\frac{\partial^2 a_2'^{DD}}{\partial T^2} = -\pi\rho \sum_i \sum_j x_i x_j \frac{\epsilon_i}{kT}\frac{\epsilon_j}{kT}\frac{\sigma_i^3 \sigma_j^3}{\sigma_{ij}^3}\Bigg[&\frac{6}{T^2}\left(z_i^A z_j^A - z_i^B z_j^B\right) J_{2,ij}^{DD} - \frac{4}{T}\Big[J_{2,ij}^{DD}\left(z_i^A z_j^A - z_i^B z_j^B\right)_T \\ &+ \left(z_i^A z_j^A - z_i^B z_j^B\right)\left(J_{2,ij}^{DD}\right)_T\Big] + 2\left(z_i^A z_j^A - z_i^B z_j^B\right)_T \left(J_{2,ij}^{DD}\right)_T + J_{2,ij}^{DD}\left(z_i^A z_j^A - z_i^B z_j^B\right)_{TT} + \left(z_i^A z_j^A - z_i^B z_j^B\right)\left(J_{2,ij}^{DD}\right)_{TT}\Bigg]\end{aligned} \tag{B.38}$$

where

$$\left(z_i^A z_j^A - z_i^B z_j^B\right)_T = 2\left(z_j^A \mu_i^{*eff}\frac{\partial \mu_i^{*eff}}{\partial T} + z_i^A \mu_j^{*eff}\frac{\partial \mu_j^{*eff}}{\partial T}\right) + \frac{1}{T}\left(z_i^A z_j^B + z_j^A z_i^B - 2 z_i^B z_j^B\right)$$

$$\left(z_i^A z_j^A - z_i^B z_j^B\right)_{TT} = 2\left[4\mu_i^{*eff}\mu_j^{*eff}\frac{\partial\mu_i^{*eff}}{\partial T}\frac{\partial\mu_j^{*eff}}{\partial T} + z_i^A\left(\mu_j^{*eff}\frac{\partial^2\mu_j^{*eff}}{\partial T^2} + \left(\frac{\partial\mu_j^{*eff}}{\partial T}\right)^2\right)\right.$$
$$\left. + z_j^A\left(\mu_i^{*eff}\frac{\partial^2\mu_i^{*eff}}{\partial T^2} + \left(\frac{\partial\mu_i^{*eff}}{\partial T}\right)^2\right) + \frac{2}{T}\left(z_i^B\mu_j^{*eff}\frac{\partial\mu_j^{*eff}}{\partial T} + z_j^B\mu_i^{*eff}\frac{\partial\mu_i^{*eff}}{\partial T}\right)\right]$$

$$\frac{\partial^2 a_2'^{DD}}{\partial T\partial\mu_i^{*eff}} = -4\pi\rho\sum_j x_i x_j\frac{\epsilon_i}{kT}\frac{\epsilon_j}{kT}\frac{\sigma_i^3\sigma_j^3}{\sigma_{ij}^3}\left[z_j^A\mu_i^{*eff}\left[\left(J_{2,ij}^{DD}\right)_T - \frac{2}{T}J_{2,ij}^{DD}\right]\right.$$
$$\left. + J_{2,ij}^{DD}\left(2\mu_i^{*eff}\mu_j^{*eff}\frac{\partial\mu_j^{*eff}}{\partial T} + \frac{z_j^B}{T}\mu_i^{*eff} + z_j^A\frac{\partial\mu_i^{*eff}}{\partial T}\right)\right] \tag{B.39}$$

$$\frac{\partial^3 a_2'^{DD}}{\partial T^2\partial\mu_i^{*eff}} = -4\pi\rho\sum_j x_i x_j\frac{\epsilon_i}{kT}\frac{\epsilon_j}{kT}\frac{\sigma_i^3\sigma_j^3}{\sigma_{ij}^3}\left[\frac{J_{2,ij}^{DD}\mu_i^{*eff}}{T^2}\left(6z_j^A - 4z_j^B\right) + \frac{2z_j^B - 4z_j^A}{T}\left(\mu_i^{*eff}\left(J_{2,ij}^{DD}\right)_T + J_{2,ij}^{DD}\frac{\partial\mu_i^{*eff}}{\partial T}\right)\right.$$
$$- \frac{8}{T}J_{2,ij}^{DD}\mu_i^{*eff}\mu_j^{*eff}\frac{\partial\mu_j^{*eff}}{\partial T} + z_j^A\mu_i^{*eff}\left(J_{2,ij}^{DD}\right)_{TT} + 2\left(J_{2,ij}^{DD}\right)_T\left[2\mu_i^{*eff}\mu_j^{*eff}\frac{\partial\mu_j^{*eff}}{\partial T} + z_j^A\frac{\partial\mu_i^{*eff}}{\partial T}\right]$$
$$\left. + J_{2,ij}^{DD}\left[4\mu_j^{*eff}\frac{\partial\mu_i^{*eff}}{\partial T}\frac{\partial\mu_j^{*eff}}{\partial T} + 2\mu_i^{*eff}\left(\frac{\partial\mu_j^{*eff}}{\partial T}\right)^2 + 2\mu_i^{*eff}\mu_j^{*eff}\frac{\partial^2\mu_j^{*eff}}{\partial T^2} + z_j^A\frac{\partial^2\mu_i^{*eff}}{\partial T^2}\right]\right] \tag{B.40}$$

$$\frac{\partial a_3'^{DD}}{\partial T} = -\frac{4}{3}\pi^2\rho^2\sum_i\sum_j\sum_k x_i x_j x_k\frac{\epsilon_i}{kT}\frac{\epsilon_j}{kT}\frac{\epsilon_k}{kT}\frac{\sigma_i^3\sigma_j^3\sigma_k^3}{\sigma_{ij}\sigma_{ik}\sigma_{jk}}\times$$
$$\left[\frac{3}{T}\left(z_i^B z_j^B z_k^B - z_i^A z_j^A z_k^A\right)J_{3,ijk}^{DD} + J_{3,ijk}^{DD}\left(z_i^A z_j^A z_k^A - z_i^B z_j^B z_k^B\right)_T + \left(z_i^A z_j^A z_k^A - z_i^B z_j^B z_k^B\right)\left(J_{3,ijk}^{DD}\right)_T\right] \tag{B.41}$$

$$\begin{aligned}\frac{\partial^2 a_3'^{DD}}{\partial T^2} &= -\frac{4}{3}\pi^2\rho^2\sum_i\sum_j\sum_k x_i x_j x_k \frac{\epsilon_i}{kT}\frac{\epsilon_j}{kT}\frac{\epsilon_k}{kT}\frac{\sigma_i^3\sigma_j^3\sigma_k^3}{\sigma_{ij}\sigma_{ik}\sigma_{jk}}\left[\frac{12}{T^2}\left(z_i^A z_j^A z_k^A - z_i^B z_j^B z_k^B\right)J_{3,ijk}^{DD}\right.\\ &- \frac{6}{T}\left[J_{3,ijk}^{DD}\left(z_i^A z_j^A z_k^A - z_i^B z_j^B z_k^B\right)_T + \left(z_i^A z_j^A z_k^A - z_i^B z_j^B z_k^B\right)\left(J_{3,ijk}^{DD}\right)_T\right] + J_{3,ijk}^{DD}\left(z_i^A z_j^A z_k^A - z_i^B z_j^B z_k^B\right)_{TT}\\ &+ \left.2\left(z_i^A z_j^A z_k^A - z_i^B z_j^B z_k^B\right)_T\left(J_{3,ijk}^{DD}\right)_T + \left(z_i^A z_j^A z_k^A - z_i^B z_j^B z_k^B\right)\left(J_{3,ijk}^{DD}\right)_{TT}\right]\end{aligned} \tag{B.42}$$

where

$$\begin{aligned}\left(z_i^A z_j^A z_k^A - z_i^B z_j^B z_k^B\right)_T &= 2\left(z_j^A z_k^A \mu_i^{*eff}\frac{\partial \mu_i^{*eff}}{\partial T} + z_i^A z_k^A \mu_j^{*eff}\frac{\partial \mu_j^{*eff}}{\partial T} + z_i^A z_j^A \mu_k^{*eff}\frac{\partial \mu_k^{*eff}}{\partial T}\right)\\ &+ \frac{1}{T}\left(z_j^A z_k^A z_i^B + z_i^A z_k^A z_j^B + z_i^A z_j^A z_k^B - 3 z_i^B z_j^B z_k^B\right)\end{aligned}$$

$$\begin{aligned}\left(z_i^A z_j^A z_k^A - z_i^B z_j^B z_k^B\right)_{TT} &= 8\left(z_k^A \mu_i^{*eff}\mu_j^{*eff}\frac{\partial \mu_i^{*eff}}{\partial T}\frac{\partial \mu_j^{*eff}}{\partial T} + z_j^A \mu_i^{*eff}\mu_k^{*eff}\frac{\partial \mu_i^{*eff}}{\partial T}\frac{\partial \mu_k^{*eff}}{\partial T} + z_i^A \mu_j^{*eff}\mu_k^{*eff}\frac{\partial \mu_j^{*eff}}{\partial T}\frac{\partial \mu_k^{*eff}}{\partial T}\right)\\ &+ \frac{4}{T}\left[\mu_i^{*eff}\frac{\partial \mu_i^{*eff}}{\partial T}\left(z_k^A z_j^B + z_j^A z_k^B\right) + \mu_j^{*eff}\frac{\partial \mu_j^{*eff}}{\partial T}\left(z_k^A z_i^B + z_i^A z_k^B\right) + \mu_k^{*eff}\frac{\partial \mu_k^{*eff}}{\partial T}\left(z_j^A z_i^B + z_i^A z_j^B\right)\right]\\ &+ 2\left[z_j^A z_k^A\left(\frac{\partial \mu_i^{*eff}}{\partial T}\right)^2 + z_i^A z_k^A\left(\frac{\partial \mu_j^{*eff}}{\partial T}\right)^2 + z_i^A z_j^A\left(\frac{\partial \mu_k^{*eff}}{\partial T}\right)^2 + z_j^A z_i^A \mu_i^{*eff}\frac{\partial^2 \mu_i^{*eff}}{\partial T^2}\right.\\ &\left.+ z_i^A z_j^A \mu_k^{*eff}\frac{\partial^2 \mu_k^{*eff}}{\partial T^2} + z_i^A z_k^A \mu_j^{*eff}\frac{\partial^2 \mu_j^{*eff}}{\partial T^2} - 3\frac{z_i^B z_j^B z_k^B}{T^2} + \frac{z_k^A z_i^B z_j^B}{T^2} + \frac{z_j^A z_i^B z_k^B}{T^2} + \frac{z_i^A z_j^B z_k^B}{T^2}\right]\end{aligned}$$

$$\begin{aligned}\frac{\partial^2 a_3'^{DD}}{\partial T \partial \mu_i^{*eff}} &= -8\pi^2\rho^2\sum_j\sum_l x_i x_j x_l \frac{\epsilon_i}{kT}\frac{\epsilon_j}{kT}\frac{\epsilon_l}{kT}\frac{\sigma_i^3\sigma_j^3\sigma_l^3}{\sigma_{ij}\sigma_{il}\sigma_{jl}}\left[\frac{\mu_i^{*eff}J_{3,ijl}^{DD}}{T}\left(z_l^A z_j^B + z_j^A z_l^B - 3 z_j^A z_l^A\right)\right.\\ &\left.+ J_{3,ijl}^{DD}\left(2 z_l^A \mu_i^{*eff}\mu_j^{*eff}\frac{\partial \mu_j^{*eff}}{\partial T} + 2 z_j^A \mu_i^{*eff}\mu_l^{*eff}\frac{\partial \mu_l^{*eff}}{\partial T} + z_j^A z_l^A\frac{\partial \mu_i^{*eff}}{\partial T}\right) + z_j^A z_l^A \mu_i^{*eff}\left(J_{3,ijl}^{DD}\right)_T\right]\end{aligned} \tag{B.43}$$

$$
\begin{aligned}
\frac{\partial^3 a_3'^{DD}}{\partial T^2 \partial \mu_i^{*eff}} = & -8\pi^2\rho^2 \sum_j \sum_l x_i x_j x_l \frac{\epsilon_i}{kT}\frac{\epsilon_j}{kT}\frac{\epsilon_l}{kT}\frac{\sigma_i^3\sigma_j^3\sigma_l^3}{\sigma_{ij}\sigma_{il}\sigma_{jl}} \Bigg[\frac{2\mu_i^{*eff} J_{3,ijl}^{DD}}{T^2}\left(6z_j^A z_l^A - 3z_l^A z_j^B + z_j^B z_l^B - 3z_j^A z_l^B\right) \\
& + \frac{2\mu_i^{*eff}\left(J_{3,ijl}^{DD}\right)_T}{T}\left(z_l^A z_j^B + z_j^A z_l^B - 3z_j^A z_l^A\right) + \frac{4\mu_i^{*eff} J_{3,ijl}^{DD}}{T}\Bigg(z_l^B \mu_j^{*eff}\frac{\partial \mu_j^{*eff}}{\partial T} + z_j^B \mu_l^{*eff}\frac{\partial \mu_l^{*eff}}{\partial T} \\
& - 3z_l^A \mu_j^{*eff}\frac{\partial \mu_j^{*eff}}{\partial T} - 3z_j^A \mu_l^{*eff}\frac{\partial \mu_l^{*eff}}{\partial T}\Bigg) + \frac{2J_{3,ijl}^{DD}}{T}\frac{\partial \mu_i^{*eff}}{\partial T}\left(z_l^A z_j^B + z_j^A z_l^B - 3z_j^A z_l^A\right) \\
& + 4\mu_i^{*eff}\left(J_{3,ijl}^{DD}\right)_T\left(z_l^A \mu_j^{*eff}\frac{\partial \mu_j^{*eff}}{\partial T} + z_j^A \mu_l^{*eff}\frac{\partial \mu_l^{*eff}}{\partial T}\right) + 4J_{3,ijl}^{DD}\frac{\partial \mu_i^{*eff}}{\partial T}\left(z_l^A \mu_j^{*eff}\frac{\partial \mu_j^{*eff}}{\partial T} + z_j^A \mu_l^{*eff}\frac{\partial \mu_l^{*eff}}{\partial T}\right) \\
& + 2\mu_i^{*eff} J_{3,ijl}^{DD}\left[z_l^A \mu_j^{*eff}\frac{\partial^2 \mu_j^{*eff}}{\partial T^2} + z_j^A \mu_l^{*eff}\frac{\partial^2 \mu_l^{*eff}}{\partial T^2} + z_l^A\left(\frac{\partial \mu_j^{*eff}}{\partial T}\right)^2 + z_j^A\left(\frac{\partial \mu_l^{*eff}}{\partial T}\right)^2\right] \\
& + z_j^A z_l^A\left[\mu_i^{*eff}\left(J_{3,ijl}^{DD}\right)_{TT} + 2\left(J_{3,ijl}^{DD}\right)_T\frac{\partial \mu_i^{*eff}}{\partial T} + J_{3,ijl}^{DD}\frac{\partial^2 \mu_i^{*eff}}{\partial T^2}\right] + 8\mu_i^{*eff}\mu_j^{*eff}\mu_l^{*eff} J_{3,ijl}^{DD}\frac{\partial \mu_j^{*eff}}{\partial T}\frac{\partial \mu_l^{*eff}}{\partial T}\Bigg]
\end{aligned}
\tag{B.44}
$$

Supplements:

$$
d_{i,TT} = \frac{\partial^2 d_i}{\partial T^2} = 0.36\sigma_i \frac{\epsilon_i}{kT^3}\exp\left(-3\frac{\epsilon_i}{kT}\right)\left[2 - 3\frac{\epsilon_i}{kT}\right]
$$

$$
\zeta_{n,TT} = \frac{\pi}{6}\rho\sum_i x_i m_i n\left[d_{i,TT} d_i^{n-1} + (n-1)\, d_{i,T}^2 d_i^{n-2}\right]
$$

$$
\left(J_{2,ij}^{DD}\right)_T = \sum_{n=0}^{4}\left(a_{n,ij} + b_{n,ij}\frac{\epsilon_{ij}}{kT}\right) n\eta^{n-1}\zeta_{3,T} - \left(b_{n,ij}\frac{\epsilon_{ij}}{kT^2}\right)\eta^n
$$

$$
\left(J_{2,ij}^{DD}\right)_{TT} = \sum_{n=0}^{4}\left(a_{n,ij} + b_{n,ij}\frac{\epsilon_{ij}}{kT}\right)\left[n(n-1)\,\zeta_{3,T}^2\eta^{n-2} + n\eta^{n-1}\zeta_{3,TT}\right] + 2\left(b_{n,ij}\frac{\epsilon_{ij}}{kT^3}\right)\eta^n - 2\left(b_{n,ij}\frac{\epsilon_{ij}}{kT^2}\right) n\eta^{n-1}\zeta_{3,T}
$$

$$\left(J_{3,ijk}^{DD}\right)_T = \sum_{n=0}^{4} c_{n,ijk} n \eta^{n-1} \zeta_{3,T}$$

$$\left(J_{3,ijk}^{DD}\right)_{TT} = \sum_{n=0}^{4} c_{n,ijk} n \left[(n-1)\,\eta^{n-2}\zeta_{3,T}^2 + \zeta_{3,TT}\eta^{n-1}\right]$$

Cross density-temperature derivatives for the effective Helmholtz energy

$$\frac{\partial^2 \mu_i^{*eff}}{\partial\eta\partial T} = -\frac{\alpha_i^* T_i^*}{x_i}\left(\frac{1}{T}\frac{\partial^2 a'^{DD}}{\partial\eta\partial\mu_i^{*eff}} + \frac{\partial^3 a'^{DD}}{\partial\eta\partial T\partial\mu_i^{*eff}}\right) \tag{B.45}$$

$$\frac{\partial^2 a'^{DD,eff}}{\partial\eta\partial T} = \frac{\partial^2 a'^{DD}}{\partial\eta\partial T} + \sum_i \frac{\alpha_i^* T_i^*}{x_i}\left(\frac{1}{T}\frac{\partial a'^{DD}}{\partial\mu_i^{*eff}}\frac{\partial^2 a'^{DD}}{\partial\eta\partial\mu_i^{*eff}} + \frac{\partial^2 a'^{DD}}{\partial\eta\partial\mu_i^{*eff}}\frac{\partial^2 a'^{DD}}{\partial T\partial\mu_i^{*eff}} + \frac{\partial a'^{DD}}{\partial\mu_i^{*eff}}\frac{\partial^3 a'^{DD}}{\partial\eta\partial T\partial\mu_i^{*eff}}\right) \tag{B.46}$$

$$\begin{aligned}\frac{\partial^2 a_2'^{DD}}{\partial\eta\partial T} = {} & \frac{-\pi\rho}{\eta}\sum_i\sum_j x_i x_j \frac{\epsilon_i}{kT}\frac{\epsilon_j}{kT}\frac{\sigma_i^3\sigma_j^3}{\sigma_{ij}^3}\left[\left(z_i^A z_j^A - z_i^B z_j^B\right)\left[\left(J_{2,ij}^{DD}\right)_T - \frac{2}{T}\left(\eta J_{2,ij}^{DD}\right)_\eta + \eta\left(J_{2,ij}^{DD}\right)_{\eta T}\right]\right. \\ & + 2\left(z_j^A \mu_i^{*eff}\frac{\partial\mu_i^{*eff}}{\partial\eta} + z_i^A\mu_j^{*eff}\frac{\partial\mu_j^{*eff}}{\partial\eta}\right)\left[\eta\left(J_{2,ij}^{DD}\right)_T - \frac{2}{T}\left(\eta J_{2,ij}^{DD}\right)\right] \\ & \left. + \left(\eta J_{2,ij}^{DD}\right)_\eta\left(z_i^A z_j^A - z_i^B z_j^B\right)_T + \left(\eta J_{2,ij}^{DD}\right)\left(z_i^A z_j^A - z_i^B z_j^B\right)_{\eta T}\right]\end{aligned} \tag{B.47}$$

where

$$\begin{aligned}\left(z_i^A z_j^A - z_i^B z_j^B\right)_{\eta T} = {} & 4\mu_i^{*eff}\mu_j^{*eff}\left(\frac{\partial\mu_j^{*eff}}{\partial\eta}\frac{\partial\mu_i^{*eff}}{\partial T} + \frac{\partial\mu_i^{*eff}}{\partial\eta}\frac{\partial\mu_j^{*eff}}{\partial T}\right) + 2z_j^A\left(\frac{\partial\mu_i^{*eff}}{\partial\eta}\frac{\partial\mu_i^{*eff}}{\partial T} + \mu_i^{*eff}\frac{\partial^2\mu_i^{*eff}}{\partial\eta\partial T}\right) \\ & + 2z_i^A\left(\frac{\partial\mu_j^{*eff}}{\partial\eta}\frac{\partial\mu_j^{*eff}}{\partial T} + \mu_j^{*eff}\frac{\partial^2\mu_j^{*eff}}{\partial\eta\partial T}\right) + \frac{2}{T}\left(z_j^B\mu_i^{*eff}\frac{\partial\mu_i^{*eff}}{\partial\eta} + z_i^B\mu_j^{*eff}\frac{\partial\mu_j^{*eff}}{\partial\eta}\right)\end{aligned}$$

$$\begin{aligned}\frac{\partial^3 a_2'^{DD}}{\partial\eta\partial T\partial\mu_i^{*eff}} &= \frac{-4\pi\rho}{\eta}\sum_j x_i x_j \frac{\epsilon_i}{kT}\frac{\epsilon_j}{kT}\frac{\sigma_i^3\sigma_j^3}{\sigma_{ij}^3}\left[\left(J_{2,ij}^{DD}\right)_T\left(z_j^A\mu_i^{*eff}+2\eta\mu_i^{*eff}\mu_j^{*eff}\frac{\partial\mu_j^{*eff}}{\partial\eta}+\eta z_j^A\frac{\partial\mu_i^{*eff}}{\partial\eta}\right)\right.\\
&+\left(\eta J_{2,ij}^{DD}\right)_\eta\left(2\mu_i^{*eff}\mu_j^{*eff}\frac{\partial\mu_j^{*eff}}{\partial T}+\frac{z_j^B}{T}\mu_i^{*eff}+z_j^A\frac{\partial\mu_i^{*eff}}{\partial T}-\frac{2}{T}z_j^A\mu_i^{*eff}\right)\\
&+\left(\eta J_{2,ij}^{DD}\right)\left(2\mu_j^{*eff}\frac{\partial\mu_i^{*eff}}{\partial\eta}\frac{\partial\mu_j^{*eff}}{\partial T}+2\mu_i^{*eff}\frac{\partial\mu_j^{*eff}}{\partial\eta}\frac{\partial\mu_j^{*eff}}{\partial T}+2\mu_i^{*eff}\mu_j^{*eff}\frac{\partial^2\mu_j^{*eff}}{\partial\eta\partial T}+\frac{z_j^B}{T}\frac{\partial\mu_i^{*eff}}{\partial\eta}\right.\\
&\left.\left.+2\mu_j^{*eff}\frac{\partial\mu_j^{*eff}}{\partial\eta}\frac{\partial\mu_i^{*eff}}{\partial T}+z_j^A\frac{\partial^2\mu_i^{*eff}}{\partial\eta\partial T}-\frac{4}{T}\mu_i^{*eff}\mu_j^{*eff}\frac{\partial\mu_j^{*eff}}{\partial\eta}-\frac{2}{T}z_j^A\frac{\partial\mu_i^{*eff}}{\partial\eta}\right)+\eta z_j^A\mu_i^{*eff}\left(J_{2,ij}^{DD}\right)_{\eta T}\right]\end{aligned} \tag{B.48}$$

$$\begin{aligned}\frac{\partial^2 a_3'^{DD}}{\partial\eta\partial T} &= -\frac{4}{3}\pi^2\left(\frac{\rho}{\eta}\right)^2\sum_i\sum_j\sum_k x_i x_j x_k\frac{\epsilon_i}{kT}\frac{\epsilon_j}{kT}\frac{\epsilon_k}{kT}\frac{\sigma_i^3\sigma_j^3\sigma_k^3}{\sigma_{ij}\sigma_{ik}\sigma_{jk}}\left[\left(z_i^Az_j^Az_k^A-z_i^Bz_j^Bz_k^B\right)\left[\eta^2\left(J_{3,ijk}^{DD}\right)_{\eta T}+2\eta\left(J_{3,ijk}^{DD}\right)_T\right.\right.\\
&\left.-\frac{3}{T}\left(\eta^2J_{3,ijk}^{DD}\right)_\eta\right]+\left(z_i^Az_j^Az_k^A-z_i^Bz_j^Bz_k^B\right)_\eta\left[\eta^2\left(J_{3,ijk}^{DD}\right)_T-\frac{3}{T}\left(\eta^2J_{3,ijk}^{DD}\right)\right]\\
&+\left.\left(\eta^2J_{3,ijk}^{DD}\right)_\eta\left(z_i^Az_j^Az_k^A-z_i^Bz_j^Bz_k^B\right)_T+\left(\eta^2J_{3,ijk}^{DD}\right)\left(z_i^Az_j^Az_k^A-z_i^Bz_j^Bz_k^B\right)_{\eta T}\right]\end{aligned} \tag{B.49}$$

where

$$
\begin{aligned}
\left(z_i^A z_j^A z_k^A - z_i^B z_j^B z_k^B\right)_{\eta T} &= 4z_k^A \mu_i^{*eff} \mu_j^{*eff} \left(\frac{\partial \mu_j^{*eff}}{\partial \eta}\frac{\partial \mu_i^{*eff}}{\partial T} + \frac{\partial \mu_i^{*eff}}{\partial \eta}\frac{\partial \mu_j^{*eff}}{\partial T}\right) + 4z_j^A \mu_i^{*eff} \mu_k^{*eff} \left(\frac{\partial \mu_k^{*eff}}{\partial \eta}\frac{\partial \mu_i^{*eff}}{\partial T p} + \frac{\partial \mu_i^{*eff}}{\partial \eta}\frac{\partial \mu_k^{*eff}}{\partial T}\right) \\
&+ 4z_i^A \mu_j^{*eff} \mu_k^{*eff} \left(\frac{\partial \mu_k^{*eff}}{\partial \eta}\frac{\partial \mu_j^{*eff}}{\partial T} + \frac{\partial \mu_j^{*eff}}{\partial \eta}\frac{\partial \mu_k^{*eff}}{\partial T}\right) + 2z_j^A z_k^A \left(\frac{\partial \mu_i^{*eff}}{\partial \eta}\frac{\partial \mu_i^{*eff}}{\partial T} + \mu_i^{*eff}\frac{\partial^2 \mu_i^{*eff}}{\partial \eta \partial T}\right) \\
&+ 2z_i^A z_k^A \left(\frac{\partial \mu_j^{*eff}}{\partial \eta}\frac{\partial \mu_j^{*eff}}{\partial T} + \mu_j^{*eff}\frac{\partial^2 \mu_j^{*eff}}{\partial \eta \partial T}\right) + 2z_i^A z_j^A \left(\frac{\partial \mu_k^{*eff}}{\partial \eta}\frac{\partial \mu_k^{*eff}}{\partial T} + \mu_k^{*eff}\frac{\partial^2 \mu_k^{*eff}}{\partial \eta \partial T}\right) \\
&+ \frac{2}{T}\left(z_k^A z_i^B \mu_j^{*eff}\frac{\partial \mu_j^{*eff}}{\partial \eta} + z_j^A z_i^B \mu_k^{*eff}\frac{\partial \mu_k^{*eff}}{\partial \eta} + z_k^A z_j^B \mu_i^{*eff}\frac{\partial \mu_i^{*eff}}{\partial \eta} + z_i^A z_j^B \mu_k^{*eff}\frac{\partial \mu_k^{*eff}}{\partial \eta}\right. \\
&\left. + z_j^A z_k^B \mu_i^{*eff}\frac{\partial \mu_i^{*eff}}{\partial \eta} + z_i^A z_k^B \mu_j^{*eff}\frac{\partial \mu_j^{*eff}}{\partial \eta}\right)
\end{aligned}
$$

$$
\begin{aligned}
\frac{\partial^3 a_3'^{DD}}{\partial \eta \partial T \partial \mu_i^{*eff}} &= -8\pi^2 \left(\frac{\rho}{\eta}\right)^2 \sum_j \sum_l x_i x_j x_l \frac{\epsilon_i}{kT}\frac{\epsilon_j}{kT}\frac{\epsilon_l}{kT}\frac{\sigma_i^3 \sigma_j^3 \sigma_l^3}{\sigma_{ij}\sigma_{il}\sigma_{jl}} \left[\frac{2\mu_i^{*eff}\left(\eta^2 J_{3,ijl}^{DD}\right)}{T}\left[z_j^B \mu_l^{*eff}\frac{\partial \mu_l^{*eff}}{\partial \eta} + z_l^B \mu_j^{*eff}\frac{\partial \mu_j^{*eff}}{\partial \eta}\right.\right. \\
&- 3z_l^A \mu_j^{*eff}\frac{\partial \mu_j^{*eff}}{\partial \eta} - 3z_j^A \mu_l^{*eff}\frac{\partial \mu_l^{*eff}}{\partial \eta} + T\left(2\mu_j^{*eff}\mu_l^{*eff}\frac{\partial \mu_l^{*eff}}{\partial \eta}\frac{\partial \mu_j^{*eff}}{\partial T} + z_l^A \frac{\partial \mu_j^{*eff}}{\partial \eta}\frac{\partial \mu_j^{*eff}}{\partial T} + z_l^A \mu_j^{*eff}\frac{\partial^2 \mu_j^{*eff}}{\partial \eta \partial T}\right. \\
&\left.\left. + 2\mu_j^{*eff}\mu_l^{*eff}\frac{\partial \mu_j^{*eff}}{\partial \eta}\frac{\partial \mu_l^{*eff}}{\partial T} + z_j^A \frac{\partial \mu_l^{*eff}}{\partial \eta}\frac{\partial \mu_l^{*eff}}{\partial T} + z_j^A \mu_l^{*eff}\frac{\partial^2 \mu_l^{*eff}}{\partial \eta \partial T}\right)\right] + \left[\mu_i^{*eff}\left(\eta^2 J_{3,ijl}^{DD}\right)_\eta + \left(\eta^2 J_{3,ijl}^{DD}\right)\frac{\partial \mu_i^{*eff}}{\partial \eta}\right] \\
&\left[\frac{1}{T}\left(z_l^A z_j^B + z_j^A z_l^B - 3z_j^A z_l^A\right) + 2z_l^A \mu_j^{*eff}\frac{\partial \mu_j^{*eff}}{\partial T} + 2z_j^A \mu_l^{*eff}\frac{\partial \mu_l^{*eff}}{\partial T}\right] + \left(\eta^2 J_{3,ijl}^{DD}\right)\left(2z_l^A \mu_j^{*eff}\frac{\partial \mu_j^{*eff}}{\partial \eta}\frac{\partial \mu_i^{*eff}}{\partial T}\right. \\
&+ 2z_j^A \mu_l^{*eff}\frac{\partial \mu_l^{*eff}}{\partial \eta}\frac{\partial \mu_i^{*eff}}{\partial T} + z_j^A z_l^A \frac{\partial^2 \mu_i^{*eff}}{\partial \eta \partial T}\Bigg) + z_j^A z_l^A \left[\left(\eta^2 J_{3,ijl}^{DD}\right)_\eta \frac{\partial \mu_i^{*eff}}{\partial T} + 2\eta \mu_i^{*eff}\left(J_{3,ijl}^{DD}\right)_T + \eta^2 \left(J_{3,ijl}^{DD}\right)_T \frac{\partial \mu_i^{*eff}}{\partial \eta}\right. \\
&\left.\left. + \eta^2 \mu_i^{*eff}\left(J_{3,ijl}^{DD}\right)_{\eta T}\right] + 2\eta^2 \mu_i^{*eff}\left(J_{3,ijl}^{DD}\right)_T \left(z_l^A \mu_j^{*eff}\frac{\partial \mu_j^{*eff}}{\partial \eta} + z_j^A \mu_l^{*eff}\frac{\partial \mu_l^{*eff}}{\partial \eta}\right)\right]
\end{aligned}
\tag{B.50}
$$

Supplements:

$$\zeta_{3,\eta T} = \frac{3\sum_i x_i m_i d_i^2 d_{i,T}}{\sum_i x_i m_i d_i^3}$$

$$\left(J_{2,ij}^{DD}\right)_{\eta T} = \sum_{n=0}^{4}\left(a_{n,ij} + b_{n,ij}\frac{\epsilon_{ij}}{kT}\right)\left[n\left(n-1\right)\eta^{n-2}\zeta_{3,T} + n\eta^{n-1}\zeta_{3,\eta T}\right] - \left(b_{n,ij}\frac{\epsilon_{ij}}{kT^2}\right)n\eta^{n-1}$$

$$\left(J_{3,ijk}^{DD}\right)_{\eta T} = \sum_{n=0}^{4} c_{n,ijk} n\left[\left(n-1\right)\eta^{n-2}\zeta_{3,T} + \eta^{n-1}\zeta_{3,\eta T}\right]$$

General formulae for derivatives of a function of the form $\frac{\alpha}{\beta}$

Let α and β be arbitrary, algebraic expressions. If M, N, and P are variables such that $\alpha = f(M, N, P)$ and $\beta = f(M, N, P)$, then we can consider a function F:

$$F = \frac{\alpha}{\beta}$$

where:

$$\frac{\partial F}{\partial M} = \frac{1}{\beta}\left(\frac{\partial \alpha}{\partial M} - F\frac{\partial \beta}{\partial M}\right)$$

$$\frac{\partial^2 F}{\partial N \partial M} = \frac{1}{\beta}\left(\frac{\partial^2 \alpha}{\partial N \partial M} - \frac{\partial F}{\partial N}\frac{\partial \beta}{\partial M} - \frac{\partial \beta}{\partial N}\frac{\partial F}{\partial M} - F\frac{\partial^2 \beta}{\partial N \partial M}\right)$$

$$\begin{aligned}\frac{\partial^3 F}{\partial P \partial N \partial M} = \frac{1}{\beta}\Bigg(&\frac{\partial^3 \alpha}{\partial P \partial N \partial M} - \frac{\partial \beta}{\partial M}\frac{\partial^2 F}{\partial P \partial N} - \frac{\partial \beta}{\partial N}\frac{\partial^2 F}{\partial P \partial M} - \frac{\partial \beta}{\partial P}\frac{\partial^2 F}{\partial N \partial M} \\ &- \frac{\partial F}{\partial M}\frac{\partial^2 \beta}{\partial P \partial N} - \frac{\partial F}{\partial N}\frac{\partial^2 \beta}{\partial P \partial M} - \frac{\partial F}{\partial P}\frac{\partial^2 \beta}{\partial N \partial M} - F\frac{\partial^3 \beta}{\partial P \partial N \partial M}\Bigg)\end{aligned}$$

In the event where $M = N = P$, the above expressions simplify to

$$\frac{\partial^2 F}{\partial M^2} = \frac{1}{\beta}\left(\frac{\partial^2 \alpha}{\partial M^2} - 2\frac{\partial F}{\partial M}\frac{\partial \beta}{\partial M} - F\frac{\partial^2 \beta}{\partial M^2}\right)$$

$$\frac{\partial^3 F}{\partial M^3} = \frac{1}{\beta}\left(\frac{\partial^3 \alpha}{\partial M^3} - 3\frac{\partial \beta}{\partial M}\frac{\partial^2 F}{\partial M^2} - 3\frac{\partial F}{\partial M}\frac{\partial^2 \beta}{\partial M^2} - F\frac{\partial^3 \beta}{\partial M^3}\right)$$

APPENDIX C

Table of results for vapour-liquid equilibrium measurements

This appendix chapter presents the table of results for both low- and high-pressure vapour-liquid equilibrium (VLE) measurements. In the former case, six samples, three for the liquid and vapour phases each, were withdrawn at each equilibrium condition. Not more than six samples were taken, unless necessary, as the total volume removed from the system after six samplings is non-negligible, and care should be taken to ensure sufficient volume is in the still at all times. For high pressure VLE measurements, samples are withdrawn until repeatability is achieved within ± 1 % of the samples taken. The number of samples taken may vary somewhat, and we have indicated this alongside the data, under the column labeled n.

Table C.1: Vapour-liquid equilibrium measurements for the ethanol (1) + cyclohexane (2) system. The average uncertainties for temperature/pressure and compositions, for each equilibrium condition (row), are given as $\bar{U}(T)$ = ± 0.1 K, $\bar{U}(P)$ = ± 0.2 kPa, $\bar{U}(x)$ = ± 0.005 and $\bar{U}(y)$ = ± 0.005.

99.7 ± 0.2 kPa			323.4 ± 0.1 K		
T (K)	x_1	y_1	P (kPa)	x_1	y_1
353.5	0.000	0.000	36.0	0.000	0.000
343.2	0.029	0.286	45.4	0.011	0.210
339.1	0.123	0.395	53.9	0.071	0.346
338.2	0.238	0.424	56.2	0.189	0.385
338.0	0.402	0.445	56.7	0.298	0.402
338.2	0.505	0.459	57.1	0.483	0.417
338.4	0.631	0.480	56.6	0.621	0.433
338.6	0.725	0.504	54.6	0.750	0.466
339.4	0.795	0.538	50.5	0.853	0.529
341.1	0.865	0.600	45.5	0.912	0.607
342.2	0.893	0.638	38.8	0.958	0.734
343.2	0.913	0.672	29.4	1.000	1.000
351.2	1.000	1.000			

Table C.2: Vapour-liquid equilibrium measurements for the *n*-hexane (1) + 1-propanol (2) system. The average uncertainties for temperature and compositions, for each equilibrium condition (row), are given as $\bar{U}(T) = \pm 0.1$ K, $\bar{U}(x) = \pm 0.012$ and $\bar{U}(y) = \pm 0.012$.

99.0 ± 0.2 kPa		
T (K)	x_1	y_1
369.9	0.000	0.000
364.7	0.019	0.184
360.8	0.040	0.320
354.6	0.082	0.493
350.4	0.127	0.582
341.9	0.316	0.748
340.2	0.421	0.779
339.7	0.478	0.791
339.2	0.538	0.801
338.8	0.609	0.809
338.1	0.893	0.862
339.2	0.973	0.920
341.2	1.000	1.000

Table C.3: Vapour-liquid equilibrium measurements for the ethanol (1) + *m*-xylene (2) system. The average uncertainties for temperature/pressure and compositions, for each equilibrium condition (row), are given as $\bar{U}(T) = \pm 0.1$ K, $\bar{U}(P) = \pm 0.2$ kPa, $\bar{U}(x) = \pm 0.006$ and $\bar{U}(y) = \pm 0.006$.

94.9 ± 0.2 kPa			323.4 ± 0.1 K			333.1 ± 0.1 K			343.2 ± 0.1 K		
T (K)	x_1	y_1	P (kPa)	x_1	y_1	P (kPa)	x_1	y_1	P (kPa)	x_1	y_1
409.6	0.000	0.000	4.2	0.000	0.000	6.5	0.000	0.000	10.1	0.000	0.000
399.8	0.011	0.202	19.5	0.097	0.800	31.0	0.112	0.798	56.0	0.265	0.841
394.3	0.019	0.340	23.5	0.219	0.835	37.4	0.233	0.836	62.1	0.466	0.865
385.1	0.036	0.499	25.2	0.363	0.854	39.7	0.340	0.850	62.8	0.495	0.868
371.0	0.076	0.695	26.6	0.533	0.865	41.2	0.468	0.863	64.8	0.619	0.880
365.4	0.106	0.752	27.5	0.658	0.879	43.4	0.705	0.889	66.5	0.703	0.891
360.6	0.170	0.803	28.2	0.767	0.895	44.2	0.780	0.901	69.6	0.841	0.918
357.5	0.277	0.838	28.8	0.846	0.915	45.2	0.853	0.920	70.8	0.913	0.943
356.1	0.335	0.847	29.2	0.903	0.934	45.8	0.908	0.939	71.3	0.942	0.958
354.4	0.438	0.862	29.4	0.953	0.961	46.4	0.963	0.970	71.8	1.000	1.000
352.4	0.686	0.890	29.5	1.000	1.000	46.5	1.000	1.000			
351.6	0.749	0.899									
350.6	0.876	0.931									
350.2	0.935	0.955									
349.9	1.000	1.000									

Table C.4: Vapour-liquid equilibrium measurements for the ethanol (1) + ethylbenzene (2) system. The average uncertainties for pressure and compositions, for each equilibrium condition (row), are given as $\bar{U}(P) = \pm 0.2$ kPa, $\bar{U}(x) = \pm 0.006$ and $\bar{U}(y) = \pm 0.006$.

323.3 ± 0.1 K			343.3 ± 0.1 K		
P (kPa)	x_1	y_1	P (kPa)	x_1	y_1
4.7	0.000	0.000	11.3	0.000	0.000
17.5	0.067	0.743	34.5	0.056	0.682
21.7	0.142	0.798	44.8	0.108	0.763
24.3	0.262	0.826	56.5	0.255	0.820
26.1	0.431	0.844	63.3	0.473	0.853
27.0	0.572	0.858	66.3	0.626	0.869
27.8	0.700	0.873	68.6	0.748	0.887
28.5	0.799	0.892	70.4	0.844	0.911
29.1	0.872	0.915	71.8	0.918	0.941
29.4	0.929	0.943	72.2	0.954	0.962
29.5	0.970	0.971	72.5	0.985	0.986
29.5	1.000	1.000	72.6	1.000	1.000

Table C.5: Vapour-liquid equilibrium measurements for the benzene (1) + acetic acid (2) system. The average uncertainties for pressure and compositions, for each equilibrium condition (row), are given as $\bar{U}(P) = \pm 0.2$ kPa, $\bar{U}(x) = \pm 0.009$ and $\bar{U}(y) = \pm 0.009$.

323.4 ± 0.1 K			333.2 ± 0.1 K			343.2 ± 0.1 K		
P (kPa)	x_1	y_1	P (kPa)	x_1	y_1	P (kPa)	x_1	y_1
7.7	0.000	0.000	12.0	0.000	0.000	18.4	0.000	0.000
16.3	0.084	0.444	20.2	0.050	0.315	34.6	0.079	0.386
18.4	0.115	0.514	26.1	0.100	0.466	45.0	0.161	0.546
21.4	0.165	0.592	31.3	0.160	0.564	48.6	0.197	0.588
24.4	0.232	0.660	35.1	0.219	0.628	50.8	0.224	0.614
25.8	0.268	0.691	38.7	0.296	0.685	59.3	0.362	0.711
28.3	0.360	0.742	41.7	0.379	0.732	62.8	0.443	0.750
31.2	0.516	0.808	43.5	0.439	0.760	66.4	0.564	0.799
32.7	0.622	0.844	45.8	0.539	0.802	69.0	0.673	0.841
34.0	0.736	0.885	48.2	0.660	0.846	72.7	0.888	0.930
34.9	0.822	0.918	49.8	0.762	0.884	72.9	0.903	0.939
35.6	0.896	0.946	51.1	0.867	0.928	73.6	0.959	0.969
36.1	0.957	0.972	51.6	0.913	0.949	73.7	1.000	1.000
36.3	1.000	1.000	52.0	0.957	0.970			
			52.2	1.000	1.000			

Table C.6: Vapour-liquid equilibrium measurements for the toluene (1) + acetic acid (2) system. The average uncertainties for pressure and compositions, for each equilibrium condition (row), are given as $\bar{U}(P) = \pm 0.2$ kPa, $\bar{U}(x) = \pm 0.017$ and $\bar{U}(y) = \pm 0.017$.

353.2 ± 0.1 K			363.1 ± 0.1 K		
P (kPa)	x_1	y_1	P (kPa)	x_1	y_1
27.9	0.000	0.000	40.8	0.000	0.000
34.2	0.063	0.176	47.2	0.043	0.121
36.4	0.096	0.227	50.5	0.070	0.180
38.1	0.130	0.276	53.4	0.102	0.231
39.9	0.183	0.331	56.1	0.144	0.279
41.1	0.233	0.371	59.1	0.205	0.341
42.6	0.307	0.423	61.1	0.283	0.397
43.2	0.362	0.454	62.1	0.348	0.438
43.6	0.401	0.478	63.0	0.415	0.477
44.2	0.470	0.516	63.5	0.481	0.514
44.6	0.543	0.557	63.7	0.550	0.553
44.7	0.608	0.595	63.3	0.648	0.612
44.4	0.662	0.629	62.5	0.728	0.667
44.1	0.730	0.674	61.2	0.816	0.735
43.5	0.804	0.732	59.3	0.902	0.826
41.7	0.914	0.843	57.4	0.959	0.903
40.3	0.968	0.923	54.2	1.000	1.000
38.5	1.000	1.000			

Table C.7: Vapour-liquid equilibrium measurements for the acetone (1) + formic acid (2) system. The average uncertainties for pressure and compositions, for each equilibrium condition (row), are given as $\bar{U}(P) = \pm 0.2$ kPa, $\bar{U}(x) = \pm 0.022$ and $\bar{U}(y) = \pm 0.022$.

323.1 ± 0.1 K		
P (kPa)	x_1	y_1
15.8	0.000	0.000
16.1	0.068	0.069
16.5	0.096	0.114
16.6	0.114	0.144
17.5	0.159	0.234
18.9	0.207	0.345
20.5	0.247	0.446
22.4	0.290	0.538
25.6	0.348	0.654
33.5	0.463	0.808
39.8	0.536	0.870
45.9	0.606	0.904
55.8	0.707	0.933
65.8	0.806	
72.3	0.872	
77.0	0.918	
82.0	1.000	1.000

Table C.8: Vapour-liquid equilibrium measurements for the propane (1) + ethanol (2) system. The average uncertainties for pressure and compositions, for each equilibrium condition (row), are given as $\bar{U}(P) = \pm 0.004$ MPa, $\bar{U}(x) = \pm 0.027$ and $\bar{U}(y) = \pm 0.021$.

343.6 ± 0.02 K					353.6 ± 0.02 K				
P (MPa)	n_x	x_1	n_y	y_1	P (MPa)	n_x	x_1	n_y	y_1
0.072		0.000		0.000	0.11		0.000		0.000
0.46	9	0.038	7	0.853	0.45	7	0.025	7	0.754
1.17	6	0.132	7	0.949	0.86	7	0.069	7	0.873
1.64	7	0.211	7	0.970	1.23	8	0.110	7	0.907
1.80	8	0.256	7	0.972	1.60	7	0.161	6	0.929
2.01	7	0.333	7	0.976	2.03	9	0.240	7	0.942
2.21	5	0.459	7	0.977	2.42	7	0.351	7	0.950
2.37	10	0.685	9	0.978	2.84	8	0.699	7	0.955
2.44	9	0.802	7	0.984	2.94	7	0.822	7	0.957
2.51	11	0.918	7	0.988	3.17		1.000		1.000
2.58		1.000		1.000					

383.6 ± 0.02 K					403.0 ± 0.02 K				
P (MPa)	n_x	x_1	n_y	y_1	P (MPa)	n_x	x_1	n_y	y_1
0.32		0.000		0.000	0.58		0.000		0.000
0.88	7	0.037	7	0.635	1.30	6	0.040	7	0.538
1.52	8	0.084	6	0.779	2.15	7	0.090	6	0.715
2.06	7	0.131	8	0.835	2.82	7	0.141	7	0.781
2.61	7	0.190	7	0.868	3.50	7	0.204	7	0.817
3.10	7	0.269	7	0.884	4.53	7	0.334	7	0.837
3.66	7	0.376	7	0.899	5.02	7	0.447	9	0.834
4.31	7	0.580	6	0.904	5.42	7	0.555	6	0.829
4.72	7	0.796	7	0.903	5.56	7	0.626	7	0.815
					5.66	7	0.677	6	0.804

Table C.9: Vapour-liquid equilibrium measurements for the *n*-butane (1) + ethanol (2) system. The average uncertainties for pressure and compositions, for each equilibrium condition (row), are given as $\bar{U}(P) = \pm 0.002$ MPa, $\bar{U}(x) = \pm 0.024$ and $\bar{U}(y) = \pm 0.028$.

323.25 ± 0.02 K					353.26 ± 0.02 K				
P (MPa)	n_x	x_1	n_y	y_1	P (MPa)	n_x	x_1	n_y	y_1
0.028		0		0.000	0.110		0.000		0.000
0.381	11	0.193	7	0.919	0.561	10	0.110	7	0.782
0.402	6	0.238	7	0.922	0.669	8	0.155	7	0.818
0.430	9	0.301	7	0.928	0.783	6	0.210	7	0.847
0.465	8	0.428	7	0.936	0.886	7	0.321	7	0.871
0.487	7	0.686	7	0.943	0.953	8	0.476	7	0.885
0.495	7	0.811	6	0.948	1.010	7	0.748	7	0.904
0.501	7	0.900	7	0.954	1.029	7	0.882	7	0.922
0.503_2	6	0.952	6	0.962	1.035	7	0.930	7	0.935
0.502_8	7	0.974	6	0.970	1.032	7	0.962	7	0.953
0.495		1.000		1.000	1.013		1.000		1.000

373.3 ± 0.02 K					403.6 ± 0.02 K				
P (MPa)	n_x	x_1	n_y	y_1	P (MPa)	n_x	x_1	n_y	y_1
0.225		0.000		0.000	0.586		0.000		0.000
0.426	6	0.025	7	0.428	0.951	7	0.035	7	0.353
0.747	7	0.082	7	0.669	1.33	6	0.088	7	0.528
0.996	7	0.155	7	0.743	1.69	7	0.152	7	0.626
1.10	6	0.196	8	0.768	2.16	7	0.297	7	0.713
1.21	8	0.253	7	0.792	2.36	7	0.391	7	0.744
1.30	7	0.319	8	0.810	2.55	7	0.583	7	0.771
1.40	7	0.426	8	0.830	2.68	7	0.744	7	0.812
1.49	7	0.627	7	0.852	2.73	7	0.812	7	0.846
1.52	7	0.728	7	0.864	2.73	7	0.922	8	0.912
1.55	6	0.796	6	0.876	2.69	7	0.973	7	0.965
1.57	7	0.926	7	0.922	2.65		1.000		1.000
1.55	7	0.976	7	0.965					
1.53		1.000		1.000					

423.2 ± 0.02 K				
P (MPa)	n_x	x_1	n_y	y_1
0.981		0.000		0.000
1.33	7	0.027	7	0.210
1.65	7	0.061	7	0.338
1.97	5	0.100	7	0.429
2.31	7	0.149	7	0.504
2.65	7	0.208	7	0.565
2.97	7	0.296	7	0.619
3.20	7	0.387	7	0.652
3.43	7	0.506	7	0.687
3.67	7	0.676	7	0.745
3.77	7	0.765	7	0.791
3.79_8	7	0.905	7	0.902
3.79_3	7	0.915	7	0.911
3.76	7	0.949	7	0.945
3.71	7	0.975	7	0.973
3.65		1.000		1.000

APPENDIX D

Worked example illustrating the estimation of uncertainties

This appendix section illustrates the procedure for evaluating the experimental uncertainties, using the high pressure propane (1) + ethanol (2) system as an example.

Calibration

We will calculate the uncertainties in the same sequence that the experiment is carried out, starting with the calibrations. It is possible to identify two sources of uncertainties pertaining to the temperature calibration, given below:

- Maximum possible error in converting the resistance of the 25 Ω reference thermometer to true temperature: ± 0.013 K.
- Maximum possible error from usage of the calibration polynomial, $T_{\text{true}} = 1.27\text{E-}05T_{\text{read}}^2 + 0.998T_{\text{read}} - 0.04$: ± 0.010 K.

Designating a rectangular distribution to each of these errors, we get the following uncertainties:

$$u_{\text{ref}}(T) = \frac{0.013}{\sqrt{3}} = 0.0075 \text{ K}$$

$$u_{\text{corr}}(T) = \frac{0.010}{\sqrt{3}} = 0.0058 \text{ K}$$

In addition:

$$u_{\text{calib}}(T) = \sqrt{u_{\text{ref}}(T)^2 + u_{\text{corr}}(T)^2}$$

These uncertainties are treated as constants. Similarly for the pressure, we are hereby concerned only with the maximum possible error from usage of the calibration polynomial. Since there are two pressure transducers, the uncertainties of both must be considered. From § 3.2.3, we have mentioned the error to be 1 kPa and 8 kPa for the low and high pressure transducers, respectively. With a rectangular distribution:

$$u_{\text{calib, LPT}}(P) = u_{\text{corr, LPT}}(P) = \frac{0.01}{\sqrt{3}} = 0.006 \text{ bar}$$

$$u_{\text{calib, HPT}}(P) = u_{\text{corr, HPT}}(P) = \frac{0.08}{\sqrt{3}} = 0.05 \text{ bar}$$

Care must be taken to use the appropriate uncertainty value. At pressures below 40 bars, the reading from the low pressure transducer is preferred, while pressures above 40 bars are read exclusively from the high pressure transducer. One does not use both uncertainties (0.006 and 0.5 bar) in the same calculation.

One notes that propane (1) is calibrated as a gas and ethanol (2) as a liquid at room temperature. This implies that $u(n_1)$ will have a $u_{\text{ig}}(n_1)$ contribution, whereas $u(n_2)$ will have the $u_{\text{ld}}(n_2)$. From Eqn. (3.19):

$$u_{\text{ig}}(n_1) = n_1 \sqrt{\left(\frac{u(P)}{P}\right)^2 + \left(\frac{u(V)}{V}\right)^2 + \left(\frac{u(T)}{T}\right)^2}$$

The error associated with the DRUCK DPI 141 is given from the manufacturer as ± 0.01 mbar. The Leris Pt-100 was calibrated as with any other temperature probe, and thus contains both an error from the reference thermometer (± 0.013 K, see above), and from its own calibration polynomial. The latter was indicated to be ± 0.025 K (see § 3.2.3). We have thus:

$$u(P) = \frac{0.01}{\sqrt{3}} = 0.006 \text{ mbar}$$

$$\begin{aligned} u(T) &= \sqrt{u_{\text{ref}}(T)^2 + u_{\text{corr}}(T)^2} \\ &= \sqrt{\left(\frac{0.013}{\sqrt{3}}\right)^2 + \left(\frac{0.025}{\sqrt{3}}\right)^2} \\ &= 0.016 \text{ K} \end{aligned}$$

From the assumption that an approximate 2 % human error results from reading the syringe with a magnifying loop. It follows that:

$$u(V) = \frac{0.02 \times V}{\sqrt{3}} = 0.012\ V$$

The calibrations were carried at relatively constant conditions ($T = \sim 296$ K and $P = \sim 1004$ mbar). Substituting the above results into Eqn. (3.19):

$$\begin{aligned} u_{\text{ig}}(n_1) &= n_1 \sqrt{\left(\frac{0.006}{1003}\right)^2 + \left(\frac{0.012\ V}{V}\right)^2 + \left(\frac{0.016}{296}\right)^2} \\ &= 0.012 n_1 \end{aligned}$$

In other words, most of the error incurred in calculating the number of moles of propane injected into the TCD, by the ideal gas law, comes from the error in reading the syringe (the human error). Continuing, the calibration polynomial for propane is given by $n_{\text{calc}} = 8.92\text{E-}14 S^2 + 4.94\text{E-}09 S$, from which $\left|n_{1,\text{ true}} - n_{1,\text{ calc}}\right|_{\text{max}} = 7.35\text{E-}08$ mols. This is treated using a type B evaluation with rectangular distribution:

$$u_{\text{corr}}(n_1) = \frac{7.35\text{E-}08}{\sqrt{3}} = 4.24\text{E-}08 \text{ mols}$$

For component 2 (ethanol), there is a dilute and concentrated region, with two calibration polynomials giving two different $u_{\text{corr}}(n_2)$ depending on the area of the TCD peak observed (see Fig. 3.18). The two

calibrations were carried out in similar ambient conditions. In calculating $u_{\text{ld}}(n_2)$, we once again observe that the square root in Eqn. (3.22) can be regarded as a constant, with the error in volume dominating. Noting that the calibration is carried out at a constant temperature of ~ 296 K for any injection, we have for ethanol, with empirical constants $\{A, B, C, T_c\} = \{1.648, 0.27627, 0.2331, 513.92\}$ taken from [68]:

$$\begin{aligned} u_{\text{ld}}(n_2) &= n_2 \sqrt{\left(\frac{C \ln B \left(1 - \frac{T}{T_c}\right)^{C-1}}{T_c} u_{\text{ld}}(T) \right)^2 + \left(\frac{u_{\text{ld}}(V)}{V} \right)^2} \\ &= n_2 \sqrt{\left(\frac{0.2331 \ln(0.27627) \left(1 - \frac{296}{513.92}\right)^{0.2331-1}}{513.92} 0.016 \right)^2 + 0.012^2} \\ &= 0.012 n_2 \end{aligned}$$

In the above calculation, $u_{\text{ld}}(T) = u_{\text{ig}}(T)$ since the temperature measurement used for each model originates from the same Leris Pt-100. In addition, the 2 % error in syringe volume reading is applied. To finish off, we have the uncertainty from the calibration polynomial for ethanol:

$$u_{\text{corr, dil}}(n_2) = \frac{1.94\text{E-}07}{\sqrt{3}} = 1.12\text{E-}07 \text{ mols}$$

$$u_{\text{corr, conc}}(n_2) = \frac{1.33\text{E-}06}{\sqrt{3}} = 7.67\text{E-}07 \text{ mols}$$

Experimental

We will consider the first equilibrium state for the propane (1) + ethanol (2) system at 343.6 K, given in Table D.1. In total, sixteen samples were taken from the equilibrium mixture, 9 liquid samples and 7 vapour samples. We can calculate immediately the error in repeatability from the average values, using Eqn. (3.8):

$$\begin{aligned} u_{\text{rep}}(T) &= \sqrt{\frac{1}{16 \times 15} \left[(343.6659 - 343.6640)^2 + \ldots + (343.6559 - 343.6640)^2 \right]} \\ &= 0.0023 \text{ K} \end{aligned}$$

$$u_{\text{rep}}(P) = 0.0012 \text{ bar}$$

$$u_{\text{rep}}(x_1) = 1.80\text{E-}04$$

$$u_{\text{rep}}(y_1) = 6.38\text{E-}04$$

The combined standard uncertainty for temperature is thus:

$$\begin{aligned} u_c(T) &= \pm \sqrt{u_{\text{ref}}(T)^2 + u_{\text{corr}}(T)^2 + u_{\text{rep}}(T)^2} \\ &= \pm \sqrt{0.0075^2 + 0.0058^2 + 0.0023^2} \\ &= \pm 0.01 \text{ K} \end{aligned}$$

Table D.1: Experimental records of the first equilibrium condition for the propane (1) + ethanol (2) system, at 343.6 K. The temperatures, pressures, and mole numbers for propane and ethanol shown here have already been subjected to their respective calibration polynomials.

Liquid samples				
T (K)	P (bar)	n_1 (mols)	n_2 (mols)	x_1 [a]
343.6659	4.6713	2.078E-06	5.279E-05	0.0379
343.6659	4.6713	1.748E-06	4.323E-05	0.0389
343.6659	4.6695	1.776E-06	4.545E-05	0.0376
343.6659	4.6708	1.737E-06	4.312E-05	0.0387
343.6659	4.6688	1.534E-06	3.791E-05	0.0389
343.6759	4.6700	1.297E-06	3.191E-05	0.0391
343.6759	4.6700	2.653E-06	6.711E-05	0.0380
343.6759	4.6700	3.254E-06	8.203E-05	0.0382
343.6759	4.6765	2.643E-06	6.706E-05	0.0379
Vapour samples				
T (K)	P (bar)	n_1 (mols)	n_2 (mols)	y_1 [a]
343.6659	4.6850	1.093E-05	1.823E-06	0.857
343.6559	4.6777	1.614E-05	2.774E-06	0.853
343.6559	4.6795	1.597E-05	2.753E-06	0.853
343.6559	4.6787	1.571E-05	2.704E-06	0.853
343.6559	4.6725	1.544E-05	2.672E-06	0.853
343.6459	4.6695	1.572E-05	2.706E-06	0.853
343.6559	4.6703	1.553E-05	2.701E-06	0.852
$\bar{T}$ (K)	$\bar{P}$ (bar)		$\bar{x}_1$	$\bar{y}_1$
343.6640	4.6732		0.0383	0.853

[a] $x_i = n_i / \sum_j n_j$

For pressure, note we will be using $u_{\text{corr, LPT}}(P)$ since the pressure measurement was done at below 40 bars:

$$\begin{aligned} u_c(P) &= \pm\sqrt{u_{\text{corr, LPT}}(P)^2 + u_{\text{rep}}(P)^2} \\ &= \pm\sqrt{0.006^2 + 0.0012^2} \\ &= \pm 0.01 \text{ bar} \end{aligned}$$

For molar compositions, it is necessary to examine each sample, starting with the first liquid sample (first line in Table D.1). We have for propane:

$$\begin{aligned} u_{\text{ig}}(n_1) &= 0.012 n_1 \\ &= 0.012 \times 2.078\text{E-}06 \\ &= 2.400\text{E-}08 \text{ mols} \end{aligned}$$

$$\begin{aligned} u(n_1) &= \sqrt{u_{\text{ig}}(n_1)^2 + u_{\text{corr}}(n_1)^2} \\ &= \sqrt{2.400\text{E-}08^2 + 4.24\text{E-}08^2} \\ &= 4.876\text{E-}08 \text{ mols} \end{aligned}$$

For ethanol, we need to select the correct $u_{\text{corr}}(n_2)$, depending on the area of the TCD peaks. In this case, the liquid sample is rich in ethanol (area $S > 1606$); thus $u_{\text{corr}}(n_2) = u_{\text{corr, conc}}(n_2) = 7.67\text{E-}07$ mols. The inverse is applied for the vapour sample, where the ethanol is lean ($S < 1606$). To determine $u_{\text{ld}}(n_2)$ for the first liquid sample:

$$\begin{aligned} u_{\text{ld}}(n_2) &= 0.012 n_2 \\ &= 0.012 \times 5.279\text{E-}05 \\ &= 6.096\text{E-}07 \text{ mols} \end{aligned}$$

$$\begin{aligned} u(n_2) &= \sqrt{u_{\text{ld}}(n_2)^2 + u_{\text{corr}}(n_2)^2} \\ &= \sqrt{6.096\text{E-}07^2 + 7.67\text{E-}07^2} \\ &= 9.79\text{E-}07 \text{ mols} \end{aligned}$$

Recall that $u_{\text{calib}}(x_1)$ is calculated using a root-sum-squared formulation, given by Eqn. (3.17):

$$\begin{aligned} u_{\text{calib}}(x_1) &= \sqrt{\left(\frac{x_2}{n_1+n_2}u(n_1)\right)^2 + \left(\frac{x_1}{n_1+n_2}u(n_2)\right)^2} \\ &= \sqrt{\left(\frac{(1-0.0379)}{2.078\text{E-}06 + 5.279\text{E-}05}4.876\text{E-}08\right)^2 + \left(\frac{0.0379}{2.078\text{E-}06 + 5.279\text{E-}05}9.79\text{E-}07\right)^2} \\ &= 0.0172 \end{aligned}$$

An Excel spreadsheet can be conveniently set-up to carry out the uncertainties for all the samples taken. The results are shown in Table D.2.

Table D.2: Calculation of the uncertainties on molar composition, due to imprecisions in the calibration procedure, for both the liquid and vapour samples.

n_1 (mols)	n_2 (mols)	x_1	$u(n_1)$	$u(n_2)$	$u_{\text{calib}}(x_1)$
2.078E-06	5.279E-05	0.0379	4.876E-08	9.794E-07	0.0172
1.748E-06	4.323E-05	0.0389	4.700E-08	9.148E-07	0.0195
1.776E-06	4.545E-05	0.0376	4.714E-08	9.291E-07	0.0189
1.737E-06	4.312E-05	0.0387	4.695E-08	9.141E-07	0.0196
1.534E-06	3.791E-05	0.0389	4.600E-08	8.828E-07	0.0215
1.297E-06	3.191E-05	0.0391	4.501E-08	8.506E-07	0.0246
2.653E-06	6.711E-05	0.0380	5.235E-08	1.091E-06	0.0150
3.254E-06	8.203E-05	0.0382	5.669E-08	1.219E-06	0.0137
2.643E-06	6.706E-05	0.0379	5.228E-08	1.090E-06	0.0150
n_1 (mols)	n_2 (mols)	y_1	$u(n_1)$	$u(n_2)$	$u_{\text{calib}}(y_1)$
1.093E-05	1.823E-06	0.8571	1.332E-07	1.137E-07	0.00904
1.614E-05	2.774E-06	0.8533	1.911E-07	1.163E-07	0.00867
1.597E-05	2.753E-06	0.8530	1.892E-07	1.162E-07	0.00867
1.571E-05	2.704E-06	0.8532	1.863E-07	1.160E-07	0.00868
1.544E-05	2.672E-06	0.8525	1.832E-07	1.159E-07	0.00868
1.572E-05	2.706E-06	0.8531	1.864E-07	1.161E-07	0.00868
1.553E-05	2.701E-06	0.8519	1.843E-07	1.160E-07	0.00866
$\bar{u}_{\text{calib}}(x_1)$	0.0183			$\bar{u}_{\text{calib}}(y_1)$	0.00873

Finally, we can combine both the uncertainty of molar composition from the calibration, with that from the repeatability, as in Eqn. (3.9):

$$\begin{aligned} u_c\,(x_1) &= \pm\sqrt{\bar{u}_{\text{calib}}\,(x_1)^2 + u_{\text{rep}}\,(x_1)^2} \\ &= \pm\sqrt{0.0183^2 + 1.80\text{E-}04^2} \\ &= \pm\,0.0183 \end{aligned}$$

Note that the uncertainties arising from repeated measurements are negligible, i.e. $u_c \simeq \bar{u}_{\text{calib}}$. The value for $u_c\,(y_1)$ is $\pm\,0.00875$.

The reporting of the final uncertainties takes into account a coverage factor $k = 2$. Applying Eqn. (3.15) for T, P, and compositions x, y:

$$\begin{aligned} T &= (343.7 \pm 0.02)\ \text{K} \\ P &= (0.47 \pm 0.002)\ \text{MPa} \\ x &= 0.038 \pm 0.037 \\ y &= 0.853 \pm 0.018 \end{aligned}$$

At the extremities of the composition range, the uncertainty estimations given in this work can be particularly harsh, as can be seen for the liquid mole fraction x. Finally, an uncertainty statement, in accordance to the NIST standards (http://physics.nist.gov/cuu/Uncertainty/index.html), shown here for temperature, would be:

$T = (343.7 \pm 0.02)$ K, where the number following the symbol $\pm$ is the numerical value of an expanded uncertainty $U = k\,u_c$, with U determined from a combined standard uncertainty (i.e. estimated standard deviation) $u_c = 0.01$ K and a coverage factor $k = 2$. It can be assumed that the error is distributed in such a way that the unknown value of the standard is believed to lie in the interval defined by U with a level of confidence of approximately 95 %.

APPENDIX E

Table of results for critical point measurements

This section presents the table of results for the critical point measurements of binary and ternary mixtures. The uncertainties on the mole fractions are considered negligible; thus have not been indicated.

Table E.1: Critical temperatures and pressures for binary mixtures at different mole fractions.

x_1	T_c (K)	P_c (MPa)
	C_3H_8 (1) + C_4H_{10} (2)	
0.1200	420.28 ± 0.04	3.911 ± 0.001
0.2900	412.10 ± 0.04	4.066 ± 0.001
0.3922	407.46 ± 0.07	4.138 ± 0.001
0.6268	395.11 ± 0.23	4.270 ± 0.001
0.9214	375.69 ± 0.04	4.283 ± 0.001
	C_4H_{10} (1) + C_2H_6O (2)	
0.2067	490.60 ± 0.22	5.959 ± 0.002
0.2912	481.11 ± 0.25	5.802 ± 0.005
0.3941	470.44 ± 0.24	5.555 ± 0.006
0.4842	460.32 ± 0.21	5.274 ± 0.009
0.6063	446.55 ± 0.17	4.824 ± 0.006
0.7112	435.42 ± 0.07	4.410 ± 0.004
0.8075	428.16 ± 0.03	4.113 ± 0.001
0.8997	425.19 ± 0.03	3.951 ± 0.001
0.9104	424.99 ± 0.04	3.938 ± 0.001
0.9250	424.89 ± 0.03	3.911 ± 0.001
0.9394	424.86 ± 0.03	3.888 ± 0.001
0.9646	424.86 ± 0.03	3.851 ± 0.001
0.9855	425.04 ± 0.03	3.821 ± 0.001

x_1	T_c (K)	P_c (MPa)
	C_5H_{12} (1) + C_2H_6O (2)	
0.1441	498.65 ± 0.14	5.664 ± 0.004
0.1986	493.69 ± 0.15	5.466 ± 0.002
0.2544	488.33 ± 0.13	5.259 ± 0.003
0.3326	481.85 ± 0.13	4.988 ± 0.002
0.4974	470.44 ± 0.12	4.441 ± 0.002
0.5830	466.74 ± 0.12	4.234 ± 0.001
0.6642	464.81 ± 0.12	4.053 ± 0.001
0.6862	464.50 ± 0.12	4.002 ± 0.001
0.7716	464.49 ± 0.12	3.853 ± 0.001
0.7933	464.75 ± 0.12	3.789 ± 0.002
0.8703	466.21 ± 0.12	3.669 ± 0.002
	C_2H_6O (1) + C_6H_{14} (2)	
0.1042	503.10 ± 0.12	3.330 ± 0.002
0.2147	498.50 ± 0.13	3.608 ± 0.003
0.4017	491.60 ± 0.13	4.037 ± 0.004
0.4997	489.58 ± 0.13	4.275 ± 0.002
0.6028	489.82 ± 0.12	4.514 ± 0.002
0.7546	495.02 ± 0.12	5.004 ± 0.001
0.8974	504.63 ± 0.13	5.607 ± 0.002
0.9429	508.64 ± 0.12	5.830 ± 0.002
	C_2H_6O (1) + C_7H_{16} (2)	
0.4679	513.83 ± 0.16	4.249 ± 0.007
0.5656	508.59 ± 0.14	4.495 ± 0.005
0.6768	504.67 ± 0.12	4.760 ± 0.003
0.7757	503.82 ± 0.12	5.050 ± 0.001
0.8303	504.75 ± 0.13	5.239 ± 0.002
0.9348	509.28 ± 0.12	5.735 ± 0.001

x_1	T_c (K)	P_c (MPa)
	C_2H_6O (1) + C_8H_{18} (2)	
0.5862	528.57 ± 0.39	4.676 ± 0.011
0.6914	519.54 ± 0.15	4.958 ± 0.005
0.7949	513.08 ± 0.13	5.201 ± 0.003
0.8909	510.96 ± 0.18	5.516 ± 0.003
	C_5H_{12} (1) + C_6H_{14} (2)	
0.1685	502.37 ± 0.12	3.109 ± 0.002
0.3177	497.40 ± 0.12	3.181 ± 0.001
0.4444	492.88 ± 0.12	3.230 ± 0.001
0.6033	486.91 ± 0.12	3.287 ± 0.001
0.7491	481.05 ± 0.12	3.328 ± 0.001
0.8632	476.15 ± 0.12	3.352 ± 0.001
	C_2H_6O (1) + C_3H_8O (2)	
0.2690	531.17 ± 0.12	5.475 ± 0.002
0.4725	526.77 ± 0.12	5.692 ± 0.001
0.5174	525.67 ± 0.12	5.734 ± 0.001
0.6786	521.91 ± 0.12	5.886 ± 0.001
0.7915	519.16 ± 0.12	5.985 ± 0.001
0.8992	516.60 ± 0.12	6.061 ± 0.001
	C_3H_8 (1) + R134a (2)	
0.0569	371.23 ± 0.04	4.077 ± 0.001
0.1511	366.45 ± 0.05	4.101 ± 0.002
0.2641	361.22 ± 0.05	4.079 ± 0.001
0.3511	357.82 ± 0.04	4.047 ± 0.001
0.4675	354.92 ± 0.03	4.016 ± 0.001
0.5534	354.12 ± 0.03	4.016 ± 0.001
0.6605	355.12 ± 0.03	4.059 ± 0.001
0.7526	357.56 ± 0.04	4.119 ± 0.001
0.8545	361.86 ± 0.05	4.195 ± 0.001
0.9309	365.84 ± 0.04	4.236 ± 0.001

Table E.2: The critical temperatures and pressures for the ternary mixture *n*-pentane (1) + ethanol (2) + *n*-hexane (3).

x_1	x_2	T_c (K)	P_c (MPa)
0.0504	0.1978	496.99 ± 0.13	3.628 ± 0.005
0.0940	0.1636	497.16 ± 0.12	3.545 ± 0.002
0.1248	0.3932	486.89 ± 0.14	4.090 ± 0.007
0.1409	0.5945	485.06 ± 0.12	4.576 ± 0.001
0.1444	0.0631	500.19 ± 0.12	3.293 ± 0.003
0.1575	0.0905	498.42 ± 0.12	3.374 ± 0.002
0.1629	0.3304	487.15 ± 0.13	3.977 ± 0.003
0.2471	0.5030	480.38 ± 0.12	4.376 ± 0.001
0.3361	0.1639	487.97 ± 0.13	3.644 ± 0.003
0.4004	0.1099	488.50 ± 0.13	3.519 ± 0.002
0.5053	0.2413	476.50 ± 0.12	3.869 ± 0.002
0.5860	0.1556	478.03 ± 0.14	3.679 ± 0.002

APPENDIX F

Communications

Publications

1. X. Courtial, C.-B. Soo, C. Coquelet, P. Paricaud, D. Ramjugernath and D. Richon. *Vapor-liquid equilibrium in the n-butane + methanol system, measurement and modeling from 323.2 to 443.2 K*. Fluid Phase Equilibr., 277:152-161, 2009.
2. R. Zehioua, C. Coquelet, C.-B. Soo, D. Richon and A.-H. Meniai. *Experimental and predicted excess molar enthalpies of some working pairs for absorption cycles*. Thermochim. Acta, 495:72-80, 2009.
3. C.-B. Soo, E. El Ahmar, C. Coquelet, D. Ramjugernath and D. Richon. *Vapor-liquid equilibrium measurements and modeling of the n-butane + ethanol system from 323 to 423 K*. Fluid Phase Equilibr., 286:69-77, 2009.
4. C. Coquelet, C.-B. Soo, A. Valtz, D. Richon, D. Amoros and H. Guyet. *"Vapor-liquid" equilibrium measurements and modeling for the cyclohexane + cyclohexanol binary system*. Fluid Phase Equilibr., 298:33-37, 2010.
5. C. Coquelet, C.-B. Soo, A. Valtz, D. Richon, D. Amoros and H. Guyet. *Vapor-Liquid Equilibrium Measurements and Modeling for Cyclohexane + Cyclohexanone*. J. Chem. Eng. Data, 55:4521-4524, 2010.
6. C.-B. Soo, P. Théveneau, C. Coquelet, D. Ramjugernath and D. Richon. *Determination of critical properties of pure and multi-component mixtures using a "dynamic-synthetic" apparatus*. J. of Supercritical Fluids, 55:545-553, 2010.

Conferences

A. X. Courtial, C.-B. Soo, C. Coquelet, P. Paricaud, D. Ramjugernath and D. Richon. *Phase diagram of methanol and alkane binary systems in the field of natural gas fractionators: experimental work and modeling*. Communication at the Annual AIChE congress. 100, Philadelphia PA, November 16-21, 2008.

B. C.-B. Soo, P. Théveneau, C. Coquelet, D. Ramjugernath and D. Richon. *Determination of critical properties using a "dynamic-synthetic" apparatus: experimental work and modeling*. Communication at the Annual AIChE congress. 101, Nashville TN, November 8-13, 2009.

C. M. Dicko, C.-B. Soo, C. Coquelet and P. Paricaud. *Étude et détermination des points critiques: mesures expérimentales et modélisation*. Récents progrès en Génie des Procédés, SFGP. 98, Paris, 2009

D. C. Coquelet, C.-B. Soo, A. Valtz, D. Richon, D. Amoros and H. Guyet. *Vapor-Liquid Equilibria Measurements and Modeling of Cyclohexane + Cyclohexanol & Cyclohexane + Cyclohexanone*. Données thermophysiques: Acquisition, traitement et utilisation des banques. Lyon/Villeurbanne, June 18, 2010.

Fluid Phase Equilibria 277 (2009) 152–161

Contents lists available at ScienceDirect

Fluid Phase Equilibria

journal homepage: www.elsevier.com/locate/fluid

Vapor–liquid equilibrium in the *n*-butane + methanol system, measurement and modeling from 323.2 to 443.2 K

Xavier Courtial[a], Chien-Bin Soo[a], Christophe Coquelet[a], Patrice Paricaud[b], Deresh Ramjugernath[c], Dominique Richon[a,*]

[a] *MINES ParisTech, CEP/TEP - Centre énergétique et procédés, CNRS FRE 2861, 35, Rue Saint Honoré, 77305 Fontainebleau, France*
[b] *Laboratoire de Chimie et Procédés, ENSTA, ParisTech, 32 Boulevard Victor, 75739 Paris Cedex 15, France*
[c] *Thermodynamic Research Unit, School of Chemical Engineering, University KwaZulu Natal, Howard College Campus, Durban 4041, South Africa*

ARTICLE INFO

Article history:
Received 11 September 2008
Received in revised form 1 December 2008
Accepted 4 December 2008
Available online 11 December 2008

Keywords:
Experimental VLE measurement
n-Butane
Methanol
Critical temperature
Thermodynamic model

ABSTRACT

New experimental vapor–liquid equilibrium (VLE) data for the *n*-butane + methanol binary system are reported over a wide temperature range from 323.2 to 443.2 K and pressures up to 5.4 MPa. A static–analytic apparatus, taking advantage of two pneumatic capillary samplers, was used. The phase equilibrium data generated in this work are in relatively good agreement with previous data reported in the literature. Three different thermodynamic models have been used to represent the new experimental data. The first model is the cubic-based Peng–Robinson equation of state (EoS) combined with the Wong–Sandler mixing rules. The two other models are the non-cubic SAFT-VR and PC-SAFT equations of state. Temperature-dependent binary interaction parameters have been adjusted to the new data. The three models accurately represent the new experimental data, but deviations are seen to increase at low temperature. A similar evolution of the binary parameters with respect to temperature is observed for the three models. In particular a discontinuity is observed for the k_{ij} values at temperatures close to the critical point of butane, indicating the effects of fluctuations on the phase equilibria close to critical points.

1. Introduction

The phase behavior of the system *n*-butane + methanol is very interesting due to the combination of a non-polar and a polar component forming an azeotrope. The modeling of such binary mixtures is often a challenge due to self-association between the polar methanol molecules, which makes the behavior of the mixture highly non-ideal.

Several sets of vapor–liquid equilibrium data for the binary mixture can be found in the literature. Kretschmer and Wiebe [1] were the first to report measurements of bubble pressures for the mixture at 298.15 K, although only three points were presented. The authors then used a self-designed apparatus, and thereafter a non-linear empirical equation to relate *n*-butane mole fractions to total pressure. Petty and Smith [2] obtained bubble and dew pressures for temperatures from 322 to 410 K, at liquid and vapor *n*-butane compositions of 0, 0.25, 0.50, 0.75 and 1. They used an equipment characterized by a mercury compressibility bomb, although there is some disparity between these results and others reported. More consistent data were later published in the works of Leu et al. [3,4], who presented VLE measurements using a variable-volume vapor–liquid equilibrium cell in the whole range of composition, and temperatures of 273.2, 323.2, 372.5 [3], and 469.9 K [4], with good agreements with two other Refs. [5,6] at 323.2 K. A recent publication by Dell'Era [7] presented data at 364.5 K with a static total pressure apparatus and modeling with Wilson, NRTL and other solution models. In this case, except for the COSMO-RS model, most solution models are quite inaccurate for the mixture, but there is a strong lack in all models in predicting the behavior at the azeotrope.

The aim of this paper is to present new isothermal VLE data for the *n*-butane + methanol binary mixture from 323.2 to 443.2 K, focusing on the phase behavior above and below the *n*-butane critical temperature. The isotherms reported in this paper were determined using an apparatus based on the static–analytic method, which takes advantage of two ROLSI™ capillary samplers [8] for analysis in a gas chromatograph.

Three different models are chosen for the treatment of the new data. The Peng–Robinson (PR) [9] is a cubic equation of state (EoS), well-established in the oil industry for its simplicity and accuracy in describing the behavior of hydrocarbon systems. However, as with most cubic EoS, association interactions between molecules (hydrogen bonding) remain unaccounted for. In recent years, the use of statistical thermodynamics has provided a sounder, more rigorous theoretical basis to fluid models. This has led to the development of a new family of EoS, which is able to describe associating interactions of polar systems, at the expense of mathematical com-

* Corresponding author.
E-mail address: dominique.richon@mines-paristech.fr (D. Richon).

0378-3812/$ – see front matter © 2009 Published by Elsevier B.V.
doi:10.1016/j.fluid.2008.12.001

Thermochimica Acta 495 (2009) 72–80

Contents lists available at ScienceDirect

Thermochimica Acta

journal homepage: www.elsevier.com/locate/tca

Experimental and predicted excess molar enthalpies of some working pairs for absorption cycles

Raouf Zehioua[a,b], Christophe Coquelet[b], Chien-Bin Soo[b], Dominique Richon[b,*], Abdeslam-Hassen Meniai[a]

[a] Laboratoire de l'ingénierie des procédés de l'environnement (LIPE), Département de Chimie Industrielle, Université Mentouri Constantine, Route Ain El Bey, Constantine 25017, Algérie
[b] MINES ParisTech, CEP/TEP - Centre énergétique et procédés, 35 Rue Saint Honoré, 77305 Fontainebleau, France

ARTICLE INFO

Article history:
Received 11 February 2009
Received in revised form 22 April 2009
Accepted 5 June 2009
Available online 16 June 2009

Keywords:
Excess enthalpies
C80 calorimeter
Redlich–Kister
Water
Ethanol
Glycol
Glycerol
UNIFAC
UNIQUAC
Absorption cycles

ABSTRACT

In this work, the measured excess molar enthalpies of absorption heat pump working pairs (refrigerant + absorbent), *viz.* water + mono-, di- and tri-ethylene glycol, water + glycerol, and ethanol + di- and tri-ethylene glycol mixtures are presented at 298.15 K and ambient pressure using a Setaram Calvet C80 calorimeter. The experimental results are represented and correlated by a Redlich–Kister type equation. Modeling of the excess enthalpies has been performed using the UNIFAC molecular group-contribution method, and UNIQUAC Gibbs energy model. In addition, the data and results are used to predict the Gibbs energy of all binary systems. This allows a preliminary evaluation of the suitability of the binary systems as heat pump working pairs.

1. Introduction

The knowledge of excess thermodynamic properties is very important in several industrial-related processes. These properties quantify the deviation from ideality of the thermodynamic functions of mixtures, which result essentially from molecular interactions. In industrial mixing processes, an understanding of the nature and magnitude of excess properties is mandatory.

A more specific industrial application of excess properties is the conception of an absorption heat pump. The usual methods to evaluate the performance of such pumps are based on the interaction and behavior of the two components making working pairs, i.e. a refrigerant, such as water or ethanol, with an absorbent—glycols or glycerol. According to the selection criteria for efficient working pairs, as listed by Narodoslawsky et al. [1] and Zheng et al. [2], dominant factors are the magnitude and location of the extremum of the excess Gibbs free energy function (g^E). Morrissey and O'Donnell [3] state that system pairs exhibiting highly negative deviations from Raoult's law give the best result. As a more refined guideline, a strong non-ideality with a g^E extremum between: −1000 J/mol and −2000 J/mol located at high concentrations of the refrigerant, is usually recommended for good absorption heat pump performance [3]. Thus, the search for ideal working pairs requires the knowledge of excess Gibbs free energies of binary mixtures of refrigerants and absorbents, which is thermodynamically related to the excess enthalpy (h^E). Hence g^E can be easily obtained through experimental measurements of h^E thanks to a convenient solution model. Consequently, the aim of this work is to provide such datasets, which will be essential for the exergy analysis and the simulation of absorption heat pumps.

The polar–polar combination of water + glycol systems is known to exhibit negative excess enthalpies, essentially due to the presence of the hydroxyl group in both components. Molar excess enthalpies for the water + ethylene glycol (EG) system were measured by Rehm and Bittrich [4] at 298.15 K by thermometric titration, and later by Matsumoto et al. [5] at 298.15 K using an isothermal dilution calorimeter. Huot et al. [6] obtained water + EG h^E values from measurements of enthalpies of solution and of dilution at 298 K, although the values were more negative than both afore-mentioned references. More recently, Kracht et al. [7] used an LKB flow microcalorimeter for the same system and conditions. Their results compared favorably with that of Mat-

* Corresponding author. Tel.: +331 64 69 49 65; fax: +31 64 69 49 68.
E-mail address: dominique.richon@mines-paristech.fr (D. Richon).

0040-6031/$ – see front matter © 2009 Elsevier B.V. All rights reserved.
doi:10.1016/j.tca.2009.06.004

Fluid Phase Equilibria 286 (2009) 69–77

Contents lists available at ScienceDirect

Fluid Phase Equilibria

journal homepage: www.elsevier.com/locate/fluid

Vapor–liquid equilibrium measurements and modeling of the *n*-butane + ethanol system from 323 to 423 K

Chien-Bin Soo [a], Elise El Ahmar [a], Christophe Coquelet [a], Deresh Ramjugernath [b], Dominique Richon [a,*]

[a] *MINES ParisTech, CEP/TEP, Centre Energétique et Procédés, Rue Saint Honoré, 77305 Fontainebleau, France*
[b] *Thermodynamic Research Unit, School of Chemical Engineering, University KwaZulu-Natal, Howard College Campus, Durban 4041, South Africa*

ARTICLE INFO

Article history:
Received 14 April 2009
Received in revised form 7 August 2009
Accepted 10 August 2009
Available online 20 August 2009

Keywords:
Experimental VLE data
Ethanol
n-Butane
Peng–Robinson EoS
PC-SAFT EoS

ABSTRACT

Vapor–liquid equilibrium (VLE) data are presented for the *n*-butane + ethanol system in the temperature range from 323 to 423 K. Measurements were performed using a "static-analytic" apparatus, equipped with two electromagnetic ROLSI™ capillary samplers, and thermally regulated via an air bath. This work presents vapor compositions which have not been explicitly measured previously. The modeling of the data was performed using two models: the Peng–Robinson equation of state with the Wong and Sandler mixing rule and NRTL excess function (PR/WS/NRTL); and the perturbed-chain statistical associating fluid theory (PC-SAFT) equation of state. To assess the effect of dipole–dipole interactions present, a dipolar contribution developed by Jog and Chapman (1999) [20] was tested with the second model. Temperature dependent binary interaction parameters have been adjusted to the new data. The PR/WS/NRTL equation of state shows good correlation with the results, while the PC-SAFT is slightly less accurate.

1. Introduction

Over the past few decades, there has been a steady accumulation of alkane + alcohol VLE data, albeit some more complete than others [1]. The apolar–polar combination of such mixtures is highly non-ideal due to the formation of hydrogen bonds; thus theoretical approaches and model predictions are often insufficient without the support of experimental data. Even so, cubic equations of state (EoS) require complex mixing rules with at least three fitting parameters to describe quantitatively the behavior of such mixtures [2]. The development of more rigorous models based on real fluids, such as the statistical association fluid theory (SAFT) family of EoS [3], improved the situation by accounting for association-type interactions that were neglected previously. However, when used with minimal modifications, even these models require fitting parameters that are unusually large in magnitude to model alkane + alcohol systems [4–6].

The *n*-butane + alcohol systems have attracted much attention in the field of research, not only due to the several industrial applications of *n*-butane, but also for the numerous phenomena present in the phase equilibria. The *n*-butane + methanol system has been measured by Leu et al. [7,8], and more recently by Courtial et al. [5], with maximum pressure azeotropes observed at subcritical temperatures. For the *n*-butane + ethanol system, Kretschmer and Wiebe [9] reported solubility data for low *n*-butane concentrations (less than 10% on a mole basis) from 298 to 323 K. Miyano and Hayduk [10] performed similar experiments at 1 atm and 298–323 K. More complete data for the whole range of *n*-butane composition were later published by Holderbaum et al. [11] at 300, 326 and 348 K, although it was Deák et al. [12] who provided the most extensive VLE dataset by measuring bubble point pressures at given liquid mole fractions from 323 to 500 K. All literature suggests maximum pressure azeotropes within the system, although only bubble point curves (*P*–*x*) have been measured. Dew point curves have been constructed based on experimental and modeling results. As shown by Deák et al. [12], ethanol is the 1-alkanol with the highest carbon number with which *n*-butane forms an azeotrope. This is possibly due to the masking of the hydrogen bond effect (and hence non-ideality) by the increasing number of methyl groups.

In this paper, we continue these previous studies and present the complete *P*–*T*–*x*–*y* dataset for the binary system *n*-butane + ethanol at 323, 353, 373, 404 and 423 K. The measurements have been conducted using an apparatus based on the "static-analytic" method, where phases are sampled via two ROLSI™ capillary samplers [13] for analysis by gas chromatography. The data have been modeled using two equations of state, one from each of the aforementioned classifications. The cubic Peng–Robinson (PR) EoS [14] combined with complex mixing rules has had reasonable successes in simi-

* Corresponding author.
E-mail address: dominique.richon@mines-paristech.fr (D. Richon).

0378-3812/$ – see front matter © 2009 Published by Elsevier B.V.
doi:10.1016/j.fluid.2009.08.007

Fluid Phase Equilibria 298 (2010) 33–37

Contents lists available at ScienceDirect

Fluid Phase Equilibria

journal homepage: www.elsevier.com/locate/fluid

"Vapor–liquid" equilibrium measurements and modeling for the cyclohexane + cyclohexanol binary system

Christophe Coquelet[a,b,*], Chien-Bin Soo[a], Alain Valtz[a], Dominique Richon[a], Daniel Amoros[c], Hubert Gayet[c]

[a] MINES ParisTech, CEP/TEP – Centre Energétique et Procédés, 35 Rue Saint Honoré, 77305 Fontainebleau Cedex, France
[b] Thermodynamics Research Unit, School of Chemical Engineering, University of KwaZulu-Natal, Howard College Campus, Durban, South Africa
[c] Rhodia, Centre de Recherches et Technologies de Lyon, 85 avenue des Frères Perret, BP62, 69192 Saint-Fons Cedex, France

ARTICLE INFO

Article history:
Received 5 March 2010
Received in revised form 23 June 2010
Accepted 24 June 2010
Available online 1 July 2010

Keywords:
"Vapor–liquid" equilibrium data
Static-analytic
High-pressure
Cyclohexane
Cyclohexanol
Equation of states

ABSTRACT

To simulate cyclohexane oxidation reactors using a dynamic model linking kinetics, thermodynamics and hydrodynamics, the acquisition and modeling of vapor–liquid equilibria of the key components, under the process conditions, are essential. In this work, the vapor–liquid equilibria of the cyclohexane + cyclohexanol system were determined at temperatures 424, 444, 464 and 484 K. The measurements were carried out using an apparatus based on the "static-analytic" method, with two ROLSI™ pneumatic capillary samplers. The generated data are successfully correlated using two equations of state, the Peng–Robinson (PR) and the Perturbed-Chain Statistical Association Fluid Theory (PC-SAFT). A comparison of model performances reveals the former being better in data representation, while the latter has a broader applicability over larger range of temperatures.

1. Introduction

The oxidation of cyclohexane is a significant process in the chemical industry, not only for the production of nylon intermediates: cyclohexanol and cyclohexanone, but also it has been the focus of catalysis research for several decades [1]. The conventional technology, using cobalt-based catalysts, is known to be low in efficiency, with a conversion of cyclohexane of less than 5%, and selectivities of cyclohexanol and cyclohexanone between 70% and 85% [2]. Careful control of reaction temperature, around 423 K, needs to be maintained to avoid the formation of byproducts [2]. Over the years, considerable research on catalysts have been carried out to balance the conversion and selectivity, without losing focus on environmental feasibility. Numerous possible catalysts have been reported in open literature, but with the exception of gold [3], most processes are nevertheless carried out at 400–430 K, and separated downstream.

For unit operations and process design, experimental equilibrium data at such high temperatures are necessary. In this study, the vapor–liquid equilibrium (VLE) data for the cyclohexane + cyclohexanol binary system are presented at 424, 444, 464 and 484 K. Careful bibliographic studies have shown that previous experimental VLE work on the cyclohexane + cyclohexanol system were carried out predominantly at low temperatures up to 433 K [4–7]. Susarev and Lyzlova measured the ternary system cyclohexane + cyclohexanol + cyclohexanone at atmospheric pressure [8]. At low temperatures and pressures, the system exhibits large relative volatilities, often exceeding 100 or more for cyclohexanol-rich regions. No data on liquid–liquid equilibrium have been reported for this system, while solid–liquid equilibrium has been reported for temperatures between 280 and 298 K [9]. Good VLE representations of the system have been achieved in the past using the NRTL local composition model [5,6], and treating the vapor as an ideal phase [6]. In this work, we have tested modeling of our new measured data using cubic and non-cubic equation of states (EoS). The former is based on the Peng–Robinson (PR) cubic equation [10], using the Wong–Sandler (WS) mixing rule [11], and the NRTL Gibbs free energy model [12]. The latter model is the Perturbed-Chain (PC) modification of the SAFT equation [13,14], which we have enhanced for this application through an additional dipolar contribution proposed by Jog and Chapman (JC) [15] and Jog et al. [16].

* Corresponding author at: MINES ParisTech, CEP/TEP – Centre Energétique et Procédés, 35 Rue Saint Honoré, 77305 Fontainebleau Cedex, France.
Tel.: +33 1 64694962; fax: +33 1 64694968.
E-mail address: christophe.coquelet@mines-paristech.fr (C. Coquelet).

0378-3812/$ – see front matter © 2010 Elsevier B.V. All rights reserved.
doi:10.1016/j.fluid.2010.06.013

J. Chem. Eng. Data **2010,** *55,* 4521–4524 **4521**

Vapor−Liquid Equilibrium Measurements and Modeling for Cyclohexane + Cyclohexanone†

Christophe Coquelet,*,‡,§ Chien-Bin Soo,‡ Alain Valtz,‡ Dominique Richon,‡ Daniel Amoros,|| and Hubert Gayet||

MINES ParisTech, CEP/TEP - Centre Energétique et Procédés, 35 Rue Saint Honoré, 77305 Fontainebleau Cedex, France, Thermodynamics Research Unit, School of Chemical Engineering, University of KwaZulu-Natal, Howard College Campus, Durban, South Africa, and Rhodia, Centre de Recherches et Technologies de Lyon, 85 Avenue des Frères Perret, BP62, 69192 Saint-Fons Cedex, France

The characteristically low conversion in the oxidation of cyclohexane to form cyclohexanol and cyclohexanone requires significant recovery work via distillation. In this study, new isothermal vapor−liquid equilibria (VLE) are presented for the cyclohexane + cyclohexanone binary system. Measurements were performed at temperatures of (423, 444, 464, and 484) K, using an apparatus based on the "static−analytic" method, with two ROLSI pneumatic capillary samplers. The generated data are correlated using two equations of state, namely, the Peng−Robinson coupled with the Wong−Sandler mixing rules and the perturbed-chain statistical associating fluid theory (SAFT) with a dipolar contribution by Jog and Chapman. While both models perform reasonably well in describing the phase equilibria, the Peng−Robinson is slightly better than the perturbed-chain SAFT equation of state and tends to be more easily implemented in industrial process simulators.

Introduction

It is well-known that the commercial synthesis of adipic acid and caprolactum, raw materials in Nylon production, follows two possible reaction routes, namely, the oxidation of cyclohexane or the hydrogenation of phenol. Certainly, at an economic level, the oxidation of cyclohexane is favored, using cobalt naphthenate or stearate catalysts[1] to produce a mixture of cyclohexanol, cyclohexanone, and unreacted cyclohexane. In 1990, over 90 % of the global output of adipic acid was produced using this route.[2]

In spite of this, the conversion of cyclohexane oxidation is characteristically low, reaching 5 % conversion and maximum selectivities of 85 % of the desired products.[3] The recovery of downstream chemicals for recycling are usually carried out by distillation, where knowledge of the relative volatilities of cyclohexane + cyclohexanol and cyclohexane + cyclohexanone are vital. This work focuses on the measurement of vapor−liquid equilibria (VLE) data for cyclohexane (1) + cyclohexanone (2). In this study, new isothermal VLE data for cyclohexane + cyclohexanone are presented at temperatures of (423, 444, 464, and 484) K. Bibliographic studies have confirmed that previous experimental VLE work on this system was carried out at temperatures up to only 433 K.[4−9] Susarev and Lyzlova measured the only ternary cyclohexane + cyclohexanol + cyclohexanone system at atmospheric pressure.[4]

The measured data are first treated using the Peng−Robinson[10] (PR) equation of state with the Mathias−Copeman[11] α function. The mixing rule employed herein is that of Wong−Sandler[12] (WS), involving the nonrandom two-liquid (NRTL) Gibbs free energy model.[13] In view of the rapid rise of the theoretically sound statistical associating fluid theory (SAFT) models, we have tested the perturbed-chain[14] (PC) modification of the SAFT equation, including the dipolar contribution proposed by Jog and Chapman[15] (JC) and Jog et al.[16]

Experimental Section

Materials. Cyclohexane (C_6H_{12}, CAS number: 110-82-7) was supplied by Fluka. Cyclohexanone ($C_6H_{10}O$, CAS number: 108-94-1) was obtained from Sigma Aldrich. Both compounds have a certified mass fraction purity of > 0.998 as determined by GC. The compounds, both being liquids at room temperature, were carefully degassed prior to measurements using a vacuum pump.

Apparatus. The apparatus used in this work is based on a "static−analytic" method with liquid and vapor phase samplings. This apparatus is similar to that described by Valtz et al.[17]

The equilibrium cell is contained in a thermostatted liquid bath. Temperatures are measured thanks to two platinum resistance thermometer probes (Pt100) inserted inside the walls of the equilibrium cell. These Pt100 probes are calibrated against a 25 Ω reference probe (Tinsley Precision Instrument) calibrated by the Laboratoire National d'Essais (Paris) following the 1990 International Temperature Scale protocol.

Pressures are measured using a pressure transducer (Druck, type PTX611, range: (0 to 6) MPa). This pressure sensor was calibrated against a dead weight pressure balance (5202S model from Desgranges and Huot). Pressure and temperature data acquisitions are performed with a computer linked to a Hewlett-Packard unit (HP34970A). The uncertainties in this work, combining both the errors from calibration and repeatability of the measurements, are not higher than ± 0.06 K and ± 0.001 MPa.

The analytical work was carried out using a gas chromatograph (Varian model CP-3800) equipped with a thermal

† Part of the "Sir John S. Rowlinson Festschrift".

* Corresponding author. E-mail: christophe.coquelet@mines-paristech.fr. Telephone: +33164694962. Fax: +33164694968.
‡ MINES ParisTech, CEP/TEP - Centre Energétique et Procédés.
§ University of KwaZulu-Natal.
|| Rhodia, Centre de Recherches et Technologies de Lyon.

10.1021/je100474b
Published on Web 08/09/2010

J. of Supercritical Fluids 55 (2010) 545–553

Contents lists available at ScienceDirect

The Journal of Supercritical Fluids

journal homepage: www.elsevier.com/locate/supflu

Determination of critical properties of pure and multi-component mixtures using a "dynamic–synthetic" apparatus

Chien-Bin Soo[a], Pascal Théveneau[a], Christophe Coquelet[a,b], Deresh Ramjugernath[b], Dominique Richon[a,*]

[a] MINES ParisTech, CEP/TEP - Centre Energétique et Procédés, Rue Saint Honoré, 77305 Fontainebleau, France
[b] Thermodynamic Research Unit, School of Chemical Engineering, University KwaZulu-Natal, Howard College Campus, Durban 4041, South Africa

ARTICLE INFO

Article history:
Received 29 March 2010
Received in revised form 13 October 2010
Accepted 16 October 2010

Keywords:
Dynamic–synthetic method
Critical properties
Refrigerants
Ethanol
Ternary methods

ABSTRACT

In this work, we use an efficient and reliable "dynamic–synthetic" method for the measurement of critical properties of a variety of pure compounds, binary mixtures, and one ternary mixture. The critical phenomenon is observed via the critical opalescence in a view cell, which withstands conditions up to 543 K and 20 MPa. Excellent agreements were obtained between the measured pure compounds' properties and those listed in recent databases. Among the pure compounds measured, several refrigerants less well described in open literature (C_3F_6, C_3F_6O, R365mfc) have been compared with conventional predictive models. The critical profiles of associating, azeotropic systems ethanol + *n*-alkanes (C_4–C_8) are presented, as well as the critical surfaces for the ternary system *n*-pentane + ethanol + *n*-hexane. We present forms of the Cibulka and Singh's equation suitable for correlating ternary critical properties.

1. Introduction

Despite the growing interests in supercritical fluid processes, mixture critical data comprise only a small percentage of the open literature. According to the Dortmund Data Bank of 2009 [1], data sets dedicated to mixture critical data form less than 1% of the database, that is excluding the occasional critical points reported in vapor–liquid equilibria (VLE), which themselves appear few and far between. This is not to undermine their importance, but rather to stress the lack of data in this regard.

From a modeling point of view, knowledge of critical data is important as they provide information about real fluids, as well as characterize phase change boundaries in mixture phase diagrams. This is a result of the classification of binary phase diagrams proposed by van Konynenburg and Scott [2]. By correlating simultaneously critical data, excess properties, and phase equilibrium data, one encompasses the major thermodynamic aspects of fluid mixtures.

The prediction of phase behavior at critical regions remains difficult. One of the reasons is mentioned above, *i.e.* the insufficient amount of critical data incorporated in the development of predictive models, compared to other types of fluid phase data. Secondly, it is often risky to extrapolate mixture parameters to the critical region, unless following in a rigorous manner the renormalization-group theory [3], or some form of the rectilinear scaling law [4]. It is for these reasons that experimental measurements of critical data remain of high value. Accurate critical data, readily achievable with the ideas proposed in this work, are being used to improve the performance of non-cubic equation of states, such as those of the SAFT-type equations [5], which lack constraints in the critical region.

This communication focuses on the experimental aspect of attaining mixture critical profiles. A "dynamic–synthetic" apparatus, which allows the observation of the critical opalescence, has been used for pure compounds and mixtures. The performance of the apparatus is illustrated in a series of measurements involving pure compounds, and binary mixtures of ethanol and *n*-alkanes. The critical *P*–*T* projections for the ternary *n*-pentane (1) + ethanol (2) + *n*-hexane (3) system are also presented.

2. Materials and methods

Table 1 summarizes the purities of the chemicals used in the study. A large inventory of materials is required for the duration of the experimental, due to the flow nature of the apparatus.

Experimental techniques for the measurement of critical properties can be classified as static or dynamic methods, and are almost all synthetic as opposed to analytic in operation. A comprehensive review on recent methods is provided by Teja and Mendez-Santiago [6]. The apparatus presented in this work is a typical flow-type

* Corresponding author. Tel.: +33 01 64694965; fax: +33 01 64694968.
E-mail address: dominique.richon@mines-paristech.fr (D. Richon).

0896-8446/$ – see front matter © 2010 Elsevier B.V. All rights reserved.
doi:10.1016/j.supflu.2010.10.022

Vapor-Liquid Equilibria Measurements and Modeling of Cyclohexane + Cyclohexanol & Cyclohexane + Cyclohexanone

Christophe Coquelet[†,‡], Chien-Bin Soo[†], Alain Valtz[†], Dominique Richon[†], Daniel Amoros[§], Hubert Gayet[§]

[†]MINES ParisTech, CEP/TEP - Centre Energétique et Procédés, 35 Rue Saint Honoré, 77305 Fontainebleau Cedex, France. [‡]Thermodynamics Research Unit, School of Chemical Engineering, University of KwaZulu-Natal, Howard College Campus, Durban, South Africa. [§] Rhodia, Centre de Recherches et Technologies de Lyon, 85 avenue des Frères Perret, BP62, 69192 Saint-Fons Cedex, France

Introduction

It is known that the commercial synthesis of cyclohexanol and cyclohexanone - raw materials in Nylon - follows two possible reaction routes, *viz.* the oxidation of cyclohexane or the hydrogenation of phenol. From an economic point of view, the oxidation of cyclohexane is favored, despite the conversion of the process being characteristically low: ~ 5 % conversion and ~ 80 % selectivities toward the desired products.

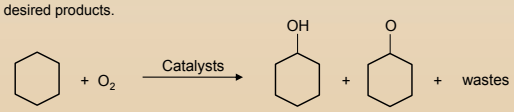

In this project, we are concerned in the phase behavior of cyclohexane + cyclohexanol / cyclohexanone at various temperatures, for the separation and recycling of downstream reactor products.

Modeling

Two equations of state have been used in the data treatment,

Peng-Robinson: $P = \frac{RT}{v-b} - \frac{a(T)}{v^2+2bv-b^2}$ — Mathias-Copeman (1983); Wong-Sandler (1992) mixing rule + NRTL (1968) g^E function

Polar PC-SAFT: $A^{res} = A^{seg} + A^{chain} + A^{assoc} + A^{dipolar}$ — Square-well u(*r*); Association; Chain Formation; Jog and Chapman (1999)

Experimental Apparatus

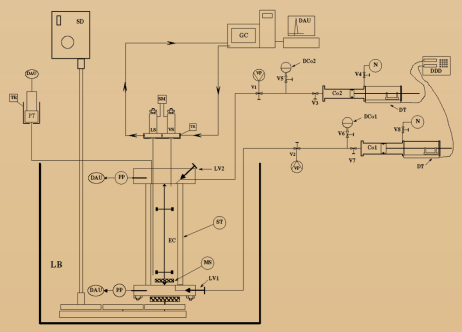

DAU: Data acquisition system; DCoi: Degassed component i; DDD: Piston displacement display; DT: Displacement tranducer; EC: Equilibrium cell; GC: Gas chromatograph; LB: Liquid bath; LS: Liquid sampler; LVi: Loading valve; MS: Magnetic stirrer; N: Pressurization fluid (N_2); PP: Platinum probe; PT: Pressure transducer; SD: Stirring device; SM: Sampling controller; ST: Sapphire tube; TC_1 & TC_2: Thermal presse; Th: Thermocouple; TR: Temperature regulator; VS: Vapour sampler; VSS: Variable speed stirrer; Vi: Loading valve i; VP: Vacuum pump.

Results

◆ *Cyclohexane* (1) + *Cyclohexanol* (2):

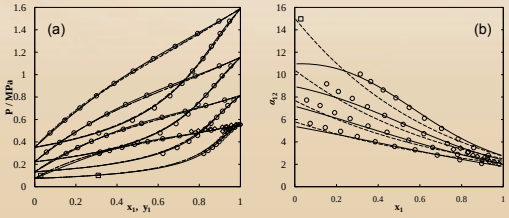

(a) Experimental VLE data and (b) relative volatilities of the cyclohexane (1) + cyclohexanol (2) system at 424, 444, 464, and 484 K. ○ : This work; □ : Steyer and Sundmacher (2004); ◇: Li et al. (2010); — : Modeling via Peng-Robinson; – – : Modeling via Polar PC-SAFT.

◆ *Cyclohexane* (1) + *Cyclohexanone* (2):

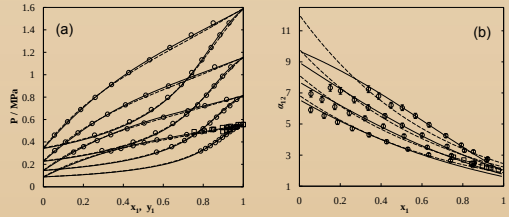

(a) Experimental VLE data and (b) relative volatilities of the cyclohexane (1) + cyclohexanone (2) system at 423, 444, 464, and 484 K. ○ : This work; □ : Li et al. (2010); — : Modeling via Peng-Robinson; – – : Modeling via Polar PC-SAFT.

Model Comparisons

C_6H_{12} + $C_6H_{12}O$	AAD_x (%)[†]		AAD_y (%)	
T / K	PR	Polar PC-SAFT	PR	Polar PC-SAFT
424	**1.0**	1.8	**0.3**	1.1
444	**1.3**	1.7	**0.8**	1.6
464	**1.5**	1.7	**1.3**	2.0
484	**0.8**	1.6	2.2	**1.7**

C_6H_{12} + $C_6H_{10}O$	AAD_x (%)		AAD_y (%)	
T / K	PR	Polar PC-SAFT	PR	Polar PC-SAFT
423	**0.9**	3.3	**0.3**	0.4
444	**1.3**	2.3	0.7	**0.3**
464	2.5	**2.4**	1.9	**1.3**
484	**2.1**	2.3	1.8	**1.4**

[†] Absolute average deviation : 100 / no. of points × $\sum$ | $\sigma_{exp} - \sigma_{cal}$ | / σ_{exp}

Conclusion

- Accurate *pTxy* VLE data for the cyclohexane + cyclohexanol / cyclohexanone systems have been measured using a "static-analytic" apparatus
- The Peng-Robinson equation of state correlates better the data.
- The Polar PC-SAFT equation of state requires only one interaction parameter for each system to correlate the entire range of temperatures

Presented at *Données thermophysiques: Acquisition, traitement et utilisation des banques, Lyon/Villeurbanne, 18 June 2010*

APPENDIX G

In-house PC-SAFT Program

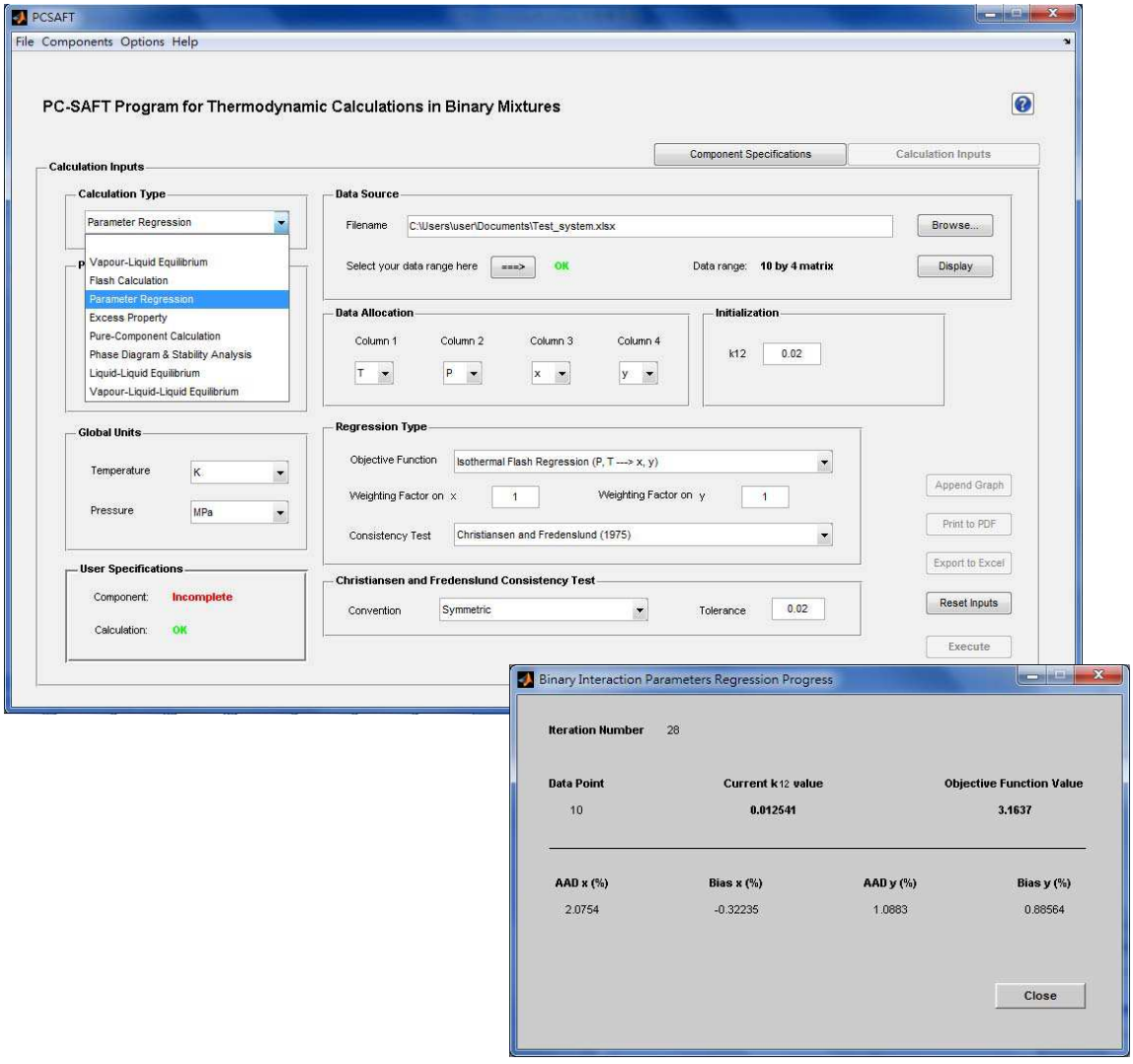

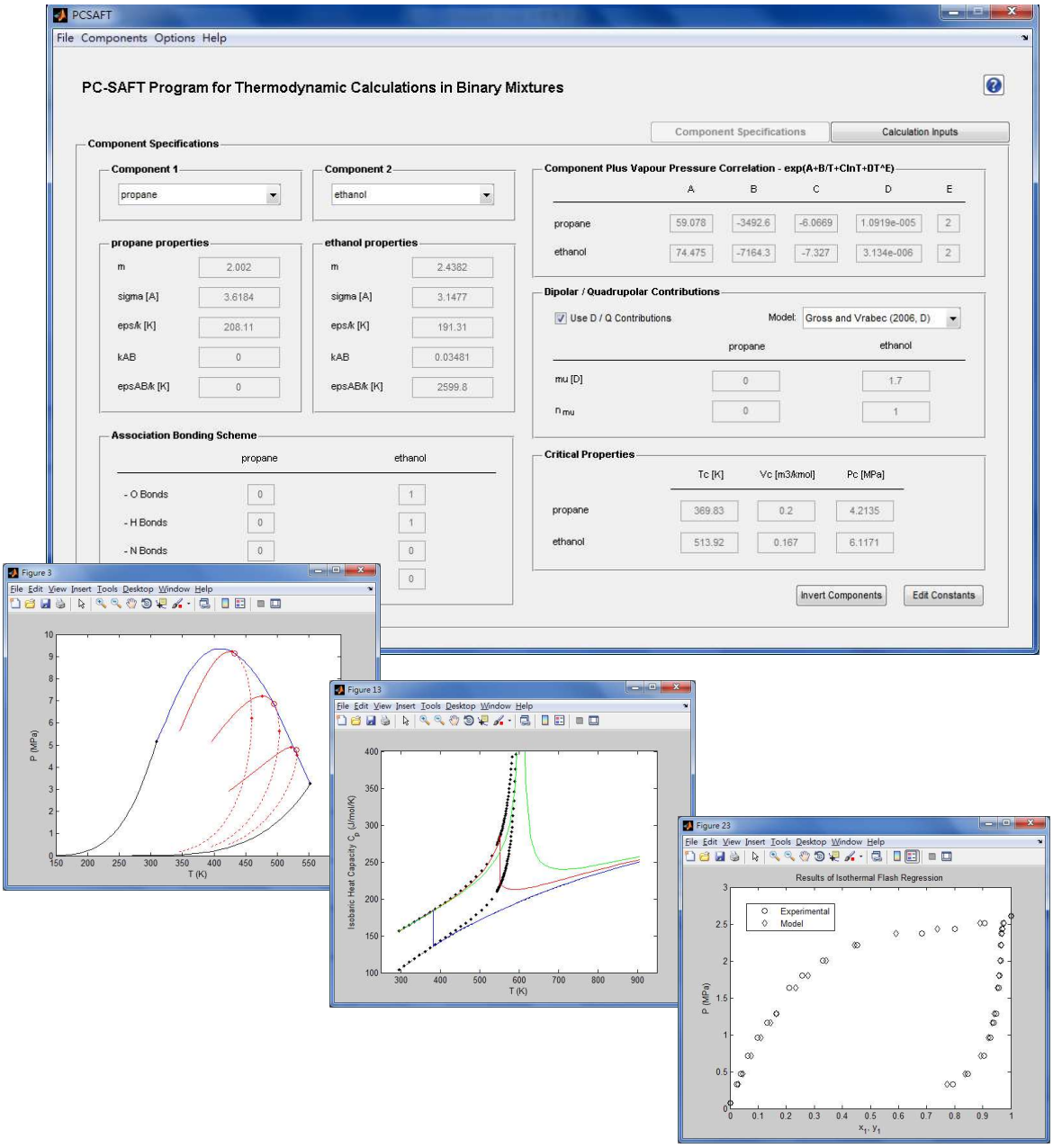
PCSAFT
File Components Options Help
PC-SAFT Program for Thermodynamic Calculations in Binary Mixtures
Component Specifications
Calculation Inputs
Component Specifications
Component 1
propane
Component 2
ethanol
Component Plus Vapour Pressure Correlation - exp(A+B/T+ClnT+DT^E)
A B C D E
propane 59.078 -3492.6 -6.0669 1.0919e-005 2
ethanol 74.475 -7164.3 -7.327 3.134e-006 2
propane properties
m 2.002
sigma [A] 3.6184
eps/k [K] 208.11
kAB 0
epsAB/k [K] 0
ethanol properties
m 2.4382
sigma [A] 3.1477
eps/k [K] 191.31
kAB 0.03481
epsAB/k [K] 2599.8
Dipolar / Quadrupolar Contributions
Use D / Q Contributions
Model: Gross and Vrabec (2006, D)
propane ethanol
mu [D] 0 1.7
n mu 0 1
Association Bonding Scheme
propane ethanol
- O Bonds 0 1
- H Bonds 0 1
- N Bonds 0 0
0 0
Critical Properties
Tc [K] Vc [m3/kmol] Pc [MPa]
propane 369.83 0.2 4.2135
ethanol 513.92 0.167 6.1171
Invert Components
Edit Constants
Figure 3
File Edit View Insert Tools Desktop Window Help
P (MPa)
T (K)
Figure 13
File Edit View Insert Tools Desktop Window Help
Isobaric Heat Capacity C_p (J/mol/K)
T (K)
Figure 23
File Edit View Insert Tools Desktop Window Help
Results of Isothermal Flash Regression
Experimental
Model
P (MPa)
x1, y1

Notes

Mesures Expérimentales “Thermodynamiques” de Composés Associatifs dans les Mélanges de Biocarburants et Modélisation avec l’Équation d’État PC-SAFT

Résumé : Le rôle croissant des biocarburants dans le marché de l’énergie a stimulé un regain d’intérêt dans l’étude des composés oxygénés. Les avancés dans le domaine des biocarburants proviennent de l’acquisition de données éxperimentales fiables, et du développement de modèles thermodynamiques qui rendent compte des phénomènes associatifs. Les mesures des constituants des biocarburants montrent souvent la coexistantes de phases multiples dont les interactions complexes ne se conforment que rarement aux méthodes conventionnels de modélisation.

L’objectif de ce travail est de résoudre cette équation soumis à deux aspects distincts par deux sections. La première section présente des dispositifs experimentaux permettant de mesurer de certaines propriétés thermo-physiques, incluant des équilibres liquide-vapeur à haute et basse pressions, des points critiques, et dans une moindre mesure des enthalpies d’excès. Les appareillages sont validés en fournissant des mesures représentative d’autres données de la littérature existantes. De nouvelles mesures ont été réalisées pour des mélanges associés aux biocarburants contienent des alcools et des acides. Une légère modification des procédures usuelles de mesure des points critiques laisse paraître des résultats prometteurs.

La deuxième section aborde de la modélisation de systèmes de biocarburants, comprenant entre autres les données mesurées dans la première section. Les mélanges contenant des groupements hydroxyles et/ou carbonyles comptent au moins un type d’interaction moléculaire mal représentés par les précédentes approches du *mean field*. Dans ce travail, nous utilisons les pleines capacités de l’équation d’état PC-SAFT basé sur des paramètres physique, et concevons au cas par cas des stratégies qui permettent de pallier aux problèmes dus aux nombreuses non-idéalités issues de ces systèmes. L’équation PC-SAFT couplée avec la théorie de groupe de renormalisation de White est appliquée pour modéliser la région critique. Cette forme améliorée à été testée avec des données experimentales critiques issues de ce travail, et emmène à des observations positives.

Mots clés : biocarburants, PC-SAFT, mesures expérimentales, points critiques, modélisation, théorie de groupe de renormalisation.

Experimental Thermodynamic Measurements of Biofuel-related Associating Compounds and Modeling using the PC-SAFT Equation of State

Abstract: The increasing role of biofuels in the energy market has stimulated a renewed interest in the study of oxygenated compounds. Biofuel research can be regarded as an interplay between the acquisition of reliable experimental data, and the application of associating thermodynamic models. Measurements of biofuel constituents often involve multiple coexisting phases, and complex interactions that rarely conform to conventional means of modeling.

The aim of the thesis is to address this seemingly two-part *conundrum* via two sections. The first section presents experimental apparatus for the measurement of selected thermo-physical properties, including high and low pressure vapour-liquid equilibria, critical points, and to a lesser extent excess enthalpies. The equipment are validated through good agreement with existing literature data. New measurements were performed for biofuel-related mixtures containing alcohols and acids. The measurement of critical points, in particular, introduces a slight modification to commonly documented procedures, with promising results.

The second section deals with the modeling of biofuel systems, including but not limited to the measured data of the first part. Mixtures containing hydroxyl and/or carbonyl groups exhibit at least one type of molecular interaction poorly modeled by previous mean field approaches. In this work we harvest the full capabilities of the physically-based PC-SAFT equation of state, devising in each case strategies for tackling different non-idealities present in the systems. The PC-SAFT coupled with White’s renormalization group theory is applied to modeling of the critical region. This improved form of the model was tested with experimental critical data performed in this work, with positive observations.

Keywords: biofuels, PC-SAFT, experimental measurements, critical points, modeling, renormalization group theory.

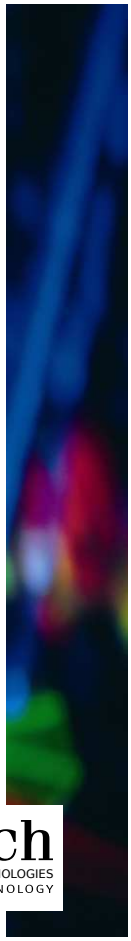

MINES ParisTech

ParisTech
INSTITUT DES SCIENCES ET TECHNOLOGIES
PARIS INSTITUTE OF TECHNOLOGY